Physics of the Solid State, Vol. 46, No. 2, 2004, pp. 193–212. Translated from Fizika Tverdogo Tela, Vol. 46, No. 2, 2004, pp. 193–211.
Original Russian Text Copyright © 2004 by Dunaevskiĭ.

REVIEWS

Magnetic Phase Diagrams of Manganites in the Electron Doping Region

S. M. Dunaevskiĭ

Konstantinov St. Petersburg Nuclear Physics Institute, Russian Academy of Sciences, Gatchina, Leningrad oblast, 188300 Russia

e-mail: dunaevsk@mail.pnpi.spb.ru

Received June 2, 2003

Abstract—The paper reviews the physical properties of the $R_{1-x}A_xMnO_3$ manganites (R = La, Pr, Nd, Sm, etc., A = Ca, Sr, Ba) in the region of their electron doping where the divalent atom concentration x in the compound lies in the interval $0.5 < x < 1.0$. Experimental magnetic phase diagrams of the most well-studied compounds and the results of theoretical calculations of these diagrams made in the tight-binding approximation within the degenerate double-exchange model for $T = 0$ are presented. The experimental section of the review deals primarily with neutron diffraction studies of the magnetic and crystal structures of the manganites, and the theoretical part, with the relation between their magnetic and orbital structures. The review describes, in considerable detail, the method of calculation of the energy spectrum $\varepsilon(\mathbf{k})$ and of the total carrier energy for all possible magnetic and orbital configurations of the system corresponding to the translation symmetry of the lattice. The theoretical analysis is carried out separately for two models of the crystal structure, with two and four manganese atoms in the unit cell. All equilibrium magnetic and orbital configurations of the four-sublattice manganite model were determined by minimizing the total energy of the system with respect to the directions of the local manganese magnetic moments and orbital states of the e_g electrons. It is shown that, by using the effective Hamiltonian of the degenerate double-exchange model for the e_g electrons, which takes into account the e_g level splitting, and the Heisenberg Hamiltonian of the localized t_{2g} electrons, one can describe the diversity of the magnetic phases, the sequence of their alternation with increasing x, and the correlation between the spin and orbital degrees of freedom, which are observed in most electron-doped manganites. © *2004 MAIK "Nauka/Interperiodica".*

CONTENTS

1. INTRODUCTION

Transition-metal oxides doped by divalent elements of the type $R_{1-x}A_xMnO_3$ (R = La, Pr, Nd, Sm, etc., A = Ca, Sr, Ba, Pb, etc.), the manganites, have recently been attracting intense interest from both experimentalists and theoreticians. As the concentration x of the divalent element A varies from zero to unity, the physical properties of the manganites change substantially and the system passes through a sequence of phase transitions featuring various types of structural, magnetic, charge, and orbital ordering. One can presently find a number of experimental [1–3] and theoretical [4–6] reviews summing up the main physical properties of the manganites and outlining the various approaches to their theoretical description. These reviews deal primarily with the properties of the manganites in the dopant concentration region $0 < x < 0.5$, where holes in the split manganese e_g band act as free carriers. In this region, the manganites demonstrate a unique property of negative colossal magnetoresistance (CMR), with the electrical resistivity of a sample to which an external magnetic

field is applied decreasing by a few times. The CMR effect is the largest at temperatures close to the transition point at which the system transfers from a paramagnetic insulator to a ferromagnetic metal. This anomalous behavior of the electrical resistivity of the manganites near the Curie temperature T_C was first discovered as far back as in 1950 [7]. At about the same time, neutron diffraction was employed to establish the crystal and magnetic structures of the $La_{1-x}Ca_xMnO_3$ system for the whole range of variation in the calcium divalent ion concentration (x = 0–1) [8]. In the 1990s, the CMR effect was applied in magnetoresistive magnetic reading heads employed in present-day computer technology, which initiated an explosive growth of studies of the physical properties of these and related compounds (cobaltites, nickelates, etc.) all over the world. The present considerable interest of experimenters and theorists in the manganites is also prompted by the fact that their electrical resistivity and the CMR effect are intimately connected with the specific types of magnetic, charge, and orbital ordering in a system.

The theoretical treatment of the magnetic and transport properties of doped manganites of the type $La_{1-x}Ca_xMnO_3$ (x = 0–1) is based actually on the double-exchange (DE) model [9, 10] of Zener–Anderson–Hasegawa. This DE model considers only the manganese sublattice of the real perovskite crystal structure, in which the hopping integral for the e_g electron connecting the nearest manganese ions depends on the mutual ordering of their local magnetic moments formed by three t_{2g} electrons. The conduction bandwidth, which is proportional to the hopping integral, turns out in the DE model to be maximal for the ferromagnetic (FM) ordering and vanishes under antiferromagnetic (AFM) ordering of the nearest spins. When the antiferromagnetic $LaMnO_3$ is doped by atoms of a divalent element (Ca, Sr, Ba, Pb, etc.), which substitute for the trivalent lanthanum, holes appear in the filled e_g band of manganese. Because their energy is minimal under FM ordering of the local spins, at a certain hole concentration the FM state becomes the ground state, with the insulating character of conduction in the paramagnetic phase switching to metallic near the Curie point with decreasing temperature. Thus, the DE model offers a qualitative interpretation of both the metal–insulator transition and the CMR effect in the vicinity of the Curie point in the manganites. Both effects are observed at hole concentrations $0.15 < x < 0.5$.

The original version of the DE model [10] assumed the e_g band to derive from one atomic e_g orbital of manganese. Treated within this nondegenerate DE model, the system should behave in the same way both at $x \sim 0$, where holes in the half-filled e_g band are free carriers, and at $x \sim 1$, where the e_g band contains a small number of conduction electrons.

The latter situation can be identified with the case of doping antiferromagnetic $CaMnO_3$ by atoms of lanthanum and other trivalent elements. Experiments have not, however, demonstrated such a symmetry of the phase diagrams with respect to the value x = 0.5 [11, 12]. A system is found to be ferromagnetic in the electron doping region very rarely, whereas in the "hole" region the ferromagnetic state occupies the larger part of the phase diagram.

In actual fact, the manganese e_g band is derived in the tight binding approximation not of one but rather of two degenerate atomic e_g manganese orbitals of the type $|z^2\rangle$ and $|x^2 - y^2\rangle$, with each of the latter being twofold spin degenerate. Because of the strong intraatomic (Hund) interaction between the e_g and t_{2g} electrons, the spin e_g subbands turn out to be split. This is why the e_g band in $LaMnO_3$ is filled to one quarter, while in $CaMnO_3$ there are no carriers in the band altogether. Obviously enough, the observed asymmetry in the properties of the manganites can be accounted for only in terms of the orbitally degenerate DE model, with simultaneous inclusion of the effects responsible for the splitting of the lower e_g manganese spin subband.

Strictly speaking, symmetry in the properties should be looked for not at the transition from $LaMnO_3$ to $CaMnO_3$ in the $La_{1-x}Ca_xMnO_3$ system but rather when the divalent dopant (Ca, etc.) in $LaMnO_3$ is replaced by a quadrivalent impurity (Ce, etc.) in the same concentration x. Because the e_g band in $LaMnO_3$ is filled to one-quarter and split, doping this compound with atoms of a quadrivalent element should produce free electrons in the upper empty band. It is this type of symmetry that is discussed in [13], where both $La_{0.7}Ca_{0.3}MnO_3$ and $La_{0.7}Ce_{0.3}MnO_3$ are reported to be metallic ferromagnets having the same Curie temperature T_C = 250 K. However, $La_{0.3}Ca_{0.7}MnO_3$, a compound that is "symmetric" from the standpoint of the number of free carriers in the lower split-off band, becomes an AFM insulator rather than an FM metal with decreasing temperature.

This review deals with the physical properties of the $R_{1-x}A_xMnO_3$ manganites (R = La, Pr, Nd, Sm, etc.; A = Ca, Sr, Ba) in the region of their electron doping, the condition where the concentration of divalent atoms in the compound exceeds x = 0.5. The review presents experimental magnetic phase diagrams of the most well-studied compounds and discusses the main models used in their theoretical description. The free carriers in the electron doping region are the d electrons, which fill the degenerate e_g manganite band with increasing concentration $y = 1 - x$ by not more than one-eighth. The small number of carriers in the conduction band permits one to disregard, in the first approximation, the inter- and intraatomic Coulomb repulsion, thus somewhat simplifying the Hamiltonian of the compounds under study.

2. CRYSTAL AND MAGNETIC STRUCTURES OF THE MANGANITES

The $R_{1-x}A_xMnO_3$ manganites doped to low x crystallize most frequently in the orthorhombic (phases O', O^*) and rhombohedral (phase R) structures [14]. A comprehensive crystallochemical analysis of these structures is reported in [15]. The latter review shows that the orthorhombicity of phase O^* is an order of magnitude smaller than that of phase O'. Therefore, phase O^* is quite frequently called pseudocubic in the literature. The formation of the structure of this phase primarily involves rotation of the oxygen octahedra (the tilting modes), while the fraction of the Jahn–Teller lattice distortions is extremely small. Both orthorhombic phases belong to the same nonsymmorphic space group *Pnma* (or *Pbnm*), and they differ only topologically in the way the ions touch. Figure 1 shows the manganese sublattice of the orthorhombic cell nested in the original cubic ABO_3 perovskite structure. The orthorhombic cell contains four translationally inequivalent manganese atoms. In the electron doping region, one meets also quite frequently, besides the orthorhombic *Pnma*, the monoclinic $P2_1/m$, tetragonal $I4/mcm$, and cubic $Pm3m$ crystal structures. In the limiting case of $x = 0$, $LaMnO_3$ and $RMnO_3$, where R stands for a rare earth element from Ce to Dy, crystallize under normal conditions of synthesis in the distorted orthorhombic perovskite structure [16]. $SrMnO_3$ and $RMnO_3$ single crystals with heavy rare earth elements from Ho to Lu crystallize under atmospheric pressure in the $P6_3cm$ hexagonal structure [17]. All these compounds can be transferred to the orthorhombic phase by annealing at $T =$ 900°C under high atmospheric pressure [18]. $CaMnO_3$ ($x = 1$) has a cubic ABO_3 perovskite structure.

The four manganese atoms, numbered accordingly in Fig. 1, are related through symmetry transformations of the *Pnma* space group. By virtue of the local magnetic moment of the manganese ions being an axial vector, this imposes certain constraints on the possible magnetic structures. The magnetic structures in a system of *Pnma* symmetry can be of the following main types:

(1) Ferromagnetic (FM) ordering of all local manganese magnetic moments along one of the axes x, y, or z (F_x, F_y, or F_z);

(2) AFM structure of type A, which represents antiferromagnetic alternation of (010)-type ferromagnetic planes;

(3) AFM structure of type C, which is made up of antiferromagnetically ordered, ferromagnetic spin chains oriented along one of the axes x, y, or z;

(4) AFM structure of type G with conventional antiferromagnetic ordering of the nearest neighbor magnetic moments.

In addition to these "pure" magnetic structures observed, as a rule, in an experiment, the orthorhombic structure allows the possibility of observing more complex magnetic structures (of the types C_xA_z, $G_zA_yF_x$, etc.) belonging to one of the irreducible representations of the Hamiltonian of the system. There are four such irreducible representations for the manganese magnetic moments in *Pnma* symmetry and eight for the magnetic moments of rare earth ions. The noncoplanar structure $G_zA_yF_x$ corresponds to ferromagnetic ordering of the S_x component of the manganese spin magnetic moment, type-A ordering for S_y, and type-G for S_z. The magnetic structures of rare earth ions allow only pair products, C_xA_y, etc. All possible types of magnetic ordering of both the manganese atoms and rare earth ions in the *Pnma* orthorhombic structure (*Pbnm* in the other reference frame) can be found in [19]. The magnetic structures corresponding to the monoclinic, tetrahedral, hexagonal, and cubic crystal symmetries are presented in [20].

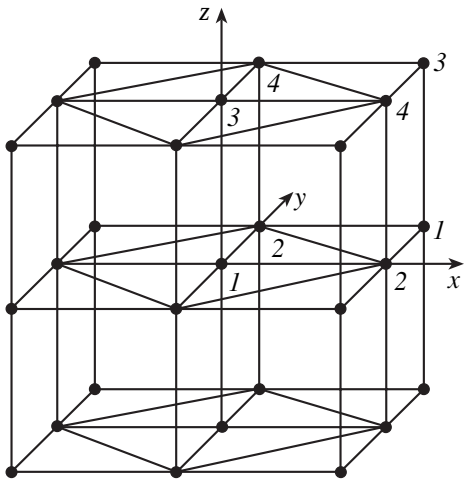

Fig. 1. Manganese sublattice of the orthorhombic unit cell nested in the original perovskite cubic structure. The figures label the four translationally inequivalent manganese atoms.

Besides the above-mentioned magnetic structures, manganites with x close to 0.5 exhibit, in some cases, an AFM charge-exchange (CE) structure with staggered charge ordering which consists of zigzag ferromagnetic chains of Mn^{3+} and Mn^{4+} ions arranged in the (110) plane of the orthorhombic perovskite structure. The magnetic moments of the nearest chains in the plane and the neighboring planes along the (001) direction are antiferromagnetically ordered, which doubles the corresponding lattice periods and gives rise to the appearance of new reflections in the x-ray and neutron diffraction spectra. A detailed description of the properties of manganites related to charge ordering would require a separate review.

Neutron diffraction is at present the main experimental technique employed to establish magnetic and crystal structures. Present-day neutron diffraction permits one not only to determine the crystal and magnetic structure of a manganite but to obtain complete information on bond lengths and distortions of the oxygen

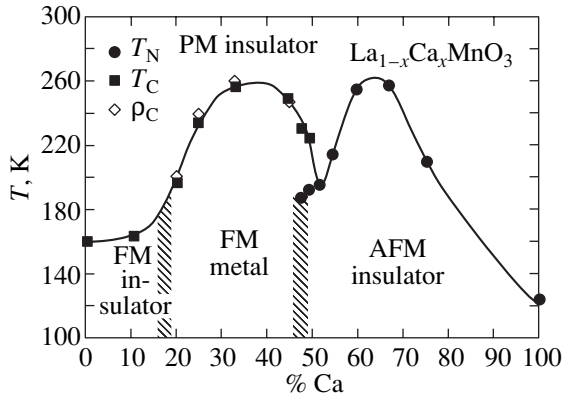

Fig. 2. Phase diagram of the $La_{1-x}Ca_xMnO_3$ ceramic [26] derived from measurements of the magnetization (T_C and T_N points) and of the electrical resistivity (ρ_C points).

octahedra surrounding the manganese ions. Two universally accepted programs for processing x-ray and neutron diffraction experimental data by the Rietveld refinement method, namely, FULLPROF [21] and RIETAN [22] are, as a rule, employed for this purpose. The character of distortions of the oxygen octahedra makes it possible to judge the type of orbital ordering in a manganite as well.

3. EXPERIMENTAL PHASE DIAGRAMS OF THE $R_{1-x}A_xMnO_3$ MANGANITES (R = La, Pr, Nd, Sm, etc.; A = Ca, Sr, Ba,…)

The properties of the $R_{1-x}A_xMnO_3$ compounds depend both on the type of the divalent ion A and on the type of the R trivalent ions. Replacement of the nonmagnetic lanthanum by trivalent magnetic ions of rare earth (RE) elements brings about a substantial change in the transport and magnetic properties of a manganite. In the region of hole doping, the magnetic ordering temperature and the magnitude of the CMR effect decrease noticeably, down to complete disappearance of the latter in $Gd_{0.7}Ca_{0.3}MnO_3$ [23]. At the same time, many new properties associated with the formation of one more RE magnetic sublattice are formed. Substitution of various divalent elements for trivalent elements also substantially affects the structural and transport properties of manganites. The observed structural changes correlate with the variation in the tolerance factor $t = (\langle r_A\rangle + r_O)/[\sqrt{2}\,(r_{Mn} + r_O)]$, where $\langle r_A\rangle$ is the average radius of the ions occupying the A position in the cubic structure of the ABO_3 perovskite. It was established in [24, 25] that the more the t parameter of a given compound differs from unity, the stronger the structural distortions observed in the system. As the t parameter decreases, the width of the conduction band usually decreases too, which, in the end, results in the metallic conduction switching to the insulating or hopping mechanism.

Thus, the available experimental phase diagrams of the manganites can be classified according to either lanthanide type or divalent atom type. The present review makes use of the traditional method of classifying experimental data by the type of the lanthanide in the manganite formula.

3.1. Phase Diagrams of the Lanthanum Manganites $La_{1-x}A_xMnO_3$ (A = Ca, Sr, Ba,…)

The first experiment that clearly revealed the "asymmetry" of the magnetic properties of $La_{1-x}Ca_xMnO_3$ (x = 0–1) was described in the above-mentioned classical study of Wollan and Koehler [8]. These authors observed an alternation of crystal and magnetic structures with increasing x in the following sequence: orthorhombic structure A (x = 0), orthorhombic or monoclinic ($x < 0.25$), cubic ferromagnetic ($0.25 < x < 0.5$), cubic CE (x = 0.5), cubic C (x = 0.8), and cubic G (x = 1). A more complete phase diagram of the same system with identification of the conduction types but without specification of the AFM structure types was published recently in [26]. This diagram (Fig. 2) draws from measurements of the magnetization and electrical resistivity of ceramic samples carried out over a broad range of magnetic fields and temperatures. The most important piece of information here is the absence, in the "electronic" part of the diagram ($x > 0.5$), of ferromagnetic regions with metallic conduction, which occupy a sizable area in the "hole" part of the phase diagram ($0.17 \le x \le 0.5$). In their place, a transition from the paramagnetic insulating phase to the AFM insulating state is observed to occur in the manganites for $x > 0.5$ with decreasing temperature. Further experimental studies of the manganites confirmed the "asymmetry" in the properties with respect to the value x = 0.5. These studies revealed that single crystals, polycrystals, and ceramics of the same composition may differ noticeably in their transport properties in the "electronic" part of the diagram ($x > 0.5$). At low temperatures, AFM states of a certain kind may feature metallic conduction in single crystals, whereas polycrystals and ceramics in analogous AFM states are insulators [27, 28]. In the electron-doping region, one may observe, at certain calcium concentrations (x = 2/3, 0.75, and other concentrations corresponding to stoichiometric compositions), crystalline and magnetic structures (Wigner crystal and bi-stripe structures), which are due, like the CE structure, to manganese charge ordering effects [29, 30]. These structures, which form below the Néel temperature T_N = 140 K in the magnetic phase of type C, are accompanied by a threefold increase in parameter a and a twofold increase in parameter c of the averaged orthorhombic lattice (in the *Pnma* notation) [29].

The crystal structure of $La_{1-x}Ca_xMnO_3$ was refined for a ceramic with x = 0.8 and 0.85 [31]. Neutron diffraction measurements showed that, below T_N = 150 K, the system undergoes a structural transition from the

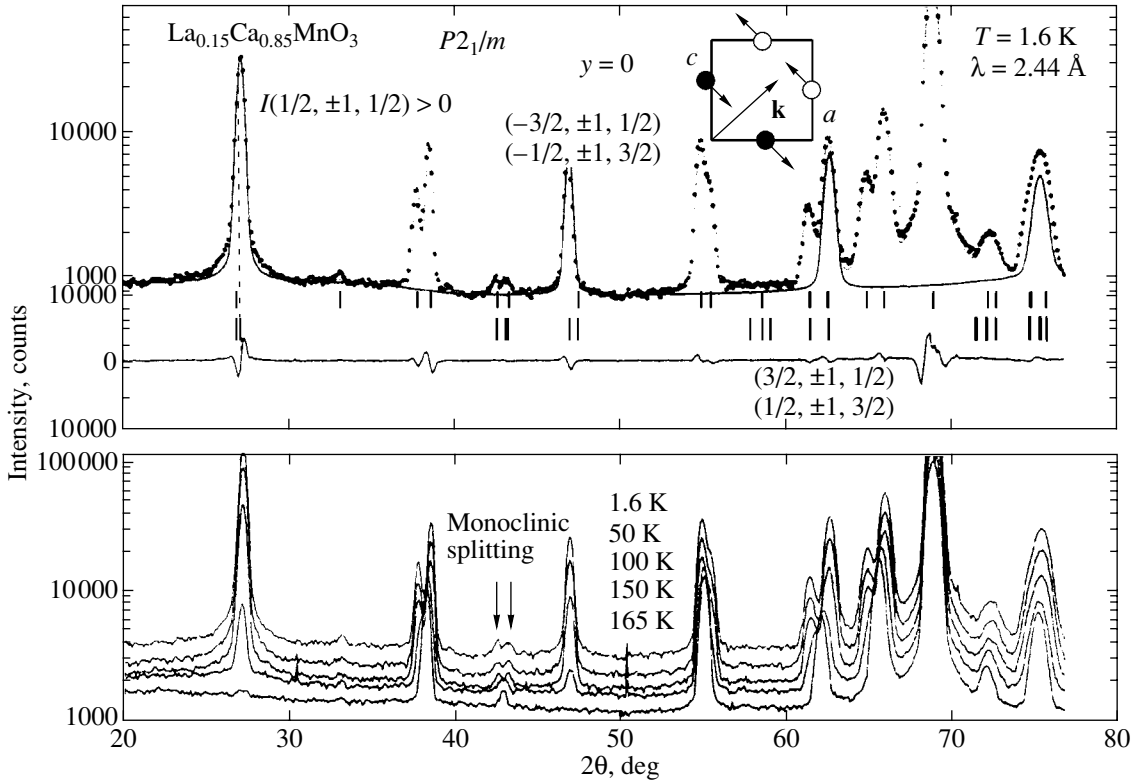

Fig. 3. Experimental (points) and theoretical (solid lines) neutron diffraction spectra obtained at 1.6 K and experimental spectra of the $La_{0.15}Ca_{0.85}MnO_3$ ceramic measured at 50, 100, 150, and 165 K [31]. The arrows identify the splitting of the (111) reflection caused by the triclinic lattice distortions.

orthorhombic *Pnma* to monoclinic $P2_1/m$ AFM phase of the *C* type (Fig. 3). In addition, it revealed the first experimental indication of the static Jahn–Teller (JT) effect. It was earlier believed [32] that the static JT effect is not observed in transition metal oxides with so large an x (i.e., for a small number of Mn^{3+} ions).

The phase diagram of the $La_{1-x}Sr_xMnO_3$ system [33] shown in Fig. 4 is the most complete of those available for the manganites; it agrees qualitatively with the preceding phase diagram. It is based on structural (x-ray), magnetic, and transport measurements performed on single crystals with strontium concentrations in the range $0 < x < 0.85$. The part of the diagram near $x = 1$ was constructed using data on the properties of the $SrMnO_3$ hexagonal compound. As the temperature is lowered, the system undergoes magnetic ordering, with the actual type of magnetic order depending on the specific dopant concentration x. In the interval $0.16 < x < 0.5$, the paramagnetic phase transfers to ferromagnetic metallic, which is qualitatively in line with the double-exchange theory. In the interval $0.5 < x < 0.6$, however, the ground state at low temperatures $T < 200$ K is not

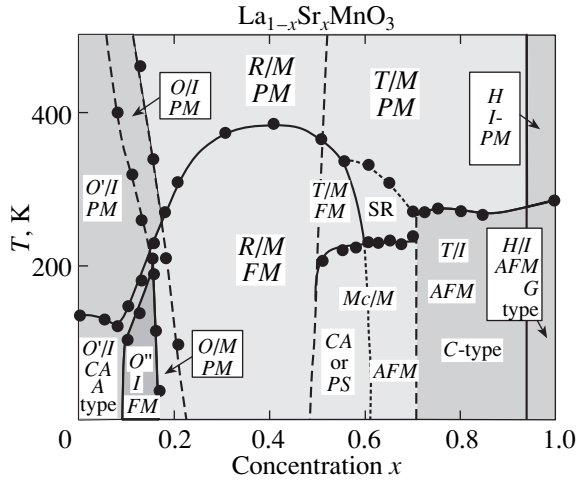

Fig. 4. Phase diagram of $La_{1-x}Sr_xMnO_3$ single crystals [33]. Crystal structures: *O*, *O*', and *O*" are orthorhombic; *T* is tetragonal, *Mc* is monoclinic, *H* is hexagonal, and *R* is rhombohedral. Magnetic structures: *PM* is paramagnetic, *FM* is ferromagnetic, *AFM* is antiferromagnetic, and *CA* is canted antiferromagnetic. Electronic states: *PS* is phase separated, *I* is insulating, and *M* is metallic.

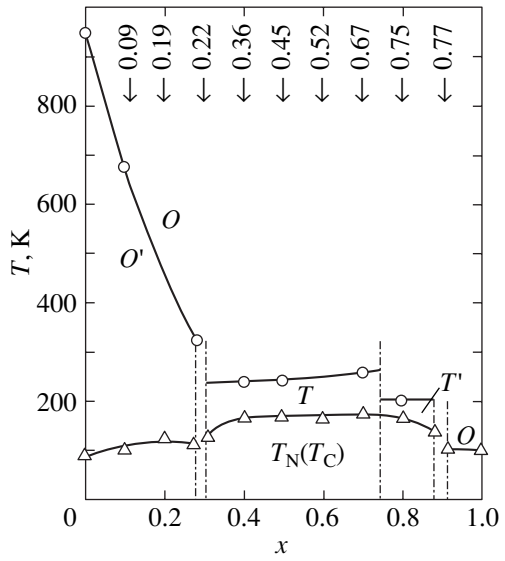

Fig. 5. Crystal and magnetic structures of the $Pr_{1-x}Ca_xMnO_3$ ceramic [35]. Circles identify structural transition temperatures, and triangles, Néel temperatures T_N. Crystal structures: *T* and *T*' are pseudotetragonal and *O* and *O*' are orthorhombic.

the ferromagnetic but either the canted (*CA*) metallic AFM or nonuniform *PS* (phase-separated) state. For $0.6 < x < 0.7$ and low temperatures $T < 200$ K, the ground state is the metallic collinear AFM phase (most probably, the *A* type). As *x* increases, this state is replaced by the *C*-type insulating AFM state, and for $x > 0.9$, by the *G* type phase. The AFM order was identified in [33] from neutron diffraction studies of the magnetic structure of manganites with similar compositions; these studies were carried out by other researchers. The existence of AFM order itself was deduced from measurements of the temperature and field dependences of the magnetization and magnetic susceptibility of the compounds in question. Thus, as the electron concentration $y = 1 - x$ in $La_{1-x}Sr_xMnO_3$ increases to $x = 0.5$, in the electron-doping region, the system undergoes the same sequence of antiferromagnetic ordering types, *G–C–A*, as $La_{1-x}Ca_xMnO_3$ but with higher Curie and Néel temperatures. As the system enters the "hole" doping region, the metallic AFM state is replaced by the metallic FM phase.

Since the $La_{1-x}Ba_xMnO_3$ system has been poorly studied, its phase diagram is still incomplete. However, a study [34] of the $La_{1/3}B_{2/3}MnO_3$ ceramic (*B* = Ca, Sr, Ba) should be mentioned in this connection. It reported a transition to the metallic state to occur only in the orthorhombic barium system at temperatures $T_P \sim 230$ K, whereas the calcium and strontium systems remain insulators in the electron-doped side at all temperatures. Interestingly, negative CMR appears in weak magnetic fields, 0.17 T, slightly above T_P and increases down to liquid-helium temperature. The magnetic structure of $La_{1/3}Ba_{2/3}MnO_3$ was neither determined nor discussed in [34].

3.2. Phase Diagrams of the Praseodymium Manganites $Pr_{1-x}A_xMnO_3$ *(A = Ca, Sr,…)*

Substitution of praseodymium for lanthanum brings about a very strong change in the manganite properties. The crystal and magnetic structures of the $Pr_{1-x}Ca_xMnO_3$ ceramic were studied with considerable detail for all *x* about 20 years ago [35] using neutron diffraction. The results of these measurements are presented in Fig. 5. At room temperature, all the compounds have the orthorhombic *Pbnm* symmetry. At low temperatures and for $0.3 < x < 0.75$, the crystal structure becomes pseudotetragonal, with the oxygen octahedra compressed along [001]. Within the interval $0.75 < x < 0.9$, the structure remains pseudotetragonal, but the oxygen octahedra are now stretched along [001], thus indicating a change in orbital order. Finally, for $x > 0.9$, the structure becomes pseudocubic.

The praseodymium manganite $PrMnO_3$, like the lanthanum manganite, is a type-*A* antiferromagnet with a Néel temperature $T_N = 91$ K. At $x = 0.5$ ($x = 0.6$), the *CE* phase forms below 175 K (165 K). At $x = 0.7$, and below $T_N = 180$ K, two phases, *C* and the ground magnetic spiral phase with an (010)-oriented wave vector, appear in the compound. At $x = 0.8$ and below $T_N = 170$ K, a *C* phase with magnetic moments of $2.56\mu_B$ aligned along the (001) pseudotetragonal axis appears. For $x = 0.8$ and below $T_N = 140$ K, a mixture of two phases, *C* and *G*, is observed to exist. Below $T_N = 110$ K, the $CaMnO_3$ compound represents a pseudocubic *G*-type antiferromagnet ($a = b = c/\sqrt{2}$). No magnetic *A* phase was found in this study in the region $0.5 < x < 0.7$. Thus, one observes here a *G–C–CE* sequence of AFM phases which differs from those found in the above systems.

Figure 6 presents a more complete phase diagram of $Pr_{1-x}Ca_xMnO_3$ showing the regions of existence of the CMR effect under electron and hole doping [36]. Note the existence in the system for $0.85 < x < 0.95$ of macroscopic F formations with a spontaneous magnetic moment of about one Bohr magneton per manganese atom. The ground state in this region is a nonuniform mixture of the *G* and *F* phases ($G_z + F_z$) called "cluster glass" by the authors. The measurements of the temperature dependences $\rho(T)$ suggest these ferromagnetic formations to have metallic conduction [37].

In its properties in the hole-doping region, the $Pr_{1-x}Sr_xMnO_3$ compound resembles $La_{1-x}Ca_xMnO_3$. The magnetic phase diagram of $Pr_{1-x}Sr_xMnO_3$ is shown in Fig. 7 without identification of the crystal structure [36]. In the electron-doping region, neutron diffraction studies of the crystal and magnetic structures of ceramic samples of this system were performed only for the range $x = 0.8$–0.95 [38, 39], where in the

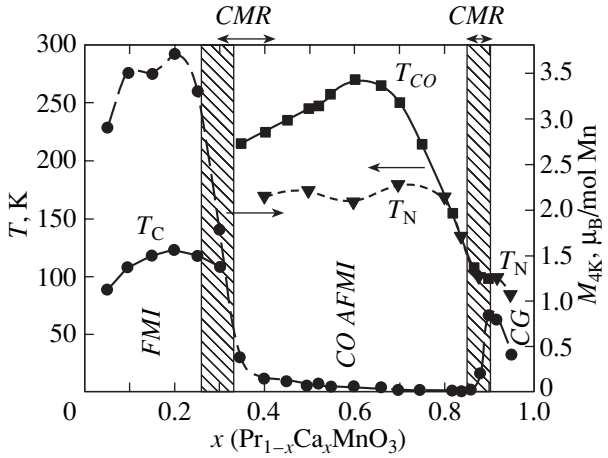

Fig. 6. Phase diagram of the $Pr_{1-x}Ca_xMnO_3$ ceramic [36] with identification of the regions within which the ferromagnetism and the CMR effect exist. *FMI* is ferromagnetic insulator, *AFMI* is antiferromagnetic insulator, T_CO is charge ordering (CO) temperature, T_C is Curie temperature, T_N is Néel temperature, and *CG* is cluster glass state.

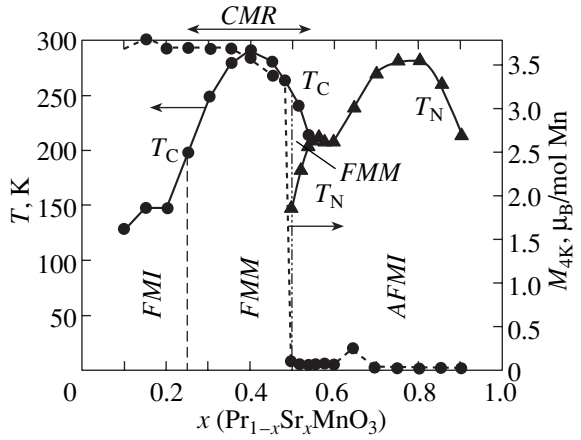

Fig. 7. Phase diagram of the $Pr_{1-x}Sr_xMnO_3$ ceramic [36]. Same notation as in Fig. 6.

low-temperature domain at $x = 0.8$ one observed a *C* phase, at $x = 0.9$—a *G* phase, and in the intermediate region of $x = 0.85$ coexisting *G* and *C* phases. Based on unpublished data, the authors of [36] suggest the *A* structure to be the ground state for the interval $0.5 < x < 0.6$. Thus $Pr_{1-x}Sr_xMnO_3$ again exhibits the *G–C–A* alternation of magnetic phases.

3.3. Phase Diagrams of the Neodymium Manganites $Nd_{1-x}A_xMnO_3$ (*A* = Ca, Sr,…)

The manganites of neodymium are much closer in their properties to those of lanthanum than of praseodymium throughout the whole range of variation of *x* for the main types of divalent ions. The observed differences among these compounds are of a quantitative rather than qualitative character. On the electron-doped side, the strontium system $Nd_{1-x}Sr_xMnO_3$ ($0.3 \le x \le 0.8$) is the most completely studied [40]. Figure 8 shows a detailed phase diagram of this polycrystalline system based on the results of neutron diffraction measurements. Close to the value $x = 0.5$, at low temperatures one observes an insulating AFM *CE* phase, which transforms with increasing *x* first to the metallic AFM *A* and, subsequently, to the insulating AFM *C*-type phase. The diffraction patterns are presented in Fig. 9 together with the results of the Rietveld refinement processing. In this figure, crosses show measurement data on the intensity of various reflections and the solid line plots the corresponding theoretical calculation for nuclear scattering. The antiferromagnetic Bragg reflections appearing at low temperatures are shown as hatched. The corresponding antiferromagnetic structures described above are also shown. In the limiting case of $x = 1$, where there are no free carriers in the e_g band, the manganites exhibit a *G*-type AFM structure. As already mentioned, neutron diffraction makes it possible to determine local distortions of the oxygen octahedra. In $Nd_{1-x}Sr_xMnO_3$, these octahedra were found to be stretched along the *z* axis for $x > 0.6$. This distortion implies that the filled *d* orbital of the Mn^{3+} ion has the $|z^2\rangle$ character. In the *A* structure, the oxygen octahedra are contracted along *z*, with the result that the filled orbital is of the $|x^2 - y^2\rangle$ character. Figure 10 displays a schematic of the main types of oxygen octahedron distortions. Thus, this system likewise exhibits the

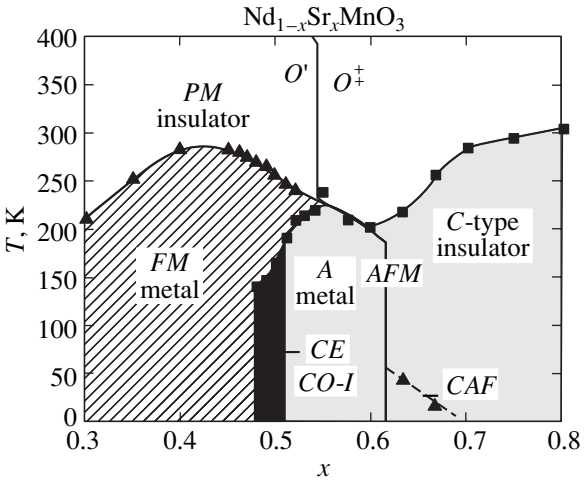

Fig. 8. Phase diagram of $Nd_{1-x}Sr_xMnO_3$ polycrystals [40] derived from neutron diffraction studies of the crystal and magnetic structures. Crystal structures: *O*' is *Ibmm* orthorhombic structure, O^+_+ is *I*4/*mcm* tetragonal phase, *CE* is structure associated with charge ordering (CO), and *CAF* is canted AFM structure.

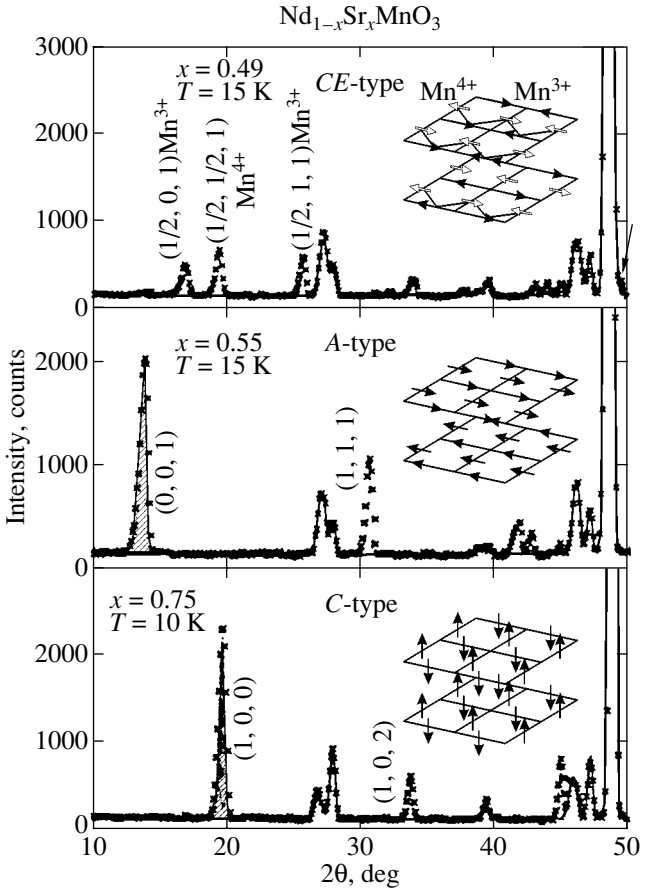

Fig. 9. Neutron diffraction patterns of $Nd_{1-x}Sr_xMnO_3$ [40]. Crosses are experimental data, solid lines plot Rietveld-refined theoretical calculations of nuclear scattering intensities. The AFM Bragg reflections appearing in the low-temperature domain are hatched. The insets show spin configurations of the corresponding AFM structures (*CE*, *A*, and *C*).

G–C–A magnetic structure sequence with increasing number of carriers $y = 1 - x$.

Calcium-doped neodymium manganites $Nd_{1-x}Ca_xMnO_3$ have practically not been studied for $x > 0.5$. One should mention here, however, in this connection a neutron diffraction study of ceramics with $x = 0.4$–0.6 [41]. In this composition region, one first observes at $T_{CO} \approx 250$ K a transition from the paramagnetic phase to a charge-ordered (paramagnetic) phase, which is followed by a transformation at $T_N \approx 160$ K to the AFM *CE* phase. At $x = 0.6$, this latter transition to the AFM state may not occur altogether.

3.4. Phase Diagrams of the Samarium Manganites $Sm_{1-x}A_xMnO_3$ *(A = Ca, Sr,…)*

Although the magnetic and transport properties of the samarium manganites $Sm_{1-x}A_xMnO_3$ were studied fairly long ago [42, 43], the first neutron diffraction measurements of the crystal and magnetic structures of these compounds were carried out only a few years ago. This is accounted for by the impossibility of making these measurements on samples based on natural samarium because of its very high neutron absorption cross section. Therefore, the first precision studies of the crystal and magnetic structures were performed only after ceramic samples with the ^{154}Sm isotope had been prepared [44, 45].

The magnetic phase diagram of $Sm_{1-x}Ca_xMnO_3$ was first derived [36] from measurements of the magnetic and transport properties of this system. The first neutron diffraction studies of the structure of this compound (using the ^{152}Sm isotope) have thus far been made only for the $Sm_{0.1}Ca_{0.9}MnO_3$ and $Sm_{0.15}Ca_{0.85}MnO_3$ compositions [38, 39]. The phase diagram of $Sm_{1-x}Ca_xMnO_3$ presented in Fig. 11 resembles, in general, that of the $Pr_{1-x}Ca_xMnO_3$ system with the *G–C–CO* alternation sequence. The particular type of the charge-ordered (*CO*) AFM structure was not specified. The unusual properties of the calcium-doped samarium system indicating phase separation at $x = 0.8$–0.95 were subsequently confirmed in the case of $Sm_{0.15}Ca_{0.85}MnO_3$ [46], a compound that also exhibits CMR. The above paper is interesting also in that it reports the observation of a *G*-type ground-state antiferromagnetic phase. Such a magnetic structure may be treated either as a manifestation of phase separation taking place in the $G_z + F_z$ system or as the onset of a $C_xF_yA_z$-type noncoplanar magnetic ordering, which was first observed to occur in $Ho_{0.1}Ca_{0.9}MnO_3$ [47].

Figure 12 shows the phase diagram of $Sm_{1-x}Sr_xMnO_3$ [36], which differs radically for $x > 0.5$ from that of the $Sm_{1-x}Ca_xMnO_3$ compound. First, we witness here the disappearance of the cluster glass region and second, for $x > 0.6$, the ground state is the AFM insulator. *CO* structures can exist only in the $x = 0.4$–0.6 range, which is evident from electron diffraction data. Therefore, one cannot rule out the possibility that the universal magnetic structure alternation *G–C–A* also takes place here. The CMR effect is observed in $Sm_{1-x}Sr_xMnO_3$ only in the region of hole doping, $0.3 < x < 0.5$.

3.5. Phase Diagrams of the Gadolinium and Holmium Manganites

The manganites of other RE elements have been studied to a considerably lesser extent. Nevertheless, it is appropriate to draw particular attention to the two already mentioned papers dealing with the manganites of gadolinium [23] and holmium [47].

The first of these papers revealed the absence of both the metal–insulator transition and of the CMR in the $Gd_{0.67}Ca_{0.33}MnO_3$ ceramics, poly-, and single crystals, with the samples becoming ferrimagnetic below $50 < T_N < 80$ K. In addition, synchrotron XAFS studies (x-ray absorption fine structure) did not reveal any

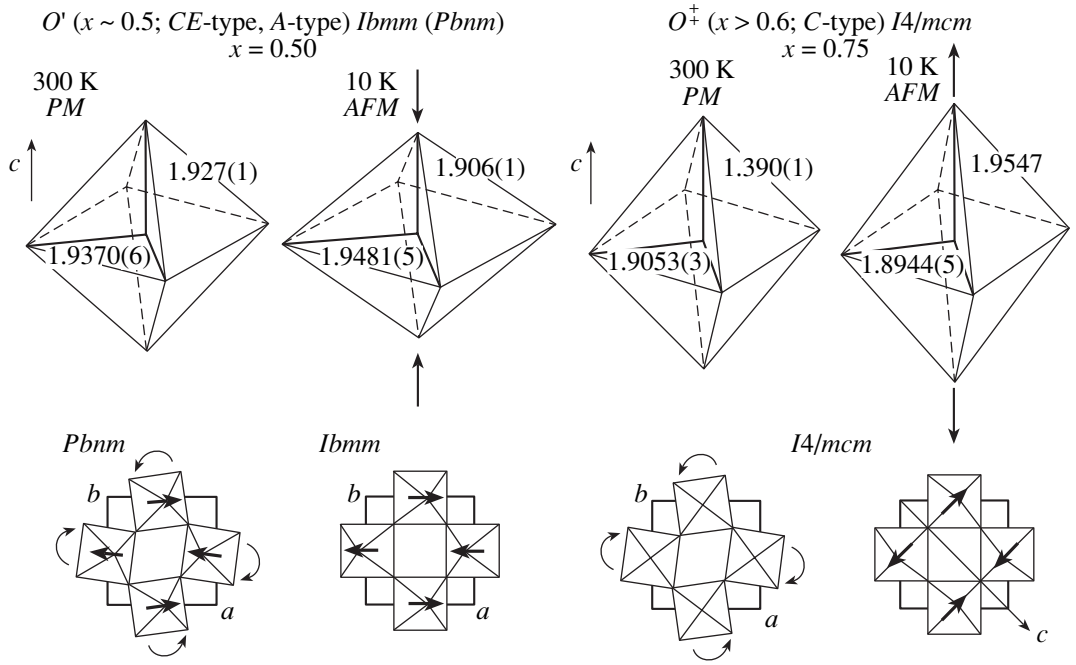

Fig. 10. Main types of distortions of the oxygen octahedra in $Nd_{1-x}Sr_xMnO_3$ polycrystals [40] for $x = 0.5$ and 0.75 and for $T = 330$ and 10 K, which make it possible to judge the type of orbital ordering corresponding to a specific type of AFM order.

changes in the orthorhombic structure in the vicinity of the magnetic transition to within 0.005 Å. The existence, in the low-temperature domain, of the ferromagnetic insulator state for such high hole doping levels is difficult to explain on the basis of modern theory.

Neutron diffraction studies of the holmium manganite $Ho_{0.1}Ca_{0.9}MnO_3$ are of interest, first, because they revealed noncoplanar $C_xF_yA_z$ canted antiferromagnetic order in the manganites, which is allowed by the *Pnma* space group (Fig. 13), and, second, the static JT effect was observed in the magnetically ordered phase in a region of fairly low electron doping. Near $T_N = 106$ K, the temperature dependence of electrical resistivity exhibits an anomaly (a section with metallic conduction) typical of CMR compounds. As the holmium concentration increases still further, the AFM structure canting decreases and disappears altogether at a concentration of ≈17.5% Ho. At the same time, the orthorhombic *Pnma* crystal structure switches to the monoclinic $P2_1/m$ structure.

Thus, as follows from the above experimentally obtained phase diagrams, at low enough temperatures, most of the manganites with various combinations of di- and trivalent elements pass with increasing electron

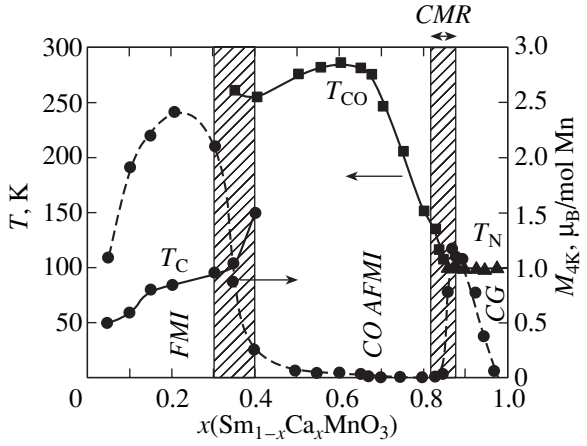

Fig. 11. Phase diagram of the $Sm_{1-x}Ca_xMnO_3$ ceramic [36]. Same notation as in Fig. 6.

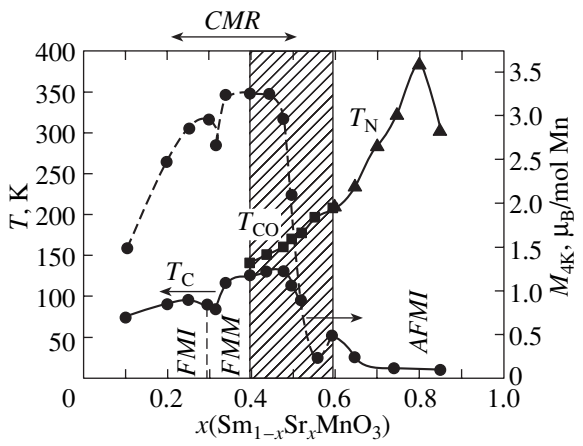

Fig. 12. Phase diagram of the $Sm_{1-x}Sr_xMnO_3$ ceramic [36]. Same notation as in Fig. 6.

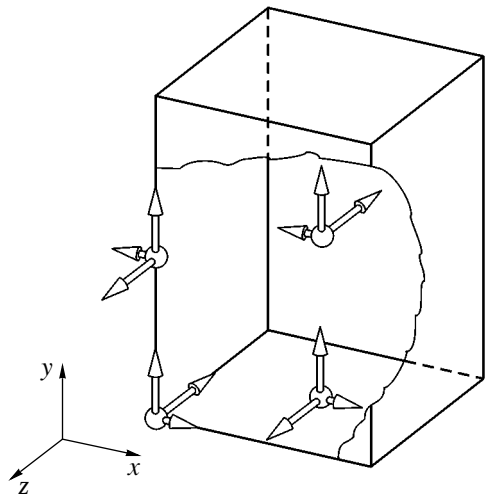

Fig. 13. Noncoplanar antiferromagnetic structure $C_xF_yA_z$ of the holmium manganite $Ho_{0.1}Ca_{0.9}MnO_3$ [47]. Only the manganese atoms are shown.

concentration in the conduction band $y = 1 - x$ from 0 to 0.5 through the same antiferromagnetic phase sequence *G–C–A*. As a rule, the ferromagnetic phase does not form here, but if it does, it happens within a narrow concentration range only and at fairly high temperatures. This pattern differs radically from the case of hole doping, where the metallic ferromagnetic phase remains the ground state for $x \geq 0.17$ up to $x \approx 0.5$. Close to $x \approx 0.5$, some compounds exhibit an antiferromagnetic insulating *CE* phase. Interestingly, the antiferromagnetic phases *G* and *A* in single crystals have metallic conduction, whereas the *C* phase is an insulator. The insulating properties of the *C* phase are usually assigned to its quasi-one-dimensional magnetic structure being destroyed by impurities. In these conditions, double exchange forbids electron hopping between neighboring chains of AFM-ordered ions, while coherent carrier motion within an FM chain is destroyed by the presence of impurities (Ca, Sr, etc.).

4. THEORETICAL MODEL OF THE MANGANITES

4.1. Effective Hamiltonian of the Degenerate DE Model

The formation of a specific state in a system is governed by its total energy, which is a sum of the kinetic (band) energy of carriers and the magnetic energy of localized spins. Considered within the DE model, the carrier kinetic energy depends on the actual type of magnetic ordering of the system. Therefore, in order to determine the ground-state energy and to construct a phase diagram, one has to know how to calculate the carrier spectrum $\varepsilon(\mathbf{k})$ for all possible magnetic configurations of the system allowed by the translational symmetry of the lattice.

The first step in determining the total energy is proper choice of the Hamiltonian of the system under study and specifying its crystal structure. As an effective Hamiltonian describing the properties of the manganites on the electron-doped side, one customarily uses the model Hamiltonian of the generate DE model [48–50], which in the local atomic basis can be written as

$$H = H_{DE} + H_H,$$

$$H_{DE} = \sum_{i\alpha\sigma} \varepsilon_{i\alpha} d^\dagger_{i\alpha\sigma} d_{i\alpha\sigma} - J_H S \sum_{i\alpha\sigma} \sigma d^\dagger_{i\alpha\sigma} d_{i\alpha\sigma}$$

$$+ \sum_{ij\alpha\beta\sigma'\sigma} t^{\sigma\sigma'}_{ij\alpha\beta} d^\dagger_{i\alpha\sigma} d_{j\beta\sigma'},$$

$$H_H = \sum J_{AF} \mathbf{S}_i \mathbf{S}_j,$$

$$t^{\sigma\sigma'}_{ij\alpha\beta} = \begin{cases} t_{ij\alpha\beta} \cos(\theta_{ij}/2) (\sigma = \sigma') \\ \pm t_{ij\alpha\beta} \sin(\theta_{ij}/2) (\sigma \neq \sigma'). \end{cases} \quad (1)$$

This Hamiltonian considers only the manganese sublattice of the real manganite crystal structure. It consists of the double-exchange Hamiltonian H_{DE} for the degenerate e_g manganese level and a finite value of the intraatomic (Hund) parameter J_H and of the Heisenberg Hamiltonian of the t_{2g} localized electrons. A detailed derivation of this model Hamiltonian for the case of an infinitely large J_H can be found in [5].

Hamiltonian (1) includes only the strong intraatomic Coulomb interaction between the e_g and t_{2g} electrons, which obeys Hund's rule. All the other interelectron Coulomb interactions are disregarded, which in a first approximation appears justified for a small number of e_g electrons in the conduction band.

The indices α and β in Eq. (1) label the degenerate e_g atomic orbitals $|1\rangle = |z^2\rangle$ and $|2\rangle = |x^2 - y^2\rangle$, and the indices *i* and *j*, the atoms. The operators $d^\dagger_{i\alpha\sigma}$ and $d_{j\beta\sigma'}$ are the operators of creation and annihilation of electrons at site *i* with the spin aligned either along or opposite to that of the localized t_{2g} electrons $\mathbf{S}_i$ ($\sigma = \uparrow, \downarrow$).

Turning back to Eq. (1), $\varepsilon_{i\alpha}$ is the energy of the type-α atomic orbital; J_H is the intraatomic Hund integral, which for the e_g electrons in Mn^{3+} is ~0.25–0.3 eV [49]; J_{AF} is the exchange integral of the Heisenberg model for the localized t_{2g} electrons (for $CaMnO_3$, $T_N = 141$ K, $J_{AF} = 1.5$ meV); and $t_{ij\alpha\beta}$ are the effective hopping integrals between local components of the spinor states of the nearest manganese ions. The e_g electrons in the double-exchange model hop without spin-flip, and therefore the hopping integral $t_{ij\alpha\beta}$ depends on the mutual orientation (the θ_{ij} angle) of the neighboring $\mathbf{S}_i$ and $\mathbf{S}_j$ spins and its value for the manganites lies within the interval 0.10–0.3 eV [51]. The part played by oxygen ions, which in the perovskite structure are located

between the manganese ions, reduces to the effective hopping integral $t_{ij\alpha\beta}$ being expressed through the hopping integral between the e_g manganese orbital and the p orbital of the nearest oxygen ion (the Koster–Slater parameter $V_{pd\sigma}$) in the second order of perturbation theory. Since the hopping integral $t_{ij\alpha\beta}$ is anisotropic in real space, it is usually written in the form of a matrix with indices α and β assigned to the x, y, and z directions:

$$t_{ij\alpha\beta} \equiv t_{ij}^{\alpha\beta} = -t\begin{pmatrix} \frac{1}{4} & \frac{-\sqrt{3}}{4} \\ \frac{-\sqrt{3}}{4} & \frac{3}{4} \end{pmatrix} \quad \text{along} \quad x,$$

$$-t\begin{pmatrix} \frac{1}{4} & \frac{\sqrt{3}}{4} \\ \frac{\sqrt{3}}{4} & \frac{3}{4} \end{pmatrix} \quad \text{along} \quad y, \quad -t\begin{pmatrix} 1 & 0 \\ 0 & 0 \end{pmatrix} \quad \text{along} \quad z,$$

$$t = \frac{V_{pd\sigma}^2}{\varepsilon_\alpha - \varepsilon_p}. \tag{2}$$

As follows from the form of Hamiltonian (1), in a system having free carriers there is always competition between the ferromagnetic and antiferromagnetic types of ordering. The ferromagnetism is associated with the double-exchange kinetic energy, whereas antiferromagnetic ordering is related to the Heisenberg part of the Hamiltonian. In the simplest case (neglecting orbital degeneracy), there exist at least two possibilities for reaching a balance between these tendencies. The first of them is the uniform canted state of the de Gennes antiferromagnetism [52], where the θ_{ij} angle between the spins of the nearest manganese ions is other than π. The second possibility involves the onset of electron phase separation, where the carriers (holes or electrons) become nonuniformly distributed in space to form FM-enriched regions against an AFM background [53].

The Hamiltonian H_{DE} allows diagonalization in the tight-binding approximation, thus permitting one to obtain the carrier spectrum $\varepsilon(\mathbf{k})$. Obviously enough, this spectrum depends on what magnetic structure is being considered. In the simplest case of an F manganite structure (with one atom in a cubic unit cell), the problem of determining $\varepsilon(\mathbf{k})$ in the limit of an infinitely large intraatomic Hund interaction $J_H \longrightarrow \infty$ reduces to the solution of a second-order secular equation,

$$\det[H_{\alpha\beta}(\mathbf{k}) - \varepsilon\delta_{\alpha\beta}] = 0. \tag{3}$$

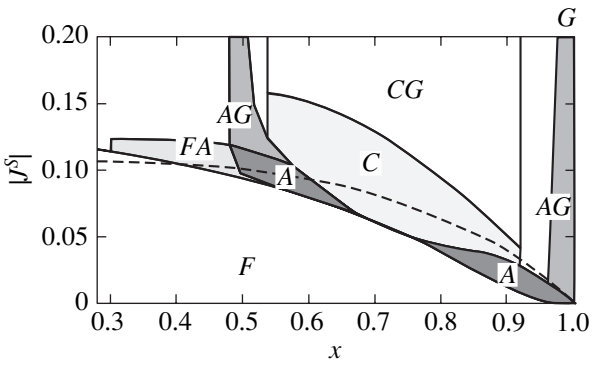

Fig. 14. Phase diagram of manganites with allowed magnetic configurations of the type (θ_{xy}, θ_z) [55]. J^S is interatomic exchange integral (J_{AF}, in units of t), and $x = 1 - y$ is the hole concentration. The phases F, C, and A (black area) are collinear. Phases FA (0, θ_z), $AG(\theta_{xy}, \pi)$, and $CG(\pi, \theta_z)$ are canted with $\theta_{xy} \neq \pi$ and $\theta_z \neq \pi$.

Analytic expressions were obtained [54] for two branches of the spectrum (for the spin-up electrons):

$$\varepsilon_\pm(\mathbf{k}) = \varepsilon_0(\mathbf{k}) \pm \sqrt{\varepsilon_1^2(\mathbf{k}) + \varepsilon_2^2(\mathbf{k})},$$
$$\varepsilon_0(\mathbf{k}) = -t(\cos k_x + \cos k_y + \cos k_z),$$
$$\varepsilon_1(\mathbf{k}) = \frac{1}{2}t(\cos k_x + \cos k_y - 2\cos k_z), \tag{4}$$
$$\varepsilon_2(\mathbf{k}) = -\frac{\sqrt{3}}{2}t(\cos k_x - \cos k_y).$$

The lattice constants a, b, and c entering Eq. (4) were assumed to equal unity. For finite J_H, the dimension of the secular equation doubles. The parameter J_H was derived in [49] from the relation $J_H(2S + 1) = E_{\text{tot}}[Mn^{3+}(S = 2)] - E_{\text{tot}}[Mn^{3+}(S = 1)]$, where E_{tot} is the total energy of the Mn^{3+} ion in the corresponding spin state, using Hartree–Fock calculation of the Mn^{3+} electronic structure with the well-known codes RAINE. For $S = 3/2$, this parameter was found to be ≈0.97 eV and the parameter $J_H \approx 0.25$ eV.

Besides the ferromagnetic (F) phase, the manganites exhibit a variety of the above-mentioned AFM structures, whose unit cell contains at least two inequivalent atoms. These are the collinear structures A, which are observed in $LaMnO_3$ ($\theta_{ij} = \theta_z = \pi$), G of $CaMnO_3$ ($\theta_{ij} = \pi$), and C ($\theta_{ij} = \theta_{xy} = \pi$), as well as the canted magnetic structures allowed by the crystal lattice symmetry, for which $\theta_{ij} \neq \pi$.

The manganite phase diagram involving Hamiltonian (1) was first theoretically calculated in [48] using a modified dispersion law (4). The modification consisted in introducing into the expressions for $\varepsilon(\mathbf{k})$ two hopping integrals $t_{xy} = t\cos(\theta_{xy}/2)$ and $t_z = t\cos(\theta_z/2)$, which depended on the angles between the neighboring spins of the manganese ions located either in the same (θ_{xy}) or neighboring (θ_z) planes.

The phase diagram constructed by minimizing the energy in the two angles θ_{xy} and θ_z [48] disagreed in some respects with experiment. First, the diagram did not have the *G* phase, and second, the larger part of the diagram (for $y \geq 0.2$) was occupied by the *F* phase, which is not observed experimentally. Nevertheless, this paper stirred considerable interest among scientists and initiated a large number of theoretical studies of the phase diagrams of electron-doped manganites.

The most comprehensive and rigorous investigation of the phase diagram of manganites performed within the framework of the model with two angles, θ_{xy} and θ_z, was reported in [55]. The carrier spectrum $\varepsilon(\mathbf{k})$ was calculated in terms of the band formalism of the spin density functional in the limit $J_H \longrightarrow \infty$, and the variation in the total energy under variation of the angles was found using the Lloyd relation from the theory of multiple scattering. The resulting phase diagram is displayed in Fig. 14. The diagram is constructed in the J^s vs. *x* coordinates, where J^s is the Heisenberg exchange integral (J_{AF} in units of *t*) and $x = 1 - y$ is the hole concentration. The phases *F*, *C*, and *A* (the black region) are collinear. The other phases, $FA(0, \theta_z)$, $AG(\theta_{xy}, \pi)$, and $CG(\pi, \theta_z)$, are canted; i.e., the angles θ_{xy} and θ_z are not equal to π. The dashed line plots the renormalized interatomic exchange interaction. The remaining regions relate to canted structures of the most general type. The orbital structure of the manganites was considered fixed under variation of the magnetic structure [55]. On the electron-doped side, near the value $J^s = 0.1$, which appears to be overestimated, the magnetic phases alternate in the sequence *G–C–A*.

4.2. Phase Diagrams of the Two-Sublattice Model of Manganites in the Tight-Binding Approximation

The dimension of the matrix of the Hamiltonian used in the tight-binding approximation to calculate the spectrum for a finite value of J_H is twice the product of the number of atoms in the unit cell multiplied by the number of independent atomic functions. Therefore, the minimum dimension of the Hamiltonian matrix employed in calculations of the spectrum of collinear *A*, *C*, and *G* structures with two translationally inequivalent manganese atoms in the tetragonal (orthorhombic) cell is eight. Within this two-sublattice manganite model, the matrix of the Hamiltonian of canted antiferromagnetic structures can be presented in the form

$$H(\mathbf{k}) = \begin{pmatrix} H_{11}(\mathbf{k}) & H_{12}(\mathbf{k}) \\ \tilde{H}^*_{12}(\mathbf{k}) & H_{22}(\mathbf{k}) \end{pmatrix}, \quad (5)$$

where the matrices H_{11} and H_{22} describe the interaction of like orbitals with $\sigma = \uparrow, \downarrow$ and matrix H_{12}, that between unlike orbitals. A similar representation was used to calculate the carrier spectrum in layered (two-dimensional) manganites in [50], where the matrices H_{11} and H_{22} described, however, interaction between orbitals within a sublattice and H_{12}, that between orbitals of neighboring atoms located on different sublattices.

The matrices $H_{\alpha\beta}$ are given for various magnetic structures in [49]. For instance, the matrix $H_{\alpha\alpha}$ for the *G* type can be written as

$$H_{\alpha\alpha}(\mathbf{k}) = \begin{pmatrix} \varepsilon_\alpha - J_H S & 0 & t_{\alpha\alpha}(\mathbf{k})\cos\frac{\theta}{2} & t_{\alpha\alpha}(\mathbf{k})\sin\frac{\theta}{2} \\ 0 & \varepsilon_\alpha + J_H(S+1) & -t_{\alpha\alpha}(\mathbf{k})\sin\frac{\theta}{2} & t_{\alpha\alpha}(\mathbf{k})\cos\frac{\theta}{2} \\ t_{\alpha\alpha}(\mathbf{k})\cos\frac{\theta}{2} & -t_{\alpha\alpha}(\mathbf{k})\sin\frac{\theta}{2} & \varepsilon_\alpha - J_H S & 0 \\ t_{\alpha\alpha}(\mathbf{k})\sin\frac{\theta}{2} & t_{\alpha\alpha}(\mathbf{k})\cos\frac{\theta}{2} & 0 & \varepsilon_\alpha + J_H(S+1) \end{pmatrix}, \quad (6)$$

where

$$t_{11}(\mathbf{k}) = -\frac{1}{2}t(\cos k_x + \cos k_y) - 2t\cos k_z,$$

$$t_{22}(\mathbf{k}) = -\frac{3}{2}t(\cos k_x + \cos k_y), \quad t = \frac{V^2_{pd\sigma}}{\varepsilon_\alpha - \varepsilon_p}.$$

Here, ε_α are the energies of the manganese e_g levels, ε_p is the energy of the oxygen *p* level, and *t* is the effective hopping integral between e_g orbitals of the nearest manganese ions written in second order of perturbation theory for the Koster–Slater integral $V_{pd\sigma}$ between the e_g orbital of the manganese and the *p* orbital of the nearest oxygen ion. The parameter *t* for the manganites is positive, because, in accordance with numerical cluster calculations [56], the ε_p level lies lower than the ε_α levels. Because transitions along the *z* axis can occur only between $|z^2\rangle$ type orbitals, the matrix $H_{12}(\mathbf{k})$ depends only on the perpendicular component of the wave vector $\mathbf{k}_\perp$ and can be written as

$$H_{12}(\mathbf{k}_\perp) = \begin{pmatrix} 0 & 0 & t_{12}(\mathbf{k}_\perp)\cos\frac{\theta}{2} & t_{12}(\mathbf{k}_\perp)\sin\frac{\theta}{2} \\ 0 & 0 & -t_{12}(\mathbf{k}_\perp)\sin\frac{\theta}{2} & t_{12}(\mathbf{k}_\perp)\cos\frac{\theta}{2} \\ t_{12}(\mathbf{k}_\perp)\cos\frac{\theta}{2} & -t_{12}(\mathbf{k}_\perp)\sin\frac{\theta}{2} & 0 & 0 \\ t_{12}(\mathbf{k}_\perp)\sin\frac{\theta}{2} & t_{12}(\mathbf{k}_\perp)\sin\frac{\theta}{2} & 0 & 0 \end{pmatrix}, \quad (7)$$

$$t_{12}(\mathbf{k}_\perp) = \frac{\sqrt{3}}{2}t(\cos k_x - \cos k_y).$$

For the *A* type, we obtain

$$H_{\alpha\alpha}(\mathbf{k}) = \begin{pmatrix} \varepsilon_\alpha + t_{\alpha\alpha}(\mathbf{k}_\perp) - J_H S & 0 & t_{\alpha\alpha}(\mathbf{k}_z)\cos\frac{\theta}{2} & t_{\alpha\alpha}(\mathbf{k}_z)\sin\frac{\theta}{2} \\ 0 & \varepsilon_\alpha + t_{\alpha\alpha}(\mathbf{k}_\perp) + J_H(S+1) & -t_{\alpha\alpha}(\mathbf{k}_z)\sin\frac{\theta}{2} & t_{\alpha\alpha}(\mathbf{k}_z)\cos\frac{\theta}{2} \\ t_{\alpha\alpha}(\mathbf{k}_z)\cos\frac{\theta}{2} & -t_{\alpha\alpha}(\mathbf{k}_z)\sin\frac{\theta}{2} & \varepsilon_\alpha + t_{\alpha\alpha}(\mathbf{k}_\perp) - J_H S & 0 \\ t_{\alpha\alpha}(\mathbf{k}_z)\sin\frac{\theta}{2} & t_{\alpha\alpha}(\mathbf{k}_z)\cos\frac{\theta}{2} & 0 & \varepsilon_\alpha + t_{\alpha\alpha}(\mathbf{k}_\perp) + J_H(S+1) \end{pmatrix}, \quad (8)$$

where

$$t_{11}(\mathbf{k}_\perp) = -\frac{1}{2}t(\cos k_x + \cos k_y),$$

$$t_{22}(\mathbf{k}_\perp) = -\frac{3}{2}t(\cos k_x + \cos k_y),$$

$$t_{11}(\mathbf{k}_z) = -2t\cos k_z, \quad t_{22}(k_z) \equiv 0.$$

Equations (5)–(8) are written under the assumption that index 1 labels the *d* orbital of type $|z^2\rangle$ and index 2, the $|x^2 - y^2\rangle$ orbital. As follows from Eq. (8), $H_{22}(\mathbf{k})$ for the *A* type is diagonal. In this case, obviously, matrix $H_{12}(\mathbf{k})$ will also have the diagonal form:

$$H_{mn}(\mathbf{k}_\perp) = t_{12}(\mathbf{k}_\perp)\delta_{mn} \qquad (m, n = 1, 2, 3, 4).$$

For the *C* type, we have

$$H_{\alpha\alpha}(\mathbf{k}) = \begin{pmatrix} \varepsilon_\alpha + t_{\alpha\alpha}(\mathbf{k}_z) - J_H S & 0 & t_{\alpha\alpha}(\mathbf{k}_\perp)\cos\frac{\theta}{2} & t_{\alpha\alpha}(\mathbf{k}_\perp)\sin\frac{\theta}{2} \\ 0 & \varepsilon_\alpha + t_{\alpha\alpha}(\mathbf{k}_z) + J_H(S+1) & -t_{\alpha\alpha}(\mathbf{k}_\perp)\sin\frac{\theta}{2} & t_{\alpha\alpha}(\mathbf{k}_\perp)\cos\frac{\theta}{2} \\ t_{\alpha\alpha}(\mathbf{k}_\perp)\cos\frac{\theta}{2} & -t_{\alpha\alpha}(\mathbf{k}_\perp)\sin\frac{\theta}{2} & \varepsilon_\alpha + t_{\alpha\alpha}(\mathbf{k}_z) - J_H S & 0 \\ t_{\alpha\alpha}(\mathbf{k}_\perp)\sin\frac{\theta}{2} & t_{\alpha\alpha}(\mathbf{k}_\perp)\cos\frac{\theta}{2} & 0 & \varepsilon_\alpha + t_{\alpha\alpha}(\mathbf{k}_z) + J_H(S+1) \end{pmatrix}, \quad (9)$$

and matrix $H_{12}(\mathbf{k}) = H_{12}(\mathbf{k}_\perp)$ coincides with the analogous matrix of type *G*.

Equations (5)–(9) were used [49] to calculate dispersion relations for various canted AFM structures both with and without inclusion of the JT static distortions of the ideal perovskite cubic lattice structure. These distortions account for the values of the hopping integral being different along various directions and for

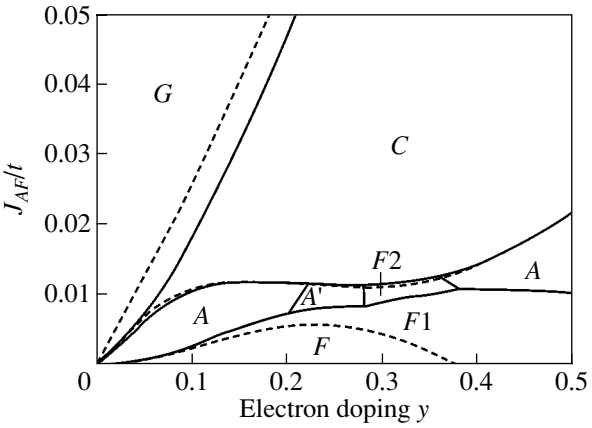

Fig. 15. Phase diagram of manganites constructed in y vs. J_{AF}/t coordinates with inclusion of the e_g level splitting for $J_H = 1.7t$. Within the narrow region $y = 0.21$–0.28, the equilibrium magnetic configuration is the canted A phase labeled by A'. The ferromagnetic phase $F2$ forms from the split phase C, and ferromagnetic phase $F1$, from the split phase A. Phases C and A are collinear, and phase G is canted. The G–C–A phase alternation sequence coincides with experimental observations. The dashed line plots the collinear approximation.

the level splitting $\varepsilon_\alpha \neq \varepsilon_\beta$. The dependence of the hopping integrals (the $V_{pd\sigma}$ parameter) on distance, which was determined by the method developed by Harrison [57], has practically no effect on the calculation of the dispersion curves. The most essential result of the JT distortions is the splitting of the manganese e_g level. After this splitting has reached a certain critical value, an insulating gap opens in the lower degenerate band of the type-A magnetic structure ($LaMnO_3$). If the JT effect is neglected, the degeneracy of the e_g level results in the A structure (even without doping) being always metallic, which is at odds with numerous experimental data. For the G structure, the gap appears for any value of JT distortion. In collinear structures ($\theta = \pi$), all bands are twofold degenerate. In this case, one can derive analytic expressions for the dispersion curves $\varepsilon(\mathbf{k})$ for some points and directions in the Brillouin zone (BZ). It is simpler, however, to perform numerical diagonalization of an eighth-order secular equation for arbitrary values of angle θ and wave vector $\mathbf{k}$ in the BZ of the crystal structure under study.

Numerical calculations of the total energies (in units of t) per manganese atom and of all collinear and canted magnetic configurations of the two-sublattice manganite model are presented in [58, 59] for the electron-doping region. The total energy calculations were performed for various electron concentrations $y = 1 - x$ and sets of parameters J_H/t and J_{AF}/t, where J_{AF} is the exchange coupling parameter for the G structure characteristic of the system under study without doping, $CaMnO_3$ (J_{AF} = 1.5 meV, T_N = 141 K). The results obtained did not extend to the $y = 0.5$ region. The total energies of all antiferromagnetic configurations were minimized in the angle θ; this procedure allowed us to find an equilibrium magnetic configuration for each $y < 0.5$.

The energy per manganese atom in the G phase was calculated as

$$E_G\left(x, \frac{\theta}{2}\right) = -3J_{AF}S^2\cos(\theta) + \int_{-\infty}^{\varepsilon_F} \varepsilon n_G\left(\varepsilon, \cos\frac{\theta}{2}\right)d\varepsilon, \quad (10)$$

where $S = 3/2$, ε_F is the Fermi level, $n_G(\varepsilon, \cos\theta/2)$ is the normalized density of states for the G phase, and J_{AF} is the exchange parameter in the Heisenberg model for the nearest neighbors. The density of states was found by summation over the corresponding BZ of the spectrum $\varepsilon(\mathbf{k}, \cos\theta/2)$, which was calculated through diagonalization of the G structure Hamiltonian matrix. The total energies of all other magnetic structures were derived in a similar manner. In this procedure, the first term in Eq. (10) was $-J_{AF}S^2(1 + 2\cos(\theta))$ for the C, $+J_{AF}S^2(2 + \cos(\theta))$ for the A, and $+3J_{AF}S^2$ for the F phase.

In the absence of free electrons, the magnetic phases are arranged in the sequence G, C, A, and F in order of increasing magnetic energy. As y increases, the interplay between the kinetic and magnetic energies of the system gives rise to one of the possible magnetic states. If the e_g level splitting is neglected, the collinear A phase can exist only within a narrow electron concentration region near $y = 0.2$ for very large values of the J_H/t parameter. The ferromagnetic phase remains an equilibrium magnetic structure within a broad range of values of J_{AF} and y. In this approximation, which is in agreement with [60], the "right" phase sequence G–C–A with increasing y can be observed only in a fairly narrow interval $0.033 < J_{AF}/t < 0.043$ for very large values of J_{AF}. The canting of the magnetic sublattices only aggravates the situation, because the only phases remaining in the diagram are G, F, and A (see [58]).

Figure 15 presents in the y vs. J_{AF}/t coordinates the phase diagram of the $La_{1-y}Ca_yMnO_3$ system in the region y = 0–0.5 calculated with an e_g-level splitting $2\Delta = \varepsilon_1 - \varepsilon_2$ for $J_H/t = 1.7$, which is characteristic of $CaMnO_3$ for $t = 0.15$ eV. The splitting was assumed to be proportional to the electron concentration such that for $y = 1$ it would be equal to the value typical of the JT splitting in $LaMnO_3$, namely, $\varepsilon_{d\alpha} = \pm 1.5ty$ for the A structure and $\varepsilon_{d\alpha} = -(\pm 1.5ty)$ for the C structure. The upper sign related to the $|z^2\rangle$ orbital, and the lower one related to the $|x^2 - y^2\rangle$ orbital. Thus, in the A phase, primarily the $|x^2 - y^2\rangle$ orbital that is filled and, in the C phase, the $|z^2\rangle$ orbital of the e_g level.

The dashed lines in Fig. 15 identify the phase boundaries determined in the collinear approximation. Minimization in the angle θ makes the canted A phase, denoted by A', for the first time an equilibrium magnetic configuration within a narrow interval $y = 0.21$–0.28 for small $0.006 < J_{AF}/t < 0.01$. As y increases, this phase transfers to the ferromagnetic phase $F2$ forming from

the split phase *C*. Slightly below *F*2, one can see a ferromagnetic phase *F*1 formed from the split *A* phase. In this region of parameters, the total energy of the unsplit ferromagnetic phase *F* turns out larger than that of the phases *F*1 or *F*2.

In the region of real values $0.012 < J_{AF}/t < 0.02$, the magnetic phase sequence *G*–*C*–*A* and the position of the phase boundaries are in good agreement with experimental values. The magnetic sublattice canting does not noticeably affect the qualitative pattern of the phase diagram while shifting the boundary separating the *G* and *C* phases.

While the possibility that the degeneracy of the e_g level can be partially lifted under low electron doping was allowed for by some authors, it was not considered earlier because of the low concentration of the Mn^{3+} ions. Calculations [58] showed, however, a qualitative rearrangement of the phase diagrams resulting from the inclusion of the e_g level splitting caused by the variation in the carrier spectrum $\varepsilon(\mathbf{k})$ in the tetragonal *G*, *C*, and *A* structures. In collinear structures, the level splitting does not lift the twofold band degeneracy in the symmetric BZ directions. Degeneracy is removed as a result of the canting of neighboring spins belonging to various sublattices. In the case of the *C* and *A* structures, the lower bands are found to be less sensitive to canting, which accounts qualitatively for the experimentally observed collinearity of these phases. Only the inclusion of the e_g level splitting and identification of each AFM structure with a specific type of orbital ordering permits one to obtain the "right" phase sequence, *G*–*C*–*A*, with increasing electron concentration for actual values of the J_H/t and J_{AF}/t parameters.

Thus, it was shown in [58, 59] that the inclusion of orbital degeneracy not only changes the carrier spectrum $\varepsilon(\mathbf{k})$ in a transition from one magnetic structure to another but also affects the conditions conducive to the formation of either collinear or canted (*A*, *G*, *C*, and *F*) magnetic structures corresponding to the minimum of total energy. As already mentioned, earlier calculations [48, 60, 61] of the kinetic energy of the *A*, *G*, and *C* structures made use of the modified spectrum $\varepsilon(\mathbf{k})$ of ferromagnetic (*F*) ordering, which resulted in inadequate description of the experimental situation.

The next step in studying the two-sublattice model of the manganites was made in [50, 62, 63], where the type of orbital ordering depending on the oxygen octahedron distortions, rather than being specified, was found by minimizing the total energy in the angle θ and two angles of orbital intraatomic mixing θ_i^o. This was achieved by invoking an arbitrary atomic basis $|\alpha\rangle_i$ and

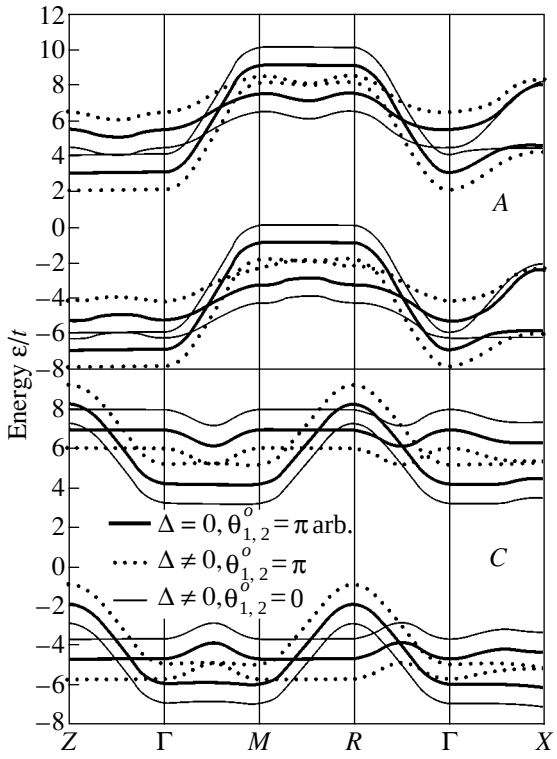

Fig. 16. Dependence of the lower energy bands $\varepsilon(\mathbf{k})$ of the magnetic *A* and *C* phases on the type of their OO. With the e_g level splitting neglected, the band structure (bold solid line) does not depend on the orbital mixing angles. Points and the thin line identify the energy bands appearing in the case of inclusion of the splitting of this level for OO of the $|x^2 - y^2\rangle$ and $|3z^2 - r^2\rangle$ types, respectively. For the magnetic *A* structure, OO of the $|x^2 - y^2\rangle$ type is obviously preferable. For the *C* structure, the reverse situation applies.

$|\beta\rangle_i$ connected with the original basis through the transformation

$$\begin{pmatrix} |\alpha\rangle_i \\ |\beta\rangle_i \end{pmatrix} = \begin{pmatrix} \cos\frac{\theta_i^o}{2} & \sin\frac{\theta_i^o}{2} \\ -\sin\frac{\theta_i^o}{2} & \cos\frac{\theta_i^o}{2} \end{pmatrix} \begin{pmatrix} |1\rangle_i \\ |2\rangle_i \end{pmatrix}. \qquad (11)$$

In this transformation, θ_i^o is the angle of intraatomic orbital mixing at the *i*th atom. After the transformation, the hopping integral $t_{ij\alpha\beta}$ is already dependent on the angles θ_{ij}, θ_i^o, and θ_j^o. Because this study considered only antiferromagnetic structures consisting of two magnetic sublattices, the possible types of orbital order (OO) coincide with those of magnetic configurations (*A*, *G*, *C*, *F*, etc.). The orbital "ferromagnetic" structure *F* could be identified only with one mixing angle θ_i^o at all sites of the system under study. In the "antiferromagnetic" orbital *A*, *G*, and *C* structures, to each sublattice corresponded a specific orbital mixing angle θ_1^o and

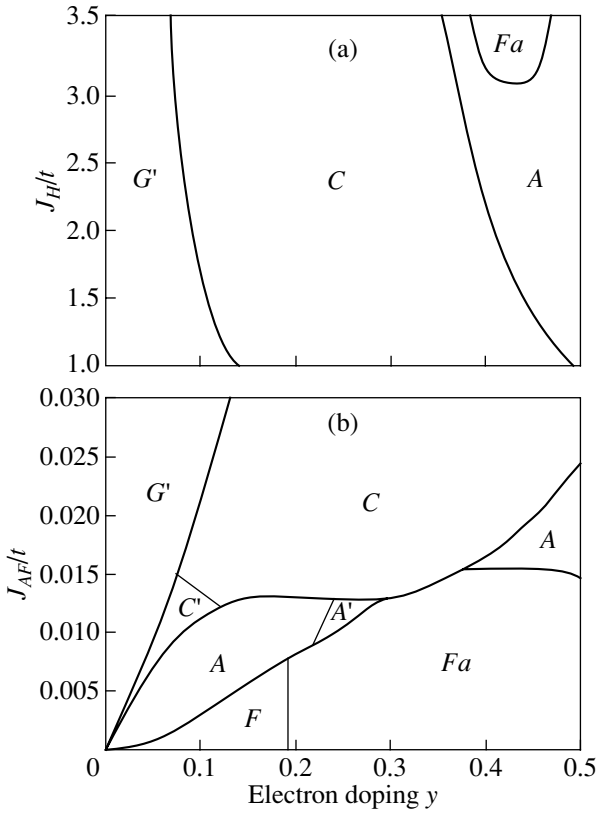

Fig. 17. Phase diagrams plotted in y vs. J_H/t and y vs. J_{AF}/t coordinates with optimization in one angle between neighboring spins and two orbital angles, calculated for J_H/t = 2.5 (b) and J_{AF}/t = 0.016 (a), $\Delta/t = 1.5y$.

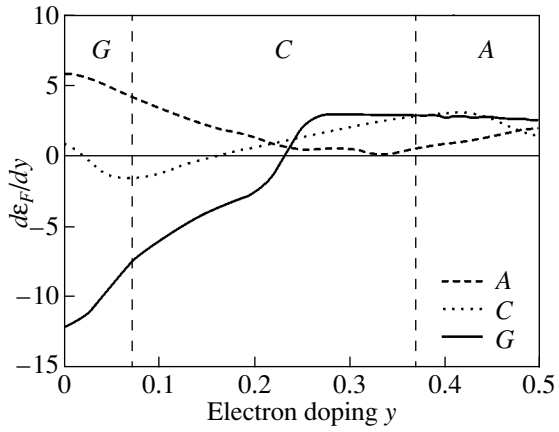

Fig. 18. $d\varepsilon_F/dy$ dependences on y calculated for various magnetic phases [63]. Vertical lines separate the regions in which G, C, and A are equilibrium magnetic phases. J_{AF} = $0.015t$.

θ_2^o and the sublattices themselves were defined in the same way as the magnetic configurations.

In the case of orbital mixing, one should add to Hamiltonian (1) a term corresponding to the JT splitting of the e_g level:

$$H_{JT} = \sum_{i\sigma}\Delta_i(d^+_{i\alpha\sigma}d^+_{i\beta\sigma})\begin{pmatrix}\cos\theta_i^o & \sin\theta_i^o\\ \sin\theta_i^o & -\cos\theta_i^o\end{pmatrix}\begin{pmatrix}d_{i\alpha\sigma}\\ d_{i\beta\sigma}\end{pmatrix}. \quad (12)$$

Without this term in Hamiltonian (1), the energy of the system is degenerate with respect to the ferromagnetic OO, to which a minimum in total energy corresponds. However, when the JT splitting of the e_g level is included, the electronic part of the total energy of the system begins to depend already on the orbital order (the values of θ_1^o and θ_2^o) in the case of $\theta_1^o = \theta_2^o$ as well. It is known that $(La–Nd)_{1-x}Sr_xMnO_3$ revealed an AFM A structure for x = 0.52–0.62 with preferential filling of type $|2\rangle$ orbitals [64]. Obviously enough, the subband splitting in the magnetic A phase, which is defined as $2\Delta = \varepsilon_1 - \varepsilon_2$, should be positive and in the magnetic C phase, negative [65]. Therefore, the splitting 2Δ for the A and C structures was chosen proportional to y in such a way as to obtain, in the limiting case of y = 1 (x = 0), the value $\varepsilon_1 - \varepsilon_2$ = 0.3–0.5 eV [56] for the A phase in $LaMnO_3$.

Numerical calculations of the total energies of manganites in this model were carried out in a way similar to that employed in [58]. The total energies of all configurations were minimized in the corresponding angles θ_{ij}^s and θ_i^o, which permitted determination of the equilibrium magnetic and orbital structures for each value of the electron concentration.

Figure 16 illustrates the dependence of the spectrum $\varepsilon(\mathbf{k})$ of the magnetic A and C phases on the type of their OO. If the e_g level splitting is neglected, the band structure turns out not to depend on the orbital mixing angles. If this level is split, ferromagnetic orbital ordering of the $|x^2 - y^2\rangle$ type for the antiferromagnetic structure A is preferable over that of type $|3z^2 - r^2\rangle$. For the C structure, we have the reverse situation.

Figure 17 shows the resulting phase diagrams plotted in the y vs. J_H/t and y vs. J_{AF}/t coordinates and calculated with optimization in one angle between neighboring spins and two orbital angles for J_H/t = 2.5 (b), J_{AF}/t = 0.016 (a), and $\Delta/t = 1.5y$. All canted phases are primed. In the canted G' phase, we have ferromagnetic OO of the $|3z^2 - r^2\rangle$ type ($\theta_i^o = 0$), which is threefold degenerate, because at the same energy there can be OOs of the $|3y^2 - r^2\rangle$ ($\theta_i^o = 2\pi/3$) and $|3x^2 - r^2\rangle$ ($\theta_i^o = 4\pi/3$) types. Phase C is collinear, with the exclusion of a small region C' with ferromagnetic OO of the $|3z^2 - r^2\rangle$ type. Most of the magnetic phases have ferromagnetic orbital order. The only exclusion is the collinear FM phase with type-A antiferromagnetic OO ($\theta_{1,2}^o = \pm\pi/2$) denoted by Fa.

In the region $0.013 < J_{AF}/t < 0.02$, the magnetic phase sequence and the position of the phase boundaries are in good agreement with experiment.

In addition to the total energies, the inverse compressibility $k^{-1} \sim d\varepsilon_F/dy$, which is proportional to the first derivative of the Fermi level with respect to concentration, was also calculated [63]. The $d\varepsilon_F/dy$ vs. y dependences are plotted in Fig. 18 for various magnetic phases. Also shown are the electron-doping regions where *G*, *C*, and *A* are the ground magnetic phases. It is known (see, e.g., [6]) that a negative derivative indicates the possibility of the onset of phase separation in the system. It was found that electron phase separation can occur only in the *G* phase for $0 < y < 0.07$ and only in the *C* phase for $0.07 < y < 0.15$. For $y > 0.15$, the inverse compressibility of phase *c* becomes positive. For the *A* phase, the inverse compressibility is positive for all *y*. Phase separation in the canted *G* structure should most probably give rise to the formation of electron-enriched ferromagnetic "clusters" within the electron-depleted collinear *G* phase. The question of what phases the *C* structure can separate into remains unclear. Additional theoretical calculations would be needed to answer this question. The theoretical pattern obtained is qualitatively in agreement with the experimental observations of phase separation effects in manganites for $0.07 < y < 0.15$ reported in [46, 66]. Nevertheless, the statement that the onset of phase separation occurs in manganites at low electron concentrations cannot be considered final because of the various approximations made. The most serious of these simplifications in the theoretical approach considered here is the neglect of interatomic Coulomb repulsion, which should favor the obtainment of a uniform charge distribution.

4.3. Phase Diagrams of the Four-Sublattice Model of Manganites in the Tight-Binding Approximation

As already mentioned, the crystal structure of most manganites contains four manganese atoms per unit cell. Therefore, a consistent calculation of the band structure and carrier kinetic energy in the tight-binding approximation for the manganites requires analysis of the Hamiltonian matrices in **k** space with dimensions no less than 16×16 to accommodate all versions of magnetic ordering (C_xA_z, $G_zA_yF_x$,… in *Pnma*, etc.).

In this case, the Hamiltonian matrix of the system can be written, as before, in the form

$$H(\mathbf{k}) = \begin{pmatrix} H_{11}(\mathbf{k}) & H_{12}(\mathbf{k}) & H_{13}(\mathbf{k}) & 0 \\ H_{21}(\mathbf{k}) & H_{22}(\mathbf{k}) & 0 & H_{24}(\mathbf{k}) \\ H_{31}(\mathbf{k}) & 0 & H_{33}(\mathbf{k}) & H_{34}(\mathbf{k}) \\ 0 & H_{42}(\mathbf{k}) & H_{43}(\mathbf{k}) & H_{44}(\mathbf{k}) \end{pmatrix}, \quad (13)$$

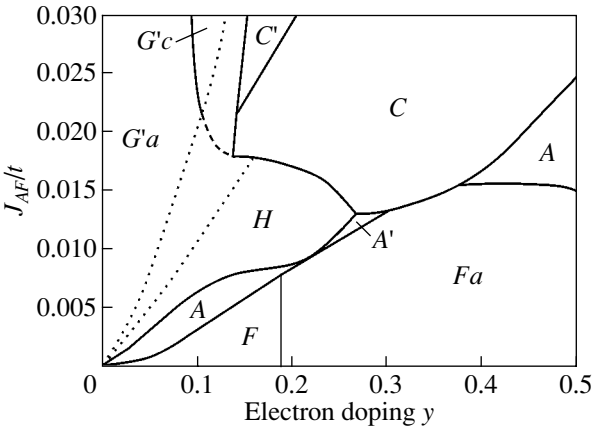

Fig. 19. Phase diagram of the model with four manganese atoms in the unit cell [68]. Capital letters denote magnetic structures, and lower-case letters, orbital structures. All canted phases are primed. Old phases: *A* and *C* are collinear AFM structures with ferromagnetic OO of the $|x^2 - y^2\rangle$ and $|3z^2 - r^2\rangle$ type, respectively; *A*' is *A* structure with ferromagnetic OO and intersublattice canting; *F* is threefold degenerate with ferromagnetic OO; and *Fa* is ferromagnetic with antiferromagnetic OO of type *A* ($\pi/2, -\pi/2$). New phases: *C*' is *C* structure with ferromagnetic OO of type $|3z^2 - r^2\rangle$ with intrasublattice spin canting and *G*'*a* and *G*'*c* are coplanar spin-canted *G* structures with antiferromagnetic OO of type *A* and *C*, respectively.

where the H_{ij} matrices describe interaction among the nearest Mn ions in the lattice from Fig. 1.

If we do not impose any constraints on possible types of magnetic and orbital structures, the three angles θ_i^s, φ_i, and θ_i^o defining the local spin direction and the type of orbital mixing will have to specified for each manganese atom in the unit cell. For an *i*th atom, one should use as a local atomic basis the $|\alpha\rangle'$ and $|\beta\rangle'$ spinors, which are connected with the atomic orbitals (11) through the well-known transformation

$$\begin{pmatrix} |\gamma\rangle'_{i\uparrow} \\ |\gamma\rangle'_{i\downarrow} \end{pmatrix} = \begin{pmatrix} \cos\dfrac{\theta_i^s}{2} & i\sin\dfrac{\theta_i^s}{2}\exp(-i\varphi_i) \\ -i\sin\dfrac{\theta_i^s}{2}\exp(i\varphi_i) & \cos\dfrac{\theta_i^s}{2} \end{pmatrix} \begin{pmatrix} |\gamma\rangle_{i\uparrow} \\ |\gamma\rangle_{i\downarrow} \end{pmatrix}. \quad (14)$$

The primes in Eq. (14) denote the spinor components in the local reference frame, and the arrows identify the electron spin projections on an arbitrarily chosen axis, $\gamma = \alpha, \beta$.Considered in the local basis, the hopping integral between identical orbitals of the nearest manganese atoms has the form (see [5])

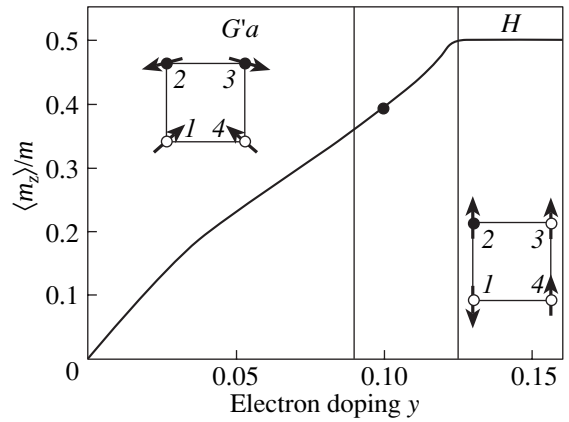

Fig. 20. Doping-level dependence of the cell-averaged ferromagnetic moment $\langle m_z \rangle / m$ calculated for $J_{AF} = 0.015t$, $J_H = 2.5t$, and $\Delta = 1.5ty$. Here, $m = 3\mu_B$ is the magnetic moment of the Mn^{4+} ion. The point specifies the experimental value of the ferromagnetic component in $Ho_{0.1}Ca_{0.9}MnO_3$ [47].

$$t_{ij\alpha\alpha}^{\uparrow\uparrow} = \langle \alpha_i^{\uparrow} | \alpha_j^{\uparrow} \rangle = t_{ij\alpha\alpha}[\cos(\theta_i/2)\cos(\theta_j/2) + \sin(\theta_i/2)\sin(\theta_j/2)e^{i(\varphi_i - \varphi_j)}]. \quad (15)$$

One can readily derive in a similar manner all the other hopping integrals and specify the Hamiltonian matrix (13) for an arbitrary spin and orbital structure of the four manganese sublattices of the manganites in an explicit way. Earlier calculations of the Hamiltonian matrices for two sublattices actually used expressions of the type of Eq. (15), in which all azimuthal angles were assumed equal and the magnetic structures could be either collinear or coplanar-canted only.

In this approach, the spectrum of the carriers and their kinetic energy depend on 12 parameters; it is these parameters that determine the ground state of the system. In the absence of magnetic anisotropy, the spin structure is not fixed relative to the crystallographic axes. By arbitrarily specifying the spin direction of one of the four manganese atoms and the point from which the azimuthal angle φ is reckoned with respect to this atom, we can reduce the number of variables (angles) to nine. Obviously enough, all the above-considered Hamiltonian matrices of the two-sublattice model can be derived from the general matrix (13). However, while all the previous calculations were limited only to the FM orbital order, in this model the OO type (*A*, *C*, etc.) is not specified but rather fixed by the minimum of total energy. In contrast to the previous models, this model allows only two types of magnetic moment canting. Besides the conventional intersublattice canting, each sublattice may have now spin and orbital canting.

Figure 19 plots the phase diagram calculated in the model assuming the presence of four manganese atoms in the unit cell [67]. Despite the existence of a large number of local minima of similar energy, the absolute minima of energy were successfully determined for all magnetic phases and turned out to be nondegenerate. On the whole, this diagram resembles the phase diagram of the two-sublattice model, although the calculations did not impose any constraints on the possible types of magnetic and orbital order. Nevertheless, all the equilibrium magnetic phases in the four-sublattice model turned out to be either collinear or coplanar. Separate calculations were carried out of the total energies for all irreducible representations allowed in *Pnma*, which is a particular case of the model with four manganese atoms in the unit cell. These calculations also showed the coplanar magnetic structures of this space group to have minimum energy. All noncoplanar magnetic structures in *Pnma* are energetically unfavorable.

Phases *A* and *C* are the well-known collinear AFM structures with FM OO of the $|x^2 - y^2\rangle$ and $|3z^2 - r^2\rangle$ types, respectively. The small central region *A*' is actually the same structure *A* with FM OO but with small intersublattice canting. Phase *F* is, as before, ferromagnetic with threefold degenerate ferromagnetic OO, and *Fa* is ferromagnetic with antiferromagnetic OO of the *A* type $(\pi/2, -\pi/2)$. The other phases in the diagram are new. Phase *C*' is the spin *C* structure with ferromagnetic OO of the $|3z^2 - r^2\rangle$ type but with intrasublattice spin canting. Phases *G*'*a* and *G*'*c* are coplanar, spin-canted *G* structures with antiferromagnetic OO of the *A* and *C* types, respectively. The spin canting in these phases can be described by two angles, $\gamma = \theta_{14}(\theta_{12})$ and $\eta = \theta_{13} = \theta_{24}$, which are the angles of inter- and intrasublattice canting with respect to the *G* structure, respectively. Such a spin configuration cannot be specified by the angles θ_{xy} and θ_z [48, 55], which describe only canting of the types *A* ($\gamma = \theta_z = \theta_{12} = \theta_{34}$, $\eta = \theta_{xy} = \theta_{14} = \theta_{23}$) and *C* ($\eta = \theta_z = \theta_{12} = \theta_{34}$, $\gamma = \theta_{xy} = \theta_{14} = \theta_{23}$). If the axis along which a magnetic moment appears in the *G*'*a* structure coincides with one of the crystallographic axes, the magnetic and orbital structures will be described by the monoclinic space group $P2_1/b$, which is a subgroup of *Pbnm*. As the electron concentration increases, triclinic distortions form in the *G*'*a* phase, which initiate its smooth transition to a new collinear ferrimagnetic phase *H* (Fig. 20) in which one of the spins opposes the other three. Each of the manganese atoms in this phase has a collinear environment, more specifically, *G* for atom *1*, *A* for atom *2*, *F* for atom *3*, and *C* for atom *4*.

Figure 20 shows the doping-level dependence of the cell-averaged local ferromagnetic moment $\langle m_z \rangle / m$ calculated for $J_{AF} = 0.015t$, $J_H = 2.5t$, and $\Delta = 1.5ty$. This magnetic moment per Mn^{4+} ion reaches a maximum value $0.5m_{Mn^{4+}} = 1.5\mu_B$ in the *H* phase and goes to zero for $y > 0.25$. Similar behavior of the spontaneous magnetization was observed in another experiment [68], where the magnetization first grew with increasing *y*, only to vanish near $y = 0.2$. Remarkably, the theoretical value of $\langle m_z \rangle / m$ coincides for $y = 0.1$ with the experimental value of the ferromagnetic component in $Ho_{0.1}Ca_{0.9}MnO_3$ [47], although this compound has non-

coplanar magnetic structure. A comparison of the theoretical curve with data on the magnetization of the manganites of samarium and praseodymium would be difficult, because the ground state of these compounds at low electron concentrations is phase separated (see [46, 66]).

Thus, the double-exchange model for e_g electrons combined with the Heisenberg model for the localized t_{2g} electrons and applied to the crystal structure of manganites with four manganese atoms per unit cell in the region of parameters $0.018 < J_{AF}/t < 0.022$, $J_H = 2.5t$, and $\Delta = 1.5ty$ also predicts the *G–C–A* magnetic phase sequence. When used for the values $J_{AF}/t < 0.018$ and $y < 0.28$, this model allows for the existence of a new collinear phase *H*.

5. CONCLUSIONS

The main goal of the present review was to demonstrate that the degenerate double-exchange model, which includes the splitting of the e_g manganese level, qualitatively describes the ground state of the manganites at $T = 0$ on the electron-doped side correctly. Despite the number of simplifications made in choosing the Hamiltonian for the system, for most of the manganites, the DE model produces an experimentally observed diversity of magnetic phases at low temperatures and their *G–C–A* alternation sequence with increasing electron doping and is capable of predicting the possible types of orbital ordering and their relation to the magnetic structure. The carrier spectrum $\varepsilon(\mathbf{k})$ calculated in the tight-binding approximation can be subsequently employed to interpret the optical and photoemission properties of the manganites and in modeling electron phase separation effects.

The ways in which the model should be generalized to permit not only qualitative but also quantitative comparison with experimental values for specific compounds and at nonzero temperatures are generally known. In choosing the Hamiltonian, one should take into account the Coulomb interaction and renormalization of the interatomic exchange between the localized t_{2g} electrons at the expense of the e_g electrons. Moreover, when specifying the manganite crystal structure, one should consider, in addition to the manganese sublattice, the sublattice formed by the rare earth elements. This should not complicate the calculations too much in the tight-binding approximation and will permit one to obtain phase diagrams of specific manganites of rare earth elements.

ACKNOWLEDGMENTS

The author expresses deep gratitude to V.V. Deriglazov for fruitful discussions and assistance in preparing this review.

This study was supported by the Russian Foundation for Basic Research, project no. 02-02-81012 Bel2002-a.

REFERENCES

1. *Colossal Magnetoresistance, Charge Ordering and Related Properties of Manganese Oxides*, Ed. by C. N. R. Rao and B. Raveau (World Sci., Singapore, 1998).
2. J. Coey, M. Viret, and S. Molnar, Adv. Phys. **48**, 167 (1999).
3. M. B. Salamon and M. Jaime, Rev. Mod. Phys. **73**, 583 (2001).
4. K. I. Kugel' and D. I. Khomskiĭ, Usp. Fiz. Nauk **136** (4), 621 (1982) [Sov. Phys. Usp. **25**, 231 (1982)].
5. Yu. A. Izyumov and Yu. N. Skryabin, Usp. Fiz. Nauk **171** (2), 121 (2001) [Phys. Usp. **44**, 109 (2001)].
6. M. Yu. Kagan and K. I. Kugel', Usp. Fiz. Nauk **171** (6), 577 (2001) [Phys. Usp. **44**, 563 (2001)].
7. G. H. Jonker and J. H. van Santen, Physica (Amsterdam) **16**, 337 (1950).
8. E. O. Wollan and W. C. Koehler, Phys. Rev. **100**, 545 (1955).
9. C. Zener, Phys. Rev. **82**, 403 (1951).
10. P. W. Anderson and H. Hasegawa, Phys. Rev. **100**, 675 (1955).
11. S. Mori, C. H. Chen, and S. W. Cheong, Nature **392**, 473 (1998).
12. R. Maezono, S. Ishihara, and N. Nagaosa, Phys. Rev. B **57**, R13993 (1998).
13. C. Mitra, P. Raychaudhuri, K. Dörr, *et al.*, Phys. Rev. Lett. **90**, 017202 (2003).
14. H. Kawano, R. Kajimoto, M. Kubota, and H. Yoshizava, Phys. Rev. B **53**, 14709 (1996).
15. V. E. Naĭsh, Fiz. Met. Metalloved. **85** (6), 5 (1998).
16. E. F. Bertaut and F. Forrat, J. Phys. Radium **17**, 129 (1956).
17. H. L. Yakel, W. C. Koehler, E. F. Bertaut, and E. F. Forrat, Acta Crystallogr. **16**, 957 (1963).
18. A. Waintal and J. Chenavas, Mater. Res. Bull. **218**, 819 (1967).
19. E. F. Bertaut, in *Magnetism*, Ed. by G. T. Rado and H. Suhl (Academic, New York, 1963), Vol. 3, Chap. 4.
20. *International Tables for Crystallography*, Ed. by T. Hahn (Reidel, Dordrecht, 1983), Vol. A.
21. J. Rodriguez-Carvajal, Physica B (Amsterdam) **192**, 55 (1993).
22. F. Izumi, in *The Rietveld Method*, Ed. by R. A. Young (Oxford Univ. Press, Oxford, 1993), Chap. 13.
23. G. J. Snyders, C. H. Booth, F. Briges, *et al.*, Phys. Rev. B **55**, 6453 (1997).
24. H. Y. Hwang, S.-W. Cheong, P. G. Radaelli, *et al.*, Phys. Rev. Lett. **75**, 914 (1995).
25. Y. Tokura, H. Kuwahara, Y. Moritomo, *et al.*, Phys. Rev. Lett. **76**, 3184 (1996).
26. P. Schiffer, A. P. Ramirez, W. Bao, and S. W. Cheong, Phys. Rev. Lett. **75**, 3336 (1995).
27. Y. Moritomo, T. Akimoto, A. Nakamura, *et al.*, Phys. Rev. B **58**, 5544 (1998).
28. H. Fujishiro, T. Fukase, and M. Ikebe, J. Phys. Soc. Jpn. **67**, 2582 (1998).
29. P. C. Radaelli, D. E. Cox, L. Capogna, *et al.*, Phys. Rev. B **59**, 14440 (1999).

30. S. Mori, C. H. Chen, and S. W. Cheong, Nature **392**, 473 (1998).
31. M. Pisas, G. Kallias, M. Hoffmann, and D. M. Többens, Phys. Rev. B **65**, 064413 (2002).
32. S. Krupička, *Physik der Ferrite und der Verwandten Magnetischen Oxide* (Academia, Praha, 1973; Mir, Moscow, 1976), Vol. 1.
33. J. Hemberger, A. Krimmel, T. Kurz, *et al.*, Phys. Rev. B **66**, 094410 (2002).
34. S. L. Yuan, Y. Jiang, X. Y. Zeng, *et al.*, Phys. Rev. B **62**, 11347 (2000).
35. Z. Jiràk, S. Krupička, Z. Šimša, *et al.*, J. Magn. Magn. Mater. **53**, 153 (1985).
36. C. Martin, A. Maignan, M. Hervieu, and B. Raveau, Phys. Rev. B **60**, 12191 (1999).
37. A. Maignan, C. Martin, F. Damay, *et al.*, Phys. Rev. B **58**, 2758 (1998).
38. C. Martin, A. Maignan, M. Hervieu, *et al.*, J. Magn. Magn. Mater. **205**, 184 (1999).
39. C. Martin, A. Maignan, M. Hervieu, *et al.*, Phys. Rev. B **62**, 6442 (2000).
40. R. Kajimoto, H. Yoshizawa, H. Kuwahara, *et al.*, Phys. Rev. B **60**, 9506 (1999).
41. F. Millange, S. de Brion, and G. Chouteau, Phys. Rev. B **62**, 5619 (2000).
42. F. Damay, N. Nguyen, A. Maignan, *et al.*, Solid State Commun. **98**, 997 (1996).
43. S. M. Dunaevskiĭ, A. L. Malyshev, V. V. Popov, and V. A. Trunov, Fiz. Tverd. Tela (St. Petersburg) **39**, 1831 (1997) [Phys. Solid State **39**, 1636 (1997)].
44. S. M. Dunaevskiĭ, A. I. Kurbakov, V. A. Trunov, *et al.*, Fiz. Tverd. Tela (St. Petersburg) **40**, 1271 (1998) [Phys. Solid State **40**, 1158 (1998)].
45. I. D. Luzyanin, V. A. Ryzhov, D. Yu. Chernyshov, *et al.*, Phys. Rev. B **64**, 094432 (2001).
46. R. Mahendiran, A. Maignan, C. Martin, *et al.*, Phys. Rev. B **62**, 11644 (2000).
47. K. Hagdorn, D. Hohlwein, J. Ihringer, *et al.*, Eur. Phys. J. B **11**, 243 (1999).
48. J. van den Brink and D. I. Khomskii, Phys. Rev. Lett. **82**, 1016 (1999).
49. S. M. Dunaevskiĭ, Fiz. Tverd. Tela (St. Petersburg) **43**, 2161 (2001) [Phys. Solid State **43**, 2257 (2001)].
50. T. Ohsawa and J. Inoue, Phys. Rev. B **65**, 134442 (2002).
51. S. Satpathy, Z. S. Popović, and F. R. Vukajlović, Phys. Rev. Lett. **76**, 960 (1996).
52. P. G. de Gennes, Phys. Rev. **118**, 141 (1960).
53. E. L. Nagaev, Zh. Éksp. Teor. Fiz. **57**, 1274 (1970) [Sov. Phys. JETP **30**, 693 (1970)].
54. H. Shiba, R. Shina, and A. Takahashi, J. Phys. Soc. Jpn. **66** (9), 41 (1997).
55. I. V. Solovyev and K. Terakura, Phys. Rev. B **63**, 174425 (2001).
56. J. W. Liu, Z. Zeng, Q. Q. Zheng, and H. Q. Lin, Phys. Rev. B **60**, 12968 (1999).
57. W. A. Harrison, *Electronic Structure and the Properties of Solids: The Physics of the Chemical Bond* (Freeman, San Francisco, 1980; Mir, Moscow, 1983), Vol. 1.
58. S. M. Dunaevskiĭ and V. V. Deriglazov, Fiz. Tverd. Tela (St. Petersburg) **44**, 2169 (2002) [Phys. Solid State **44**, 2271 (2002)].
59. S. M. Dunaevsky and V. V. Deriglazov, J. Magn. Magn. Mater. **258–259**, 283 (2003).
60. G. Venketeswara Pai, Phys. Rev. B **63**, 064431 (2001).
61. Liang-Jian Zou, Phys. Rev. B **63**, 155103 (2001).
62. S. M. Dunaevskiĭ and V. V. Deriglazov, Fiz. Tverd. Tela (St. Petersburg) **45** (4), 681 (2003) [Phys. Solid State **45**, 714 (2003)].
63. S. M. Dunaevsky and V. V. Deriglazov, Phys. Rev. B **67**, 014409 (2003).
64. T. Akimoto, Y. Maruyama, Y. Moritomo, *et al.*, Phys. Rev. B **57**, R5594 (1998).
65. R. Maezono, S. Ishihara, and N. Nagaosa, Phys. Rev. B **58**, 11583 (1998).
66. P. A. Algarabel, J. M. De Teresa, B. Garsia-Landa, *et al.*, Phys. Rev. B **65**, 104437 (2002).
67. S. M. Dunaevskiĭ and V. V. Deriglazov, Fiz. Tverd. Tela (St. Petersburg) **46** (3) (2004) (in press).
68. J. J. Neumeier and J. L. Cohn, Phys. Rev. B **61**, 14319 (2000).

Translated by G. Skrebtsov

Physics of the Solid State, Vol. 46, No. 2, 2004, pp. 213–218. Translated from Fizika Tverdogo Tela, Vol. 46, No. 2, 2004, pp. 212–217.
Original Russian Text Copyright © 2004 by Baranov, Dubov, Dyatlova, Chernykh.

METALS AND SUPERCONDUCTORS

Atomic–Discrete Description of the Effect of Anisotropic Interatomic Interactions on the Elastic Properties of Metals with a Hexagonal Close-Packed Lattice

M. A. Baranov, E. A. Dubov, I. V. Dyatlova, and E. V. Chernykh

Altaĭ State Technical University, pr. Lenina 46, Barnaul, 656038 Russia

e-mail: fap@agtu.secna.ru

Received May 7, 2003

Abstract—Anisotropic interatomic potentials that account for the symmetry of hexagonal crystal lattices and ensure their stability are proposed. Numerical parameters of the potential functions are determined for the majority of metals with a hexagonal close-packed lattice. Analytical expressions are derived for elastic moduli of hexagonal crystals, and their values are calculated using the interatomic potentials obtained in the framework of the isotropic and anisotropic models. It is demonstrated that the anisotropic model offers a more adequate description of the elastic properties of metals with a hexagonal close-packed lattice as compared to the isotropic model. The potentials obtained can be successfully used for modeling lattice defects. © *2004 MAIK "Nauka/Interperiodica".*

1. INTRODUCTION

Considerable progress in transport, aerospace, high-voltage, and manufacturing engineering has brought to the fore the necessity of designing materials with high specific strength, shock resistance, and stability against corrosive media, high temperatures, and cavitation. However, only metallic systems, namely, alloys, uniquely combine these properties. It is known that the physicochemical properties of an alloy depend both on the crystal lattices of the phases comprising the material and on the character of interaction and distribution of the lattice defects. The effect of these factors on the properties of an alloy can be quantitatively described in terms of interatomic interaction potentials with the use of computer simulation. One of the main criteria for the adequacy of a model for the interatomic interaction under consideration is agreement between the calculated and experimental values for the greatest possible number of reliably determined characteristics of the crystal. Among these characteristics are the elastic moduli and energies of formation of crystal defects.

At present, a large number of models describing the properties and interatomic interaction potentials have been proposed for a wide variety of crystals with a cubic lattice [1, 2]. However, hexagonal crystals have received little attention [3], even though these materials are very promising for use in practice. This is associated with the severe difficulties encountered in constructing model interatomic interaction potentials with allowance made for the anisotropy of a hexagonal close-packed (hcp) crystal. Without considering this anisotropy, it is difficult if not impossible to adequately describe the stability of hcp metal lattices with experimentally observed unit cell parameters and, consequently, to model the lattice defects.

The purpose of the present work was to construct model interatomic potentials that ensure the stability of hcp metal lattices, to devise a technique for calculating elastic moduli of hexagonal crystals, and to determine the range of applicability of the spherically symmetric interatomic potentials for hcp metals. Agreement between the calculated and experimental elastic moduli served as a criterion for the adequacy of the model potentials for a particular interatomic interaction. The interatomic interaction potentials proposed in this work can be used for describing interatomic interactions in alloys containing hcp metals.

2. CONSTRUCTION OF THE INTERATOMIC POTENTIALS

For a metal with a hcp lattice, the internal energy U_0 of the lattice per atom can be represented by the energy of pair atomic interactions:

$$U_0 = \frac{1}{2}\sum_j \varphi(\mathbf{r}_j), \qquad (1)$$

where $\varphi(\mathbf{r}_j)$ is the interatomic potential, i.e., the energy of interaction of a pair of atoms related by the lattice vector $\mathbf{r}_j$. In expression (1), the summation is extended over all bonds of an atom located at a zeroth site of the lattice. In what follows, the subscript "j" on the summation sign and summable expressions will be omitted from the relationships for brevity. For a sublimation energy E_s and bulk modulus B, the crystal lattice with

Table 1. Initial data and parameters of the interatomic potentials [relationships (4) and (5)] ensuring the stability of hcp lattices in the framework of the isotropic and anisotropic models

Metal	Initial experimental data				Model	Parameters of the interatomic potentials			
	a_0, Å	η	E_s, eV	B, $\frac{\text{eV}}{\text{Å}^3}$		ξ	α, Å^{-1}	β	D, eV
Be	2.283	1.5799	3.33	0.6261	Isotropic	–	1.03639	15.5321	0.28540
					Anisotropic	−0.47003	1.02984	15.5631	0.33018
Cd	2.973	1.8859	1.16	0.2915	Isotropic	–	1.57346	148.6845	0.166490
					Anisotropic	5.12969	1.50880	147.4930	0.055273
Co	2.514	1.6329	4.387	1.1948	Isotropic	–	1.41301	45.7857	0.494230
					Anisotropic	−0.25480	1.41228	45.8561	0.537950
Hf	3.195	1.5830	6.35	0.6804	Isotropic	–	0.97716	30.1948	0.653940
					Anisotropic	−0.48839	0.97173	30.3060	0.767107
Mg	3.208	1.6240	1.53	0.2210	Isotropic	–	1.16852	54.1921	0.17832
					Anisotropic	−0.28759	1.16757	54.2811	0.19633
Re	2.761	1.6148	8.10	2.3221	Isotropic	–	1.54337	85.2601	1.01990
					Anisotropic	−0.32127	1.54212	85.3768	1.13721
Ru	2.706	1.5824	6.615	2.0025	Isotropic	–	1.56400	80.7498	0.82891
					Anisotropic	−0.52657	1.55942	80.9837	0.99296
Sc	3.309	1.5935	3.93	0.2715	Isotropic	–	0.76943	18.3760	0.35341
					Anisotropic	−0.44311	0.76583	18.4222	0.40655
Tl	3.456	1.6002	1.87	0.2241	Isotropic	–	1.10367	56.45925	0.22008
					Anisotropic	−0.41616	1.10165	56.6069	0.25319
Ti	2.950	1.5885	4.855	0.6561	Isotropic	–	1.05291	30.0089	0.49888
					Anisotropic	−0.46777	1.04914	30.1143	0.581327
Zn	2.665	1.8563	1.35	0.3733	Isotropic	–	1.53691	85.3287	0.17560
					Anisotropic	2.57957	0.83722	84.5847	0.08887
Zr	3.232	1.5925	6.316	0.5200	Isotropic	–	0.84079	21.3823	0.59309
					Anisotropic	−0.44977	0.83722	21.4452	0.68484

experimentally observed unit cell parameters can attain a stable state under the following conditions:

$$\begin{aligned} U_0(a_0, \eta_0) &= -E_s, \\ \left.\frac{dU_0}{da}\right|_{a_0, \eta_0} &= 0, \\ V_0\left(\left.\frac{d^2U_0}{dV^2}\right)\right|_{a_0, \eta_0} &= B, \\ \left.\frac{dU_0}{d\eta}\right|_{a_0, \eta_0} &= 0, \end{aligned} \tag{2}$$

where $\eta = c/a$ is the ratio of the height c to the edge a of the unit cell; a_0 and η_0 are the experimental values of the parameters a and η for the studied metal, respectively; and $V_0 = (\sqrt{3}/4)\eta_0 a_0^2$ is the atomic volume.

The system of equations (2) takes the simplest form in the case when the interatomic potential φ is isotropic, i.e., when it depends only on the interatomic distance r:

$$\begin{aligned} \sum \varphi(r) &= -2E_s, \\ \sum\left(r\frac{d\varphi}{dr}\right) &= 0, \\ \frac{2\sqrt{3}}{27a_0^3\eta_0}\sum\left(r^2\frac{d^2\varphi(r)}{dr^2}\right) &= B, \\ \sum\left(r\frac{d\varphi}{dr}\right)\left(\frac{1}{r}\frac{dr}{d\eta}\right) &= 0. \end{aligned} \tag{3}$$

The derivatives $(1/r\,dr/d\eta)$ are close to unity for the fourth and seventh coordination shells, i.e., for vectors **r** whose direction coincides very closely with the principal lattice direction. The second and fourth equations of system (3) are satisfied depending on the form of the interatomic potential only for particular ratios η that are close to the ideal value (1.633) but do not necessarily coincide with the experimental values. The construction of the model isotropic interatomic potentials for describing hcp crystals is of undeniable interest, as it makes it possible to ascertain the potentialities of the traditional method and to compare the results obtained with and without considering the anisotropy of interatomic interactions.

The majority of spherically symmetric functions that approximate interatomic interaction potentials (for example, the Born, Born–Mayer, Morse, Dominguez, and Finnis–Sinclair potentials) are two- or three-parameter functions. Consequently, the first three equations of system (3) will suffice to determine the parameters of the interatomic interaction potentials. It should be kept in mind that the lattice can attain a stable state not only at a particular experimental value of η_0. In such a manner, the parameters of the interatomic potentials defined by the Morse function

$$\varphi_M(r) = D\beta\exp^{-\alpha r}(\beta e^{-\alpha r} - 2) \qquad (4)$$

can be determined for a number of metals with a hexagonal lattice. In our calculations, we took into account the bonds of atoms in the first six coordination shells (i.e., 38 bonds). For cubic crystals, approximately the same number of bonds are involved in the first three coordination shells: 42 and 26 bonds in face-centered and body-centered cubic crystals, respectively. The parameters of the interatomic potentials D, α, and β are listed in Table 1.

In order to satisfy all four conditions in system (3) and, hence, to ensure complete stability of the lattice, it is necessary to transform the potential function in such a way that the vector of the interatomic bond will be taken into account in an explicit form. In this case, the potential function should account for the symmetry of the crystal lattice. Since the basal planes have close packing, it can be assumed that the interatomic potential does not depend on the projection of the bond vector onto the basal plane but depends on the polar angle θ between the bond vector and the principal axis of the crystal. Moreover, the magnitude of the interatomic potential should remain unchanged when the bond vector suffers reflection from the principal plane. Therefore, the function describing the interaction of atoms in an hcp crystal can be represented in the form of a radial function $R(r)$ dependent on the polar angle θ. For example,

$$\varphi(\mathbf{r}) = (1 + \xi\cos^2\theta)R(r), \qquad (5)$$

where ξ is the anisotropy parameter. It is obvious that the interatomic potential becomes isotropic at $\xi = 0$.

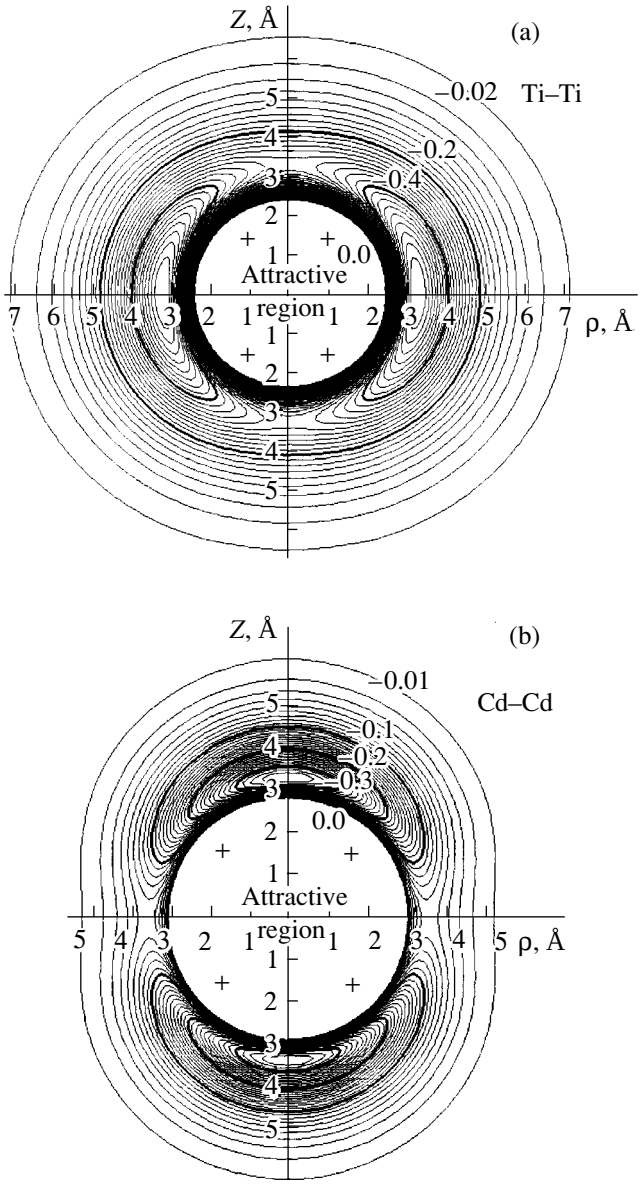

Fig. 1. Contours of the potentials (eV) in the plane through the ⟨0001⟩ direction (the Z axis) and the projection ρ of the bond vector onto the principal plane of (a) titanium and (b) cadmium crystals.

The values of $\cos^2\theta$ are determined only by the coordination shell number and the axial ratio η. If the interatomic potential is defined by function (5), the fourth stability condition in system (2) differs from the fourth equation in system (3) and can be written in the form

$$\sum\left[\xi\frac{d\cos^2\theta}{d\eta}R(r) + (1 + \xi\cos^2\theta) \times\left(\frac{1}{r}\frac{dr}{d\eta}\right)\left(r\frac{dR}{dr}\right)\right] = 0. \qquad (6)$$

Table 2. Experimental elastic moduli and theoretical values calculated from the isotropic and anisotropic interatomic potentials of metals with a hexagonal lattice

Metal	Method of determining the elastic moduli	Elastic moduli, eV/Å^3				
		C_{11}	C_{12}	C_{13}	C_{33}	C_{44}
Be	Experimental	1.824	0.167	0.087	2.100	1.014
	Isotropic	1.0681	0.3437	0.3515	1.4063	0.3423
	Anisotropic	1.3106	0.4369	0.2218	1.2526	0.2296
Cd	Experimental	0.723	0.248	0.253	0.321	0.127
	Isotropic	0.8360	0.2868	0.0134	0.3503	0.0187
	Anisotropic	0.3843	0.1281	0.1459	1.0812	0.1492
Co	Experimental	1.916	1.030	0.643	2.235	0.487
	Isotropic	2.1903	0.7236	0.5521	2.7195	0.5472
	Anisotropic	2.4159	0.8053	0.4521	2.5022	0.4534
Hf	Experimental	1.130	0.482	0.413	1.229	0.348
	Isotropic	1.1546	0.3755	0.3688	1.5896	0.3618
	Anisotropic	1.4235	0.4745	0.2346	1.3891	0.2387
Mg	Experimental	0.373	0.163	0.135	0.385	0.102
	Isotropic	0.4014	0.1326	0.1046	0.5031	0.1037
	Anisotropic	0.4480	0.1493	0.0842	0.4575	0.0845
Re	Experimental	3.823	1.685	1.286	4.262	1.014
	Isotropic	4.1819	1.3827	1.1319	5.2466	1.1234
	Anisotropic	4.7062	1.5687	0.9125	4.6988	0.9144
Ru	Experimental	–	–	–	–	–
	Isotropic	3.3921	1.1134	1.0887	4.6611	1.0757
	Anisotropic	4.1796	1.3932	0.7407	3.9143	0.7455
Sc	Experimental	–	–	–	–	–
	Isotropic	0.4670	0.1511	0.1471	0.6194	0.1437
	Anisotropic	0.5660	0.1887	0.0956	0.5519	0.0980
Tl	Experimental	–	–	–	–	–
	Isotropic	0.3918	0.1288	0.1146	0.5179	0.1132
	Anisotropic	0.4619	0.1540	0.1831	0.4530	0.0835
Ti	Experimental	1.014	0.574	0.431	1.128	0.291
	Isotropic	1.1213	0.3651	0.3507	1.5303	0.3443
	Anisotropic	1.3689	0.4563	0.2279	1.3426	0.2316
Zn	Experimental	1.005	0.213	0.312	0.381	0.239
	Isotropic	0.9831	0.3368	0.0402	0.6122	0.0452
	Anisotropic	0.5732	0.1911	0.1694	1.2593	0.1694
Zr	Experimental	0.895	0.454	0.498	1.029	0.200
	Isotropic	0.8925	0.2894	0.2797	1.1984	0.2736
	Anisotropic	1.0844	0.3615	0.1811	1.0636	0.1851

Here, the radially symmetric function $R(r)$ has the form of Morse function (4). In this case, four parameters of potential (5), namely, ξ, α, β, and D, can be uniquely determined by solving the system of equations (3), provided the fourth equation is replaced by expression (6). Table 1 presents numerical values of the above parameters obtained with allowance made for the bonds involved in the first–sixth coordination shells. The behavior of the anisotropic interatomic potentials is clearly illustrated by the equipotential lines in the plane through the principal axis of the crystal, i.e., the Z axis (see Fig. 1).

For metals with $\eta > 1.633$, the interatomic potential reaches a minimum at $\theta = 0$ or when the bond vectors are directed along the principal axis. For metals with $\eta < 1.633$, the interatomic potential reaches a minimum at $\theta = 90°$ or when the bond vectors are aligned parallel to the basal plane. The anisotropy parameter ξ correlates well with the axial ratio η. Specifically, the anisotropy parameter ξ has negative sign at $\eta < 1.633$ and increases to 5.13 at $\eta = 1.88$ (as is the case with cadmium).

3. ELASTIC MODULI

Let us assume that $\mathbf{r}_0 = (x_0, y_0, z_0)$ is a vector specified by Cartesian coordinates and relating any two points (particles) in an unstrained material and $\mathbf{r} = (x, y, z)$ is a vector relating these points in the material subjected to random elastic strain. The coordinates of the vectors $\mathbf{r}$ and $\mathbf{r}_0$ in strained and unstrained materials are related by the expressions [4–6]

$$\begin{aligned} x &= (1 + e_1)x_0 + \frac{e_6}{2}y_0 + \frac{e_5}{2}z_0, \\ y &= \frac{e_5}{2}x_0 + (1 + e_2)y_0 + \frac{e_4}{2}z_0, \\ z &= \frac{e_5}{2}x_0 + \frac{e_4}{2}y_0 + (1 + e_3)z_0, \end{aligned} \tag{7}$$

where e_1, e_2, e_3, …, e_6 are the components of the strain tensor in the Voight notation. By definition [4, 5], the elastic moduli can be represented in the form

$$C_{mn} = \frac{d^2U}{de_m de_n}, \tag{8}$$

where $m, n = 1, 2, \ldots, 6$; and $U = U_0/V_0$ is the internal energy density. For a hexagonal crystal, there are five independent elastic stiffness constants, namely, C_{11}, C_{12}, C_{13}, C_{33}, and C_{44}. Making allowance for the fact that the argument of the interatomic potential is the interatomic bond vector $\mathbf{r}$, the derivatives of the internal energy density with respect to strains can be determined from relationship (1) for the internal energy U_0; that is,

$$\begin{aligned} \frac{dU}{de_1} &= \frac{1}{2V_0}\sum\frac{d\varphi}{dx}x_0, \\ \frac{dU}{de_2} &= \frac{1}{2V_0}\sum\frac{d\varphi}{dy}y_0, \\ \frac{dU}{de_3} &= \frac{1}{2V_0}\sum\frac{d\varphi}{dz}z_0, \\ \frac{dU}{de_4} &= \frac{1}{2V_0}\sum\left[\frac{d\varphi}{dy}\frac{z_0}{2} + \frac{d\varphi}{dz}\frac{y_0}{2}\right]. \end{aligned} \tag{9}$$

Hereafter, as in the system of equations (3), the summation is taken over all sites of the hcp metal lattice and all the expressions are calculated at equilibrium points of the crystal. Upon differentiating expressions (9) with respect to strains, we derive the following relationships for the elastic moduli:

$$\begin{aligned} C_{11} &= \frac{1}{2V_0}\sum\left(x^2\frac{d^2\varphi}{dx^2}\right), \\ C_{12} &= \frac{1}{2V_0}\sum\left(xy\frac{d^2\varphi}{dxdy}\right), \\ C_{13} &= \frac{1}{2V_0}\sum\left(xz\frac{d^2\varphi}{dxdz}\right), \\ C_{33} &= \frac{1}{2V_0}\sum\left(z^2\frac{d^2\varphi}{dz^2}\right), \\ C_{44} &= \frac{1}{8V_0}\sum\left(z^2\frac{d^2\varphi}{dy^2} + 2yz\frac{d^2\varphi}{dydz} + y^2\frac{d^2\varphi}{dz^2}\right). \end{aligned} \tag{10}$$

By substituting the interatomic potential φ in the form of expression (5) into relationships (10), taking into account that $\cos^2\theta = z^2/r^2$, $dr/dx = x/r$, $dr/dy = y/r$, and $dr/dz = z/r$, and performing the appropriate differentiation, we obtain the following expressions for the elastic moduli in terms of the radial function:

$$\begin{aligned} C_{11} &= \frac{1}{2V_0}\sum\left[\frac{8\xi x^4z^2 - 2\xi x^2z^2r^2}{r^6}R\right. \\ &+ \frac{x^2r^4 - x^4r^2 + \xi x^2z^2r^2 - 5\xi z^2x^4}{r^6}\left(r\frac{dR}{dr}\right) \\ &\left.+ \frac{x^4r^2 + \xi x^4z^2}{r^6}\left(r^2\frac{d^2R}{dr^2}\right)\right], \\ C_{12} &= \frac{1}{2V_0}\sum\left[\frac{8\xi x^2y^2z^2}{r^6}R - \frac{x^2y^2r^2 + 5\xi x^2y^2z^2}{r^6}\left(r\frac{dR}{dr}\right)\right. \\ &\left.+ \frac{x^2y^2r^2 + \xi x^2y^2z^2}{r^6}\left(r^2\frac{d^2R}{dr^2}\right)\right], \\ C_{33} &= \frac{1}{2V_0}\sum\left[\frac{2\xi z^2r^4 - 10\xi\xi z^4r^2 + 8\xi z^6}{r^6}R\right. \\ &+ \frac{z^2r^4 + (5\xi - 1)z^4r^2 - 5\xi z^6}{r^6}\left(r\frac{dR}{dr}\right) \\ &\left.+ \frac{z^4r^2 + \xi z^6}{r^6}\left(r^2\frac{d^2R}{dr}\right)\right], \\ C_{13} &= \frac{1}{2V_0}\sum\left[\frac{8\xi x^2z^4 - 4\xi x^2z^2r^2}{r^6}R\right. \end{aligned} \tag{11}$$

$$+\frac{(2\xi-1)x^2z^2r^2-5\xi x^2z^4}{r^6}\left(r\frac{dR}{dr}\right)$$

$$+\frac{x^2z^2r^2+\xi x^2z^4}{r^6}\left(r^2\frac{d^2R}{dr^2}\right)\Bigg],$$

$$C_{44}$$

$$=\frac{1}{8V_0}\sum\Bigg[\frac{32\xi y^2z^4-18\xi y^2z^2r^2+2\xi y^2r^4-2\xi z^4r^2}{r^6}R$$

$$+\frac{y^2r^4+z^2r^4+(9\xi-4)y^2z^2r^2-20\xi y^2z^4+\xi z^4r^2}{r^6}\left(r\frac{dR}{dr}\right)$$

$$+\frac{4y^2z^2r^2+4\xi y^2z^4}{r^6}\left(r^2\frac{d^2R}{dr^2}\right)\Bigg].$$

It is evident that, in the framework of the isotropic model, the elastic moduli can be obtained by setting $\xi = 0$. For metals with a hexagonal lattice, we calculated the elastic moduli in terms of the models of isotropic and anisotropic interatomic potentials. A comparison of the calculated elastic moduli with available experimental data is given in Table 2. The radial function $R(r)$ was taken as the Morse function with the parameters presented in Table 1. As was done in constructing the interatomic potentials, the elastic moduli were calculated with inclusion of the bonds involved in the first–sixth coordination shells.

It can be seen from Table 1 that, for metals with an axial ratio close to the ideal value, the elastic moduli calculated within the isotropic and anisotropic models are in close agreement with the experimental data. However, for cadmium and zinc, i.e., metals with a large axial ratio, the C_{13} and C_{44} elastic moduli calculated in the framework of the isotropic model are approximately one order of magnitude smaller than the experimental values. In order to overcome this disagreement, the calculated elastic moduli must be corrected for the anisotropy of interatomic interactions. On the other hand, the anisotropic model offers overestimated values of C_{33} for cadmium and zinc. This is not surprising, because, at large ratios η and, hence, at large parameters ξ [see relationship (5)], the role played by the bonds aligned nearly parallel to the Z axis becomes more significant. For beryllium, the ratios between the calculated values of the aforementioned elastic moduli are approximately equal to those for other metals.

However, the experimental values of the elastic moduli exhibit an anomaly. The point is that the elastic moduli C_{11}, C_{33}, and C_{44} slightly exceed the elastic moduli C_{12} and C_{13}. Specifically, the ratio between the experimental values of C_{33} and C_{13} for beryllium is equal to 24.1. This can be explained by the fact that the beryllium electron shells have a complicated configuration, which is ignored in the model.

The difference between the experimental and calculated elastic moduli can be reduced using another, more suitable dependence of the potential function on the vector of the interatomic bond. However, even if the above differences were to be still larger, the construction of the anisotropic interatomic potentials would be justified because of the necessity of modeling extended lattice defects, such as dislocations, shear-type defects, and grain boundaries. In actual fact, the interatomic potentials that are incapable of ensuring stability of the crystal lattice can give rise to an additional relaxation not related to the lattice defects.

4. CONCLUSIONS

Thus, the interatomic potentials obtained in this work ensure the stability of crystal lattices for the majority of hcp metals with respect to their geometric and elastic characteristics and, therefore, can be successfully used for modeling lattice defects. This will make it possible to reveal the specific features of the crystal structure associated with the presence of a particular defect in the lattice.

The proper choice of the potential function is of fundamental importance in describing the elastic properties of crystals. In particular, the model with a potential function in the form of expression (5) provides close agreement between the calculated and experimental elastic moduli even for metals with a large axial ratio η.

ACKNOWLEDGMENTS

This work was supported by MO PD, grant no. 02-1.2-31.

REFERENCES

1. L. A. Girifalco and V. G. Weizer, Phys. Rev. **114**, 687 (1959).
2. E. S. Machlin, Acta Metall. **22**, 9 (1974).
3. V. Vitek and M. Igarashi, Phys. Mag. **63A**, 1059 (1991).
4. C. Kittel, *Introduction to Solid State Physics*, 5th ed. (Wiley, New York, 1976; Nauka, Moscow, 1978).
5. M. P. Shaskol'skaya, *Crystallography* (Vysshaya Shkola, Moscow, 1984).
6. G. Schulze, *Metallphysik* (Academie, Berlin, 1967; Mir, Moscow, 1971).

Translated by O. Borovik-Romanova

Physics of the Solid State, Vol. 46, No. 2, 2004, pp. 219–225. Translated from Fizika Tverdogo Tela, Vol. 46, No. 2, 2004, pp. 218–223.
Original Russian Text Copyright © 2004 by Yakunkin.

METALS AND SUPERCONDUCTORS

Mechanism of High-Temperature Heat Capacity of Tungsten: Study of Relaxation Processes

M. M. Yakunkin

Moscow State Institute of Electronics and Mathematics, Moscow, 109028 Russia

e-mail: Yakunkin@mail.ru

Received May 13, 2003

Abstract—It is experimentally shown that, in addition to fast relaxation, a slow relaxation process controlled by vacancy diffusion contributes to the high-temperature heat capacity C_p of tungsten. To account for the existence of contributions from two relaxation processes to C_p, it is suggested to consider the finite time required for the equilibrium density of transient complexes to set in. © *2004 MAIK "Nauka/Interperiodica".*

1. INTRODUCTION

In a phenomenological model of vacancy diffusion in solids [1, 2], transient complexes (TCs) are introduced on the basis of the Eyring theory of absolute reaction rates. In this model, a vacancy hopping to a new position is preceded by the formation of a TC, i.e., an excited metastable atomic configuration near the vacancy. The problem is whether a TC is a real crystal lattice defect or is introduced artificially as a virtual atomic configuration in order to give the simplest explanation for the observed exponential temperature dependence of the vacancy diffusion coefficient [3].

Although the concept of TCs has been used for a long time in the theories describing atom transitions across a barrier [2, 4], the first reliable confirmation of their existence was obtained in the study of the fast kinetics of chemical reactions in [5]. The possible experimental detection of TCs in the study of diffusion kinetics was discussed in [6]. It was noted that, while the equilibrium density of TCs $N_a^e = N_0\exp(-E_a^f/kT)$ is introduced to describe the process of vacancy migration in the presence of a density gradient, it is also necessary to assume the existence of N_a^e in the absence of a density gradient for vacancy mobility to be nonzero in thermal equilibrium. Thus, if the model developed in [1, 2] adequately describes the real physical process of diffusion, there must be an equilibrium contribution from TCs to the heat capacity C_a^e that varies exponentially with temperature.

In [1], the equilibrium density was assumed to be instantaneously established, so that at any time t it is given by the Boltzmann distribution. In [2], the kinetics of the density N_a^e setting in was described by using the kinetic balance equation with the coefficients Γ_{12} and Γ_{21} equal to the frequencies of formation and dissociation of TCs. Thus the fast relaxation process describing the establishment of the value $N_a^e = \Gamma_{12}/\Gamma_{21}$ with characteristic time $\tau_a = (\Gamma_{12} + \Gamma_{21})^{-1}$ is introduced into the theory; this time is longer than the thermal relaxation time but much shorter than the vacancy relaxation time $\tau_v \sim L^2/D_v$ determined by the diffusion kinetics and depending on the distance L between vacancy sources and drains.

In [6], it was suggested that the fast relaxation process of the establishment of the nonlinear component of the heat capacity C_p^n with $\tau_a \sim 7 \times 10^{-9}$ s at the melting point T_m [7] is related to the kinetics of the establishment of N_a^e and that $C_p^n \approx C_p^a$. Thus one can account for the more than two orders of magnitude disagreement between the equilibrium vacancy densities N_v^e obtained for tungsten by quenching methods [8] and their values found from measurements of C_p^n [9]. However, this interpretation implies that the high-temperature heat capacity of tungsten C_p must exhibit not only fast relaxation but also a slow relaxation associated with the process of establishing the equilibrium vacancy contribution to the heat capacity C_v^e with time $\tau_v(T_m) \sim 10^{-4}$ s [8] characteristic of annealed samples with densities of dislocation sources (drains) of $\sim 10^7$ cm^{-2}.

In this study, we observed and analyzed the contribution from the slow relaxation process to C_p of tungsten. We showed that the thermal and kinetic characteristics of the defects responsible for this process agree (to within experimental error) with those calculated for vacancies in quenched samples. We suggest a method

1063-7834/04/4602-0219$26.00 © 2004 MAIK "Nauka/Interperiodica"

that includes both the "fast" (τ_a) and "slow" (τ_v) relaxation times in the description of the vacancy diffusion kinetics.

2. EXPERIMENTAL

We assume that there is an equilibrium density N_a^e and that the equilibrium TC density setting in is characterized by a short time τ_a, in addition to the long time τ_v characterizing the establishment of the equilibrium vacancy concentration. In this case, the equation of thermal balance for a thin metal wire heated by passing periodic electric current pulses through it has the form

$$\alpha_l\dot{\Theta} + \beta_a\dot{N}_a + \beta_v\dot{N}_v = P(t) - \bar{P}, \qquad (1)$$

where

$$\dot{N}_a = -(N_a - N_a^e)/\tau_a, \quad N_a^e = \bar{N}_a^e + \delta_a\Theta,$$

$$\delta_a = \bar{N}_a^e E_a^f/k\bar{T}^2,$$

$$\dot{N}_v = -(N_v - N_v^e)/\tau_v, \quad N_v^e = \bar{N}_v^e + \delta_v\Theta,$$

$$\delta_v = \bar{N}_v^e E_v^f/k\bar{T}^2,$$

$$\alpha_l = mC_l, \quad \beta_a = mE_a^f, \quad \beta_v = mE_v^f,$$

$$\tau_{a,v} = \tau_0^{a,v}\exp(E_{a,v}^m/k\bar{T}),$$

$$P(t) = \begin{cases} P_0, & 0 \le t \le t_u \\ 0, & t_u \le t \le t_n, \end{cases}$$

$$P(t) = P(t + \nu t_n), \quad \nu = 1, 2, \ldots.$$

Here, subscripts a and v refer to the TCs and vacancies, respectively; $N_{a,v}$ and $N_{a,v}^e$ are the instantaneous and equilibrium vacancy densities at temperature $T(t) = \bar{T} + \Theta(t)$; $E_{a,v}$ and $\bar{N}_{a,v}^e$ are the formation energies of TCs and vacancies and their equilibrium densities at temperature $\bar{T}$; $\Theta(t)$ and $\bar{T}$ are the oscillating and constant components of the temperature; C_l is the lattice component of the heat capacity; $P(t)$, $\bar{P} = \gamma P_0$, and P_0 are the instantaneous, average, and pulse powers dissipated in pulse heating; t_u and t_n are the electric current pulse duration and repetition period; and $\gamma = t_u/t_n$ is the duty factor.

The times τ_v and τ_a in Eq. (1) determine the long- and short-time scales for measurements of the heat capacity C_p; the solution of Eq. (1) essentially depends on the time scale considered. If we neglect relaxation effects, then, by using Eq. (1) for $t \gg \tau_v$ and $(\tau_v, \tau_a) \longrightarrow 0$, we obtain an expression for calculating the equilibrium heat capacity $C_p^e = C_l + C_a^e + C_v^e$ from the measurements using the method of periodic pulse heating [10]. The choice of time scale τ_v ($\tau_a \longrightarrow 0$) corresponds to coarse-grained averaging and transition to the hydrodynamic time scale; in this case, Eq. (1) describes macroscopic processes of the equilibrium vacancy density N_v^e setting in and of the heat capacity varying from $(C_l + C_a^e)$ to C_p^e [6, 11]. Finally, on the short time scale τ_a ($\tau_v \longrightarrow \infty$), the vacancy density is almost equal to the equilibrium density, $N_v \approx \bar{N}_v^e$, and the rate of its variation vanishes. Therefore, by passing in Eq. (1) to the short time scale, we can study the microscopic process of the variation of C_p from C_l to $(C_l + C_a^e)$ related to the kinetics of the density N_a^e setting in.

In this situation, the measured value of C_p depends on the time scale chosen in the experiment and the possibility of observation of the relaxation process depends on the relation between its scale τ_a or τ_v and the time characteristics of the heating process t_u and t_n. The main difficulty in such studies is that it is necessary to use two different oscillation frequencies of temperature $\Theta(t)$ (differing by several orders of magnitude) and to measure small values of $C_{a,v}(t)$ against a large constant contribution C_l. However, since a single relaxation process corresponds to each of the time scales, the kinetics of the equilibrium values $C_{a,v}^e$ setting in can be studied using the method suggested in [6].

In this method, we choose a time interval (t_u, t_n) whose ends correspond to different time scales and use the dual character of the method of periodic pulse heating in the experiment. Indeed, in a single measurement, we can obtain heat capacity values that depend on the pulse duration, $C_p(t_u)$, and on the pulse repetition rate, $C_p(\omega)$ ($\omega = 2\pi/t_n$), and their relative difference $\delta C_{a,v} = [C_p(\omega) - C_p(t_u)]/C_p(\omega) = 1 - A\Theta_a^1/\Theta_a$ related to the contribution from relaxation effects to C_p. Here, $A = \pi^2\gamma(1 - \gamma)/\sin\pi\gamma$ and Θ_a^1 and Θ_a are the first-harmonic amplitude and the amplitude of oscillations in temperature $\Theta(t)$, respectively. From the $\delta C_{a,v}(T)$ dependence thus obtained and Eqs. (1), we calculate the temperature dependence of the defect relaxation time $\tau_{a,v}$ and the equilibrium defect contributions to the heat capacity $C_{a,v}^e = (E_{a,v}^{f2}/kT^2)N_{a,v}^e$.

The scheme of our experimental setup is similar to that described in [6]. For computer-aided measurements, the setup was designed as a chip programmable module; the data from the module, namely, the values

$\Theta(t_i)$ $(1 \le i \le 4096)$ over the period t_n, were converted by the input–output controller and then transmitted through the parallel port of a personal computer. The computer calculated the values $\delta C_{a,v}$, $\tau_{a,v}$, and $C^e_{a,v}$, as well as visualized the measurement results and controlled the programmable module.

The measurements were performed in vacuum at a pressure of 2×10^{-8} Torr on wire samples (diameter 25 μm, length 100 mm, $\rho(273\text{ K})/\rho(4.2\text{ K}) = (2.2\text{–}2.8) \times 10^3$) in the temperature range 2000–3420 K. The time interval was taken to be $(t_u, t_n) = (10^{-3}\text{ s}, 10^{-2}\text{ s})$ in accordance with the data on the vacancy relaxation time in tungsten [8]. The relative error in measuring δC_v was determined by the error in the measurement of the ratio Θ^1_a/Θ_a and did not exceed 0.1%, which is almost an order of magnitude smaller than the contribution from quenched vacancies to the heat capacity near T_m. To make the experiment complete, we reproduced the results of the studies of the contribution from the fast relaxation process to C_p for tungsten [6] with $(t_u, t_n) = (0.8 \times 10^{-6}\text{ s}, 10^{-4}\text{ s})$. The results of the experiment are shown in the figure.

From the figure it is seen that two relaxation effects with characteristic times $\tau_a = (1.2 \times 10^{-16}\text{ s}) \times \exp(5.4\text{ eV}/kT)$ and $\tau_v = (1.82 \times 10^{-6}\text{ s})\exp(1.84\text{ eV}/kT)$ contribute to the high-temperature heat capacity of tungsten; near T_m, these relaxation times differ by five orders of magnitude. The equilibrium contribution to the heat capacity coming from the defects responsible for the slow relaxation effect is $C^e_v = (4.82 \times 10^8\text{ J/g K})T^{-2} \exp(-2.82\text{ eV}/kT)$, and the relaxation time is $\tau_v(T_m) \sim 6 \times 10^{-4}$ s; these values are characteristic of vacancies [8]. The ratio C^e_v/C_p at temperature T_m does not exceed 2%. Therefore, the anomalous increase in the high-temperature heat capacity C^n_p is mainly due to defects characterized by fast relaxation, whose contribution to the heat capacity is $C^e_a = (1.02 \times 10^{10}\text{ J/g K})T^{-2} \exp(-2.77\text{ eV}/kT)$. Without going into the possible reasons for the difference between the experimental values of E^f_a and E^m_v, we note that the obtained values of the formation energies E^f_a and E^f_v agree with the existing concepts [3, 12]; namely, their sum is close to the activation energy for self-diffusion in tungsten [13] and the formation energies themselves almost coincide.

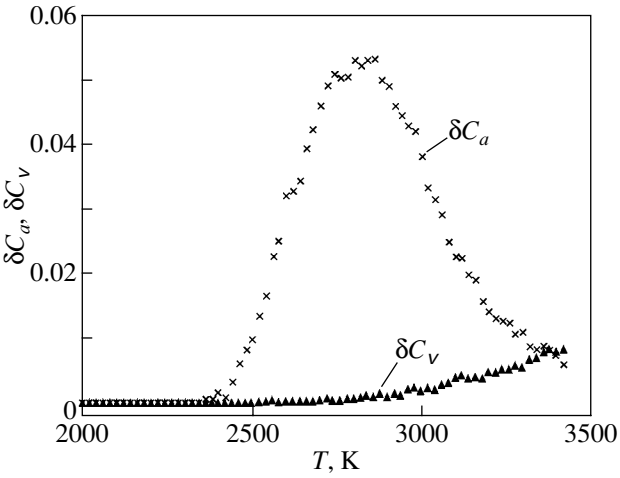

Temperature dependence of the relative change in heat capacity δC_a for $(t_u, t_n) = (0.8 \times 10^{-6}\text{ s}, 10^{-4}\text{ s})$ and δC_v for $(t_u, t_n) = (10^{-3}\text{ s}, 10^{-2}\text{ s})$.

3. THEORY

The above explanation of the contribution from relaxation effects to C_p involves the problem that the fast kinetics of N^e_a setting in should be included in the description of transport, i.e., that the short time τ_a scale must be taken into account in the diffusion equation. The inclusion of different time scales is inconsistent with the well-known procedure for deriving differential-balance equations [14]; indeed, according to this procedure, fast fluctuations are averaged over the hydrodynamic scale and, therefore, are eliminated. However, this procedure is frequently used in constructing models in which the terms describing a small-scale process are kept when passing to the hydrodynamic approximation [15, 16]. A typical example is the inclusion of the "fast" time τ controlling the establishment of the Chapman–Enskog regime in the kinetic theory of gases [17].

In our approach, a uniform distribution of vacancies in the crystal is established due to the fluctuation process of a redistribution of atoms between the ground and metastable states. Obviously, if the process of establishing the equilibrium value N^e_a is inertial, then there will always be a lag between the instantaneous density $N_a(t)$ of diffusing vacancies and their equilibrium density. We can establish the relation between the two phenomena, namely, the diffusion of vacancies [characterized by $N_v(t)$] and the fast kinetics of atomic transitions between the two states, by considering them as a unified fluctuation–dissipation process. However, a quantitative first-principles description of this process in solids encounters well-known difficulties [18]. Therefore, to simplify the derivation of analytical expressions describing the transition of the densities $N_a(t)$ and $N_v(t)$ to their equilibrium values, we consider a semiphenomenological model.

To construct the model, we first derive a well-known result by using the expression for the flux

$$J = -D_v dn_v/dx, \quad D_v = \lambda^2 \nu N_a, \quad \nu = kT/h, \quad (2)$$

where, in accordance with the experimental results, we replace the equilibrium TC density N_a^e by the instantaneous density $N_a(t)$. Using Eq. (2), the expression for $N_a = N_2/N_1$ [2] determined by the equation of kinetic balance

$$\dot{\mathbf{N}} = \mathbf{\Gamma N}, \quad \mathbf{\Gamma} = \begin{pmatrix} -\Gamma_{12} & \Gamma_{21} \\ \Gamma_{12} & -\Gamma_{21} \end{pmatrix}, \quad \mathbf{N} = \begin{pmatrix} N_1(t) \\ N_2(t) \end{pmatrix}, \quad (3)$$

and the obvious relation $N_a \ll 1$, we find

$$\tau_a \dot{J} + J = -D_v^e dn_v/dx, \quad D_v^e = \lambda^2 \nu N_a^e. \quad (4)$$

The continuity equation for Eq. (4) gives

$$\hat{L} n_v = 0,$$
$$\hat{L} = \tau_a \partial^2/\partial t^2 + \partial/\partial t - D_v^e \partial^2/\partial x^2, \quad n_v = n_v(t, x). \quad (5)$$

Here, n_v is the instantaneous vacancy density, N_1 and N_2 are the numbers of atoms in the ground and metastable states, D_v and D_v^e are the vacancy diffusion coefficients corresponding to the instantaneous and equilibrium TC densities, ν is the vibration frequency for atoms in the ground state, and λ is the hop distance.

This type of modification of the diffusion equation (and of the thermal conductivity equation) has been studied in detail in the mathematical and physical literature. Apparently, this modification was first applied to describe diffusion processes in [19]. Its probabilistic interpretation is given in [20]. In [21], this modification was applied to study transport in locally nonequilibrium systems. The possibility of introducing the inertial term $\tau_a \dot{J}$ in the equations of nonequilibrium thermodynamics was discussed in [22]. We can only add that the equation itself implies no conservation law that would determine the character of its solutions (see Appendix 1). The conservation law must be introduced on the basis of other independent physical reasons.

We note that the absence of a conservation law is due to the fact that Eq. (5) takes into account two different time scales. Indeed, this equation permits factorization; namely, the operator $\hat{L}$ can be represented as the product of two differential operators,

$$\hat{L} = \hat{L}_- \hat{L}_+,$$
$$\hat{L}_\mp = \partial/\partial t + \frac{1}{2\tau_a}(I \mp \sqrt{I + 4D_v^e \tau_a \partial^2/\partial x^2}) \quad (6)$$

(here, I is the unity operator). The operators in Eq. (6) correspond to fast and slow relaxation processes with the parameters τ_a and τ_v defining the time scales.

The equation $\hat{L}_- n_v = 0$ describes a slow relaxation process on a hydrodynamic time scale and reduces to the classical diffusion equation as $\tau_a \longrightarrow 0$. It is the solution of this equation $n_v^-(t, x)$ (expressed in terms of a Bessel function) that is cited in most relevant papers and is considered a solution to Eq. (5).

For this reason, the equation $\hat{L}_+ n_v = 0$, which is in no way related to the diffusion process (the evolution of its solutions is determined by the time τ_a), has not been considered earlier. Since the differential operators $\hat{L}_-$ and $\hat{L}_+$ appear symmetrically in expression (6) for the operator $\hat{L}$, one cannot exclude this equation simply by setting $\tau_a \longrightarrow 0$. It is this equation that results in the loss of the conservation law in Eq. (5).

If we ignore this fact, then the departure from the classical description allows us to explain the existence of two contributions from relaxation processes to the heat capacity C_p of tungsten in the simplest way. However, the operators $\hat{L}_\mp$ act on the same function $n_v(t, x)$. In other words, in the framework of this approach, vacancies would have different kinetic parameters and their contributions to the heat capacity would differ by almost two orders of magnitude, depending on the experimental time scales τ_a and τ_v. This is in poor agreement with the existing concepts related to the properties of point defects in crystals [3].

We separate the fast relaxation process from slow diffusion by separating the two time scales in Eq. (5). To this aim, we pass from the integral equation (3) to the differential equation of kinetic balance for a two-component vector function **n,**

$$\mathbf{n} = \begin{pmatrix} n_1(t, x) \\ n_2(t, x) \end{pmatrix}, \quad N_{1,2}(t) = \int_{-\infty}^{+\infty} n_{1,2}(t, x) dx,$$

chosen such that each component of this solution satisfies the initial equation (5). As a constraint relating n_1 and n_2, we choose the conservation law determined by Eq. (3):

$$N = N_1(t) + N_2(t)$$
$$= \int_{-\infty}^{+\infty} (n_1(t, x) + n_2(t, x)) dx, \quad \dot{N} = 0. \quad (7)$$

If we consider only matrix coefficients with real elements, then the equation for the vector function **n** will be

$$\partial \mathbf{n}/\partial t + \partial(\mathbf{V}\mathbf{n})/\partial x = \mathbf{\Gamma}\mathbf{n}, \quad (8)$$

where

$$\mathbf{V} = \lambda\left(\frac{\nu\Gamma_{12}}{2\Gamma_{21}}\frac{\Gamma_{12}+\Gamma_{21}}{\Gamma_{12}^2+\Gamma_{21}^2}\right)^{1/2}\begin{pmatrix} -\Gamma_{12}-\Gamma_{21} & -\Gamma_{12}+\Gamma_{21} \\ -\Gamma_{12}+\Gamma_{21} & \Gamma_{12}+\Gamma_{21}\end{pmatrix}.$$

In this equation, the velocity matrix operator **V** has eigenvalues $V_a = \pm(D_v^e/\tau_a)^{1/2}$. Since Eq. (8) is invariant under the group of linear orthogonal transformations, these eigenvalues determine the limiting relaxation rate of spatial inhomogeneities in the system. The matrix **Γ** of the source **Γn** is defined in Eq. (3). It guarantees the validity of the conservation law (7) in Eq. (8).

Equation (8) describes the evolution of the vector function **n** (the distribution of atoms in the ground and metastable states) to the equilibrium distribution $\mathbf{n}^e$. At times $t \gg \tau_a$, the ratio of the solution components tends to the constant $n_2^e/n_1^e = \Gamma_{12}/\Gamma_{21}$, which is equal to $N_a^e = \exp(-\Delta F_a/kT)$. From the first-order equation for the vector function **n**, we obtain second-order equations for the components n_1 and n_2:

$$\hat{L}n_{1,2} = 0, \quad \hat{L} = -\partial^2/\partial t^2 + \mathrm{Sp}\,\mathbf{\Gamma}\partial/\partial t - \mathrm{Det}\,\mathbf{V}\partial^2/\partial x^2.$$

By comparing this equation with Eq. (5), we obtain a relation between the coefficients $\tau_a = -(\mathrm{Tr}\mathbf{\Gamma})^{-1}$ and $D_v^e = (\mathrm{Det}\mathbf{V}/\mathrm{Tr}\mathbf{\Gamma})$. According to the above assumptions, Eq. (8) describes the fast kinetics of the equilibrium TC density setting in with characteristic time $\tau_a = (\Gamma_{12}+\Gamma_{21})^{-1}$ (and the corresponding contribution to C_p of tungsten).

To introduce the hydrodynamic scale and describe the contribution of the slow relaxation process to C_p, it is convenient to consider Eq. (8) as a system with two basic states using a vector analogy [23]:

$$\partial \mathbf{n}/\partial t = \hat{\mathbf{H}}\mathbf{n}, \quad \hat{\mathbf{H}} = \mathbf{\Gamma} - \mathbf{V}\partial/\partial x. \quad (9)$$

This approach is based on the fact that, when we pass to Eq. (8), we represent the crystal (for the process considered) as a two-level nondegenerate system in contact with a heat bath that induces transitions between the levels.

In such an approach, the off-diagonal elements $\hat{H}_{ij}(\partial/\partial x)$ $(i \neq j)$ of the matrix operator $\hat{\mathbf{H}}$ describe atomic transitions between the ground state $\langle 1|$ and the metastable state $\langle 2|$ and the fast process involves a superposition state $\langle n| = n_1\langle 1| + n_2\langle 2|$ in which the densities $n_{1,2}(t, x)$ have the meaning of the probability densities of finding atoms in different states. The total probability of finding an atom in at least one of the basic states is determined by the conservation law (7) and (after normalization $N = 1$) is equal to unity.

An analog of the hydrodynamic approximation is obtained when we pass over to a new system of basic states $\langle \mathrm{I}|$ and $\langle \mathrm{II}|$ and to a new state vector $\langle n_v| = n_v^-\langle \mathrm{I}| + n_v^+\langle \mathrm{II}|$ such that the matrix operator $\hat{\mathbf{H}}$ is diagonal with respect to these states. To this end, we perform a canonical transformation $\hat{\mathbf{H}} = \mathbf{T}\hat{\mathbf{L}}\mathbf{T}^{-1}$ in system (9) (with **T** being a unitary matrix) and arrive at the following equation for stationary states:

$$\frac{\partial \mathbf{n}_v}{\partial t} = \hat{\mathbf{L}}\mathbf{n}_v, \quad \mathbf{n}_v = \begin{pmatrix} n_v^-(t, x) \\ n_v^+(t, x)\end{pmatrix}, \quad \hat{\mathbf{L}} = \begin{pmatrix} \hat{L}_- & 0 \\ 0 & \hat{L}_+\end{pmatrix}. \quad (10)$$

Here, $\mathbf{n}_v = \mathbf{T}^{-1}\mathbf{n}$ and the operators $\hat{L}_\mp$ are defined by Eq. (6). The operator $\hat{\mathbf{L}}$ acts on the vector function $\mathbf{n}_v$, whose components $n_v^\mp(t, x)$, according to Eq. (5), are the vacancy densities or (for the state vector $\langle n_v|$) the probability densities of finding a vacancy in the stationary state $\langle \mathrm{I}|$ or $\langle \mathrm{II}|$.

We see that for system (10) the parts of the solution to Eq. (5) that are invariant (n_v^-) and noninvariant (n_v^+) in time appear to refer to different stationary states. However, the probability of finding a vacancy in a stationary state must be time-independent. Therefore, even without performing any calculations, we can state that the state vector $\langle n_v|$ coincides with the basis state vector $\langle \mathrm{I}|$ and that the probability of finding a vacancy in this state is unity (see Appendix 2). For the new system, the operator $\hat{L}_+$, which produces the violation of the conservation law in Eq. (5), is eliminated and the relaxation process controlled by vacancy diffusion is described by the equation $\hat{L}_- n_v = 0$ alone.

4. CONCLUSIONS

Thus, we have established that the high-temperature heat capacity of tungsten contains contributions from two relaxation processes whose characteristic times differ by almost five orders of magnitude at the melting temperature. The slow relaxation process describes the kinetics of the equilibrium vacancy density setting in through diffusion in the sample. To explain the existence of the fast relaxation process, we have taken into account the finite time of formation and decay of TCs. We have shown that both effects can be described as a unified fluctuation–dissipation process in terms of a single kinetic equation for a two-component vector function.

APPENDIX 1

Taking the Fourier transform of Eq. (5) with respect to the variable x, we obtain

$$\hat{n}_v(t, \zeta) = \hat{n}_v^-(t, \zeta) + \hat{n}_v^+(t, \zeta),$$

$$\hat{n}_v^\mp(t, \zeta) = N_v^\mp(\zeta)\exp[-t(1 \mp \varphi)],$$

$$\varphi = \sqrt{1-\zeta^2}, \quad D_v^e = \tau_a = 1/2.$$

It follows that the total vacancy density, expressed in terms of the Fourier transform of the solution for $\zeta = 0$, is

$$N_v = \int_{-\infty}^{+\infty} n_v(t, x)dx = \hat{n}_v(t, 0)$$
$$= N_v^-(0) + N_v^+(0)\exp(-2t),$$
$$\dot{N}_v \neq 0,$$

i.e., the total density of the diffusing component is not conserved. For physical reasons, we cannot ignore the solution $\hat{n}_v^+(t, \zeta)$: both solutions $\hat{n}_v^\mp(t, \zeta)$ are bounded and behave similarly to $\zeta \longrightarrow \pm\infty$.

In this respect, there is a distinction between the solutions to Eq. (5) and the solutions to the related system

$$\frac{\partial}{\partial t}\begin{pmatrix} J \\ n_v \end{pmatrix} = \begin{pmatrix} 0 & -D_v^e/\tau_a \\ -1 & 0 \end{pmatrix}\frac{\partial}{\partial x}\begin{pmatrix} J \\ n_v \end{pmatrix}$$
$$+\begin{pmatrix} -1/\tau_a & 0 \\ 0 & 0 \end{pmatrix}\begin{pmatrix} J \\ n_v \end{pmatrix},$$

which includes the continuity equation and Eq. (4) for the flux. The Fourier transform of the component n_v of the solution is $\hat{n}_v = \hat{n}_v^-(t, \zeta)$. Therefore, $\dot{\hat{n}}_v^-(t, 0) = \dot{N}_v^- = 0$; i.e., in contrast to Eq. (5), the conservation law is valid. Note that, to within a dimensional factor, we have $\hat{J} = \hat{n}_v^+(t, \zeta)$ and, therefore, $J \propto \exp(-t/\tau_a)$. Thus, on the hydrodynamic scale $t \sim \tau_v \gg \tau_a$, the flux vanishes for any external conditions.

APPENDIX 2

By expressing the probabilities $N_{1,2}$ and $N_v^\mp$ of finding an atom in the basis states $\langle 1|$, $\langle 2|$ and $\langle \mathrm{I}|$, $\langle \mathrm{II}|$, respectively, through the Fourier transforms of the probability densities $N_{1,2}(t) = \hat{n}_{1,2}(t, 0)$ and $N_v^\mp(t) = \hat{n}_v^\mp(t, 0)$, we establish the relation between the probability vector functions $\mathbf{N}$ and $\mathbf{N}_v$ for the states $\langle n|$ and $\langle n_v|$:

$$\mathbf{N} = \exp(\mathbf{\Gamma}t)\mathbf{N}_0 = \mathbf{P}(\exp\mathbf{R}t)(\mathbf{P}^{-1}\mathbf{N}_0) = \mathbf{P}(\exp\mathbf{R}t)\mathbf{N}_v^0.$$

Here, $\mathbf{N}_0$ and $\mathbf{N}_v^0$ are the initial values of the vector functions $\mathbf{N}$ and $\mathbf{N}_v$, respectively; $\mathbf{R}$ is the diagonal form of the matrix $\mathbf{\Gamma}$; and $\mathbf{P}$ and $\mathbf{P}^{-1}$ are the eigenvector matrix and its inverse.

Now we can express the vector function $\mathbf{N}$ in terms of the probabilities $N_v^\mp$ of finding a vacancy in the stationary basis states $\langle \mathrm{I}|$ and $\langle \mathrm{II}|$:

$$\mathbf{N} = \begin{pmatrix} N_1(t) \\ N_2(t) \end{pmatrix} = \begin{pmatrix} \Gamma_{21}\tau_a N_v^-(0) + N_v^+(0)\exp(-t/\tau_a) \\ \Gamma_{12}\tau_a N_v^-(0) - N_v^+(0)\exp(-t/\tau_a) \end{pmatrix}.$$

Using Eq. (7), we obtain the desired result:

$$N_1(t) + N_2(t) = N_v^- = \int_{-\infty}^{\infty} n_v^-(t, x)dx = 1.$$

We see that, in contrast to Eq. (5), the solution $n_v^+(t, x)$ does not manifest itself in system (10); this solution does not contribute to the conservation law, and the probability of finding a vacancy in state $\langle \mathrm{II}|$ of this solution is equal to zero.

REFERENCES

1. G. H. Vineyard, J. Phys. Chem. Solids **3** (2), 121 (1957).
2. P. Haggi, J. Stat. Phys. **42** (1/2), 105 (1986).
3. A. C. Damask and G. J. Dienes, *Point Defects in Metals* (Gordon and Breach, New York, 1963; Mir, Moscow, 1966).
4. P. Hanggi, P. Talkner, and M. Borcovec, Rev. Mod. Phys. **62** (2), 251 (1990).
5. M. Gruebele and A. H. Zewail, Phys. Today **33** (5), 24 (1990).
6. M. M. Yakunkin, Fiz. Tverd. Tela (Leningrad) **33** (9), 2682 (1991) [Sov. Phys. Solid State **33**, 1515 (1991)].
7. Ya. A. Kraftmakher, Fiz. Tverd. Tela (Leningrad) **27** (1), 235 (1985) [Sov. Phys. Solid State **27**, 141 (1985)].
8. Bu K.-D. Rasch, R. W. Siegel, and G. Schultz, Philos. Mag. A **41** (1), 91 (1980).
9. Ya. A. Kraftmakher and P. G. Strelkov, Fiz. Tverd. Tela (Leningrad) **4** (8), 2271 (1962) [Sov. Phys. Solid State **4**, 1662 (1962)].
10. M. M. Yakunkin, Teplofiz. Vys. Temp. **21** (6), 1115 (1983).
11. J. van den Sype, Phys. Status Solidi **39** (2), 659 (1970).
12. B. S. Bokshteĭn, S. Z. Bokshteĭn, and A. A. Zhukhovitskiĭ, *Thermodynamics and Kinetics of Diffusion in Solids* (Metallurgiya, Moscow, 1974).
13. W. Danneberg, Metall (Heidelberg) **15** (4), 977 (1961).

14. K. P. Gurov, *Phenomenological Thermodynamics of Irreversible Processes* (Nauka, Moscow, 1978).
15. R. A. Guyer and J. A. Krumhansl, Phys. Rev. B **148** (3), 778 (1966).
16. D. D. Joseph and L. Preziosi, Rev. Mod. Phys. **61** (1), 41 (1989); Rev. Mod. Phys. **62** (2), 375 (1990).
17. S. Chapman and T. G. Cowling, *Mathematical Theory of Non-Uniform Gases*, 2nd ed. (Cambridge Univ. Press, Cambridge, 1952; Inostrannaya Literatura, Moscow, 1961).
18. R. Balescu, *Equilibrium and Non-Equilibrium Statistical Mechanics* (Wiley, New York, 1975; Mir, Moscow, 1978), Vol. 2.
19. V. A. Fok, Tr. Gos. Opt. Inst. **4** (34), 1 (1920).
20. M. Kac, *Some Stochastic Problems in Physics and Mathematics* (Magnolia Petrolium Co., Dallas, Texas, 1956; Nauka, Moscow, 1967).
21. S. V. Sobolev, Usp. Fiz. Nauk **161** (3), 5 (1991) [Sov. Phys. Usp. **34**, 217 (1991)].
22. L. Onsager and S. Machlup, Phys. Rev. **91** (6), 1512 (1953); D. Jou, J. Casas-Vazquez, and G. Lebon, Rep. Prog. Phys. **51** (8), 1105 (1988).
23. R. P. Feynman, R. B. Leighton, and M. Sands, *The Feynman Lectures on Physics* (Addison-Wesley, Reading, Mass., 1964; Mir, Moscow, 1966), Vol. 8.

Translated by I. Zvyagin

Physics of the Solid State, Vol. 46, No. 2, 2004, pp. 226–230. Translated from Fizika Tverdogo Tela, Vol. 46, No. 2, 2004, pp. 224–227.
Original Russian Text Copyright © 2004 by Kochelaev, Safina.

METALS AND SUPERCONDUCTORS

Electron-Bottleneck Mode for Paramagnetic Impurities in Metals in the Case of Anisotropic Exchange Interaction

B. I. Kochelaev and A. M. Safina

Kazan State University, Kremlevskaya ul. 18, Kazan, 420008 Tatarstan, Russia

e-mail: boris.kochelaev@ksu.ru, alsu.safina@ksu.ru

Received June 5, 2003

Abstract—Equations of the Bloch–Hasegawa type are derived in the case of anisotropic exchange interaction between the subsystems of the magnetic moments of paramagnetic impurities and conduction electrons under conditions of their collective motion. Expressions describing the effective linewidth of electron paramagnetic resonance and the effective g factor are obtained. © *2004 MAIK "Nauka/Interperiodica".*

1. INTRODUCTION

Electron paramagnetic resonance (EPR) of paramagnetic impurities in normal metals and superconductors has been investigated in a large number of experimental and theoretical works (see, for example, the reviews by Barnes [1] and Alekseevskii *et al.* [2]). Paramagnetic impurities are often used as probes in examining the characteristics of conduction electrons. Exchange interaction is the main interaction between conduction electrons and paramagnetic impurities. For a crystal with axial symmetry, the exchange interaction between paramagnetic impurities and conduction electrons can be represented in the form

$$H_{\text{ex}} = \sum_i \{J_\perp[S_i^x\sigma^x(\mathbf{r}_i) + S_i^y\sigma^y(\mathbf{r}_i)] + J_\parallel S_i^z\sigma^z(\mathbf{r}_i)\}, \quad (1)$$

where $\mathbf{S}_i$ is the spin operator of the ith paramagnetic impurity, $\sigma(\mathbf{r}_i)/2$ is the spin-density operator of conduction electrons, and $J_\parallel$ and $J_\perp$ are the exchange interaction parameters. If the exchange interaction and the concentration of paramagnetic impurities are sufficiently small, the spin system of conduction electrons is in equilibrium with the lattice (as a rule, the spin–lattice relaxation rate $\Gamma_{\sigma L}$ of conduction electrons is determined by their spin–orbit scattering by different lattice defects and phonons). In this case, the EPR linewidth of paramagnetic impurities is governed by the Korringa relaxation rate $\Gamma_{s\sigma}$ due to the exchange interaction described by expression (1), because the spin–lattice relaxation rate Γ_{sL} of magnetic impurities in metals is negligible.

If the interaction between the subsystems is strong and the Zeeman frequencies ω_s and ω_σ are close in magnitude, that is,

$$\Gamma_{s,\sigma}, \Gamma_{\sigma s} \gg \Gamma_{\sigma L}, \Gamma_{sL}, |\omega_s - \omega_\sigma|, \quad (2)$$

the subsystems of the conduction electrons and localized magnetic moments are coupled and relax toward nonmagnetic degrees of freedom together. In relationship (2), $\Gamma_{\sigma s}$ is the rate of spin relaxation of conduction electrons toward the localized moments. This effect is referred to as the electron bottleneck (bottleneck mode).

The isotropic exchange interaction in normal metals has been studied in sufficient detail and described thoroughly, for example, in review [1]. Here, we present only the main results.

In the isotropic case, the motion of the transverse components of magnetization can be described by the following equations [1]:

$$\begin{aligned}\dot{\mathbf{M}}_s &= g_s\mu_B\mathbf{M}_s\times(\mathbf{H}_{\text{ext}} + \lambda\mathbf{M}_\sigma) - (\Gamma_{s\sigma} + \Gamma_{sL})\delta\mathbf{M}_s \\ &\quad + \left(\frac{g_s}{g_\sigma}\Gamma_{\sigma s}\right)\delta\mathbf{M}_\sigma, \\ \dot{\mathbf{M}}_\sigma &= g_\sigma\mu_B\mathbf{M}_\sigma\times(\mathbf{H}_{\text{ext}} + \lambda\mathbf{M}_s) - (\Gamma_{\sigma s} + \Gamma_{\sigma L})\delta\mathbf{M}_\sigma \\ &\quad + \left(\frac{g_\sigma}{g_s}\Gamma_{s\sigma}\right)\delta\mathbf{M}_s,\end{aligned} \quad (3)$$

$$\begin{aligned}\delta\mathbf{M}_s &= [\mathbf{M}_s - \chi_s^0(\mathbf{H}_{\text{ext}} + \lambda\mathbf{M}_\sigma)], \\ \delta\mathbf{M}_\sigma &= [\mathbf{M}_\sigma - \chi_\sigma^0(\mathbf{H}_{\text{ext}} + \lambda\mathbf{M}_s)],\end{aligned} \quad (4)$$

where $\mathbf{M}_s$ and $\mathbf{M}_\sigma$ are the magnetizations of the localized magnetic moments and conduction electrons, respectively; $\mathbf{H}_{\text{ext}}$ is the total external magnetic field; λ is the constant of the molecular field; χ_s^0 and χ_σ^0 are the static susceptibilities of the noninteracting localized magnetic moments and conduction electrons, respectively; and g_s and g_σ are the g factors of the noninteract-

ing localized magnetic moments and conduction electrons, respectively. In the molecular field approximation, we have

$$\chi_\sigma^0 = \frac{1}{2}(g_\sigma\mu_B)^2\rho_F, \quad \chi_s^0 = \frac{n}{3k_BT}S(S+1)(g_s\mu_B)^2, \quad (5)$$

$$\lambda = \frac{2J}{g_s g_\sigma \mu_B^2}, \quad (6)$$

where ρ_F is the density of states of conduction electrons at the Fermi level, k_B is the Boltzmann constant, μ_B is the Bohr magneton, and S and n are the spin and the concentration of localized magnetic moments, respectively.

It follows from these equations that, in the electron-bottleneck mode, there should appear a single EPR line with an effective g factor and an effective linewidth, which are determined by the expressions

$$g_{\text{eff}} \cong \left(\frac{\chi_s g_s + \chi_\sigma g_\sigma}{\chi_s + \chi_\sigma}\right), \quad (7)$$

$$\Gamma_{\text{eff}} \cong \left(\frac{\chi_s^0\Gamma_{sL} + \chi_\sigma^0\Gamma_{\sigma L}}{\chi_s + \chi_\sigma}\right). \quad (8)$$

Here, the renormalized susceptibilities χ_σ and χ_s are defined as follows:

$$\chi_\sigma = \chi_\sigma^0(1+\lambda\chi_s), \quad \chi_s = \chi_s^0(1+\lambda\chi_\sigma). \quad (9)$$

It should be emphasized that the rates of relaxation of the localized magnetic moments toward the conduction electrons and in the opposite direction satisfy the relationship of detailed balance:

$$\frac{1}{g_s^2}\chi_s^0\Gamma_{s\sigma} = \frac{1}{g_\sigma^2}\chi_\sigma^0\Gamma_{\sigma s}. \quad (10)$$

Here, the Korringa relaxation rate $\Gamma_{s\sigma}$ is determined by the following expression:

$$\Gamma_{s\sigma} = \frac{4\pi}{\hbar}(\rho_F J)^2 k_B T. \quad (11)$$

It can be seen that the isotropic exchange interaction does not contribute to the linewidth, because the total spin of the two spin subsystems commutes with the Hamiltonian.

When the exchange interaction is anisotropic in character, this contribution should appear even though the exchange interaction parameters $J_\parallel$ and $J_\perp$ differ insignificantly; that is,

$$|J_\parallel - J_\perp| \ll J_\perp. \quad (12)$$

In this case, the total spin does not commute with Hamiltonian (1) and there should appear terms containing $\Gamma_{s\sigma}$ and $\Gamma_{\sigma s}$, which, with allowance made for inequalities (2) and large values of $J_\parallel$ and $J_\perp$ can substantially affect the spin kinetics of the system. A preliminary treatment of this problem is presented in [3].

2. BLOCH–HASEGAWA EQUATIONS FOR ANISOTROPIC EXCHANGE INTERACTION

Let us consider in detail the case where a constant magnetic field is directed along the symmetry axis of a crystal. The Hamiltonian of the system of interacting spins and conductivity electrons can be represented in the form

$$\begin{aligned} H(t) &= H_z + H_{\text{ex}} + H_{\sigma L} + H_t + H_L, \\ H_z &= -(M_s^z + M_\sigma^z)H_0, \\ M_s^z &= g_{s\parallel}\mu_B\sum_k S_k^z, \quad M_\sigma^z = g_{\sigma\parallel}\mu_B\sum_k \frac{1}{2}\sigma_i^z, \\ H_t &= -\frac{1}{2}h\{(M_s^+ + M_\sigma^+)\exp(-i\omega t) \\ &\quad + (M_s^- + M_\sigma^-)\exp(i\omega t)\}, \end{aligned} \quad (13)$$

where H_z is the Hamiltonian of the system of noninteracting localized spins and conduction electrons in a static magnetic field H_0, H_{ex} is the Hamiltonian of interaction of the subsystems of the localized magnetic moments and conduction electrons [relationship (1)], H_t is the Hamiltonian of these subsystems in an external alternating field with amplitude h, $H_{\sigma L}$ is the Hamiltonian of interaction of the conduction electrons with the lattice, and H_L is the Hamiltonian of the lattice.

Now, we use the Zubarev method of a nonequilibrium statistical operator [4] and, by analogy with the algorithm described by Fazleev [5], derive a system of kinetic equations for the Fourier components of the transverse magnetizations at frequency ω'; that is,

$$\begin{aligned} (\omega' - \varepsilon_s)\langle M_s^-\rangle_{\omega'} + \xi_s\langle M_\sigma^-\rangle_{\omega'} &= 2\pi h\delta(\omega-\omega')\eta_s, \\ \xi_\sigma\langle M_s^-\rangle_{\omega'} + (\omega' - \varepsilon_\sigma)\langle M_\sigma^-\rangle_{\omega'} &= 2\pi h\delta(\omega-\omega')\eta_\sigma, \end{aligned} \quad (14)$$

where

$$\begin{aligned} \varepsilon_s &= \omega_s^* - i\left(\Gamma_{ss} + \Gamma_{sL} + \Gamma_{\sigma s}\lambda_\perp\chi_{\sigma\perp}^0\frac{g_{s\perp}}{g_{\sigma\perp}}\right), \\ \varepsilon_\sigma &= \omega_\sigma^* - i\left(\Gamma_{\sigma\sigma} + \Gamma_{\sigma L} + \Gamma_{s\sigma}\lambda_\perp\chi_{s\perp}^0\frac{g_{\sigma\perp}}{g_{s\perp}}\right), \\ \xi_s &= \lambda_\perp\chi_{s\perp}^0(\omega_s^* - i\Gamma_{ss} - i\Gamma_{sL}) - i\Gamma_{\sigma s}\frac{g_{s\perp}}{g_{\sigma\perp}}, \\ \xi_\sigma &= \lambda_\perp\chi_{\sigma\perp}^0(\omega_\sigma^* - i\Gamma_{\sigma\sigma} - i\Gamma_{\sigma L}) - i\Gamma_{s\sigma}\frac{g_{\sigma\perp}}{g_{s\perp}}, \end{aligned} \quad (14a)$$

$$\eta_s = \chi^0_{s\perp}\omega^*_s + i\left(\chi^0_{s\perp}\Gamma_{ss} - \chi^0_{\sigma\perp}\Gamma_{\sigma s}\frac{g_{s\perp}}{g_{\sigma\perp}} + \chi^0_{s\perp}\Gamma_{sL}\right),$$

$$\eta_\sigma = \chi^0_{\sigma\perp}\omega^*_\sigma + i\left(\chi^0_{\sigma\perp}\Gamma_{\sigma\sigma} - \chi^0_{s\perp}\Gamma_{s\sigma}\frac{g_{\sigma\perp}}{g_{s\perp}} + \chi^0_{\sigma\perp}\Gamma_{\sigma L}\right).$$

Here, $\langle M^-\rangle_\omega = \langle M^x - iM^y\rangle_\omega$ is the Fourier component of the transverse components of the average magnetic moments $\langle M^-\rangle_t = \mathrm{Tr}(M^-\rho_q(t))$ is the quasi-equilibrium statistical operator of the system; and ω^*_s and ω^*_σ are the renormalized frequencies, which are determined as follows:

$$\omega^*_s = \frac{1+\lambda_\parallel\chi^0_{\sigma\parallel}}{1-\lambda^2_\parallel\chi^0_{s\parallel}\chi^2_{\sigma\parallel}}\omega_s, \quad \omega^*_\sigma = \frac{1+\lambda_\parallel\chi^0_{s\parallel}}{1-\lambda^2_\parallel\chi^0_{s\parallel}\chi^2_{\sigma\parallel}}\omega_\sigma. \quad (15)$$

Here, by analogy with relationship (6), the molecular field constants are expressed in terms of the exchange interaction parameters,

$$\lambda_\parallel = \frac{2J_\parallel}{g_{s\parallel}g_{\sigma\parallel}\mu_B^2}, \quad \lambda_\perp = \frac{2J_\perp}{g_{s\perp}g_{\sigma\perp}\mu_B^2}; \quad (16)$$

$g_{s,\sigma;\parallel}$, and $g_{s,\sigma;\perp}$ are the longitudinal and transverse g factors of the localized magnetic moments and conduction electrons, respectively; and $\chi^0_{s\parallel}$, $\chi^0_{\sigma\parallel}$, $\chi^0_{s\perp}$, and $\chi^0_{\sigma\perp}$ are the longitudinal and transverse static susceptibilities.

The kinetic coefficients in expression (14a) have the form

$$\Gamma_{kj} \approx \Gamma_{kj}(\omega) = \frac{g_{k\perp}}{g_{j\perp}}\int_{-\infty}^{0} dt\Sigma_{kj}(t)\exp(-i\omega t), \quad (17)$$

$$\Sigma_{kj}(t) = (2\delta_{kj}-1)\frac{\beta e^{\varepsilon t}}{2\chi^0_{j\perp}}\int_0^1 d\tau\,\mathrm{Tr}\{\dot M^-_k\rho_0^\tau\dot M^+_j(t)\rho_0^{1-\tau}\}. \quad (18)$$

Here, δ_{kj} is the Kronecker delta ($k, j = s, \sigma$), $\dot M^{+,-}_{k,j} = [M^{+,-}_{k,j}, \tilde H_{ex}]/i\hbar$, $A(t)$ is the Heisenberg representation of the operator A with Hamiltonian $\tilde H_0$, $\tilde H_{ex}$, and $\tilde H_0$ are the renormalized terms of Hamiltonian (13),

$$\tilde H_{ex} = -\sum_{kj}\left\{J^\parallel_{s\sigma}\delta S^z_k\delta\sigma^z_j + \frac{1}{2}J^\perp_{s\sigma}(\delta S^-_k\delta\sigma^+_j + \delta S^+_k\delta\sigma^-_j)\right\},$$

$$\tilde H_0 = \hbar\omega^*_s\sum_k S^z_k + \hbar\omega^*_\sigma\sum_j\frac{1}{2}\sigma^z_j, \quad (19)$$

ρ_0^τ is the equilibrium statistical operator,

$$\rho_0^\tau = \frac{\exp(-\tilde H_0\beta\tau)}{\mathrm{Tr}\exp(-\tilde H_0\beta)}, \quad (20)$$

and $\beta = 1/(k_BT)$ is the inverse temperature.

It is easily seen that the system of equations (14) in the isotropic case is transformed into the system of equations (3) and the introduced quantities $\Gamma_{s\sigma}$, $\Gamma_{\sigma s}$, Γ_{sL}, and $\Gamma_{\sigma L}$ have the meaning of the corresponding rates of relaxation.

In the anisotropic case, the relationships of detailed balance, which correspond to expression (10), take the following form:

$$\Gamma_{\sigma s} = \frac{\chi^0_{s\perp}}{\chi^0_{\sigma\perp}}\Gamma_{s\sigma}\left(\frac{g_{\sigma\perp}}{g_{s\perp}}\right)^2, \quad \Gamma_{\sigma\sigma} = \frac{\chi^0_{s\perp}}{\chi^0_{\sigma\perp}}\Gamma_{ss}\left(\frac{g_{\sigma\perp}}{g_{s\perp}}\right)^2,$$
$$\Gamma_{\sigma\sigma} = \frac{(J_\parallel)^2 + (J_\perp)^2}{2J_\parallel J_\perp}\Gamma_{s\sigma}. \quad (21)$$

3. EFFECTIVE g FACTOR AND THE EFFECTIVE LINEWIDTH

In order to solve the system of equations (14), we will use the approach proposed in [1]; i.e., we will choose a change of variables that allows us to disregard the cross term of the determinant formed from the equations. Then, we can easily obtain the resonance frequencies

$$\omega_{res1} = \frac{\varepsilon_s\chi_{s\perp} + \varepsilon_\sigma\chi_{\sigma\perp} - \xi_s\chi_{\sigma\perp}\frac{g_{\sigma\perp}}{g_{s\perp}} - \xi_\sigma\chi_{s\perp}\frac{g_{s\perp}}{g_{\sigma\perp}}}{\chi_{s\perp}+\chi_{\sigma\perp}}, \quad (22)$$

$$\omega_{res2} = \frac{\varepsilon_s\chi_{\sigma\perp} + \varepsilon_\sigma\chi_{s\perp} + \xi_s\chi_{\sigma\perp}\frac{g_{\sigma\perp}}{g_{s\perp}} + \xi_\sigma\chi_{s\perp}\frac{g_{s\perp}}{g_{\sigma\perp}}}{\chi_{s\perp}+\chi_{\sigma\perp}}. \quad (23)$$

The renormalized susceptibilities have the form

$$\chi_{s\parallel} = \chi^0_{s\parallel}\frac{1+\lambda_\parallel\chi^0_{\sigma\parallel}}{1-\lambda_\parallel\chi^0_{s\parallel}\chi^0_{\sigma\parallel}}, \quad \chi_{\sigma\parallel} = \chi^0_{\sigma\parallel}\frac{1+\lambda_\parallel\chi^0_{s\parallel}}{1-\lambda_\parallel\chi^0_{s\parallel}\chi^0_{\sigma\parallel}}. \quad (24)$$

It is seen that the resonance frequencies contain quantities consisting of real and imaginary parts. By considering these parts separately, we can determine the effective linewidth and the effective g factor of the system.

We are not interested in the broad resonance line at frequency ω_{res2} corresponding to the individual motion of the subsystems. Let us consider the narrow resonance line at frequency $\omega_{res} = \omega_{res1}$ corresponding to the collective mode (the effect of narrowing).

The effective linewidth is the imaginary part of the resonance frequency, which can be determined by substituting expressions (14a) into relationship (22); that is,

$$\Gamma_{\text{eff}} = \{\chi^0_{s\perp}(\Gamma_{sL} + \alpha_J\Gamma_{s\sigma})[1 + \lambda_\perp\chi_{\sigma\perp}\beta_s] + \chi^0_{\sigma\perp}(\Gamma_{\sigma L} + \alpha_J\Gamma_{\sigma s})[1 + \lambda_\perp\chi_{s\perp}\beta_\sigma]\}(\chi_{s\perp} + \chi_{\sigma\perp})^{-1}. \quad (25)$$

Here, we introduced the following designations:

$$\alpha_J = \frac{(J_\parallel - J_\perp)^2}{2J_\parallel J_\perp}, \quad \beta_s = \left(1 - \frac{g_{\sigma\perp}}{g_{s\perp}}\right), \quad \beta_\sigma = \left(1 - \frac{g_{s\perp}}{g_{\sigma\perp}}\right). \quad (26)$$

From the real part of the resonance frequency determined by expression (22), we can obtain the effective g factor, which is defined in the form

$$\hbar\,\text{Re}(\omega_{\text{res}}) = g^\parallel_{\text{eff}}\mu_B H_0. \quad (27)$$

Substituting expressions (14a) into relationship (22), separating out the real part, and taking into account formulas (24) and (27), we derive the following expression for the effective g factor:

$$g^\parallel_{\text{eff}} = [\chi_{s\perp}g_{s\parallel}(1 + \delta\lambda_\parallel\chi_{\sigma\parallel}) + \chi_{\sigma\perp}g_{\sigma\parallel}(1 + \delta\lambda_\parallel\chi_{s\parallel})](\chi_{s\perp} + \chi_{\sigma\perp})^{-1}, \quad (28)$$

where $\delta\lambda_\parallel = 2(J_\parallel - J_\perp)/g_{s\parallel}g_{\sigma\parallel}\mu_B^2$.

Similarly, we can obtain the expression for the g factor in the case when the constant magnetic field is perpendicular to the symmetry axis of the crystal:

$$g^\perp_{\text{eff}} = \left[\chi_{s\perp}g_{s\parallel}\left(1 - \frac{1}{2}\delta\lambda_\perp\chi_{\sigma\perp}\right) + \chi_{\sigma\perp}g_{\sigma\perp}\left(1 - \frac{1}{2}\delta\lambda_\perp\chi_{s\perp}\right)\right](\chi_{s\perp} + \chi_{\sigma\perp})^{-1}, \quad (29)$$

where $\delta\lambda_\perp = \delta\lambda_\parallel(g_{s\parallel}g_{\sigma\parallel}/g_{s\perp}g_{\sigma\perp})$.

4. RESULTS AND DISCUSSION

An analysis of the expressions obtained for the linewidth and g factors [formulas (25), (28), and (29), respectively] shows that the anisotropic part of the exchange interaction contributes to both the linewidth and the g factor. In the expression for the effective linewidth, the rates of relaxation of the localized magnetic moments toward the conduction electrons and in the opposite direction ($\Gamma_{s\sigma}$, $\Gamma_{\sigma s}$) do not vanish because the total spin does not commute with Hamiltonian (1). By virtue of inequalities (2), the product $\alpha_J\Gamma_{s\sigma}$ is sufficiently large and the contribution of the anisotropic part can become dominant. In the isotropic case, this radically changes the results obtained from expressions (7) and (8) for the effective g factor and the effective linewidth, respectively, which can be derived from formulas (25), (28), and (29) by setting $g_{\sigma\parallel} = g_{\sigma\perp}$, $g_{s\parallel} = g_{s\perp}$, and $\lambda_\parallel = \lambda_\perp$. Let us analyze this contribution by comparing two systems, namely, gadolinium in a metal and copper in a metal.

Since gadolinium is in the S state, its exchange interaction with conduction electrons is isotropic in character. Copper is in the D state, and the exchange interaction in the copper–metal system becomes anisotropic when the symmetry of the crystal deviates from cubic symmetry. Data on electron paramagnetic resonance in the Al : Gd system are presented in [1]. The concentration dependence of the linewidth indicates that, in this case, the mode of an electron bottleneck takes place even though the degree of overlapping of the Gd f electrons and conduction electrons is relatively small. Actually, in the denominator of expression (8) for the EPR linewidth, the susceptibility χ_σ of conduction electrons is small compared to the susceptibility χ_s and can be disregarded. As a result, it follows from expressions (9) for χ_s and (5) for χ^0_s that the linewidth in the case of the electron-bottleneck mode is inversely proportional to the concentration of magnetic impurities (as was noted above, the spin–lattice relaxation rate Γ_{sL} can be ignored).

In the copper–metal system, the interaction of Cu d electrons with conduction electrons is substantially stronger than that of Gd f electrons. Consequently, owing to the large exchange integral J, the Korringa relaxation rate is considerably higher than the rate $\Gamma_{s\sigma}$ for the gadolinium system [see expression (11)]. Hence, inequalities (2) become still stronger and the electron-bottleneck mode for copper in the metal is more pronounced than that for gadolinium in the metal. In this case, the linewidth of magnetic resonance is determined by formula (24). If the contribution of the anisotropic part of the exchange interaction were to be insignificant, it would be possible to observe electron paramagnetic resonance by varying the concentration and temperature, as is the case in the gadolinium–metal system. The spin–lattice relaxation in the copper system cannot affect the linewidth, because the relaxation rate Γ_{sL} is negligible (the Cu ground state is the Kramers doublet, which does not relax in the lattice). However, as was noted by Elshner and Loidl [6], for copper in metal, many attempts to observe not only a situation similar to that which occurs in the aluminum–gadolinium system but also to observe the electron paramagnetic resonance signal have failed. This can be

explained by the large contribution of the anisotropic part of the interaction, which leads to a substantial broadening of the line and makes it unobservable.

ACKNOWLEDGMENTS

This work was supported by the grants BRHE REC-007, SNSF 7 IP 62 595, and INTAS-01-0654.

REFERENCES

1. S. E. Barnes, Adv. Phys. **30**, 801 (1981).
2. N. E. Alekseevskii, A. V. Mitin, V. I. Nizhankovskii, *et al.*, J. Low Temp. Phys. **77** (1/2), 87 (1989).
3. B. I. Kochelaev, J. Sichelschmidt, B. Elschner, *et al.*, Phys. Rev. Lett. **79** (21), 4274 (1997).
4. D. N. Zubarev, *Nonequilibrium Statistical Thermodynamics* (Nauka, Moscow, 1971; Consultants Bureau, New York, 1974).
5. N. G. Tazleev, Fiz. Nizk. Temp. **6**, 1422 (1980) [Sov. J. Low Temp. Phys. **6**, 693 (1980)].
6. B. Elshner and A. Loidl, *Electron–Spin Resonance on Localized Magnetic Moments in Metals* (Inst. für Festkörperphysik/Experimentalphysik, Darmstadt, Germany, 1996).

Translated by O. Moskalev

Physics of the Solid State, Vol. 46, No. 2, 2004, pp. 231–233. Translated from Fizika Tverdogo Tela, Vol. 46, No. 2, 2004, pp. 228–230.
Original Russian Text Copyright © 2004 by Nemov, Seregin, Kozhanova, Troitskaya, Volkov, Seregin, Shamraĭ.

METALS AND SUPERCONDUCTORS

Variation of Electronic Density in the Superconducting Phase Transition in Nb_3Al

S. A. Nemov*, P. P. Seregin*, Yu. V. Kozhanova*, N. N. Troitskaya*, V. P. Volkov*, N. P. Seregin, and V. F. Shamraĭ*****

**St. Petersburg State Polytechnic University, Politekhnicheskaya ul. 25, St. Petersburg, 195251 Russia*
***Institute of Analytical Instrumentation, Russian Academy of Sciences, St. Petersburg, 198103 Russia*
****Institute of Metallurgy, Russian Academy of Sciences, Leninskiĭ pr. 49, Moscow, 117911 Russia*
Received May 20, 2003

Abstract—The variation of electronic density in the superconducting phase transition in the classical superconductor Nb_3Al with critical temperature T_c = 18.6 K was studied using ^{73}Ge emission Mössbauer spectroscopy. A comparison of the results obtained and the data available for the ^{67}Zn isotope in the lattices of high-temperature superconductors revealed a correlation between the electronic density variation at the Mössbauer probe nuclei sites and the value of T_c. This correlation is assumed to be related to the dependence of the electronic density variation on the standard correlation length. © *2004 MAIK "Nauka/Interperiodica".*

The phenomenon of superconductivity originates from the creation of Cooper pairs and the formation of the Bose condensate, which is described by a unique coherent wave function [1]. This implies that the electronic density at the lattice sites of a superconductor should be distributed differently at temperatures above and below the superconducting phase transition point. Mössbauer spectroscopy is one of the most efficient tools for probing such a variation in the electronic density.

Experimental investigation of the formation of Cooper pairs and of their Bose condensation by using Mössbauer spectroscopy is based on measuring the temperature dependence of the center of gravity of the Mössbauer probe spectrum both above and below the superconducting transition temperature; in the normal phase this dependence is determined by the relativistic Doppler shift alone, whereas in the superconducting phase the major contribution comes from the formation of Cooper pairs and their Bose condensation, which brings about a redistribution of the electronic density in the crystal and, as a result, a variation in the electronic density at the nucleus sites under study.

However, attempts at detecting the formation of Cooper pairs and their Bose condensation in both classical (of the type of Nb_3Sn [2]) or high-temperature superconductors (of the $YBa_2Cu_3O_7$ type [3]) by measuring the temperature dependence of the center of gravity of the ^{119}Sn and ^{57}Fe Mössbauer spectra have not met with success, which can be attributed to the low resolution of Mössbauer spectroscopy on these isotopes. For this reason, it was proposed to use emission Mössbauer spectroscopy (EMS) with the ^{67}Zn probe for determination of the electronic density variation in the course of a superconducting transition [4]. Indeed, this isotope features a record-high resolution (which is at least 200 times that for ^{57}Fe and ^{119}Sn) and the ^{67}Zn probe can be incorporated into a variety of superconductor sublattices through the parent isotopes (^{67}Cu, ^{67}Ga).

Experiments performed on a large number of high-temperature superconductors by using EMS on the $^{67}Cu(^{67}Zn)$ and $^{67}Ga(^{67}Zn)$ isotopes have shown the observed electronic density variation on the ^{67}Zn nuclei to depend on both the measurement temperature (because of the density of the superconducting electrons being temperature-dependent) and the phase transition temperature T_c (which is a manifestation of the electronic density variation being dependent on the effective size of the Cooper pair) [5]. The latter factor imposes certain difficulties on the observation of a variation in the electronic density using EMS on the ^{67}Zn isotope in superconductors with phase transition temperatures below 20 K. This is why ^{73}Ge EMS was proposed for the investigation of Cooper-pair Bose condensation in such materials [6]; indeed, the resolution provided by this isotope exceeds that for ^{57}Fe and ^{119}Sn by at least 2000 times.

We present the results of a study of the electronic density variation occurring at the superconducting phase transition in Nb_3Al (T_c = 18.6 K), a classical superconductor, by using EMS on the $^{73}As(^{73}Ge)$ isotope. It was assumed that the arsenic parent atoms substitute isoelectronically for the niobium atoms in the Nb_3Al lattice, so that the daughter isotope ^{73}Ge should also stabilize on the niobium sublattice.

Nb_3Al is a classical superconductor; it forms incongruently at a temperature of ~2300 K and exists on the phase diagram within a broad region of homogeneity

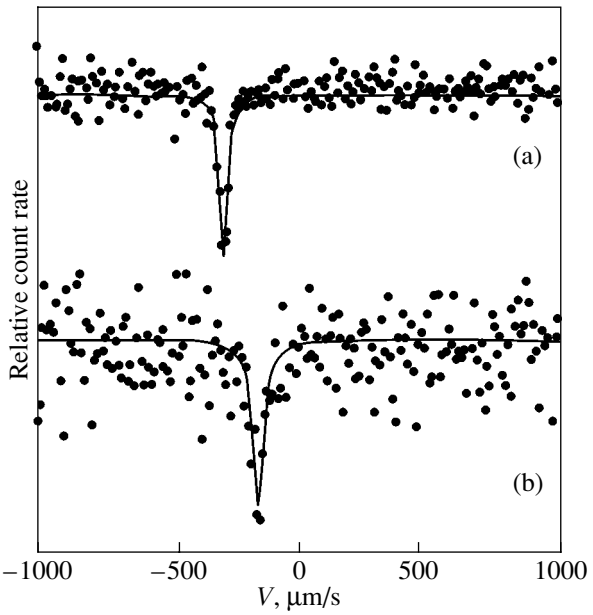

Fig. 1. Emission Mössbauer spectra of Nb_3Al : ^{73}As obtained at (a) 297 K and (b) 4.2 K.

(from 21.2 to 23.4 at. % Al) [7]. This compound crystallizes in the *A*15 structural type [the structurally equivalent positions 2(*a*) in the unit cell are occupied by aluminum atoms, and the niobium atoms sit at positions 6(*c*)], with the niobium atoms forming chains stretching through the crystal lattice.

The samples were prepared using levitation melting. The charge consisted of metallic niobium (99.9%) and aluminum (99.999%). Because a high T_c in Nb_3Al is known to become realized only after a low-temperature anneal [7], the homogenizing annealing of the ingots was carried out in two steps, first at 1820 K (for 5 h) and afterwards at 970 K (for 100 h). The chemical analysis of the samples for aluminum was made using the atomic absorption method. The superconducting transition temperature was derived from the change in the inductance of the measuring coil into which the sample was placed. The x-ray structural analysis was performed on a DRON-3.0 x-ray diffractometer using copper radiation and a graphite beam monochromator. Because the superconducting transition temperature T_c depends on the aluminum concentration and the highest value of T_c was found in alloys with the maximum aluminum content [7], we chose for the study a composition containing 75.5 at. % Nb and 24.5 at. % Al, which produced T_c = 18.6 K.

The radioactive isotope ^{73}As was prepared in the reaction $^{74}Ge(p, 2n)^{73}As$ with subsequent isolation of the carrier-free ^{73}As using the technique based on a large difference in volatility between the target and parent atoms; a proton-irradiated single-crystal germanium film (containing ~98% ^{74}Ge) was stored for three months (to reduce the content of the radioactive ^{74}As) and placed in an evacuated quartz ampoule; next, its end housing the target was heated at 900 K, after which ~80% of the ^{73}As atoms were found sorbed on the inner walls of the quartz ampoule; the carrier-free ^{73}As was washed off with a nitric acid solution.

The ^{73}As parent isotope was incorporated into Nb_3Al through diffusion in the course of an additional low-temperature homogenizing anneal. The ^{73}Ge Mössbauer spectra were measured with a commercial MS-2201 spectrometer with a ^{73}Ge single crystal used as an absorber (the enrichment in the ^{73}Ge isotope was ~90%).The temperature of the source was varied from 4.2 to 300 K, whereas that of the absorber was fixed at 297 K. All the spectra were single lines whose center of gravity varied noticeably with temperature (Fig. 1).

The temperature dependence of the center of gravity *S* of a Mössbauer spectrum at constant pressure *P* is given by the relation [5]

$$\left(\frac{\delta S}{\delta T}\right)_P = \left(\frac{\delta I}{\delta \ln V}\right)_T \left(\frac{\delta \ln V}{\delta T}\right)_P + \left(\frac{\delta D}{\delta T}\right)_P + \left(\frac{\delta I}{\delta T}\right)_V. \quad (1)$$

In Eq. (1), the first term relates the isomer shift *I* to the volume *V* (this term is significant only in structural phase transitions), the second term describes the temperature dependence of the relativistic Doppler shift *D*, and the third term reflects the temperature dependence of the isomer shift (it is this term that accounts for the variation in electronic density at the Mössbauer probe nuclei expected to occur as the matrix transfers to the superconducting state). In the Debye approximation, the temperature dependence of the Doppler shift can be written as [5]

$$\left(\frac{\delta D}{\delta T}\right)_P = -\frac{3kE_0}{2Mc^2} F\left(\frac{T}{\theta}\right), \quad (2)$$

where *k* is the Boltzmann constant, E_0 is the isomer transition energy, *M* is the probe nucleus mass, *c* is the velocity of light in vacuum, θ is the Debye temperature, and $F(T/\theta)$ is the Debye function. Note that although the Debye model is applicable for describing the vibrational properties of primitive lattices only, Eq. (2) applies equally well to experimental $S(T)$ relations obtained for compounds with a complex crystalline and chemical structure [5]. The reason for this is that the temperature dependence of the Doppler shift is determined primarily by the short-wavelength region of the phonon spectrum, which is fitted well by the Doppler model.

Figure 2 presents the $S(T)$ plot obtained for the ^{73}Ge impurity atoms occupying the niobium sites in the Nb_3Al lattice. The temperature dependence of the center of gravity of the spectrum *S* measured relative to its value at T_c is seen to fit well to Eq. (2) within the temperature interval 19–297 K if the Debye temperature is assumed to be 300 K. Said otherwise, the variation in the isomer shift, both through a change in the volume

and as a result of a change in temperature, has practically no effect on the $S(T)$ relation in the normal state. Because Nb_3Al does not undergo any structural phase transitions in the interval 19–297 K, this behavior of $S(T)$ might be expected.

In the temperature region $T < T_c$, the quantity S depends on temperature more strongly than follows from Eq. (2) and the third term in Eq. (1), which describes the temperature dependence of the isomer shift, now becomes significant.

According to BCS theory [1], a finite fraction of electrons in superconductors is condensed in a superfluid, which extends throughout the crystal and is assumed to be formed of electron pairs bound by the lattice polarization forces. At zero temperature, the condensation is complete and all electrons participate in the formation of the superfluid (although condensation noticeably affects only the motion of the electrons close to the Fermi surface). As the temperature increases, part of the electrons "evaporate" from the condensate to form a "normal fluid." As the temperature approaches the critical value T_c, the fraction of the electrons in the superfluid tends to zero and the system undergoes a second-order phase transition. This scenario of the temperature-induced variation in the fraction of the superfluid made up by the Cooper pairs is represented in the $S(T)$ plot in Fig. 2, Namely, in the low-temperature domain ($T \ll T_c$), the Bose condensate exerts the maximum influence on the variation in electronic density and the deviation of S from the value calculated from Eq. (2) is the largest; as the temperature increases (in the range of the superconducting state), the fraction of the Bose condensate decreases, as does its influence on the variation in electronic density, with the result that the quantity S tends to the value predicted by the Debye model.

As in the case of the ^{67}Zn EMS, one observes a clearly pronounced correlation between the variation in electronic density at the ^{73}Ge nuclei sites (the quantity $\Delta S = S - D$, where S is the position of the center of gravity of an experimental spectrum for $T \ll T_c$ and D is the relativistic Doppler shift at the same temperature, may serve as a measure of this variation) and the value of T_c. Indeed, for T_c = 18.6 K (Nb_3Al compound), we have $\Delta S = 30 \pm 7$ μm/s, whereas for $T_c \approx 4$ K (the $(Pb_{0.4}Sn_{0.6})_{0.84}In_{0.16}Te$ alloy [6]) we have $\Delta S = 15 \pm 5$ μm/s. The dependence of the variation in electronic density at lattice sites during a superconducting phase transition on the value of T_c can be understood if we take into account that the standard correlation length ξ_0 (the "size" of the Cooper pair for $T \longrightarrow 0$) for anisotropic superconductors is defined as $\xi_0 \sim T_c^{-1}$. Thus, the above relation actually reflects the dependence of the variation in electronic density on the standard correlation length ξ_0.

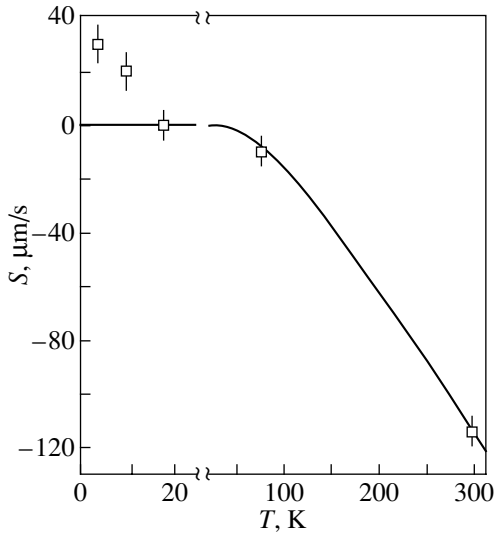

Fig. 2. Temperature dependence of the center of gravity S of the Nb_3Al : ^{73}As Mössbauer spectrum. Solid line plots the temperature dependence of the relativistic Doppler shift calculated in the Debye approximation for a Debye temperature of 300 K.

ACKNOWLEDGMENTS

This study was supported by the Russian Foundation for Basic Research, project no. 02-02-17306.

REFERENCES

1. J. R. Schrieffer, *Theory of Superconductivity* (Benjamin, New York, 1964; Nauka, Moscow, 1970).
2. J. S. Shier and R. D. Taylor, Phys. Rev. B **174**, 346 (1968).
3. Y. Wu, S. Pradhan, and P. Boolchand, Phys. Rev. Lett. **67**, 3184 (1991).
4. N. P. Seregin and P. P. Seregin, Zh. Éksp. Teor. Fiz. **118**, 1421 (2000) [JETP **91**, 1230 (2000)].
5. N. P. Seregin, Fiz. Tverd. Tela (St. Petersburg) **45** (1), 10 (2003) [Phys. Solid State **45**, 11 (2003)].
6. S. A. Nemov, P. P. Seregin, Yu. V. Kozhanova, *et al.*, Fiz. Tverd. Tela (St. Petersburg) **45** (11), 1938 (2003) [Phys. Solid State **45**, 2036 (2003)].
7. V. F. Shamraĭ and A. M. Postnikov, Metally, No. 3, 208 (1977).

Translated by G. Skrebtsov

Physics of the Solid State, Vol. 46, No. 2, 2004, pp. 234–237. Translated from Fizika Tverdogo Tela, Vol. 46, No. 2, 2004, pp. 231–234.
Original Russian Text Copyright © 2004 by Chigarev.

SEMICONDUCTORS AND DIELECTRICS

A New Mechanism of Optoacoustic Response in Semiconductors

N. V. Chigarev

International Laser Center, Faculty of Physics, Moscow State University, Moscow, 119992 Russia

e-mail: cnv@mail.ru

Received May 13, 2003

Abstract—Recently grown semiconductors exhibiting ferromagnetic properties can be very promising materials for optoacoustic applications. In these materials, the ferromagnetic phase transition controlled by the density of photoexcited carriers can bring about the generation of sound. The efficiency of this mechanism and the electron–deformation mechanism of photoexcitation of sound are compared. The duration of acoustic pulses generated by the change in the magnetic susceptibility of the sample is estimated. © *2004 MAIK "Nauka/Interperiodica".*

1. INTRODUCTION

The problems involved in laser optoacoustics require the generation of shorter and more powerful acoustic pulses. Semiconductors are promising materials for dealing with optoacoustic problems, since they are widely used in microelectronics. Numerous experimental studies have been performed to apply the methods of laser optoacoustics for testing and contactless quality monitoring of semiconductor materials. The optoacoustic response in semiconductors was studied in [1]. Two mechanisms of optoacoustic transformation (the thermoelastic and electron–deformation mechanisms) are known to operate in nonpiezoelectric semiconductors. The first mechanism is universal in the sense that it is characteristic of gases, fluids, and solids. The second mechanism operates in the interband optical excitation of an electron–hole plasma in semiconductors. The dynamics of the electron–hole plasma determines the profile of an acoustic pulse excited by the deformation potential of electrons and holes. Study of the profiles of the generated acoustic pulses provides information on short-time processes in the electronic subsystem.

Ultrasonic waves generated by an electron–deformation potential in Ge and Si were studied in [2] using nanosecond laser pulses. With the development of techniques for generating short optical pulses, the possibility appeared of using first pico- and then femtosecond lasers for optoacoustic applications. In [3, 4], the photoexcitation and propagation of hypersound pulses was studied with a time resolution of about 100 ps in crystalline germanium. The conclusion was made that hypersound photoexcitation in germanium on the subpicosecond time scale is due to the electron–deformation mechanism. Similar experiments with single-crystalline Si and GaAs were described in [5]. In [6], the generation of ultrashort acoustic pulses in single-crystalline GaAs was studied using a femtosecond laser with a time resolution of about 100 fs. It was shown that the electron–deformation mechanism of sound photoexcitation is very efficient in semiconductors on the nano-, pico-, and subpicosecond time scales. However, the duration of generated acoustic pulses is limited by diffusion and recombination of electron–hole plasma. Therefore, the search for new efficient mechanisms of photoexcitation of short acoustic pulses is an important problem. In this respect, recently prepared semiconductors that have a ferromagnetic phase under certain conditions [7, 8] are very promising materials.

2. PLASMA-INVOLVING MECHANISMS OF HYPERSOUND PHOTOGENERATION IN SEMICONDUCTORS

We consider a semiconductor sample in a static electric field E directed normally to the sample surface. The semiconductor surface is irradiated with pumping pulse laser radiation, which generates an electron–hole plasma in a surface layer with a thickness equal to the inverse light absorption coefficient, α^{-1}. We consider the behavior of the system for times exceeding ~1 ps, so that the electron–hole plasma can be assumed to be in equilibrium. Suppose that a free carrier packet moves in a static electric field with speed $v = \mu E$, where μ is the carrier packet mobility in the electron–hole plasma. In this case, the dynamics of the electron–hole plasma in the surface layer is described by the following equation taking into account the diffusion, recombination, and drift of the plasma:

$$\frac{\partial N}{\partial t} = D\frac{\partial^2 N}{\partial x^2} - v\frac{\partial N}{\partial x} - \gamma(N)N + \frac{(1-R)e^{-\alpha x}I(t)}{h\nu}. \quad (1)$$

Here, $N = N(t, x)$ is the electron–hole plasma density, D is the ambipolar diffusion coefficient, and $\gamma = \gamma(N)$ is the inverse recombination lifetime, which depends on the plasma density and takes into account different recombination processes. Since the laser beam diame-

ter d_p is usually such that $d_p \gg \alpha^{-1}$, the dynamics of the electron–hole plasma can be described by the one-dimensional equation (1). In Eq. (1), the time dependence of the laser pulse energy density is described by the function $I(t)$, R is the reflection factor of the semiconductor surface, and $h\nu$ is the photon energy. In indirect-band semiconductors, the dynamics of the electron–hole plasma is affected by linear recombination and Auger recombination [9],

$$\gamma = \gamma_0 + \gamma_1 N^2,$$

where γ_0 and γ_1 are the corresponding coefficients for these processes. Linear recombination is efficient for times $\gamma_0^{-1} \geq 10$ μs. Auger recombination essentially affects the dynamics of an electron–hole plasma if the plasma density is sufficiently high. For example, for crystalline Ge with $N \approx 5 \times 10^{18}$ cm^{-3}, we have $\gamma_1^{-1} \approx 0.3$ μs [9]. The diffusion speed for electron–hole plasma can be defined by

$$v_D = D\frac{1}{N}\frac{\partial N}{\partial x}.$$

Taking into account that $N(x, 0) \sim \exp(-\alpha x)$, we can estimate the diffusion speed as $v_D \approx \alpha D$. We consider the case where diffusion in electron–hole plasma can be neglected compared to the drift, $v \gg v_D$. Experimentally, the following values of the parameters are realistic: $v \sim 10^5$ cm/s, $D \sim 10$ cm^2/s, and $\alpha \ll 10^4$ cm^{-1}. We also consider the processes of a duration shorter than γ_0^{-1} and γ_1^{-1}, thereby neglecting recombination. Then, Eq. (1) becomes

$$\frac{\partial N}{\partial t} = -v\frac{\partial N}{\partial x} + \frac{(1-R)e^{-\alpha x}I(t)}{h\nu}. \quad (2)$$

The boundary conditions correspond to zero electron–hole plasma flux across the boundary, $N(t, x = 0) = 0$. Equation (2) can be solved using the Laplace transformation (see, e.g., [1]); in the spectral form, this solution is

$$N_\omega(z) = \frac{e^{-\alpha x} - e^{-\frac{i\omega}{v}x}}{i\omega - \alpha v}I_\omega, \quad (3)$$

where I_ω is the Fourier transform of the envelope of the laser pulse, which is usually Gaussian in shape, $I_\omega = I_0\exp(-(\omega/\omega_0)^2)$. The frequency ω_0 is determined by the laser pulse duration. We set $\omega_0 \sim 10^{10}$ Hz; this frequency can be easily obtained using modern lasers [3]. Solution (3) describes the propagation of an electron–hole plasma profile along the x axis at a constant speed v (Fig. 1).

Now we assume that the free carriers generated by pump light pulses through interband absorption initiate a phase transition to the ferromagnetic phase in the surface layer. The paramagnetic-to-ferromagnetic phase

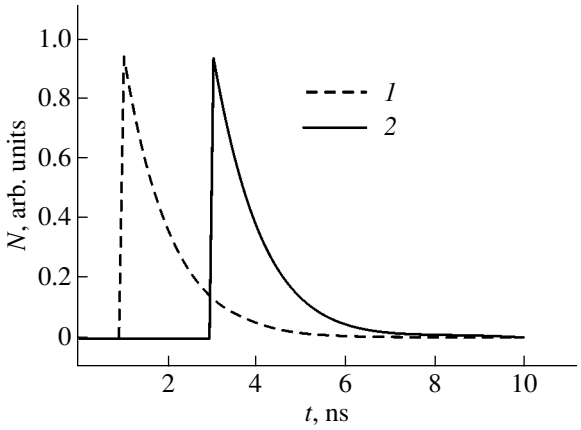

Fig. 1. Time dependence of the electron–hole plasma density for x equal to (*1*) 10 and (*2*) 12 μm.

transition has been observed in PbSnMnTe for impurity concentrations exceeding $>3 \times 10^{20}$ cm^{-3} and temperatures ≤4 K [10]. The ferromagnetic state has also been observed in $(Zn_{1-x}Mn_x)GeP_2$ samples at $T \approx 300$ K [8]. In what follows, we demonstrate that the photoinduced transition to the ferromagnetic state can be accompanied by the excitation of hypersound pulses. We consider the generation of acoustic pulses using the theory developed in [1, 9]. The mechanical displacement $u(t, x)$ in a sample is described by the wave equation with sources of sound $G(t, x)$

$$\frac{\partial^2 u}{\partial t^2} - c_a^2\frac{\partial^2 u}{\partial x^2} = -\frac{1}{\rho}\frac{\partial G}{\partial x}, \quad (4)$$

where c_a is the speed of sound and ρ is the sample mass density. Suppose that photoinduced free charge carriers concentrated in the surface layer of the semiconductor induce the transition to the ferromagnetic state in this layer.

In this case, sound sources are determined by the bulk energy density of the magnetic field in the material:

$$G(t, x) = \frac{\mu(t, x)\mu_0 H^2}{2}, \quad (5)$$

where $\mu(t, x)$ is the magnetic susceptibility of the material, which depends on the density of free charge carriers. For excitation of acoustic pulses, it is important to have a transition layer in which the electron–hole plasma density is close to a certain critical value N_C and μ varies from a minimum to a maximum value. This region can be a source of sound (Fig. 2).

Let us estimate the sound generation efficiency in the region with varying μ. Assuming that the saturation magnetic field is $H \sim 10$ kOe and that the change in magnetic susceptibility due to the phase transition is $\Delta\mu \sim 1$ (these values are typical of experiments with semiconductor materials [7]), we find the energy den-

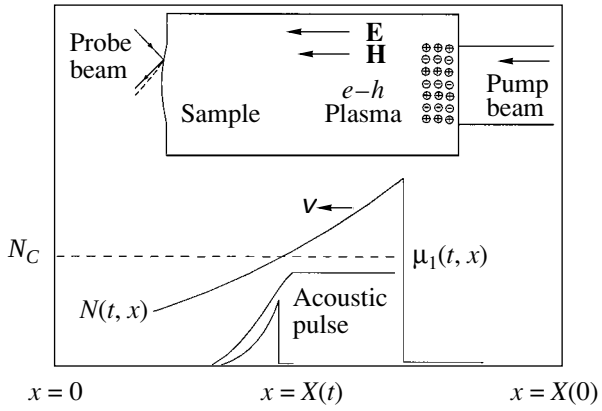

Fig. 2. Spatial distributions of the electron–hole plasma density $N(x)$ and magnetic susceptibility $\mu_1(x)$ at time t (schematic). The directions of the magnetic field **H** and of the electric field **E** are shown. The position $X(t)$ of the shape of $\mu_1(x)$ is determined by the critical electron–hole plasma density N_C corresponding to the ferromagnetic phase transition in the semiconductor.

sity transferred to acoustic vibrations to be $\Delta G_M \approx 5 \times 10^3$ J/m^3.

Now we compare the energies of generated pulses through the mechanism considered above and the electron–deformation mechanism studied in [4] on the nanosecond time scale. The efficiency of the latter mechanism can be evaluated from the relation

$$G_E \approx -dN\frac{\alpha^{-1}}{\lambda_a},$$

where d is the deformation potential for the electron–hole plasma and $\lambda_a \approx 50$ μm is the characteristic wavelength of an acoustic pulse generated in the course of plasma diffusion. Hypersound pulses were photoexcited in crystalline germanium using laser radiation with a wavelength of 1.06 μm, pulse duration of ≈100 ps, pulse repetition frequency of 100 MHz, and excitation pulse energy density of $\omega \approx 10$ μJ/cm^2 [3]. Using these parameters and setting the light penetration depth for germanium to $\alpha^{-1} \approx 1$ μm, we evaluate the electron–hole plasma density to be $N \approx w\alpha/h\nu \approx 6 \times 10^{17}$ cm^{-3}. Accordingly, for $|d| \approx 7$ eV, the energy density for the electron–deformation mechanism in germanium is $|G_E| \approx 1.4 \times 10^4$ J/m^3. Thus, under certain conditions, the efficiency of the mechanism of sound generation in a magnetic field can be comparable to the efficiency of the electron–deformation mechanism.

In our experiments with crystalline germanium, the efficiency of excitation pulse energy conversion into sound is

$$k_E = \frac{|G_E|}{w\alpha}\frac{\partial u}{\partial x} \approx 1.5 \times 10^{-7}.$$

The duration of generated acoustic pulses at available excitation densities is determined by electron–hole plasma diffusion and is about 1 ns; i.e., it is much longer than the limiting sound pulse duration of ~1 ps [1].

3. MODELING OF SOUND GENERATION

To model the spatial distribution of the semiconductor magnetic permeability $\mu(t, x)$ in the tail of the $N(t, x)$ distribution, we use the function (Fig. 2)

$$\mu(t, x) = \begin{cases} \mu_1, & x \le X(t) \\ \mu_1 \exp\left(-\dfrac{x - X(t)}{\delta}\right), & x > X(t), \end{cases}$$

where δ is the layer thickness and μ_1 is the magnetic susceptibility of the semiconductor in the ferromagnetic state. The transition point $X(t)$ is determined by the critical electron–hole plasma density $N \approx N_C$ corresponding to the semiconductor transition from the nonferromagnetic to the ferromagnetic state.

In the experiment, an acoustic pulse is often photoexcited at one of the sample faces and is probed at the opposite face (Fig. 2) [4]. Let the magnetization front propagate at a constant speed $v < c_a$ towards the origin $x = 0$ in accordance with the motion of the electron–hole plasma. Since the acoustic pulse is generated only in the region of the gradient of $\mu(t, x)$, for further analysis we use the acoustic pulse source in the form

$$G(t, x) = \begin{cases} 0, & x \le X(0) - vt \\ G_0 \exp\left(-\dfrac{x + vt - X(0)}{\delta}\right), & x > X(0) - vt, \end{cases} \quad (6)$$

where $G_0 = \mu_1\mu_0 H^2/2$ is the amplitude of the energy density (5).

Taking the Fourier transform of Eq. (6) with respect to t and the Laplace transform with respect to x, we obtain

$$\hat{G}(\omega, p) = \frac{G_0}{\left(i\omega + \dfrac{v}{\delta}\right)\left(p - \dfrac{i\omega}{v}\right)}. \quad (7)$$

In Eq. (7), the factor $\exp(-i\omega X(0)/v)$ corresponding to the displacement of the acoustic pulse profile along the t axis is eliminated. The spectrum of the surface displacements is given by the corresponding Laplace and Fourier transforms of the wave equation (4) and has the form [9]

$$\hat{u}(\omega) = \frac{-i\omega}{\rho c_a^3}\left(\hat{G}\left(\omega, i\frac{\omega}{c_a}\right) - \hat{G}\left(\omega, -i\frac{\omega}{c_a}\right)\right). \quad (8)$$

From Eq. (8), we obtain the deformation of the semiconductor surface $x = 0$:

$$u(t) = \frac{2G_0}{\rho c_a^2\left(\frac{c_a^2}{v^2} - 1\right)} \exp\left(-\frac{vt}{\delta}\right).$$

Thus, the duration of the acoustic pulse generated by magnetization reversal can be evaluated as $\delta/v \approx 10$ ps for a layer thickness of $\delta \approx 10$ nm (several interatomic distances) and for a drift speed of the carrier packet of $\approx 10^5$ cm/s.

Experimentally, the speed of propagation of the front of magnetization reversal can vary with time and is determined by the dynamics of the electron–hole plasma, which can be affected by different processes. By studying the profile of acoustic pulses generated due to the mechanism in question, it is possible to estimate a number of important parameters, such as the thickness δ of the layer in which the magnetization reversal occurs and the speed v of the propagating front of magnetization reversal. Note that supersonic plasma expansion has been observed at room temperature; this expansion affected the dynamics of the acoustic pulses generated [4]. Low-temperature studies of hypersonic pulse amplification for semiconductors in a magnetic field also appear to be quite promising. Such studies were performed earlier on garnets, where the energy transfer from the spin subsystem to the crystal lattice was observed to occur and to be accompanied by ultrasonic pulse amplification [11].

REFERENCES

1. V. É. Gusev and A. A. Karabutov, *Laser Optoacoustics* (Nauka, Moscow, 1991).
2. S. M. Avanesyan, V. E. Gusev, and N. I. Zheludev, Appl. Phys. A **40**, 163 (1986).
3. N. V. Chigarev, D. Yu. Parashchuk, Yu. S. Pan, and V. É. Gusev, Zh. Éksp. Teor. Fiz. **121**, 728 (2002) [JETP **94**, 627 (2002)].
4. N. V. Chigarev, D. Yu. Paraschuk, X. Y. Pan, and V. E. Gusev, Phys. Rev. B **61**, 15837 (2000).
5. N. V. Chigarev and D. Yu. Paraschuk, Proc. SPIE **4749**, 167 (2002).
6. O. B. Wright, B. Perrin, O. Matsuda, and V. E. Gusev, Phys. Rev. B **64**, 81202 (2001).
7. I. O. Troyanchuk, D. A. Efimov, D. D. Khalyavin, *et al.*, Fiz. Tverd. Tela (St. Petersburg) **42** (1), 81 (2000) [Phys. Solid State **42**, 84 (2000)].
8. S. Cho, S. Choi, G. Cha, *et al.*, Phys. Rev. Lett. **88**, 257203 (2002).
9. S. A. Akhmanov and V. É. Gusev, Usp. Fiz. Nauk **162** (3), 3 (1992) [Sov. Phys. Usp. **35**, 153 (1992)].
10. T. Story, R. R. Gatazka, R. B. Frankel, and P. A. Wolff, Phys. Rev. Lett. **56**, 777 (1986).
11. E. B. Tucker, Phys. Rev. Lett. **6**, 547 (1961).

Translated by I. Zvyagin

Physics of the Solid State, Vol. 46, No. 2, 2004, pp. 238–246. Translated from Fizika Tverdogo Tela, Vol. 46, No. 2, 2004, pp. 235–242.
Original Russian Text Copyright © 2004 by Davydov.

SEMICONDUCTORS AND DIELECTRICS

Energy of Substitution of Group-III and V Elements for Si and C Atoms in Silicon Carbide

S. Yu. Davydov

Ioffe Physicotechnical Institute, Russian Academy of Sciences, Politekhnicheskaya ul. 26, St. Petersburg, 194021 Russia

Received June 24, 2003

Abstract—The Harrison bonding-orbital approximation is used to calculate the energy of substitution δE of Group-III and V elements for Si and C atoms in silicon carbide. The surface and bulk locations of the substitutional atoms are considered. The difference between the surface and bulk substitution energies is estimated with allowance for the image forces. The effect of the relaxation of the impurity–host bond is discussed. © *2004 MAIK "Nauka/Interperiodica".*

1. INTRODUCTION

The calculation of substitution energy, i.e., the energy required to remove a host atom from the crystal lattice and replace it by an impurity atom, is an old labor-consuming and, to some extent, speculative problem. This is the case because direct experimental verification of the theoretical results has been impossible up till now. Even such a standard characteristic as the enthalpy of solution of one semiconductor in another has not been experimentally studied yet, since semiconductors are almost insoluble in each other. This problem, however, became urgent when it was found that some elements added during semiconductor growth can change the semiconductor properties, namely, suppress the nucleation of three-dimensional islands, which, in turn, results in layer-by-layer growth of a semiconductor film through the Franck–van der Merve mechanism. This effect is observed if an additional atom *X* incorporated during the growth remains on the surface and does not diffuse deep into the crystal. Thus, we should theoretically analyze what is energetically favorable for the atom *X*, to be on the surface or in the bulk of the crystal.

In this paper, we use the Harrison bonding-orbital approximation [5]. Like any tight-binding approximation, the Harrison method seems to be too simplified for calculating any characteristic of a particular system. However, if the problem is to find a general regularity (the functional dependence of a physical quantity on one or another parameter of the problem), the bonding-orbital approximation is quite appropriate. In this paper, this method is used for Group-III and V substitutional atoms in silicon carbide.

2. COHESIVE ENERGY OF SILICON CARBIDE

First, let us calculate the cohesive energy E_{coh} of silicon carbide following the approach developed in [6, 7]. In what follows, we use superscripts + and – to denote the parameters of the silicon and carbon sublattices, respectively. The energy required for the formation of the two-center bond in silicon carbide (the so-called promotion energy) is

$$E_{\text{pro}} = (\varepsilon_p^+ - \varepsilon_s^+) + (\varepsilon_p^- - \varepsilon_s^-), \quad (1)$$

where the quantities $\varepsilon_{s(p)}^{+(-)}$ are the energies of the atomic $s(p)$ terms. Taking into account that there are eight electrons per atom pair, the formation of this bond results in a gain in energy,

$$E_{BF} = -8(V_2^2 + V_3^2)^{1/2}. \quad (2)$$

Here, the covalent and polar energies are given by

$$V_2 = 3.22\frac{\hbar^2}{md^2}, \quad V_3 = (\varepsilon_h^+ - \varepsilon_h^-)/2, \quad (3)$$

where $\varepsilon_h^\pm = (\varepsilon_s^\pm + 3\varepsilon_p^\pm)/4$ is the energy of the hybridized $|sp^3\rangle$ orbitals for silicon and carbon atoms, respectively; $\hbar$ is Planck's constant; m is the electron mass; and d is the distance between the nearest neighbors in the SiC volume. One of the fundamental characteristics of the bond is its polarity, which is defined as

$$\alpha_p = |V_3|/(V_2^2 + V_3^2)^{1/2}. \quad (4)$$

The bond covalence is $\alpha_c = V_2/(V_2^2 + V_3^2)^{1/2}$; therefore, we have $\alpha_c^2 + \alpha_p^2 = 1$.

Another contribution to the cohesive energy of the silicon carbide is from the so-called repulsion energy E_{rep}, that is, the additional kinetic energy due to bond-

ing between two isolated atoms. The repulsion energy per atom pair is [7]

$$E_{\text{rep}} = 8(SV_2 + \Delta E_{\text{rep}}),$$
$$S = [S_0(n^+)S_0(n^-)]^{1/2}(a_0/d), \quad (5)$$
$$\Delta E_{\text{rep}} = (\hbar^2/2ma_0^2)[C(n^+)C(n^-)]^{1/2}(a_0/d)^{12}.$$

Here, $S_0(n^\pm)$ and $C(n^\pm)$ are dimensionless coefficients depending on the Group n of the Periodic Table to which the atom belongs (for silicon, $n^+ = 3$; for carbon, $n^- = 2$ [7]) and a_0 is the Bohr radius.

The last contribution to the cohesive energy is from the so-called metallization energy. Up to this point, we have considered the two-center bond, that is, an isolated SiC molecule. To extend our consideration to the whole crystal, we must take into account the coupling between the $|s\rangle$ and $|p\rangle$ orbitals of the same atom, that is, to link these bonds to the other bonds of the crystal. The corresponding coupling matrix element is

$$V_1^\pm = (\varepsilon_s^\pm - \varepsilon_p^\pm)/4. \quad (6)$$

The metallization energy, considered as a perturbation, can be written as

$$E_{\text{met}} = -3\alpha_c^2[(V_1^+)^2 + (V_1^-)^2]/(V_2^2 + V_3^2)^{1/2}. \quad (7)$$

Thus, the cohesive energy is

$$E_{\text{coh}} = -(E_{\text{pro}} + E_{BF} + E_{\text{rep}} + E_{\text{met}}). \quad (8)$$

A numerical calculation carried out using Mann's tables of atomic terms [8] (see also [6]) and by putting $d = 1.88$ Å gives $\alpha_p = 0.26$, $E_{\text{pro}} = 15.51$ eV, $E_{BF} = -57.52$ eV, $E_{\text{rep}} = 28.15$ eV, and $E_{\text{met}} = -2.94$ eV.[1] As a result, we have $E_{\text{coh}} = 16.80$ eV, whereas the experimental value of the cohesive energy is 12.68 eV [6, 7]. As mentioned above, such a difference between the experimental and theoretical results is typical of the tight-binding approximation.

An impurity atom coupled with the crystal lattice by the $|sp^3\rangle$ bond and a valence band of the crystal can exchange electrons. Thus, for our calculations, we need to determine the top of the valence band E_V. According to the Harrison method, this energy is

$$E_V = E_V^{TB} + (1.28/3.22)^2(E_{\text{over}}/8),$$
$$E_V^{TB} = (\varepsilon_p^+ + \varepsilon_p^-)/2 \quad (9)$$
$$- \{[(\varepsilon_p^+ - \varepsilon_p^-)/2]^2 + (1.28\hbar^2/md^2)^2\}^{1/2}.$$

[1] We calculate the repulsion energy following the approach developed in [7] but, as in [6], take the experimental value of the distance d between the nearest neighbors.

3. SUBSTITUTION ENERGY OF AN ATOM IN THE BULK

Now, let us estimate the energy required to replace a Si or a C atom in the SiC lattice by a Group-III or V atom. In what follows, we use superscript s to denote the parameters of the substitutional atom X. Thus, we need to calculate the energy of substitution

$$\Delta E_B^\pm = E^{s\pm} - (-E_{\text{coh}}), \quad (10)$$

where $E^{s\pm}$ is the energy of the system in which a Si or a C atom is substituted for by impurity atom X; δE_B^+ corresponds to the C–X bond, and δE_B^- corresponds to the Si–X bond.

We assume that the Si–X and C–X bond lengths are equal to the distance between the nearest neighbors in silicon carbide $d = 1.88$ Å [5] and neglect the relaxation of the bonds between the substitutional atom and its nearest neighbors. In this case, the change in the promotion energy per atom pair is given by

$$\delta E_{\text{pro}}^\pm = (\varepsilon_p^s - \varepsilon_s^s) + (4 - Z^s)(\varepsilon_p^s - E_V) - (\varepsilon_p^\pm - \varepsilon_s^\pm). \quad (11)$$

As before, superscript + refers to substitutional atoms at the Si site and superscript – refers to substitutional atoms at the C site; for Group-III (V) elements, $Z^s = 3$ (5). The change in the bond-formation energy δE_{BF} (per atom pair) is determined by

$$\delta E_{BF}^+ = 8\{(V_2^2 + V_3^2)^{1/2} - [V_2^2 + (V_3^{s\mp})^2]^{1/2}\}, \quad (12)$$

where $V_3^{s\pm} = (\varepsilon_h^s - \varepsilon_h^\pm)/2$, with ε_h^s being the energy of the $|sp^3\rangle$ orbitals of the impurity atom.

The change in the repulsion energy δE_{rep} is

$$\delta E_{\text{rep}}^\pm = E_{\text{rep}}^{s\pm} - E_{\text{rep}}, \quad (13)$$

where $E_{\text{rep}}^{s\pm}$ is given by Eq. (5), in which n is replaced by the number n^s of the group to which the impurity atom belongs.

An equation for the change in the metallization energy δE_{met} is given in the Appendix.

For calculations, we used the energies of the atomic terms taken from [9]. For the X atoms incorporated into the silicon or the carbon sublattice of SiC and located in the bulk, the energy of substitution is

$$\delta E_{\text{B}}^\pm = \delta E_{\text{pro}}^\pm + \delta E_{BF}^\pm + \delta E_{\text{rep}}^\pm + \delta E_{\text{met}}^\pm. \quad (14)$$

The calculation results shown in Fig. 1 indicate that the substitution for a carbon atom in SiC (curve *1*) is energetically favored for Group-V elements, whereas the substitution for a Si atom is favored for As and Sb atoms only. Note that we neglected relaxation of impurity–host bonds.

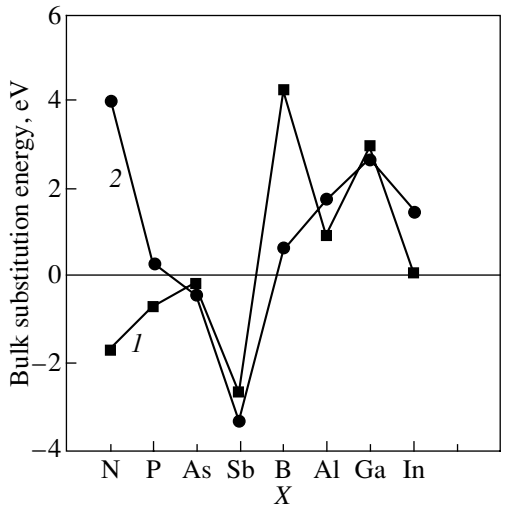

Fig. 1. Bulk substitution energy $\delta E_B^{\pm}$ for (*1*) Si*X* and (*2*) C*X*.

4. SUBSTITUTION ENERGY OF A SURFACE ATOM

The binding energy between a substitutional atom and the surface was calculated in terms of the bonding-orbital approximation in [10, 11]. Our approach, however, is simpler. We assume that a surface atom of silicon carbide (Si or C) is bound with $N < 4$ atoms of the substrate (C or Si, respectively). Let us suppose that this atom is substituted for an *X* atom (which is an adatom in this case) and that the length of the Si–*X* (C–*X*) bond remains equal to *d*. Taking into account that there are four bonds per atom pair, the substitution energy δE_S of the C or Si surface atom can be written as

$$\delta E_S^{\pm} = \frac{N}{4}[E^{s\pm} - (-E_{\text{coh}})] = \frac{N}{4}\delta E_B^{\pm}. \quad (15)$$

Let us introduce the parameter

$$\Delta_0^{\pm} = \delta E_S^{\pm} - \delta E_B^{\pm} = -\frac{4-N}{4}\delta E_B^{\pm}, \quad (16)$$

which characterizes the difference between the substitution energies of the surface and bulk atoms of SiC.

Table 1. Initial parameters, adatom charges $Z_{\pm}$, and the ion binding energies E_i (eV) calculated in terms of the Anderson–Newns model

	X					
	Al	Ga	In	P	As	Sb
a, Å	1.43	1.39	1.66	1.30	1.48	1.61
ε_a	0.93	0.99	0.78	0.88	1.17	1.07
$Z_{\pm}$	0.84	0.85	0.82	0.16	0.18	0.14
$-E_i$	2.49	1.82	1.74	0.07	0.08	0.04

Now we take into account the image forces, which appear if an adatom located on the substrate surface has a charge. The corresponding ion energy of the adsorption bond E_i can be estimated by the classical formula (see, e.g., [12])

$$E_i = -Z^2 e^2/4a, \quad (17)$$

where $2a$ is the distance between the charge and its image in the substrate and Z is the charge of the adsorbed atom. Here, we neglected the small dielectric correction $(\varepsilon_0 - 1)/(\varepsilon_0 + 1) \sim 1$ [13], because the static dielectric constant of silicon carbide is $\varepsilon_0 \sim 10$ [14]. Now we can calculate the charge Z using the Anderson–Newns model [15–17] and assuming that only one electron of the outer shell of the adatom is involved in the adsorption. In this case, Group-III atoms are positively charged, because they donate one electron to the substrate. The charge of these ions Z_+ is

$$Z_+ = \frac{1}{2} + \frac{1}{\pi}\arctan(\varepsilon_a/\Gamma), \quad (18)$$

where ε_a is the energy of the highest initially occupied quasi-level of the adatom reckoned from the affinity of the substrate $\chi = 4.4$ eV [18] and Γ is the half-width of the adatom quasi-level. The energy ε_a can be written as [19]

$$\varepsilon_a = \chi - (I - e^2/4a), \quad (19)$$

where I is the ionization energy of the Group-III atom. The last term in parentheses is the Coulomb repulsion energy between the electron of the adatom and the electrons of the substrate.

For Group-V atoms, which are acceptors and capture substrate electrons on an unoccupied orbital, the charge Z_- is

$$Z_- = \frac{1}{2} - \frac{1}{\pi}\arctan(\varepsilon_a/\Gamma). \quad (20)$$

Here, $\varepsilon_a = \chi - (A + e^2/4a)$, where A is the affinity of the electron to a Group-V atom.

For a rough estimate of this charge, we can assume that $\Gamma = 0.5$ eV for any adatom and that this quantity is independent of the surface atom (C or Si) to which the adatom is directly bound. The charges $Z_{\pm}$ and ion energies E_i calculated using the values of A and I from [20] (the values of a are supposed to be equal to the atomic radii of the corresponding adatoms taken from [21]) are listed in Table 1. For B and N atoms, the results are not presented because Eqs. (16)–(19) are invalid for the B atom, whose adatom level falls within the forbidden band and does not overlap with the conduction band, in contrast to the other atoms; the affinity A of the N atom is unknown. The calculated values of the parameter

$$\Delta^{\pm} = \Delta_0^{\pm} + E_i^{\pm} \quad (21)$$

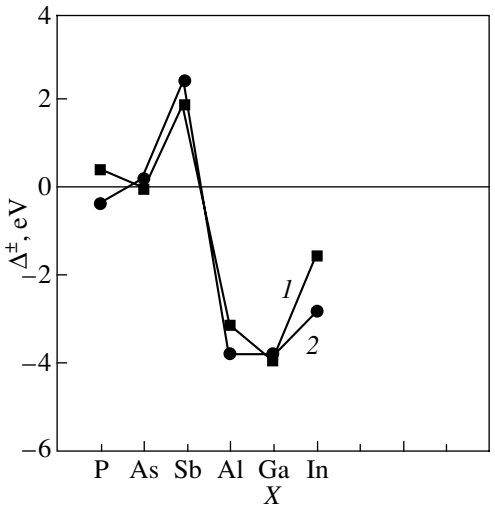

Fig. 2. Values of $\Delta^{\pm}$ calculated in the Anderson–Newns model ($N = 1$) for (*1*) Si*X* and (*2*) C*X*.

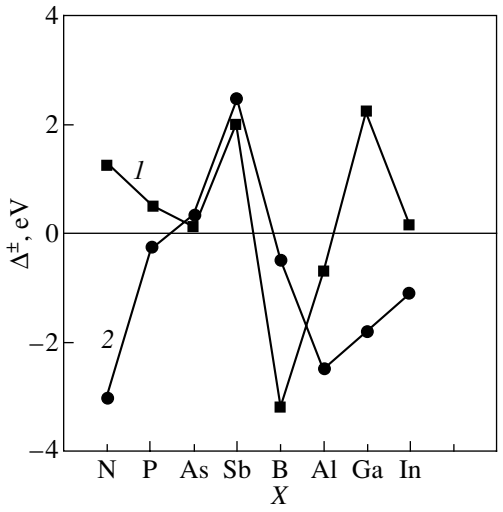

Fig. 3. Values of $\Delta^{\pm}$ calculated in the bonding-orbital approximation ($N = 1$) for (*1*) Si*X* and (*2*) C*X*.

for $N = 1$ are shown in Fig. 2. If $\Delta^{\pm} < 0$, then the surface location of the impurity atom is energetically favored; if $\Delta^{\pm} > 0$, the location in the bulk is favored. It should be noted that, in the theory of adsorption (see, e.g., [22]), the adatom position is usually denoted by index *a* (atop) for $N = 1$, by index *b* (bridge) for $N = 2$, and by index *c* (center) for $N = 3$.

The charge of the adatom can also be calculated within the bonding-orbital approximation. If the adatom is a metal atom, then for its $|sp^3\rangle$ orbital we have $n_+^{\pm} = (1 - \alpha_p^{s\pm})/2$ and the corresponding charge is

$$Z_+^{\pm} = 1 - n_+^{\pm} = (1 + \alpha_p^{s\pm})/2. \quad (22)$$

Similarly, for a nonmetal atom, we have $n_-^{\pm} = (1 + \alpha_p^{s\pm})/2$ and

$$Z_-^{\pm} = 1 - n_-^{\pm} = (1 - \alpha_p^{s\pm})/2. \quad (23)$$

Substituting these charges into Eq. (16) and assuming that the length of the absorption bond is $a = d/2$, we find the ionic component of the binding energy of the adatom. The calculated charges and ionic energies are listed in Table 2, and the calculated values of $\Delta^{\pm}$ are shown in Fig. 3 (for $N = 1$).

A comparison of the data presented in Figs. 2 and 3 shows that there is no qualitative difference between the values of $\Delta^{\pm}$ calculated using the Anderson–Newns and Harrison methods. For example, according to both methods, the surface location of Al, Ga, and In atoms substituting for C atoms in SiC is favored (curve *1*). According to the Harrison method, this is also true for P, As, and B atoms. If the Si atom is substituted (curve *2*), the location of P, Al, Ga, and In atoms on the SiC surface is favored in both schemes for calculating the ionic energy. According to the Harrison method, the surface location of N and B atoms is also favored. On the other hand, the location in the SiC bulk is always favored for N and Sb atoms. It should be noted that the results shown in Figs. 2 and 3 are as though a mirror reflection of the data presented in Fig. 1. This comes as no surprise, because the results follow from Eqs. (15) and (21).

5. IMPURITY–HOST BOND RELAXATION IN THE BULK

Calculating the bond relaxation in a crystal containing impurities is quite difficult, because minimization of the total energy of the crystal is required. On the other hand, we calculated the cohesive energy of silicon carbide without minimizing the crystal energy using the experimental value $d = 1.88$ Å (the minimization carried out in [7] yielded $d = 2.22$ Å). For this reason, we make a simplified estimate of the relaxation. Let us assume, as in [6, 7], that only the length of the impu-

Table 2. Adatom charges $Z_{\pm}$ and ion binding energy E_i (eV) calculated in the Harrison bonding-orbital approximation

	X							
	B	Al	Ga	In	N	P	As	Sb
$Z_{\pm}^{C-X}$	0.62	0.70	0.70	0.71	0.37	0.45	0.44	0.40
$Z_{\pm}^{Si-X}$	0.51	0.59	0.58	0.60	0.26	0.41	0.43	0.47
$-E_i^{C-X}$	1.47	1.88	1.88	1.93	0.52	0.78	0.74	0.61
$-E_i^{Si-X}$	1.00	1.33	1.29	1.38	0.26	0.64	0.71	0.85

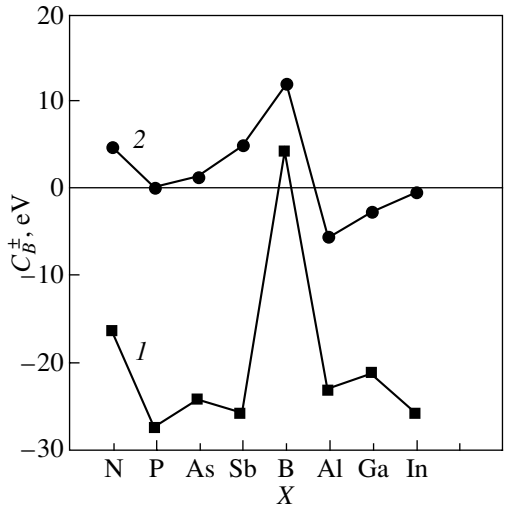

Fig. 4. Calculated values of $C_B^{\pm}$ for (*1*) Si*X* and (*2*) C*X*.

rity–host bond changes ($d \longrightarrow \tilde{d} = d + \Delta d$), whereas all other bonds of the crystal remain unchanged. We calculate the relaxation energy (the first-order correction to the substitution energy of the atom in the crystal volume), which can be written as

$$\Delta\delta E_B^{\pm} = C_B^{\pm}(\Delta d/d),$$
$$C_B^{\pm} = C_{BF}^{\pm} + C_{\text{rep}}^{\pm} + C_{\text{met}}^{\pm}, \quad (24)$$

where $C_B^{\pm} = d(\partial\delta E_B^{\pm}/\partial d)$ and $(\Delta d/d)$ is the relative change in the length of the impurity–host bond. According to Eqs. (5), (12), and (13), we have

$$C_{BF}^{\pm} = -16V_2(\alpha_c - \alpha_c^{s\mp}), \quad (25)$$

$$C_{\text{rep}}^{\pm} = -3(S^{s\mp}V_2 + 4\Delta E_{\text{rep}}^{s\mp}). \quad (26)$$

A formula for $C_{\text{met}}^{\pm}$ is given in the Appendix; the calculated values of $C_B^{\pm}$ are shown in Fig. 4. First, it should be noted that curves *1* and *2*, corresponding to the relaxation of the Si–*X* and C–*X* bonds, respectively, are qualitatively similar. For the Si–*X* bonds, however, $C_B^- < 0$ for all impurity atoms except the B atom, whereas, for the C–*X* bonds, the parameter C_B^+ is negative for Al, Ga, and In only.

As shown in [7], the relaxation type is usually determined by the relative position of the impurity and substituted atoms in the corresponding group in the Periodic Table. If the position of the impurity atom is below the position of the substituted atom, then so-called outward relaxation ($\Delta d > 0$) usually occurs, whereas if the impurity atom is above the substituted atom in the Periodic Table, then inward relaxation ($\Delta d < 0$) takes place. If the impurity and the substituted atoms are in the same row of the Periodic Table, then we have $\Delta d < 0$ for an impurity atom situated on the left of the substituted atom and $\Delta d > 0$ for an impurity atom situated on the right. Thus, when C is replaced by B, the relaxation of the Si–*X* bond is inward; for the other substitutional atoms, the relaxation of this bond is outward in this case. In what follows, we follow this empirical rule.

For Al, Ga, In, P, As, and Sb impurity atoms in silicon, the average value of the ratio $\Delta d/d$ is smaller than 0.04 and only for the carbon atom is this ratio $(\Delta d/d) \approx -0.15$ [7]. If we assume that, for the boron atom substituting for carbon in silicon carbide, this ratio is $(\Delta d/d) \approx -0.15$, then the relaxation correction is $\Delta\delta E_B^- \approx -0.62$ eV ($C_B^- \approx 4.15$ eV), which is not sufficient to change the sign of the substitution energy of Si for C, $\delta E_B^- \approx 4.27$ eV (Fig. 1). Thus, the substitution of boron for carbon in SiC remains energetically unfavorable. On the other hand, for the In atom, for which $\delta E_B^- \approx 0.12$ eV and $C_B^- \approx -25.60$ eV, the substitution energy with allowance for relaxation ($\delta\tilde{E}_B^+ = \delta E_B^+ + \Delta\delta E_B^+$) is negative. For aluminum, $\delta E_B^- \approx 0.95$ eV, $C_B^- \approx -23.09$ eV, and $\delta\tilde{E}_B^+$ becomes negative at $(\Delta d/d) > 0.04$. In general, this is possible, although the substitution of Al for Si in the silicon crystal is characterized by $(\Delta d/d) = 0$ [7]. For the Ga atom, we have $\delta E_B^- \approx 2.95$ eV and $C_B^- \approx -21.08$ eV and $\delta\tilde{E}_B^+$ becomes negative at $(\Delta d/d) > 0.14$, which is unlikely. For the other atoms, the relaxation leads to an increase in the absolute value of their negative substitution energy (Fig. 1). Thus, incorporation into the carbon sublattice is energetically favored for N, P, As, Sb, In and, possibly, Al atoms. For comparison, according to [7], incorporation into the Si lattice is energetically favored for P, As, and Sb and is unfavorable for In and Al. The latter conclusion is also valid for Ga, which is consistent with our results.

Now let us consider the C–*X* bond, where the Si atom is replaced. This band relaxes inward only if the Si atom is replaced by B, N, or Al. A comparison of curves *2* in Figs. 1 and 4 allows the following conclusions to be made. If we again assume that $(\Delta d/d) \approx -0.15$ for the boron atom, then we have $\Delta\delta E_B^+ \approx -1.79$ eV ($C_B^+ \approx 11.94$ eV). Since for the boron $\delta E_B^+ \approx 0.68$ eV, the correction changes the sign of the substitution energy, which corresponds to the energy gain associated with the incorporation of B into the SiC lattice. However, assuming that $(\Delta d/d) \approx -(0.05–0.06)$ results in $\Delta\delta E_B^+ \approx -(0.6–0.7)$ eV, and the energy $\delta\tilde{E}_B^+ = \delta E_B^+ + \Delta\delta E_B^+$ can be either positive or negative and $|\delta\tilde{E}_B^+| \approx 0$. A similar estimate for N at $(\Delta d/d) \approx -0.15$ yields

Table 3. Ratio $\eta^+ = \tilde{\Delta}^+/\Delta^+$ at $|\Delta d/d| = 0.05$ calculated for the C–*X* bond in the Anderson–Newns model (rows 1–3) and in the bonding-orbital approximation (rows 4–6) for adatom positions *a* (*N* = 1), *b* (*N* = 2), and *c* (*N* = 3)

No.	Adatom position	*X*							
		B	Al	Ga	In	N	P	As	Sb
1	*a*	–	1.09	0.95	0.96	–	0.99	0.80	0.93
2	*b*	–	1.08	0.95	0.96	–	0.99	0.76	0.92
3	*c*	–	1.07	0.95	0.95	–	0.98	0.40	0.92
4	*a*	0.81	1.09	0.95	0.96	0.96	0.96	1.03	0.92
5	*b*	0.88	1.07	0.95	0.95	0.97	0.96	0.99	0.91
6	*c*	0.95	1.06	0.95	0.95	0.98	0.95	0.97	0.86

Table 4. Ratio $\eta^- = \tilde{\Delta}^-/\Delta^-$ at $|\Delta d/d| = 0.05$ calculated for the Si–*X* bond within the Anderson–Newns model (rows 1–3) and within the bonding-orbital approximation (rows 4–6) for adatom positions *a* (*N* = 1), *b* (*N* = 2), and *c* (*N* = 3)

No.	Adatom position	*X*							
		B	Al	Ga	In	N	P	As	Sb
1	*a*	–	0.69	0.78	0.36	–	3.51	–	1.50
2	*b*	–	0.76	0.81	0.69	–	3.75	–	1.50
3	*c*	–	0.85	0.86	0.80	–	4.84	–	1.52
4	*a*	0.97	0.54	0.76	0.19	1.62	–5.61	–0.57	1.90
5	*b*	0.98	0.64	0.79	0.64	1.72	–1.24	–0.02	2.45
6	*c*	1.00	0.77	0.84	0.77	2.34	0.22	0.50	2.91

$\Delta\delta E_B^+ \approx -0.69$ eV ($C_B^+ \approx 4.58$ eV), which is insufficient to change the sign of the substitution energy δE_B^+, whose value (provided the relaxation is ignored) is 4.02 eV. For the Al atom, we have $\Delta\delta E_B^+ > 0$ ($\Delta d < 0$, $C_B^+ < 0$) and $\delta E_B^+ > 0$.

For the other atoms substituting for silicon, $\Delta d > 0$. Thus, the corrections $\Delta\delta E_B^+$ are positive for P (≈ 0), As, and Sb. Since for the P atom we have $\delta E_B^+ > 0$, the relaxation correction increases the positive value of δE_B^+. For arsenic, $\delta E_B^+ \approx -0.40$ eV and $C_B^+ \approx 1.29$ eV. Hence, the substitution energy remains negative at a reasonable value of $(\Delta d/d) < 0.2$. This is also valid for Sb, for which $\delta E_B^+ \approx -3.30$ eV and $C_B^+ \approx 4.90$ eV. Therefore, the incorporation into the silicon sublattice is energetically favored for As, Sb, and, probably, for B.

6. RELAXATION OF THE IMPURITY–HOST BOND ON THE SURFACE

Let us consider the effect of the relaxation on the ionic component of the binding energy between an adatom and the substrate. According to Eq. (17), we have

$$\Delta E_i^\pm = \left|E_i^\pm\right|(\Delta a/a). \tag{27}$$

Now the energy difference $\Delta^\pm$ should be recalculated with allowance for the relaxation. Using Eqs. (16), (21), (24), and (27), we find

$$\tilde{\Delta}^\pm = \Delta^\pm - \left(\frac{4-N}{4}C_B^\pm + E_i^\pm\right)(\Delta d/d), \tag{28}$$

where, for simplicity, we assumed that $(\Delta a/a) = (\Delta d/d)$.

The values of the parameter $\eta^\pm = \tilde{\Delta}^\pm/\Delta^\pm$ calculated at $|\Delta d/d| = 0.05$ and $N = 1, 2, 3$ are listed in Tables 3 and 4. When $\eta^\pm$ is positive, $\Delta^\pm$ and $\tilde{\Delta}^\pm$ are of the same sign. This means that the conclusion concerning the surface or bulk location of an impurity being energetically favorable (or unfavorable) drawn in the theory ignoring

relaxation remains valid. At $\eta^{\pm} < 0$, the signs of $\Delta^{\pm}$ and $\tilde{\Delta}^{\pm}$ are different. Thus, the inclusion of relaxation gives rise to a qualitatively new result: the location that was considered energetically unfavorable becomes favorable (and vice versa).

It follows from Table 3 that the parameter η^+ is positive for all the substitutional impurities considered. Moreover, η^+ is approximately unity (i.e., the relaxation correction is small) and depends only slightly on the particular atom or the number of adsorption bonds. It should also be noted that an arbitrary increase in $|\Delta d/d|$ at $\eta^+ > 1$ does not qualitatively change the conclusion regarding the favorable impurity location. At $\eta^+ < 1$, an increase in $|\Delta d/d|$ can lead to the opposite result; i.e., favored positions can become unfavorable and vice versa. However, it follows from Table 3 that even if the elongation of the bond increases by a factor of 5, that is, $|\Delta d/d| = 0.25$ (which is an unlikely bond relaxation), the parameter η^+ remains positive. Thus, according to Figs. 2 and 3, it is energetically favored for N, P, B, Al, Ga, and In atoms to substitute for surface silicon atoms, whereas for the Sb atom it is favored to substitute for Si in the bulk of SiC. For the As atom, the conclusion is ambiguous; the Anderson–Newns model yields $\Delta^+ > 0$, whereas in the bonding-orbital approximation, $\Delta^+ < 0$.

Now let us consider the data from Table 4 corresponding to the substitution for the carbon atom. In this case, the parameter η^- depends significantly on the particular atom and the number of adsorption bonds. For B, Al, Ga, In, and Sb atoms, η^- is positive and, therefore, does not generally change the energy relationships; namely, if $\Delta^- > 0$ (<0), then $\tilde{\Delta}^- > 0$ (<0). It should be noted, however, that the relaxation corrections are not small, because for all the atoms except boron the parameter η^- differs from unity significantly. For N and Sb impurities, this does not lead to any crucial changes, because for these atoms we have $\eta^- > 1$. Thus, the location of N and Sb atoms in the SiC bulk (curves *1* in Figs. 2, 3) are favored. Since the value of η^- for the B atom differs from unity by less than 3%, we can assert (curve *1* in Fig. 3) that the surface location of B is favored regardless of the specific value of the elongation of the impurity–host bond. For In atoms, the situation is different. For example, if the adatom charge is calculated for an *a*-type bond ($N = 1$) using the Harrison method, then an increase in $|\Delta d/d|$ up to 0.062 results in a negative value of η^-. For aluminum, the result is similar ($N = 1$, calculation by the Harrison method); namely, at $|\Delta d/d| = 1$, the parameter η^- is negative. It should be noted, however, that in all these cases, η^- increases as the number of adsorption bonds grows. Thus, the surface location of Al, Ga, and In atoms at the *b* and *c* positions is energetically favored at $|\Delta d/d| \le 0.2$.

Now let us consider the behavior of the As impurity. Estimating the adatom charge in terms of the Anderson–Newns model, we obtain $\Delta^- \approx 0$; for this reason, the corresponding values of η^- are not given in Table 4. However, since $C_B^- < 0$ (Fig. 4) and $(\Delta d/d) > 0$, it is obvious that $\tilde{\Delta}^- > 0$. Calculation of the charge in terms of the Harrison method shows that the surface position of As atoms is favored only in the *c* position and only if $(\Delta d/d) < 0.1$. Thus, it is most likely that the bulk location of As atoms substituting for C atoms in the SiC crystal is energetically favored. As is seen from Table 4, the behavior of the P impurity atom is also ambiguous. In the framework of the Anderson–Newns model, we have $\eta^- > 1$ and the bulk position of this impurity in SiC is always favored (Fig. 2). In terms of the bonding-orbital approximation, however, this conclusion is valid if the P adatom can form only one or two bonds with surface silicon atoms (curve *1* in Fig. 3). If three surface Si–P bonds are formed (position *c*), the surface position of the P atom is favored provided the condition $(\Delta d/d) < 0.06$ is satisfied. Thus, as for the As atom, the volume position of the P atom is more probable.

Thus, our calculation suggests that the surface position of B, Al, Ga, In, and N atoms in SiC is always favored, irrespective of the atom (C or Si) they substitute for. The surface position of P is also favored if it substitutes for Si. In [1–4], such substances are referred to as surfactants (surface-active substances). Unfortunately, we know only two papers whose data can be compared with our results. According to the experimental data from [23], aluminum is a surface-active impurity upon epitaxial growth of the 6*H*-SiC layers. Al and B atoms were also considered surfactants with respect to SiC(111) in theoretical paper [24]. The silicon substrate has been considered in much more papers (see, e.g., [1–4]). It is also worth mentioning that, according to [25] (see also references therein), Al, Ga, and In atoms are surface-active impurities with respect to Si(100), whereas for C, B, P, As, and Sb atoms the bulk position is more favored. In this case, these results depend significantly on the position of the adsorbed atom and the geometry of the substrate surface. For example, As and Sb, as well as Ga and In impurities, are surfactants at the Si epitaxy on the Si(111) surface [4]. In the case of silicon carbide, polytypism is also likely to be of importance, which should be taken into account while analyzing the question of whether a given impurity *X* is a surfactant.

ACKNOWLEDGMENTS

The author is grateful to V.V. Zelenin and A.A. Lebedev for valuable discussions.

This work was supported by the Russian Foundation for Basic Research (project no. 03-02-16054), INTAS (grant no. 01-0603), and NATO SfP (grant no. 978011).

APPENDIX

The change in the metallization energy can be written as

$$\begin{aligned}\delta E^{\pm}_{\text{met}} &= -3(V_1^s)^2(\alpha_c^{s\mp})^2/[V_2^2 + (V_3^{s\mp})^2]^{1/2} \\ &- 6(V_1^{\mp})^2(1+\alpha_p^{s\mp})(1-\alpha_p)/I_-^{\pm} \\ &- 6(V_1^{\mp})^2(1-\alpha_p^{s\mp})(1+\alpha_p)/I_+^{\pm},\end{aligned} \tag{A1}$$

where

$$\alpha_p^{s\pm} = \left|V_3^{s\pm}\right|/[V_2^2 + (V_3^{s\pm})^2]^{1/2},\ (\alpha_c^{s\pm})^2 = 1 - (\alpha_p^{s\pm})^2, \tag{A2}$$

$$I_{\pm}^{\pm} = (V_2^2 + V_3^2)^{1/2} + [V_2^2 + (V_3^{s\mp})^2]^{1/2} \pm \left|V_3^{s\pm}\right|. \tag{A3}$$

The subscripts in Eq. (A3) denote the sign of the last term.

According to Eqs. (24) and (A1)–(A3), C_{met} is

$$\begin{aligned}C^{\pm}_{\text{met}} &= -6\frac{(V_1^s)^2}{V_2}(\alpha_c^{s\mp})^3[3(\alpha_c^{s\mp})^2 - 2] \\ &- 12\frac{(V_1^{\mp})^2}{I_-^{\pm}}[(1-\alpha_p)(\alpha_p^{s\mp})(\alpha_c^{s\mp})^2 - (1+\alpha_p^{s\mp})\alpha_p\alpha_c^2] \\ &- 12\frac{V_2(V_1^{\mp})^2}{(I_-^{\pm})^2}(1+\alpha_p^{s\mp})(1-\alpha_p)(\alpha_c+\alpha_c^{s\mp}) \\ &- 12\frac{(V_1^{\mp})^2}{I_+^{\pm}}[-(1+\alpha_p)(\alpha_p^{s\mp})(\alpha_c^{s\mp})^2 + (1-\alpha_p^{s\mp})\alpha_p\alpha_c^2] \\ &- 12\frac{V_2(V_1^{\mp})^2}{(I_+^{\pm})^2}(1-\alpha_p^{s\mp})(1+\alpha_p)(\alpha_c+\alpha_c^{s\mp}).\end{aligned} \tag{A4}$$

Equation (A4) is cumbersome. Taking into account that our aim is to estimate the effect of the relaxation only, let us simplify this equation. First, we assume that $\alpha_p \approx \alpha_p^{s\pm} \approx 0$ and $\alpha_c \approx \alpha_c^{s\pm} \approx 1$. Second, we neglect the last term in Eq. (A3) (because it is much smaller than the sum of the first and second terms) and assume that $(V_3^{s\pm})^2 \approx V_3^2$ (the most radical simplification). Thus, we have $I_{\pm}^{\pm} \approx (V_2^2 + V_3^2)^{1/2}$. Finally, taking into account that the matrix elements are $V_1^+ = -1.80$ eV and $V_1^- = -2.08$ eV, we replace them by $\tilde{V}_1 = (V_1^+ + V_1^-)/2$. In this case, we have

$$C_{\text{met}} = -6\frac{(V_1^s)^2}{V_2} - 12\frac{V_2\tilde{V}_1^2}{V_2^2 + V_3^2} + 9\frac{\tilde{V}_1^2}{(V_2^2 + V_3^2)^{1/2}}. \tag{A5}$$

It should be noted that the coefficient C_{met} is usually much smaller (in magnitude) than C_{BF} and C_{rep}. In addition, it will be recalled that, in the bonding-orbital approximation, the metallization energy is calculated using perturbation theory [5–7]. Thus, the error associated with our simplification is negligible.

REFERENCES

1. M. Copel, M. C. Reuter, E. Kaxiros, and R. M. Tromp, Phys. Rev. Lett. **63** (6), 632 (1989).
2. Y. W. Mo, J. Kleiner, M. B. Webb, and M. G. Lagally, Phys. Rev. Lett. **66** (15), 1998 (1991).
3. J. Massies and N. Grandjean, Phys. Rev. B **48** (11), 8502 (1993).
4. B. Voigtlander, A. Zinner, T. Weber, and H. P. Bonzel, Phys. Rev. B **51** (12), 7583 (1995).
5. W. A. Harrison, *Electronic Structure and the Properties of Solids: The Physics of the Chemical Bond* (Freeman, San Francisco, 1980; Mir, Moscow, 1983).
6. W. A. Harrison and E. A. Kraut, Phys. Rev. B **37** (14), 8244 (1988).
7. F. Bechstedt and W. A. Harrison, Phys. Rev. B **39** (8), 5041 (1989).
8. J. B. Mann, *Atomic Structure Calculations. I. Hartree-Fock Energy Results for Elements from Hydrogen to Laurencium* (National Technical Information Service, Springfield, VA, 1967).
9. W. A. Harrison, Phys. Rev. B **31** (4), 2121 (1985).
10. J. E. Klepeis and W. A. Harrison, J. Vac. Sci. Technol. B **6** (4), 1315 (1988).
11. J. E. Klepeis and W. A. Harrison, Phys. Rev. B **40** (8), 5810 (1989).
12. S. Yu. Davydov, Fiz. Tverd. Tela (Leningrad) **19** (11), 3376 (1977) [Sov. Phys. Solid State **19**, 1971 (1977)].
13. D. V. Sivukhin, *General Course of Physics: Electricity* (Nauka, Moscow, 1996).
14. V. I. Gavrilenko, A. M. Grekhov, D. V. Korbutyak, and V. G. Litovchenko, *Optical Properties of Semiconductors* (Naukova Dumka, Kiev, 1987).
15. P. W. Anderson, Phys. Rev. **124** (1), 41 (1961).
16. D. M. Newns, Phys. Rev. **178** (3), 1123 (1969).
17. L. A. Bol'shov, A. P. Napartovich, A. G. Naumovets, and A. G. Fedorus, Usp. Fiz. Nauk **122** (1), 125 (1977) [Sov. Phys. Usp. **20**, 432 (1977)].

18. S. Yu. Davydov, A. A. Lebedev, O. V. Posrednik, and Yu. M. Tairov, Fiz. Tekh. Poluprovodn. (St. Petersburg) **35** (12), 1437 (2001) [Semiconductors **35**, 1375 (2001)].
19. J. W. Gadzuk, Phys. Rev. B **1** (5), 2110 (1970).
20. A. A. Radtsig and B. M. Smirnov, *Reference Data on Atoms, Molecules, and Ions*, 2nd ed. (Springer, Berlin, 1985; Énergoatomizdat, Moscow, 1986).
21. *Physical Quantities. Handbook*, Ed. by I. S. Grigor'ev and E. Z. Meĭlikhov (Énergoatomizdat, Moscow, 1991).
22. T. L. Einstein and J. R. Schrieffer, Phys. Rev. B **7** (8), 3629 (1973).
23. V. V. Zelenin, M. L. Korogodskiĭ, and A. A. Lebedev, Fiz. Tekh. Poluprovodn. (St. Petersburg) **35** (10), 1172 (2001) [Semiconductors **35**, 1120 (2001)].
24. U. Grossner, J. Furthmuller, and F. Bechstedt, Surf. Sci. **454–456**, 127 (2000).
25. M. Ramamoorthy, E. L. Briggs, and J. Bernholc, Phys. Rev. Lett. **81** (8), 1642 (1998).

Translated by A. Pushnov

Physics of the Solid State, Vol. 46, No. 2, 2004, pp. 247–248. Translated from Fizika Tverdogo Tela, Vol. 46, No. 2, 2004, pp. 243–244.
Original Russian Text Copyright © 2004 by Rozman.

SEMICONDUCTORS AND DIELECTRICS

Correlations between Thermodynamic Characteristics of Alkali Halide Crystals and the Binding Energy of Dipolons

G. A. Rozman

Pskov State Pedagogical Institute, Pskov, 180760 Russia

e-mail: info@pgpi.pskpv.ru

Received December 5, 2002; in final form, February 7, 2003

Abstract—The thermodynamic properties of alkali halide crystals are considered. Correlations between the thermodynamic characteristics (such as the melting temperature, the melting energy, and the jump in the entropy upon melting) and the binding energy of dipolons are established for 16 alkali halide crystals. © *2004 MAIK "Nauka/Interperiodica".*

Theoretical investigations into the properties of crystal lattice defects, including dipolons (neutral pairs of vacancies) [1], in alkali halide crystals are of practical significance, because ionic crystals are model objects in solid-state physics. It has been established that dipolons make a dominant contribution to the dielectric processes and internal friction of pure alkali halide crystals; participate in the generation of color centers, electrical conduction, and diffusion; etc. [2].

The main characteristic of a dipolon is its binding energy. Earlier [3], I devised a method for determining the binding energy of dipolons in all 16 alkali halide crystals. This method is based on an analysis of graphs of the transcendental equation

$$c = A\exp\left(-\frac{E-\gamma c}{2kT}\right), \quad (1)$$

where c is the concentration of all vacancies (both single vacancies and vacancies associated into dipolons), E is the energy of formation of two isolated vacancies of opposite sign, $\gamma = 2\alpha U\exp U/kT$, U is the binding energy of a dipolon, and α is the orientational factor determining the different positions of the dipolon in the crystal lattice. For $U = 0$, relationship (1) is transformed into a standard formula for the concentration of single vacancies: $c = A\exp(-E/2kT)$.

This paper reports data on the binding energies of all alkali halide crystals [3], their melting temperatures T_{melt} [4], and the calculated jumps in the entropy ΔS_{melt} and in the energy of melting ΔQ upon the crystal–melt first-order phase transition (see table). It is known that the first-order phase transition is accompanied by a jump in the entropy S of the crystal in accordance with the principle of the increase in entropy:

$$\Delta S_{melt} = \frac{\Delta Q_{melt}}{T_{melt}}. \quad (2)$$

The jumps in the entropy ΔS_{melt} for all alkali halide crystals with a NaCl-type lattice were calculated using the data obtained by Shenkin [5], who demonstrated theoretically that a decisive role in the thermodynamic relationships for alkali metal halides is played by the anion size.

The calculations performed in this work revealed a correlation between the jumps in the entropy ΔS_{melt} and in the melting energy ΔQ_{melt} and the binding energy U of dipolons in alkali halide crystals.

A comparison of the parameters presented in rows 1 and 4 of the table shows that the "strength" U of a dipolon is nearly proportional to the melting energy of the alkali halide crystals. Physically, this proportionality is justified because both parameters are determined by the energy of interaction of structural species of the lattice.

A comparison of the parameters in rows 1 and 3 demonstrates an inverse proportion between the binding energies of dipolons and the jumps in the entropy. This corresponds to relationship (2) if the increase in the melting temperature with an increase in the strength of the crystal is taken into account.

Moreover, from a comparison of the parameters presented in rows 6 and 7, we can reveal correlations between the corresponding ratios in each family of alkali halide crystals.

The calculated jumps in the entropy upon the crystal–melt phase transition in alkali halide crystals can be used in the design of binary crystals. The established correlations confirm the general tendency for different thermodynamic characteristics of crystals (including the binding energy of dipolons) to be interrelated with the energy of a crystal–melt phase transition and the jump in the entropy due to this transition.

The above inference suggests that dipolons can be involved in the crystal–melt phase transition; in this case, the concentration of dipolons should increase in the vicinity of the phase transition. In my opinion, this

1063-7834/04/4602-0247$26.00 © 2004 MAIK "Nauka/Interperiodica"

Thermodynamic characteristics of alkali halide crystals and the binding energies of dipolons

No.	Parameter	LiI	LiBr	LiCl	LiF	NaI	NaBr	NaCl	NaF
1	U, eV [1]	0.38	0.56	0.67	0.85	0.38	0.45	0.58	0.76
2	T_{melt}, K [4]	719	820	879	1143	934	1013	1073	1268
3	ΔS^{calc}_{melt}, kcal/(mol K)	6.36	6.23	6.10	5.15	6.47	5.99	5.81	4.89
4	ΔQ^{calc}_{melt}, kJ/mol	19.1	21.3	22.4	24.6	25.2	25.4	26.0	26.0
5	ΔQ_{melt}, kJ/mol [4]	–	12.95	13.4	26.4	–	–	28.8	33.6
6	$\lvert\Delta Q^{calc}_{melt}/U\rvert$	50	38	33	28	95	56	44	34
7	$\lvert\Delta S^{calc}_{melt}/U\rvert$	16.7	11.1	9.1	6.1	17.0	13.3	10.0	6.4
No.	Parameter	KI	KBr	KCl	KF	RbI	RbBr	RbCl	RbF
1	U, eV [1]	0.48	0.56	0.62	0.78	0.57	0.63	0.68	0.74
2	T_{melt}, K [4]	959	1003	1043	1130	915	955	990	1048
3	ΔS^{calc}_{melt}, kcal/(mol K)	6.02	6.02	5.83	5.28	5.48	5.48	5.73	5.50
4	ΔQ^{calc}_{melt}, kJ/mol	24.1	25.3	25.4	25.0	20.1	21.8	23.7	24.0
5	ΔQ_{melt}, kJ/mol [4]	–	24.8	25.5	27.2	–	–	18.4	17.3
6	$\lvert\Delta Q^{calc}_{melt}/U\rvert$	50	45	40	32	21	34	34.8	32
7	$\lvert\Delta S^{calc}_{melt}/U\rvert$	12.5	10.7	9.4	6.8	9.4	8.7	8.4	7.4

statement is significant because a unique theory of melting of alkali halide crystals does not, as yet, exist.

REFERENCES

1. G. A. Rozman, Fiz. Tverd. Tela (Leningrad) **19** (9), 1840 (1977) [Sov. Phys. Solid State **19**, 1665 (1977)].
2. *Proceedings of the All-Union Conference on Physics of Dielectrics and Perspective of Its Development* (Leningrad, 1973), Vols. 1, 2; *Proceedings of the International Conference on Physics of Dielectrics* (Tula, 1997); *Proceedings of the International Conference on Physics of Dielectrics* (St. Petersburg, 2000).
3. G. A. Rozman, Available from VINITI, No. 2325-76.
4. *Tables of Physical Data: A Reference Book*, Ed. by I. K. Kikoin (Atomizdat, Moscow, 1976).
5. Ya. S. Shenkin, Fiz. Tverd. Tela (Leningrad) **23** (9), 1896 (1981) [Sov. Phys. Solid State **23**, 1110 (1981)].

Translated by O. Moskalev

Physics of the Solid State, Vol. 46, No. 2, 2004, pp. 249–253. Translated from Fizika Tverdogo Tela, Vol. 46, No. 2, 2004, pp. 245–249.
Original Russian Text Copyright © 2004 by Zarochentsev, Troitskaya, Chabanenko.

SEMICONDUCTORS AND DIELECTRICS

Elastic Constants of Noble-Gas Crystals under Pressure and the Cauchy Relations

E. V. Zarochentsev, E. P. Troitskaya, and Val. V. Chabanenko

Donetsk Physicotechnical Institute, National Academy of Sciences of Ukraine, Donetsk, 83114 Ukraine

e-mail: zero@zero.fti.ac.donetsk.ua

Received February 13, 2003; in final form, June 21, 2003

Abstract—The equations of state are solved and the elastic constants responsible for the propagation of sound in strongly compressed crystals of noble gases are calculated in the next-to-nearest neighbor approximation using the interatomic potential proposed by the authors. The results of calculations are in satisfactory agreement with the experimental data. Slightly worse agreement is achieved in calculating the shear modulus $\mathcal{B}_{44}$. The validity of the Cauchy relation for krypton is confirmed in the experiment. On this basis, the inference is drawn that the interatomic interaction in the krypton crystal has a central character. *© 2004 MAIK "Nauka/Interperiodica".*

1. INTRODUCTION

It is known that pressure is a key parameter in many fields of physics. As the pressure acting on a solid increases, interatomic interactions are enhanced to such a degree that, in a number of cases, they will radically change the physical and chemical properties of the material. In recent years, considerable advances have been made in the theory of materials under high pressure, including calculations for a wide variety of properties and substances, approximate methods, and analytical theory. Theoretical treatment plays an important role in interpreting experimental results and realizing useful predictions.

The last decade has brought significant advances to the field of research into high pressures due to the great progress achieved in the technology of cells with diamond anvils [1, 2]. At present, static pressures of up to several megabars can be attained in laboratory experiments. A more important point is that, under laboratory conditions, the physical properties of materials can be determined in a local region and, in the majority of cases, the accuracy in high-pressure measurements approaches the accuracy achieved for samples subjected to hydrostatic compression. Under high pressure, virtually any solid undergoes a sequence of phase transitions. Moreover, under high pressure, apart from the well-known structural phase transitions, during which the type of chemical bond does not change, there can occur phase transitions accompanied by a changeover of the chemical bond from one type to another (for example, insulator–metal transitions). Furthermore, compounds differing in the type of chemical bond under atmospheric pressure can exhibit one type of bond under high pressure. In particular, under a pressure in the range 1.0–1.5 Mbar, cesium, iodine, and xenon transform into the hexagonal close-packed metallic state with identical density [3]. The problem of theoretical *ab initio* description of the state of matter and phase transitions under ultrahigh pressure is particularly important, because experimental investigations only in combination with theoretical studies can provide deeper insight into both the structure of matter and the mechanisms of related processes and phenomena. In order to describe a particular phase transition, it is necessary to devise and employ theoretical methods that will be equally suitable for analyzing several types of chemical bonds expected in a compound upon phase transition.

It is believed that, under high pressure, the decisive role is played by the energy band structure and its transformations. Hence, it follows that, in this case, the theory should be (i) *a priori* microscopic (quantum-mechanical), (ii) constructed from first principles without fitting parameters, and (iii) quantitative. On the other hand, since we deal with a multielectron system, it is expedient to use the Hartree–Fock method. This method is clearly formulated, provides sufficient accuracy, and is not overly cumbersome for use in computer calculations (see, for example, [4]).

The pressure range in which the fundamental band gap separating occupied and unoccupied states reduces to zero and an insulator–metal phase transition occurs [5] is of great interest from both the theoretical and practical standpoint.

The results obtained in our previous studies and used in the present work can be summarized as follows.

(1) We proved the theorems substantiating the applicability of the Abarenkov–Antonova cluster expansion for the Bloch functions [6].

(2) An analytical expression for the energy (adiabatic potential) of a crystal was derived in the constructed Wannier function basis. A pair interatomic

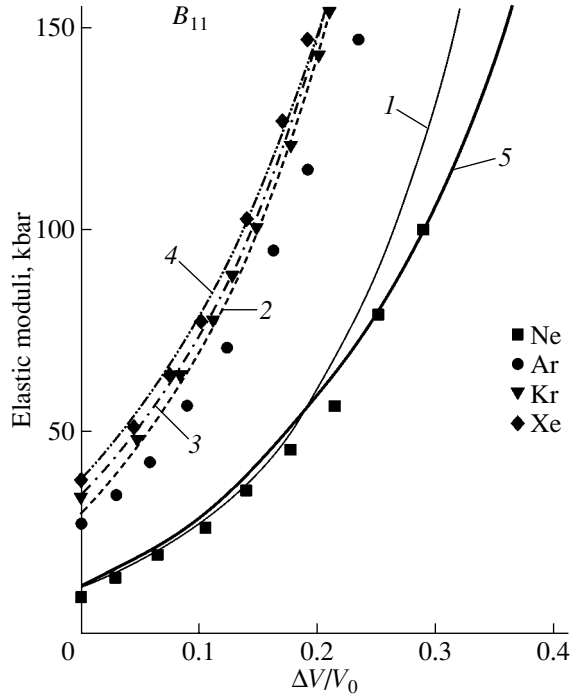

Fig. 1. Dependences of the Fuchs elastic moduli B_{11} on the compression $\Delta V/V_0$ according to the results of calculations for (*1*) neon, (*2*) argon, (*3*) krypton, and (*4*) xenon. Points are the experimental data taken from [14]. (*5*) Calculation for neon with inclusion of the cluster expansion.

potential was obtained using the cluster expansion. The short-range part of the interatomic potential was calculated from first principles [5–10].

In this work, we considered the first- and second-order derivatives of the interatomic potential in the compression range 0–0.9 and compared the obtained results with the latest experimental data. The results of the calculations of the elastic constants and discussion are presented in Sections 3–5.

2. ELASTIC PROPERTIES OF COMPRESSED CRYSTALS

When processing experimental data on the elastic properties of a strained crystal, it is necessary to use the theory of finite deformations [11, 12]. Under stresses, there are three types of elastic moduli: (i) the coefficients of expansion of the free energy C_{ikl} (Brugger moduli), (ii) the proportionality coefficients in the Hooke law for a strained crystal $\mathcal{B}_{ikl}$ (Birch moduli), and (iii) the coefficients of propagation of sound in the strained crystal A_{ikl}. In this case, it is common practice to use the Lagrange distortion tensor $u_{\alpha\beta}$ as the parameters of the expansion. The strain parameters can be conveniently taken as the quantities γ_i. For a monoatomic-gas crystal, the quantities γ_i are given, for example, in [13].

In our case, we consider only cubic crystals and, hence, are especially interested in the parameter γ_1. This parameter describes the change in the volume under deformation. The other five parameters $\gamma_2, \ldots, \gamma_6$ characterize the shear deformations of the cell. The derivative of the free energy F with respect to the parameters γ_1–γ_6 determines the Fuchs elastic moduli, which are more significant under stronger deformations. In the subsequent treatment, the behavior of a strained crystal will be described in terms of the Fuchs elastic moduli B_{ik}.

The Brugger (C_{ik}), Fuchs (B_{ik}), and Birch ($\mathcal{B}_{ik}$) elastic moduli for a strained crystal ($p \neq 0$) are related by the following expressions:

$$C_{11} = B_{11} + \frac{4}{3}B_{33} + p, \tag{1}$$

$$C_{12} = B_{11} - \frac{2}{3}B_{33} - p, \tag{2}$$

$$C_{44} = B_{44} + p, \tag{3}$$

$$\mathcal{B}_{\alpha\beta\gamma\vartheta} = C_{\alpha\beta\gamma\vartheta} - p(\delta_{\alpha\gamma}\delta_{\beta\vartheta} + \delta_{\alpha\vartheta}\delta_{\beta\gamma} - \delta_{\alpha\beta}\delta_{\gamma\vartheta}),$$
$$\mathcal{B}_{11} = B_{44} + \frac{4}{3}B_3 = C_{11} - p, \tag{4}$$

$$\mathcal{B}_{12} = B_{11} - \frac{2}{3}B_3 = C_{12} + p, \tag{5}$$

$$\mathcal{B}_{44} = B_{44} = C_{44} - p. \tag{6}$$

It follows from the above expressions that, under pressure, the measured slopes of the dispersion curves determine not the moduli C_{ik} but the moduli $\mathcal{B}_{ik}$ [13] (formally, this is done by simply replacing C_{ik} by $\mathcal{B}_{ik}$). Ignoring this circumstance leads to confusion between the numerical coefficients of elasticity of strained crystals. For this reason, in some works, numerical values of elastic moduli of one type are given in place of elastic moduli of another type; more precisely, the Birch elastic moduli $\mathcal{B}_{ik}$ are mistakenly referred to as the Brugger elastic moduli C_{ik}.

3. RESULTS OF THE CALCULATIONS

For the entire series of compressed crystals of noble gases, we derived and solved the equations of states $p = p(V)$ and calculated the Brugger (C_{11}, C_{12}, C_{44}), Fuchs (B_{11}, B_{33}, B_{44}), and Birch ($\mathcal{B}_{11}$, $\mathcal{B}_{12}$, $\mathcal{B}_{44}$) elastic moduli in the nearest and next-to-nearest neighbor approximation using the interatomic potential proposed in our earlier works [7, 8].

Figure 1 presents the results of calculations of the bulk moduli for neon, argon, krypton, and xenon crystals in the face-centered cubic phase. As can be seen from Fig. 1, the calculated and experimental data are in close agreement, especially in the case where the clus-

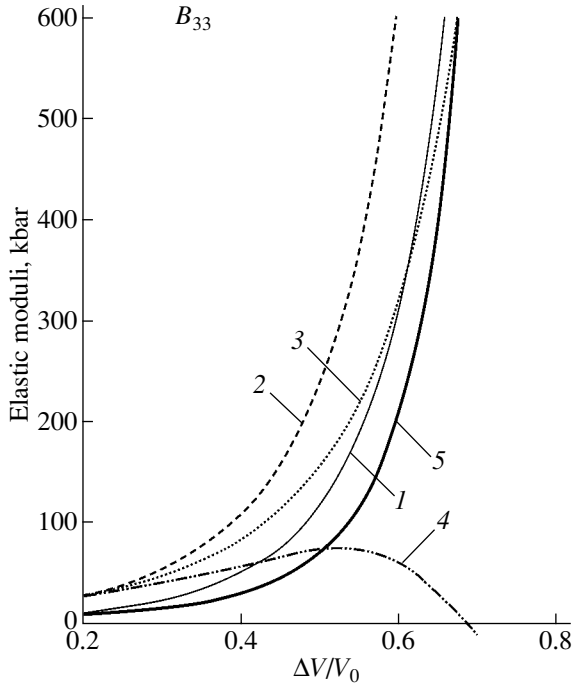

Fig. 2. Dependences of the Fuchs elastic moduli B_{33} on the compression $\Delta V/V_0$ according to the results of calculations for (*1*) neon, (*2*) argon, (*3*) krypton, and (*4*) xenon. (*5*) Calculation for neon with inclusion of the cluster expansion.

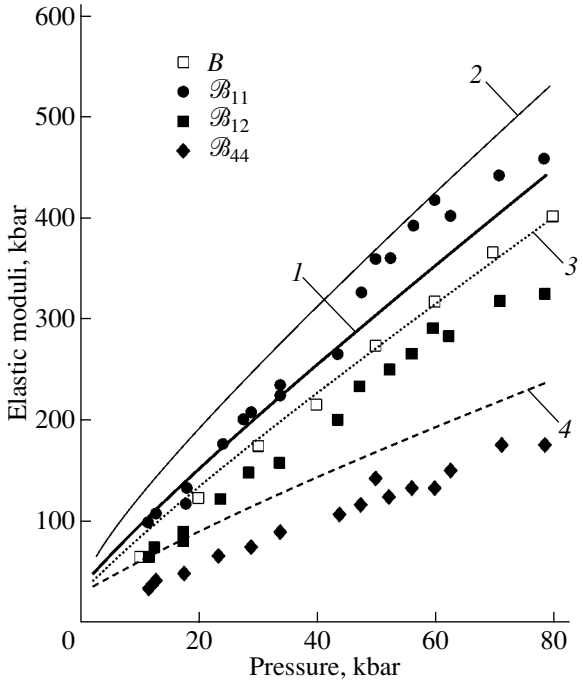

Fig. 3. Dependences of the calculated Birch moduli on the pressure for krypton: (*1*) B, (*2*) $\mathcal{B}_{11}$, (*3*) $\mathcal{B}_{12}$, and (*4*) $\mathcal{B}_{44}$. Points are the experimental data taken from [17].

ter expansion for neon is included in the calculation. This agreement is retained for large compressions.

The behavior of the shear modulus B_{33} as a function of the pressure for noble-gas crystals is shown in Fig. 2. In this case, experimental data are not available. Hence, it is of interest to compare the theoretical curves. In particular, it is clearly seen that, as the compression increases, the elastic moduli B_{33} for xenon decrease and become zero when the compression $\Delta V/V_0$ reaches 0.7. This suggests that, under pressure, the xenon crystal should undergo a phase transition. In actual fact, a pressure-induced phase transition in solid xenon was experimentally observed in [15]. This is a transition from an intermediate close-packed phase to a hexagonal close-packed phase at $p = 0.75$ Mbar immediately prior to metallization observed under compression $\Delta V/V_0 = 0.7$ (1.5 Mbar) [16].

The elastic moduli B_{44} for noble-gas crystals exhibit trivial dependences on the pressure p (an increase in the elastic moduli B_{44} with increasing p); hence, these curves are not given in the present work.

Figure 3 shows the dependences of the calculated Birch moduli $\mathcal{B}_{ik}$ on the pressure for krypton and their experimental values taken from [17]. The pressure dependence of the bulk modulus $B = 1/3(\mathcal{B}_{11} + 2\mathcal{B}_{12})$ is also depicted in Fig. 3. As is clearly seen, the calculated and experimental data are in satisfactory agreement.

Moreover, it can be seen that the dependences $\mathcal{B}_{ik}(p)$ and $B(p)$ remain linear at pressures up to 10 Mbar.

4. CAUCHY RELATIONS FOR STRAINED CRYSTALS

Let us now assume that lattice atoms (ions) interact with each other through pair central forces and that each atom is a center of symmetry. In this case, the elastic moduli of the crystal are related by exact mathematical expressions, which are referred to as the Cauchy relations. For cubic crystals, these relations are reduced to one expression,

$$C_{12} - C_{44} = 0,$$

where C_{ik} are the Brugger elastic moduli. It should be emphasized that, under the above assumptions, this relation also holds for crystals in a strained state. Then, the Cauchy relation, which is satisfied at any pressure p, can be more conveniently written in terms of the Birch elastic moduli $\mathcal{B}_{ik}$:

$$\mathcal{B}_{12} - \mathcal{B}_{44} = 2p.$$

However, until recently, it was believed that the violation of the Cauchy relation has been proved experimentally for all types of crystals, namely, metals, semiconductors, and insulators.

Actually, detailed analysis of the results obtained in the most precise experiment [17] demonstrates that,

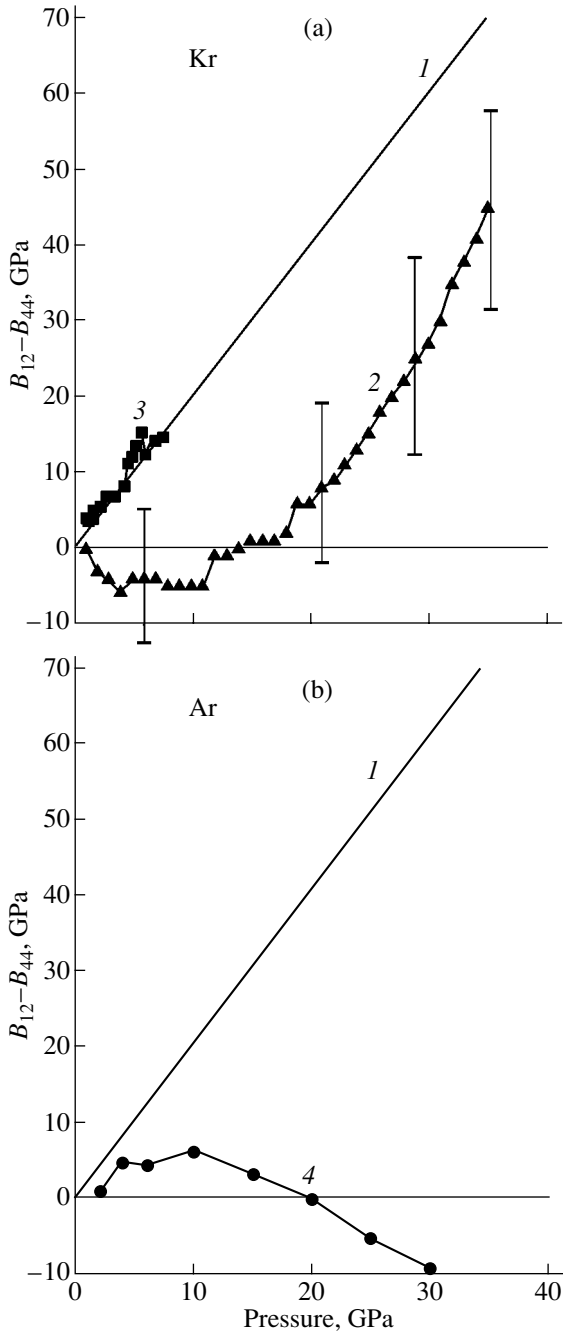

Fig. 4. Illustration of the validity of the Cauchy relation for (a) krypton and (b) argon: (*1*) theory, (*2*) [18], (*3*) [17], and (*4*) [19] (experiment). Vertical segments indicate the scatter in the experimental data taken from [18].

when the elastic constants are used accurately, the Cauchy relation for krypton holds true with a high accuracy over a wide range of compressions (Fig. 4a). It should be emphasized that the applicability of the Cauchy relations at high pressures cannot substantially depend on temperature and zero-point vibrations, because their contribution is small compared to the pressure contribution. Figure 4b illustrates the applicability of the Cauchy relation for argon (theory and experiment [19]). As can be seen from Fig. 4b, the validity of the Cauchy relation for argon is out of the question. In our opinion, this large discrepancy is due to the inaccurate determination of pressure in [18, 19].

Thus, we proved that the interatomic forces, at least, in krypton, have a central character. The Cauchy relation is a good criterion for accuracy in measuring the elastic moduli under pressure.

5. DISCUSSION

In [20], it was demonstrated that none of the existing simple model potentials can be used to describe adequately the thermodynamic and elastic properties of neon at $p = 0$. Among the numerous attempts to improve the interatomic potential under normal conditions, mention should be made of the work by Rościszewski *et al.* [21], who used an approach similar (in some sense) to our approach, namely, cluster expansion.

The general approach [6–10] to constructing the adiabatic potential E for the series Ne–Xe makes it possible to reveal the most important interactions in these gases, i.e., the structure of the interatomic potentials. Although the justified, sufficiently exact form of the adiabatic potential was obtained in the pair interatomic interaction approximation, it can be extended to the case of n-atom interaction. For a neon crystal, the repulsive short-range potential involved in the adiabatic potential should include terms of higher orders in overlap integrals. For other crystals of this series, the approximation quadratic in overlap integrals will suffice to describe the short-range potential adequately. Thus, the developed theory allows one to calculate the repulsive short-range potential for each crystal in the series Ne–Xe without fitting or variational parameters.

On the other hand, the properly introduced parameters of the theory, provided the functional relationship of the long-range and cross potentials is derived analytically, permit one to avoid cumbersome calculations of three-particle forces, quadrupole interactions, and distortion of the electron shells of atoms due to lattice vibrations. Although these interactions in a crystal are of fundamental importance, they do not make a significant contribution to the atomic properties of noble-gas crystals.

The above analysis of the equation of state and the theoretical and experimental data on the elastic constants of a strained crystal revealed a number of specific features.

First and foremost, the comparison of the theory and experiment enables us to assert that, despite its simplicity, the interatomic potential proposed accounts for all the important features in the behavior of noble-gas crystals under pressure. On this basis, we obtained a number of interesting results, for example, an inference regarding the character of the interatomic potential and

a criterion that makes it possible to determine the applied pressure accurately and, in some cases, to ascertain the stability of particular phases.

In conclusion, we point out some factors that should be taken into account in experimental and theoretical investigations into the lattice properties of crystals at high temperatures and pressures.

(1) From a comparison of different experimental data [17–19] (Fig. 4), it is evident that the results of measurements of elastic moduli are very sensitive to the particular technique and initial conditions used.

(2) Correct interpretation of the types of elastic modules measured is of great importance.

(3) At high pressures, it is very important to check the validity of the Cauchy relation $C_{\alpha\beta\gamma\delta} - C_{\alpha\gamma\beta\delta} = 0$, which must be completely satisfied for elemental cryocrystals (noble-gas crystals).

(4) The role of the accuracy in solving the equation of state increases with an increase in pressure.

REFERENCES

1. R. J. Hemley and H.-K. Ashcroft, Phys. Today **51**, 26 (1998).
2. R. J. Hemley and H. K. Mao, Encycl. Appl. Phys. **18**, 555 (1997).
3. R. Jeanloz, Annu. Rev. Phys. Chem. **40**, 237 (1989).
4. I. V. Abarenkov, I. M. Antonova, V. G. Bar'yakhtar, V. L. Bulatov, and E. V. Zarochentsev, *Computer Physics Methods in the Solid-State Theory: Electronic Structure of Ideal and Defect Crystals* (Naukova Dumka, Kiev, 1991).
5. E. V. Zarochentsev and E. P. Troitskaya, Fiz. Tverd. Tela (St. Petersburg) **44** (7), 1309 (2002) [Phys. Solid State **44**, 1370 (2002)].
6. Yu. V. Eremeĭchenkova, E. V. Zarochentsev, and E. P. Troitskaya, Teor. Mat. Fiz. **102** (3), 498 (1996).
7. V. L. Dorman, E. V. Zarochentsev, and E. P. Troitskaya, Fiz. Nizk. Temp. **8** (1), 94 (1982) [Sov. J. Low Temp. Phys. **8**, 47 (1982)].
8. V. L. Dorman, E. V. Zarochentsev, and E. P. Troitskaya, Fiz. Tverd. Tela (Leningrad) **23** (6), 1581 (1981) [Sov. Phys. Solid State **23**, 925 (1981)].
9. E. P. Troitskaya, Doctoral Dissertation in Physics and Mathematics (Kiev, 1987).
10. E. V. Zarochentsev and E. P. Troitskaya, Fiz. Tverd. Tela (St. Petersburg) **43** (7), 1292 (2001) [Phys. Solid State **43**, 1345 (2001)].
11. F. D. Murnaghan, *Finite Deformation of an Elastic Solid* (Wiley, New York, 1951).
12. D. Wallace, Solid State Phys. **25**, 301 (1970).
13. V. G. Bar'yakhtar, E. V. Zarochentsev, and E. P. Troitskaya, *Theory of Adiabatic Potential and Atomic Properties of Simple Metals* (Gordon and Breach, London, 1999).
14. M. S. Anderson and C. A. Swenson, J. Phys. Chem. Solids **36**, 145 (1975).
15. A. P. Jephcoat, H. K. Mao, L. W. Finger, *et al.*, Phys. Rev. Lett. **59** (2), 2670 (1987).
16. K. F. Goettel, J. H. Eggert, J. F. Silvera, and W. C. Moss, Phys. Rev. Lett. **62** (6), 665 (1989).
17. H. Shimizu, N. Saitoh, and S. Sasaki, Phys. Rev. B **57**, 230 (1998).
18. A. Polian, J. V. Desson, M. Grimsditch, and W. A. Grosshans, Phys. Rev. B **39** (2), 1332 (1989).
19. M. Grimsditch, P. Loubeyre, and A. Polian, Phys. Rev. B **33** (10), 7192 (1986).
20. D. Acocella, G. K. Horton, and E. R. Cowley, Phys. Rev. B **61** (13), 8753 (2000).
21. K. Rościszewski, B. Paulus, P. Fulde, and H. Stoll, Phys. Rev. B **60** (11), 7905 (1999).

Translated by O. Borovik-Romanova

Physics of the Solid State, Vol. 46, No. 2, 2004, pp. 254–257. Translated from Fizika Tverdogo Tela, Vol. 46, No. 2, 2004, pp. 250–252.
Original Russian Text Copyright © 2004 by Akimov, Marinin, Kameneva.

Evolution of the Phase Composition and Physicomechanical Properties of ZrO_2 + 4 mol % Y_2O_3 Ceramics

G. Ya. Akimov, G. A. Marinin, and V. Yu. Kameneva

Donetsk Physicotechnical Institute, National Academy of Sciences of Ukraine, Donetsk, 83114 Ukraine

e-mail: akimov@host.dipt.donetsk.ua

Received April 22, 2003; in final form, June 21, 2003

Abstract—The evolution of the phase composition and physicomechanical properties of ZrO_2 + 4 mol % Y_2O_3 ceramics subjected to hot isostatic pressing and subsequent calcining in air is investigated. It is found that hot isostatic pressing results in the formation of an easily transformed phase T_{et} with a degree of tetragonality c/a = 1.035, which determines high fracture toughness. After calcining in air, the phase T_{et} decomposes to form a nontransformed phase T' with a degree of tetragonality c/a = 1.005, which determines low fracture toughness.
© 2004 MAIK "Nauka/Interperiodica".

1. INTRODUCTION

It is known that diffusion and diffusionless phase transformations can proceed in partially stabilized zirconia ceramics, depending on the content of stabilizing impurities, pressure, temperature, surrounding gas medium, moisture content, and duration of external actions [1]. These transformations lead to substantial variations in the phase composition and physicomechanical properties of the ceramic material. To date, these phenomena have been investigated intensively. This provides deeper insight into the nature of physical transformations in partially stabilized zirconia and makes it possible not only to control the properties of stabilized zirconia ceramics but also to specify its behavior.

The purpose of this work was to investigate how the variations in the phase composition affect the physicomechanical properties of partially stabilized zirconia ceramics ZrO_2 + 4 mol % Y_2O_3, in which the monoclinic, tetragonal, and cubic phases exist at room temperature [2, 3].

2. SAMPLES PREPARATION AND EXPERIMENTAL TECHNIQUE

A powder of partially stabilized zirconia (ZrO_2 + 4 mol % Y_2O_3) was prepared by coprecipitation. The powder was compacted into samples under cold isostatic pressing at a pressure of 0.6 GPa and was then sintered in air at a temperature T = 1773 K for 2 h. Sintered samples were divided into two groups. Samples of the first group were subjected to hot isostatic pressing in an argon atmosphere at a pressure P = 0.2 GPa and temperature T = 1723 K for 4 h [3]. The samples subjected to hot isostatic pressing were also divided into two groups, one of which was calcined in air at T = 1773 K for 2 h. In what follows, the samples sintered in air, subjected to hot isostatic pressing, and calcined in air will be referred to as samples of series **1**, **2**, and **3**, respectively.

The phase composition was determined using x-ray powder diffraction at room temperature on a DRON-3M diffractometer (CoK_α radiation, wavelength λ = 0.17902 nm) with computer recording and plotting of the x-ray powder diffraction patterns. The phase composition was calculated quantitatively according to a procedure described earlier in [4, 5]. In our calculations, we used x-ray powder diffraction patterns for the (111) reflections in the angle range $33° \le 2\theta \le 39°$ and x-ray powder diffraction patterns for the (400) reflections in the range $85° \le 2\theta \le 90°$. The intensity of reflection at one point was measured upon scanning for 10 s with a step of $\Delta 2\theta = 0.01°$. The results of measurements at large angles were averaged over five points.

The strength σ_F and fracture toughness K_{1c} were measured by three-point bending of the sample with an incision and without one [6]. All samples were $3 \times 4 \times 30$ mm in size. The incision depth was equal to 1.0 mm, and the incision width was 0.4 mm. The base length of the gauge was 14.5 mm. The velocity of a movable traverse of the testing machine was 0.5 mm/min. All the samples were polished prior to testing. The density ρ_{exp} of ceramic samples was determined by hydrostatic weighing on a VLR-200 balance. The theoretical density ρ_{th} was calculated from the x-ray powder diffraction data. The porosity was determined according to the formula $P = (1 - \rho_{exp}/\rho_{th}) \times 100$. The strength and fracture toughness were calculated from standard formulas [7]. According to [3], the mean grain size was equal to 0.5 μm.

3. RESULTS AND DISCUSSION

Figure 1a shows the x-ray powder diffraction patterns of samples of three series in the angle range $33° \le 2\theta \le 39°$ for the (111) reflections of the *F* and *T* phases and the $(11\bar{1})$ reflections for the *M* phase. It can be seen that the x-ray powder diffraction pattern of samples of series **1** (curve *1*) differs significantly from the patterns of samples of series **2** and **3** (curves *2* and *3*, respectively). After hot isostatic pressing, the intensity of the (111) reflections of the *T* phase decreases and the peak becomes broader toward smaller angles 2θ, i.e., toward larger interplanar spacings $d_{(111)}$. Calcining in air (curve *3*) leads to a decrease in the width of the peak and a substantial increase in its height. As a result, the peak shifts toward smaller values of $d_{(111)}$. This change in the intensity of the (111) reflections of the *T* phase indicates that the lattice parameters of the *F* and *T* phases and the degree of tetragonality *c*/*a* of the *T* phase change. The mean *c*/*a* value increases for the samples subjected to hot isostatic pressing and decreases after their calcining in air. The content of the monoclinic phase was almost identical in samples of series **1** and **3** and slightly higher in samples of series **2** (Table 1).

The x-ray powder diffraction patterns of samples of the three series in the angle range $85° \le 2\theta \le 90°$ for reflections from the (400) and (004) planes of the *T* and *F* phases are shown in Fig. 1b. An analysis of the x-ray powder diffraction pattern of the sample of series **1** (curve *1*) suggests that the characteristic feature of the phase composition for this series is the high content of the *F* phase (~25%) (Table 1). After hot isostatic pressing, the content of the *F* phase decreases to 17%. However, the content of the *T* phase increases (Table 1) and the *T* phase transforms into two tetragonal modifications T_t and T_{et} with a change in the lattice parameters *c* and *a* (Table 2). After calcining (series **3**), the peak associated with the T_{et} phase in the x-ray diffraction pattern disappears but the splitting of the reflections of the T_t phase is retained. In addition to the T_t and *F* phases, there appears a *T*' phase with a degree of tetragonality $c/a = 1.005$. By analogy with the polymorph method of calculating the content of the *M*, *T*, and *F* phases [4], we determined the relative content of modifications of the *T* phase [5]. In the case when reflections from modifications of the *T* phase appeared in the range of the (400) and (004) reflections, their intensities were added together. The contents of different modifications of the *T* phase, lattice parameters, and the degrees of tetragonality *c*/*a* are given in Table 2.

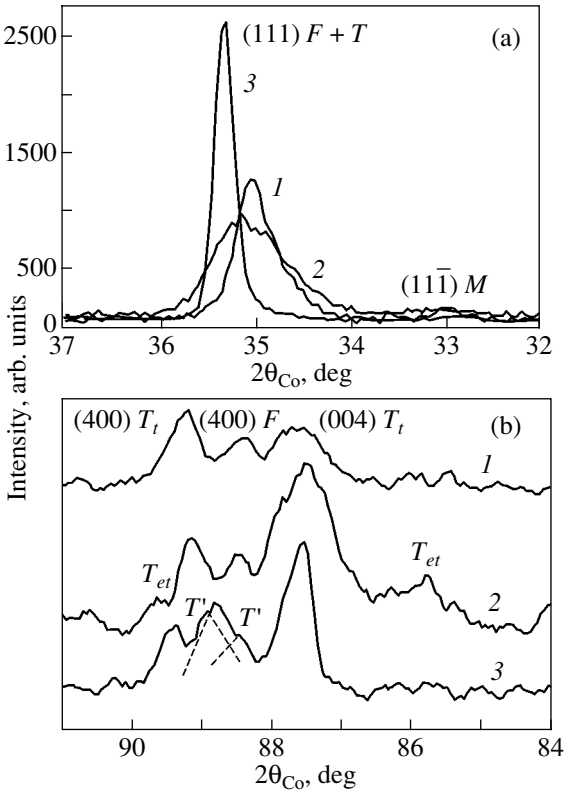

Fig. 1. X-ray powder diffraction patterns of ZrO_2 + 4 mol % Y_2O_3 ceramic samples measured in the angle ranges (a) $33° \le 2\theta \le 39°$ and (b) $85° \le 2\theta \le 90°$ after (*1*) cold isostatic pressing and sintering in air, (*2*) hot isostatic pressing in argon, and (*3*) hot isostatic pressing and calcining in air.

Our investigations into the physicomechanical properties demonstrate that the largest values of σ_F and K_{1c} are characteristic of ceramic samples subjected to hot

Table 1. Phase composition and physicomechanical properties of ZrO_2 + 4 mol % Y_2O_3 ceramic samples after different thermomechanical treatments

Treatment	Phase composition, %			Density, g/cm^3		Porosity *P*, %	σ_F, MPa	K_{1c}, MPa m$^{1/2}$	Color
	M	*T*	*F*	ρ^*_{th}	ρ_{exp}				
Sintering after cold isostatic pressing (series **1**)	4	71	25	6.08	5.98	1.64	1023	11.0	White
Hot isostatic pressing (series **2**)	8	75	17	**	6.13	–	1400	18.0	Black
Calcining in air (series **3**)	5	80	15	6.09	5.90	3.12	720	5.7	White

* $\rho_M = 5.83$ g/cm^3, $\rho_T = 6.10$ g/cm^3, and $\rho_F = 6.09$ g/cm^3 [8].

** Exact theoretical densities for black (oxygen-deficient) ceramics are unknown.

Table 2. Relative contents of modifications of the *T* phase in ZrO_2 + 4 mol % Y_2O_3 after different treatments

Modification of the *T* phase	Relative contents of the modifications after treatment			*c*/*a*	*c*, nm	*a*, nm
	sintering (series **1**)	hot isostatic pressing (series **2**)	calcining (series **3**)			
T'	–	–	32	1.005	0.5131	0.5105
T_t	71	61	57	1.017	0.5180	0.5095
T_{et}	–	14	–	1.035	0.5260	0.5080

Note: *T*' is the nontransformed *T* phase, T_t is the transformed *T* phase, and T_{et} is the easily transformed *T* phase.

isostatic pressing. After calcining in air, the mechanical properties deteriorate drastically (Table 1). It can be seen from Table 1 that the variation in the strength correlates well with the variation in the porosity. In order to evaluate how the density affects the strength, it is necessary to take into account the possible change in the grain size. However, there are grounds to believe that no substantial increase in the grain size occurs, because, otherwise, this increase should lead to a decrease in the stability of the *T* phase, which, in turn, should lead to an increase in K_{1c} at a given content of the stabilizer [6]. Actually, as can be seen from Table 1, this is not the case.

The fracture toughness is governed by the phase composition of the ceramic samples, or, more exactly, by the ability of the *T* phase to undergo a transformation under applied stresses. It is known that the fracture toughness and, to a lesser extent, the strength of partially stabilized zirconia ceramics is determined by the mechanically activated martensitic transformation $T \longrightarrow M$ [6, 9]. However, this transition is not always equally possible. For example, the *T*' phase formed upon the martensitic $F \longrightarrow T$ transition does not transform into the *M* phase even during vigorous grinding of the sample, i.e., during its destruction [10]. Nikol'skiĭ *et al.* [11] showed that there exist a large variety of modifications of the tetragonal phase, which is determined by the degree of tetragonality *c*/*a*. It is reasonable that the larger degree of tetragonality *c*/*a*, the more readily the *T* phase undergoes a transformation under elastic stresses due to the crack.

Analysis of the splitting of the (004) and (400) reflections of the tetragonal *T* phase in the x-ray powder diffraction pattern (Fig. 1b) and the intensity and width of the (111) diffraction peak of the *T* phase (Fig. 1a) demonstrates (Table 2) that, for series **1**, the tetragonal T_t phase is characterized by the degree of tetragonality $c/a = 1.017$. After hot isostatic pressing (series **2**), a decrease in the content of the *F* phase is accompanied by the formation of the T_{et} phase with a degree of tetragonality $c/a = 1.035$ and the content of the T_t phase decreases by 10% (Tables 1, 2). After calcining in air (series **3**), the T_{et} modification disappears; however, there arises a *T*' phase with a degree of tetragonality $c/a = 1.005$, the content of the T_t phase decreases to 23%, and the amount of the *F* phase decreases.

One of the important results of this study is the finding of the T_{et} phase in the samples subjected to hot isostatic pressing. Let us consider the processes occurring in the ceramic samples during hot isostatic pressing in more detail. First, hot isostatic pressing in argon brings about a partial reduction of zirconia and the formation of a large amount of oxygen vacancies. As a consequence, the ceramic sample turns a black color. It is known that oxygen vacancies can participate in the stabilization of the *T* and *F* phases [12] and, probably, decrease the stabilizing effect of yttrium ions under certain conditions. Second, during hot isostatic pressing, the material becomes increasingly denser due to the dilution of the intercrystallite material and accommodation of the shape of a grain to the shape of the neighboring grains through plastic deformation. As was shown in [13], plastic deformation of dislocation nature in partially stabilized zirconia starts at a temperature of about 973 K. Therefore, hot isostatic pressing is accompanied by two complementary processes: a loss of oxygen and plastic deformation of the ceramic grains. When the dislocations meet yttrium ions, they can also reduce the stabilizing effect of yttrium.

Thus, the formation of the T_{et} phase upon hot isostatic pressing can be associated with the additive effect of oxygen vacancies and dislocations. This phase can be easily transformable, as is the case with zirconia at a low content of the stabilizer [1]. Therefore, the existence of the T_{et} phase and the high density of samples of series **2** are responsible for the large values of K_{1c} and σ_F.

The second, no less important result of this study is that the phase composition of the ceramic samples changes after calcining in air. The T_{et} phase disappears, the content of the T_t and *F* phases decreases, and the *T*' phase is formed in large amounts. These variations in the composition of the tetragonal phase and the decrease in the ceramic density manifest themselves in a decrease in K_{1c} and σ_F for samples of series **3**.

The above effect of calcining in air can be explained as follows. Recall that, after hot isostatic pressing, grains of the ceramic samples, first, already contained dislocations and vacancies and, second, were in a strained state apparently due to incomplete accommo-

dation of the grain shape. We assume that, upon calcining in air, the yttrium ions could be more uniformly distributed throughout the grain bulk both under the action of internal stresses and owing to the dislocation pipes. This brought about the formation of the T' phase, whereas the drastic decrease in the amount of oxygen vacancies led to the disappearance of the T_{et} phase.

ACKNOWLEDGMENTS

We would like to thank O.N. Potapskaya for her participation in processing the experimental results.

REFERENCES

1. M. Yoshimura, Am. Ceram. Soc. Bull. **67** (12), 1950 (1988).
2. K. Tsukuma and M. Shimada, Am. Ceram. Soc. Bull. **64** (2), 310 (1985).
3. G. A. Marinin, G. Ya. Akimov, V. N. Varyukhin, and O. N. Potapskaya, Fiz. Tverd. Tela (St. Petersburg) **44** (7), 1266 (2002) [Phys. Solid State **44**, 1323 (2002)].
4. R. C. Garvie and P. S. Nikolson, J. Am. Ceram. Soc. **55** (6), 303 (1972).
5. M. I. Kabanova and V. A. Dubok, Poroshk. Metall. (Kiev), No. 5, 85 (1992).
6. G. Ya. Akimov, V. M. Timchenko, and N. G. Labinskaya, Fiz. Tverd. Tela (St. Petersburg) **37** (7), 2146 (1995) [Phys. Solid State **37**, 1167 (1995)].
7. Yu. V. Zaĭtsev, *Fracture Mechanics for Builders* (Moscow, 1991), p. 288.
8. V. N. Strekalovskiĭ, Yu. M. Polezhaev, and S. F. Pal'guev, *Oxides with Impurity Disordering* (Nauka, Moscow, 1987).
9. M. Rühle and A. G. Evans, Prog. Mater. Sci. **33**, 85 (1989).
10. T. Noma, M. Yoshimura, M. Kato, *et al.*, Yogyo Kyokaishi, No. 8, 887 (1986).
11. V. Yu. Nikol'skiĭ, S. K. Filatov, T. A. Zhuravina, and V. A. Frank-Kamenetskiĭ, Izv. Akad. Nauk SSSR, Neorg. Mater. **8** (8), 1506 (1972).
12. B. Ya. Sukharevskiĭ, A. N. Gavrish, and B. G. Alapin, in *Theoretical and Technical Studies of Refractory Materials*, Ed. by K. G. Romanenko (Metallurgizdat, Moscow, 1968), No. 9(56).
13. M. Bauteld, U. Messerschmidt, M. Bartsch, and D. Baither, Rev. Eng. Mater. **97–98**, 431 (1994).

Translated by N. Korovin

Physics of the Solid State, Vol. 46, No. 2, 2004, pp. 258–264. Translated from Fizika Tverdogo Tela, Vol. 46, No. 2, 2004, pp. 253–258.
Original Russian Text Copyright © 2004 by Basun, Razdobarin, Sochava, Evans.

SEMICONDUCTORS AND DIELECTRICS

Optical Alignment of Cu^{2+} Axial Centers in $KTaO_3$: Spectral Dependence of the Effect

S. A. Basun*, A. G. Razdobarin*, L. S. Sochava*, and D. R. Evans**

**Ioffe Physicotechnical Institute, Russian Academy of Sciences, Politekhnicheskaya ul. 26, St. Petersburg, 194021 Russia*
e-mail: Lev.Sochava@pop.ioffe.rssi.ru
***Air Force Research Laboratory, Wright-Patterson Air Force Base, Dayton, Ohio, 45433 USA*
Received July 14, 2003

Abstract—The Cu_{Ta}^{2+}–V_O axial centers in crystalline $KTaO_3$ were found to undergo alignment under the action of polarized light. The sign of the effect is shown to change depending on the wavelength of the aligning light. A parallel study of the spectral response of photoconductivity of the same samples led to the conclusion that the alignment of the copper centers is driven not by reorientation but rather by an anisotropic recharging of the centers, which involves both the conduction and valence bands of the crystal. This interpretation was supported by a study of the kinetics of thermal destruction of the copper center alignment. © *2004 MAIK "Nauka/Interperiodica".*

1. INTRODUCTION

Elucidation of the physical mechanisms responsible for the defect center orientation ordering in a crystal due to an external anisotropic action is a topical issue both in solid-state physics and for applications where the symmetry of the object is crucial (for instance, second harmonic generation, photorefraction, etc.). The illumination of a crystal with polarized light, which can bring about alignment of low-symmetry defect centers, can serve as a simple illustration of such an anisotropic action. The optical ordering of the center orientation can be of various natures. As follows, for instance, from the well-known studies by Lüty (see [1] and references therein), the alignment of F_A centers in alkali halide crystals is caused by the orientation-sensitive excitation of the centers and their subsequent reorientation in the excited state. Another mechanism of alignment associated with anisotropic photoinduced recharging of the centers was considered, in particular, by Berney and Cowan [2] for the Fe^+–V_O centers in $SrTiO_3$. Obviously, in the cases where centers may reside in two different charge states, preferential recharging of centers of the same orientation manifests itself as alignment.

It was shown in [3, 4] that optical alignment of two tetragonal iron complexes (Fe_{Ta}–V_O and Fe_K–O_i) in a potassium tantalate crystal results from orientation-sensitive photoionization of these centers. It was found that the photoionization efficiency of both centers depends on the mutual orientation of the center axis and the light polarization vector. As a result, the axes of defects with a given charge state are no longer distributed with equal probability over the three ⟨100⟩ directions. This mechanism, while not including actual reorientation of the Fe_{Ta}–V_O and Fe_K–O_i complexes, brings about, nevertheless, alignment of the centers in each of the two charge states along (or perpendicular to) the light polarization vector.

An analysis of the total experimental data obtained in [3, 4] led to the conclusion that two competing photorecharging processes take part in the alignment. Thus, in the case of the Fe_K–O_i center, both the photoionization of Fe_K^{2+}–O_i (with the promotion of one electron to the conduction band and the formation of Fe_K^{3+}–O_i) and the phototransfer of an electron from the valence band to Fe_K^{3+}–O_i (with the formation of a hole in the valence band and the appearance of Fe_K^{2+}–O_i) take place.

These processes have, generally speaking, different spectral thresholds; therefore, illumination in various spectral regions may, in principle, give rise to alignments that are opposite in sign (depending on which of the two processes dominates in a given spectral region). It is this situation that was observed in the case of the Cu_{Ta}^{2+}–V_O centers in crystalline potassium tantalate, where alignment reverses sign when the wavelength of the polarized light is changed.

As follows from an analysis of the available literature data, the determination of the mechanism of optical alignment in each given case (actual reorientation of the centers or their orientation-sensitive photorecharging) is a very complex problem. In this study, we succeeded in solving it by performing a parallel investiga-

tion of the spectral responses of the photoconductivity and alignment, as well as of the thermal relaxation kinetics of the aligned centers.

2. EXPERIMENTAL TECHNIQUES

We studied $KTaO_3$: Cu single crystals grown at the Ioffe Physicotechnical Institute by spontaneous crystallization from a slowly cooled melt. The growth took place in an oxygen environment at a cooling rate of 0.5 K/h. The crystals grown from a batch with copper contents of 0.5 and 5 at. % were transparent in the former case and greenish in the latter. We also studied crystals obtained from a batch containing, in addition to copper, a few percent of niobium and a very low vanadium impurity. The results on the optical alignment of copper centers reported below were obtained primarily on crystals grown from the batch with 5 at. % copper content.

The EPR spectra were measured with a modified 3-cm Radiopan SE/X2544 spectrometer.

The light sources were laser diodes operating at various wavelengths in the range 450–850 nm, a tunable (Spectra Physics 164-05) argon laser, a helium–neon laser, and a copper-vapor laser, as well as a mercury lamp (100 W). The measurements in the red and IR spectral regions were conducted with a tungsten halogen incandescent lamp (70 W) and a xenon lamp (250 W), provided by a set of wide-band and interference (pass band 10 nm) filters.

On passing through a crystal polarizer, the light from the source was focused on the upper face of a quartz rod (4 mm diameter, 270 mm length, end faces plane and polished), which served as a light guide. A sample was fixed to the lower rod face. The bottom part of the rod with the sample was inserted in the cold finger of a nitrogen Dewar vessel mounted in the spectrometer cavity. The polarizer provided a high enough degree of polarization (>95%) throughout the spectral range covered (350–2000 nm). Most of the depolarization occurred in the quartz rod and did not exceed 10%.

The studies of the temperature behavior were carried out in a nitrogen-flow cryostat (temperature range 90–500 K, stability ±0.1 K).

Figure 1 shows the sample orientation with respect to the magnetic field $\mathbf{H}_0$ and to the light wave vector.

The steady-state photocurrent was measured with an electrometric amplifier (sensitivity 10^{-14} A) at room temperature, with excitation provided by a xenon or the incandescent lamp through the interference filters. The dark conductivity was extremely low. The photocurrent excitation spectrum was normalized against the photon flux.

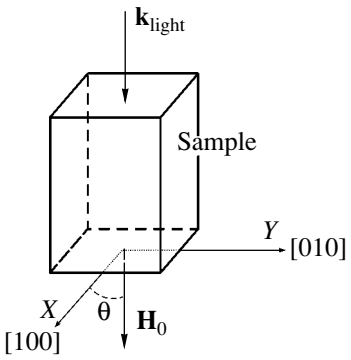

Fig. 1. Geometry of the photo-EPR experiment. Magnetic field $\mathbf{H}_0$ is in the (001) plane.

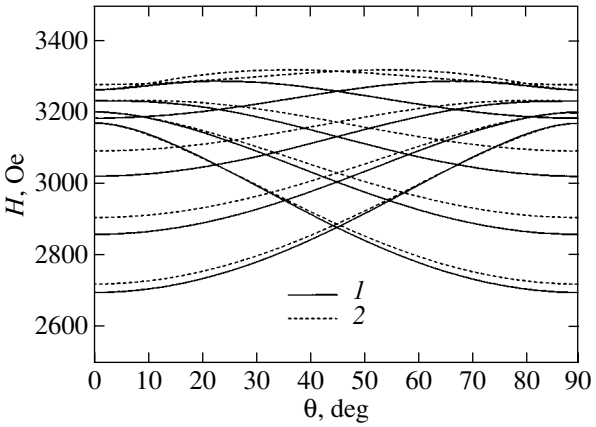

Fig. 2. Calculated angular dependences of the resonance fields of the Cu^{2+} EPR lines (without inclusion of the superhyperfine structure) in $KTaO_3$ in the {100} plane (ν = 9.29 GHz, T = 78 K). Curves *1* and *2* refer to spectra I and II, respectively. The experimental points fall on the calculated curves and are omitted to make the figure more revealing.

3. MAIN RESULTS

3.1. EPR Spectrum

The $KTaO_3$: Cu crystals studied exhibit two intense spectra of Cu^{2+} (S = 1/2, I = 3/2) of tetragonal symmetry. The spectral parameters are very similar and coincide with those reported in [5, 6]. Figure 2 shows the angular response of both spectra in the (100) plane. The spectra contain not only the hyperfine but also a superhyperfine structure, whose resolution depends, to a considerable extent, on both the crystal orientation in the magnetic field and the batch composition. The analysis of the superhyperfine interaction of copper ions performed in [6] revealed that Cu^{2+} ions substitute for Ta^{5+} (I = 7/2) and that the interaction of the unpaired electron with the nuclei of the four tantalum ions accounts for the total width of each of the hyperfine components (about 30 Oe).

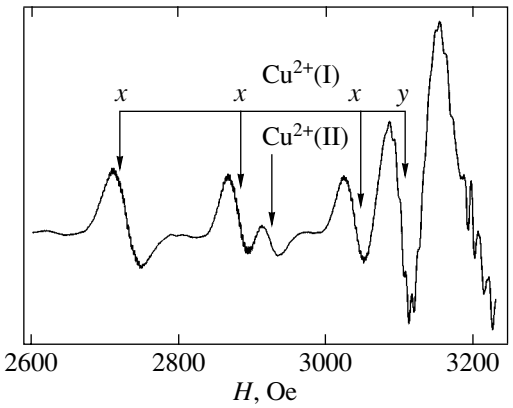

Fig. 3. EPR spectrum of $KTaO_3$: Cu (5%) obtained in the *X* range at $T = 78$ K and $\theta = 14°$. The strong-field components of the *x* and *y* centers superpose on the *z*-center lines in spectrum I. Only one of the *x*-center components could be resolved in spectrum II. The other lines are overlaid by the stronger lines in spectrum I.

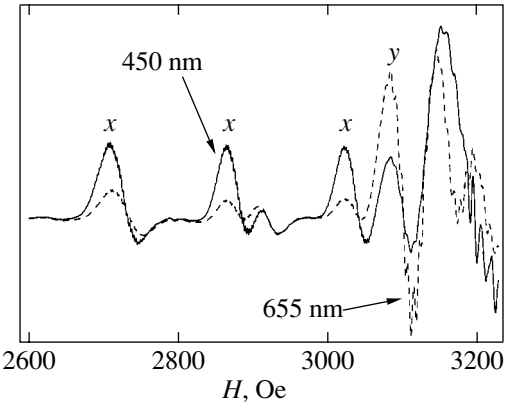

Fig. 4. Optical alignment of the $Cu_{Ta}^{2+}-V_O$ centers in $KTaO_3$. Dashed line is the EPR spectrum measured after illumination of the sample by **e** ∥ *y* light with a wavelength of 655 nm. Illumination with light of wavelength 450 nm (solid line) reverses the alignment sign.

The tetragonal symmetry of the two observed centers is apparently due to two types of local compensation of the effectively negative charge of the impurity ion by oxygen vacancies. The possible mechanisms of formation of the center structure were associated with charge compensation by one or two oxygen vacancies [6] or with a more complex model taking into account charge transfer and lattice distortion in the vicinity of the Cu^{2+} ion [7].

Optical alignment was observed for center I ($g_{\|} = 2.24$, $g_{\perp} = 2.04$, $A_{\|} = 173 \times 10^{-4}$ cm^{-1}), whose spectral intensity was found to substantially exceed that of center II (Fig. 3). (The EPR spectrum of center II in crystals grown from a batch with a copper content of 0.5 at. % was only slightly above the background.)

We performed measurements for the crystal orientation corresponding to $\theta = 14°$ (Fig. 2), in which the spectral components of the two centers *x* and *y* with mutually perpendicular orientations in the horizontal plane specified in Fig. 3 (spectrum I) were not superposed on the EPR lines of the *z* center.

3.2. Spectral Dependence of the Alignment

Illumination of a sample with polarized light within a broad spectral range (370–920 nm) distorts the uniform distribution of the centers over their possible orientations along the three ⟨100⟩ axes. Experimentally, we were able to detect variations only in the concentration of the *x* and *y* centers (n_x, n_y), because the strong-field components of the x and *y* centers (Figs. 2, 3) superposed on the EPR lines of the *z* centers. Thus, we measured the intensities of the third component of the *x* centers and of the first (weak-field) component of the *y* centers (Fig. 3).

Figure 4 (dashed line) illustrates the variation of the ratio of the *x* and *y* center concentrations after illumination of the sample by light with $\lambda = 655$ nm and the **e** ∥ *y* electric vector orientation. The degree of alignment $A = (n_y - n_x)/(n_x + n_y)$ reaches 0.66 in this case and the concentration ratio n_y/n_x increases from 1 to 4.9. At the same time, light with a wavelength of 450 nm brings about a reverse variation in the relative values of n_x and n_y, i.e., a reversal of the sign of the alignment (solid curve in Fig. 4); the value of $|A|$ in this case is 0.41. Light with the electric vector **e** ∥ *x* gives rise to changes in n_x and n_y opposite to those described above.

In the course of the alignment, the total spectral intensity (measured as $2I_x + I_y$ for **e** ∥ *y*) remains constant to within experimental error (±5%).

Below ~230 K, the alignment produced by polarized light persists in the dark for an indefinite period of time.

Figure 5a shows the spectral response of the quantity *A* measured in the range 370–920 nm. Two qualitative features of this relation are noteworthy:

(i) The existence of two broad spectral regions differing in the sign of alignment and having a fairly sharp boundary between them near 520 nm (~2.4 eV).

(ii) The existence of a long-wavelength alignment threshold; namely, light with a wavelength in excess of 870 nm (~1.4 eV) does not initiate alignment of the centers.

The reversal of the alignment sign can be associated with the light-induced change in the charge state of the copper ion and with the involvement of two rather than one electronic bands of the crystal in this process [4]. In

the crystals under study, the copper ions reside apparently in two charge states, Cu^{2+} (its EPR spectrum is observed) and Cu^{3+} (its spectrum is not observed at 77 K [8]). Thus, the alignment threshold (1.45 eV) corresponds to the energy gap between the $Cu^{2+/3+}$ level and the edge of one of the electronic bands of the crystal (for instance, the conduction band bottom). After the photon energy has reached 1.45 eV, the ionization process $Cu^{2+} \longrightarrow Cu^{3+}$ begins (process *1* in Fig. 6) and its anisotropy results in alignment of the centers. After the photon energy has reached ~1.9 eV, process *2* is initiated and, being more efficient, brings about a fast decrease in the alignment factor and a subsequent reversal of its sign.

3.3. Photoconductivity of $KTaO_3$: Cu Crystals

The light-induced recharging of the copper ions should obviously contribute to the photoconductivity of the crystals under study. Therefore, if the operating optical-alignment mechanism is related to the photoionization of copper ions, a correlation between the spectral dependences of these two effects could serve as direct evidence of this mechanism. This correlation was observed to exist and is shown in Fig. 5.

The excitation spectrum of photoconductivity (Fig. 5b) exhibits two broad bands differing strongly in intensity (by three to four orders of magnitude). A remarkable feature in this curve is the presence of a long-wavelength photocurrent excitation threshold at 860–880 nm, which coincides with the spectral threshold for the alignment (Fig. 5a). In our opinion, such an exact coincidence of the two thresholds cannot be accidental and indicates that the observed alignment is due to the photoionization of the copper ions. It is also remarkable that the boundary between the two photoconductivity bands is close to the photon energy (~1.9 eV, Fig. 5) at which a sharp decrease in the positive alignment factor is observed to occur.

3.4. Thermal Destruction of Center Alignment

As already mentioned, at temperatures below ~230 K, the alignment of the centers persists in the dark for an indefinite period of time. However, a rise in temperature up to ~250 K leads to its fast destruction, i.e., to restoration of the uniform distribution of the centers over their orientations along the three ⟨100⟩ axes.

The decay rate of the alignment depends very strongly on temperature and, therefore, can be measured only within a narrow temperature interval. Figure 7a presents the curves describing the decay of alignment (produced by light with λ = 578 nm) in the dark with time at three temperatures in the range 245–265 K. Each of these curves is very well fitted with one exponential,

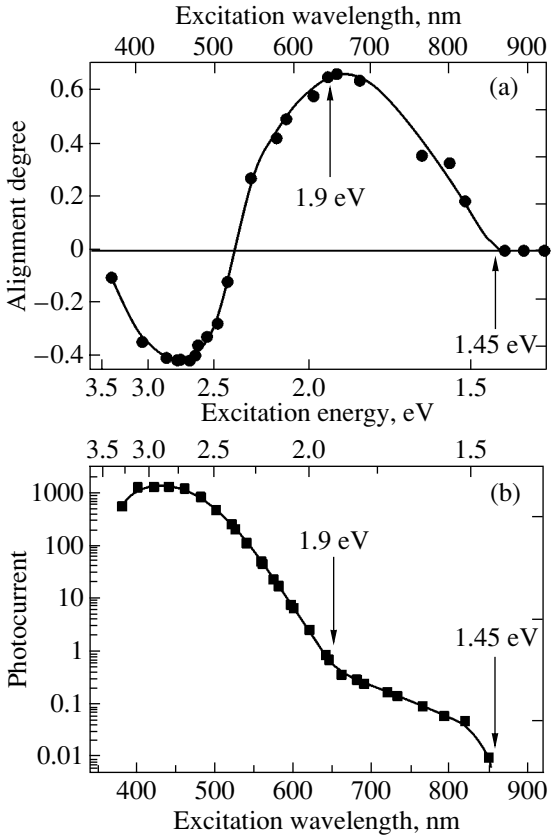

Fig. 5. (a) Stationary alignment of the Cu^{2+}–V_O centers in $KTaO_3$ plotted vs. incident light wavelength at T = 78 K. (b) The thresholds in the two spectral regions opposite in alignment sign coincide with the boundaries of the corresponding bands in the photoconductivity spectrum. The photocurrent is normalized against the incident photon flux. T = 300 K.

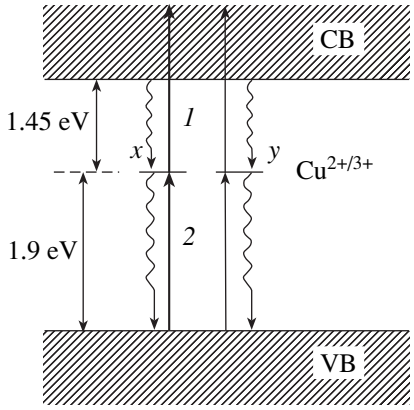

Fig. 6. Schematic diagram of the levels and transitions associated with the Cu_{Ta}–V_O tetragonal complexes. The light-induced electronic transitions are identified by straight arrows. The thickness of the arrows conventionally reflects the difference between the ionization cross sections for the *x* and *y* centers for the case of the light polarization **e** ∥ *y*.

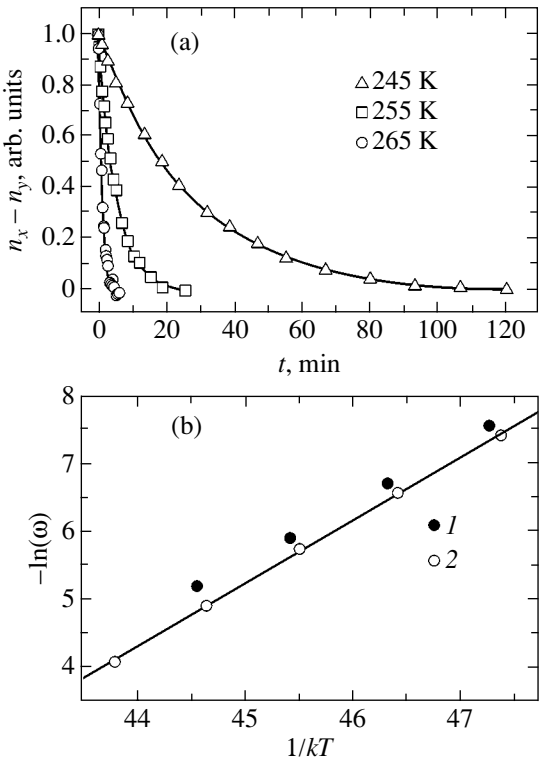

Fig. 7. (a) Thermal destruction of the Cu^{2+}–V_O center alignment in $KTaO_3$ found to occur at T = 245, 255, and 265 K. Points are the experimental data, and solid lines are obtained by fitting with a single exponential with characteristic decay time τ. (b) Rate of thermal destruction of the alignment ($w = 1/\tau$) of Cu^{2+}–V_O centers in $KTaO_3$ plotted vs. temperature. The initial alignment was created by polarized light with a wavelength of (*1*) 436 nm and (*2*) in the spectral interval 600–800 nm.

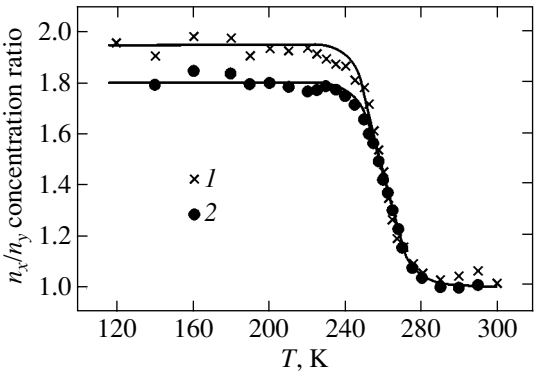

Fig. 8. Stationary alignment of the Cu^{2+}–V_O centers: (*1*) concentration ratio n_x/n_y vs. temperature obtained under simultaneous illumination with polarized light with a wavelength of 436 nm, P = 2 mW, and (*2*) concentration ratio n_y/n_x obtained as a function of temperature for the case of illumination by polarized light in the spectral interval 600–800 nm, P = 15 mW. Points are experimental data, and curves are calculated using parameters ΔE and w_0 derived from Fig. 7.

exp(–t/τ). The relaxation time τ for these three curves varies by nearly a factor of 30, from 1620 s (at 245 K) to 59 s (at 265 K). Figure 7b demonstrates an exponential dependence of $w = 1/\tau$ on $1/T$, which makes it possible to determine the activation energy of the process $\Delta E = 0.90 \pm 0.02$ eV and the prefactor $w_0 = (2 \pm 0.5) \times 10^{15}$ s^{-1}.

A similar study of thermal destruction of the alignment created by light with λ = 436 nm yielded values of ΔE and w_0 that coincide with the above figures.

Figure 8 displays temperature dependences of the steady-state degree of alignment (characterized by the n_x/n_y concentration ratio) under illumination of the sample with polarized light. Assuming that the concentration of the Cu_{Ta}^{3+} centers substantially exceeds the concentration of Cu_{Ta}^{2+}, the variation of the stationary value of the ratio n_y/n_x with increasing temperature can be described by the following expression (obtained using the equations from [4]):

$$\frac{n_y}{n_x} = \frac{R1 + w_0 \exp\left(-\frac{\Delta E}{kT}\right)}{R2 + w_0 \exp\left(-\frac{\Delta E}{kT}\right)}.$$

Here, $R1$ and $R2$ are fitting parameters, which can be expressed in terms of the corresponding ionization cross sections of the copper centers: (i) $R1 = \sigma_1^{\parallel} P_x + \sigma_1^{\perp} P_y$, and $R2 = \sigma_1^{\parallel} P_y + \sigma_1^{\perp} P_x$ for alignment with light in the interval 600–800 nm and (ii) $R1 = (\sigma_2^{\parallel} P_y + \sigma_2^{\perp} P_x)\frac{\Sigma Cu^{3+}}{\Sigma Cu^{2+}}$ and $R2 = (\sigma_2^{\parallel} P_x + \sigma_2^{\perp} P_y)\frac{\Sigma Cu^{3+}}{\Sigma Cu^{2+}}$ for alignment with light with a wavelength of 436 nm. The absorption cross sections $\sigma_i^{\parallel}$ and $\sigma_i^{\perp}$ (i = 1, 2) refer to photoionization transitions *1* and *2* in Fig. 6 for light polarized parallel and perpendicular to the center axis, respectively; P_x and P_y are the flux densities of photons with polarizations along the corresponding axes; and $\frac{\Sigma Cu^{3+}}{\Sigma Cu^{2+}}$ is the concentration ratio of the Cu_{Ta}^{3+} and Cu_{Ta}^{2+} centers.

We readily see that the curves calculated for the values of ΔE and w_0 derived from the data from Fig. 7 are in good agreement with the experiment.

4. DISCUSSION OF THE RESULTS

The remarkably good coincidence of the two characteristic energies derived from the spectral dependence of the copper center alignment, 1.45 and 1.90 eV; (Fig. 5a), with the cutoff energy of photoconductivity (1.45 eV) and the energy separating the two photoconductivity bands (1.90 eV; Fig. 5b) in $KTaO_3$ crystals unambiguously indicates the alignment effect to be related to the photoionization of copper ions and, thus, identifies the mechanism of alignment of the defect centers under study to be their orientation-sensitive photoionization. Note that the correlation between the spectral responses of the photoconductivity and of the alignment effect revealed in our earlier studies on the optical alignment of two tetragonal iron centers in the same $KTaO_3$ crystal [4] was substantially weaker and, therefore, could not be considered a convincing argument for establishing the real alignment mechanism.

Now let us discuss the involvement of both electron bands of the crystal in the alignment effect and the interpretation of the experimentally observed sign reversal of the alignment. The proposed explanation for the reversal of the alignment sign is convincingly argued for by the values of the alignment threshold (1.45 eV) and of the photon energy (1.9 eV) at which the degree of alignment starts to decrease rapidly and eventually change the sign of the effect (Fig. 5b); these values indicate that a second mechanism (process *2* in Fig. 6) becomes operative. Indeed, in accordance with the Born–Haber thermodynamic cycle [9–11], the sum of the threshold energies for photoionization of the Cu_{Ta}^{2+} tetragonal center and for electron transfer from the valence band to Cu_{Ta}^{3+} should be equal to the band gap energy E_g. The sum of the experimental values of these two threshold energies is 3.35 eV, which is close to the available estimates of E_g in $KTaO_3$, namely, 3.6–3.8 eV [12, 13].

Let us now discuss the results obtained in studying the kinetics of thermal destruction of the alignment of the centers. What physical process resulting in the decrease of the degree of alignment could be identified with the experimentally found energy ΔE? Such processes could be:

(1) thermally induced recharging $Cu_{Ta}^{2+} \rightleftharpoons Cu_{Ta}^{3+}$, i.e., transitions *1* or *2* in Fig. 6;

(2) thermal ionization of traps followed by the capture of electrons or holes by copper ions; and

(3) thermal reorientation of the centers under study (oxygen vacancy hopping).

If the alignment was destroyed by thermal ionization of Cu_{Ta}, the long-wavelength thresholds for alignment and for photocurrent (1.45 eV) would coincide with the value of ΔE (0.90 eV) extracted from the experimental data on the thermal destruction of alignment of the centers.

If the alignment (of either sign) occurred through thermal ionization of the traps, then transitions connecting the copper ions with the two energy bands of the crystal would require the existence of traps of two types, namely, of the electronic and hole types. The exact coincidence of the two values of ΔE obtained from the experimental data on the thermal destruction of the center alignment of either sign argues against the above mechanism.

Furthermore, recapture of the carriers released from the traps by Cu_{Ta} ions should have resulted, in addition to a decrease in the degree of alignment [4], in a change in the total spectral intensity. A special measurement of the intensity of the spectrum of aligned centers conducted in the 245- to 265-K interval revealed that the total intensity remains unchanged (within an experimental accuracy of, ±5%) after the light is turned off, although the degree of alignment becomes zero fairly rapidly at these temperatures.

Thus, we come to the conclusion that it is mechanism 3 that provides the only viable interpretation for the energy ΔE; namely, the energy found, $\Delta E = 0.90$ eV, is the height of the barrier separating various orientations of the center (for instance, the neighboring positions of the oxygen vacancy in the model of the center proposed in [6]).

Thus, the alignment of the copper centers created in $KTaO_3$ crystals in the course of anisotropic photoionization is destroyed thermally through real reorientations of the centers.

5. CONCLUSIONS

The results obtained in this study offer convincing proof that the optical alignment of the Cu_{Ta}^{2+} tetragonal centers in the potassium tantalate crystal occurs, similarly to that of Fe_K^{3+}–O_i and Fe_{Ta}^{4+}–V_O centers in the same crystal, through orientation-sensitive center recharging, as a result of which the axes of the defects with a given charge state become no longer equally distributed over the three ⟨100⟩ crystallographic directions. Thus, the mechanism of optical alignment of axial defect centers studied by us does not involve actual reorientations of them. At the same time, thermal relaxation of the aligned copper centers occurs through hopping of the oxygen vacancy belonging to the defect center.

ACKNOWLEDGMENTS

The authors are indebted to A.G. Badalyan and V.S. Vikhnin for helpful discussions, P.P. Syrnikov for

growing the copper-doped potassium tantalate crystals, and A.A. Kaplyanskiĭ for discussion of the results of the study and continuous encouragement.

This study was supported by the Russian Foundation for Basic Research (project no. 03-02-17632) and the European Office of Aerospace Research and Development (CRDF grant no. RPO-1385-ST-03).

REFERENCES

1. F. Lüty, in *Physics of Color Centers*, Ed. by W. B. Fowler (Academic, New York, 1968).
2. R. L. Berney and D. L. Cowan, Phys. Rev. B **23**, 37 (1981).
3. S. A. Basun, L. S. Sochava, V. E. Bursian, *et al.*, in *Proceedings of the XIII International Conference on Defects in Insulating Materials, Wake Forest Univ., USA* (1996); Mater. Sci. Forum **239–241**, 345 (1997).
4. S. A. Basun, V. É. Bursian, A. G. Razdobarin, and L. S. Sochava, Fiz. Tverd. Tela (St. Petersburg) **43**, 1025 (2001) [Phys. Solid State **43**, 1059 (2001)].
5. I. P. Bykov, V. V. Laguta, M. D. Glinchuk, *et al.*, Fiz. Tverd. Tela (Leningrad) **27**, 1908 (1985) [Sov. Phys. Solid State **27**, 1149 (1985)].
6. A. G. Badalyan, P. G. Baranov, D. V. Azamat, *et al.*, J. Phys.: Condens. Matter **14**, 6855 (2002).
7. V. S. Vikhnin, A. G. Badalyan, and P. G. Baranov, Ferroelectrics **283**, 149 (2003).
8. W. E. Blumberg, J. Eisinger, and S. Geschwind, Phys. Rev. **130**, 900 (1963).
9. M. Born, Verh. Dtsch. Phys. Ges. **21/22**, 679 (1919).
10. F. Haber, Verh. Dtsch. Phys. Ges. **21/22**, 750 (1919).
11. W. C. Wong, D. S. McClure, S. A. Basun, and M. R. Kokta, Phys. Rev. B **51**, 5682 (1995).
12. W. S. Baer, J. Phys. Chem. Solids **28**, 677 (1967).
13. A. Frova and P. J. Boddy, Phys. Rev. **153**, 606 (1967).

Translated by G. Skrebtsov

Physics of the Solid State, Vol. 46, No. 2, 2004, pp. 265–271. Translated from Fizika Tverdogo Tela, Vol. 46, No. 2, 2004, pp. 259–265.
Original Russian Text Copyright © 2004 by Avdyukhina, Anishchenko, Katsnel'son, Revkevich.

DEFECTS, DISLOCATIONS, AND PHYSICS OF STRENGTH

Role of Vacancies in the Structural Relaxation of Pd–Mo Alloys Saturated with Hydrogen

V. M. Avdyukhina, A. A. Anishchenko, A. A. Katsnel'son, and G. P. Revkevich

Moscow State University, Vorob'evy gory, Moscow, 119899 Russia

Received March 25, 2003; in final form, June 11, 2003

Abstract—The presence of an anomalously large number of vacancies in Pd–Mo alloys subjected to hydrogenation is revealed using precise x-ray diffractometry. These alloys are found to undergo nonmonotonic structural evolution during long-term relaxation. The evolution is characterized by aperiodic time variations in the number of coexisting phases, in the volume of each of them, and in the defect structure and by the cooperative motion of vacancies (as well as hydrogen in the early stage) between the matrix and defect regions. The key features of this evolution are an anomalously high concentration of not only hydrogen but also vacancies and a high concentration of defect regions, which causes thermodynamic instability of the system. The structural evolution has an oscillating character, because the maxima of thermodynamic instability of the matrix and of an ensemble of defect regions are separated in time. © *2004 MAIK "Nauka/Interperiodica".*

1. INTRODUCTION

The kinetics of structural transformations in palladium alloys after hydrogenation has been shown to be nonmonotonic [1–6]. Long-term variations in the defect structure were found in Pd–W–H alloys [1, 2]. Multiphase decomposition and stochastic changes in the number and volume fractions of coexisting phases during long-term relaxation were observed in binary alloys of Pd with Er, Ta, or Mo after their saturation with hydrogen [3–6]. Synergetic models, based on the "predator–prey" and Lorenz schemes, were proposed for some of these phenomena [1, 3, 7].

Oscillations in structural characteristics have been detected not only in metal–hydrogen systems but also in a number of other nonequilibrium systems, e.g., in severely irradiated [8] or plastically deformed [9] metals and alloys.

Analysis of the reported data showed that different palladium alloys exhibit radically different characters of structural changes after hydrogenation. To reveal possible causes of this phenomenon, we chose a Pd–Mo alloy. This alloy is a convenient subject for study, since the atomic radii of its components are virtually the same and the binding energy between hydrogen and palladium is substantially higher than that between hydrogen and molybdenum. The study of nonmonotonic evolution in Pd–Mo–H systems can offer some insight into the processes occurring in other nonequilibrium condensed systems.

In this work, we analyze the characteristic features of the structural evolution of Pd–Mo–H alloys after their saturation with hydrogen and the key factors determining these features and propose approaches to constructing a microscopic scheme of the phenomena that occur in these alloys during long-term relaxation.

2. EXPERIMENTAL

For examination, we used x-ray diffraction (monochromatized Cu$K_{\alpha 1}$ radiation) following the technique described in detail in [2–6]. A Pd–5 at. % Mo alloy was melted from high-purity metals in an electric-arc furnace and then homogenized at 900°C for 24 h. After cutting, the surface of the samples was polished; for this reason, the thickness of the deformed surface layer was greater than the x-ray penetration depth (less than 10 μm) for all reflection planes under study. The alloy was saturated with hydrogen electrolytically at a current density of 80 mA/cm^2 for one hour and then stored in air under normal conditions. The profiles of the (111), (200), (220), (311), and (222) diffraction lines were analyzed with the Origin software package.

The angular positions of the diffraction peaks for the initial state corresponded to the Reuss formula for deformed materials [10]; according to this formula, the dependence of a_{hkl} on the Miller indices has the form

$$a_{hkl} = a_0 + a_0 \sigma K_{hkl}. \quad (1)$$

Here, a_0 is the lattice parameter of the cubic matrix; σ is the elastic stress in the surface; and

$$K_{hkl} = S_{12} + \left(S_{11} - S_{12} - \frac{S_{44}}{2}\right)\frac{h^2k^2 + k^2l^2 + l^2h^2}{(h^2 + k^2 + l^2)^2},$$

where S_{11}, S_{12}, and S_{44} are the elastic compliance coefficients.

The elastic stresses appearing as a result of polishing the palladium alloys cause tensile strains along the normal to the sample surface [5, 11], which are induced by defect complexes generating image forces. The saturation of such alloys with hydrogen leads to a change

Dependence of σ_{comp} and a_{0comp} on the time t after hydrogenation

t, h	$\langle\sigma\rangle$, kg/mm^2	$\langle a_0\rangle$, Å	σ_{comp}, kg/mm^2	a_{0comp}, Å
0 (initial state)	–43	3.8873		
2–2.4	30	3.9070		
4.4–4.7	44	3.9007		
7.2–7.7	44	3.8953		
22.7–25.3	48	3.8886	112	3.8963
			–1	3.8886
26.5–28.6	55	3.8889	112	3.8954
			–9	3.8799
29.4–31.9	45	3.8877	118	3.8952
			3	3.8874
52.3–55.0	49	3.8853	139	3.8938
			10	3.8785
96.7–99.5	42	3.8827	134	3.8889
			–6	3.8795
120–123	49	3.8827	63	3.8855
			20	3.8755
193–196	52	3.8831	108	3.8903
			–13	3.8760
218–224	55	3.8831	115	3.8909
			18	3.8844
241–268	54	3.8830	85	3.8851
			–1	3.8793
16300	55	3.8841		
18400	57	3.8831		
20568	47	3.8855	95	3.8893
			10	3.8834
21672	19	3.8828		

in the sign of the elastic stresses in the system before hydrogenation (i.e., to compression) [5, 11].

We find the values of a_0 and σ from the least squares fits to the set of equations (1) for the (111), (200), (220), and (222) planes with an accuracy of 0.0004 Å and 3 kg/mm^2, respectively. After diffraction peaks were resolved into components corresponding to different coexisting phases of Pd–Mo–H alloys, the errors of measuring a_{0comp} and σ_{comp} (the lattice parameter and the level of elastic stresses for the corresponding phase) were 0.0015 Å and 10 kg/mm^2, respectively.

3. EXPERIMENTAL RESULTS

3.1. Time Dependence of $\langle a_0\rangle$ in the Pd–Mo–H Alloys: Effect of Vacancies

Analysis of the lattice parameter $\langle a_0\rangle$ of the cubic matrix averaged over all phases in the hydrogenated state (see table) showed that it varies nonmonotonically during relaxation. Indeed, after saturation of a Pd–Mo alloy with hydrogen, $\langle a_0\rangle$ first increases because of dissolved hydrogen (up to 8 at. %) and then decreases. In the range 22–28.6 h after saturation, the lattice parameter $\langle a_0\rangle$ eases to decrease, then again starts to decrease, and reaches its minimum (3.8827 Å) in 96 h after saturation; then, up to time t = 18400 h, it oscillates only slightly. The values of $\langle a_0\rangle$ measured in Pd–Mo alloys in the initial state coincide with the reported data [12, 13]. Four days after saturation, the lattice parameter was found to be 0.004 Å smaller. This decrease can be due to the appearance of vacancies, whose concentration can be calculated by the formula

$$\Delta v/v_0 = 3\Delta a_0/a_0 = n_{vac}\Delta v_{at}, \qquad (2)$$

where n_{vac} is the vacancy concentration, v_0 is the atomic volume, and Δv_{at} is the relative decrease in the atomic volume due to the formation of one vacancy ($0.2v_0$). The decrease in the lattice parameter indicated above corresponds to a vacancy content of 1.5% in the system, which is several orders of magnitude higher than their content in the equilibrium state of Pd. This high vacancy concentration in the hydrogen-saturated Pd–Mo–H alloys remains unchanged up to 18400-h storing. Then, in 2200 h, their amount considerably decreases, but, in the next 1100 h, it again increases to the values measured after 96- to 120-h relaxation.

Note that a high vacancy concentration has been found experimentally in Pd–H and Pd–Cu–H alloys [14–16]. The theoretical analysis performed in [17] showed that, in the Pd–H system, the vacancy concentration in the presence of hydrogen (e.g., 6 at. %) should exceed its equilibrium value for pure Pd by three orders of magnitude. However, such a theory has not yet been obtained for the more complex systems considered in this work.

3.2. Elastic Stresses and H–D–M–V Complexes in Pd–Mo–H Alloys

Measurements of elastic stresses after saturation of a Pd–Mo alloy with hydrogen (see table) showed that $\langle\sigma\rangle$ changes sign and increases in magnitude, first rapidly (over the first 5 h) and then slowly (up to time t = 25–26 h). During further relaxation, $\langle\sigma\rangle$ remains virtually unchanged to time t = 18400 h and then decreases by 10 kg/mm^2 over the period to t = 20570 h and additionally by 28 kg/mm^2 over the next period to t = 21670 h. Note that the time position of the weakly pronounced maximum of $\langle\sigma\rangle$ coincides with the instant of time at which $\langle a_0\rangle$ ceases to vary.

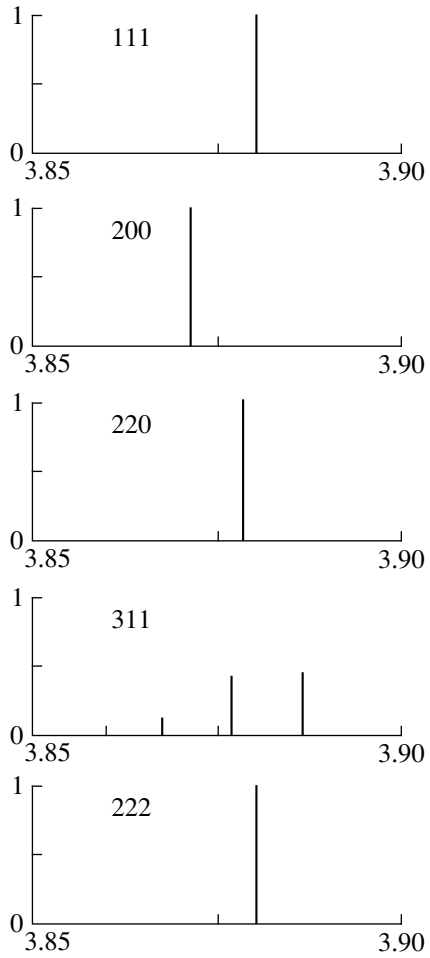

Fig. 1. Bar x-ray diffraction patterns of all diffraction peaks recorded within 16300 h. The abscissa is the lattice parameter (in Å), and the ordinate is the relative peak intensity.

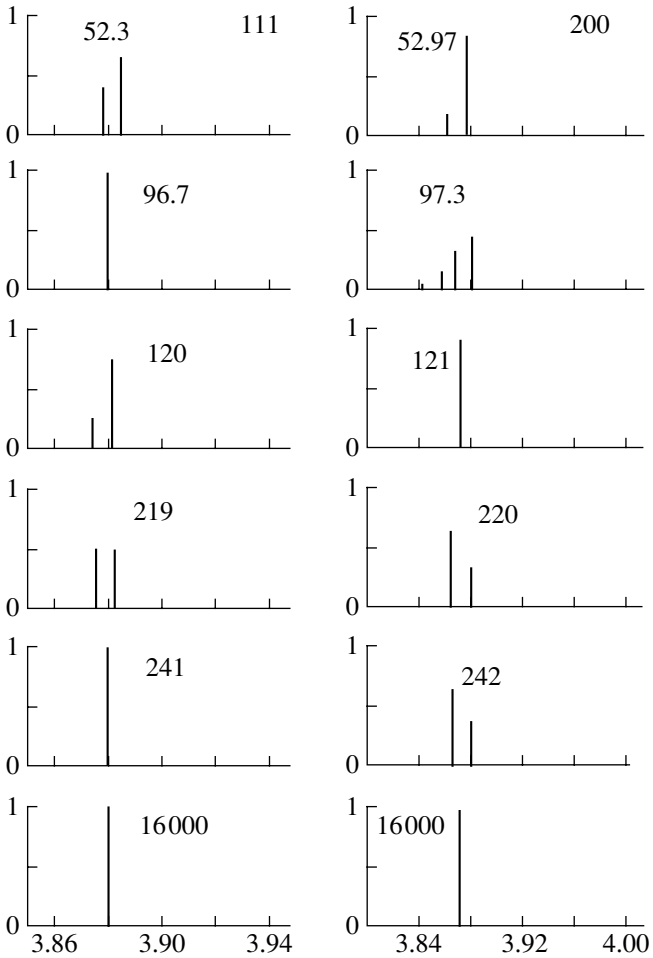

Fig. 2. Bar x-ray diffraction patterns of the (111) and (200) reflections for certain states of the system. The abscissa is the lattice parameter (in Å), and the ordinate is the relative peak intensity. Numerals at the peaks show the storing time (in hours).

The increase in $\langle a_0 \rangle$ when $\langle \sigma \rangle$ decreases slightly at $t = 20570$ h can be due to the removal of a significant portion of vacancies from the matrix to the surface (a small quantity of vacancies pass from defect regions to the matrix during this process). The simultaneous decrease in these parameters at $t = 21670$ h is explained by the passage of a significant portion of vacancies from the defect regions to the matrix.

By taking into account the variation of both $\langle a_0 \rangle$ and $\langle \sigma \rangle$, we can refine the composition of defect complexes appearing in the system upon hydrogenation. As was shown in [6], vacancies should enter into the defect complexes along with hydrogen. This model of the defect complexes (H–*D*–*M*–*V* complexes) explains a decrease in the specific volumes of the defect regions upon hydrogenation and, therefore, seems preferable to the model proposed earlier in [2]. The H–*D*–*M*–*V* complexes should be about a few nanometers in size, and their structure needs to be revealed.

3.3. Coexisting Elastically Stressed Cubic Phases in Saturated Pd–Mo–H Alloys

Figure 1 shows a bar x-ray diffraction pattern calculated from the experimental x-ray diffraction data obtained 16300 h after the saturation of a Pd–Mo alloy with hydrogen. As is seen, the (111), (200), (220), and (222) diffraction peaks again become single peaks (as before saturation) passing through various states (from a single-phase to a multiphase state and vise versa) during structural evolution (Fig. 2; see also [5]). The values of a_{111}, a_{200}, a_{220}, and a_{222} were found to correspond to the Reuss formula with a high accuracy. We found that $a_0 = 3.8873 \pm 0.0002$ Å and $\sigma = -43 \pm 2$ kg/mm^2 before saturation and $a_0 = 3.8841 \pm 0.0002$ Å and $\sigma = 55 \pm 2$ kg/mm^2 after saturation and storing under normal conditions for 16300 h. These data unambiguously indicate that the phase under study is an elastically stressed cubic phase having a decreased lattice parameter and stresses σ of opposite sign as compared to

those in the initial state. The vacancy content in the matrix of this phase is more than 1%, and the level of stresses is about 3–5% of the elastic modulus.

Figure 2 shows bar x-ray diffraction patterns for the (111) and (200) reflections at different instants of time during relaxation. The abscissa is a_{hkl} (in Å), and the ordinate is the volume fraction occupied by coherent-scattering domains (CSDs) of the phases found by decomposing the diffraction peaks. As is seen, in a number of states, one of the lines to be analyzed is a single line, whereas the other ones, as a rule, consist of several constituents. These patterns can be explained by the presence of states with several cubic phases having different $a_{0\text{comp}}$ and σ_{comp}. Note that each of the clearly resolved constituents of a multipeak reflection is attributed to a phase, which is defined as a homogeneous part of a heterogeneous system [18, 19].

An alternative interpretation of the experimental data obtained in this study could be the appearance of low-symmetry phases in Pd–Mo–H alloys upon hydrogenation. However, a special analysis showed that no such phases correspond to the set of experimentally measured d_{hkl}.

Thus, the phases that appear after hydrogenation can be represented as a set of several cubic phases having different lattice parameters and different levels of elastic stresses (or no stresses). The values of $\langle a_{0\text{comp}}\rangle$ and $\langle\sigma_{\text{comp}}\rangle$ calculated from the experimental data for a number of states are given in the table.

3.4. Correlated Variations of σ_{comp} and $a_{0\text{comp}}$

The table gives the data for CSDs with the maximum and minimum values of σ_{comp} and $a_{0\text{comp}}$. Analysis showed that the maximum values of $a_{0\text{comp}}$ always correspond to the maximum values of σ_{comp}. We failed to find a strong correlation between other (not maximum) values of σ_{comp} and $a_{0\text{comp}}$.

The effects detected can primarily be due to the saturation of alloys with vacancies after hydrogenation, as was noted above. The presence of vacancies in the matrix decreases the lattice parameters $a_{0\text{comp}}$ of coexisting phases; hence, lower values of this parameter should correspond to higher vacancy concentrations in the matrix. The removal of vacancies from the matrix should increase $a_{0\text{comp}}$. If vacancies were to go to the surface, the only detectable effect would be an increase in $a_{0\text{comp}}$. The fact that a considerable increase in $a_{0\text{comp}}$ is accompanied by an increase in σ_{comp} can be explained only by the motion of vacancies from the matrix (Pd-rich phase) to the defect regions (H–*D*–*M*–*V* complexes) rather than to the surface.

3.5. Hydrogen–Vacancy Complexes

The decreased values of $\langle a_0\rangle$ as compared to its value in the initial state observed 96 hours after hydrogenation and its further small oscillations mean that a significant part of the most mobile component of the system ("free" hydrogen atoms) leaves the matrix and that the matrix contains a large number of vacancies. However, there are experimental data indicating that part of the hydrogen is retained in the matrix for a long time to form H–*V* complexes in it. These complexes can appear due to vacancies capturing both free hydrogen and the hydrogen that escapes from (H–*D*–*M*–*V*) complexes. Depending on the hydrogen-to-vacancy content ratio in the H–*V* complexes, the formation of such complexes can result either in an isotropic increase or in an isotropic decrease in the lattice parameter. It should be noted that the presence of hydrogen that is bound to vacancies to form H–*V* complexes in Pd has been reported in the literature [15]; therefore, our assumption is based not only on our results. Note that these complexes can even be at equilibrium [16], but only at sufficiently high temperatures ($T > 700$°C).

Experimental data indicating the presence of H–*V* complexes are given in the table (σ_{comp}, $a_{0\text{comp}}$). It is seen that the lattice parameter of the phase where it is higher exceeds the lattice parameter of Pd (3.8907 Å) by 0.005–0.006 Å within 20–30 h after hydrogenation, which can be caused only by the presence of hydrogen in the system. At $t = 96$ h, the parameter becomes equal to 3.8890 Å and, a day later, decreases by 0.0035 Å. This decrease can be caused only by the presence of a fairly large quantity of vacancies in this phase. However, the presence of vacancies is insufficient to account for the subsequent 0.005-Å increase in the lattice parameter of this phase (in the range 190–219 h) followed by the 0.005-Å decrease (in the range 241–268 h). It is reasonable to suppose that free hydrogen leaves the matrix during these time intervals of sample storage after hydrogenation and that hydrogen is retained in the matrix in the form of small hydrogen–vacancy (H–*V*) complexes.

Thus, we can conclude that the phases having high values of $a_{0\text{comp}}$ represent Pd–Mo alloys with a low Mo concentration and with comparatively stable hydrogen–vacancy complexes. A phase with a smaller value of $a_{0\text{comp}}$ is characterized by a considerably higher Mo concentration; therefore, such a phase cannot contain much hydrogen but can contain many vacancies.

4. DISCUSSION OF THE RESULTS AND DEVELOPMENT OF A MICROSCOPIC MODEL

An increase in the relaxation time of a Pd–Mo–H alloy to 21500 h allowed us to reveal new (as compared to the data reported in [5, 6, 11]) features of its structural evolution and the related key factors. These are an anomalously high (about 1.5%) vacancy concentration

and correlated (cooperative) nonmonotonic processes of migration of vacancies and hydrogen and metal atoms between the matrix and defect regions, which take place even when the hydrogen concentration in the matrix becomes insignificant. The latter means that the decisive factor in the late evolution stages is a high concentration of vacancies migrating between the matrix (probably, H–*V* complexes) and defect (H–*D*–*M*–*V*) regions.

A microscopic model of the nonmonotonic structural evolution can be based on the following points. The introduction of hydrogen to the system followed by the formation of a new defect structure (vacancies and various complexes of hydrogen, vacancies, and, probably, dislocations) can cause the system to loose stability, as is the case in systems with a high dislocation density [20, 21]. As a result, at the initial stage of evolution, according to the theory [7] based on the Edwards thermodynamic representation and the Lorenz scheme, a substantially multilevel system forms in which multiphase decomposition is energetically favorable. During the subsequent relaxation, the defect structure of the system is continuously rearranged due to hydrogen removal and to redistribution and annihilation of defects. Since the rates of these processes are different, the thermodynamic stability of this system can change with time in a complicated manner. The evolution is determined by a number of factors operating in different directions, such as the migration of hydrogen atoms from Pd-rich CSDs in the matrix to the surface or grain boundaries and the formation of various small and large (like H–*D*–*M*–*V*) hydrogen–defect complexes. Note that these complexes can be identified from isotropic or anisotropic expansion or compression of the lattice. For example, isotropic expansion or compression of the lattice can be induced by the appearance of small H–*V* complexes (depending on the hydrogen-to-vacancy concentration ratio in these complexes), whereas anisotropic compression can be due to the formation of larger H–*D*–*M*–*V* complexes resulting in an increase in σ. The formation of these complexes can affect the thermodynamic stability of both the complexes and the matrix, thereby causing differently directed processes. As a result, transformations in the hydrogen-containing system produce a complex unstable defect structure, which initiates various processes of vacancy migration; the most important of such processes is likely the cooperative motion of vacancies between the matrix (probably, H–*V* complexes) and defect (H–*D*–*M*–*V*) regions.

Note that the time evolution of $a_{0\text{comp}}$ and σ_{comp} is characterized not only by the variation in their values with time but also by their scatter in each state; e.g., the single-phase state corresponds to no scatter in these parameters. Therefore, the process of migration of vacancies and of hydrogen and metal atoms can also be a factor affecting the variation in the phase composition of the system with time.

Now, we develop a consistent model of this process. We denote the vacancy concentration in the system by n; the vacancy concentrations in the matrix and defect regions by n_M and n_D, respectively; and the volumes of the matrix and defect regions by V_M and V_D, respectively. It is obvious that $n = (n_M V_M + n_D V_D)/V$.

If the process under analysis is reduced to vacancy redistribution between the matrix and defect regions, then $\Delta(n_M V_M) = -\Delta(n_D V_D)$ and only three variables of the four introduced above are independent. Let these variables be n_M, V_M, and V_D. The variables V_M and V_D characterize the volume fractions occupied by "predators," and n_M characterizes the concentration of "prey." In this notation, a set of equations describing the $n_M(t)$, $V_M(t)$, and $V_D(t)$ dependences can be written as [1]

$$\frac{dn_M}{dt} = \frac{n_M}{t_0}\left(1 - \frac{n_M}{n_{0M}} - \frac{V_D}{V_{0D}} + \frac{V_M}{V_{0M}}\right), \quad (3)$$

$$\frac{dV_D}{dt} = -\frac{V_D}{t_D}\left(1 - \frac{n_M}{n_M^0}\right), \quad (4)$$

$$\frac{dV_M}{dt} = -\frac{V_M}{t_{DM}}\left(1 - \frac{n_M}{n_M^0}\right). \quad (5)$$

In this work, we are interested only in the general character of the oscillating process. Therefore, it is sufficient to introduce the following characteristic scales: time scales t_0, t_D, and t_M that specify changes in the corresponding quantities in the off-line mode; scales of changes in the concentrations in the matrix regions due to vacancy adsorption n_M^0 and changes in the vacancy concentration in the matrix n_{0M}; and the corresponding scales V_{rm} and V_{dr} for the matrix and defect regions, respectively. In this case, in Eq. (3), the first term describes the vacancy generation under external action (upon hydrogenation), the second term allows for mutual annihilation (if any occurs) of free vacancies due to their clustering (note that, in the presence of hydrogen, this term can also characterize the formation of hydrogen–vacancy clusters), the third term describes a decrease in the vacancy concentration in the defect regions (in the corresponding time interval), and the last term represents an increase in this concentration in the matrix regions. Equations (4) and (5) describe the behavior of the defect and matrix regions, respectively; the first terms describe their Debye relaxation, and the second terms, an increase in the volume of predators (in other words, an increase in V_M or V_D) due to vacancy absorption. The directions of the changes in V_M and V_D are opposite, and the sign symmetry of Eqs. (4) and (5) means that changes in V_M and V_D are measured from the values most distant from their average levels. The experimental data on the structural evolution in the late stage (20570–21670 h) indicate that vacancies pass from the defect regions to the matrix; therefore, as an effective variable, we can take the difference in the vol-

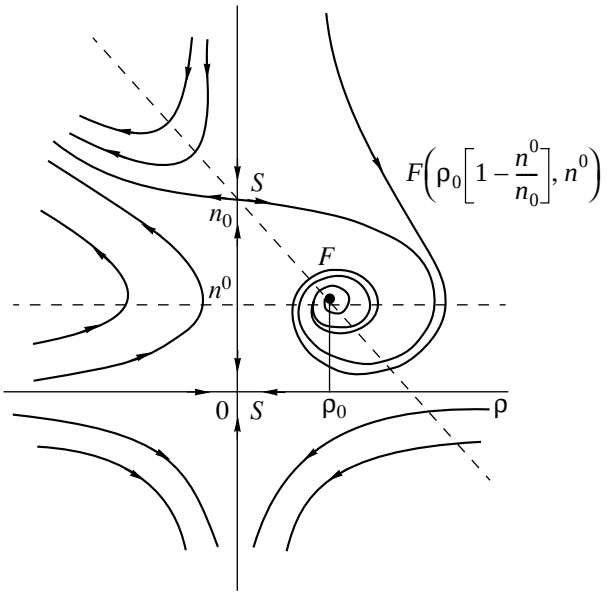

Fig. 3. Phase portrait.

umes V_M and V_D rather than the volumes themselves. In this case, the set of equations (3)–(5) can be simplified. With the notation $V_M - V_D = V_{MD} = \rho$, we can write

$$\frac{dn_M}{dt} = \frac{n_M}{t_0}\left(1 - \frac{n_M}{n_{0M}} - \frac{\rho}{\rho_0}\right), \quad (6)$$

$$\frac{d\rho}{dt} = -\frac{\rho}{t_0}\left(1 - \frac{n_M}{n_M^0}\right). \quad (7)$$

The physical meaning of the terms in the set of equations (6) and (7) is clear from the above description of the terms in Eqs. (3)–(5). The advantage of this set is in the transition to a simpler two-dimensional scheme, which makes it possible to construct a clear two-dimensional phase portrait describing the structural evolution of the system.

This phase portrait is shown in Fig. 3. As is seen, the (ρ, n_M) phase plane contains three singular points, namely, focus F with coordinates $\rho_F = \left(1 - \frac{n^0}{n_0}\right)\rho_0$ and $n_F = n^0$ and two saddles at (0, 0) and (0, n^0).

In the physical region (ρ, n) > 0, the evolution of the system is described by a phase path spiraling onto the focus F for any initial values of the volume fraction of the matrix regions and of the vacancy concentration.

This behavior corresponds to the experimentally observed oscillatory behavior of the system under study. If vacancies leave the system by reaching the surface or form new vacancy clusters (mainly, bivacancies), the oscillating processes have a damping character. Otherwise, they are steady (the classical predator–prey scheme). As shown in [1], this behavior of the system corresponds to a shift of the upper saddle to infinity and the transformation of the focus into a center.

Our analysis is not exhaustive, since we analyzed the situation where only vacancies are involved in the processes. A detailed analysis requires more variables in order to take into account at least the simultaneous motion of vacancies and hydrogen. However, solving this multidimensional problem is beyond the scope of this work and will be discussed in future publications.

Another problem is of interest. The recorded diffraction peaks or their constituents are fairly narrow, which indicates that the structural states in the same CSDs in the whole scattering volume of a crystal are virtually the same. This means that the processes proceeding in different regions of a crystal are synchronized. This phenomenon can be caused by the following factors. For example, collective modes of migrating hydrogen atoms, vacancies, etc., can appear in the system [22]; atomic motion in these modes is synchronized to a certain degree. Another explanation is based on the ideas put forward in [5, 7]. According to [7], the multilevel system under study consists of regions of intermediate size (peculiar quasi-cells similar to the Bénard cells [5, 23]), each of which corresponds to one of the long-lived (in the thermodynamic aspect) energy states, whose number is not large. The system evolves in such a way that only a small number of these states arise at different times because of vacancy and hydrogen migration. Therefore, the x-ray reflections consist of a few peaks and their widths are determined by the size and defect structure of CSDs of the corresponding phases, which were found to vary only slightly with time. For this explanation of the synchronization of the relaxation processes in different regions of a crystal, the role of vacancy and/or hydrogen migration is important. Due to the motion of vacancies and hydrogen not only between the defect regions and matrix (this process was considered in detail above) but also between the CSDs of different phases, the number of phases whose CSDs are in the reflecting position varies with time.

ACKNOWLEDGMENTS

We are grateful to V.A. Bushuev, A.I. Olemskiĭ, and I.A. Lubashevskiĭ for helpful discussions.

This work was supported by the Russian Foundation for Basic Research, project nos. 02-02-16537 and 03-02-06690.

REFERENCES

1. A. A. Katsnel'son, A. I. Olemskoĭ, I. V. Sukhorukova, and G. P. Revkevich, Vestn. Mosk. Univ., Ser. 3: Fiz. Astron. **35** (3), 94 (1994); Usp. Fiz. Nauk **165** (3), 331 (1995) [Phys. Usp. **38**, 317 (1995)].
2. V. M. Avdyukhina, A. A. Katsnel'son, and G. P. Revkevich, Kristallografiya **44** (1), 49 (1999) [Crystallogr. Rep. **44**, 44 (1999)].

3. A. A. Katsnel'son, V. M. Avdyukhina, D. A. Olemskoĭ, *et al.*, Fiz. Met. Metalloved. **88** (6), 63 (1999).
4. V. M. Avdyukhina, A. A. Katsnel'son, G. P. Revkevich, *et al.*, Al'tern. Énerg. Ékol., No. 1, 11 (2000).
5. V. M. Avdyukhina, A. A. Anishchenko, A. A. Katsnel'son, and G. P. Revkevich, Perspekt. Mater., No. 6, 12 (2001).
6. V. M. Avdyukhina, A. A. Anishchenko, A. A. Katsnel'son, and G. P. Revkevich, Perspekt. Mater., No. 4, 5 (2002).
7. V. M. Avdyukhina, A. A. Katsnel'son, D. A. Olemskoĭ, *et al.*, Fiz. Tverd. Tela (St. Petersburg) **44** (6), 979 (2002) [Phys. Solid State **44**, 1022 (2002)].
8. V. S. Khmelevskaya and V. G. Malynkin, Materialovedenie, No. 2, 25 (1998).
9. A. A. Katsnel'son and P. Sh. Dazhaev, Fiz. Met. Metalloved. **30**, 663 (1970).
10. Ya. S. Umanskiĭ, *X-ray Diffraction Methods for Studying Metals and Semiconductors* (Metallurgiya, Moscow, 1969).
11. M. K. Mitkova, G. P. Revkevich, and A. A. Katsnelson, J. Alloys Compd. **216**, 183 (1995).
12. M. Ura, Y. Haraguchi, F. L. Chen, and Y. Sakamoto, J. Alloys Compd. **231**, 436 (1995).
13. E. Kudielka-Arther and B. B. Argent, Proc. Phys. Soc. London **80**, 1143 (1962).
14. G. P. Revkevich, A. A. Katsnel'son, V. M. Khristov, and M. A. Knyazeva, Izv. Akad. Nauk SSSR, Met. **4**, 180 (1990).
15. Y. Fukai and N. Okuma, Phys. Rev. Lett. **73**, 1640 (1994).
16. Y. Fukai, Y. Ichii, Y. Goto, and K. Watanabe, J. Alloys Compd. **313**, 121 (2000).
17. V. M. Bugaev, V. A. Tatarenko, C. L. Tsinman, *et al.*, Int. J. Hydrogen Energy **24**, 135 (1999).
18. L. D. Landau and E. M. Lifshitz, *Course of Theoretical Physics*, Vol. 5: *Statistical Physics*, 2nd ed. (Nauka, Moscow, 1964; Pergamon, Oxford, 1976).
19. M. A. Leontovich, *Introduction to the Thermodynamics. Statistical Physics* (Nauka, Moscow, 1983).
20. G. A. Malygin, Usp. Fiz. Nauk **169** (6), 979 (1999) [Phys. Usp. **42**, 887 (1999)].
21. B. A. Grinberg and M. A. Ivanov, *Intermetallic Compounds Ni_3Al and TiAl: Microstructure and Deformation Behavior* (Ural. Otd. Ross. Akad. Nauk, Yekaterinburg, 2002).
22. A. I. Olemskoĭ and A. A. Katsnel'son, Usp. Fiz. Met. **3**, 5 (2002).
23. G. Nicolis and I. Prigogine, *Exploring Complexity* (Freeman, New York, 1989; Mir, Moscow, 1990).

Translated by K. Shakhlevich

Physics of the Solid State, Vol. 46, No. 2, 2004, pp. 272–276. Translated from Fizika Tverdogo Tela, Vol. 46, No. 2, 2004, pp. 266–270.
Original Russian Text Copyright © 2004 by Zhitaru, Durum.

DEFECTS, DISLOCATIONS, AND PHYSICS OF STRENGTH

Mobility of Edge and Screw Dislocations in γ-Irradiated LiF Crystals

R. P. Zhitaru and T. S. Durum

Institute of Applied Physics, Academy of Sciences of Moldova, Chisinau, 2028 Moldova

e-mail: mechprop@phys.asm.md

Received March 27, 2003; in final form, June 5, 2003

Abstract—The free path lengths of ensembles of edge and screw dislocations in the stress field of a concentrated load are studied in γ-irradiated LiF crystals. The relative mobility of edge and screw dislocations is found to depend substantially on the irradiation dose and temperature. The results obtained are discussed in the context of additional retardation of screw dislocations with dislocation debris that appears during double cross slip.
© 2004 MAIK "Nauka/Interperiodica".

1. INTRODUCTION

It was found in [1, 2] that the type of an impurity and its state in NaCl crystals doped with bivalent cation impurities substantially affect the relative mobility of edge and screw dislocations and the parameters of double cross slip (DCS). The results obtained were explained by additional retardation of screw dislocations with dislocation debris formed during DCS. However, some researchers [3, 4] believe that the relative mobility of dislocations appearing during the indentation of ionic crystals depends on the surface free energy of the crystals. It was found in [3, 4] that there is a surface potential barrier for screw dislocations and that this barrier depends on the surface energy and can be lowered by adsorption.

Thus, there are two standpoints: (i) the mobility of dislocations moving in the stress field of a concentrated load is determined by the volume properties of a crystal [1, 2] and (ii) the characteristics of dislocation rosettes depend on the surface free energy of the crystal [3, 4].

In this work, we aimed to study the dependence of the dislocation mobility in the stress field of an indenter on the internal energy of a crystal related to its defect structure rather than on the surface energy. Point defects and their complexes are known to change the parameters of dislocation double cross slip [5, 6]. Therefore, we can expect that their introduction in a crystal will affect the retardation of mobile dislocations with debris [debris-induced retardation (DR)] consisting of dislocation dipoles and other defects and appearing upon double cross slip of screw dislocations [5, 7]. This retardation can be significant [8, 9]; however, this effect has been studied insufficiently and is not always taken into account. Dislocation rosettes that appear on the (001) face of alkali-halide crystals near indentations consist of arms made up of ensembles of edge and screw dislocation half-loops [10]; therefore, their length should change differently as DR changes, since only screw segments of dislocation half-loops are mainly retarded.

The purpose of this work was to study the effect of stable radiation defects on the mobility and relative mobility of dislocations in the edge and screw arms of dislocation rosettes appearing in the stress field of an indenter in LiF single crystals. We chose LiF because the surface energy of LiF single crystals affect the arm lengths of dislocation rosettes only weakly [3, 4].

2. EXPERIMENTAL

LiF single crystals were grown at LOMO (St. Petersburg) and irradiated using γ radiation from a Co^{60} source. The irradiation doses were varied from 5×10^4 to 5×10^6 Gy. The irradiated samples were stored at room temperature in the dark for ~30 years; therefore, we studied single crystals with stable radiation defects and their complexes [11]. This conclusion follows from the study reported in [12], where it was found that, in the course of storing γ-irradiated LiF crystals at room temperature in the dark, unstable radiation-induced defects were destroyed and stable radiation defects formed. The fact that stable radiation defects are present in the LiF samples under study is supported by absorption spectra recorded with a spectrophotometer in the wavelength range 390–1000 nm.

The (001) cleavage plane of the crystals was deformed in a PMT-3 microhardness tester with a load P = 10–50 g applied to a diamond indenter. The deformation temperature was 77–573 K. Dislocation rosettes appearing around indentations and consisting of arms of edge and screw dislocation half-loops were revealed by chemical selective etching in a 10% aqueous solution of $FeCl_3$.

As a measure of the dislocation mobility in the stress field of the indenter, we took the free path lengths of dislocation ensembles in the $\{110\}_{90}$ edge and

$\{110\}_{45}$ screw slip planes (l_e and l_s, respectively). To compare the mobilities of edge and screw dislocation ensembles, we used the parameter $\xi = l_e/l_s$. The error in measuring l_e and l_s was 10%.

3. EXPERIMENTAL RESULTS AND DISCUSSION

Figure 1 shows dislocation rosettes near indentations on the (001) plane made at two temperatures in the initial and irradiated LiF single crystals. It is seen that both irradiation and a decrease in the indentation temperature result in changes in the structure of the rosettes, in particular, in the lengths of their dislocation arms.

Quantitative data on the effect of γ radiation on the arm lengths for edge and screw components at 293 K under various loads are given in Table 1 as the ratio between these lengths before (l_0) and after (l_{ir}) irradiation. At all loads and doses, γ radiation is seen to decrease the both types of arm lengths, with this effect being more pronounced for the screw components than for the edge ones (at all values of *P*, the length ratio in the second columns in Table 1 is higher than in the first ones).

The results of measuring the relative mobility of edge and screw dislocations in γ-irradiated LiF samples are shown in Fig. 2. After irradiation in the case of indentation at 293 K (curves *1*–*3*), the parameter ξ (characterizing the relative change in the lengths of the edge and screw arms of dislocation rosettes) increases. This effect manifests itself even at the minimum irradiation dose ($D = 5 \times 10^4$ Gy) and occurs at all loads, slightly decreasing with increasing *P*. As *D* increases further, ξ varies insignificantly and randomly. In the case of indentation at 77 K, ξ decreases rather than increases after irradiation (Fig. 2, curve *4*).

Thus, the results obtained indicate that, at *P* = const, the effect of the natural shortening of the arm lengths of dislocation rosettes at 293 K in the irradiated LiF crystals is found to be more significant for screw dislocations than for edge ones. In other words, the introduction of radiation defects leads to an increase in ξ; i.e., such defects retard the motion of screw half-loops more strongly than edge ones. This is most likely due to the fact that the radiation defects intensify the double cross slip of crew dislocations, which results in the formation of dislocation jogs and dipoles and thereby additionally retards these dislocations [5, 6].

The effect of the surface free energy on the free path length of leading dislocations in the stress field of the indenter in the screw and edge arms of a dislocation rosette is unlikely to be substantial for the γ-irradiated LiF crystals under study, which agrees with the results reported in [7, 13].

The above interpretation of the effect of the debris-induced retardation on the mobility of screw dislocations and the increased values of ξ in the irradiated LiF samples agree well with the γ-radiation-induced variation in the lengths of edge and screw dislocation arms (Table 1). Table 1 indicates that the decrease in the arm lengths after the introduction of radiation defects is more pronounced for screw half-loops than for edge ones and that this effect manifests itself clearly at all loads and irradiation doses. At each load and irradiation dose, screw dislocations are more sensitive to the introduction of radiation defects than are edge ones; their shortening is greater than that of edge dislocations. Thus, the data from Table 1 indicate that the retardation

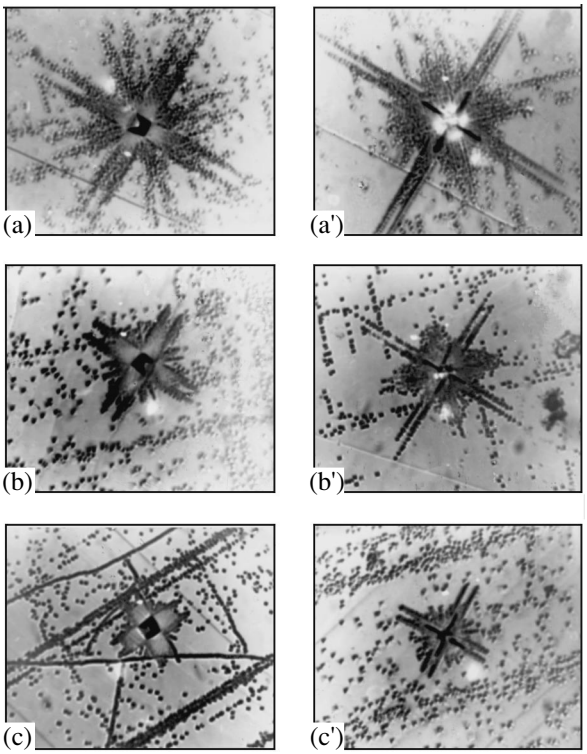

Fig. 1. Dislocation rosettes on the (001) plane of LiF single crystals (200×) produced under load *P* = 50 g at (a–c) *T* = 293 and (*a*'–*c*') 77 K for (*a*, *a*') nonirradiated samples and (*b*, *b*', *c*, *c*') γ-irradiated samples. (*b*, *b*') $D = 5 \times 10^4$ and (*c*, *c*') 5×10^5 Gy.

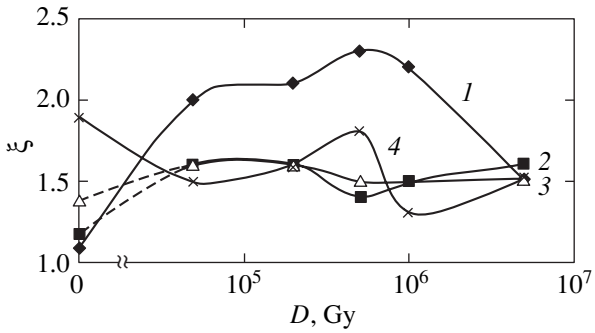

Fig. 2. Effect of the irradiation dose on the relative mobility ξ of edge and screw dislocations in LiF crystals at (*1*–*3*) 293 and (*4*) 77 K. (*1*) *P* = 10, (*2*) 30, and (*3*, *4*) 50 g. The indentation dimensions in cases (*1*) and (*4*) are the same.

Table 1. Effect of γ irradiation of LiF single crystals on the arm length of a dislocation rosette (l_0/l_{ir}) at T = 293 K

D, Gy	P = 10 g		P = 30 g		P = 50 g	
	edge	screw	edge	screw	edge	screw
5×10^4	1.6	2.2	1.9	2.5	2.3	2.5
2×10^5	2.2	4.0	2.3	3.1	–	–
5×10^5	2.6	5.3	3.6	4.2	6.0	6.3
10^6	3.0	5.7	3.7	4.7	4.0	4.2
5×10^6	3.0	4.0	4.1	5.3	4.0	5.0

Table 2. Relative mobility of edge and screw dislocations ($\xi = l_e/l_s$) in the stress field of an indenter at P = 10 g

D, Gy	T = 293 K	T = 373 K	T = 423 K	T = 473 K*
0	1.1	0.9	0.8	
5×10^4	2.0	1.1	0.8	0.8
2×10^5	2.1	1.3	1.3	0.7
5×10^5	2.3	1.4	1.5	1.2
10^6	2.2	1.2	1.9	1.3
5×10^6	1.5	1.3	1.6	1.0

* At T > 473 K, the arm lengths cannot be measured, because the dislocation mobility is high and arms are smeared.

of screw dislocations after the introduction of radiation defects is greater than that of edge dislocations. Although this effect takes place at all values of P, it is most pronounced at P = 10 g (Fig. 2).

The state of point defects and the effective stresses affect the DCS parameters. Depending on the applied load P, different states of stress form under an indenter [14]. Therefore, in a field of the same defects but under different effective stresses, the behavior of dislocations created upon indenting is different, which will affect the relative mobility of edge and screw dislocations, i.e., the value of ξ. Figure 2 shows that, at 293 K, the values of ξ at 50 g (ξ_{50}) in the irradiated and nonirradiated LiF crystals differ from those at 10 g (ξ_{10}). The introduction of radiation defects changes the sign of this difference: $\xi_{10} < \xi_{50}$ for the nonirradiated crystals and, on the contrary, $\xi_{10} > \xi_{50}$ for the γ-irradiated LiF crystals. This effect is likely due to the intensification of DCS in the irradiated LiF samples as compared to the nonirradiated ones. However, the fact that $\xi_{10} \neq \xi_{50}$ for the same type of LiF samples is likely caused by different states of stress at 10 and 50 g. At P = 50 g, the effective stresses under the indenter in the nonirradiated and γ-irradiated LiF crystals are higher than those at P = 10 g [15].

However, the state of radiation defects in the stress field of the indenter can also change, which causes changes in the character of DCS and in its effect on the mobility of dislocations, especially screw dislocations. These processes proceed differently depending on the applied stresses (i.e., the applied load). Hence, the conditions at 50 and 10 g are different for dislocations. This difference is likely the cause of the fact that ξ_{50} becomes smaller than ξ_{10} in the irradiated LiF samples. The data obtained by us also allow the conclusion that radiation defects mainly affect screw dislocations and that the deformation-induced stresses in the field of radiation defects, on the contrary, mainly affect the mobility of edge dislocations. The former effect manifests itself clearly at 10 g; the latter, at 50 g.

The experiments performed in a wide temperature range (293–573 K) and at 77 K showed that the effects detected at room temperature after indenting the γ-irradiated LiF crystals are also observed at other temperatures. At $T \geq 293$ K, as seen from Table 2, the relative dislocation mobility in the γ-irradiated LiF samples (i.e., the samples with radiation defects) is higher, $\xi_{ir} > \xi_0$ (ξ_0 and ξ_{ir} correspond to a sample before and after irradiation, respectively). This effect, being most pronounced at 293 K, decreases with increasing temperature; i.e., the parameter ξ at T > 293 K is smaller that its values at T = 293 K. Table 2 contains data at P = 10 g. These phenomena are even more pronounced at P = 50 g; however, because of the presence of spreading arms, the measurements are performed in a narrower temperature range. Table 2 also shows the absence of a clear dependence of ξ on the irradiation dose. It should be noted that, at T > 293 K, the values of ξ at the maximum irradiation dose (5×10^8 Gy) are larger than at the minimum dose (5×10^5 Gy); however, the opposite effect is detected at T = 293 K. This difference indicates that the effect of the irradiation dose on the variation in ξ depends on the temperature.

The effects observed at T > 293 K can also be explained in terms of the additional retardation of screw dislocations caused by the defects that form during cross slip. An increase in temperature is known to cause complexes and clusters of point defects to be finer. Hence, at T > 293 K, the quantity of radiation defects in the γ-irradiated LiF crystals becomes higher. However, thermal stresses are favorable for mobile dislocations to overcome these defects. Therefore, the higher T, the higher the thermal activation and the longer the dislocation path length in the basic slip plane. An increase in the number of retardation centers as a result of radiation complexes becoming finer also leads to an increase in the number of DCS events. At high temperatures, shear stresses in the basic slip plane and in the transverse planes differ only slightly. Therefore, as a result of DCS, dislocations undergo intense multiplication, screw dislocations are subjected to weak DR, the length l_s becomes longer, and $\xi = l_e/l_s$ decreases (Table 2). The higher the temperature, the weaker the retardation of screw dislocations with the debris, since at high T the debris (dislocation dipoles) becomes a source of dislo-

cation multiplication. This process affects the structure of a dislocation rosette appearing around an indentation. Screw arms become substantially wider and extend far from an indentation (prick), which correlates with a decrease in the screw dislocation retardation with the debris. At temperatures $T \geq 573$ K, this retardation is virtually absent.

The variation of ξ at a low temperature (77 K) is of interest. After the introduction of radiation defects, ξ decreases (rather than increases, as in the case of $T >$ 293 K) and depends on the irradiation dose only weakly (Fig. 2). Moreover, a decrease from 293 to 77 K affects the relative mobility of edge and screw dislocations differently in the nonirradiated and irradiated LiF crystals; the parameter ξ increases in the former samples and decreases in the latter. For the nonirradiated samples, we have $\xi_{77} > \xi_{293}$, and for the irradiated samples, on the contrary, we have $\xi_{77} < \xi_{293}$ (in Fig. 2, curve *4* is below curve *1*).

A decrease in temperature from 293 to 77 K for a number of alkali-halide crystals is known to cause anomalous dislocation mobility in the stress field of a concentrated load [14–17]. The dislocation half-loops of the edge arms of dislocation rosettes are especially sensitive to a decrease in temperature. In particular, in the LiF crystals studied in this work (Fig. 3) and in [16, 17], the edge arms become longer and the screw-arm lengths remain virtually unchanged as the temperature decreases from 293 to 77 K.

The introduction of radiation defects also causes elongation of arms at 77 K. However, not only edge arms but also screw arms elongate (Fig. 3) and the increase in l_e and l_s upon the temperature decrease is approximately the same. This means that at 77 K radiation defects change the mobility of edge half-loops only weakly and increase the mobility of screw half-loops. The latter is likely determined by a decrease in the additional retardation of screw dislocations with the debris. While being somewhat sensitive to the radiation defects, the mobility of edge half-loops is mainly specified by the temperature decrease. The increase in l_e becomes smaller only at very high irradiation doses ($D \geq 10^6$ Gy); the dependence of l_s on the irradiation dose is weak.

Thus, the sensitivities of edge and screw dislocations to stable radiation defects produced during γ irradiation of LiF crystals are different at 77 K. The clearly pronounced elongation of l_s and the weak change in l_e due to the temperature decreasing from 293 to 77 K cause a decrease in the parameter ξ in the γ-irradiated LiF crystals as compared to the nonirradiated ones and lead to the inequality $\xi_{ir} < \xi_0$ at 77 K (Fig. 2, curve *4*).

Intense cross slip of screw dislocations obviously plays an important role in the effects observed at 77 K [18]. As the temperature decreases, the cross slip is retarded; this retardation is greater in the irradiated samples, where the probability of cross slip is higher.

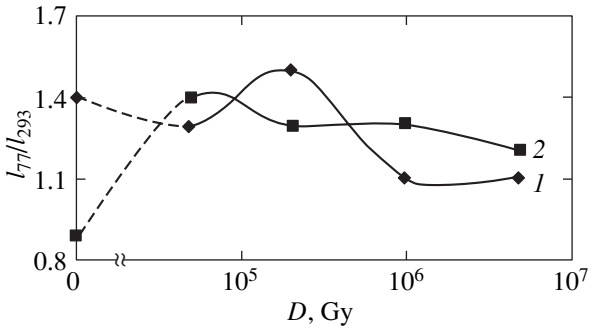

Fig. 3. Relative variation of the lengths of (*1*) edge and (*2*) screw dislocation arms as the temperature decreases from 293 to 77 K. P = 10 g.

Therefore, the screw dislocation retardation with the debris is weaker at low temperatures. The temperature dependence of the mobility of edge half-loops is specified by double cross slip to a smaller degree. Therefore, as the temperature decreases from 293 to 77 K, the parameter $\xi = l_e/l_s$ should decrease in the γ-irradiated samples to a greater extent than in the initial samples, which was observed experimentally.

4. CONCLUSIONS

Thus, we have shown that radiation defects in LiF crystals substantially affect the relative mobility of edge and screw dislocations. The radiation-induced variation of the parameter ξ in a wide temperature range (77–473 K) is explained by a change in the character of DCS and by the related additional retardation of screw dislocations with dislocation debris. The results obtained allow the conclusion that the parameter ξ can be used to estimate the role of secondary defects appearing upon the cross slip of screw dislocations in strain hardening of crystals. The variation of ξ with external and internal factors gives information on the character of the double cross slip.

REFERENCES

1. Yu. S. Boyarskaya, R. P. Zhitaru, and M. A. Linte, Kristallografiya **41** (4), 737 (1996) [Crystallogr. Rep. **41**, 700 (1996)].
2. R. P. Zhitaru and N. A. Palistrant, Fiz. Tverd. Tela (St. Petersburg) **41** (6), 1041 (1999) [Phys. Solid State **41**, 947 (1999)].
3. E. D. Shchukin, V. I. Savenko, and L. A. Kochanova, Dokl. Akad. Nauk SSSR **200** (2), 406 (1971).
4. V. I. Savenko, L. A. Kochanova, and E. D. Shchukin, Kristallografiya **17** (5), 995 (1972) [Sov. Phys. Crystallogr. **17**, 874 (1972)].
5. B. I. Smirnov, *Dislocation Structure and Strengthening of Crystals* (Nauka, Leningrad, 1981).
6. R. P. Zhitaru, O. V. Klyavin, B. I. Smirnov, and A. V. Stepanov, in *Physical Processes of Plastic Deformation at*

Low Temperatures (Naukova Dumka, Kiev, 1974), p. 112.

7. F. Appel, H. Grube, U. Messerschmidt, and B. I. Smirnov, Cryst. Lattice Defects **7**, 65 (1977).
8. J. J. Gilman, J. Appl. Phys. **33** (9), 2703 (1962).
9. W. J. Johnston and J. J. Gilman, J. Appl. Phys. **31**, 632 (1960).
10. A. A. Predvoditelev, V. N. Rozhanskiĭ, and V. M. Stepanova, Kristallografiya **7**, 418 (1962) [Sov. Phys. Crystallogr. **7**, 330 (1962)].
11. Yu. S. Boyarskaya and R. P. Zhitaru, Phys. Status Solidi **42**, 29 (1970).
12. M. P. Abramishvili, Z. G. Akhvlediani, T. L. Kalabegishvili, *et al.*, Fiz. Tverd. Tela (St. Petersburg) **42** (10), 1794 (2000) [Phys. Solid State **42**, 1840 (2000)].
13. F. Appel and U. Messerschmidt, Phys. Status Solidi **35** (2), 1003 (1969).
14. Yu. S. Boyarskaya, D. Z. Grabko, and M. S. Kats, *Physics of Microindentation Processes* (Shtiintsa, Chisinau, 1986).
15. Yu. S. Boyarskaya, *Deformation of Crystals in Microhardness Tests* (Shtiintsa, Chisinau, 1972).
16. Yu. S. Boyarskaya, S. S. Shutova, R. P. Zhitaru, and E. I. Purich, *Deformation of Crystals under a Concentrated Load* (Shtiintsa, Chisinau, 1978).
17. Yu. S. Boyarskaya, D. Z. Grabko, and R. P. Zhitaru, *Pseudomobility of Dislocations in Pure and Doped Alkali–Halide Crystals* (Shtiintsa, Chisinau, 1986).
18. O. V. Klyavin, *Physics of Crystal Plasticity at Liquid-Helium Temperatures* (Nauka, Moscow, 1987).

Translated by K. Shakhlevich

Physics of the Solid State, Vol. 46, No. 2, 2004, pp. 277–282. Translated from Fizika Tverdogo Tela, Vol. 46, No. 2, 2004, pp. 271–276.
Original Russian Text Copyright © 2004 by Shutyĭ, Sementsov.

MAGNETISM AND FERROELECTRICITY

Dynamic Magnetization Reversal and Bistable States in Antiferromagnetic Multilayer Structures

A. M. Shutyĭ and D. I. Sementsov

Ulyanovsk State University, ul. Tolstogo 42, Ulyanovsk, 432700 Russia

e-mail: shuty@mail.ru

Received May 6, 2003

Abstract—The dynamic behavior of the magnetization under a transverse microwave field is investigated in a system of magnetic layers with cubic crystallographic anisotropy coupled through interlayer antiferromagnetic exchange interaction. An orientational phase transition is found to occur as the microwave field frequency and amplitude are varied. It is established that there is a frequency range in which several steady-state regimes of precession of magnetic moments exist. The limits of this range can be efficiently controlled both by varying the strength of the bias magnetic field and the amplitude of the microwave field. *© 2004 MAIK "Nauka/Interperiodica".*

1. The unique static and dynamic properties of periodic multilayer structures consisting of thin magnetic metallic layers separated by nonmagnetic metallic spacers [1–4] are primarily determined by the character of the magnetic-moment coupling due to strong indirect exchange, which gives rise to ferromagnetic (FM), antiferromagnetic (AFM), or noncollinear ordering of magnetic moments of adjacent layers [5, 6]. The properties of such structures near the critical value of the applied field at which an orientational phase transition occurs are of particular interest. In the vicinity of such phase transition points, favorable conditions are created for the excitation (by using a weak microwave field) of various dynamic regimes sensitive to small changes in the parameters of the system and of the controlling fields. The structures with AFM exchange coupling are the most favorable for the occurrence of various equilibrium orientation states and dynamic regimes [7–9]. One of the effects of practical importance that are exhibited by such structures is the nonlinear dynamic magnetization reversal caused by a microwave (mw) field. We showed in [9] that, for films with uniaxial in-plane anisotropy and with dipole–dipole coupling between the layers, there exists a certain frequency-dependent critical value $h_c(\omega)$ of the mw field amplitude for the case when the bias field is close to the value at which the orientation of magnetic moments in opposite directions becomes unstable. At $h < h_c$, magnetic moments precess in an AFM configuration, whereas at $h \geq h_c$ dynamic magnetization reversal occurs under the action of the mw field and the magnetic moments precess either in an FM collinear configuration or in a noncollinear configuration, i.e., about axes making a certain angle depending on the value of the coupling constant. In this paper, we investigate the dynamic behavior of an AFM multilayer structure with strong exchange interaction and cubic crystallographic anisotropy subjected to an mw field in the vicinity of an orientational phase transition point.

2. We consider a system consisting of a fairly large number ($n \gg 1$) of magnetic metallic layers with thickness d_i and magnetization $\mathbf{M}_i$, where i is the number of a magnetic layer. The layers are separated by nonmagnetic spacers whose thickness is such that AFM exchange coupling takes place between adjacent magnetic layers. In such structures, according to the available experimental data, e.g., for $(Fe/Cr)_n$ multilayers [10], the magnetic anisotropy of magnetic layers consists of induced uniaxial (easy-axis) anisotropy and cubic crystallographic anisotropy. The [100] and [010] axes lie in the plane of a layer, and the easy axis of the induced anisotropy is perpendicular to this plane. In this case, the free energy of the system (per unit area) is given by

$$E = \sum_{i=1}^{n} d_i \Big[-\mathbf{H}\mathbf{M}_i + \frac{K_{1i}}{4}(\sin^2 2\psi_i + \cos^4\psi_i \sin^2 2\varphi_i) + \frac{K_{2i}}{16}\sin^2 2\psi_i \cos^2\psi_i \sin^2 2\varphi_i + (K_{ui} - 2\pi M_i^2)\cos^2\psi_i \Big] + J\sum_{i=1}^{n} \frac{\mathbf{M}_i \mathbf{M}_{i+1}}{M_i M_{i+1}}, \quad (1)$$

where J is the bilinear coupling constant characterizing the indirect exchange interaction between magnetic moments of adjacent layers and depending, in general, on the thickness, material, and structural parameters of the spacer layer; K_{1i} and K_{2i} are the first and second cubic anisotropy constants, respectively; K_{ui} is the growth anisotropy constant; $\mathbf{H}$ is the dc bias field; φ_i is the azimuthal angle defining the orientation of the mag-

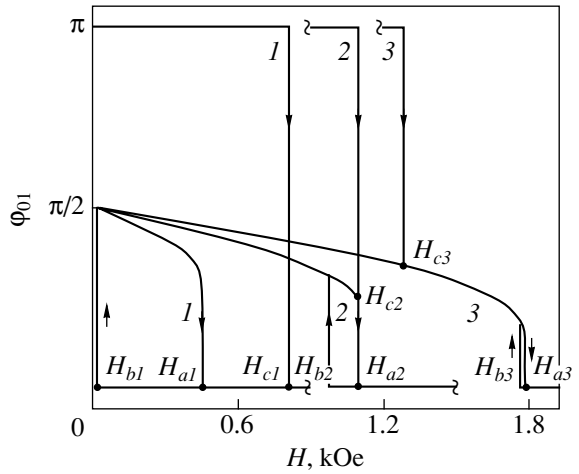

Fig. 1. Field dependences of the equilibrium angle φ_{01} in the cases of 180° and 90° magnetization reversal for different values of the coupling constant J: (*1*) 0.05, (*2*) 0.132, and (*3*) 0.2 erg/cm^2.

netic moment of the corresponding layer measured from the [100] axis; and ψ_i is the deflection angle of the magnetization $\mathbf{M}_i$ from the layer plane. All magnetic layers are assumed to be identical; i.e., $M_i = M$, $d_i = d$, $K_{ui} = K_u$, $K_{1i} = K_1$, and $K_{2i} = K_2$. It is also assumed that the coupling constant J is positive; therefore, the coupling between the magnetic moments of adjacent layers is antiferromagnetic and they are oppositely directed in a zero bias field.

Thus, all magnetic layers are separated into two subsystems ($j = 1, 2$) in each of which the behavior of the layers is identical. For actual layered structures, the demagnetizing fields are large ($4\pi M \gg 2K_u/M$, JM); therefore, in the case of in-plane bias field $\mathbf{H}$, the magnetic moments lie in the layer plane and we have $\psi_{0j} = 0$ in equilibrium. The equilibrium azimuthal angles $\varphi_{0j}(H)$ can be found from the equilibrium conditions $\partial E/\partial\varphi_j = 0$ and $\partial^2 E/\partial\varphi_j^2 > 0$. Using these conditions and Eq. (1), we obtain

$$\begin{aligned} &2HM\sin(\varphi_{0j} - \varphi_H) + K_1\sin 4\varphi_{0j} \\ &\quad - 2\bar{J}\sin(\varphi_{0j} - \varphi_{03-j}) = 0, \\ &HM\cos(\varphi_{0j} - \varphi_H) + 2K_1\cos 4\varphi_{0j} \\ &\quad - \bar{J}\cos(\varphi_{0j} - \varphi_{03-j}) > 0, \\ &\quad j = 1, 2, \end{aligned} \tag{2}$$

where $\bar{J} = 2J/d$ and φ_H is the azimuthal angle defining the direction of the in-plane field $\mathbf{H}$ measured from the [100] axis.

The motion of the magnetization vectors of the layers $\mathbf{M}_i$ can be described by the Landau–Lifshitz equations, which have the following form in a spherical system of coordinates:

$$\begin{aligned} \dot{\varphi}_j Md\cos\psi_i &= \gamma\frac{\partial E}{\partial\psi_j} + \frac{\lambda}{M}\frac{1}{\cos\psi_j}\frac{\partial E}{\partial\varphi_j}, \\ \dot{\psi}_j Md &= \frac{\lambda}{M}\frac{\partial E}{\partial\psi_j} - \gamma\frac{1}{\cos\psi_j}\frac{\partial E}{\partial\varphi_j}, \end{aligned} \tag{3}$$

where γ is the gyromagnetic ratio and λ is the damping parameter [11]. In a linear approximation with respect to small deviations from the equilibrium position ($\delta_j = \varphi_j - \varphi_{0j}$, ψ_j), the high-frequency magnetic susceptibility of the system can be written as the sum $\chi = \chi_1 + \chi_2$, where the susceptibilities of the individual subsystems are

$$\chi_j = \frac{M^2}{\Delta_1\Delta_2 - D^2}(D\cos\varphi_{03-j} - \Delta_{3-j}\cos\varphi_{0j}). \tag{4}$$

Here, $D = \bar{J}\cos(\varphi_{01} - \varphi_{02})$, $\Delta_j = (\omega_{0j}^2 - \omega^2 + 4\pi i\lambda\omega)/4\pi\gamma^2 - D$, and the resonance frequencies of the noninteracting magnetic subsystems are

$$\omega_{0j}^2 = 4\pi\gamma^2[HM\cos(\varphi_{0j} - \varphi_H) + 2K_1\cos 4\varphi_{0j}]. \tag{5}$$

We will perform numerical calculations using the parameters of an actual $(Fe/Cr)_n$ structure. For Fe layers, $M = 1620$ G, $K_1 = 4.6\times10^5$ erg/cm^3, $K_2 = 1.5\times10^5$ erg/cm^3, $K_u = 2.06\times10^6$ erg/cm^3, $d = 21.2\times10^{-8}$ cm, $\lambda = 5\times10^7$ s^{-1}, and $\gamma = 1.76\times10^7$ (Oe s)$^{-1}$. The parameters of Cr layers are not involved explicitly in Eq. (1), but they determine the value of the coupling constant J [3]. For the films under study, the amplitude of oscillation of the polar angle is always significantly smaller than that of the azimuthal angle.

3. Analysis of the equilibrium conditions (2) shows that, in the systems under study, orientation hysteresis loops and the bistable states associated with them arise as the bias field changes in value. Figure 1 shows the equilibrium azimuthal angle of the magnetic moment of one of the subsystems of magnetic layers φ_{01} as a function of bias field H calculated for three values of the coupling constant $J = 0.05$, 0.132, and 0.2 erg/cm^2 (curves *1–3*). In the case where the initial orientation of the magnetic moments is $\varphi_{01} = \pi$ and $\varphi_{02} = 0$ and the orientation of the bias field corresponds to $\varphi_H = 0$, the initial state remains stable as the bias field varies from $H = 0$ to $H = H_c$, where

$$H_c = \frac{2}{M}\sqrt{K_1(\bar{J} + K_1)}. \tag{6}$$

When the field reaches this limiting value, an orientational phase transition occurs in a jump. If the coupling constant is small, $\bar{J} < \bar{J}_{ca}$ (curve 1), 180° magnetization reversal of the first magnetic subsystem takes place, while the azimuthal angle in the second subsystem remains unchanged. If the coupling constant is

sufficiently large, $\bar{J} > \bar{J}_{ca}$, the magnetization direction of the layers $j = 2$ is also changed because of the AFM coupling; in this case, we have $\varphi_{02}(H_c) = -\varphi_{01}(H_c)$.

A further increase in the bias field causes the angle between the magnetizations of adjacent layers $\Delta\varphi_0 = \varphi_{01} - \varphi_{02}$ to decrease. When the field reaches another critical value

$$H = H_a = \frac{4}{3M}\sqrt{\frac{\bar{J} + K_1}{6K_1}}(\bar{J} + K_1) \quad (7)$$

this angle becomes minimal, $\Delta\varphi_0 = 2\varphi_a(J)$ (this minimum is smaller, the greater the coupling constant), and another phase transition occurs to a state in which the magnetic moments are aligned with the field. The minimal angle between the magnetic moments in the case of their noncollinear configuration can be found from Eqs. (2) and (7) to be

$$\varphi_a = \arccos\sqrt{\frac{\bar{J} + K_1}{6K_1}}. \quad (8)$$

The critical value of the coupling constant $\bar{J}_{ca}$ introduced above corresponds to the case of $H_c = H_a$ and is given by

$$\bar{J}_{ca} = \frac{3\sqrt{6} - 2}{2}K_1. \quad (9)$$

As the bias field decreases from a value $H > H_a$, for which the state with parallel magnetic moments of the layers is stable, this state persists down to the field value

$$H_b = \frac{2}{M}(\bar{J} - K_1). \quad (10)$$

At $H = H_b$, the inverse orientational phase transition occurs, with the result that the angle between the vectors $\mathbf{M}_1$ and $\mathbf{M}_2$ becomes nonzero and their equilibrium angles become equal to $\varphi_{01}(H_b) = -\varphi_{02}(H_b)$ in a jump. As the bias field is decreased further, the angle between the magnetizations increases smoothly and again becomes equal to π at $H = 0$. However, each of the magnetization vectors does not return to its original position; instead, they form a configuration with angles $\varphi_{01} = \pi/2$ and $\varphi_{02} = -\pi/2$.

In the case of in-plane 90° magnetization reversal, which takes place when the initial state is $\varphi_{01} = -\varphi_{02} = \pi/2$ and $\varphi_H = 0$, an increase in the bias field to the value H_a causes the angle between the magnetic moments to decrease smoothly. At $H = H_a$, as in the case considered above, an orientational phase transition occurs to the state with a parallel alignment of the magnetic moments. If the bias field is then decreased, the noncollinear configuration recovers when the field becomes equal to H_b and the inverse phase transition occurs. Thus, at small values of the coupling constant, we have an orientation hysteresis loop, which becomes narrower as the value of J increases. If the coupling constant is large, we have $H_b = H_a$ and the hysteresis loop does not arise.

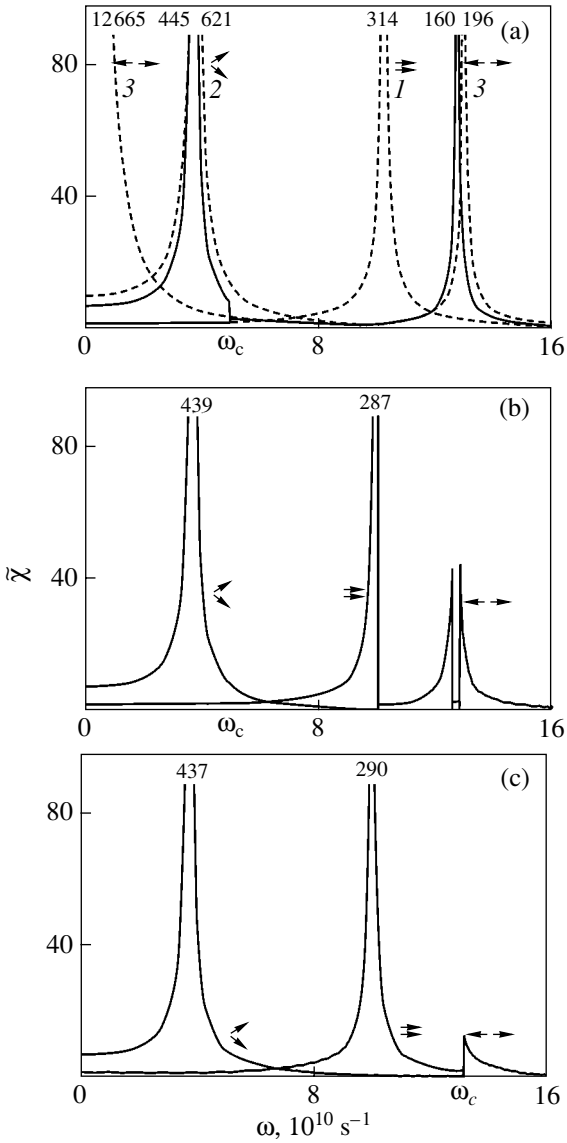

Fig. 2. Frequency dependences of the high-frequency magnetic susceptibility of the system under study for J = 0.132 erg/cm^2, H = 1093.2 Oe, and different values of h: (a) 0.2, (b) 0.4, and (c) 1.0 Oe.

4. Near the critical values of the bias field corresponding to orientational phase transitions, the system with AFM exchange coupling is most sensitive to mw fields. In the system with cubic crystallographic anisotropy, the parameters can be such that $\bar{J} \approx \bar{J}_{ca}$ and the two critical values H_a and H_c of the bias field become close to each other. Figure 2 shows the frequency dependences of the mw magnetic susceptibility of the system $\tilde{\chi} = (M_1\cos\varphi_{1m} + M_2\cos\varphi_{2m})/h$, where φ_{jm} are the amplitudes of steady-state oscillations of the azi-

muthal angles of the magnetic moments in the corresponding layers, for the case where the coupling constant $J = 0.132$ erg/cm^2 is close to the critical value $J_{ca} \equiv \bar{J}_{ca}d/2 \approx 0.131$ erg/cm^2. These dependences were calculated for mw field amplitudes $h = 0.2$, 0.4, and 1.0 Oe and the bias field $H = 1093.2$ Oe, which is close to the critical values $H_c \approx 1093.4$ Oe and $H_a \approx 1103.2$ Oe. For these parameters of the structure, the state with oppositely directed magnetic moments of the layers, $\varphi_{01} = 0$ and $\varphi_{02} = \pi$, is stable in the absence of an mw field. In Fig. 2, dashed curves correspond to the linearized solutions calculated from Eq. (4) for equilibrium orientations $\varphi_{01} = \varphi_{02} = 0$ (curve *1*), $\varphi_{01} = \pi$ and $\varphi_{02} = 0$ (curve *2*), and a symmetrical noncollinear configuration (curve *3*). It can be seen that, at frequencies lower than a certain value ω_c, the precession of the magnetic moments in an AFM configuration in the initial state becomes unstable and dynamic magnetization reversal occurs in the system. As a result, the magnetic moments of the layers begin either to precess in an FM collinear configuration or to precess about axes that make a certain angle in the case where the magnetic moments form a noncollinear configuration corresponding to the given bias field. Therefore, dynamic bistability occurs at $\omega < \omega_c$. Which of the two configurations of the axes of precession will be realized when the initial AFM phase becomes unstable depends on fluctuations in the parameters of the layers and of the magnetic fields, e.g., on the initial phase of the mw field. Since the magnetic structure of layers typically consists of small crystallites with slightly different parameters [12], the precession of the magnetization after the occurrence of bistability can proceed about various axes and has various amplitudes depending on the crystallites.

The critical frequency and, therefore, the frequency range of the dynamic bistability are easily controlled, because ω_c depends strongly on the mw field amplitude. The frequency ω_c increases and the frequency range of dynamic bistability broadens to higher frequencies as the field h increases. For example, for $h = 0.2$ Oe (Fig. 2a), the range of dynamic bistability covers only the resonance frequency corresponding to precession about symmetrically oriented noncollinear axes; for $h = 0.4$ Oe (Fig. 2b), the critical frequency ω_c is close to the resonance frequency corresponding to the case where the magnetic moments precess in an FM collinear configuration; and for $h = 1$ Oe (Fig. 2c), the range of dynamic bistability covers resonance frequencies corresponding to both cases of precession in a noncollinear and in an FM collinear configuration.

At $\omega > \omega_c$, dynamic magnetization reversal does not occur and magnetic moments precess in an AFM configuration. However, if the mw field amplitude is sufficiently large (but such that ω_c is less than the AFM resonance frequency ω_{ar}), there is a narrow frequency range near ω_{ar} (Fig. 2b) in which dynamic magnetization reversal occurs and the system passes over to one of the two orientation states of dynamic bistability. If h is increased further, dynamic magnetization reversal does not occur only in the frequency range above the resonance frequency corresponding to AFM precession ($\varphi_{01} = \pi$, $\varphi_{02} = 0$; Fig. 2c).

The frequency ω_c also depends strongly on the bias field strength. As the difference between the value of H and the critical value H_c increases in magnitude, the frequency ω_c decreases. For example, for $H = 1093$ Oe and $h = 1$ Oe, the frequency range of dynamic bistability does not reach as far as the resonance frequency corresponding to precession in an FM collinear configuration and covers only the resonance corresponding to precession about noncollinear axes. Near the resonance frequency corresponding to AFM precession, there is a frequency range of dynamic bistability that is several times narrower than the corresponding range in Fig. 2b. The dynamic bistability can be initiated not only by the bias field approaching the critical value H_c but also by an increase in the mw field amplitude.

It should be noted that, in the frequency range lying below the resonance frequency corresponding to AFM precession, magnetization reversal does not occur if the initial phase of an mw field is close to $\pi/2$; moreover, the mw field has virtually no effect on the system in this case. This state is stable against small variations in the initial positions of the magnetic moments of the layers ($\varphi_{01} = 180° \pm 1°$, $\varphi_{02} = \pm 1°$) and in the initial phase of the mw field ($\alpha = 90° \pm 5°$). Figure 3 shows the time dependences of the angles φ_j of the magnetic moments approaching a steady state in the case where their initial positions correspond to $\varphi_{01} = \pi$ and $\varphi_{02} = 0$ and dynamic bistability occurs ($H = 1093.2$ Oe, $\omega = 3.7 \times 10^{10}$ s^{-1}, $h = 1$ Oe). In Fig. 3a, curves *1* correspond to the zero initial phase of the mw field and to resonance precession about symmetrically oriented noncollinear axes. Curves *2* correspond to the above-mentioned case where the magnetic moments are antiparallel and the system is not affected by an mw field with initial phase $\alpha = \pi/2$. Figure 3b corresponds to the case where the initial phase is $\alpha = 10°$ and small-amplitude precession takes place in an FM collinear configuration.

The character of the dependence of the high-frequency magnetic susceptibility of the system on the bias field strength varies with the mw field frequency. Figure 4 shows the field dependence of $\tilde{\chi}(H)$ calculated for $h = 1$ Oe and two values of the mw field frequency: $\omega_1 = 3.7 \times 10^{10}$ s^{-1}, which is close to the resonance frequency corresponding to a noncollinear configuration of magnetic moments (curve *1*), and $\omega_2 = 12.7 \times 10^{10}$ s^{-1}, which is close to the AFM resonance frequency (curve *2*). The initial state of the system corresponds to the AFM configuration. The dashed curve represents the linearized solution calculated from Eq. (4) for the case where the magnetic moments precess about noncollinear axes. When the mw field frequency is equal to ω_1, there are three critical values of the bias field. At $H < H_{11}$, small-

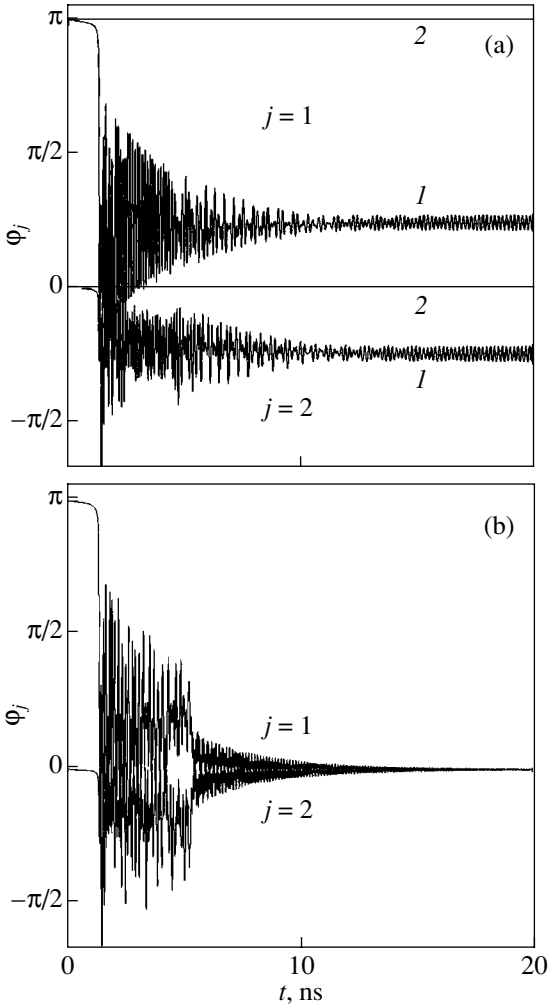

Fig. 3. Time dependences of the angles φ_j in the case of dynamic bistability: (a) resonance precession about noncollinear axes (curve *1*), the regime in which the system is not affected by an mw field (line *2*), and (b) small-amplitude precession in an FM collinear configuration. $H = 1093.2$ Oe, $h = 1$ Oe, and $\omega = 3.7 \times 10^{10}$ s^{-1}; $\varphi_{01} = \pi$ and $\varphi_{02} = 0$.

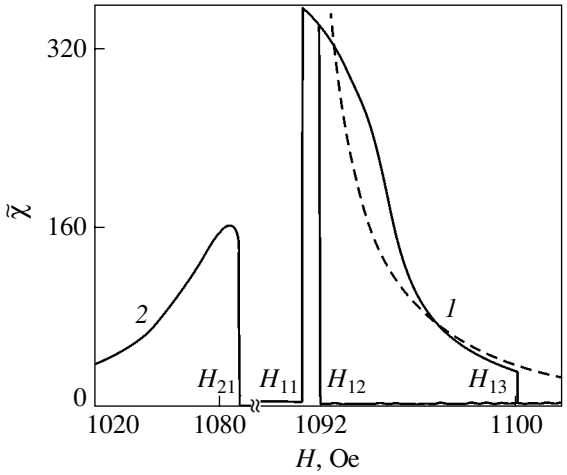

Fig. 4. Field dependences of the magnetic susceptibility of the system (*1*) at the frequency $\omega_1 = 3.7 \times 10^{10}$ s^{-1} close to the resonance frequency for a noncollinear configuration and (*2*) at $\omega_2 = 12.7 \times 10^{10}$ s^{-1} close to the AFM resonance frequency. $h = 1$ Oe.

amplitude precession in an AFM configuration occurs. In the range $H_{11} < H < H_{12}$, only precession about noncollinear axes takes place. In the field range $H_{12} < H < H_{13}$, dynamic bistability occurs and magnetic moments can either precess in an FM collinear configuration or precess about noncollinear axes. At $H > H_{13}$, only precession in an FM configuration takes place. Note that the critical fields H_{11} and H_{12} are higher than H_c and that $H_{13} = H_a$. In the case of frequency ω_2, there are two critical values of the bias field. In the range $H < H_{21}$, AFM resonance arises. In the range $H_{21} < H < H_{22}$ (the value $H_{22} = H_a$ is not indicated in Fig. 4), dynamic magnetization reversal occurs and low-amplitude precession takes place either in an FM configuration or about noncollinear axes. At $H > H_{22}$, the precession about noncollinear axes becomes impossible. The $\tilde{\chi}(H)$ dependence and the occurrence of dynamic bistability are determined by the relative values of critical fields H_c and H_a; therefore, the properties of the magnetic multilayer structures considered above depend significantly on the value of the exchange coupling constant.

The analysis performed above has shown that, in a multilayer structure such as $(Fe/Cr)_n$ with cubic crystallographic anisotropy and AFM coupling due to indirect exchange interaction, an mw field initiates dynamic magnetization reversal with the result that the initial configuration with oppositely directed magnetic moments is replaced by precession in an FM collinear configuration or precession about noncollinear axes. It has been found that, in structures with $J \approx J_{ca}$, in a fairly wide frequency range, dynamic bistability occurs and, depending on fluctuations in the parameters of the system or on the initial mw field phase, one of two precession regimes sets in; these regimes differ in the orientation of the axes of magnetic-moment precession and in its amplitude. The frequency range in which the dynamic bistability arises can be efficiently controlled by varying the mw field amplitude or the bias field strength near the critical value $H_c(J_{ca})$.

ACKNOWLEDGMENTS

This study was supported by the Ministry of Education of the Russian Federation, project no. RD 02-1.2-72.

REFERENCES

1. V. V. Ustinov, M. M. Kirillova, I. D. Lobov, *et al.*, Zh. Éksp. Teor. Fiz. **109** (2), 477 (1996) [JETP **82**, 253 (1996)].
2. V. V. Kostyuchenko and A. K. Zvezdin, Phys. Rev. B **57** (6), 5951 (1998).
3. N. G. Bebenin and V. V. Ustinov, Fiz. Met. Metalloved. **84** (2), 29 (1997).
4. A. K. Zvezdin and V. V. Kostyuchenko, Fiz. Tverd. Tela (St. Petersburg) **41** (3), 461 (1999) [Phys. Solid State **41**, 413 (1999)].
5. A. Schreyer, J. F. Anhner, Th. Zeidler, *et al.*, Phys. Rev. B **52** (12), 16066 (1995).
6. G. S. Patrin, N. V. Volkov, and V. P. Kononov, Pis'ma Zh. Éksp. Teor. Fiz. **68** (4), 287 (1998) [JETP Lett. **68**, 307 (1998)].
7. D. S. Sementsov and A. M. Shutyĭ, Pis'ma Zh. Éksp. Teor. Fiz. **74** (6), 339 (2001) [JETP Lett. **74**, 306 (2001)].
8. D. I. Sementsov and A. M. Shutyĭ, Fiz. Met. Metalloved. **93** (4), 10 (2002).
9. A. M. Shutyĭ and D. I. Sementsov, Fiz. Met. Metalloved. **95** (3), 5 (2003).
10. M. A. Milyaev, L. N. Romashev, V. V. Ustinov, *et al.*, in *Abstracts of International School–Seminar HMMM-XVIII* (Moscow, 2000), Part 1, p. 102.
11. A. G. Gurevich and G. A. Melkov, *Magnetic Oscillations and Waves* (Nauka, Moscow, 1994).
12. A. V. Semerikov, T. P. Krinitsina, V. V. Popov, *et al.*, in *Abstracts of International School–Seminar HMMM-XVI* (Moscow, 1998), Part 1, p. 33.

Translated by Yu. Epifanov

Physics of the Solid State, Vol. 46, No. 2, 2004, pp. 283–288. Translated from Fizika Tverdogo Tela, Vol. 46, No. 2, 2004, pp. 277–281.
Original Russian Text Copyright © 2004 by Bezus, Leonov, Mamaluĭ, Siryuk.

MAGNETISM AND FERROELECTRICITY

Phase Transitions in Bubble-Domain Structures upon Spin Reorientation in Garnet Ferrite Films

A. V. Bezus, A. A. Leonov, Yu. A. Mamaluĭ, and Yu. A. Siryuk

Donetsk State University, Universitetskaya ul. 24, Donetsk, 83055 Ukraine

e-mail: coyote@skif.net

Received May 6, 2003

Abstract—The behavior of a hexagonal bubble lattice in a $(BiTm)_3(FeGa)_5O_{12}$ garnet ferrite uniaxial film with a compensation point of 120 K is investigated experimentally in the range of the crossover from easy-axis magnetization anisotropy to easy-plane magnetization anisotropy. It is demonstrated that the spin reorientation occurs in the temperature range 185–160 K, in which the angular phase $\Phi_\angle$ (or $\bar{\Phi}_\angle$) coexists with the axial phase $\Phi_{\langle 111\rangle}$. At 172 K, when the percentage of the angular phase becomes equal to the percentage of the axial phase, the bubble-lattice parameters and domain-wall width are characterized by a jump. In the range $T < 160$ K, there exists only the easy-plane phase. © *2004 MAIK "Nauka/Interperiodica".*

1. INTRODUCTION

As is known, garnet ferrite uniaxial films with a variation in temperature undergo spin-reorientation phase transitions during which the magnetization vector aligned with the ⟨111⟩ axis perpendicular to the film plane changes direction. The spin-reorientation phase transitions are accompanied by a transformation of the domain structure of the film. Belyaeva *et al.* [1, 2] visually observed the domain structure of garnet ferrite thin films upon spin-reorientation phase transitions with the use of the magneto-optical Faraday effect. In those works, the parameters of the spiral-type domain structure were determined by magneto-optical diffraction. It was found that, in garnet ferrite thin films, the magnetization reversal in domains leads to a jumpwise increase in the domain period and the spin-reorientation transition from the phase with easy-axis anisotropy to the phase with easy-plane anisotropy occurs without a hysteresis but is attended by the coexistence of two phases in a temperature range of approximately 3 K.

Apart from the spin-reorientation phase transitions, garnet ferrite films undergo considerable transformations of the domain structure in the vicinity of the magnetic compensation point T_C. The most interesting situation occurs when the temperature of the spin-reorientation phase transition is close or equal to the magnetic compensation temperature T_C. In [3, 4], the domain structure was examined in the temperature range including the magnetic compensation temperature T_C and spin-reorientation phase transitions both in the absence of external magnetic fields (spontaneous transitions) and in different magnetic fields (induced transitions). In particular, Kandaurova and Pamyatnykh [3] studied the domain structure with the use of the magneto-optical Faraday effect and identified the observed phases by the color contrast method. Belyaeva *et al.* [4] investigated the domain structure in the $Er_3Fe_5O_{12}$ garnet ferrite and revealed that the temperature of the first-order spin-reorientation phase transition between phases with magnetization orientations along the ⟨111⟩ and ⟨100⟩ directions coincides with the magnetic compensation temperature T_C. In [3], it was also found that, in substituted erbium garnet, the temperature ranges of the magnetic compensation and spin reorientation overlap.

The purpose of this work was to perform an experimental investigation of the behavior of a hexagonal bubble lattice in a garnet ferrite film with a variation in temperature in the range of spin reorientation near the magnetic compensation point T_C.

2. EXPERIMENTAL TECHNIQUE AND RESULTS

In our experiments, we used a $(BiTm)_3(FeGa)_5O_{12}$ garnet ferrite uniaxial film in which it was possible to induce a bubble lattice. The film was grown through liquid-phase epitaxy on a gadolinium gallium garnet with the (100) plane. The film had a thickness $h = 8.2$ μm, quality factor $q > 1$, and $4\pi M_S = 160$ G at room temperature. The ⟨111⟩ axis was perpendicular to the film plane. The bubble lattice was induced by a monopolar pulsed magnetic field with a frequency of 400 Hz and an amplitude of 60 Oe in the absence of a bias field, and the magnetic field was then switched off [5]. The spin reorientation in the film was observed in the temperature range 185–160 K. The magnetic compensation point was determined to be $T_C = 120$ K. The domain structure was examined using the Faraday effect. The spin-reorientation phase transitions were visually identified by color.

1063-7834/04/4602-0283$26.00 © 2004 MAIK "Nauka/Interperiodica"

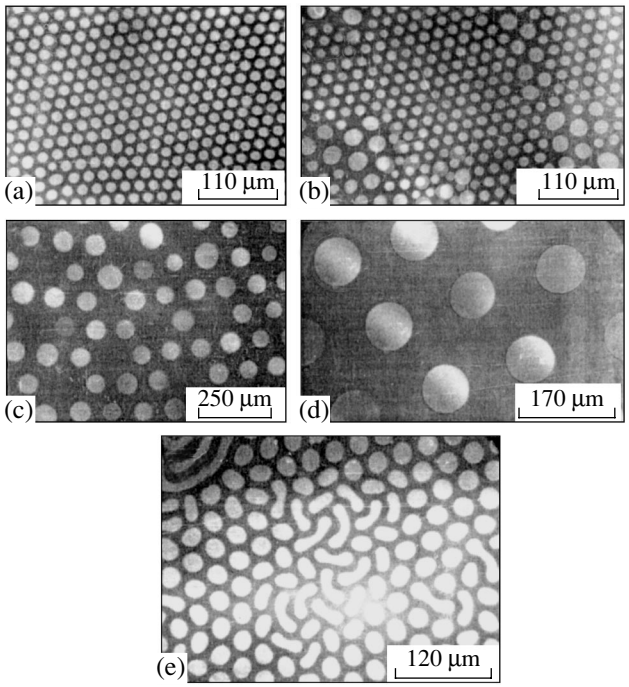

Fig. 1. Domain structures of the $(BiTm)_3(FeGa)_5O_{12}$ film at temperatures of (a) 300, (b) 215, (c, d) 172, and (e) 205 K.

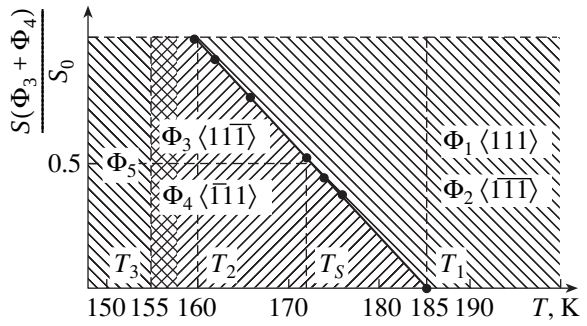

Fig. 2. Temperature dependence of the ratio between the areas occupied by the domain phases.

There exist two methods for analyzing the characteristics of a bubble lattice. According to the first method, the bubble lattices are induced at different temperatures. In this case, the measured dependences of the lattice parameter $a(T)$ and the bubble-domain diameter $d(T)$ are continuous functions of temperature [6]. These lattices are in an equilibrium state at the temperature of formation; i.e., their parameters correspond to an energy minimum. The parameter $y = d/a = 0.74$ remains constant over the entire temperature range in which the equilibrium lattice can exist [7]. A different behavior of the dependences $a(T)$ and $d(T)$ is observed with a variation in the temperature of the film in the case when the bubble lattice is induced at a constant temperature. The lattice is retained over a particular temperature range and then undergoes a spontaneous phase transformation into a lattice with other parameters corresponding to an equilibrium lattice at the transformation temperature [6, 8]. It is this technique that was used in the present work.

Let us now consider in detail the phase transitions induced in a bubble lattice by a change in the temperature upon cooling of the film. The bubble lattice is induced at $T = 300$ K (Fig. 1a). In this case, the film contains two collinear magnetic phases $\Phi_1\langle 111\rangle$ (orange bubble domains) and $\Phi_2\langle\bar{1}\bar{1}\bar{1}\rangle$ (brown background), whose magnetization vectors are perpendicular to the film plane. The lattice with parameter $a = 18$ μm is retained upon cooling to 215 K; i.e., the parameter a remains unchanged to 215 K. With further decrease in the temperature, this lattice undergoes a phase transformation into a lattice with a larger parameter a; during this process, part of the bubble domains contract and disappear and another part of the domains increase in diameter and occupy the sites of adjacent domains (Fig. 1b). Exposure to a pulsed magnetic field induces an equilibrium bubble lattice with a larger parameter $a = 25$ μm and a smaller number of bubble domains. The magnetic phases Φ_1 and Φ_2 are retained. At 185 K, some regions change color from brown to green and the orange color of part of the bubble domains changes to white. This indicates the onset of spin reorientation and the formation of two new phases, Φ_3 (white bubble domains) and Φ_4 (green background), whose magnetization vectors make an angle with the film plane. A decrease in the temperature to 172 K results in collapse of the bubble lattice (Fig. 1c). Then, the film is again exposed to a pulsed field, which induces a lattice with parameter $a = 118$ μm (Fig. 1d) and a wide, very contrast domain wall. This is accompanied by a jumpwise change in the bubble-domain size; or, more precisely, there occurs a threefold increase in the bubble-domain diameter (as compared to the diameter of bubble domains at 185 K) and the corresponding change in the ratio $y = d/a$ to $y = 0.45$ (nonequilibrium lattice). The domain-wall width also changes jumpwise; i.e., it increases by a factor of five as compared to the domain-wall width at 185 K. The film contains four phases; in this case, the area of the Φ_3 and Φ_4 phases is equal to the area of the phases Φ_1 and Φ_2 (Fig. 2). A decrease in the temperature is attended by an increase in the area of the phases Φ_3 and Φ_4: the green component becomes dominant and displaces the brown color, and virtually all bubble domains acquire a white color. At $T_2 = 160$ K, large-sized isolated bright white bubble domains with clearly defined wide dark domain walls are observed against the bright green background. This indicates that the film contains only two angular phases, Φ_3 and Φ_4. At 158 K, the bubble domains become unstable and drift with a change in the shape. Furthermore, the domain-wall width in different domain regions turns out to be different. A further decrease in the temperature brings about a deterioration of the contrast due to a

decrease in the specific Faraday rotation, and virtually nothing is seen at 150 K. This suggests the appearance of in-plane anisotropy, i.e., the formation of the magnetic phase Φ_5.

During heating of the film, a very large whitish stripe domain appears at 155 K. Exposure of the film to a pulsed field at 160 K induces unstable isolated white bubble domains against the green background. This implies the formation of the phases Φ_3 and Φ_4. Moreover, a small number of orange and brown regions (phases Φ_1 and Φ_2) are observed in the film. Upon heating of the film to 172 K, bubble domains lose their shape and transform into stripes. At 172 K, the film is exposed to a pulsed field, which induces a lattice with a smaller parameter a = 166 μm and narrow domain walls. With a further increase in the temperature, we observe the appearance of an orange color in a number of white bubble domains and brown regions against the green background, which indicates an increase in the area of the phases Φ_1 and Φ_2. At 185 K, the white and green colors are virtually not observed (the phases Φ_3 and Φ_4 disappear), bubble domains lose their shape, and the bubble lattice collapses. Exposure of the film to a pulsed field at 185 K induces a new lattice (with a smaller parameter a = 120 μm) that involves only the collinear phases Φ_1 and Φ_2 (orange bubble domains and brown background). This lattice is retained up to 205 K. Then, the lattice breaks down into regions (separated by stripes) with a new bubble lattice characterized by a smaller parameter a = 40 μm, which corresponds to the equilibrium lattice at the given temperature (Fig. 1e). Note that, upon this phase transition, the total number of domains remains unchanged. Subsequent exposure to a pulsed field induces a bubble lattice that has a smaller parameter a and occupies the entire visible region of the film. Several phase transitions of this type are observed away from the magnetic compensation temperature T_C.

3. DISCUSSION

Let us now interpret the experimental data. The change in the orientation of the magnetization vector will be treated as a spin-reorientation phase transition between homogeneous states in an infinite ideal crystal. The expression for the free energy of the infinite crystal in a zero field involves only the magnetic anisotropy energy. In the coordinate system, in which the x, y, z axes coincide with the $\langle 1\bar{1}0\rangle$, $\langle 11\bar{2}\rangle$, and $\langle 111\rangle$ crystallographic axes, respectively, the anisotropy energy density can be represented in the form [9, 10]

$$F_A = K_u\sin^2\theta + K_1\left(\frac{1}{3}\cos^4\theta + \frac{1}{4}\sin^4\theta - \frac{\sqrt{2}}{3}\cos\theta\sin^3\theta\sin 3\varphi\right), \quad (1)$$

where θ and φ are the polar and azimuthal angles of the magnetization vector, respectively; K_u is the uniaxial anisotropy constant; and K_1 is the cubic anisotropy constant.

In subsequent treatment, we will use the dimensionless parameter $\nu = K_u/K_1$. With due regard for this parameter, relationship (1) takes the form

$$f = \frac{F_A}{K_1} = \nu\sin^2\theta + \left(\frac{1}{3}\cos^4\theta + \frac{1}{4}\sin^4\theta - \frac{\sqrt{2}}{3}\cos\theta\sin^3\theta\sin 3\varphi\right). \quad (2)$$

By minimizing expression (2) with respect to the angles θ and φ, we obtain the system of equations

$$\frac{\partial f}{\partial\theta} = 0, \quad (3a)$$

$$\frac{\partial f}{\partial\varphi} = 0. \quad (3b)$$

An analysis of this system of equations demonstrates that the magnetic phases can exist only at the following angles θ and φ:

$$\text{(i)}\ \ \theta = 0; \quad (4a)$$

$$\text{(ii)}\ \theta = \pi/2, \quad \varphi = 0; \quad (4b)$$

(iii) $\varphi = \pi/6$ and the angle θ determined from the solution of the cubic equation

$$y^3 + y^2\left(\frac{-14(2\nu+1)-16}{27}\right) + y\left(\frac{(2\nu+1)^2+2}{9}\right) - \frac{2}{81} = 0, \quad (5)$$

where $y = \cos^2\theta$.

The dependence of the discriminant D of this cubic equation on the dimensionless parameter ν is plotted in Fig. 3. It can be seen from this figure that, at $\nu > 0.76$ and $\nu < -0.22$, the discriminant $D > 0$ and the cubic equation possesses a unique real solution. However, for the interval $\nu \in (-0.22, 0.76)$, there exist three real roots of Eq. (5). In the general form, the expressions for these roots are very cumbersome and are not presented in this work. The dependences of these three roots on the dimensionless parameter ν are depicted in Fig. 4. It is clear that these roots correspond to the angular phases in the range $0 < \theta < \pi/2$.

For each of the orientations of the magnetization vector (4a), (4b), and (5), the free energy has minima at specific values of the dimensionless parameter ν, i.e., at specific ratios between the anisotropy constants. At the next stage of constructing the phase diagram, we reveal the stability regions of the magnetic phases. The stabil-

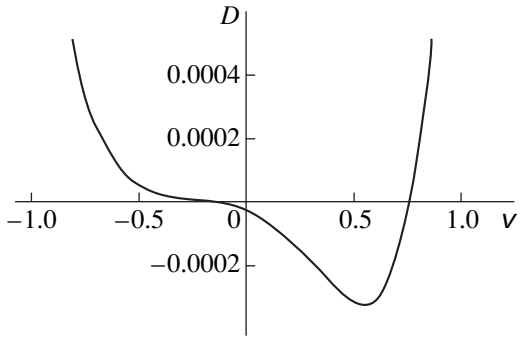

Fig. 3. Dependence of the discriminant D of cubic equation (5) on the dimensionless parameter v.

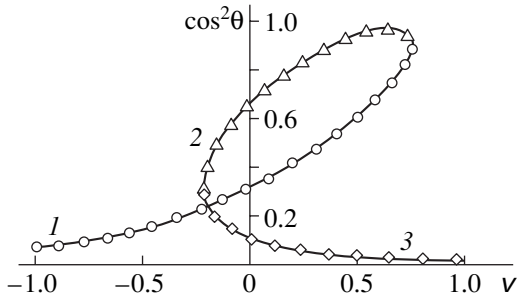

Fig. 4. Dependences of the roots of cubic equation (5) on the dimensionless parameter v: (*1*) y_1, (*2*) y_2, and (*3*) y_3.

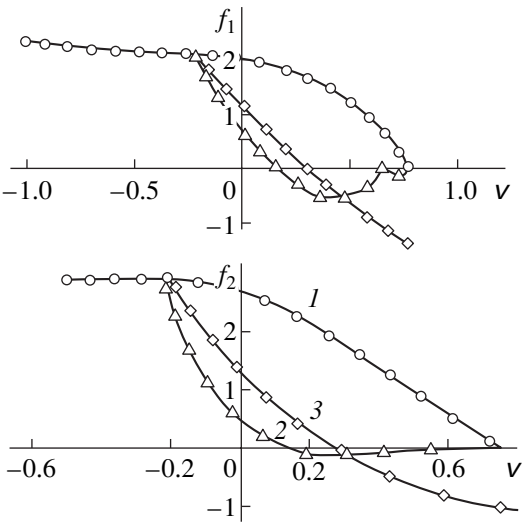

Fig. 5. Dependences $f_1(v)$ [relationship (8a)] and $f_2(v)$ [relationship (8b)] for the roots of cubic equation (5). Designations are the same as in Fig. 4.

ity condition for a function with two variables $f(\theta, \varphi)$ has the form

$$\frac{\partial^2 f}{\partial \theta^2} > 0, \tag{6a}$$

$$\frac{\partial^2 f}{\partial \theta^2}\frac{\partial^2 f}{\partial \varphi^2} - \frac{\partial^2 f}{\partial \theta \partial \varphi} > 0. \tag{6b}$$

The condition for loss of stability of the function $f(\theta, \varphi)$ implies that either of these expressions vanishes (with a subsequent change in sign). In the K_uK_1 plane, this condition determines a critical line that can correspond to a second-order phase transition or loss of stability of the metastable phase.

By using conditions (6a) and (6b) for solutions (4a), (4b), and (5), we obtain the following results.

(i) At $\theta = 0$, the stability condition for the magnetic phase is determined by the inequality

$$-2 + 3v < 0 \tag{7}$$

or, what is the same, by the relationship

$$-2K_1 + 3K_u < 0. \tag{7a}$$

(ii) At $\theta = \pi/2$ and $\varphi = 0$, condition (6b) is not satisfied. This means that the magnetic phase is not an extremum of function (2).

(iii) For the roots y_1, y_2, and y_3 of cubic equation (5), the stability region can be graphically determined by constructing a plot of the functions

$$\frac{\partial^2 f}{\partial \theta^2} = f_1(v), \tag{8a}$$

$$\frac{\partial^2 f}{\partial \theta^2}\frac{\partial^2 f}{\partial \varphi^2} - \frac{\partial^2 f}{\partial \theta \partial \varphi} = f_2(v) \tag{8b}$$

(see Fig. 5).

As can be seen from Fig. 5, the magnetic phases corresponding to the roots y_1, y_2, and y_3 are stable at $v < 0.76$, $-0.22 < v < 0.15$, and $-0.22 < v < 0.28$, respectively, or, what is the same, under the conditions

$$K_u < 0.76K_1 \quad \text{for} \quad y_1, \tag{9a}$$

$$-0.22 < K_u < 0.15K_1 \quad \text{for} \quad y_2, \tag{9b}$$

$$-0.22 < K_u < 0.28K_1 \quad \text{for} \quad y_3. \tag{9c}$$

The construction of the graph of the anisotropy energy (2) for different solutions (θ, φ) provides better insight into the processes under investigation and makes it possible to determine the lines corresponding to the phase transitions. These lines can be obtained by comparing the free energies of the magnetic phases with different orientations of the magnetization vector (Fig. 6). It can be seen from Fig. 6 that, at $v < 0.76$, the phase y_1 has the lowest energy and, at $v > 0.76$, there exists only the easy-axis phase. Note that only the portions of the curves that correspond to the minimum of the anisotropy energy (2) are shown in Fig. 6.

By using the data presented in Fig. 6 and conditions (7a) and (9a)–(9c), we constructed the phase diagram in the K_u–K_1 coordinates (Fig. 7).

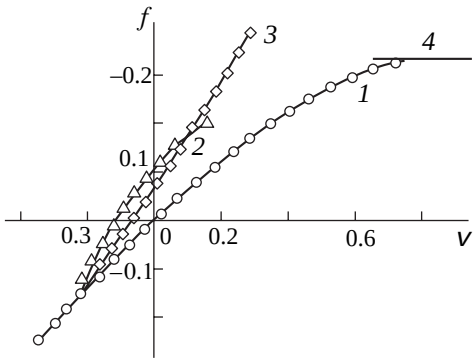

Fig. 6. Dependences of the anisotropy energy [relationship (2)] on the dimensionless parameter ν for the solutions obtained. Designations are the same as in Fig. 4. Line *4* corresponds to the easy-axis state.

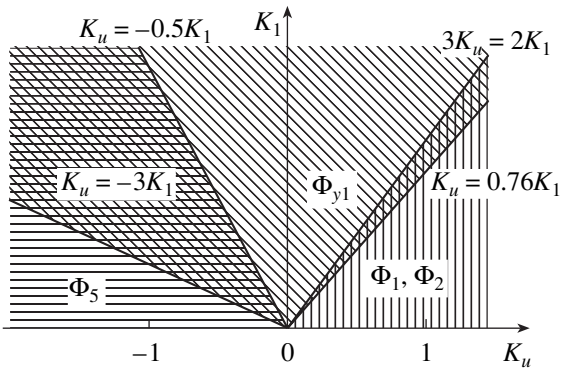

Fig. 7. Regions of existence of the easy-plane phase Φ_5 (horizontal hatching), the angular phase Φ_{y_1} (tilted hatching), and the easy-axis phases Φ_1 and Φ_2 (vertical hatching).

An analysis of the phase diagram shows that the reorientation of the magnetization vector from the easy-axis state to the angular state y_1 is a first-order phase transition. This can be judged from the existence of the regions of metastable states, i.e., the overlap of the stability regions of the relevant phases. The phase y_1 at $\nu = -3$ transforms into the easy-plane state ($\theta = \pi/2$, $\varphi = \pi/6$). Substitution of these angles into relationships (6a) and (6b) gives the stability condition for the easy-plane phase; that is,

$$\nu < -\frac{1}{2}, \tag{10a}$$

or, what is the same,

$$K_u < -\frac{1}{2}K_1. \tag{10b}$$

Therefore, the transition from the angular phase y_1 to the easy-plane phase ($\theta = \pi/2$, $\varphi = \pi/6$) is a first-order phase transition. This can be explained in the following way. The easy-plane phase with $\theta = \pi/2$ and $\varphi = \pi/6$ becomes more favorable at large angles θ close to $\pi/2$.

An analysis of the results presented in Fig. 6 demonstrates that the application of a magnetic field can render a particular angular magnetic phase favorable. In this case, it is necessary to consider the ranges of the parameter ν in which the corresponding angular phases are stable.

The results of the calculations allow us to draw the following inferences.

The transformation from the easy-axis state into the easy-plane state should occur along the direction with $\varphi = \pi/6$. In the plane, this direction coincides with the $\langle \bar{2}11 \rangle$ direction. The easy-plane state is observed at $\nu = -1/2$. The easy-plane phase is formed upon a gradual change in the angle θ for the angular phase y_1. At angles θ close to $\pi/2$, the phase with $\theta = \pi/2$ and $\varphi = \pi/6$ becomes more favorable. In this process, the magnetization vector lies in the plane involving the $\langle 111 \rangle$ and $\langle \bar{2}11 \rangle$ directions and passes through the $\langle 11w \rangle$ direction.

Now, we use the results obtained to interpret the experimental data on the transformation of the domain structure in garnet ferrite films with a variation in the temperature. At room temperature, only the easy-axis phase Φ_1 with magnetization orientation along the $\langle 111 \rangle$ direction is observed in the film. A decrease in the temperature (in the dimensionless parameter $\nu = K_u/K_1$) leads to the formation of the angular phase y_1 (Φ_3 and Φ_4) due to the first-order spin-reorientation phase transition at $\nu = 0.66$. At $\nu = -0.5$, the y_1 angular phase undergoes a first-order transition to the easy-plane phase Φ_5.

4. CONCLUSIONS

The results obtained in this work can be summarized as follows. In the temperature range above T_1 (Fig. 2), there coexist two magnetic collinear phases, namely, $\Phi_1\langle 111 \rangle$ and $\Phi_2\langle \bar{1}\bar{1}\bar{1} \rangle$. This range is characterized by the formation of a hexagonal bubble lattice with a lattice equilibrium parameter $y = 0.74$ and narrow Bloch domain walls. The lattice remains stable over a particular temperature range. In the case when the boundary of the stability range approaches the magnetic compensation temperature T_C, the lattice undergoes a phase transformation into an equilibrium bubble lattice with larger parameters. This is accompanied by the collapse of part of the domains. At the other boundary of the stability range (far from the magnetic compensation temperature T_C), the bubble lattice transforms into a two-phase structure that consists of regions of a new bubble lattice and stripe domains. Upon this transformation, the total number of domains remains unchanged. Although the above transformations are qualitatively different, both phase transitions in the lattice spontaneously occur in a

jumpwise manner over a temperature range of 2–3 K. The phase transitions are characterized by a hysteresis which manifests itself both in the difference between the temperatures of collapse of the bubble lattice upon heating and cooling and in different character of this collapse.

In the temperature range T_1–T_2 (Fig. 2), there coexist four magnetic phases, namely, the collinear phases $\Phi_1\langle 111\rangle$ and $\Phi_2\langle \bar{1}\bar{1}\bar{1}\rangle$ and the angular phasesΦ_3 and Φ_4. The percentage of these phases is identical at the temperature of the spin-reorientation phase transition T_S = 172 K. This transition is attended by a jump in the phase volume in the bubble lattice due to a change in the parameters *a* and *d*. The lattice equilibrium parameter *y* changes from 0.74 to 0.45. The domain-wall width slowly increases in the temperature range T_1–T_S. At the temperature T_S, the domain-wall width increases drastically: the Bloch domain wall transforms into the Néel domain wall. In the case when the film contains only the angular phases Φ_3 and Φ_4 (at the temperature T_2), no bubble lattice is formed but isolated bubble domains are observed.

REFERENCES

1. A. I. Belyaeva, A. V. Antonov, and V. P. Yur'ev, Fiz. Tverd. Tela (Leningrad) **22** (6), 1621 (1980) [Sov. Phys. Solid State **22**, 947 (1980)].
2. A. I. Belyaeva, A. V. Antonov, G. S. Egiazaryan, and V. P. Yur'ev, Fiz. Tverd. Tela (Leningrad) **24** (7), 2191 (1982) [Sov. Phys. Solid State **24**, 1247 (1982)].
3. G. S. Kandaurova and L. A. Pamyatnykh, Fiz. Tverd. Tela (Leningrad) **31** (8), 132 (1989) [Sov. Phys. Solid State **31**, 1351 (1989)].
4. A. I. Belyaeva, V. P. Yur'ev, and V. A. Potakova, Zh. Éksp. Teor. Fiz. **83** (3), 1104 (1982) [Sov. Phys. JETP **56**, 626 (1982)].
5. E. F. Khodosov, A. O. Khrebtov, and Yu. A. Siryuk, Pis'ma Zh. Tekh. Fiz. **8** (6), 363 (1982) [Sov. Tech. Phys. Lett. **8**, 157 (1982)].
6. V. G. Bar'yakhtar, É. A. Zavadskiĭ, Yu. A. Mamaluĭ, and Yu. A. Siryuk, Fiz. Tverd. Tela (Leningrad) **26** (8), 2381 (1984) [Sov. Phys. Solid State **26**, 1443 (1984)].
7. V. A. Zablotskiĭ, Yu. A. Mamaluĭ, and Yu. A. Siryuk, Ukr. Fiz. Zh. **33** (3), 403 (1988).
8. Yu. A. Mamaluĭ, Yu. A. Siryuk, and E. F. Khodosov, Ukr. Fiz. Zh. **30** (1), 103 (1985).
9. A. Hubert and R. Schaffer, *Magnetic Domains* (Springer, Berlin, 1998).
10. K. P. Belov, A. K. Zvezdin, A. M. Kadomtseva, and R. Z. Levitin, *Orientational Transitions in Rare-Earth Magnets* (Nauka, Moscow, 1979).

Translated by O. Borovik-Romanova

Physics of the Solid State, Vol. 46, No. 2, 2004, pp. 289–293. Translated from Fizika Tverdogo Tela, Vol. 46, No. 2, 2004, pp. 282–286.
Original Russian Text Copyright © 2004 by Pleshchev, Korolev, Dorofeev.

MAGNETISM AND FERROELECTRICITY

Magnetic State of Intercalation Compounds in the Cr_xTiTe_2 System

V. G. Pleshchev*, A. V. Korolev, and Yu. A. Dorofeev****

** Ural State University, pr. Lenina 51, Yekaterinburg, 620083 Russia*

*** Institute of Metal Physics, Ural Division, Russian Academy of Sciences, ul. S. Kovalevskoĭ 18, Yekaterinburg, 620219 Russia*

e-mail: Valery.Pleschov@usu.ru

Received May 13, 2003

Abstract—The temperature and field dependences of the magnetic characteristics of chromium-intercalated titanium ditelluride compounds are investigated over a wide range of chromium concentrations. The $Cr_{0.5}TiTe_2$ compound is studied by neutron diffraction. It is revealed that the system under investigation can occur in different magnetic states depending on the chromium concentration. An analysis of the experimental results demonstrates that the interaction between magnetic moments of chromium ions is predominantly ferromagnetic in character. An increase in the chromium concentration leads to ferromagnetic behavior with a pronounced magnetic hysteresis. The magnetic moments of chromium ions in these compounds are estimated. © *2004 MAIK "Nauka/Interperiodica".*

1. INTRODUCTION

The considerable interest expressed by researchers in compounds prepared through intercalation of transition elements into titanium dichalcogenides TiX_2 (X = S, Se, Te) is associated with the possibility of producing structures with alternating layers of magnetic and nonmagnetic ions [1, 2]. In the structure, the intercalated transition metal atoms occupy empty octahedral sites of the so-called van der Waals gap between trilayer X–Ti–X fragments. This feature of the crystal structure offers strong possibilities for modifying the physical properties of the compounds under consideration. The intercalation of transition metal atoms leads to hybridization of the 3d electron states of the intercalated atoms with the band states of the TiS_2 and $TiSe_2$ matrices. The contribution of the 3d states to the formation of new molecular orbitals depends on the type of intercalated atoms. The formation of the new orbital states is accompanied by a distortion of the crystal lattice along the direction perpendicular to the X–Ti–X layers and a change in the electrical conductivity and the effective magnetic moment [3, 4]. As was shown earlier in [5–7], the intercalation of 3d metal atoms into titanium disulfide and titanium ditelluride provides a means for producing compounds in different magnetic states with both long-range magnetic order and frustrated bonds. For example, it was revealed [8] that Cr_xTiSe_2 compounds at a chromium content $x = 0.5$ are in the antiferromagnetic state characterized by spin reorientation with a relatively low magnetic field strength.

Although the aforementioned intercalation compounds have been studied extensively, the problem of their magnetic ordering remains unsolved, in particular, because of the lack of reliable experimental information. In order to complement the available data on the magnetism of layered materials, we examined compounds based on titanium ditelluride. In this work, the magnetic properties of Cr_xTiTe_2 compounds were experimentally investigated for the first time. These investigations provide important information on the influence of the TiX_2 matrix on the magnetic properties of intercalated systems.

2. SAMPLES AND EXPERIMENTAL TECHNIQUE

Polycrystalline samples of Cr_xTiTe_2 were prepared using solid-phase synthesis in two stages. The synthesis procedure was described in detail in [5]. The $TiTe_2$ binary compound was synthesized at the first stage, and Cr_xTiTe_2 samples ($0 < x \le 0.5$) were prepared at the second stage. At both stages, intermediate products were carefully ground, the powders thus obtained were pressed into compact pellets, and the pellets were subjected to prolonged high-temperature treatment. As was established earlier for other systems, this synthesis procedure provides homogeneity of the composition throughout the volume of the sample. X-ray diffraction analysis and the determination of the structural parameters were carried out using a DRON-3M x-ray diffractometer (CuK_α radiation). The magnetic measurements were performed on a QUANTUM DESIGN MPMS-5XL SQUID magnetometer. The ac and dc susceptibilities and the field dependences of the magnetization were measured in magnetic fields up to 5 T in the temperature range 2–300 K. The neutron diffraction investigations were performed at temperatures

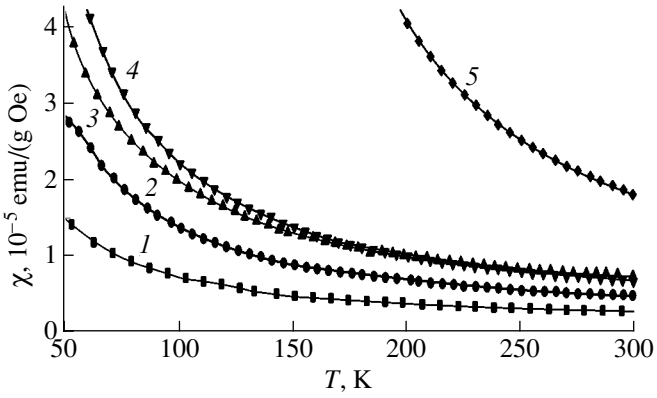

Fig. 1. Temperature dependences of the static magnetic susceptibility of Cr_xTiTe_2 compounds at chromium contents x = (*1*) 0.1, (*2*) 0.2, (*3*) 0.25, (*4*) 0.33, and (*5*) 0.5.

of 295 and 4.2 K with the use of a D3 diffractometer (wavelength, 0.243 nm) installed on the horizontal channel of an IVV-2M reactor. The neutron diffraction patterns were numerically processed using the Rietveld full-profile method with the Fullprof program package [9].

3. RESULTS AND DISCUSSION

According to the x-ray diffraction data, the crystal structure of Cr_xTiTe_2 compounds at a chromium content $x \le 0.33$ retains the symmetry (space group $P\bar{3}m1$) characteristic of the initial matrix $TiTe_2$. The structure of the sample with $x = 0.5$ belongs to the monoclinic system (space group $I2/m$) due to the ordering of chromium ions, which occupy half of all possible octahedral sites in the van der Waals gaps. A similar change in symmetry of the unit cell was revealed earlier in Fe_xTiSe_2 compounds [1].

The magnetic susceptibility χ of Cr_xTiTe_2 compounds increases with an increase in the chromium content (Fig. 1). The dependence $\chi(T)$ in the temperature range covered is adequately described by the generalized Curie–Weiss law:

$$\chi = \chi_0 + C/(T - \Theta),$$

where C is the Curie constant; Θ is the Weiss constant; and χ_0 is the temperature-independent contribution, which accounts for the diamagnetism of the filled electron shells and paramagnetism of the electron gas. The values of χ_0, C, and Θ (see table) were determined by approximating the experimental dependence $\chi(T)$ according to the above expression.

An analysis of the data presented in the table shows that, upon intercalation, the temperature-independent contribution χ_0 increases in the initial stages as compared to the Pauli magnetic susceptibility of the $TiTe_2$ compound, reaches a maximum in the concentration range $x = 0.2$–0.25, and then decreases. Since the diamagnetic component is determined primarily by the electron shells of the matrix, this component should very weakly depend on the chromium concentration. Therefore, it can be inferred that the concentration dependence of the diamagnetic contribution correlates qualitatively with the change in the Pauli susceptibility. Unfortunately, correct analysis of this dependence is complicated, because necessary data on the kinetic characteristics of these phases and on the state of the electronic subsystem are not available in the literature. The value of χ_0 for the $Cr_{0.5}TiTe_2$ compound is not given in the table. This is explained by the fact that the high susceptibility of this material leads to a large error in determining the contribution χ_0.

As can be seen from the table, the effective magnetic moments $\mu_{eff} = (4.0 \pm 0.2)\mu_B$ for samples of different compositions are virtually identical to within the experimental error and almost coincide with the effective magnetic moment of a free Cr^{3+} ion (3.87 μ_B). A different situation was observed earlier for the Co_xTiSe_2 and Fe_xTiSe_2 compounds [6], for which the effective magnetic moments appreciably decrease with an increase in the concentration of intercalant atoms. It was found that the positive Weiss constant Θ increases from 6 K for $Cr_{0.2}TiTe_2$ to 115 K for $Cr_{0.5}TiTe_2$. This indicates that, as the chromium content increases, the ferromagnetic interactions dominate and ferromagnetic ordering becomes possible in the low-temperature range.

As follows from analyzing the magnetizations measured at low temperatures, the paramagnetic state of samples with $x = 0.1$ is retained down to $T = 2$ K. The temperature dependences of the magnetization measured for samples with $x = 0.2$ and 0.25 after cooling in the absence of a magnetic field and after cooling in a magnetic field exhibit a temperature hysteresis at temperatures below 8 and 10 K, respectively. However, no hysteresis is observed in the field dependences of the magnetization measured for these samples under conditions where the magnetic fields are changed in opposite directions. In order to elucidate the nature of the mag-

Temperature-independent contributions χ_0, effective (μ_{eff}) and spontaneous (μ_s) magnetic moments of chromium ions, Weiss constants Θ, and critical temperatures T_c of magnetic phase transformations in the Cr_xTiTe_2 compounds

Parameter	x					
	0	0.1	0.2	0.25	0.33	0.5
χ_0, 10^{-7} emu/(g Oe)	2	1.77	4.33	3.67	2.36	–
μ_{eff}/Cr, μ_B	–	4.1	3.9	4.1	3.8	4.2
μ_s/Cr, μ_B	–	–	–	–	0.2	0.9
Θ, K	–	≅0	6	8	20	115
T_c, K	–	–	8	10	12	78

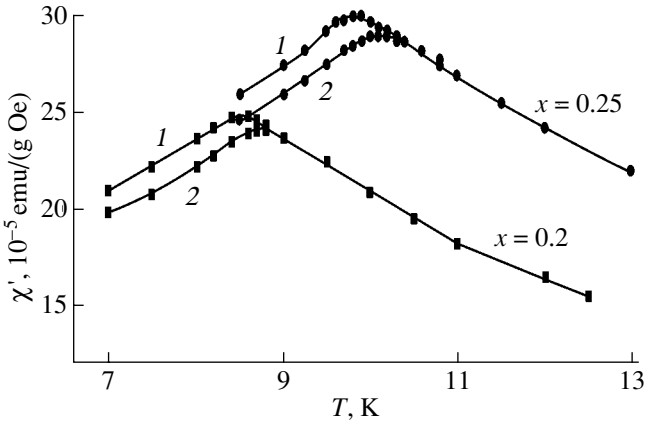

Fig. 2. Temperature dependences of the real part of the magnetic susceptibility of the $Cr_{0.2}TiTe_2$ and $Cr_{0.25}TiTe_2$ compounds at ac magnetic field frequencies of (*1*) 8 and (*2*) 800 Hz.

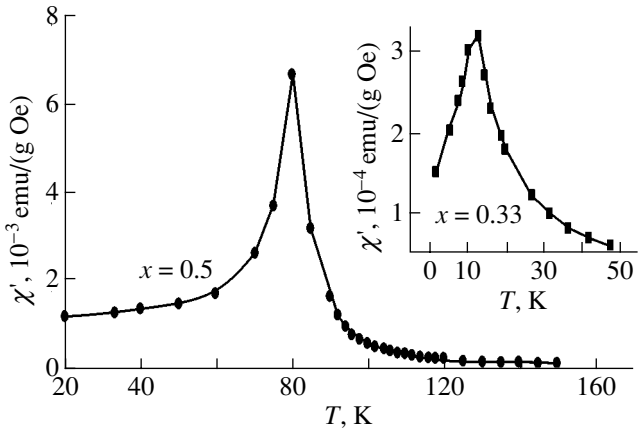

Fig. 3. Temperature dependences of the real part of the magnetic susceptibility of the $Cr_{0.33}TiTe_2$ and $Cr_{0.5}TiTe_2$ compounds.

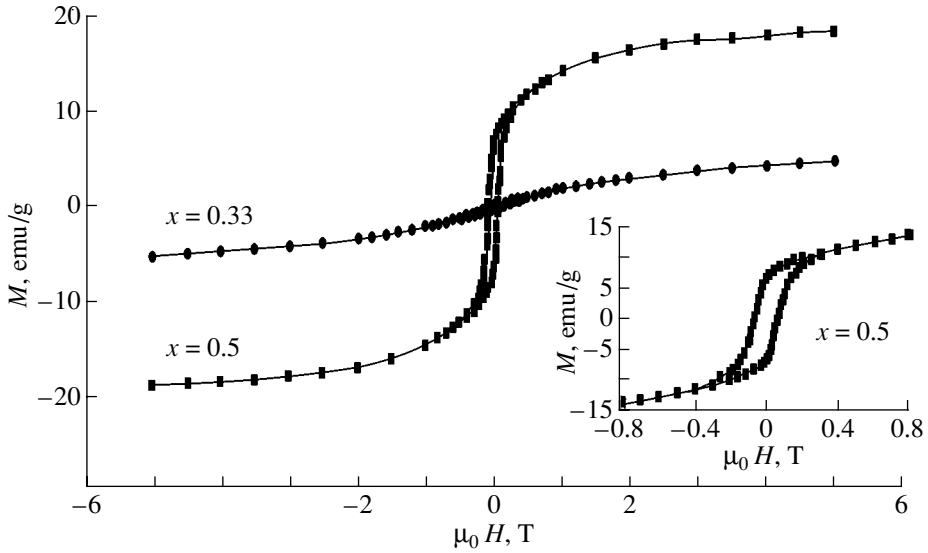

Fig. 4. Field dependences of the specific magnetization of the $Cr_{0.33}TiTe_2$ and $Cr_{0.5}TiTe_2$ compounds at a temperature of 2 K.

netic state in the compounds with chromium contents $x = 0.2$ and 0.25 at temperatures in the vicinity of the observed maxima, we measured the susceptibility in an ac magnetic field with an amplitude of 4 Oe at frequencies of 8 and 800 Hz. The experimental data obtained for these samples are presented in Fig. 2. It can be seen from this figure that, as the frequency of the magnetic field increases, the real part χ' of the magnetic susceptibility at temperatures below the temperature of the maxima decreases and the maxima observed in the dependence $\chi'(T)$ shift toward the high-temperature range. This suggests that relaxation processes proceed in the course of magnetization. The results obtained allow us to draw the inference that samples with chromium contents $x = 0.2$ and 0.25 are characterized by the spin-glass state with critical temperatures $T_c = 8$ and 10 K, respectively.

The dependences $\chi'(T)$ for samples with $x = 0.33$ and 0.5 also exhibit maxima at temperatures of 12 and 78 K, respectively (Fig. 3). The Weiss constants Θ of these samples are larger than those of the compounds with a lower chromium content, which reflects enhancement of the ferromagnetic interactions. In this respect, we measured the field dependences of the magnetization M for samples with $x = 0.33$ and 0.5 at $T = 2$ K. It was found that the dependences $M(H)$ exhibit a pronounced magnetic hysteresis. The hysteresis loops obtained for these samples after cooling in the absence of a magnetic field and after cooling in a magnetic field are symmetric in shape (Fig. 4). The coercive forces for compounds with $x = 0.33$ and 0.5 are equal to

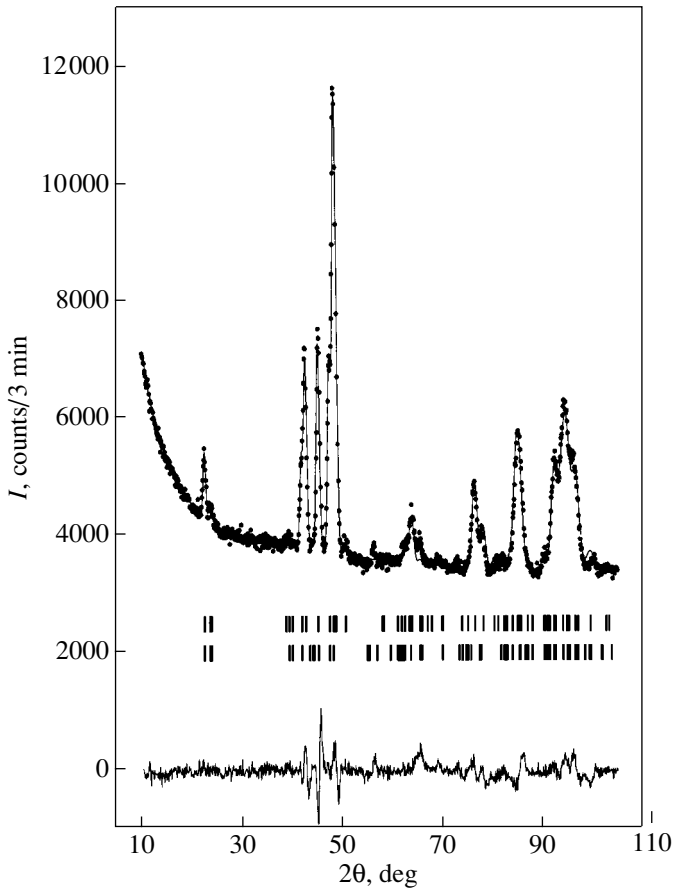

Fig. 5. Neutron diffraction pattern of the $Cr_{0.5}TiTe_2$ compound at temperature $T = 4.2$ K. Points are the experimental intensities. The upper solid line corresponds to the results of calculations. The lower solid line is the difference curve. The upper and lower tick marks indicate the angular positions of the nuclear and magnetic reflections, respectively.

200 and 700 Oe, respectively. The field dependences are characterized by a very strong paraprocess, and, consequently, saturation for relatively weak coercive forces is not attained up to a field strength of 5 T. The spontaneous magnetic moments of chromium ions, which were determined by extrapolating the magnetization to a zero magnetic field, are equal to 0.2 μ_B for $Cr_{0.33}TiTe_2$ and 0.9 μ_B for $Cr_{0.5}TiTe_2$.

The neutron diffraction pattern of the $Cr_{0.5}TiTe_2$ compound (Fig. 5) indicates ferromagnetic ordering of the magnetic moments of chromium ions. An analysis of the neutron diffraction data demonstrates that the magnetic unit cell coincides with the crystal chemical unit cell. The magnetic structure is described by the (000) magnetic vector. Consequently, the greater part of the magnetic reflections overlap with nuclear reflections. Since the intensity of the magnetic reflections is very weak, we failed to obtain a reliability factor better than 20%. Making allowance for the high chromium content in this compound, the weak intensity of the magnetic reflections can be explained by the fact that only part of the chromium atoms form an ordered structure. The calculations were performed for different models of magnetic moment orientation with respect to the principal crystallographic directions in the monoclinic unit cell. The best agreement with the experimental diffraction pattern was achieved in the case when the magnetic moments of chromium ions in the layer plane were aligned parallel to each other and to the [010] direction of the monoclinic structure. Moreover, the magnetic moment of chromium ions was determined to be $(0.8 \pm 0.2)\mu_B$, which agrees well with the spontaneous magnetic moment obtained from the magnetic measurements. It can be seen that the magnetic moments determined by independent methods in the experiment are considerably less than the calculated value, which, for a Cr^{3+} ion with a $3d^3$ electron configuration, should be equal to $3\mu_B$. From analyzing the experimental results, we assume that the magnetic state of the $Cr_{0.5}TiTe_2$ compound at temperatures below $T =$ 78 K can be represented as a mixture of magnetically ordered and spin-glass states. The possible coexistence of these states was considered in [10]. Probably, a similar mixed state, but with a smaller contribution of the magnetically ordered phase, can be observed in the compound with $x = 0.33$.

4. CONCLUSIONS

Thus, the results obtained in the above investigation indicate that chromium-intercalated titanium ditelluride can occur in different magnetic states (from a typical paramagnetic state to spin-glass and ferromagnetic states), depending on the intercalant content. The spin-glass and ferromagnetic states coexist in some regions. A comparison of the data obtained in this work with the results of our earlier investigation into the magnetic properties of Cr_xTiSe_2 compounds [8] clearly demonstrates that the specific features of the crystal and electronic structures of the matrix substantially affect both the magnetic properties of intercalation materials of this type and the magnitude and character of the interaction between intercalated 3*d* transition metal atoms.

ACKNOWLEDGMENTS

This work was supported by the US Civilian Research and Development Foundation for the Independent States of the Former Soviet Union (US CRDF) (project no. REC-005), the scientific program “Russian Universities” (project no. UR.01.01.005), and the Russian Federal program “Integration.”

REFERENCES

1. G. Calvarin, J. Calvarin, M. Buhannic, *et al.*, Rev. Phys. Appl. **22**, 1131 (1987).

2. M. Inoue, H. P. Hughes, and A. D. Yoffe, Adv. Phys. **38**, 565 (1989).
3. A. Titov, S. Titova, M. Neumann, *et al.*, Mol. Cryst. Liq. Cryst. **311**, 161 (1998).
4. A. N. Titov, A. V. Kuranov, V. G. Pleschev, *et al.*, Phys. Rev. B **63**, 035106 (2001).
5. Yu. Tazuke and T. Takeyama, J. Phys. Soc. Jpn. **66**, 827 (1997).
6. V. G. Pleshchev, A. N. Titov, and A. V. Kuranov, Fiz. Tverd. Tela (St. Petersburg) **39** (9), 1618 (1997) [Phys. Solid State **39**, 1442 (1997)].
7. A. V. Kuranov, V. G. Pleshchev, A. N. Titov, *et al.*, Fiz. Tverd. Tela (St. Petersburg) **42**, 2029 (2000) [Phys. Solid State **42**, 2089 (2000)].
8. V. Pleschov, N. Baranov, A. Titov, *et al.*, J. Alloys Compd. **320**, 13 (2001).
9. J. Rodriquez-Carvayal, Physica B (Amsterdam) **192**, 55 (1993).
10. M. Gabay and G. Toulouse, Phys. Rev. Lett. **47**, 201 (1981).

Translated by O. Borovik-Romanova

Physics of the Solid State, Vol. 46, No. 2, 2004, pp. 294–302. Translated from Fizika Tverdogo Tela, Vol. 46, No. 2, 2004, pp. 287–295.
Original Russian Text Copyright © 2004 by Korolev, Bazuev.

MAGNETISM AND FERROELECTRICITY

Paramagnetic and Spin-Glass Properties of Pyrochlore-Like Oxides $Ln_2Mn_{2/3}Mo_{4/3}O_7$ (Ln = Sm, Gd, Tb, or Y)

A. V. Korolev* and G. V. Bazuev**

** Institute of Metal Physics, Ural Division, Russian Academy of Sciences, ul. S. Kovalevskoĭ 18, Yekaterinburg, 620219 Russia*

*** Institute of Solid-State Chemistry, Ural Division, Russian Academy of Sciences, ul. Pervomaĭskaya 91, Yekaterinburg, 620219 Russia*

Received June 4, 2003

Abstract—The magnetic properties of complex oxides $Ln_2Mn_{2/3}Mo_{4/3}O_7$ (Ln = Sm, Gd, Tb, or Y) with a pyrochlore-type structure are studied in the temperature range 2–300 K. For all compounds in the paramagnetic state, the temperature dependence of the magnetic susceptibility is described by a generalized Curie–Weiss law with a temperature-independent component of ~10^{-6} cm^3/g and with a Weiss constant $\Theta < 0$ and $|\Theta| < 16$ K. At low temperatures (T < 10–12 K), the compounds have spin-glass properties; they exhibit magnetic and temperature hysteresis and the typical dependences of the imaginary and real parts of the dynamic magnetic susceptibility on temperature and the frequency of an ac magnetic field in a wide range of magnetization relaxation times. The data obtained suggest that d electrons are responsible for the formation of frustrated exchange interactions in the compounds and that $4f$ electrons in the compounds with Sm or Tb provide strong magnetic-anisotropy effects. © *2004 MAIK "Nauka/Interperiodica".*

1. INTRODUCTION

The family of chemical compounds isostructural to pyrochlore $NaCaTa_2O_6(OH, F)$ [1] is considerable. It contains a large group of complex oxides $A_2B_2O_7$, where A is a bivalent alkaline earth element or a trivalent rare earth element [2]. The positions of B atoms are occupied by penta- and tetravalent elements, respectively. These cases correspond to the chemical formulas $A_2^{2+}B_2^{5+}O_7$ and $A_2^{3+}B_2^{4+}O_7$, respectively. The compounds under study have a face-centered cubic lattice (space group $Fd3m$) and eight formula units in the unit cell. Atoms A are located in the 16d positions and coordinated by eight oxygen ions. Atoms B are located in the octahedra (16c positions). Unlike ABO_3 perovskites, where the BO_6 octahedra are connected by their vertices and form linear chains in three directions, the octahedra in pyrochlores are connected to form zigzag chains along the (110) direction with a B–O–B bond angle of ~135°. In order to emphasize the presence of two independent cation subsystems in the lattice, the pyrochlore formula can be written as $A_2O'(B_2O_6)$.

Cations A and B in the $A_2B_2O_7$ structure form a sublattice of tetrahedra connected by their vertices, which can result in intense frustration of the magnetic interaction and unusual low-temperature properties [3]. This cation environment prohibits antiferromagnetic interaction between cations located along the same directions [4]. This is likely the cause of the absence of long-range magnetic order in many pyrochlores. As a rule, complex oxides with pyrochlore structure demonstrate spin-glass behavior. However, according to [5], such compounds can also be in a ferromagnetic state. For example, semiconductor vanadium(IV)-based oxides $Ln_2V_2O_7$ (Ln = Lu, Yb, or Tm) are ferromagnets [6, 7].

Note that pyrochlore-type compounds have superconducting properties (e.g., $Cd_2Re_2O_7$ [8]) and, probably, exhibit spin-ice behavior (e.g., $Ln_2Ti_2O_7$ [9]).

Mn-containing pyrochlores $Ln_2Mn_2O_7$ exhibit a complex dependence of their magnetic properties on the type of element in the A position. For example, the oxides with Ln = Sc, Y, or Lu are characterized by spin-glass behavior and have semiconductor properties [10], whereas $Tl_2Mn_2O_7$ and $In_2Mn_2O_7$ compounds are ferromagnets (at $T \le 120$ K) and metallic conductors [11]. Mo-containing pyrochlores $Ln_2Mo_2O_7$ exhibit ferromagnetic properties in the case of Ln = Nd–Gd and spin-glass behavior for most heavy rare earth metals (Ln = Tb–Er, Y) [12, 13]. $Ln_2Mo_2O_7$ compounds of the former group have metallic conduction, whereas those of the latter group exhibit pronounced semiconductor properties. The character of conduction is likely to play the determining role in establishing magnetic order in these compounds.

In [14–16] (see also references therein), more complex oxides were reported to be synthesized: $Ln_2A_{2/3}B_{4/3}O_7$, where Ln stands for trivalent rare earth $4f$ ions, A are bivalent Mn, Co, or Ni ions, and B are pentavalent Nb, Ta, Mo, or Re ions; $Ln_2A_{4/3}B_{2/3}O_7$, where A are trivalent Fe or Mn ions and B is cation W^{6+}; and $Ln_2M^{3+}BO_7$, where B is Nb^{5+} or Ta^{5+}. These oxides were

found to have pyrochlore structure with rhombohedral distortions. Examination of these compounds by using high-resolution electron spectroscopy, electron diffraction, and x-ray diffraction [17, 18] showed that they could exist in two modifications, namely, in a trigonal one (space group $P3_121$, $z = 6$, zirkelite structure) and in a monoclinic one (space group $C2/c$, $z = 8$, zirconolite $CaZrTi_2O_7$ structure).

The magnetic properties of $Ln_2A_{2/3}B_{4/3}O_7$ pyrochlore-like oxides at low temperatures are almost completely unknown. Bazuev *et al.* [16] found that the $Y_2Mn_{2/3}Re_{4/3}O_7$ compound has a spontaneous magnetic moment below 190 K. Presumably, the magnetic structure of $Y_2Mn_{2/3}Re_{4/3}O_7$ is noncollinear [16]. As the temperature decreases, this compound undergoes a metal–semiconductor transition at $T \sim 120$ K [19]. At high temperatures (300–400 K), the magnetic susceptibility χ obeys the Curie–Weiss law

$$\chi = C/(T - \Theta), \quad (1)$$

where C and Θ are the Curie and Weiss constants, respectively. The value of Θ is negative, and the value of the effective magnetic moment μ_{eff} indicates the presence of a $Mn^{2+}(d^5)$–$Re^{5+}(d^2)$ cation combination. Note that the data on μ_{eff} for the $Er_2Mn_{2/3}Mo_{4/3}O_7$ compound obtained in [18] suggest a Mn^{2+}–Mo^{5+} cation combination; therefore, the manganese in both compounds is in the bivalent state. Similar to $Ln_2Mn_{2/3}Mo_{4/3}O_7$, $Ln_2Mn_{2/3}Re_{4/3}O_7$ oxides are semiconductors at low temperatures [14].

The data given above indicate that these compounds have a wide spectrum of magnetic states depending both on the degree of electron localization and on their crystal structure. However, the roles of these factors in the formation of the magnetic states in pyrochlore-like compounds are still unknown. Solving this problem requires, in particular, more information on the magnetic properties of $Ln_2A_{2/3}B_{4/3}O_7$ compounds. As noted above, the magnetic properties of these compounds are poorly understood. The purpose of this work is to find possible magnetic states in the series of complex oxides $Ln_2Mn_{2/3}Mo_{4/3}O_7$, where Ln = Y, Tb, Gd, or Sm. By analogy with the $Y_2Mn_{2/3}Re_{4/3}O_7$ compound studied earlier in [16], we can assume the existence of a Mn^{2+}–Mo^{5+} cation combination and, hence, long-range magnetic order in these oxides. Bazuev *et al.* [20] found that such a cation combination in the $LaMn_{2/3}Mo_{1/3}O_3$ perovskite leads to ferrimagnetism with a Curie temperature $T_C = 89$ K.

2. EXPERIMENTAL

The compounds to be studied were prepared, by solid-phase reactions, from oxides Ln_2O_3 (Ln = Y, Sm, Gd, or Tb) of the base material (99.95%), MnO produced from MnO_2 (99.9%) by reduction in hydrogen at 800°C, and metallic molybdenum (99.9%). They were synthesized in vacuum at a pressure of 10^{-3} Pa and a temperature of 1423 K. The completion of chemical reactions was controlled using x-ray diffraction (CuK_α radiation). The lattice parameters were calculated, using the least squares method, from the interplanar spacings measured with a STADI-P (STOE) diffractometer. As an external standard, we used polycrystalline silicon ($a = 5.43075(5)$ Å), and, as an internal standard, we used Al_2O_3 (NIST SRM 676 standard sample from the US National Institute of Standards and Technology with $a_h = 4.75919(44)$ Å, $c_h = 12.99183(174)$ Å).

Table 1. Lattice parameters of $Ln_2Mn_{2/3}Mo_{4/3}O_7$

Compound	Parameters	
	a, Å	c, Å
$Sm_2Mn_{2/3}Mo_{4/3}O_7$	15.075(2)	17.398(3)
$Gd_2Mn_{2/3}Mo_{4/3}O_7$	14.95(1)	17.37(1)
$Tb_2Mn_{2/3}Mo_{4/3}O_7$	14.90(1)	17.33(1)
$Y_2Mn_{2/3}Mo_{4/3}O_7$	14.80(1)	17.24(1)

Magnetic measurements were performed on an MPMS-XL-5 (QUANTUM DESIGN) SQUID magnetometer in the temperature range 2–300 K at the Center of Magnetometry of the Institute of Metal Physics. The strength H of the applied magnetic field was varied up to 50 kOe. The static magnetic moment of a sample was used to determine its magnetization M and static magnetic susceptibility $\chi = M/H$. By measuring the dynamic magnetic susceptibility, we determined the real part χ' and imaginary part χ'' of the dynamic susceptibility at an ac magnetic field amplitude of up to 4 Oe and a frequency f varying from 1 to 642 Hz.

3. RESULTS AND DISCUSSION

According to the x-ray diffraction data, all complex oxides produced are isostructural and do not contain any additional phases. As an example, Fig. 1 shows the x-ray diffraction pattern of the $Sm_2Mn_{2/3}Mo_{4/3}O_7$ compound typical of the series of compounds under study. Table 1 gives the lattice parameters of all compounds. The parameters were calculated assuming the crystal lattice to be rhombohedral with $a_{hex} \sim a_c \times 2^{1/2}$ and $c_{hex} \sim c_c \times 3^{1/2}$, where a_c and c_c are the lattice parameters for the cubic pyrochlore structure. We did not refine the atomic positions in the lattice; however, we believe that they can be specified using the data from [17], where an $Er_2Mn_{2/3}Mo_{4/3}O_7$ compound (which could be considered an analog of the oxides to be studied) was investigated. This compound was considered to have monoclinic structure with space group $C2/1$ and parameters $a = 12.781$ Å, $b = 7.378$ Å, $c = 11.643$ Å, and $\beta = 100.53°$. In the unit cell of this oxide, there are two types of Er^+ cations in the 8*a* positions, the Mo^{5+} ion is

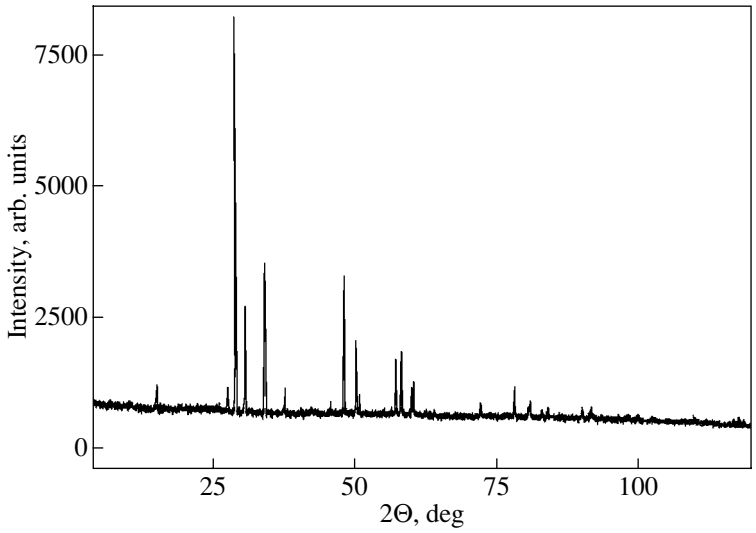

Fig. 1. X-ray diffraction pattern of $Sm_2Mn_{2/3}Mo_{4/3}O_7$.

in the 8*f* position, the Mn^{2+} cations of the first type are in the 4*e* positions, and the Mn^{2+} cations of the second type and the Mo^{5+} ion occupy the second 4*e* position (in the proportion 0.33Mn + 0.67Mo).

The basic magnetic data, especially for the paramagnetic state of the samples, are given in Fig. 2. Note that, to comprehensively analyze such data obtained for real samples, it is necessary to take into account the contributions to the magnetic susceptibility χ coming not only from a Curie–Weiss-type mechanism but also from other magnetization mechanisms. This is especially important at small values of the effective magnetic moment μ_{eff} and, correspondingly, small values of the experimentally determined susceptibility at fairly high temperatures $kT \gg \mu H$ (μ is the *z* component of the magnetic moment of an ion). Taking into account the nonlinear character of the temperature dependence of the reciprocal susceptibility for the compounds under study, we use the generalized Curie–Weiss law

$$\chi = \chi_0 + C/(T - \Theta), \qquad (2)$$

where χ_0 is the susceptibility due to other magnetization mechanisms. Assuming χ_0 to be virtually independent of temperature, we put $\chi_0(T)$ = const when processing the experimental data. Expression (2) describes the real magnetization of a material more exactly than does Eq. (1), and the additional contributions to the susceptibility, such as diamagnetic and Van Vleck- or Pauli-type contributions, as a rule, depend on temperature only weakly. The fact that susceptibility χ_0 of any nature, as a rule, weakly depends on temperature as compared to the function C/T serves as a basis for using the condition χ_0 = const in Eq. (2) to analyze the experimental $\chi(T)$ dependences for paramagnetic samples with localized magnetic moments. It should be noted that, apart from the physical reasons for introducing the additional term χ_0 in Eq. (1), there are trivial reasons, such as technological contamination of samples with ferromagnetic or other impurities with high values of susceptibility or magnetization.

At first glance, the nonlinear $\chi^{-1}(T)$dependence (Fig. 2a) can be considered a sign of a ferrimagnetic ground state in the $Y_2Mn_{2/3}Mo_{4/3}O_7$ and $Sm_2Mn_{2/3}Mo_{4/3}O_7$ compounds. Based on such a nonlinear character of the $\chi^{-1}(T)$ dependence in the range 77–1050 K, Bazuev *et al.* [14] supposed that $Y_2Mn_{2/3}Mo_{4/3}O_7$ has ferrimagnetic properties. However, the $\chi^{-1}(T)$ data obtained (Fig. 2) are not described by the Néel hyperbolic law. As will be shown below, the magnetic ground state of $Y_2Mn_{2/3}Mo_{4/3}O_7$ turns out to be spin glass rather than ferrimagnetic. In the case of the compound with Sm, we might consider another cause of the nonlinear character of the function $\chi^{-1}(T)$, namely, possible mixing of the ground multiplet of the Sm^{3+} ion (ground state $^6H_{5/2}$) and the next, higher lying state. However, this problem requires separate consideration. In this work, we analyze the experimental data for the compounds in question (including $Sm_2Mn_{2/3}Mo_{4/3}O_7$) only in the paramagnetic state in terms of Eq. (2).

As already mentioned, the susceptibility $\chi = M/H$ and the experimental data obtained at various values of *H* allow us to reveal contamination of samples with ferromagnetic impurities. The experiments were performed at $H \geq 500$ Oe (up to $H = 50$ kOe). In all cases in the region of a paramagnetic state, the $\chi(T)$ dependences merge with each other to form a line, within the measurement error. This result suggests that the content of ferromagnetic impurities in the samples is negligible ($<10^{-4}$–10^{-5}%). Therefore, the susceptibility χ_0 is likely to be related to the physics of magnetic phenomena in the compounds in question. The values of χ_0, Θ, *C*, and

effective magnetic moment μ_{eff} per formula unit are given in Table 2. They are obtained by fitting Eq. (2) to the experimental $\chi(T)$ curves with the use of standard methods for determining the three parameters involved in Eq. 2. The representation of the results in the form of $\chi(T)$ curves is not sufficiently illustrative. By contrast, the functions $\chi^{-1}(T)$ and $(\chi - \chi_0)^{-1}(T)$ clearly demonstrate (Fig. 2) the advantage of applying the generalized Curie–Weiss law to analyze the experimental data and determine the physical parameters χ_0, Θ, and C of the compounds. In the case of the $Gd_2Mn_{2/3}Mo_{4/3}O_7$ and $Tb_2Mn_{2/3}Mo_{4/3}O_7$ compounds, the susceptibility χ is found to be substantially higher than χ_0 over the whole temperature range studied; therefore, the $\chi^{-1}(T)$ dependence differs only weakly from the $(\chi - \chi_0)^{-1}(T)$ straight line (Fig. 2b).

Table 2 shows that, for all compounds, the values of the susceptibility χ_0 are positive and typical of most paramagnetic materials without localized magnetic moments. The susceptibility χ_0 is likely due to the magnetization of the matrix of the compounds, i.e., of the electronic subsystem that is not involved in the formation of localized moments. It is difficult to say anything more definite about this characteristic at the present time.

The Weiss constant Θ is negative and does not exceed ~16 K in magnitude for all compounds (Table 2). This result indicates the presence of antiferromagnetic interactions in the compounds under study. The absolute values of Θ for the compounds with Gd and Tb are several times greater than those for the compounds with Y and Sm, which can be understood as a result of interactions in both the 3*d*- and 4*f*- electron subsystems with possible *d–d*, *f–f*, and *d–f* exchange couplings. Note that our results are too scarce to establish standard correlations between Θ and de Gennes's parameter; however, the low values of Θ suggest that the antiferromagnetic interactions are weak.

Table 2 gives the values of Curie constant C and μ_{eff} determined from the experimental data and calculated using the free-ion model

$$\mu_{eff}^2 = 2\mu_R^2 + (2/3)\mu_{Mn}^2 + (4/3)\mu_{Mo}^2, \qquad (3)$$

where μ_R is the effective magnetic moment for the free Ln^{3+} ion and μ_{Mn} and μ_{Mo} are the effective spin magnetic moments for the manganese and molybdenum ions, respectively. The calculation was performed for two cation combinations of these ions, namely, $Mn^{2+}(d^5)$–$Mo^{5+}(d^1)$ and $Mn^{4+}(d^3)$–$Mo^{4+}(d^2)$. For the former combination (Table 2), the calculated values of μ_{eff} and C are seen to be substantially higher than the experimental values for all compounds under study. In the Mn^{4+}–Mo^{4+} model, the calculated results are much closer to the experimental data. However, as noted above, analysis of the experiments on determining the Curie constant C for the $Ln_2Mn_{2/3}Mo_{4/3}O_7$ (Ln = Y or Er [14, 16]) and $LnMn_{2/3}Mo_{1/3}O_3$ [20] compounds in the temperature range 77–1000 K gave a $Mn^{2+}(d^5)$–$Mo^{5+}(d^1)$ cation combination of manganese and molybdenum ions. Bivalent Mn and pentavalent Mo were also detected in [21], where the $BaLaMnMoO_6$ perovskite was studied using x-ray fluorescence analysis. However, the analysis of the four compounds given above inclines us to the model of Mn^{4+}–Mo^{4+}. To resolve this contradiction, it is necessary to perform additional studies, e.g., high-temperature measurement of the magnetic susceptibility; it is also appropriate to study x-ray and photoemission spectra.

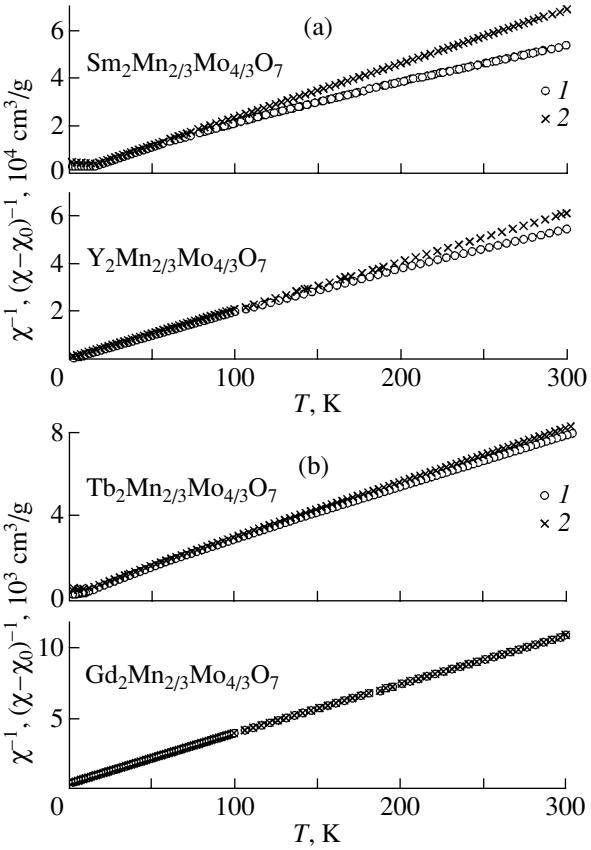

Fig. 2. (*1*) Curie–Weiss $\chi^{-1}(T)$ curve and (*2*) the same corrected for the temperature-independent magnetic susceptibility χ^0, i.e., $\chi_0(\chi - \chi_0)^{-1}(T)$, for compounds $Ln_2Mn_{2/3}Mo_{4/3}O_7$. (a) Ln = Y or Sm and (b) Ln = Gd or Tb.

If the ground state of the samples is paramagnetic, then a magnetic field H = 50 kOe is sufficient in all cases to achieve saturation of the $M(H)$ curve at T = 2 K ($\mu H \gg kT$). It is easy to calculate the saturation magnetization M_s, i.e., the limiting value of magnetization when all z projections of localized magnetic moments are oriented along an applied field H. The data calculated using the Mn^{2+}–Mo^{5+} and Mn^{4+}–Mo^{4+} models are given in Table 2. The values of M_s calculated in the former model are seen to be insignificantly lower than those calculated by the latter model. However, the cal-

Table 2. Temperature-independent magnetic susceptibility χ_0, Weiss constant Θ, Curie constant C, effective magnetic moment μ_{eff}, magnetization M_{50} measured at $T = 2$ K and $H = 50$ kOe, calculated limiting values of saturation magnetization M_s, coercive force H_c, and the spin-glass freezing temperature T_f for compounds $Ln_2Mn_{2/3}Mo_{4/3}O_7$

Property		*Ln*			
		Y	Sm	Gd	Tb
χ_0, 10^{-6} cm^3/g		2.2	4.4	1.8	5.5
Θ, K		–5.5	–4.0	–14.7	–16
C, 10^{-4} K cm^3/g	Experiment	52	46	297	400
	Calculation Mn^{2+}–Mo^{5+}	75	61	325	456
	Calculation Mn^{4+}–Mo^{4+}	57	49	311	442
μ_{eff}, μ_B	Experiment	4.3	4.6	11.8	13.8
	Calculation Mn^{2+}–Mo^{5+}	5.2	5.3	12.4	14.7
	Calculation Mn^{4+}–Mo^{4+}	4.5	4.7	12.1	14.5
M_{50}, M_s, emu/g	Experiment (50 kOe, 2K)	11.1	9.9	80.2	64.6
	Calculation Mn^{2+}–Mo^{5+}	57.5	52.1	110.4	128.6
	Calculation Mn^{4+}–Mo^{4+}	65.7	58.5	116.7	134.8
H_c, Oe	H_c^+	1070	2470	145	1380
	H_c^-	1040	1120	145	1210
T_f, K(500 Oe)		10	12.5	~5	12.5

culated values of magnetization M_s turn out to be substantially higher than the magnetization M_{50} measured at $H = 50$ kOe and $T = 2$ K (Fig. 3a; Table 2). Only in the case of the compound with Gd do the calculated and experimental results differ only weakly. These data indicate that the experimentally measured function $M(H)$ does not reach saturation; it is likely that M_s will be reached at $H \gg 50$ kOe.

The magnetic hysteresis loops given in Fig. 3 were measured with a magnetic field cycled starting from +50 kOe. The samples were cooled at $H = 0$; hereafter, we designate this regime as ZFC. For all compounds except $Gd_2Mn_{2/3}Mo_{4/3}O_7$, the hysteresis loops are asymmetrical with respect to the origin of coordinates. They are biased toward both negative values of H and positive values of M. The loop bias along the H axis can be characterized quantitatively by, for example, two values of coercive force H_c measured for a descending (from +50 to –50 kOe) branch (H_c^+) and an ascending (from –50 to +50 kOe) branch (H_c^-) of a hysteresis loop. The greater the difference $\Delta H_C = H_c^+ - H_c^-$, the greater the bias. Table 2 shows that, for the compounds with Sm, Tb, or Y, the values of ΔH_c are 1350, 170, and 30 Oe, respectively. The same sequence is characteristic of the average coercive force $(H_c^+ + H_c^-)/2$, i.e., the loop width at $M = 0$. The hysteretic properties are less pronounced for the compound with Gd. Although the coercive force in this compound is significantly lower than in the other three compounds, its value is significant (Table 2).

The study of the $M(H)$ isotherms indicates that the compounds are not in a paramagnetic state at sufficiently low temperatures.

Since the magnetic hysteresis is observed at low temperatures, it is obvious that in this case the magnetization of a sample should depend on its magnetic history, e.g., on the cooling of the sample at various values of H. Figure 4 shows the temperature dependences of the magnetization measured at $H = 500$ Oe. For each compound, measurements upon heating a sample from $T = 2$ K were performed twice, namely, after cooling the sample from room temperature at $H = 0$ (ZFC regime) and at $H = 500$ Oe (FC regime).

The character of the $M(H)$ and $M(T)$ functions for the compounds with Y, Sm, or Tb (Figs. 3, 4) is typical of systems with a spin-glass ground state. For the compounds with Y, Sm, or Tb, the spin-glass freezing temperature T_f is defined as the temperature at which two experimental $M(T)$ dependences merge near the maximum of the $M(T)$ function recorded in the ZFC regime.

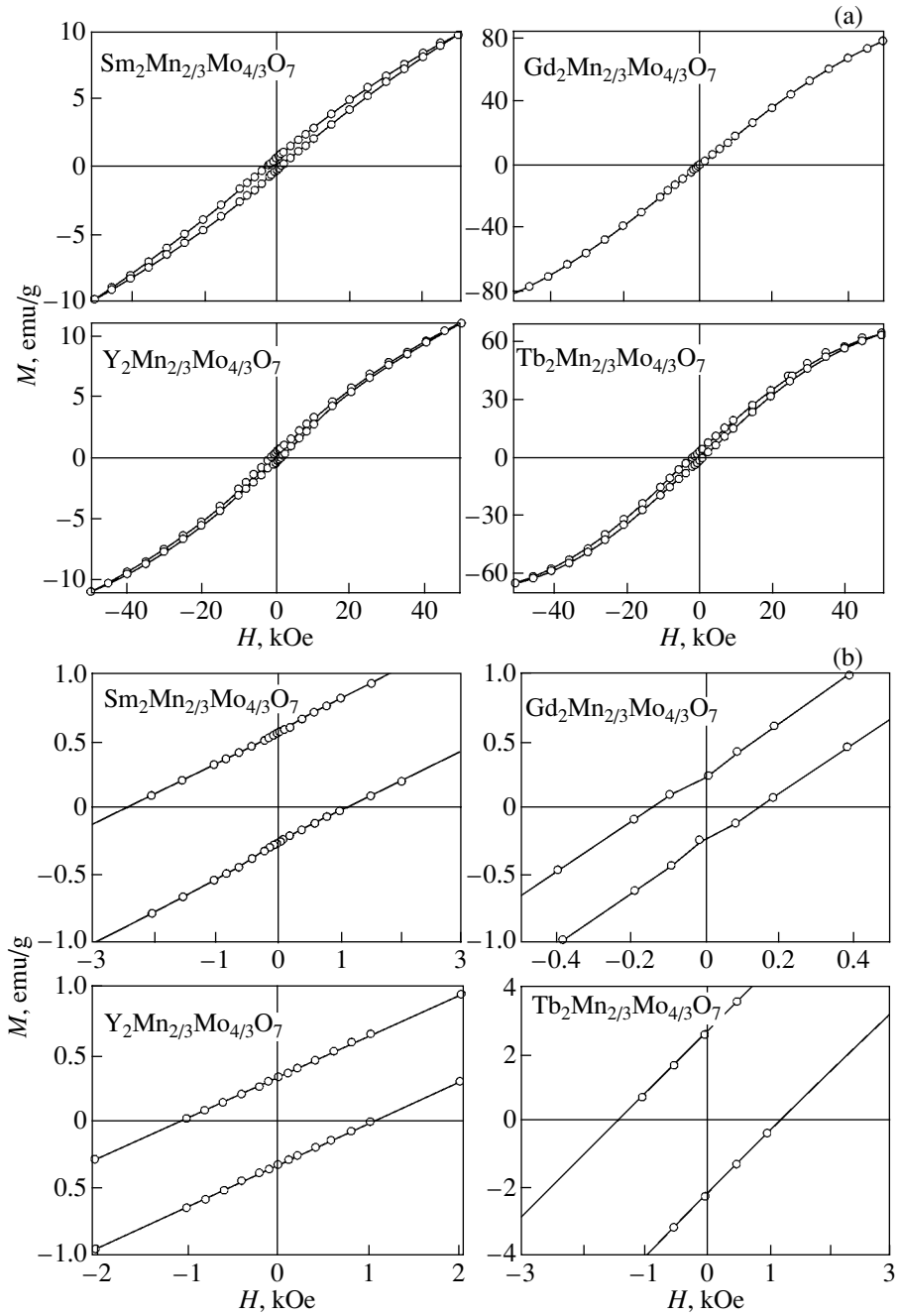

Fig. 3. Magnetization–field isotherms measured using a closed cycle +50 to 0 to –50 to 0 to +50 kOe for compounds $Ln_2Mn_{2/3}Mo_{4/3}O_7$ at $T = 2$ K. (a) Full scale and (b) fragments of magnetic hysteresis loops near the origin of coordinates.

For the compound with Gd, the $M(T)$ dependence has no maximum; in this case, the critical temperature T_f is also estimated as the point where the two $M(T)$ curves merge. In the series of compounds under study, the compounds with Sm or Tb have the highest values of T_f, the compound with Y has a slightly lower value of T_f, and the compound with Gd has the lowest T_f (Table 2).

The fact that a spin-glass state forms in the materials under study is additionally supported by the experimental investigation of the temperature and frequency dependences of the real χ' and imaginary χ'' parts of the dynamic magnetic susceptibility. The experiments were performed on $Y_2Mn_{2/3}Mo_{4/3}O_7$ samples in an ac magnetic field with an amplitude of 4 Oe. The typical frequency dependences of $\chi'(f)$ and $\chi''(f)$ for a low-temperature region ($T \le 10$ K) are shown in Fig. 5. In the range $10 < T < 12$ K, the shape of these dependences changes only slightly (the main features are retained).

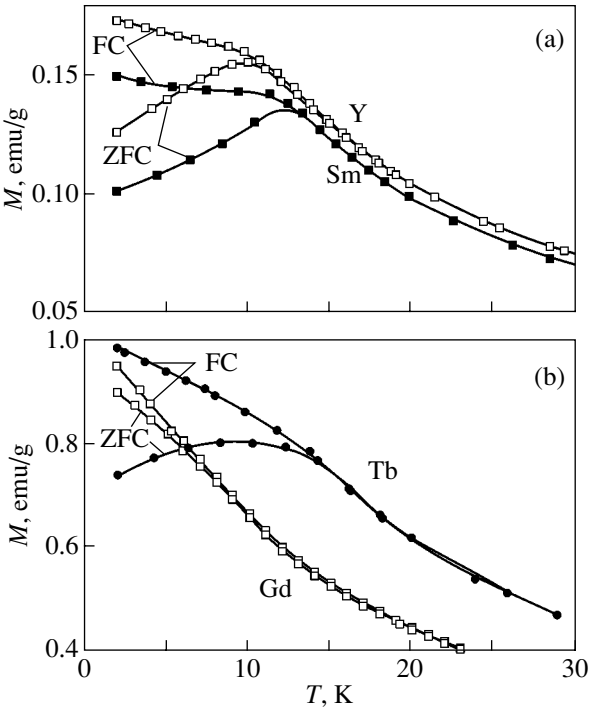

Fig. 4. Temperature dependences of the magnetization for compounds $Ln_2Mn_{2/3}Mo_{4/3}O_7$ [(a) Ln = Y or Sm; (b) Gd or Tb] measured twice upon heating a sample in a field H = 500 Oe after cooling the sample at H = 0 (ZFC curves) and after cooling the sample at H = 500 Oe (FC curves).

At T > 13–14 K, $\chi'(f)$ = const. The susceptibility χ'' at high temperatures (T > 14 K) cannot be measured under the experimental conditions used because the error in measuring this characteristic exceeds it.

The frequency dependences of $\chi'(f)$ and $\chi''(f)$ at low temperatures (Fig. 5) can be caused by specific relaxation of the magnetization in the spin-glass system of localized moments. In such systems, as a rule, the magnetization relaxation time τ has a wide range of values and is characterized by a certain distribution function $g(\tau)$. Assuming that $\tau_{min} \ll 1/f \ll \tau_{max}$ (where τ_{min} and τ_{max} are the shortest and longest relaxation times in the system under study, respectively), we can find the following relationship between χ'' and χ' [22]:

$$\chi'' \approx -(\pi/2)*\partial\chi'/\partial \ln f. \quad (4)$$

Since χ' varies insignificantly in the frequency range covered (Figs. 5, 6), the $\chi'(\ln f)$ dependence turns out to be virtually linear at temperatures T < 13 K within the limits of experimental error. It is obvious that we cannot describe the complex experimental $\chi''(T)$ dependence using Eq. (4). Nevertheless, the values of χ'' calculated from Eq. (4) are close to the experimental data (Fig. 7) and the experimental $\chi''(T)$ curves measured at various values of f lie near the calculated $\chi''(T)$ curve. The frequency dependences of the dynamic susceptibility can be analyzed more exactly by, for example, simulating the distribution function $g(\tau)$. However, solving such a problem is beyond the scope of this work. The examples given above allow us to understand semiquantitatively that relaxation processes in the spin-glass system do play a significant role in the processes of magnetization. Apparently, due to these processes, the magnetic hysteresis loops are biased (Fig. 3).

The data from Fig. 6 suggest that the shortest relaxation time τ_{min} is extremely small. As is seen, the temperature dependences of the dynamic $\chi'(T)_{f = const}$ and static $\chi(T)_{f = 0}$ ($\chi_{dc} = M/H$) susceptibilities are typical of spin-glass systems characterized by a large difference between the shortest and longest relaxation times. The freezing temperature T_f as determined from the position of the peak in the curves in Fig. 6 in the static measure-

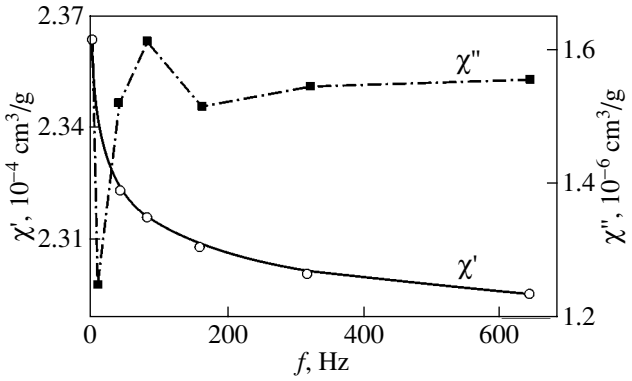

Fig. 5. Real χ' and imaginary χ'' parts of the dynamic magnetic susceptibility of $Y_2Mn_{2/3}Mo_{4/3}O_7$ at T = 2 K as functions of the frequency of an ac magnetic field with an amplitude of 4 Oe.

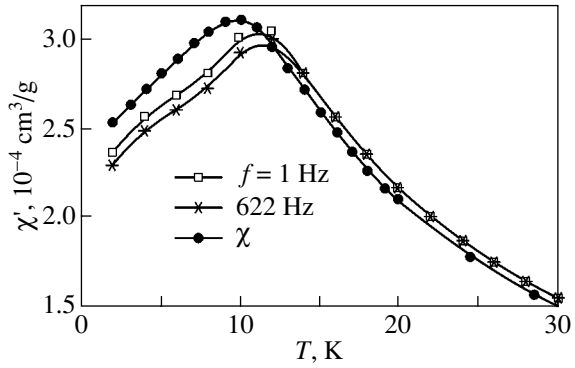

Fig. 6. Temperature dependences of the static magnetic susceptibility χ measured in the ZFC regime (see Fig. 4a) at H = 500 Oe and of the real part χ' of the dynamic magnetic susceptibility at frequencies f = 1 and 642 Hz of the applied ac magnetic field with an amplitude of 4 Oe (for compound $Y_2Mn_{2/3}Mo_{4/3}O_7$).

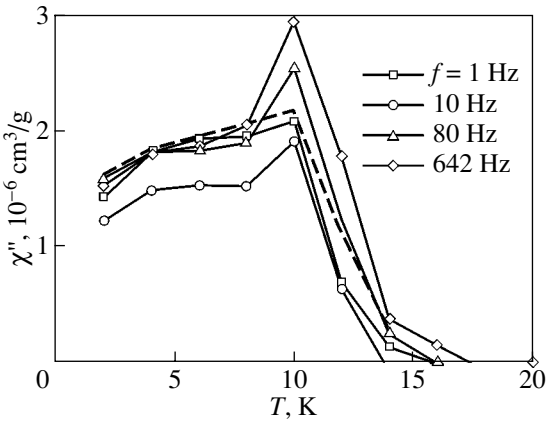

Fig. 7. Temperature dependence of the imaginary part χ" of the dynamic magnetic susceptibility of $Y_2Mn_{2/3}Mo_{4/3}O_7$ at various frequencies f of the applied ac magnetic field with an amplitude of 4 Oe. The dashed line is the calculation.

ment mode (i.e., at $f = 0$) is ~10 K. However, even at frequency $f = 1$ Hz, T_f becomes about 2 K higher and continues to increase with frequency.

4. CONCLUSIONS

The main conclusions are as follows.

First, the temperature dependences of the magnetic susceptibility $\chi(T)$ in the paramagnetic region cannot be uniquely described for all compounds $Ln_2Mn_{2/3}Mo_{4/3}O_7$ (Ln = Y, Sm, Gd, or Tb) in terms of the Curie–Weiss law. However, they can be described using a generalized Curie–Weiss law with an additional temperature-independent term, whose values are quite reasonable. The effective magnetic moments that are determined experimentally using this approach are smaller than those calculated for the Mn^{2+}–Mo^{5+} cation combination. Unique interpretation of these results requires additional investigation.

Second, exchange couplings in the compounds are weak and contain antiferromagnetic interactions. Interactions in the system of d electrons and, partly, f–d interactions likely play the main role. The interactions are most likely random and bring about the formation of an experimentally observed spin-glass state at sufficiently low temperatures. This state is characteristic of both the magnetic moments of the manganese and molybdenum ions in the case of a zero magnetic moment of the rare earth subsystem ($Y_2Mn_{2/3}Mo_{4/3}O_7$) and the magnetic moments of the rare earth ions (Sm, Gd, or Tb). Crystalline magnetic anisotropy plays a significant role in the formation of the spin-glass state in the case of rare earth ions with a nonzero orbital moment (Sm or Tb). The magnetic anisotropy is likely one of the main causes of the low values of M_{50} and wide hysteresis loops in the compounds with Sm or Tb. However, in the case of the compound with "nonmagnetic" Y, it would be surprising if only the crystalline magnetic anisotropy of 3d and 4d ions manifested itself in the formation of magnetic properties. Apparently, in this compound and the compound with Gd, exchange interactions are predominant in the hierarchy of interactions that dictate the directions of magnetic moments. The f–d interactions substantially decrease the rigidity of fixed random directions of the magnetic moments of d electrons and, hence, cause easier magnetization of the sample with Gd. The role of 4f electrons is likely ambiguous. On the one hand, their participation in the formation of exchange interactions favors magnetization of the whole ensemble of magnetic moments. On the other hand, 4f ions with a nonzero orbital moment (Sm or Tb) hinder the magnetization.

Thus, the long-range magnetic order, which could be expected due to the fact that it is characteristic of the compounds $Y_2Mn_{2/3}Re_{4/3}O_7$ [16] and $LaMn_{2/3}Mo_{1/3}O_3$ [20], having a Mn^{2+}–Re^{5+} or Mn^{2+}–Mo^{5+} cation combination, respectively, is not observed in the compounds studied. We believe that one of the important conditions for the formation of a spin-glass state in the four compounds $Ln_2Mn_{2/3}Mo_{4/3}O_7$ (Ln = Y, Sm, Tb, or Gd) studied by us consists in a random distribution of the manganese and molybdenum ions over equivalent positions in the crystal lattice.

ACKNOWLEDGMENTS

This work was supported by the Russian Foundation for Basic Research, project no. 02-03-32972.

REFERENCES

1. A. S. Povarennykh, *Crystallochemical Classification of Mineral Types* (Naukova Dumka, Kiev, 1966).
2. M. A. Subramanian, G. Aravamudan, and G. V. Subba Rao, Prog. Solid State Chem. **15**, 55 (1983).
3. J. E. Greedan, J. Mater. Chem. **11**, 37 (2001).
4. S. T. Bramwell and M. J. Harris, J. Phys.: Condens. Matter **10**, L215 (1998).
5. M. A. Subramanian, C. C. Torardi, D. C. Johnson, *et al.*, J. Solid State Chem. **72**, 24 (1988).
6. G. V. Bazuev, O. V. Makarova, V. Z. Oboldin, and G. P. Shveĭkin, Dokl. Akad. Nauk SSSR **230**, 869 (1976).
7. G. V. Bazuev, A. A. Samokhvalov, Yu. N. Morozov, *et al.*, Fiz. Tverd. Tela (Leningrad) **19**, 3274 (1977) [Sov. Phys. Solid State **19**, 1913 (1977)].
8. R. Jin, J. He, S. McCall, *et al.*, Phys. Rev. B **64**, 180503R (2001).
9. A. P. Ramirez, A. Hayashi, R. J. Cava, *et al.*, Nature **399** (6734), 333 (1999).
10. J. E. Greedan, N. P. Raju, A. Maignan, *et al.*, Phys. Rev. B **54** (10), 7189 (1996).
11. M. A. Subramanian, B. H. Toby, A. P. Ramirez, *et al.*, Science **273** (5271), 81 (1996).
12. G. V. Bazuev, G. P. Shveĭkin, T. I. Arbuzova, and V. N. Derkachenko, Dokl. Akad. Nauk SSSR **297** (2), 389 (1987).

13. K. Miyoshi, Y. Nishimura, K. Honda, *et al.*, Physica B (Amsterdam) **284–288**, 1463 (2000).
14. G. V. Bazuev, O. V. Makarova, and G. P. Shveĭkin, Zh. Neorg. Khim. **29**, 875 (1984).
15. G. V. Bazuev, O. V. Makarova, and N. A. Kirsanov, Zh. Neorg. Khim. **34**, 23 (1989).
16. G. V. Bazuev, T. I. Chupakhina, and V. N. Krasil'nikov, Pis'ma Zh. Éksp. Teor. Fiz. **74** (7), 440 (2001) [JETP Lett. **74**, 401 (2001)].
17. H. Nakano and N. Kamegashira, J. Am. Ceram. Soc. **84** (6), 1374 (2001).
18. G. Chen, K. Takasaka, and N. Kamegashira, J. Alloys Compd. **233**, 206 (1996).
19. G. V. Bazuev, T. I. Chupakhina, É. A. Neĭfel'd, and G. P. Shveĭkin, in *New Inorganic Materials and Thermodynamics* (Inst. Khim. Tverd. Tela Ural. Otd. Ross. Akad. Nauk, Yekaterinburg, 2002), p. 13.
20. G. V. Bazuev, A. S. Borukhovich, A. A. Sidorov, *et al.*, Neorg. Mater. **25** (1), 95 (1989).
21. T. Nakamura and Y. Gohski, Chem. Lett., No. 11, 1171 (1975).
22. L. Lundgren, P. Svedlindh, and O. Beckman, J. Magn. Magn. Mater. **25**, 33 (1981).

Translated by K. Shakhlevich

Physics of the Solid State, Vol. 46, No. 2, 2004, pp. 303–305. Translated from Fizika Tverdogo Tela, Vol. 46, No. 2, 2004, pp. 296–298.
Original Russian Text Copyright © 2004 by Zakharov, Titov.

MAGNETISM AND FERROELECTRICITY

Negative Magnetoresistance of Iron Single-Crystal Whiskers in the Course of Magnetization Reversal

Yu. V. Zakharov* and L. S. Titov**

** Kirensky Institute of Physics, Siberian Division, Russian Academy of Sciences, Akademgorodok, Krasnoyarsk, 660036 Russia*

*** Krasnoyarsk State University, Svobodnyĭ pr. 79, Krasnoyarsk, 660062 Russia*

Received June 5, 2003

Abstract—The change in the low-temperature resistance of iron single-crystal whiskers during magnetization reversal form a single-domain state to a state with a plane-parallel domain structure is studied theoretically. The negative magnetoresistance (~45%) is calculated from the Kubo formula with due regard for the change in the trajectories of conduction electrons in a magnetic induction field of domains. The magnetoresistance thus calculated is of the same order of magnitude as the magnetoresistance obtained in the experiment performed by Isin and Coleman. © *2004 MAIK "Nauka/Interperiodica".*

1. INTRODUCTION

In recent works [1, 2], new attempts have been made to interpret the negative magnetoresistance (up to –20%) in pure iron polycrystals [3] in terms of electron scattering by domain walls. As in earlier works performed by Cabrera and Falicov [4], the theoretical values were found to be several orders of magnitude smaller than the experimental magnetoresistance.

Earlier [5, 6], we showed that the negative magnetoresistance is caused by the change in the trajectories of electrons in a magnetic induction field near the domain walls. Taking into account the triple-domain states of electrons whose trajectories encompass a narrow domain, we obtained a negative magnetoresistance of up to –22%. The purpose of the present work was to demonstrate that our approach makes it possible to explain the negative magnetoresistance not only in iron polycrystals [3] but also in iron single-crystal thin whiskers [7].

The effect of a decrease in the electrical resistance of a ferromagnetic sample upon its magnetization in a transverse magnetic field was first revealed in the experiments performed with an iron polycrystal at 4.2 K by Sudovtsov and Semenenko [3] (the decrease observed was 20%) and in the experiments carried out with iron single-crystal whiskers by Isin and Coleman [7] (the resistance decreased to –60%). In our previous work [6], the experimental results obtained in [3] were theoretically interpreted as follows. During magnetization of a sample with the initial plane-parallel domain structure, the trajectories of conduction electrons in a magnetic induction field of the domains change as a result of displacements of the domain walls. When the width $2d$ of a decreasing domain becomes comparable to the cyclotron diameter $2R$, the size effect manifests itself and there appears a new type of electron states whose classical trajectories encompass three domains. The contribution from the other mechanisms responsible for the influence of the domain structure on the electrical conductivity of ferromagnetic metals turns out to be negligible. In [6], we calculated the electrical conductivity with allowance made for single-, double-, and triple-domain electron states and achieved quantitative agreement with the experimental data obtained in [3].

However, the situation observed in the experiments carried out by Isin and Coleman [7] was not considered and, hence, no explanation for the large negative magnetoresistance revealed in their work was offered. Coleman and Scott [8] performed detailed experimental studies of the domain structures of iron single-crystal whiskers upon magnetization reversal of samples in a transverse magnetic field. According to the results of powder experiments carried out in [8], samples in the initial state have a nearly single-domain structure, whereas the magnetization reversal in a transverse field brings about the formation and development of dagger-like and plane-parallel domain structures throughout the sample in magnetic fields up to 2 kOe. It is in these fields that the maximum negative magnetoresistance was observed by Isin and Coleman.

2. THEORETICAL BACKGROUND

In order to interpret the results obtained in [7], we considered the magnetoresistance of a multidomain sample. This sample had a single-domain structure in the initial state and involved narrow plane-parallel domains upon magnetization reversal (Fig. 1). Within this model, we obtained the dependence of the magnetoresistance on the transverse magnetization M. In our case, the relative value of M is determined by the width of new domains and the domain period is taken to be $2D$.

1063-7834/04/4602-0303$26.00 © 2004 MAIK "Nauka/Interperiodica"

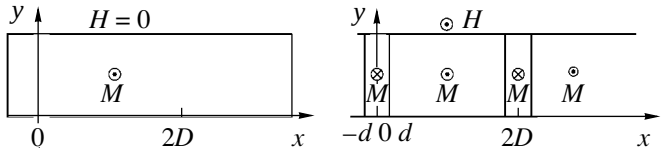

Fig. 1. Schematic diagram illustrating the formation of a domain structure in the course of magnetization reversal of a single-domain sample (the model corresponds to the experiment performed in [8]).

The calculation was performed with the use of the Kubo formula for the electrical conductivity of a compensated metal in the τ approximation [6]:

$$\sigma_{ij} = -e^2 \int d\Gamma \frac{\partial f_F}{\partial \varepsilon} \int_0^\infty \langle v_i(t') v_j(t'-t) \rangle_{t'} \exp(-t/\tau) dt. \quad (1)$$

Since the velocity correlators for different types of states differ from each other, the integration over the Fermi sphere is divided into integrations over the areas occupied by different electron states. This subdivision varies with a change in the coordinate x. The areas occupied by different electron states can be found from the relationship between the canonical and kinematic momenta and the condition that determines whether or not the domain walls are attained by the classical electron trajectories. This makes it possible to calculate analytically the averages of the velocity correlators of single-, double-, and triple-domain states and to perform the integration allowing for the collisions. As a result, the electrical conductivity across the new domains (along the whisker) in the range $0 \le x \le 2D$ can be represented in the following form:

$$\sigma_{xx}(x) = \frac{\sigma_0}{1+s^2}[1 + \Delta_3(x) + \Delta_3(2D-x) + \Delta_2(x+d) + \Delta_2(|x-d|) + \Delta_2(2D+d-x) + \Delta_2(|2D-d-x|)], \quad (2)$$

where $s = \tau\omega$ (ω is the cyclotron frequency in the magnetic field of the domain). The quantities $\Delta_2(x)$ and $\Delta_3(x)$ are the additional contributions (as compared to the single-domain states) made to the electrical conductivity by the double- and triple-domain states localized at the domain walls and in the narrow domains, respectively. These quantities represent the integrals over the Fermi surface area occupied by conduction electrons in the corresponding states. In the case when $d < R < D/2$, the quantity $\Delta_2(x)$ is the additional contribution from the double-domain states, which is truncated because of the presence of triple-domain states:

$$\Delta\sigma_2(x) = \begin{cases} \frac{1}{\pi}\int_{\varphi_2}^{\pi} F_2(\alpha) d\varphi, & 0 < x < 2d \\ 0, & 2d < x. \end{cases} \quad (3)$$

Here,

$$F_2(\alpha) = \frac{s^2}{1+s^2}\frac{2\cos^2\alpha\tanh(\alpha/s)}{\alpha} - \frac{1+3s^2}{1+s^2}\frac{\sin\alpha\cos\alpha}{\alpha}. \quad (4)$$

The parameters α and φ are related by the equation $\cos\varphi + \cos\alpha = -x/R$, because the expression is written for the domain wall located at $x = 0$ and the distance x to this domain wall is assumed to be positive in sign. The angle φ_2 is determined to be as follows: $\varphi_2 = \arccos[((2d - x)/R - 1)]$.

The relationship describing $\Delta\sigma_3(x)$ for a domain centered at $x = 0$ takes the following form at any positive x:

$$\Delta\sigma_3(x) = \begin{cases} \frac{1}{\pi}\int_{\varphi_3}^{\varphi_4} F_3(\alpha, \beta) d\varphi, & 0 < x < d < 2R \\ 0, & d + 2R < x. \end{cases} \quad (5)$$

The integrand has the form

$$F_3(\alpha, \beta) = \frac{1+3s^2}{\theta(1+s^2)}\cos\theta\sin(\theta - 2\alpha) + \frac{4s^3}{\theta(1+s^2)\sinh(2\theta/s)} \times [\cos^2\alpha\sinh(\alpha/s)\sinh((2\theta - \alpha)/s) + \cos^2\beta\sinh(\beta/s)\sinh((2\theta - \beta)/s) + 2\cos\alpha\cos\beta\sinh(\alpha/s)\sinh(\beta/s)]. \quad (6)$$

The limits of integration φ_3 and φ_4 depend on the range of definition of x. In particular, for $0 < x < d$, we have $\varphi_3 = \arccos[((x - d)/R + 1)]$ and $\varphi_4 = \arccos[((x + d)/R - 1)]$. In the case when $d < x < 3d$, the angles φ_3 and φ_4 are determined as follows: $\varphi_3 = \arccos[1 - (x - d)/R]$ and $\varphi_4 = \arccos[((3d - x)/R - 1)]$. In the range $3d < x < d + 2R$, these angles are found to be as follows: $\varphi_3 = \arccos[1 - (x - d)/R]$ and $\varphi_4 = \pi$. The parameters α, β, and φ are related by the expressions

$$\cos\varphi + \cos\alpha = -|(x - d)|/R, \quad \cos\beta + \cos\alpha = -2d/R. \quad (7)$$

Next, we performed the numerical calculation of the magnetoresistance according to the formula

$$\Delta\rho/\rho = [\rho(m) - \rho_0]/\rho_0, \quad (8)$$

where $\rho(m) = \int_0^D (1/\sigma(x))dx$ is the resistance for the relative transverse magnetization $m = M/M_0$ and ρ_0 is the resistance of the sample in the initial state.

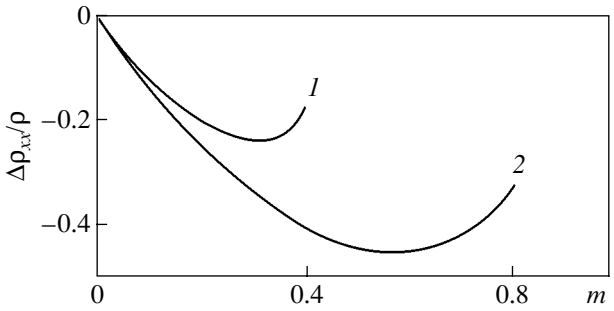

Fig. 2. Magnetoresistance of a single-domain sample in the course of transverse magnetization reversal at $2R/D$ = (*1*) 0.4 and (*2*) 0.8 for $s = 10$.

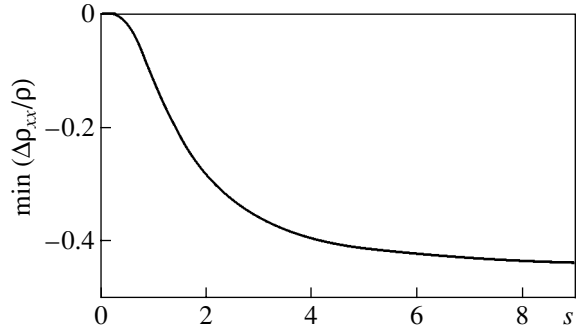

Fig. 3. Depth of the negative magnetoresistance minimum in the course of transverse magnetization reversal of the single-domain sample as a function of the ratio l/R at $2R/D = 0.8$.

3. RESULTS AND DISCUSSION

The magnetoresistance is calculated with respect to the initial single-domain state. Since the single-domain state is characterized by a higher resistance than the state with a periodic domain structure, the negative minimum in the magnetoresistance for a single-domain sample is deeper. Figure 2 presents the magnetoresistance curves obtained in our calculations for two values of the ratio $2R/D$. For example, at $2R/D = 0.8$, the depth of the magnetoresistance minimum reaches –45%.

The above expressions for electrical conductivity make it possible to calculate the magnetoresistance as a function of the quantity $s = \tau\omega = l/R$ (l is the mean free path of electrons in a metal). The depth of the magnetoresistance minimum changes most abruptly at the following ratio of the mean free path to the cyclotron radius: $l/R \gtrsim 1$–2. A typical dependence of the depth of the magnetoresistance minimum is shown in Fig. 3. It can be seen that, when the ratio l/R is relatively large, there occurs saturation. This result demonstrates that samples with a ratio $l/R \gtrsim 1$ will suffice for observations of the negative magnetoresistance effect due to changes in the electron trajectories.

The negative magnetoresistance (–45%) obtained in our calculations does not coincide with the value (–60%) observed in the experiment performed by Isin and Coleman. This difference can be explained by the fact that we did not take into account the contribution of quintuple-domain and consecutive multidomain electron states created upon magnetization reversal followed by the formation of a narrow daggerlike domain structure ($2R/D > 1$).

ACKNOWLEDGMENTS

We would like to thank Yu.I. Man'kov and S.G. Ovchinnikov for their continuous interest in our work.

REFERENCES

1. J. B. A. N. van Hoof, K. M. Schep, P. J. Kelly, and G. E. W. Bauer, J. Magn. Magn. Mater. **177–181**, 188 (1998).
2. G. Tatara and H. Fukuyama, Phys. Rev. Lett. **78**, 3773 (1997).
3. A. I. Sudovtsov and E. E. Semenenko, Zh. Éksp. Teor. Fiz. **35**, 305 (1958) [Sov. Phys. JETP **8**, 211 (1958)]; Zh. Éksp. Teor. Fiz. **47**, 486 (1964) [Sov. Phys. JETP **20**, 323 (1964)].
4. G. G. Cabrera and L. M. Falicov, Phys. Status Solidi B **61**, 539 (1974); Phys. Status Solidi B **62**, 217 (1974).
5. Yu. V. Zakharov, Yu. I. Mankov, and L. S. Titov, J. Magn. Magn. Mater. **54–57**, 1549 (1986).
6. Yu. V. Zakharov, Yu. I. Man'kov, and L. S. Titov, Fiz. Nizk. Temp. **12**, 408 (1986) [Sov. J. Low Temp. Phys. **12**, 232 (1986)].
7. A. Isin and R. V. Coleman, Phys. Rev. [Sect. A] **137**, 1609 (1965); Phys. Rev. **142**, 372 (1966).
8. R. V. Coleman and G. G. Scott, Phys. Rev. **107**, 1276 (1957).

Translated by I. Volkov

Physics of the Solid State, Vol. 46, No. 2, 2004, pp. 306–311. Translated from Fizika Tverdogo Tela, Vol. 46, No. 2, 2004, pp. 299–304.
Original Russian Text Copyright © 2004 by Voronin, Kuchin, Glazkov, Kozlenko, Savenko.

MAGNETISM AND FERROELECTRICITY

The Influence of High Pressure on the Structural and Magnetic Properties of $Y_2Fe_{17-x}M_x$ (M = Si, Al; x = 1.7) Compounds

V. I. Voronin*, A. G. Kuchin*, V. P. Glazkov, D. P. Kozlenko***, and B. N. Savenko*****

** Institute of Metal Physics, Ural Division, Russian Academy of Sciences, ul. S. Kovalevskoĭ 18, Yekaterinburg, 620219 Russia*

e-mail: Voronin@imp.uran.ru

*** Russian Research Centre Kurchatov Institute, pl. Kurchatova 1, Moscow, 123182 Russia*

**** Joint Institute for Nuclear Research, Dubna, Moscow oblast, 141980 Russia*

Received June 10, 2003

Abstract—The influence of high pressure on the crystal structure of the hexagonal intermetallic compounds Y_2Fe_{17}, $Y_2Fe_{15.3}Al_{1.7}$, and $Y_2Fe_{15.3}Si_{1.7}$ is investigated by neutron diffraction for the first time. It is shown that, under high pressure, the crystal lattice undergoes an isotropic contraction. A correlation of the changes in the Curie temperature with the distance between iron atoms in the dumbbell positions under pressure is revealed. The effect of pressure on the Y_2Fe_{17} compound is examined at low temperatures. It is found that the magnetostriction in this compound is suppressed under high pressure. *© 2004 MAIK "Nauka/Interperiodica".*

1. INTRODUCTION

The increased interest in intermetallic compounds of rare-earth metals with iron of the R_2Fe_{17} type is associated with their possible practical use as magnetic and magnetostrictive materials. The properties of these compounds are determined, to a large extent, by the real (defect) crystal structure. In particular, according to results obtained by various authors, the Curie temperature T_C of the transition to a ferromagnetic state in the Y_2Fe_{17} compound varies over a wide range (300–360 K). As was shown in our earlier work [1], this spread in the Curie temperatures T_C is caused by lattice imperfections. By introducing different elements (for example, nitrogen, carbon, or hydrogen) into the lattice [2–4] or doping the iron sublattice with silicon or aluminum [5–7], it is possible to increase the Curie temperature and to change the magnetostriction [8].

In the above works, the chemical composition of the samples was varied and, hence, the contributions of the particular structural parameters responsible for the change in the magnetic properties were difficult to separate. Kuchin *et al.* [8] analyzed the influence of high pressure on the magnetic properties of $Y_2Fe_{17-x}M_x$ (M = Si, Al) compounds but did not consider structural transformations of these materials under pressure. In the present work, we investigated the crystal structure of $Y_2Fe_{17-x}M_x$ (M = Si, Al) compounds under high pressures in order to reveal a possible correlation between the pressure-induced changes in the magnetic properties and the structural parameters.

2. EXPERIMENTAL TECHNIQUE

Samples of $Y_2Fe_{17-x}M_x$ (M = Si, Al; x = 0, 1.7) alloys were prepared by levitation melting in an induction furnace, subjected to homogenizing annealing at a temperature of 1300 K for 24 h, and quenched in water. The compression experiments were carried out with the Y_2Fe_{17}, $Y_2Fe_{15.3}Al_{1.7}$, and $Y_2Fe_{15.3}Si_{1.7}$ alloys, whose structures were precisely determined by neutron diffraction in the absence of pressure at room temperature in our previous works [1, 9]. The alloys contained α-Fe impurities in small amounts (<5%).

The crystal structure of the alloys was investigated by neutron diffraction. The experiments at pressures up to 1.0 GPa were performed on a D7a neutron diffractometer installed on the horizontal channel of an IVV-2M reactor (Zarechnyĭ, Russia) [10]. The neutron diffraction patterns were measured in the angle range 9°–111° with a step of 0.1°; the angular resolution of the diffractometer at the wavelength λ = 1.515 Å was $\Delta d/d$ = 0.003. The diffractometer was equipped with a high-pressure piston–cylinder-type chamber fabricated from a Ti–Zr alloy. A Freon-111 liquid served as a pressure-transferring medium [11]. The structural parameters (unit cell parameters, atomic coordinates, site occupancies) were refined by the Rietveld full-profile method [12] with the Fullprof program package [13]. The experiments at higher pressures (up to 4.5 GPa) were carried out in high-pressure chambers with sapphire anvils [14] with the use of a DN-12 spectrometer [15] installed on an IBR-2 pulsed high-flux reactor (Frank Laboratory of Neutron Physics, Joint Institute for Nuclear Research, Dubna). In this case, the volume V of the studied samples was approximately equal to 2 mm^3. The diffraction patterns were recorded at the

scattering angle $2\theta = 90°$. The resolution of the diffractometer for this scattering angle at the wavelength $\lambda = 2$ Å was $\Delta d/d = 0.015$. The characteristic time taken for one spectrum to be measured was equal to 20 h. The pressure in the chamber was measured from the shift of the ruby luminescence line with an accuracy of 0.05 GPa. In the experiments at low temperatures, the high-pressure chamber was placed in a helium refrigerator.

3. RESULTS

In [1, 9], we demonstrated that, under normal conditions, the crystal lattices of the Y_2Fe_{17}, $Y_2Fe_{15.3}Al_{1.7}$, and $Y_2Fe_{15.3}Si_{1.7}$ compounds have hexagonal symmetry and their real structures are disordered modifications of the Th_2Ni_{17}-type structure.

Figure 1 shows the neutron diffraction pattern of the Y_2Fe_{17} compound at pressure $P = 0.92$ GPa. The diffraction patterns of the $Y_2Fe_{15.3}Al_{1.7}$ and $Y_2Fe_{15.3}Si_{1.7}$ compounds are similar to the diffraction pattern shown in Fig. 1. The experimental results were analyzed within the model of a disordered crystal structure proposed in [1, 9]. The structural parameters obtained for the Y_2Fe_{17}, $Y_2Fe_{15.3}Si_{1.7}$, and $Y_2Fe_{15.3}Al_{1.7}$ compounds at different pressures and room temperature are given in Tables 1–3. Since the atomic coordinates in the structures of the $Y_2Fe_{15.3}Si_{1.7}$ and $Y_2Fe_{15.3}Al_{1.7}$ compounds are close to those in the structure of the Y_2Fe_{17} compound and weakly depend on the pressure, only the unit cell parameters for these compounds are presented in Tables 2 and 3.

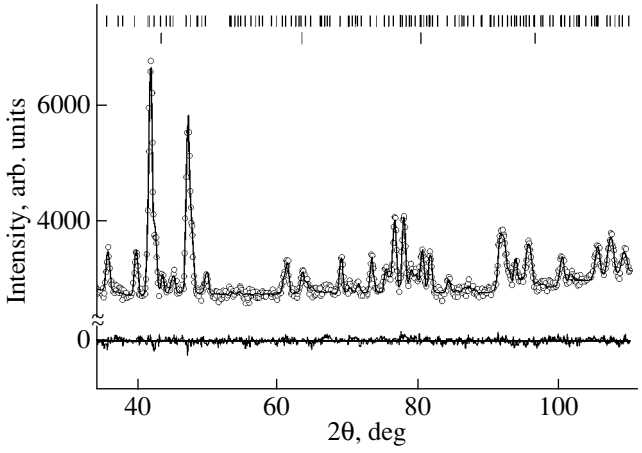

Fig. 1. Fragment of the neutron diffraction pattern of the Y_2Fe_{17} compound at room temperature and pressure $P = 0.92$ GPa. Points are the experimental data. The solid line represents the profile calculated by the Rietveld method. The difference curve is shown at the bottom. Two rows of tick marks (at the top) indicate the calculated positions of the diffraction peaks for the Y_2Fe_{17} compound and small amounts of α-Fe impurities found in the sample.

Table 1. Experimental structural parameters of the Y_2Fe_{17} compound at different pressures

Parameter		*P*, GPa			*K*, GPa^{-1}
		0	0.46	0.92	
a, Å		8.5023(9)	8.4872(9)	8.4778(8)	0.0031(4)
c, Å		8.3279(9)	8.3118(9)	8.3023(8)	0.0033(5)
V, Å^3		520.91(9)	518.50(9)	516.78(8)	0.0096(8)
c/*a*		0.9795	0.9793	0.9793	
Fe(4*f*)	*z*	0.1066(9)	0.1077(12)	0.1078(11)	
Fe_1(12*j*)	*x*	0.328(3)	0.328(3)	0.325(2)	
	y	0.373(3)	0.369(3)	0.369(2)	
Fe_2(12*j*)	*x*	0.290(7)	0.282(7)	0.281(5)	
	y	0.287(7)	0.279(7)	0.271(6)	
Fe(12*k*)	*x*	0.169(2)	0.169(2)	0.169(2)	
	z	–0.0133(6)	–0.0148(6)	–0.0164(5)	
Fe(4*e*)	*z*	0.100(9)	0.108(9)	0.106(8)	
R_P		1.79	1.56	1.59	
R_{WP}		2.44	1.97	2.04	
R_B		6.63	6.84	6.59	

Designations: *a* and *c* are the unit cell parameters; *V* is the unit cell volume; *x*, *y*, and *z* are the fractional atomic coordinates; $K_i = (1/a_{i0})(d_{ai}/dP)_T$ ($a_i = a, c$) and $K_V = (1/V_0)(dV/dP)_T$ are the linear and volume compressibility coefficients; and R_P, R_{WP}, and R_B are the reliability factors.

Table 2. Experimental structural parameters of the $Y_2Fe_{15.3}Si_{1.7}$ compound at different pressures

Parameter	*P*, GPa					*K*, GPa^{-1}
	0	0.15	0.31	0.61	0.79	
a, Å	8.4449	8.441	8.426	8.417	8.421	0.004(1)
c, Å	8.2966	8.29	8.274	8.265	8.271	0.0043(12)
V, Å^3	512.41	511.57	508.74	507.07	508.00	0.012(4)
c/*a*	0.9824	0.9821	0.9820	0.9819	0.9822	

Table 3. Experimental structural parameters of the $Y_2Fe_{15.3}Al_{1.7}$ compound at different pressures

Parameter	*P*, GPa				*K*, GPa^{-1}
	0	0.28	0.55	0.79	
a, Å	8.5261	8.515	8.521	8.502	0.0029(14)
c, Å	8.3344	8.321	8.323	8.312	0.0029(9)
V, Å^3	524.7	522.42	523.42	520.38	0.009(2)
c/*a*	0.9775	0.9772	0.9768	0.9777	

For the $Y_2Fe_{15.3}Si_{1.7}$ compound, we performed additional measurements over a wider range of pressures up to 4.5 GPa. The neutron diffraction patterns of the $Y_2Fe_{15.3}Si_{1.7}$ compound at pressures of 0 and 4.5 GPa and room temperature are shown in Fig. 2. The experimental data obtained at high pressures are adequately described within the model of a disordered crystal structure [1, 9] (Fig. 2). This suggests that no structural phase transformations occur in the pressure range covered, which agrees with the experimental results obtained earlier for the crystal structure of the $Y_2Fe_{15.3}Si_{1.7}$ compound at pressures up to 2.0 GPa [16].

The pressure dependences of the unit cell parameters and the unit cell volume for $Y_2Fe_{17-x}M_x$ (M = Si, Al) are depicted in Figs. 3a and 3b, respectively. These dependences exhibit a nearly linear behavior. The calculated coefficients of the linear compressibility for the unit cell parameters $K_i = (1/a_{i0})(da_i/dP)_T$ ($a_i = a, c$) and the volume compressibility $K_V = (1/V_0)(dV/dP)_T$ are presented in Tables 1–3. For all the compounds studied, the coefficients K_a and K_c are almost identical and the ratio of the unit cell parameters c/a remains nearly constant with an increase in the pressure. This indicates that the compressibility of these compounds is isotropic in nature.

In [8, 17–19], it was shown that R_2Fe_{17} compounds are characterized by a considerable magnetostrictive effect, which leads to a substantial increase in the unit cell parameter c with a decrease in the temperature below 270 K. With the aim of investigating the influence of high pressure on this effect, we performed the neutron diffraction experiments at pressure P = 1 GPa in the temperature range 150–300 K. The temperature dependences of the unit cell parameters for the Y_2Fe_{17} compound at P = 1 GPa and normal pressure (according to the data taken from [4]) are depicted in Fig. 4. It can be seen from this figure that the temperature dependence of the unit cell parameter c under high pressure changes significantly. A decrease in the temperature leads to a noticeable increase in the parameter c at normal pressure and to an insignificant decrease in this parameter at P = 1.0 GPa. Therefore, the magnetostrictive effect in the Y_2Fe_{17} compound under high pressure is suppressed.

4. DISCUSSION

The properties of $Y_2Fe_{17-x}M_x$ (M = Si, Al) compounds are determined, to a large extent, by the real (defect) crystal structure, which is a disordered modification of the Th_2Ni_{17}-type hexagonal structure [1, 8, 9]. The disordering is associated with the formation of vacancies at the 2*b* sites of the yttrium sublattice. A number of large-sized yttrium atoms change places with small-sized iron atoms coupled in pairs at the 4*f* positions (so-called iron "dumbbells"). Moreover, iron atoms partially occupy the 4*e* positions that are vacant in the ideal lattice and form additional dumbbell iron positions. This brings about distortions in the plane of iron atoms and, hence, splitting of the 12*j* position of iron into two positions. The degree of disordering depends on the specific synthesis conditions of the sample. This provides an explanation for the fact that, according to data obtained by different authors, the Curie temperature T_C for the Y_2Fe_{17} compound varies over a wide range (300–360 K). It was shown earlier in

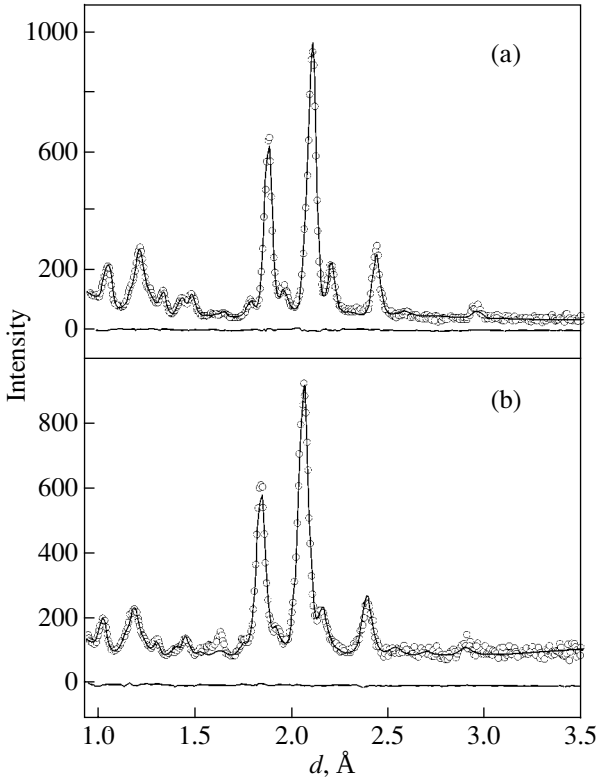

Fig. 2. Fragments of the neutron diffraction patterns of the $Y_2Fe_{15.3}Si_{1.7}$ compound at room temperature and pressures P = (a) 0 and (b) 4.5 GPa. Points are the experimental data. Solid lines represent the profiles calculated by the Rietveld method. Difference curves are shown at the bottom.

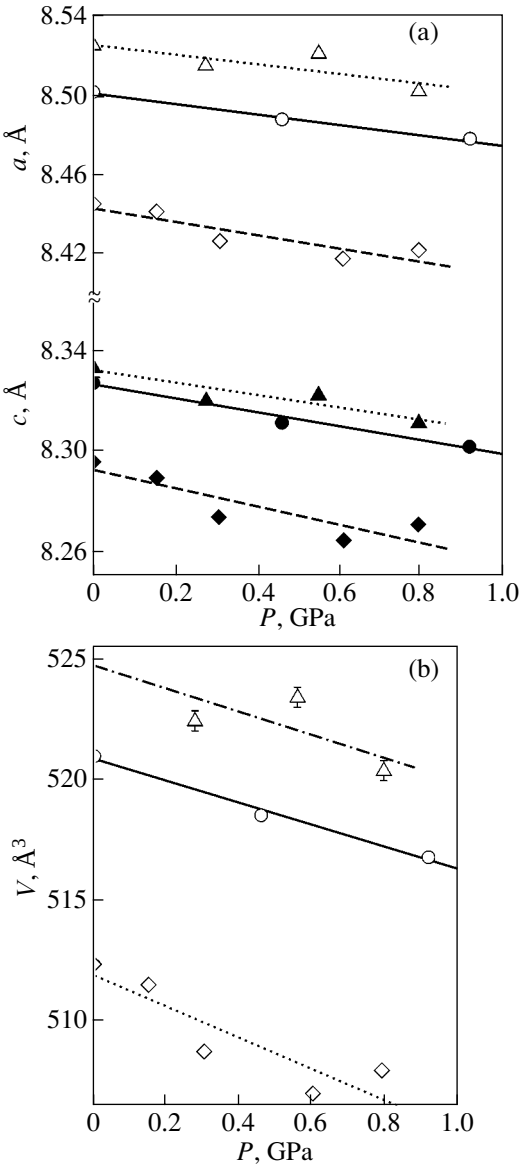

Fig. 3. Pressure dependences of (a) the unit cell parameters and (b) the unit cell volume for Y_2Fe_{17} (circles), $Y_2Fe_{15.3}Al_{1.7}$ (triangles), and $Y_2Fe_{15.3}Si_{1.7}$ (rhombs). Straight lines represent the linear interpolation of the experimental data.

[1, 9] that, upon doping of the initial Y_2Fe_{17} compound, Al and Si atoms replace Fe atoms in the 12*k* and 4*f* positions with a higher probability and in the 6*g* and 12*j* positions with a lower probability. Similar changes upon doping with Al and Si atoms were also observed in the isostructural compound Lu_2Fe_{17} [20].

Let us now analyze the interrelation of the structural and magnetic properties in terms of the model of localized moments. Within this model, iron atoms interact with each other either ferromagnetically or antiferromagnetically depending on whether the distance between them is larger or smaller than the critical distance $R_c \approx 2.45$ Å. In R_2Fe_{17} compounds, the interatomic distances between the nearest neighbor iron atoms are close to 2.45 Å. Consequently, these compounds can occur in both the ferromagnetic and antiferromagnetic states. Among the interatomic distances, the smallest distance is observed between iron atoms in the 4*f* dumbbell position. Therefore, it can be assumed that the Curie temperature of the R_2Fe_{17} alloys substantially depends on this distance. Actually, in our previous works [8, 16, 20, 21], we demonstrated that the Curie temperature T_C for R_2Fe_{17} compounds doped with aluminum and silicon increases directly with an increase in the distance between the iron atoms in dumbbell positions. It was revealed that the distance between the iron atoms in the dumbbell positions of the Y_2Fe_{17} compound increases as a result of partial replacement of both aluminum and silicon due to atomic displacements inside the crystal lattice. A similar dependence was observed for the hexagonal isostructural compound Lu_2Fe_{17} [20] upon doping with aluminum and silicon. Furthermore, an increase in the Curie temperature T_C with an increase in the distance between the iron atoms in dumbbell positions was also revealed in compounds with small-sized rare-earth atoms, for example, in the Ce_2Fe_{17} compound with a rhombohedral lattice upon

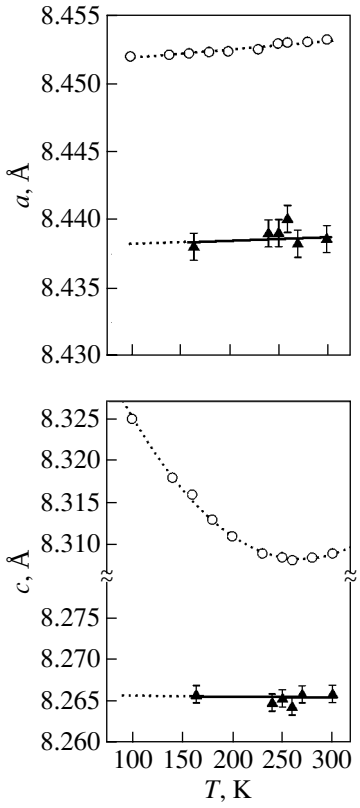

Fig. 4. Temperature dependences of the lattice parameters for the Y_2Fe_{17} compound at pressures $P = 0$ (open symbols) and 1 GPa (closed symbols).

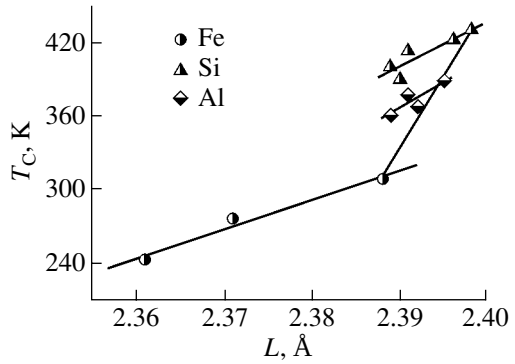

Fig. 5. Calculated dependence of the Curie temperature T_C on the distance L between the iron atoms in dumbbell positions for $Y_2Fe_{17-x}M_x$ (M = Si, Al) compounds. The calculations are performed according to the structural data obtained in this work and the data on the magnetic properties [8] at high pressures up to 1.0 GPa.

doping with aluminum and silicon [21, 22]. Thus, we can infer that there exists a parameter (the distance between the iron atoms in dumbbell positions) whose variation in all $R_2Fe_{17-x}M_x$ ternary compounds correlates with the change in the Curie temperature T_C.

Figure 5 shows the dependence of the Curie temperature T_C on the distance L between the iron atoms in dumbbell positions of the structure of $Y_2Fe_{17-x}M_x$ (M = Si, Al). This dependence was calculated from the structural data obtained in the present work and data on the magnetic properties at high pressures of up to 1.0 GPa [8] (Tables 1, 2). As can be seen from Fig. 5, the Curie temperature T_C decreases with a decrease in the distance between the iron atoms in the dumbbell positions of all three compounds. At the same time, the change in the Curie temperature T_C with a decrease in the distance L depends on the nature of the dopant and is maximum for the undoped Y_2Fe_{17} compound. These findings can be explained on the basis of the available data on doping. According to [1, 9], the occupancy of the dumbbell positions with iron atoms is approximately equal to 1.60 (lowest occupancy) in the aluminum-doped sample, 1.74 in the silicon-doped sample, and 1.91 in the initial sample. This is clearly illustrated by the dependence of dT_C/dP on the occupancy of the dumbbell positions in the three compounds (Fig. 6). Therefore, the larger the total number of iron atoms occupying the dumbbell positions, the stronger the effect of pressure on the Curie temperature T_C.

As was noted above, the R_2Fe_{17} compounds are characterized by pronounced magnetostrictive effects [19]. These effects manifest themselves in a strong dependence of the Curie temperature and the magnetic properties on the volume. The spontaneous volume magnetostriction of R_2Fe_{17} compounds is rather large: it is comparable in magnitude to the volume magnetostriction of invar alloys. It should be noted that the exchange striction and isotropic magnetoelastic interaction in hexagonal and cubic crystals exhibit specific features. In particular, the spontaneous magnetoelastic deformations that are independent of the magnetization vector direction are strongly anisotropic in R_2Fe_{17} hexagonal compounds [19]. For example, the exchange striction of the lattice parameter c of the Y_2Fe_{17} crystal is four to five times greater than that of the parameter $a = b$. The factors responsible for the anisotropy of the exchange striction remain unclear. It was assumed that the anisotropy of the exchange striction is associated with the anisotropy of the crystal lattice of R_2Fe_{17} compounds and, hence, with the anisotropy of elastic constants. However, our experiments revealed that, under pressure, the crystal lattice undergoes an isotropic contraction (the ratio c/a remains nearly constant). Consequently, it can be expected that the dependence of the exchange interaction on the distance should exhibit anisotropic behavior. In turn, this leads to high anisotropy of the spontaneous exchange magnetostriction $(\Delta c/c)^m/(\Delta a/a)^m \approx 4$ [19] and a large difference between the magnetic contributions to the linear compressibility along the crystallographic axes.

The magnetostrictive effect in the Y_2Fe_{17} compound is associated with the ferromagnetic state. Therefore,

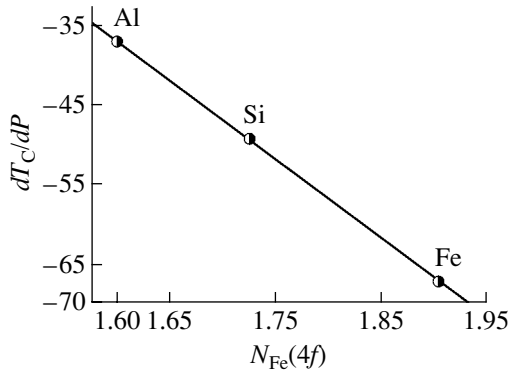

Fig. 6. Dependence of dT_C/dP on the occupancy of the dumbbell position for $Y_2Fe_{17-x}M_x$ (M = Si, Al) compounds.

the suppression of this effect at high pressures can be due to a decrease in the Curie temperature because of the decrease in the distance between the iron atoms in the dumbbell positions. In the immediate future, some effects caused by the isotropic magnetoelastic interaction in R_2Fe_{17} hexagonal crystals will be analyzed in the framework of the phenomenological theory of isotropic magnetoelastic interaction in ferromagnets and the results obtained will be reported in a separate paper.

5. CONCLUSIONS

Thus, the crystal structures of Y_2Fe_{17}, $Y_2Fe_{15.3}Al_{1.7}$, and $Y_2Fe_{15.3}Si_{1.7}$ intermetallic compounds were investigated at high pressures. It was found that, under high pressure, the crystal lattice undergoes an isotropic contraction, whereas the hexagonal crystal structure of these compounds is retained over the entire range of pressures up to 4.5 GPa.

It was established that, for these compounds, the main factors affecting the Curie temperature T_C and its derivative with respect to pressure dT_C/dP are the distance between the iron atoms in the dumbbell positions and their occupancy.

The suppression of the magnetostrictive effect in the Y_2Fe_{17} compound under high pressure was explained by the decrease in the Curie temperature. It was assumed that the magnetostrictive effect in $R_2Fe_{17-x}M_x$ compounds can also be suppressed under high pressure.

ACKNOWLEDGMENTS

This work was supported by the State Scientific and Technical Program “Topical Directions in the Physics of Condensed Matter,” State Contract no. 40.012.1.1.11.50.

REFERENCES

1. V. I. Voronin, I. F. Berger, and A. G. Kuchin, Fiz. Met. Metallogr. **89**, 88 (2000).
2. J. M. D. Coey and H. Sun, J. Magn. Magn. Mater. **87**, L251 (1990).
3. X. P. Zhong, R. J. Radwanski, F. R. de Boer, *et al.*, J. Magn. Magn. Mater. **86**, 333 (1990).
4. X. Z. Wang, K. Donnely, J. M. D. Coey, *et al.*, J. Mater. Sci. **23**, 329 (1988).
5. B. G. Shen, L. S. Kong, F. W. Wang, and L. Cao, Appl. Phys. Lett. **63**, 2288 (1993).
6. B. G. Shen, F. W. Wang, L. S. Kong, *et al.*, J. Magn. Magn. Mater. **127**, L267 (1993).
7. A. G. Kuchin, N. I. Kourov, Yu. V. Knyazev, *et al.*, Phys. Status Solidi A **155**, 479 (1996).
8. A. G. Kuchin, I. V. Medvedeva, V. S. Gaviko, and V. A. Kazantsev, J. Alloys Compd. **289**, 18 (1999).
9. V. I. Voronin, I. F. Berger, A. G. Kuchin, *et al.*, J. Alloys Compd. **315**, 82 (2001).
10. B. N. Goshchitskii and A. Z. Menshikov, Neutron News **7**, 12 (1996).
11. A. I. Ivanov, D. E. Litvin, B. N. Savenko, *et al.*, High Press. Res. **14**, 209 (1995).
12. H. M. Rietveld, J. Appl. Crystallogr. **2**, 65 (1969).
13. J. Rodriges-Carvajal, Physica B (Amsterdam) **192**, 155 (1993).
14. V. P. Glazkov and I. N. Goncharenko, Fiz. Tekh. Vys. Davleniĭ **1**, 56 (1991).
15. V. P. Glazkov, V. L. Aksenov, D. V. Sheptyakov, *et al.*, Physica B (Amsterdam) **265**, 258 (1999).
16. V. I. Voronin, A. E. Teplykh, I. V. Medvedeva, *et al.*, High Press. Res. **17**, 193 (2000).
17. D. Givord and R. Lemaire, IEEE Trans. Magn. **10**, 109 (1974).
18. M. Brouha, K. H. J. Buschow, and A. R. Miedema, IEEE Trans. Magn. **10**, 182 (1974).
19. A. V. Andreev, A. V. Deryagin, S. M. Zadvorkin, *et al.*, in *Physics of Magnetic Materials* (Kalinin, 1985), p. 21.
20. V. I. Voronin, I. F. Berger, and A. G. Kuchin, Fiz. Met. Metalloved. **93**, 39 (2002).
21. V. V. Serikov, N. M. Kleĭnerman, A. G. Kuchin, and V. I. Voronin, Fiz. Met. Metalloved. **94**, 59 (2002).
22. M. Artigas, D. Fruchart, O. Isnard, *et al.*, J. Alloys Compd. **270**, 28 (1998).

Translated by O. Borovik-Romanova

Physics of the Solid State, Vol. 46, No. 2, 2004, pp. 312–315. Translated from Fizika Tverdogo Tela, Vol. 46, No. 2, 2004, pp. 305–307.
Original Russian Text Copyright © 2004 by Akhmadullin, Migachev, Sadykov, Shakirzyanov.

MAGNETISM AND FERROELECTRICITY

Magnetic Birefringence of Sound and Magnetoacoustic Oscillations in Hematite

I. Sh. Akhmadullin, S. A. Migachev, M. F. Sadykov, and M. M. Shakirzyanov

Zavoĭskiĭ Kazan Physicotechnical Institute, Kazan Science Center, Russian Academy of Sciences, Sibirskiĭ trakt 10/7, Kazan, 420029 Russia

e-mail: i_akhm@kfti.knc.ru

Received June 23, 2003

Abstract—An experimental study of the magnetic birefringence of sound in the α-Fe_2O_3 easy-plane antiferromagnet is reported. The amplitude of transverse sound transmitted through the crystal along the $\mathbf{C}_3$ trigonal axis was found to oscillate depending on the magnitude of the magnetic field $\mathbf{H}$ applied in the basal plane ($\mathbf{H} \perp \mathbf{C}_3$). The experiments provide qualitative support for the theory of this phenomenon developed earlier by Turov. Possible reasons for the substantial quantitative disagreement between theory and experiment observed in the field dependence of the sonic-amplitude oscillation period are discussed. Unannealed samples of the hematite revealed a 60° periodic dependence of the position of the intensity oscillation extrema on magnetic field orientation in the basal plane, which is associated with basal anisotropy of higher than second order. The observation of pronounced ($\sim 6 \times 10^3$ Oe) effective magnetic anisotropy fields in the basal plane can be assigned to the existence of large residual strains in such samples. © *2004 MAIK "Nauka/Interperiodica".*

1. Linear magnetic birefringence of sound in easy-plane antiferromagnets (AFMs) is one of the various new magnetoacoustic phenomena associated with a vector order parameter (antiferromagnetism vector), whose theory was developed recently by Turov [1]. The nature of linear birefringence is related to the lifting of the degeneracy in the spectrum of transverse waves propagating along the hard axis of an easy-plane AFM by effective magnetoelastic (ME) interaction [2] and can be briefly summed up as follows. When transverse-polarized coherent sound propagates along the hard axis, only one of the two normal modes of transverse vibrations interacts effectively with the magnetic subsystem [1–3]. Because the elastic moduli are renormalized by the ME coupling, the velocity of the interacting (magnetic) mode differs from that of the noninteracting (nonmagnetic) mode and depends on an external magnetic field. This brings about a phase shift between the modes and, as a result, elliptical polarization of the wave transmitted through the AFM. The amplitude of the sound at the exit from the sample turns out to be an oscillating function of the magnetic field [1, 4].

2. We report on the first observation and results of an experimental study on the magnetic birefringence of linearly polarized transverse sound propagating along the $\mathbf{C}_3$ axis in the α-Fe_2O_3 easy-plane AFM, which, as follows from theoretical estimates [4], has the most convenient parameters for the investigation of new phenomena in an antiferromagnetoacoustic material. We measured the amplitude of the ultrasound transmitted through a hematite sample as a function of the magnitude and direction of the magnetic field $\mathbf{H}$ applied in the basal easy magnetization plane perpendicular to the axis $\mathbf{C}_3 \parallel \mathbf{Z}$. The samples were rectangular parallelepipeds with plane-parallel (to within 10″), optically polished end faces perpendicular to the $\mathbf{C}_3$ axis. Piezoelectric transducers (*X*-cut lithium) were bonded to the end faces, with one of the transducers being an emitter and the other, a detector of ultrasound. The piezoelectric transducers were arranged so that the polarizations of the excited and received waves were either parallel or perpendicular to each other. The thicknesses of the piezoelectric transducers and the frequencies at which the measurements were carried out were selected so as to achieve the maximum possible conversion efficiency for only one shear eigenmode of the piezoelectric transducer. The experiments were performed using the pulse echo method [5]. The response of the system was derived from the first acoustic pulse passed through the sample. In contrast to the stationary sound excitation technique employed in [6, 7] in observations of the linear sound birefringence in $MnCO_3$ and $FeBO_3$, respectively, this method allows one to exclude the effect of reflected waves present in the sample under stationary excitation.

The measured amplitudes of components of the outgoing wave (A_l for the parallel and A_t for the perpendicular orientation of the emitter and detector polarizations) are presented in Figs. 1a and 2a as a function of magnetic field (excited sound frequency f = 90.85 MHz). Figures 1b and 2b show the corresponding theoretical curves plotted using the equations [4]

$$A_l = \{\cos^2 2\varphi_0 + \sin^2 \varphi_0 \cos^2(\Delta k d/2)\}^{1/2}, \qquad (1)$$

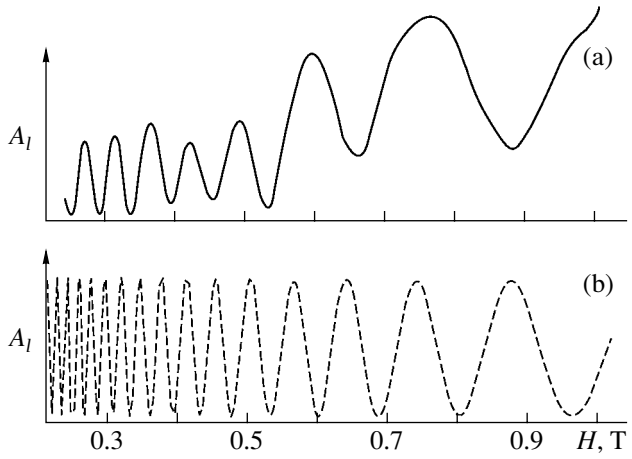

Fig. 1. Amplitude oscillations of the sound transmitted through a sample plotted vs. magnetic field for parallel polarization orientation ($\varphi_0 = 45°$, $\varphi_H \approx 140°$);(a) experiment and (b) theory.

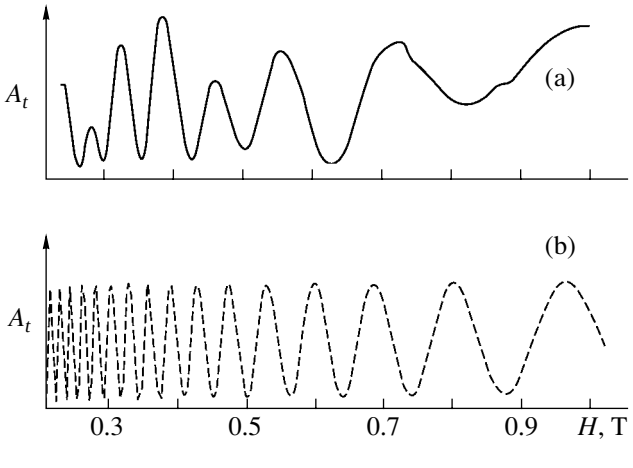

Fig. 2. Amplitude oscillations of the sound transmitted through a sample plotted vs. magnetic field for perpendicular polarization orientation ($\varphi_0 = 45°$, $\varphi_H \approx 140°$); (a) experiment and (b) theory.

$$A_t = \{\sin^2 2\varphi_0 \sin^2(\Delta k d/2)\}^{1/2}, \qquad A_l^2 + A_t^2 = 1, \tag{2}$$

$$\Delta k = \omega(1/V_\xi - 1/V_\eta), \quad V_\eta^2 = C_{44}/\rho, \tag{3}$$

$$V_\eta^2 = V_\xi^2\left(1 - \frac{2H_E(2B_{14})^2}{C_{44}M_0\omega_{f0}^2}\right), \tag{4}$$

$$\omega_{f0}^2 = H(H + H_D) + 2H_E H_{\text{ms}},$$

where φ_0 is the angle between the directions of the polarization of the excited wave and of the polarization ξ of the magnetic normal mode, ω is the circular frequency of sound, d is the sample length in the direction of the propagation of sound, V_ξ and V_η are the phase velocities of the magnetic (ξ) and nonmagnetic (η) normal vibration modes, and ω_0 is the frequency of the quasi-ferromagnetic antiferromagnetic resonance mode. Equations (1)–(4) for the trigonal AFMs in an easy-plane weakly ferromagnetic state were derived under the assumption that the magnitude of the magnetic field H is such that the conditions $\mathbf{M} \parallel \mathbf{H} \perp \mathbf{L}$ are met, where $\mathbf{L} = \mathbf{M}_1 - \mathbf{M}_2$ is the antiferromagnetism vector and $\mathbf{M} = \mathbf{M}_1 + \mathbf{M}_2$ is the ferromagnetic moment, with $M \ll L$ (M_1, M_2 are the sublattice magnetizations) [4]. It is also assumed that the effective ME coupling derives from vibrations of the antiferromagnetism vector in the basal easy magnetization plane [2]. In the case where $\mathbf{M} \parallel \mathbf{H} \perp \mathbf{L}$, the normal-mode polarization directions are found from the relations [4]

$$\boldsymbol{\xi} = \mathbf{X}\cos 3\varphi_H - \mathbf{Y}\sin 3\varphi_H,$$

$$\boldsymbol{\eta} = \mathbf{Y}\cos 3\varphi_H + \mathbf{X}\sin 2\varphi_H,$$

where $\mathbf{X}$ and $\mathbf{Y}$ are the coordinate axes ($\mathbf{X} \parallel \mathbf{M}$, $\mathbf{Y} \parallel \mathbf{L}$) and φ_H is the angle between the magnetic field $\mathbf{H}$ and the twofold symmetry axis C_2 in the basal plane. The theoretical plots were drawn using the following values of the parameters available from the literature [2–4]: the exchange field $H_E = 9.2 \times 10^6$ Oe, the Dzyaloshinski field $H_D = 2.2 \times 10^4$ Oe, the spontaneous-magnetostriction field $H_{\text{ms}} = 0.96$ Oe, the ME coupling constant $2B_{14} = 29.2 \times 10^6$ erg/cm^3, the elastic modulus $C_{44} = 9.42 \times 10^{11}$ erg/cm^3, the crystal density $\rho = 5.29$ g/cm^3, and the equilibrium sublattice magnetization $M_0 = 870$ G; the sample length d was equal to 0.6 cm.

3. As follows from Figs. 1 and 2, the experimental data support the main conclusions in the theory of magnetoacoustic linear birefringence [4] concerning the conversion of linear sound polarization to elliptical sound polarization, the dependence of the intensity oscillations of the transmitted sound wave on the external magnetic field, and the growth of the oscillation period with increasing field. The agreement obtained is, however, only qualitative, whereas the quantitative differences between the theory and experiment are substantial. A similar pattern is observed in $MnCO_3$ [6] and $FeBO_3$ [7]. First of all, we note a fairly large difference in the oscillation period ΔH and in the dependence of the oscillation amplitude on the magnitude of the magnetic field H. Furthermore, the hematite sample under study revealed a periodic (hexagonal) dependence of the position of the oscillation extrema on the direction of magnetic field $\mathbf{H}$ in the basal plane, i.e., on the angle φ_H. According to theory [4], the shift in the oscillation phase observed in a transition from mutually parallel to mutually perpendicular polarizations of the emitting and receiving piezoelectric transducers should be one-half the oscillation period. In the experiment, however,

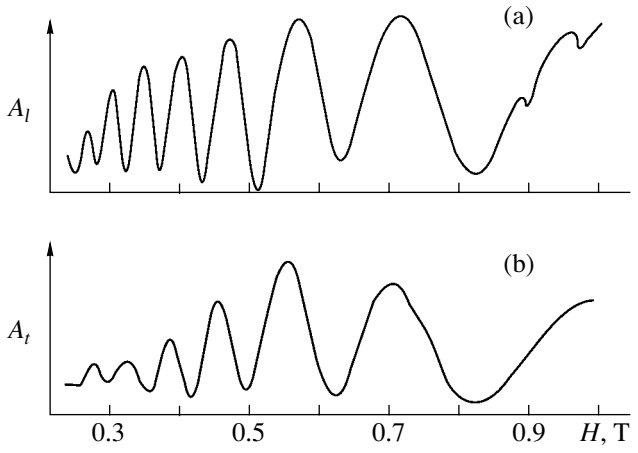

Fig. 3. Oscillations of the amplitude of the sound transmitted through a sample plotted vs. magnetic field for $\varphi_H \approx 105°$ (*l* relates to mutually parallel polarizations, and *t*, to mutually perpendicular polarizations).

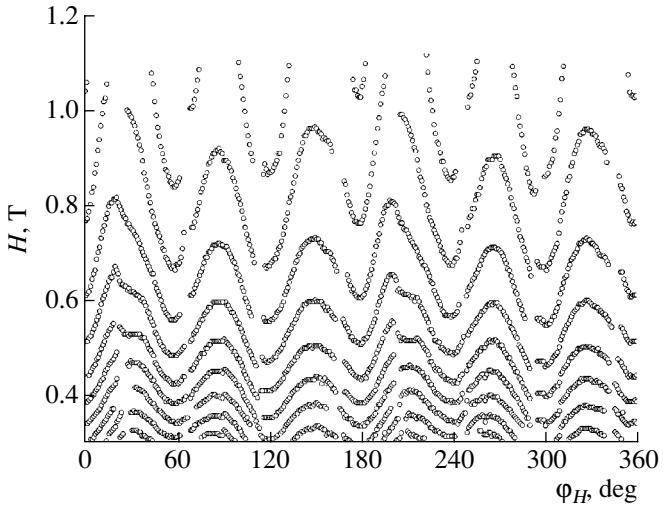

Fig. 4. Dependence of the magnetic field strength H at which the oscillation amplitude is maximal on angle φ_H.

this shift exhibited a strong dependence on both the direction and magnitude of the magnetic field. A phase shift by one half-period was observed only at certain angles φ_H and not very large values of H (Figs. 1–3).

It would not be very reasonable to expect quantitative agreement with the theory based on an isotropic model, and further development of the theory based on existing models is obviously needed. Above all, one apparently needs to take into account spontaneous strains, which are distributed nonuniformly over the sample and give rise to the formation of an additional, spatially nonuniform basal-plane magnetic anisotropy accounting for the scatter in the directions of normal vibrations $\boldsymbol{\xi}$ and $\boldsymbol{\eta}$ over the crystal [4, 8]. Nonuniform strains can originate from various causes, such as the mosaic structure of the real crystal lattice [1], mechanical boundary conditions for the excitation and reception of sound [7, 8], crystal growth conditions, etc. The goal of our further studies is to develop a theoretical model describing the experimental data on the birefringence of sound in α-Fe_2O_3. In this paper, we wish to discuss the dependence of the position of the oscillation amplitude extrema of the transmitted sound on the magnetic field orientation. Figure 4 presents experimental dependences of the magnetic field values at which maxima are observed on the field direction in the basal plane, i.e., on φ_H (the polarizations of the emitter and receiver are mutually perpendicular). As is evident from Fig. 4, the curves of magnetoacoustic vibrations oscillate with respect to a certain position exhibiting a 60° hexagonal pattern. In our opinion, this dependence can be due to a sixth-order anisotropy in the basal plane. The inclusion of basal-plane anisotropy of higher than second order brings about the appearance of the following anisotropic gap in the spectrum of low-frequency spin oscillations [9]:

$$\Delta H_\Delta^2 \cos 6\varphi_H, \quad H_\Delta = \sqrt{36 H_E H_a}, \tag{5}$$

where H_a is the effective basal-plane anisotropy field. In this case, the antiferromagnetic resonance frequency ω_{f0}, which enters Eq. (4) for the velocity of the magnetic mode of normal vibrations (ξ), is given by

$$\varphi_{f0} = \gamma^{-2}\{H(H + H_D) + 2H_E H_{\rm ms} + H_\Delta^2 \cos 6\varphi_H\}. \tag{6}$$

Thus, the phase difference $\Delta kd/2$ becomes dependent on the angle φ_H. From the experimental data presented in Fig. 3, we find H_Δ to be about $(4–6) \times 10^3$ Oe. These values of H_Δ are greater by a factor of 4 to 5 than the values available in the literature obtained for hematite using other methods (antiferromagnetic resonance [10], torque method [11]). However, it should be pointed out that the values $H_\Delta \approx 10^3–1.5 \times 10^3$ Oe were obtained in [10, 11] on annealed samples, whereas our experiments were carried out on unannealed α-Fe_2O_3. It is well known that such samples have residual strains that are relieved under annealing. It may be conjectured that it is these strains that account for the fairly high magnetic anisotropy fields in the samples we studied.

ACKNOWLEDGMENTS

The authors are indebted to V.A. Golenishchev-Kutuzov for helpful discussions and interest in this work.

REFERENCES

1. E. A. Turov, I. F. Mirsaev, and V. V. Nikolaev, Usp. Fiz. Nauk **172** (2), 193 (2002) [Phys. Usp. **45**, 185 (2002)].

2. V. I. Ozhogin and V. L. Preobrazhenskiĭ, Usp. Fiz. Nauk **155** (4), 593 (1988) [Sov. Phys. Usp. **31**, 713 (1988)].
3. M. H. Seavey, Solid State Commun. **10** (2), 219 (1972).
4. E. A. Turov, Zh. Éksp. Teor. Fiz. **96** (6), 2140 (1989) [Sov. Phys. JETP **69**, 1211 (1989)].
5. J. W. Tucker and V. W. Rampton, *Microwave Ultrasonics in Solid State Physics* (North-Holland, Amsterdam, 1972; Mir, Moscow, 1975).
6. V. R. Gakel', Pis'ma Zh. Éksp. Teor. Fiz. **9** (5), 590 (1969) [JETP Lett. **9**, 360 (1969)].
7. A. P. Korolyuk, V. V. Tarakanov, and V. I. Khizhnyĭ, Fiz. Nizk. Temp. **22** (8), 924 (1996) [Low Temp. Phys. **22**, 708 (1996)].
8. Yu. N. Mitsaĭ, K. M. Skibinskiĭ, M. B. Strugatskiĭ, and V. V. Tarakanov, Fiz. Tverd. Tela (St. Petersburg) **39** (5), 901 (1997) [Phys. Solid State **39**, 803 (1997)].
9. E. A. Turov, A. V. Kolchanov, V. V. Men'shenin, I. F. Mirsaev, and V. V. Nikolaev, *Symmetry and Physical Properties of Antiferromagnets* (Fizmatlit, Moscow, 2001).
10. H. Kumaga, H. Abe, K. Ono, *et al.*, Phys. Rev. **99** (3), 1116 (1955).
11. A. A. Bogdanov, Fiz. Tverd. Tela (Leningrad) **14** (11), 3362 (1972) [Sov. Phys. Solid State **14**, 2845 (1972)].

Translated by G. Skrebtsov

Physics of the Solid State, Vol. 46, No. 2, 2004, pp. 316–325. Translated from Fizika Tverdogo Tela, Vol. 46, No. 2, 2004, pp. 308–316.
Original Russian Text Copyright © 2004 by Busiello, Saburova, Sushkova, Chugunova.

MAGNETISM AND FERROELECTRICITY

Nonequilibrium Dynamics of Quantum Spin Glass in an AC Magnetic Field

G. Busiello*, R. V. Saburova, V. G. Sushkova**, and G. P. Chugunova*****

**Dipartimento di Fisica "E.R. Caianiello," Universitá di Salerno, 84081 Baronissi–Salerno and INFM–Unitá di Salerno, Salerno, Itali*

***Kazan State Power University, Kazan, 620066 Tatarstan, Russia*

****Kazan State University of Technology, Kazan, 420015 Tatarstan, Russia*

Received June 23, 2003

Abstract—The ageing effect is studied analytically in a disordered quantum system interacting with its surroundings and subjected to an external ac magnetic field. Energy dissipation is due to the interaction of the system with a set of independent harmonic oscillators, imitating a quantum thermal bath. Dynamic equations for the autocorrelation function and linear-response function are derived using the method of closed-path integrals. The effect of an external field is studied on the correlation function and response in the spin-glass and paramagnetic phases. Both functions are found to depend on the spin interaction strength. © *2004 MAIK "Nauka/Interperiodica".*

1. INTRODUCTION

The dissipation effects in the nonequilibrium dynamics of quantum glasses has recently begun to be studied [1]. Presently, the role played by quantum fluctuations in quantum spin glasses is being studied intensively [1–6]. Time-dependent external influences on the nonequilibrium dynamics of quantum spin glasses have not yet been considered theoretically. In [7], the effect of a time-varying external field was considered within a classical model of spin glasses and it was shown that the ageing effect (the dependence of the relaxation rate on the waiting time or age of the system) takes place under a weak disturbing external field.

We study the nonequilibrium dynamics of a quantum spin glass interacting with its surroundings (thermal bath) and a time-varying external field. Closed dynamic equations (analogous to those derived in [8]) for the symmetrized autocorrelation function and for the linear-response function are considered, and their solutions are found numerically as a function of the strengths of the interaction between spins and of the interaction between the spin system and the thermal bath for various values of the amplitude and frequency of the external field. The *p*-spin spherical model in the mean-field approximation is considered.

Experimentally, the magnetic susceptibility of a spin glass measured in an external ac magnetic field exhibits the ageing effect; namely, the magnetic response of the system to a weak external field depends on the thermal history of the sample, i.e., on the time period over which the system was in the spin-glass phase at a constant temperature. Let us consider the following experiment. A sample is cooled rapidly in the absence of an external dc magnetic field from a temperature $T > T_g$ (T_g is the spin-glass phase transition temperature) to a temperature $T_1 < T_g$ at time $t = 0$. At this moment, a weak external ac magnetic field $h(t)$ is applied to the sample. Thereafter, the temperature of the system is kept constant and the magnetic susceptibility is measured at a fixed angular frequency ω as a function of the elapsed time t from the instant ($t = 0$) at which the temperature of the sample became equal to T_1 [1, 9].

Note that the correlation function $C(t, t')$ of the system characterizes the time after which a loss of history memory occurs in the system; therefore, this function vanishes at long times. The response of the system to an external influence is described by the response function, which is related to the susceptibility of the system. The response function, as well as the correlation function, decreases with time, because the system is in contact with the thermal bath and, therefore, the perturbation gradually fades away. However, there is a significant difference between the correlation and response. A correlation between two observable quantities can exist at any time, whereas a response is absent before the beginning of an external influence. Nevertheless, the correlation and response can be treated on equal terms.

We may expect that the model of a quantum spin glass interacting with its surroundings and subjected to an external ac magnetic field will exhibit nonlinear dynamics and, in particular, the ageing effect.

In this paper, we describe this model of a spin glass and derive coupled equations of motion for the correlation function and response of the system. The equations are solved numerically, and their solution is analyzed.

1063-7834/04/4602-0316$26.00 © 2004 MAIK "Nauka/Interperiodica"

2. MODEL

We consider a quantum system consisting of N spins interacting with each other. The system is in contact with a thermal bath consisting of independent quantum harmonic oscillators and is subjected to an external ac magnetic field. The Hamiltonian of the total system is

$$\mathcal{H} = \mathcal{H}_S + \mathcal{H}_B + \mathcal{H}_{SB} + \mathcal{H}_{SF}, \quad (1)$$

where $\mathcal{H}_S$ is the Hamiltonian of the system under study, $\mathcal{H}_B$ is the Hamiltonian of the thermal bath, $\mathcal{H}_{SB}$ is the interaction Hamiltonian of the system and the bath, and $\mathcal{H}_{SF}$ is the interaction Hamiltonian of the system and the external ac field. We have

$$\mathcal{H}_S = \frac{m}{2}\sum_{i=1}^{N}\dot{\sigma}_i^2 + V, \quad (2)$$

$$\mathcal{H}_B = \frac{1}{2}\sum_{l=1}^{N_b}\left(\frac{p_l^2}{m_l} + m_l\omega_l x_l^2\right), \quad (3)$$

$$\mathcal{H}_{SB} = -\sum_{i,l} C_l^i x_l \sigma_i, \quad (4)$$

$$\mathcal{H}_{SF} = -h(t)\sum_{i=1}^{N}\sigma_i, \quad h(t) = h_t\cos\omega_0 t, \quad (5)$$

where m is the mass of the object with spin σ_i (dots indicate differentiation with respect to time); V is the spin interaction potential; N_b is the number of oscillators; x_l and p_l are the coordinate and momentum of the lth oscillator; and m_l and ω_l are the mass and angular frequency of this oscillator, respectively. The thermal bath is phonons in the crystal lattice. C_l^i is the coupling constant between the ith spin and the lth oscillator. The external ac magnetic field $h(t)$ is characterized by its amplitude h_t (in energy units) and angular frequency ω_0. We neglect the interaction between the bath and the external ac field, assuming the latter to be sufficiently weak. Let us consider diagonal p-spin interaction of the form

$$V = \sum_{i_1<\ldots<i_p}^{N} J_{i_1\ldots i_p}\sigma_{i_1}^z\ldots\sigma_{i_p}^z, \quad (6)$$

where $p \geq 2$. The quantities $J_{i_1\ldots i_p}$ are random variables characterizing the interaction between spins and are described by a Gaussian distribution with zero average and variance $\overline{(J_{i_1\ldots i_p})^2} = \tilde{J}^2 p!/2N^{p-1}$, where the over bar denotes averaging over the disorder variables. In the classical case, this model was well studied in [10–12].

We will restrict our consideration to the case of $p = 3$. The model described by Eqs. (2)–(6) exhibits a dynamic phase transition between two phases, namely, an ordered phase (spin-glass) and a disordered (paramagnetic) phase.

3. CLOSED-PATH INTEGRAL FORMALISM

We use quantum field theory [13] in what follows. Let $\boldsymbol{\xi}^+(t)$ and $\boldsymbol{\xi}^-(t)$ be external N-vector sources, where the plus and minus signs indicate the values related to the positive and negative branches of the time contour, going from 0 to $+\infty$ and in the opposite direction from $+\infty$ to 0, respectively, and the degrees of freedom are described by the field $\boldsymbol{\phi} = (\phi_1(t), \ldots, \phi_N(t))$ in the Heisenberg picture [14, 15]. The generating functional has the form [16]

$$Z[\boldsymbol{\xi}^+, \boldsymbol{\xi}^-] = \mathrm{Tr}\left[T^*\exp\left(-\frac{i}{\hbar}\int_0^\infty dt\,\boldsymbol{\xi}^-(t)\boldsymbol{\phi}(t)\right) \times T\exp\left(-\frac{i}{\hbar}\int_0^\infty dt\,\boldsymbol{\xi}^+(t)\boldsymbol{\phi}(t)\right)\hat{\rho}(0)\right], \quad (7)$$

where T is the time-ordering operator, T^* is the reversed time-ordering operator, and $\hat{\rho}(t_0)$ is the density matrix at the initial instant t_0 (we put $t_0 = 0$). The ensemble average of any operator is conventionally defined as

$$\langle A(t)\rangle = \frac{\mathrm{Tr}[A(t)\hat{\rho}(0)]}{\mathrm{Tr}\,\hat{\rho}(0)}. \quad (8)$$

The symmetrized correlation function $C_{ij}(t, t')$ can be expressed in terms of the generating functional as

$$C_{ij}(t, t') \equiv \frac{1}{2}\langle\phi_i(t)\phi_j(t') + \phi_j(t')\phi_i(t)\rangle = \frac{\hbar^2}{2}\left[\frac{\delta^2}{\delta\xi_i^+(t)\delta\xi_j^-(t')} + \frac{\delta^2}{\delta\xi_j^+(t)\delta\xi_i^-(t')}\right]\ln Z|_{\xi=0}, \quad (9)$$

where the response $R_{ij}(t, t')$ to the external ac field h_t is

$$R_{ij}(t, t') \equiv \left.\frac{\delta\langle\phi_i(t)\rangle}{\delta h_j(t')}\right|_{h=0}. \quad (10)$$

In terms of the linear-response theory, we can write

$$R_{ij}(t, t') = \frac{i}{\hbar}\theta(t-t')\langle[\phi_i(t), \phi_j(t')]\rangle = \frac{\hbar}{i}\left[\frac{\delta^2}{\delta\xi_i^+(t)\delta\xi_j^+(t')} + \frac{\delta^2}{\delta\xi_j^+(t)\delta\xi_i^-(t')}\right]\ln Z|_{\xi=0}. \quad (11)$$

Using the generating functional (7) and performing transformations as in the dynamics of a classical system [17], we can write

$$Z[\boldsymbol{\xi}^+, \boldsymbol{\xi}^-] = \int \mathcal{D}\boldsymbol{\phi}^+ \mathcal{D}\boldsymbol{\phi}^- \exp\left[\frac{i}{\hbar}(S[\boldsymbol{\phi}^+] - S[\boldsymbol{\phi}^-] + \int dt \boldsymbol{\xi}^+(t)\boldsymbol{\phi}^+(t) - \int dt \boldsymbol{\xi}^-(t)\boldsymbol{\phi}^-(t)\right)\Big] \langle \boldsymbol{\phi}^+|\hat{\rho}(0)|\boldsymbol{\phi}^-\rangle, \quad (12)$$

where $\mathcal{D}\boldsymbol{\phi}^+\mathcal{D}\boldsymbol{\phi}^-$ stands for $\int_{-\infty}^{+\infty}\Pi_{i,t}[d\phi_i^+(t)d\phi_i^-(t)]$; $\mathcal{D}\boldsymbol{\phi}^+$ and $\mathcal{D}\boldsymbol{\phi}^-$ are the functional measures corresponding to integration along all paths. In Eq. (12), we dropped the limits of time integrals (integration is performed from $t_0 = 0$ to ∞); $S[\boldsymbol{\phi}]$ is the action of the system and $\langle \boldsymbol{\phi}^+|\hat{\rho}(0)|\boldsymbol{\phi}^-\rangle$ is the density matrix element. In terms of the fields $\boldsymbol{\phi}^+$ and $\boldsymbol{\phi}^-$, the correlation function and the response function can be written as

$$C_{ij}(t, t') = \frac{1}{2}\langle \phi_i^+(t)\phi_j^-(t') + \phi_j^+(t')\phi_i^-(t)\rangle, \quad (13)$$

$$R_{ij}(t, t') = \frac{i}{\hbar}\langle \phi_i^+(t)[\phi_j^+(t') - \phi_j^-(t')]\rangle. \quad (14)$$

Within the path-integral formalism [18], the interaction between the system and the thermal bath is described in terms of the variables $\boldsymbol{\phi} = (\boldsymbol{\sigma}, \mathbf{v}_l)$, where $\boldsymbol{\sigma} = (\sigma_1, \ldots, \sigma_N)$ are variables of the system and $\mathbf{v}_l = (v_{1l}, \ldots, v_{N_b l})$ are variables of the bath ($l = 1, \ldots N_b$). The total action S is the sum of the actions corresponding to the spin system, thermal bath, system–bath interaction, and system–ac field interaction:

$$S[\boldsymbol{\phi}] = S_S[\boldsymbol{\sigma}] + S_B[\mathbf{v}_l] + S_{SB}[\boldsymbol{\sigma}, \mathbf{v}_l] + S_{SF}[\boldsymbol{\sigma}] = S_S[\boldsymbol{\sigma}] + \frac{1}{2}\sum_{l=1}^{N_b} m_l(\dot{\mathbf{v}}_l^2 - \omega_l^2\mathbf{v}_l^2) - \sum_{l=1}^{N_b} C_l\mathbf{v}_l\boldsymbol{\sigma} - h(t)\sum_{i=1}^{N}\sigma_i. \quad (15)$$

The action of the system $S_S[\boldsymbol{\sigma}, J]$ is

$$S_S[\boldsymbol{\sigma}, J] = S_0[\boldsymbol{\sigma}] - \int dt V[\boldsymbol{\sigma}, J]. \quad (16)$$

The disorder-independent part of the action has the form

$$S_0[\boldsymbol{\sigma}, J] = \int dt\left[\frac{m}{2}\dot{\boldsymbol{\sigma}}^2 - \frac{z}{2}(\boldsymbol{\sigma}^2 - N)\right], \quad (17)$$

where z is a time-dependent Lagrange multiplier introduced to impose the spherical-model constraint $\sum_{i=1}^{N}\sigma_i^2(t) = N$ for all time.

In our model for the Gaussian random potential $V[\boldsymbol{\sigma}, J]$, we have

$$\overline{V[\boldsymbol{\sigma}, J]V[\boldsymbol{\sigma}', J']} = -\frac{N}{2}\mathcal{V}\left(\frac{(\boldsymbol{\sigma} - \boldsymbol{\sigma}')^2}{N}\right), \quad (18)$$

$$P[J] = \left(\sqrt{\frac{N^{p-1}}{\tilde{J}^2\pi p!}}\exp\left(-\frac{N^{p-1}}{\tilde{J}^2 p!}\sum_{i_1 \neq \ldots \neq i_p}(J_{i_1\ldots i_p})^2\right) \to \overline{(J_{i_1\ldots i_p})^2}\right) = \frac{\tilde{J}^2 p!}{2N^{p-1}}. \quad (19)$$

These expressions correspond to the random potential-energy correlation $\mathcal{V}(x) = -(1 - x/2)^p/2$ and to the following effective (nonlocal in time) interaction between spins [19]:

$$V_D[\boldsymbol{\sigma}^+, \boldsymbol{\sigma}^-] = \frac{\tilde{J}^2 N i}{4\hbar}\int dt \int dt'\Big[\left(\frac{1}{N}\boldsymbol{\sigma}^+(t)\boldsymbol{\sigma}^+(t')\right)^p + \left(\frac{1}{N}\boldsymbol{\sigma}^-(t)\boldsymbol{\sigma}^-(t')\right)^p - \left(\frac{1}{N}\boldsymbol{\sigma}^+(t)\boldsymbol{\sigma}^-(t')\right)^p - \left(\frac{1}{N}\boldsymbol{\sigma}^-(t)\boldsymbol{\sigma}^+(t')\right)^p\Big]. \quad (20)$$

Here, σ_i are continuous dynamic variables ($-\sqrt{N} < \sigma_i < \sqrt{N}$ for all values of i) satisfying the spherical-model condition

$$\frac{1}{N}\boldsymbol{\sigma}^2(t) = \frac{1}{N}\sum_{i=1}^{N}\sigma_i^2(t) = 1 \quad (21)$$

at any instant of time. This restriction is satisfied by introducing the time-dependent Lagrange multiplier $z(t)$.

We could also consider other types of system–thermal bath interaction differing from the simplest case described by Eq. (15). Assuming that at the initial instant the density matrix is $\hat{\rho}(0) = \hat{\rho}_S(0)\hat{\rho}_B(0)$, where $\hat{\rho}_B(0)$ corresponds to a Boltzmann distribution for the bath variables at temperature $k_B T = 1/\beta$ we can integrate over the bath variables and obtain the effective thermal action $S_T[\boldsymbol{\sigma}^+, \boldsymbol{\sigma}^-]$ entering the Feynman–Vernon influence functional

$$S_T[\boldsymbol{\sigma}^+, \boldsymbol{\sigma}^-] = -\int dt \int dt'(\boldsymbol{\sigma}^+(t) - \boldsymbol{\sigma}^-(t)) \times \eta(t - t')(\boldsymbol{\sigma}^+(t) + \boldsymbol{\sigma}^-(t)) + i\int dt \int dt'(\boldsymbol{\sigma}^+(t) \times -\boldsymbol{\sigma}^-(t))\nu(t - t')(\boldsymbol{\sigma}^+(t) - \boldsymbol{\sigma}^-(t)), \quad (22)$$

where the noise and dissipation kernels ν and η are

$$\nu(t - t') = \int_0^\infty d\omega I(\omega)\coth\left(\frac{1}{2}\beta\hbar\omega\right)\cos(\omega(t - t')), \quad (23)$$

$$\eta(t-t') = -\theta(t-t')\int_0^\infty d\omega I(\omega)\sin(\omega(t-t')). \quad (24)$$

The spectral density of the bath $I(\omega)$ is given by

$$I(\omega) = 2\alpha\hbar(\omega/\omega_c)^{s-1}\omega\exp(-\omega/\omega_c), \quad (25)$$

where α is the dimensionless coupling constant between the system and bath, ω_c is a high-frequency cutoff, and $0 < s < 2$. For an Ohmic bath, $s = 1$. In this case, for small values of α (e.g., $\alpha = 0.2$) we have the paramagnetic phase and for $\alpha = 1$, the spin-glass phase [19]. In treating a disordered system, the quantities should be averaged over the disorder variables with distribution $P[J]$.

Now, we consider the dynamics of the system in real time with a random initial condition at $t_0 = 0$ when the system is brought into contact with a thermal bath and an external ac field is applied. This condition does not depend on disorder; therefore, $\hat{\rho}$ is also independent of disorder and, in the absence of external sources and field $h(t)$, the generating functional is also independent of disorder, $Z[\boldsymbol{\xi}^+ = 0, \boldsymbol{\xi}^- = 0, J] = \mathrm{Tr}[\hat{\rho}(0)]$. As in the classical case, we can use dynamic equations with random initial conditions without calculating the average of $\ln Z[\boldsymbol{\xi}^+, \boldsymbol{\xi}^-, J]$ over the disorder variables and without using the replica technique. In terms of the averaged generating functional

$$\overline{Z[\boldsymbol{\xi}^+, \boldsymbol{\xi}^-]} = \int dJP[J]Z[\boldsymbol{\xi}^+, \boldsymbol{\xi}^-, J] \quad (26)$$

the average of any operator $\boldsymbol{\sigma}(t)$ is found to be

$$\begin{aligned}\overline{\langle\boldsymbol{\sigma}(t)\rangle} &\equiv \left.\overline{\frac{\delta \ln Z[\boldsymbol{\xi}^+, \boldsymbol{\xi}^-, J]}{\delta\boldsymbol{\xi}^+(t)}}\right|_{\boldsymbol{\xi}=0, h=0} \\ &= \frac{1}{Z[0,0,J]}\left.\overline{\frac{\delta Z[\boldsymbol{\xi}^+, \boldsymbol{\xi}^-, J]}{\delta\boldsymbol{\xi}^+(t)}}\right|_{\boldsymbol{\xi}=0, h=0} \\ &= \frac{1}{\overline{Z[0,0,J]}},\end{aligned} \quad (27)$$

where the over bar denotes averaging over the disorder variables.

Thus, the system under study is described by the generating functional

$$\begin{aligned}\overline{Z[\boldsymbol{\xi}^+, \boldsymbol{\xi}^-, J]} = \int \mathcal{D}\boldsymbol{\sigma}^+\mathcal{D}\boldsymbol{\sigma}^- \exp\Big[\frac{i}{\hbar}(S_{\mathrm{EFF}}[\boldsymbol{\sigma}^+, \boldsymbol{\sigma}^-] \\ + \int dt\boldsymbol{\xi}^+(t)\boldsymbol{\sigma}^+(t) - \int dt\boldsymbol{\xi}^-(t)\boldsymbol{\sigma}^-(t) \\ + \int dth^+(t)\boldsymbol{\sigma}^+(t) - \int dth^-(t)\boldsymbol{\sigma}^-(t)\Big)\Big],\end{aligned} \quad (28)$$

where $S_{\mathrm{EFF}}[\boldsymbol{\sigma}^+, \boldsymbol{\sigma}^-] = S_0[\boldsymbol{\sigma}^+] - S_0[\boldsymbol{\sigma}^-] + S_T[\boldsymbol{\sigma}^+, \boldsymbol{\sigma}^-]$. The quantum equations of motion can be derived in the same way as in the classical case [17, 20].

Further, we introduce macroscopic order parameters and find equations of motion in the saddle-point approximation to the Schwinger–Keldysh functional (this approximation becomes exact in the mean-field approximation as $N \longrightarrow \infty$). Since we consider the dynamics of the system at long but finite times, nonequilibrium phenomena may be expected.

3.1. Dynamic Order Parameters

By introducing the operator $\mathrm{Op}(t, t')$ [19] as

$$\begin{aligned}\mathrm{Op}(t,t') &= \begin{pmatrix} \mathrm{Op}^{++}(t,t') & \mathrm{Op}^{+-}(t,t') \\ \mathrm{Op}^{-+}(t,t') & \mathrm{Op}^{--}(t,t') \end{pmatrix} \\ &= \{\mathrm{Op}^{\alpha\beta}(t,t')\},\end{aligned} \quad (29)$$

$$\begin{aligned}\mathrm{Op}^{++}(t,t') &= (m\partial_t^2 + z^+(t))\delta(t-t') - 2i\nu(t-t'), \\ \mathrm{Op}^{+-}(t,t') &= 2\eta(t-t') + 2i\nu(t-t'), \\ \mathrm{Op}^{-+}(t,t') &= -2\eta(t-t') + 2i\nu(t-t'), \\ \mathrm{Op}^{--}(t,t') &= (m\partial_t^2 + z^-(t))\delta(t-t') - 2i\nu(t-t'),\end{aligned} \quad (30)$$

we combine the quadratic terms in the action S_{EFF} into one term. In this case, we have

$$\begin{aligned}S_{\mathrm{EFF}}[\boldsymbol{\sigma}^+, \boldsymbol{\sigma}^-] = -\frac{1}{2}\int dt\int dt'\boldsymbol{\sigma}^\alpha(t)\mathrm{Op}^{\alpha\beta}(t,t')\boldsymbol{\sigma}^\beta(t') \\ - V_D[\boldsymbol{\sigma}^+, \boldsymbol{\sigma}^-],\end{aligned} \quad (31)$$

where α and β stand for + and – and a summation convention over repeated indices is adopted. By substituting the identity

$$\begin{aligned}1 &= \int\prod_{\alpha\beta} DQ^{\alpha\beta}\delta\Big(\frac{1}{N}\sigma^\alpha(t)\sigma^\beta(t') - Q^{\alpha\beta}\Big) \\ &\sim \int\prod_{\alpha\beta} DQ^{\alpha\beta}D\lambda^{\alpha\beta} \\ &\times \exp\Big(-\frac{i}{2\hbar}\lambda^{\alpha\beta}(\sigma^\alpha(t)\sigma^\beta(t') - NQ^{\alpha\beta}(t,t'))\Big),\end{aligned} \quad (32)$$

into the expression for the generating functional, we rewrite the total action in the form

$$\begin{aligned} S &= S_{\text{EFF}} + \int dt\xi^{+}(t)\sigma^{+}(t) - \int dt\xi^{-}(t)\sigma^{-}(t) \\ &+ \int dth^{+}(t)\sigma^{+}(t) - \int dth^{+}(t)\sigma^{+}(t) \\ &= S_{\text{EFF}} + \int dt(\xi^{+}(t) + h^{+}(t))\sigma^{+}(t) \\ &- \int dt(\xi^{-}(t) + h^{-}(t))\sigma^{-}(t), \end{aligned} \tag{33}$$

where

$$\begin{aligned} S_{\text{EFF}}[\sigma^{+}, \sigma^{-}] &= -\frac{1}{2}\int dt\int dt'\sigma^{\alpha}(t)(\text{Op}^{\alpha\beta}(t, t') \\ &+ \lambda^{\alpha\beta}(t, t'))\sigma^{\beta}(t') + \frac{N}{2}\int dt\int dt'\lambda^{\alpha\beta}(t, t')Q^{\alpha\beta}(t, t') \\ &+ \frac{N}{2}\int dt[z^{+}(t) - z^{-}(t)] + \frac{i\tilde{J}^{2}N}{4\hbar}\int dt\int dt'[(Q^{++}(t, t'))^{p} \\ &+ (Q^{--}(t, t'))^{p} - (Q^{+-}(t, t'))^{p} - (Q^{-+}(t, t'))^{p}]. \end{aligned} \tag{34}$$

The order parameters $Q^{\alpha\beta}(t, t')$ (with $\alpha, \beta = +, -$) can be expressed in terms of the critical correlation function and the response function, defined by Eqs. (13) and (14), as

$$\begin{aligned} NQ^{++}(t, t') &= \overline{\langle\sigma^{+}(t)\sigma^{+}(t')\rangle} \\ &= N\left(C(t, t') - \frac{i\hbar}{2}(R(t, t') + R(t', t))\right), \end{aligned} \tag{35}$$

$$\begin{aligned} NQ^{+-}(t, t') &= \overline{\langle\sigma^{+}(t)\sigma^{-}(t')\rangle} \\ &= N\left(C(t, t') + \frac{i\hbar}{2}(R(t, t') - R(t', t))\right), \end{aligned} \tag{36}$$

$$\begin{aligned} NQ^{-+}(t, t') &= \overline{\langle\sigma^{-}(t)\sigma^{+}(t')\rangle} \\ &= N\left(C(t, t') - \frac{i\hbar}{2}(R(t, t') - R(t', t))\right), \end{aligned} \tag{37}$$

$$\begin{aligned} NQ^{--}(t, t') &= \overline{\langle\sigma^{-}(t)\sigma^{-}(t')\rangle} \\ &= N\left(C(t, t') + \frac{i\hbar}{2}(R(t, t') + R(t', t))\right), \end{aligned} \tag{38}$$

and we also have

$$NC(t, t') = \frac{1}{2}\sum_{i=1}^{N}\overline{\langle\sigma_i^{+}(t)\sigma_i^{-}(t') + \sigma_i^{-}(t)\sigma_i^{+}(t')\rangle}, \tag{39}$$

$$NR(t, t') = \frac{i}{\hbar}\sum_{i=1}^{N}\overline{\langle\sigma_i^{+}(t)(\sigma_i^{+}(t') + \sigma_i^{-}(t'))\rangle}. \tag{40}$$

Further, by performing calculations analogous to those in [19], it is shown that all terms in the action depend on $\lambda^{\alpha\beta}$, $Q^{\alpha\beta}$, and z^{α} and are proportional to N.

3.2. Saddle-Point Calculations

For the sake of convenience, we rewrite the equations in the matrix form. For this purpose, we introduce two matrices

$$\mathcal{L} = \begin{pmatrix} \lambda^{++} & \lambda^{+-} \\ \lambda^{-+} & \lambda^{--} \end{pmatrix}, \quad \mathcal{Q} = \begin{pmatrix} Q^{++} & Q^{+-} \\ Q^{-+} & Q^{--} \end{pmatrix} \tag{41}$$

and define the operator

$$F[\mathcal{Q}](t, t') \equiv \begin{pmatrix} (Q^{++}(t, t'))^{p-1} & (Q^{+-}(t, t'))^{p-1} \\ (Q^{-+}(t, t'))^{p-1} & (Q^{++}(t, t'))^{p-1} \end{pmatrix}. \tag{42}$$

We also introduce symbol $\otimes$ to denote the conventional operator product

$$\begin{aligned} &A \otimes B(t, t') \\ &= \begin{pmatrix} \int dt''A^{+\gamma}(t, t'')B^{\gamma+}(t'', t')\int dt''A^{+\gamma}(t, t'')B^{\gamma-}(t'', t') \\ \int dt''A^{-\gamma}(t, t'')B^{\gamma+}(t'', t')\int dt''A^{-\gamma}(t, t'')B^{\gamma-}(t'', t') \end{pmatrix}, \end{aligned} \tag{43}$$

where summation over γ is performed.

At the saddle point, the equation for $\lambda^{\alpha\beta}(t, t')$ gives

$$\mathcal{L}(t, t') = \frac{\hbar}{2}\mathcal{Q}^{-1}(t, t') - \text{Op}(t, t'), \tag{44}$$

where $\mathcal{Q}^{-1}$ is the operator inverse of $\mathcal{Q}$. The equation for $Q^{\alpha\beta}(t, t')$ at the saddle point gives

$$\mathcal{L}(t, t') = -\frac{ip\tilde{J}^{2}}{2\hbar}F[\mathcal{Q}](t, t'). \tag{45}$$

Equations (44) and (45) can be written in compact form as

$$\frac{i}{\hbar}\text{Op}\otimes\mathcal{Q} = I - \frac{p\tilde{J}^{2}}{2\hbar^{2}}F[\mathcal{Q}]\otimes\mathcal{Q}, \tag{46}$$

where I is the identity operator, $I^{\alpha\beta}(t, t') = \delta^{\alpha\beta}\delta(t - t')$.

The equation for z^{α} at the saddle point gives

$$\frac{i}{\hbar} = (\text{Op} + \mathcal{L})^{-1}_{++}(t, t') = \frac{i}{\hbar}\mathcal{Q}^{++}(t, t'), \tag{47}$$

$$\frac{i}{\hbar} = (\text{Op} + \mathcal{L})^{-1}_{--}(t, t') = \frac{i}{\hbar}\mathcal{Q}^{--}(t, t'); \tag{48}$$

these equations lead to the spherical-model restriction.

4. DYNAMIC EQUATIONS FOR THE CORRELATION FUNCTION AND RESPONSE

Dynamic equations for the correlation function and the response function can be derived from Eqs. (42)–

(46) and (35)–(38). By subtracting the (+–) component of Eq. (46) from the (++) component, we obtain the equation of motion for the response function:

$$(m\partial_t^2 + z^+(t))R(t,t') + 4\int_{t'}^{t} dt''\eta(t-t'')R(t'',t') = \delta(t-t') - \frac{p\tilde{J}^2}{2i\hbar}\int_0^\infty dt''((Q^{++}(t,t''))^{p-1} - (Q^{+-}(t,t''))^{p-1})R(t'',t'). \quad (49)$$

The equation of motion for the autocorrelation function is obtained by subtracting the (–+) from the (+–) component of Eq. (46):

$$\left(m\partial_t^2 + \frac{1}{2}(z^+(t)+z^-(t))\right)C(t,t') + \frac{i}{2}(z^+(t)-z^-(t))\hbar(R(t',t)-R(t,t')) - 2\hbar\int_0^\infty dt''\nu(t-t'')R(t',t'') + 4\int_0^t dt''\eta(t-t'')C(t'',t') = -\frac{p\tilde{J}^2}{2\hbar}\int_0^\infty dt''\mathrm{Im}((Q^{++}(t,t''))^{p-1}Q^{+-}(t'',t') - (Q^{+-}(t,t''))^{p-1}Q^{--}(t'',t')). \quad (50)$$

The dynamic equations can be rewritten in a more compact form as

$$(m\partial_t^2 + z(t))R(t,t') = \delta(t-t') + \int_0^\infty dt''\Sigma(t,t'')R(t'',t'), \quad (51)$$

$$(m\partial_t^2 + z(t))C(t,t') = \int_0^\infty dt''\Sigma(t,t'')C(t'',t') + \int_0^{t'} dt''D(t,t'')R(t',t''). \quad (52)$$

These equations should be supplemented by the following conditions at equal times:

$$C(t,t) = 1, \quad R(t,t) = 0, \quad (53)$$

$$\lim_{t'\to t^-}\partial_t R(t,t') = \frac{1}{m}, \quad \lim_{t'\to t^+}\partial_t R(t,t') = 0, \quad (54)$$

$$\lim_{t'\to t^-}\partial_t C(t,t'') = \lim_{t'\to t^+}\partial_t C(t,t') = 0. \quad (55)$$

The response function must satisfy the causality requirement $R(t,t'')R(t'',t) = 0$. As in [19], the self-energy has the form

$$\tilde{\Sigma}' \equiv \Sigma(t,t') + 4\eta(t-t') = -\frac{p\tilde{J}^2}{\hbar}\mathrm{Im}\left[C(t,t') - \frac{i\hbar}{2}R(t,t')\right]^{p-1}, \quad (56)$$

and the vertex function is

$$\tilde{D}' \equiv D(t,t') - 2\hbar\nu(t-t') = \frac{p\tilde{J}^2}{2}\mathrm{Re}\left[C(t,t') - \frac{i\hbar}{2}(R(t,t') + R(t',t))\right]^{p-1}. \quad (57)$$

Note that the self-energy Σ and the vertex function D are real and consist of terms of different origin; namely, there are terms due to the system–bath interaction (η, ν) and terms due to the nonlinearity that arises after averaging over the disorder variables [quantities $\tilde{\Sigma}'$ and $\tilde{D}'$ in Eqs. (56), (57)]. In the case of $p = 2$, the quantities $\tilde{\Sigma}'$ and $\tilde{D}'$ become equal to their classical counterparts. In the case of $p \geq 3$, the nonlinear terms depend explicitly on $\hbar$.

The imaginary part of Eq. (50) gives

$$z(t) \equiv z^+(t) = z^-(t). \quad (58)$$

Therefore, the equation for z takes the form

$$z(t) = \int_0^t dt''(\Sigma(t,t'')C(t,t'') + D(t,t'')R(t,t'')) + m\int_0^t dt''\int_0^t dt'''[\partial_t R(t,t'')]D(t'',t''')[\partial_t R(t,t''')]. \quad (59)$$

Thus, Eqs. (51), (52), and (59) comprise a complete set of equations describing the dynamics of the system.

In what follows, we use dimensionless variables, namely, energy measured in units of $\tilde{J}$ and time measured in units of $\hbar/\tilde{J}$. In this case, the quantum tunneling effect is characterized by the parameter $\Gamma \equiv \hbar^2/\tilde{J}M$. The real time and the other parameters involved in the dynamic equations for the correlation function and response are renormalized in this case: $t \longrightarrow (\tilde{J}/\hbar)t$, the symmetrized correlation function remains unchanged, and the response function transforms as $R \longrightarrow \hbar R$. After this renormalization, the dynamic

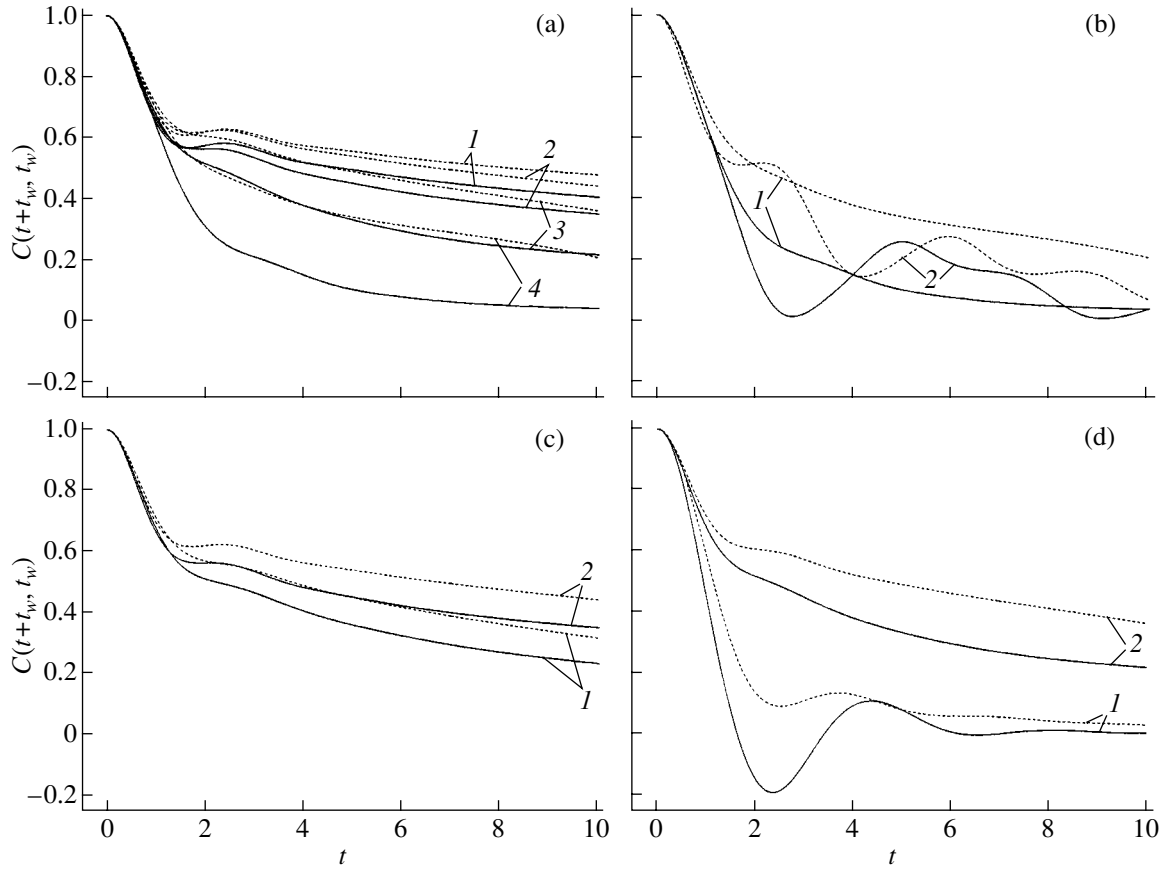

Fig. 1. Dependence of the symmetrized correlation function $C(t + t_w, t_w)$ on time t for waiting time t_w equal to 5 (solid lines) and 10 (dashed lines) and for (a) $\alpha = 1$, $\tilde{J} = 1$, $\Gamma = 1$, $T = 0.5$, $\omega_c = 0.1$, and different values of the ac field amplitude h_t: (*1*) 0, (*2*) 0.5, (*3*) 1, and (*4*) 2; (b) $\alpha = 1$, $\tilde{J} = 1$, $\Gamma = 1$, $T = 0.5$, $\omega_c = 5$, $h_t = 2$, and different values of the frequency ω_0: (*1*) 0.1 and (*2*) 1; (c) $\alpha = 1$, $\Gamma = 1$, $T = 0.5$, $\omega_c = 5$, $h_t = 0.1$, and different values of the spin interaction constant $\tilde{J}$: (*1*) 0.5 and (*2*) 1; and (d) $\tilde{J} = 1$, $\Gamma = 1$, $T = 0.5$, $\omega_c = 5$, $h_t = 1$, $\omega_0 = 0.1$, and different values of the coupling constant with the bath α: (*1*) 0.2 and (*2*) 1.

equations have the same form but with M replaced by Γ^{-1}. Thus, after renormalization, we have

$$(\Gamma^{-1}\partial_{\tilde{t}}^2 + \tilde{z}(\tilde{t}))\tilde{R}(\tilde{t}, \tilde{t}') = \delta(\tilde{t} - \tilde{t}') + \int_0^\infty d\tilde{t}''\tilde{\Sigma}(\tilde{t}, \tilde{t}'')\tilde{R}(\tilde{t}'', \tilde{t}'), \quad (60)$$

$$(\Gamma^{-1}\partial_{\tilde{t}}^2 + \tilde{z}(\tilde{t}))\tilde{C}(\tilde{t}, \tilde{t}') = \int_0^\infty d\tilde{t}''\tilde{\Sigma}(\tilde{t}, \tilde{t}'')\tilde{C}(\tilde{t}'', \tilde{t}') + \int_0^{\tilde{t}'} d\tilde{t}''\tilde{D}(\tilde{t}, \tilde{t}'')\tilde{R}(\tilde{t}', \tilde{t}'') + \tilde{\hbar}_t^2\cos(\tilde{\omega}\tilde{t})\int_0^{\tilde{t}'} d\tilde{t}''\cos(\tilde{\omega}\tilde{t}'')\tilde{R}(\tilde{t}', \tilde{t}''), \quad (61)$$

$$\tilde{z}(\tilde{t}) = \int_0^{\tilde{t}} d\tilde{t}''[\tilde{\Sigma}(\tilde{t}, \tilde{t}'')\tilde{C}(\tilde{t}, \tilde{t}'') + \tilde{D}(\tilde{t}, \tilde{t}'')\tilde{R}(\tilde{t}, \tilde{t}'')] - \Gamma^{-1}\partial_{\tilde{t}}^2\tilde{C}(\tilde{t}, \tilde{t}')\big|_{\tilde{t}' \to \tilde{t}^-} + \int_0^{\tilde{t}} d\tilde{t}''\cos(\tilde{\omega}\tilde{t}'')\tilde{R}(\tilde{t}, \tilde{t}''), \quad (62)$$

$$\tilde{\Sigma}(\tilde{t}, \tilde{t}') = -4\tilde{\eta}(\tilde{t} - \tilde{t}') - p\,\mathrm{Im}\left[\tilde{C}(\tilde{t}, \tilde{t}') - \frac{i}{2}\tilde{R}(\tilde{t}, \tilde{t}')\right]^{p-1}, \quad (63)$$

$$\tilde{D}(\tilde{t}, \tilde{t}') = 2\hbar\tilde{\nu}(\tilde{t} - \tilde{t}') + \frac{p}{2}\mathrm{Re}\left[\tilde{C}(\tilde{t}, \tilde{t}') - \frac{i}{2}(\tilde{R}(\tilde{t}, \tilde{t}') + \tilde{R}(\tilde{t}', \tilde{t}))\right]^{p-1}, \quad (64)$$

$$\tilde{\eta}(\tilde{t} - \tilde{t}') = -\theta(\tilde{t} - \tilde{t}')\int_0^\infty d\tilde{\omega}\tilde{I}(\tilde{\omega})\sin(\tilde{\omega}(\tilde{t} - \tilde{t}')), \quad (65)$$

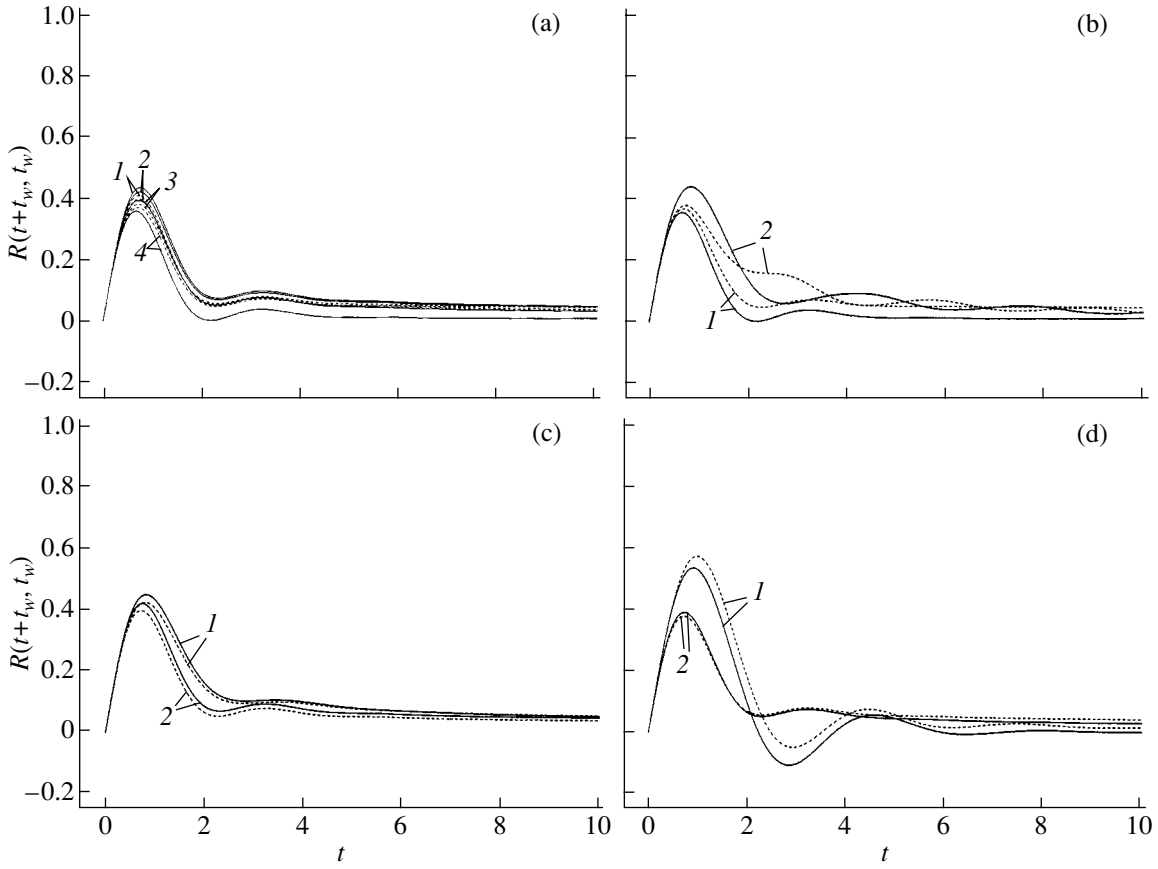

Fig. 2. Dependence of the response function $R(t + t_w, t_w)$ on time t for the waiting time t_w equal to 5 (solid lines) and 10 (dashed lines) and for (a) $\alpha = 1$, $\tilde{J} = 1$, $\Gamma = 1$, $T = 0.5$, $\omega_c = 5$, $\omega_0 = 0.1$, and different values of h_t: (*1*) 0, (*2*) 0.5, (*3*) 1, and (*4*) 2; (b) $\alpha = 1$, $\tilde{J} = 1$, $\Gamma = 1$, $T = 0.5$, $\omega_c = 5$, $h_t = 2$, and different values of ω_0: (*1*) 0.1 and (*2*) 1; (c) $\alpha = 1$, $\Gamma = 1$, $T = 0.5$, $\omega_c = 5$, $h_t = 0.5$, $\omega_0 = 0.1$, and different values of the spin interaction constant $\tilde{J}$: (*1*) 0.5 and (*2*) 1; and (d) $\tilde{J} = 1$, $\Gamma = 1$, $T = 0.5$, $\omega_c = 5$, $h_t = 1$, $\omega_0 = 0.1$, and different values of the coupling constant with the bath α: (*1*) 0.2 and (*2*) 1.

$$\tilde{\nu}(\tilde{t} - \tilde{t}') = \frac{1}{\hbar}\int_0^\infty d\tilde{\omega}\tilde{I}(\tilde{\omega})\coth\left(\frac{\beta\tilde{J}\tilde{\omega}}{2}\right)\cos(\tilde{\omega}(\tilde{t} - \tilde{t}')), \quad (66)$$

$$\tilde{I}(\tilde{\omega}) = 2\alpha\left(\frac{\tilde{\omega}}{\tilde{\omega}_{\text{ph}}}\right)^{s-1}\tilde{\omega}\exp\left(-\frac{\tilde{\omega}}{\tilde{\omega}_c}\right), \quad (67)$$

where $\tilde{h}_t = h_t/\tilde{J}$, $\tilde{\omega} = \omega\hbar/\tilde{J}$, $\tilde{\omega}_{\text{ph}} = \omega_{\text{ph}}\hbar/\tilde{J}$, $\tilde{\omega}_c = \omega_c\hbar/\tilde{J}$, and $\tilde{t} = \tilde{J}t/\hbar$. The renormalization does not affect the conditions at equal times (53)–(55) except one, which takes the form

$$\lim_{t' \to t^-} \partial_t \tilde{R}(\tilde{t}, \tilde{t}') = \Gamma. \quad (68)$$

In what follows, we drop tildes over the functions and their arguments, because we will consider only renormalized equations.

Let us consider the properties of the autocorrelation function and the response function in the spin-glass phase ($\alpha = 1$) and in the paramagnetic phase ($\alpha = 0.2$). First, we consider the effect of ac magnetic fields differing in amplitude h_t and frequency ω_0 on the system with $\alpha = 1$. Calculations were carried out for $T = 0.5$, $\Gamma = 1$, $\tilde{J} = 1$, $\omega_c = 5$, and a waiting time $t_w = 5$ and 10.

Figures 1 and 2 show the numerically calculated functions $C(t + t_w, t_w)$ and $R(t + t_w, t_w)$ for different values of the parameters of the external ac field and of the waiting time (ageing effect) and for different phases (spin-glass and paramagnetic phases). Calculations were performed using an interpolation algorithm with a step of $h = 0.01$.

Figure 1a shows the t dependence of the autocorrelation function $C(t + t_w, t_w)$ for $\alpha = 1$; $T = 0.5$; $\Gamma = 1$; $\tilde{J} = 1$, $\omega_c = 5$; $\omega = 0.1$; two values of the waiting time $t_w = 5$ and 10; and various values of the ac field amplitude $h_t = 0$, 0.5, 1, and 2. At $t = 0$, $C(t + t_w, t_w) = 1$. It can

be seen that this function first decreases rapidly with time and then smoothly approaches a nonzero limit. It is also noteworthy that the dynamics depends on the waiting time and is slow at longer times, which is characteristic of ageing. The dependence of $C(t + t_w, t_w)$ on external field becomes noticeable for field amplitudes higher than $h_t = 0.5$; the larger the amplitude, the stronger the field dependence. The autocorrelation function decreases in magnitude with increasing field amplitude. Figure 1b shows the dependence of $C(t + t_w, t_w)$ on the frequency of the external ac field. The correlation function is seen to oscillate with time, and its oscillations become more pronounced as the field frequency increases.

Figure 2a shows the t dependence of the response function $R(t + t_w, t_w)$ for two values of the waiting time t_w, 5 and 10, and various values of the external-field amplitude h_t the other parameters are the same as those in Fig. 1a). It is seen that, at short times t, this function increases sharply from zero to a maximum less than unity and then decreases rapidly; thereafter, this function slowly approaches a nonzero limit less than that for the correlation function. The dependence of the response function on an external ac field is weaker than that of the correlation function and becomes noticeable for values $h_t = 1$ and 2; the magnitude of this function at long times t decreases with increasing field amplitude. The oscillation of $R(t + t_w, t_w)$ is less pronounced than that of $C(t + t_w, t_w)$. Figure 2b shows the dependence of $R(t + t_w, t_w)$ on external-field frequency. This dependence is seen to be very weak.

For the spin-glass phase, calculations were performed for two values of the spin interaction constant $\tilde{J}$, 0.5 and 1. At the smaller value, $\tilde{J} = 0.5$, the low dynamics of $C(t + t_w, t_w)$ is suppressed more rapidly than in the case of $\tilde{J} = 1$. The values of $R(t + t_w, t_w)$ slightly increase as the spin interaction constant decreases.

Figures 1d and 2d demonstrate the effect of the coupling constant with the bath α on the functions $C(t + t_w, t_w)$ and $R(t + t_w, t_w)$. In the paramagnetic phase ($\alpha = 0.2$), these functions oscillate with time about values approaching zero at large field amplitudes. At $\alpha = 1$, the functions $C(t + t_w, t_w)$ and $R(t + t_w, t_w)$ are positive and approach nonzero limits with time, which is indicative of the spin-glass phase [2]. The behavior of the $C(t + t_w, t_w)$ and $R(t + t_w, t_w)$ curves in the spin-glass phase ($\alpha = 1$) differs noticeably from their behavior in the paramagnetic phase, where the values of these oscillating functions can be negative.

5. CONCLUSIONS

We have considered the effect of an external ac magnetic field and of the surroundings (a thermal bath of quantum oscillators) on the nonequilibrium dynamics of the quantum system. It has been shown that the symmetrized autocorrelation function and the response function decay with different rates at short and long times. The role of the spin interaction and the role of the interaction of the system with its surroundings and an external ac field were analyzed. For a quantum system, such an analysis was performed for the first time. It was shown that the relaxation of the system becomes slower as the interaction of the system with its surroundings and with the external ac field intensifies (see figures). In this case, the two different decay rates of the autocorrelation function and of the response function persist. The spin-glass state is favored by stronger interaction of the system with its surroundings, as follows from the α dependence of the functions $C(t + t_w, t_w)$ and $R(t + t_w, t_w)$. In a strong ac field, on the contrary, ageing does not persist. Therefore, quantum fluctuations, which are important at low temperatures, and a weak external ac field do not suppress spin ordering and ageing can occur in the system under study. In the case of a zero external ac field, our results are similar to the theoretical results obtained in [19].

ACKNOWLEDGMENTS

The authors are grateful to L.F. Cugliandolo, S. Franz, and M.P. Mezard for kindly providing the numerical-computation algorithm and the Physics Department of the University of Salerno for its hospitality.

This study was supported in part by the Russian Foundation for Basic Research, project no. 01-02-16368.

REFERENCES

1. *Spin-Glasses and Random Fields*, Ed. by A. P. Young (World Sci., Singapore, 1998).
2. L. F. Cugliandolo, D. R. Grempel, G. Lozano, *et al.*, Phys. Rev. B **66**, 014444 (2002).
3. M. P. Kennett, C. Chamon, and J. Ye, Phys. Rev. B **64**, 224408 (2001).
4. A. J. Leggett, S. Chakravarty, A. T. Dorsey, *et al.*, Rev. Mod. Phys. **67** (3), 725 (1995).
5. G. Busiello, R. V. Saburova, and V. G. Sushkova, Solid State Commun. **123** (1), 37 (2002).
6. G. Busiello, R. V. Saburova, V. G. Sushkova, and G. P. Chugunova, Fiz. Met. Metalloved. **95** (5), 1 (2003).
7. L. Berthier, L. F. Cugliandolo, and J. L. Iguain, Phys. Rev. E **63**, 051302 (2001).
8. L. F. Cugliandolo and J. Kurchan, Phys. Rev. Lett. **71** (1), 173 (1993).
9. H. E. Castillo, C. Chamon, L. F. Cugliandolo, and M. P. Kennett, cond-mat/01112272.
10. T. R. Kirkpatrick and D. Thirumalai, Phys. Rev. B **36** (10), 5388 (1987).

11. B. Derrida, Phys. Rev. B **24** (5), 2613 (1981).
12. D. J. Gross and M. Mezard, Nucl. Phys. B **240** (2), 431 (1984).
13. J. Zinn-Justin, *Quantum Field Theory and Critical Phenomena* (Oxford Sci., Oxford, 1996).
14. J. Schwinger, J. Math. Phys. **2** (3), 407 (1961).
15. L. V. Keldysh, Zh. Éksp. Teor. Fiz. **47** (4), 1515 (1964) [Sov. Phys. JETP **20**, 1018 (1964)].
16. K. Chou, Z. Su, B. Hao, and L. Yu, Phys. Rep. **118** (1–2), 3 (1985).
17. P. C. Martin, E. D. Siggia, and H. A. Rose, Phys. Rev. A **8** (1), 423 (1973).
18. R. P. Feynman and F. L. Vernon, Ann. Phys. (N.Y.) **24** (1), 118 (1963).
19. L. F. Cugliandolo and G. Lozano, Phys. Rev. B **59** (2), 915 (1999).
20. H. Sompolinsky and A. Zippelius, Phys. Rev. Lett. **47** (5), 359 (1981).

Translated by Yu. Epifanov

Physics of the Solid State, Vol. 46, No. 2, 2004, pp. 326–334. Translated from Fizika Tverdogo Tela, Vol. 46, No. 2, 2004, pp. 317–324.
Original Russian Text Copyright © 2004 by Kalita, Lozenko, Ryabchenko, Trotsenko, Yatkevich.

MAGNETISM AND FERROELECTRICITY

Effect of Multidomain Structure on the Field Dependences of Magnetization and Forced Striction in Easy-Plane Antiferromagnets

V. M. Kalita, A. F. Lozenko, S. M. Ryabchenko, P. A. Trotsenko, and T. M. Yatkevich

Institute of Physics, National Academy of Sciences of Ukraine, pr. Nauki 144, Kiev, 03028 Ukraine

e-mail: lozenko@iop.kiev.ua

Received March 21, 2003

Abstract—The forced magnetostriction and magnetization are measured in the easy-plane-type two-sublattice $NiCl_2$ antiferromagnet (AFM) in the case where this AFM passes from the multidomain to a single-domain state. It is shown that, in accordance with the magnetoelastic nature of the multidomain state, the field dependences of the forced magnetostriction and magnetization are interrelated and affected by the transition from the multidomain to the single-domain state. The character of these dependences corresponds to the case where the magnetization and striction are proportional to the number of domains with an energetically favored orientation with respect to the external magnetic field. *© 2004 MAIK "Nauka/Interperiodica".*

1. INTRODUCTION

In many highly symmetric antiferromagnets (AFMs) with a perfect crystal lattice, the antiferromagnetic phase is in a multidomain state [1], which strongly affects the magnetic properties of the crystals. In certain cases, the multidomain state is an equilibrium state; i.e., this state is restored when the field applied to the crystal is cyclically increased and decreased to zero and the crystal passes from the multidomain to the single-domain state and vice versa.

Unlike ferromagnets (FMs), the mechanism of formation of the equilibrium multidomain state in AFMs is still not clearly understood. Li [2] proposed an entropy mechanism according to which a decrease in the degree of ordering in a multidomain state makes an additional contribution to the entropy, thereby reducing the free energy of the multidomain state, in comparison with that of the uniform state, by the quantity $-T\Delta S$, where ΔS is the entropy increment in the multidomain state. The entropy mechanism can operate in the vicinity of T_N and has been observed to occur in a number of AFMs [3]. At lower temperatures, the AFM is in a single-domain state.

In [1], the entropy mechanism of the multidomain state was assumed to operate in layered easy-plane AFMs. However, it was shown in [4] that domains in such AFMs also exist at $T \longrightarrow 0$. Therefore, the entropy mechanism is not dominant in this case.

The first experimental data on the multidomain state in layered easy-plane AFMs were obtained in [5] from measurements of the magnetization of powders. A number of unusual phenomena were reported in [5] to occur. First, in a magnetic-field range below a certain value, the magnetization of samples was observed to be a nonlinear function of the applied magnetic field. Second, the magnetization exhibits hysteretic behavior characterized by a remanent magnetization and a coercive force. This hysteresis and the nonlinear field dependence of the magnetization were explained in [5] by the presence of ferromagnetic inclusions in the samples under study.

Neutron-scattering studies of single crystals of dihalides of iron-group elements in the antiferromagnetic state [6] showed that in this state a crystal is broken up into domains in each of which the direction of the antiferromagnetism vector **L** is the same everywhere over a domain but varies from domain to domain. The angle between the spins in neighboring domains was found to be 120°. It was also shown in [6] that, when a magnetic field **H** is applied in the easy plane, the fraction of domains with the antiferromagnetism vector perpendicular to the field becomes progressively larger with increasing field until the crystal passes to the single-domain state. The appearance of a multidomain state was assumed in [6] to be due to in-plane anisotropy and, hence, to a dependence of the energy on the direction of **L** in the easy plane. The anisotropy is such that there are three equivalent easy magnetization axes along which domains can be magnetized. The transition from a multidomain to a single-domain state was considered to be due to orientation transitions in domains to the state in which the vector **L** is perpendicular to **H**. As the field was decreased to zero, the multidomain state was restored to a large extent, but not completely; the overall volume of domains with **L** perpendicular to the field was larger than its value before the application of the field. The existence of several easy magnetization

1063-7834/04/4602-0326$26.00 © 2004 MAIK "Nauka/Interperiodica"

axes due to in-plane anisotropy affects the spin orientation but cannot explain the fact that the multidomain state is close to equilibrium (i.e., that this state is restored when the applied field is cyclically increased and decreased to zero). Indeed, a metastable multidomain state can appear when a sample is cooled in a zero field and passes through the Néel point, because in this case the antiferromagnetic state nucleates randomly at various sites of the crystal with the vector **L** oriented along different easy axes. However, anisotropy cannot provide the energy required to form domain walls (DWs) when the single-domain state again transforms into a multidomain state as the applied field **H** is decreased to zero. The effect of weak in-plane anisotropy was also discussed in [7], where it was shown that the anisotropy can affect the formation of a domain structure.

The formation of an "equilibrium" multidomain state in an easy-plane AFM can be favored by screw dislocations [8, 9]. In this case, the domain structure must be stabilized by in-plane anisotropy.

In [4, 7, 10], it was conjectured that domains in easy-plane antiferromagnetic dihalides of iron-group elements are of a magnetoelastic nature. This conjecture was based on experimental data on magnetostriction (MS) measured during rearrangement of the domain structure in this type of crystals. For example, $CoCl_2$ crystals exhibit large forced MS [4, 10] comparable to the MS of magnets with rare earth ions [11].

If the multidomain state has a magnetoelastic nature, then the nonlinear magnetization observed in layered antiferromagnetic crystals of dihalides of iron-group elements [5] is likely due to the field-induced rearrangement of the magnetoelastic multidomain antiferromagnetic state rather than to ferromagnetic inclusions. In this case, the field dependences of the magnetization and MS must be interrelated.

It is well known that magnetoelasticity strongly affects the magnetization curves of FMs [12] and influences the motion of DWs and the formation of a domain structure. For example, a uniaxial FM with domains oriented along the easy axis is magnetized by a magnetic field directed along this axis through the motion of 180° DWs, and forced MS does not arise (without regard for the paramagnetic process) [13]. Forced MS in such an FM occurs when an external magnetic field is applied perpendicular to the easy axis and, therefore, the magnetic moments of domains tilt to the field direction. Forced MS also arises in an FM when 90° DWs move [12]. In the AFM, in contrast to in the FM, any rearrangement of the multidomain structure is accompanied by sublattice spins tilting in the direction of the applied magnetic field; therefore, forced MS must arise in this case.

In this paper, we analyze the specific features of the multidomain structure rearrangement that occurs in an easy-plane AFM under the action of an external magnetic field. As an example, we use experimental data on magnetization and forced MS obtained for layered easy-plane-type two-sublattice antiferromagnetic $NiCl_2$ in a multidomain state subjected to a magnetic field cyclically increased and decreased to zero. It is shown that the field dependences of the magnetization and forced MS correlate with the rearrangement of the multidomain structure in $NiCl_2$.

2. EXPERIMENTAL

We performed measurements on plates cleaved from a $NiCl_2$ single-crystal boule grown from a melt in a sealed ampoule by lowering the ampoule through a zone of a sharp vertical temperature gradient. The $NiCl_2$ crystal has D_{3d}^5 symmetry, and the antiferromagnetic transition temperature is $T_N = 49.6$ K [14]. Measurements were performed at $T = 4.2$ K.

The MS was measured on samples in the form of a rectangular plate $5 \times 5 \times 1$ mm in size. The shortest edge was parallel to the hard magnetization axis (C_3). To measure the MS, a dilatometer from a magnetic system with two crossed magnets was used.

The magnetization was measured with an LDJ-9500 vibrating-sample magnetometer on a sample in the form of a rectangular plate $5 \times 4 \times 0.2$ mm in size; this sample is thinner than those used in measuring the MS. The magnetic field applied to samples was lower than 10 kOe, which sufficed to produce a single-domain state in $NiCl_2$ [15]. It should be noted that the samples used to measure the MS and the magnetization were grown at different times. Since $NiCl_2$ crystals are hydroscopic, the samples were kept in a dehydrated medium. However, because of the differences in the growth and storage conditions, we cannot be sure that the grown crystals are identical; they can differ in the amount of defects, which are of importance in forming and rearranging a magnetoelastic multidomain structure.

Figure 1 shows the field dependence of the forced MS of a $NiCl_2$ single crystal for two mutually perpendicular field directions in the easy plane of the crystal in the case where the field **H** is increased and then decreased to zero. It can be seen that there is hysteresis in the MS as a function of the field strength and in the remanent striction, whose sign depends on the direction of the decreasing field. The hysteresis is unusual; namely, it takes place only when the orientation of the applied field is changed; no hysteresis is observed when the field is cyclically increased and decreased in the same direction.

The experimental $\varepsilon(H)$ dependence ($\varepsilon = \Delta l/l$ is the field-induced strain of the crystal, l is the crystal length along the direction of measurement, Δl is the field-induced increase in this length) exhibits a general feature; namely, in a multidomain state, the forced MS of the crystal is anisotropic and changes sign as the direction of the magnetic field is changed from parallel to

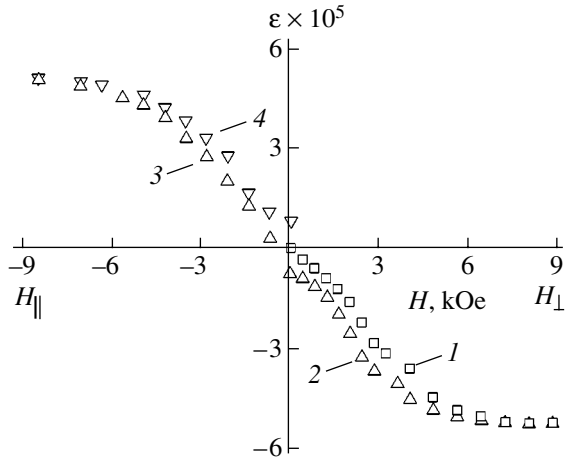

Fig. 1. Field dependences of the magnetostriction in $NiCl_2$ at $T = 4.2$ K in the case where the field $H_\perp$ perpendicular to the MS measurement direction (*1*) increases from zero and then (*2*) decreases to zero and in the case where the field $H_\perp$ parallel to the MS measurement direction (along which the crystal dimension is measured with a dilatometer) (*3*) increases from zero and then (*4*) decreases to zero.

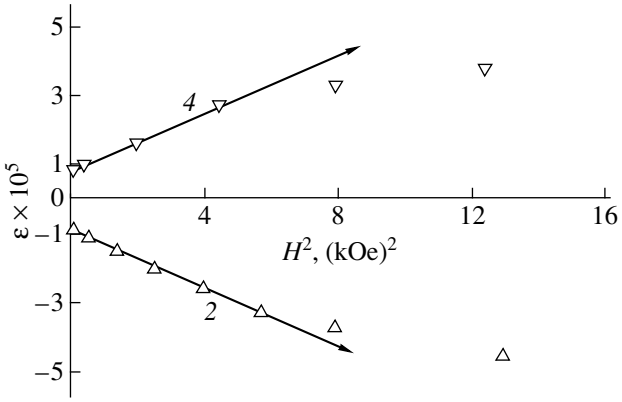

Fig. 2. Dependences of MS on the square of the magnetic field strength corresponding to curves *2* and *4* in Fig. 1, respectively (in the case where the field decreases to zero).

perpendicular. The $NiCl_2$ crystal is extended along the direction of the field **H** and contracted by the same quantity in the perpendicular direction. In strong fields (≥10 kOe), a uniform (single-domain) state sets in irrespective of the direction of field **H** in the easy plane. The behavior of the MS of $NiCl_2$ in the uniform (single-domain) state was studied in [7], and it was found that the MS in the uniform state varies slowly as the applied field is increased further; for fields up to the value at which spin flip occurs, $\varepsilon(H)$ varies in proportion to the square of the magnetic field strength, as should be the case with a homogeneous AFM subjected to an external magnetic field [16]. By extrapolating this dependence to $H = 0$, we find a hypothetical value of the spontaneous MS in the single-domain state.

It can be seen from Fig. 1 that the anisotropic spontaneous striction in the multidomain state is balanced (to within the remanent striction mentioned above). Therefore, the crystal as a whole is not strained (neglecting the possible remanent striction) in the antiferromagnetic multidomain state at $H = 0$. Note that, as follows from the experimental data on antiferromagnetic resonance [17], domains in this state, while being virtually unstrained, retain the spontaneous strain, which manifests itself in the presence of a gap due to the spontaneous strain in the low-frequency antiferromagnetic resonance spectrum. Therefore, in constructing a model of the multidomain state, one should take into account that the crystal as a whole and individual domains remain unstrained.

Figure 2 shows the dependences of the MS in the multidomain state on the square of the magnetic field strength in the case where the field is decreased to zero. These dependences correspond to the low-frequency range in curves *2* and *4* of Fig. 1. The difference in the MS sign indicates that the forced MS is anisotropic. In the range $H < 2.5$ kOe, as seen from Fig. 2, the striction can be closely approximated by the expression

$$\varepsilon = \varepsilon_r + \varepsilon_s \frac{H^2}{H_d^2}, \qquad (1)$$

where ε_r is the remanent striction, which vanishes as the field is decreased to zero; ε_s is the spontaneous striction in the single-domain state; and H_d is an empirical parameter, which should be taken to be $H_d = 3.6 \pm 0.3$ kOe to fit the experimental data. Since the value of ε_r depends on the prehistory (the previous values and direction of the applied magnetic field), the quantity ε_s should be determined, in general, as the half-sum of the asymptotic values of striction $\varepsilon(H)$ as $H \longrightarrow 0$ for successive application of the field along the two mutually perpendicular directions. When the magnetic field H is applied for the first time, the field dependence of the striction in the field range in question ($H < 2.5$ kOe) is given by Eq. (1) with $\varepsilon_r = 0$ [7].

Figure 3 shows the magnetization curve of a $NiCl_2$ single crystal for the case where the $\mathbf{H} \perp C_3$ is increased from zero. It is seen that the magnetization is a nonlinear function of H. According to the Néel theory [16], the dependence of the magnetization in the single-domain state on the field applied in the easy plane must be linear. As shown in [15], the magnetization of the easy-plane antiferromagnetic $NiCl_2$ crystal increases linearly with the field (i.e., the susceptibility is constant) up to the spin-flip field value (except for the field range where the multidomain state is rearranged). Figure 3 also shows a hypothetical magnetization curve (dashed straight line) constructed on the basis of data taken from [15, 16] for the case where the multidomain structure does not arise. It is seen that, in the range

where the multidomain structure is rearranged, the $m(H)$ curve passes below this line; that is, the magnetization in this field range is less than that expected for the single-domain state. As the field H is increased, the spacing between the straight line and the $m(H)$ curve first increases and then (for $H > 5$ kOe) decreases, so that above $H = 10$ kOe these dependences become virtually identical. The measured magnetization is normalized to a unit mass of the sample.

The $m(H)$ dependence shown in Fig. 3 can be closely approximated for $H \longrightarrow 0$ by the expression

$$m = \chi_d H\left(1 + \frac{H^2}{H_m^2}\right), \quad (2)$$

where χ_d is the magnetic susceptibility for the multidomain state at $H \longrightarrow 0$ ($\chi_d = 0.44$ emu/g kOe) and H_m is an empirical parameter, whose best fit value to the experimental data is $H_m = 4.3 \pm 0.6$ kOe. This approximation by odd powers of H agrees with the experimentally observed asymmetry of the $m(H)$ dependence with respect to a change in the sign of the applied field. Obviously, Eq. (2) is valid for $H < H_m$. Thorough measurements with the applied magnetic field cyclically increased and decreased to zero (without changes in the field direction) showed no remanent magnetization and no magnetization hysteresis, which is in agreement with the data from [15]. Unfortunately, no successive measurements have been performed with the applied field cyclically increased and decreased to zero along two mutually perpendicular directions in the easy plane; in this case, one might expect unusual hysteresis to occur with zero remanent magnetization.

By integrating the function $m(H)$ with respect to H, we can find the work done by the magnetic field when a crystal is magnetized and passes to the single-domain state. For a unit volume of the sample, this work is

$$A = \frac{1}{\rho}\int_0^{H_0} m(H)dH, \quad (3)$$

where ρ is the density of the crystal (which appears because the magnetization is normalized to unit mass) and H_0 is the upper limit of integration, corresponding to a field at which the sample is in the single-domain state (we put $H_0 = 10$ kOe). If the multidomain structure does not occur and the crystal is always in the uniform state, then, taking into account the linear field dependence of the magnetization, the work in Eq. (3) can be found to be

$$A_0 = \frac{1}{2\rho}\chi_e H_0^2, \quad (4)$$

where χ_e is the magnetic susceptibility of the single-domain crystal.

The energy E of the AFM in a magnetic field (per unit volume) is the sum of the exchange energy e_1 (in the approximation where only the intersublattice interactions are included), the Zeeman energy e_2, the domain-wall energy e_3, and the elastic accommodation energy e_4 of the domain MS and the elastic fields of defects [7] giving rise to the formation of triads of domains [18], $E = e_1 + e_2 + e_3 + e_4$. The formation of DWs at the expense of exchange energy is not favored energetically, whereas elastic accommodation of the spontaneous domain MS to defects favors the formation of a multidomain structure and, therefore, can be the reason for the formation of a multidomain structure. In actuality, the configuration, number, orientation, and shape of domains are such that the energy E becomes minimal. Let us show that, when a multidomain structure forms, the changes in e_3 and e_4 must be opposite in sign. For this purpose, we consider the change in energy E caused by the application of a field H_0, $\Delta E = \Delta e_1 + \Delta e_2 + \Delta e_3 + \Delta e_4$. In this case, $\Delta E = A$ and $\Delta e_1 + \Delta e_2 = A_0$. Therefore, we have $A - A_0 = e_3(H = 0) + \Delta e_4$, where it is taken into account that at $H = H_0$ the crystal is in a nearly uniform state and, therefore, $e_3(H = H_0) = 0$ and $\Delta e_3 = e_3(H = 0) - e_3(H = H_0) = e_3(H = 0) = e_3$. According to Eqs. (3) and (4) and the data from Fig. 3, we have $A_0 - A > 0$. The formation of DWs at the expense of the exchange energy is not favored; therefore, $e_3 > 0$ and it follows that $\Delta e_4 < 0$ and $|\Delta e_4| > e_3$. Since $\Delta e_4 = e_4(H = 0) - e_4(H_0)$, we obtain that $e_4(H = 0) < e_4(H_0)$. This property of the energy e_4 is a necessary condition for an equilibrium magnetoelastic multidomain structure to form in an AFM.

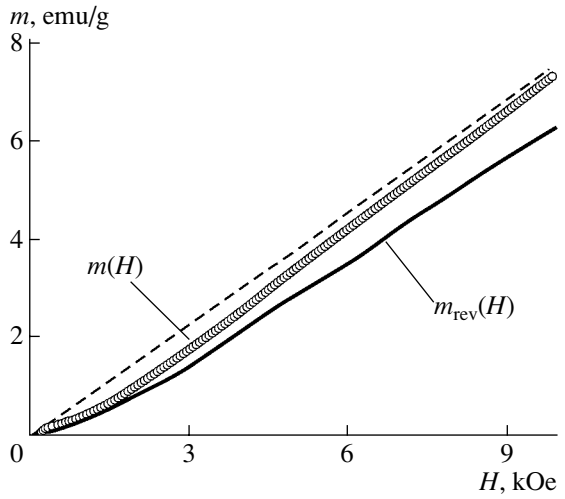

Fig. 3. Field dependence of the magnetization $m(H)$ of $NiCl_2$ at $T = 4.2$ K in the case where the field increases from zero. Also shown is the reversible part $m_{rev}(H)$ of the magnetization.

Thus, using Eqs. (3) and (4), we estimated the cost in energy of DWs and the gain in energy responsible for the formation of a domain structure. The difference between the works A_0 and A is equal to the difference

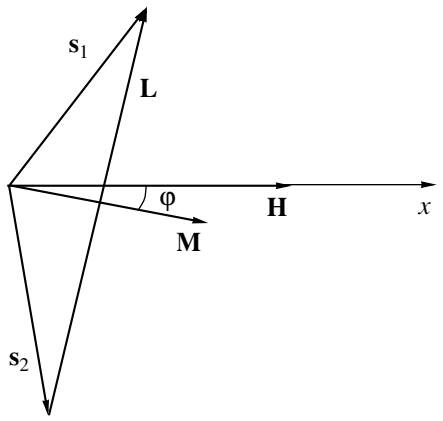

Fig. 4. Orientation of the sublattice spins $\mathbf{s}_1$ and $\mathbf{s}_2$, the magnetization vector **M**, and the antiferromagnetism vector **L** with respect to the applied magnetic field **H**.

between these two energies and determines the gain in energy due to the formation of a domain structure at $H = 0$. Geometrically, the difference between the works can be found as the area between the uniform-magnetization curve and the $m(H)$ curve in Fig. 3. The calculation gives the ratio of this gain in energy to the exchange interaction energy between the sublattices as 5.7×10^{-4} (in calculating the exchange energy, we used the fact that the spin-flip field for $NiCl_2$ is equal to $H_{ff} =$ 129 kOe at $T = 4.2$ K [19]).

In what follows, we show that the nonlinear field dependence of magnetization and the hysteresis of striction are manifestations of magnetoelastic interaction in the multidomain state of AFMs (including $NiCl_2$). The striction and magnetization (and the $\varepsilon(H)$ and $m(H)$ dependences) are shown to correlate when the domain structure is rearranged.

3. DISCUSSION OF RESULTS

We will interpret the experimental results under the assumption that domains are oriented in the easy plane and that the domain orientation distribution is continuous [4, 7]. The orientation of a domain in the easy plane is specified by the angle φ between the magnetization vector of the domain $\mathbf{M} = \mathbf{s}_1 + \mathbf{s}_2$ and the direction of the magnetic field **H**, where $\mathbf{s}_1$ and $\mathbf{s}_2$ are the sublattice magnetizations. The vectors $\mathbf{s}_1$ and $\mathbf{s}_2$, as well as **M**, are assumed to lie in the easy plane (Fig. 4).[1] The domains are considered two-dimensional. The domain orientation distribution function $p(\varphi)$ is defined as the ratio of the volume of domains of orientation φ to the total crystal volume. For the sake of definiteness, the magnetic field is assumed to be applied along the x axis in the easy plane (Fig. 4). The antiferromagnetism vector also lies in the easy plane and is defined conventionally as $\mathbf{L} = \mathbf{s}_1 - \mathbf{s}_2$. Therefore, the angle φ lies in the easy plane. The domain orientation distribution function is normalized as

$$\frac{1}{\pi}\int_{-\pi/2}^{\pi/2} p(\varphi)d\varphi = 1.$$

As shown in [4], the MS of a uniform easy-plane AFM is anisotropic in the easy plane; namely, the MS is equal to ε_s in the direction perpendicular to **L**, while along **L** it changes sign and is $-\varepsilon_s$. In this case, the striction of a multidomain crystal along the applied field is

$$\begin{aligned}\varepsilon &= \frac{1}{\pi}\int_{-\pi/2}^{\pi/2} \varepsilon_s(\cos^2\varphi - \sin^2\varphi)p(\varphi)d\varphi \\ &= \frac{\varepsilon_s}{\pi}\int_{-\pi/2}^{\pi/2} 2\left(\cos^2\varphi - \frac{1}{2}\right)p(\varphi)d\varphi.\end{aligned} \quad (5)$$

We assume that $\mathbf{s}_1$ and $\mathbf{s}_2$ are of the same magnitude, $|\mathbf{s}_1| = |\mathbf{s}_2| = s$. A domain with $\mathbf{L} \perp \mathbf{H}(\varphi = 0)$ has magnetization $\mathbf{M} = \chi_e\mathbf{H}$. In general ($\varphi \neq 0$), the vector **M** of a domain is not parallel to **H** and its magnitude is $M = \chi_e H\cos\varphi$. Therefore, the magnetization of the crystal along the field direction is

$$m = \frac{1}{\pi}\int_{-\pi/2}^{\pi/2} \chi_e H\cos^2\varphi p(\varphi)d\varphi. \quad (6)$$

Taking $\chi_e H$ out of the integral in Eq. (6) and using Eq. (5), we obtain a general relation between the magnetization and striction

$$m = \frac{1}{2}\chi_e H\left(1 + \frac{\varepsilon}{\varepsilon_s}\right). \quad (7)$$

This relation can be tested using the experimental data.

Equation (7) makes it possible to predict the field dependence of magnetization using the experimental data on striction. Figure 5 shows such $m(H)$ dependence obtained on the basis of the data on $\varepsilon(H)$ from Fig. 1; namely, we used curve *3* in Fig. 1 for the case where the external field is increased from zero and curve *4* for where the field is decreased. The $m(H)$ curve thus found is nonlinear and concave downward. Note that the striction data used were obtained after the field direction was changed (that is, the preceding cycle of the field increasing and decreasing to zero was performed for the perpendicular field direction) and, therefore, when the field was first applied, the crystal had a remanent striction of opposite sign produced in the preceding cycle. It is seen from Fig. 5 that the curves obtained for the increasing and decreasing fields coincide at $H = 0$ and at high field values ($H > 8$ kOe), thereby forming a loop (pronounced only weakly on the

[1] In the case of $H = 0$, the angle φ is taken to be the angle between the vector $\lim_{\mathbf{H}\to 0}\mathbf{M}$ and the direction of the field **H**.

scale of Fig. 5). This is the above-mentioned hysteresis without remanent magnetization. The lower (solid) curve in Fig. 5 corresponds to the increasing field, and the upper (dashed) curve, to the decreasing field.

The predicted $m(H)$ dependence correlates well with our assumption that the rearrangement of the multidomain structure proceeds through an increase in the relative volume of domains with $\mathbf{L} \perp \mathbf{H}$. The irreversibility of the rearrangement of the multidomain structure (manifested in the appearance of remanent striction and of the striction hysteresis) is weakly pronounced in the behavior of the magnetization; the difference between the values of the magnetization corresponding to increasing and decreasing fields is insignificant and becomes noticeable only in the middle of the field range where a multidomain structure exists, i.e., for H = 3–5 kOe.

Based on the experimental $m(H)$ dependence, we can also solve the inverse problem with the help of Eq. (7); namely, we can find the $\varepsilon(H)$ dependence using the experimental values of the magnetization. For this purpose, we find the quantity

$$y(H) = \frac{m(H)}{(1/2)\chi_e H} - 1, \qquad (8)$$

which is the ratio of the striction to its value for the single-domain state, $y(H) = \varepsilon/\varepsilon_s$. The $y(H)$ dependence is shown in Fig. 6 and agrees qualitatively and quantitatively with the $\varepsilon(H)$ dependence shown in Fig. 1. It should be noted that the former dependence was found from the data on $m(H)$ that were obtained after several cycles of field increasing and decreasing to zero were performed for the field direction in question. For this reason, as $H \longrightarrow 0$, the quantity $y(H)$ tends to a nonzero value exhibiting remanent striction, as does the $\varepsilon(H)$ dependence shown in Fig. 1.

Thus, the behavior of the magnetization calculated from Eq. (7) on the basis of the data on striction agrees well with the experimental $m(H)$ dependence shown in Fig. 3 and the behavior of MS calculated from Eq. (7) also agrees with its experimental field dependence. Therefore, the $m(H)$ and $\varepsilon(H)$dependences are interrelated and describe the rearrangement of the domain structure caused by the applied magnetic field.

Based on Eqs. (1) and (7), we find the $m(H)$ dependence for $H \longrightarrow 0$. For the initial magnetization curve ($\varepsilon_r = 0$), we obtain

$$m = \frac{1}{2}\chi_e H\left(1 + \frac{H^2}{H_d^2}\right). \qquad (9)$$

Equation (9) has the form of the experimental dependence (2). From comparison of Eqs. (2) and (9), it follows that the magnetic susceptibility in the beginning of the rearrangement of the multidomain structure as the magnetic field H increases from zero is half as large as

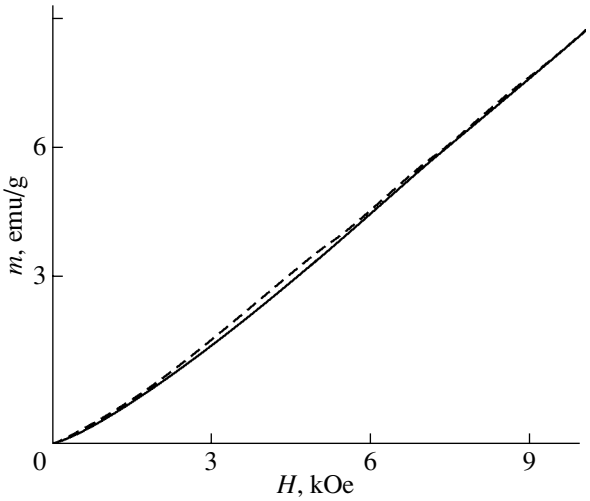

Fig. 5. Field dependences of $m(H)$ constructed on the basis of the data represented by curves *3* and *4* in Fig. 1 in the case where the magnetic field, applied along the MS measurement direction, (*1*) increases from zero and then (*2*) decreases to zero.

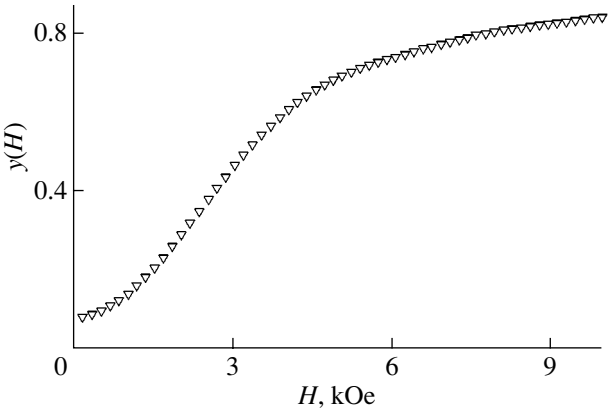

Fig. 6. Field dependence of the striction calculated from the experimental data on magnetization.

the susceptibility in the single-domain state, $\chi_d = \chi_e/2$. The experimental value of χ_d is somewhat larger. It also follows from comparing Eqs. (2) and (9) that $H_d = H_m$. The experimental values of H_d and H_m differ by 15%.

In general, the domain orientation distribution is anisotropic (because of small in-plane anisotropy). However, it was shown in [7] that, in spite of the anisotropy in this distribution, the field dependence of the striction in the easy plane remains isotropic. For the sake of simplicity, we neglect the in-plane anisotropy

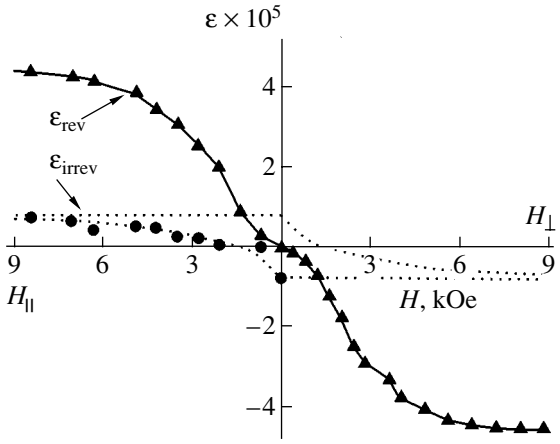

Fig. 7. Field dependences of the reversible (ε_{rev}) and irreversible (ε_{irrev}) components of the striction in the field strength range where the multidomain antiferromagnetic state is rearranged. The dotted curve represents the $\varepsilon_{irrev}(H)$ dependence in the case where fields $H_\perp$ and $H_\parallel$ (successively applied along two mutually perpendicular directions) increase from zero and then decrease to zero.

and assume that all orientations φ of domains are equiprobable before the first application of field *H*.

The appearance of remanent striction is accompanied by an anisotropic rearrangement of the domain structure. This anisotropy is related to the direction of the vanishing field *H*. For small deviations from the equiprobable distribution, we can write $p(\varphi)$ in the form [4]

$$p(\varphi) = 1 + \alpha\left(\cos^2\varphi - \frac{1}{2}\right), \tag{10}$$

where α is a parameter depending on *H* and the value of the remanent striction. Using Eq. (10), we calculated the average strain of the crystal. By comparing the result with the experimental dependence (1), we found that the domain orientation distribution for a small decreasing field has the form

$$p(\varphi) = 1 + 4\left(\frac{\varepsilon_r}{\varepsilon_s} + \frac{H^2}{H_d^2}\right)\left(\cos^2\varphi - \frac{1}{2}\right). \tag{11}$$

Substituting Eq. (11) into Eq. (6), we obtain the field dependence of the susceptibility of the crystal in low fields in the case where the field is decreased to zero or is again applied in the same direction:

$$m = \frac{1}{2}\chi_e H\left(1 + \frac{\varepsilon_r}{\varepsilon_s} + \frac{H^2}{H_d^2}\right). \tag{12}$$

Note that Eq. (12) can also be obtained by substituting Eq. (1) into Eq. (7). By differentiating Eq. (12) with respect to *H*, we find that, in accordance with Eq. (2), the magnetic susceptibility is a quadratic function of the field for $H \longrightarrow 0$

$$\chi = \frac{1}{2}\chi_e\left(1 + \frac{\varepsilon_r}{\varepsilon_s} + 3\frac{H^2}{H_d^2}\right). \tag{13}$$

It is seen from Eqs. (12) and (13) that, in accordance with Eq. (7), the magnetic susceptibility of the crystal in the multidomain state in the case of field *H* decreasing to zero is not half as large as χ_e but has a somewhat greater value,

$$\chi_d = \frac{1}{2}\chi_e\left(1 + \frac{\varepsilon_r}{\varepsilon_s}\right). \tag{14}$$

Thus, irreversibility of the rearrangement of the multidomain state increases the magnetic susceptibility for $H \longrightarrow 0$ when the external magnetic field is decreased to zero or is again applied.

According to Eq. (11), when the external magnetic field decreases to zero, the domain orientation distribution function $p(\varphi)$ contains two additive components; one of them is reversible and field-dependent and the other is irreversible and field-independent. The latter component is responsible for the remanent striction and makes a contribution to the susceptibility of the crystal in the multidomain state for $H \longrightarrow 0$. Therefore, the total striction and magnetization of the crystal can be represented as the sum of two terms,

$$\varepsilon(H) = \varepsilon_{rev}(H) + \varepsilon_{irrev}(H), \tag{15}$$

$$m(H) = m_{rev}(H) + m_{irrev}(H), \tag{16}$$

where $\varepsilon_{rev}(H)$ and $m_{rev}(H)$ are the reversible components of the striction and magnetization corresponding to the reversible rearrangement of the multidomain structure and $\varepsilon_{irrev}(H)$ and $m_{irrev}(H)$ are the irreversible components. In general, all components in Eqs. (15) and (16) are field-dependent. However, when the magnetic field decreases in the field strength range of existence of the multidomain state, the irreversible part of the striction remains constant and equal to the remanent MS; i.e., $\varepsilon_{irrev}(H) = \varepsilon_r = \text{const}$. This property makes it possible to determine the field dependences of $\varepsilon_{irrev}(H)$ and $\varepsilon_{rev}(H)$ when the field with the other direction is applied. As was mentioned above in discussing the experimental data on the striction in $NiCl_2$ crystals, the striction changes sign as the field direction is changed from transverse to longitudinal (and *vice versa*); therefore, both terms in Eq. (15) must also change sign in this case. The $\varepsilon_{rev}(H)$ dependences for the longitudinal and transverse field directions are shown in Fig. 7. Figure 7 also shows the $\varepsilon_{irrev}(H)$ dependence in another cycle, where the transverse field is decreased to zero and a longitudinal field is applied and then decreased to zero, after which the initial transverse field is again applied. Unfortunately, we did not investigate the closing section of this $\varepsilon_{irrev}(H)$ loop. In Fig. 7, this section is

constructed under the assumption that the loop is antisymmetric.

The ratio ξ between the irreversible contribution to the striction and the total striction in the single-domain state is $\xi = \varepsilon_{irrev}/\varepsilon_s = 0.16$. Therefore, the volume of domains contributing to the irreversible striction is $\delta_{irrev} = 0.16$ of the sample volume. The irreversible contribution to the striction in the case where the field decreases to zero is due to a change in the domain orientation distribution (with respect to the equilibrium distribution), namely, to an increase (proportional to ε_r) in the fraction of domains with $\mathbf{L} \perp \mathbf{H}$. It is likely that, when the field is decreased to zero or is again applied in the same direction, the magnetization of this fraction of domains is characterized by the susceptibility χ_e of the single-domain state (with $\mathbf{L} \perp \mathbf{H}$). Indeed, by comparing the experimental value of the magnetic susceptibility of the multidomain state χ_d and its predicted value $\chi_e/2$, the value of ξ is found to be close to its value determined from the data on striction, namely, $\xi = 2\chi_d/\chi_e - 1 = 0.14$.

Now, we determine the field dependence of the contribution to the sample magnetization coming from the domains that are rearranged reversibly. The volume fraction of these domains is $\delta_{rev} = 1 - \delta_{irrev}$. The $m_{rev}(H)$ dependence is shown in Fig. 3 (m_{rev} is the magnetization per unit mass). Note that the magnetic susceptibility of these domains is half as large as its value in the case where these domains transformed into the single-domain state. We also note that the value of H_m as determined from the $m_{rev}(H)$ dependence conforms more closely to the condition $H_d = H_m$.

In Eqs. (15) and (16), the striction and magnetization of a sample were formally broken down into two components in order to explain the occurrence of the remanent striction and the fact that the magnetic susceptibility in the multidomain state is not half its value in the single-domain state. However, in the case in question, this separation into two components is of fundamental importance, because the mechanism of formation of the multidomain antiferromagnetic state is magnetoelastic in nature. The reversible contributions to the striction and magnetization are associated, as mentioned above, with elastic accommodation of the spontaneous domain MS to the local elastic fields of defects [7, 18]. In [18], the formation of triads of domains near defects was considered theoretically. The angle between the vectors **L** of the domains in a triad was 120°. The triads around a defect should also accommodate elastically to each other. Such a domain structure is energetically favored and will be reversible in fields cyclically increased and decreased to zero. The irreversibility is likely due to those domain walls that are pinned at defects not involved in the formation of triads.

4. CONCLUSIONS

Thus, observations of the behavior of the forced striction and magnetization in $NiCl_2$ crystals passing from the multidomain to the single-domain state in an external magnetic field have shown that, in the multidomain antiferromagnetic state that arises in an $NiCl_2$ crystal, the overall striction is nearly balanced and the magnetic susceptibility is approximately half as large in a zero magnetic field. When a magnetic field is applied, the crystal passes from the multidomain to the single-domain state and a spontaneous striction arises that is uniform over the crystal.

As the crystal passes to the single-domain state, the magnetization and MS exhibit a nonlinear dependence on the applied field. The experimental data on the forced striction and magnetization show that their field dependences reveal the rearrangement of the multidomain state in the magnetic field. These dependences exhibit a fundamental feature; namely, the magnetization and striction are both proportional to the average number of domains with the energetically favored orientation $\mathbf{L} \perp \mathbf{H}$.

The rearrangement of the multidomain state in a magnetic field cyclically increased and decreased to zero is accompanied by striction hysteresis, while the magnetization exhibits no hysteresis. The MS hysteresis is due to the domain structure rearrangement being partially irreversible, which results in an increased volume fraction of domains with the energetically favored orientation with respect to the field direction when the field decreases to zero. For this reason, the remanent MS causes the domain orientation distribution to be anisotropic in this case.

Thus, we have explained the nonlinear field dependences of the magnetization and MS, the MS hysteresis, and the nonhysteretic behavior of the magnetization in the field strength range where the multidomain antiferromagnetic state is rearranged.

REFERENCES

1. M. M. Farztdinov, Usp. Fiz. Nauk **84** (4), 611 (1964) [Sov. Phys. Usp. **7**, 855 (1964)].
2. Y. Y. Li, Phys. Rev. **101** (5), 1450 (1956).
3. M. M. Farztdinov, *The Physics of Magnetic Domains in Antiferromagnets and Ferrites* (Nauka, Moscow, 1981).
4. V. M. Kalita and A. F. Lozenko, Fiz. Nizk. Temp. **27** (8), 872 (2001) [Low Temp. Phys. **27**, 645 (2001)].
5. W. J. De Haas, B. H. Schultz, and J. Koolhaas, Physica (Amsterdam) **7** (1), 57 (1940).
6. M. K. Wilkinson, J. W. Cable, E. O. Wollan, and W. C. Koehler, Phys. Rev. **113**, 497 (1959).
7. V. M. Kalita and A. F. Lozenko, Fiz. Nizk. Temp. **28** (4), 378 (2002) [Low Temp. Phys. **28**, 263 (2002)].
8. A. S. Kovalev and A. M. Kosevich, Fiz. Nizk. Temp. **3** (2), 259 (1977) [Sov. J. Low Temp. Phys. **3**, 125 (1977)].
9. I. E. Dzyaloshinskiĭ, Pis'ma Zh. Éksp. Teor. Fiz. **25** (2), 110 (1977) [JETP Lett. **25**, 98 (1977)].

10. V. M. Kalita, A. F. Lozenko, S. M. Ryabchenko, and P. A. Trotsenko, Ukr. Fiz. Zh. **43** (1), 1469 (1998).
11. A. K. Zvezdin, V. M. Matveev, A. A. Mukhin, and A. I. Popov, *Rare-Earth Ions in Magnetically Ordered Crystals* (Nauka, Moscow, 1985).
12. S. V. Vonsovskiĭ, *Magnetism* (Nauka, Moscow, 1971; Wiley, New York, 1974).
13. V. G. Bar'yakhtar, A. N. Bogdanov, and D. A. Yablonskiĭ, Usp. Fiz. Nauk **156** (1), 47 (1988) [Sov. Phys. Usp. **31**, 810 (1988)].
14. P. A. Lingard, R. J. Birgenau, J. Als-Nierlsen, and H. J. Guggenheim, J. Phys. C **8** (7), 1059 (1975).
15. D. Billerey, C. Terrier, A. J. Pointon, and J. P. Redoules, J. Magn. Magn. Mater. **21**, 187 (1980).
16. L. Néel, Izv. Akad. Nauk SSSR, Ser. Fiz. **21** (6), 890 (1957).
17. A. F. Lozenko, P. E. Parkhomchuk, S. M. Ryabchenko, and P. A. Trotsenko, Fiz. Nizk. Temp. **14** (9), 941 (1988) [Sov. J. Low Temp. Phys. **14**, 517 (1988)].
18. V. M. Kalita and A. F. Lozenko, Fiz. Nizk. Temp. **27** (5), 489 (2001) [Low Temp. Phys. **27**, 358 (2001)].
19. J. Gunzbourg, S. Papassimacopoulos, A. Mieden-Gros, and A. Allain, J. Phys. **32** (C1), 125 (1971).

Translated by Yu. Epifanov

Physics of the Solid State, Vol. 46, No. 2, 2004, pp. 335–338. Translated from Fizika Tverdogo Tela, Vol. 46, No. 2, 2004, pp. 325–328.
Original Russian Text Copyright © 2004 by Yakushkin.

MAGNETISM AND FERROELECTRICITY

Heat Capacity of the SBN Relaxor Ferroelectric

E. D. Yakushkin

Shubnikov Institute of Crystallography, Russian Academy of Sciences, Leninskiĭ pr. 59, Moscow, 117333 Russia
e-mail: yakushkin@ns.crys.ras.ru

Received June 10, 2003

Abstract—The temperature dependence of the heat capacity of the single-crystal relaxor ferroelectric SBN was studied. Hysteresis and a "two-level" effect were observed near the temperature of the dielectric permittivity maximum. © *2004 MAIK "Nauka/Interperiodica".*

Relaxor ferroelectrics have been studied intensively over recent years, and their main properties and qualitative differences from conventional ferroelectrics have been mainly determined. At the same time, some points of a rather fundamental nature, though being specific, remain unclear, including what the true probability distributions of states and energy levels are, what the origin of the transition between states with an ergodic and nonergodic behavior is, in what way the domain structure evolves, whether the conclusions concerning the fractal geometry of nanodomain walls have been substantiated enough, etc. There is no certainty in the choice of an adequate model for these systems either. All this calls for further comprehensive studies, in particular, of the heat capacity, a quantity connected intimately with the whole spectrum of the degrees of freedom. Moreover, it is measurements of the temperature dependence of the heat capacity that should provide the ultimate answer to the question as to whether or not the transition to the relaxor state is a thermodynamic phase transition. Here, we discuss a study of the barium–strontium niobate relaxor ferroelectric. This study was reported earlier and is apparently the first investigation of its kind [1].

The dielectric permittivity of crystalline solid solutions of barium–strontium niobate passes through a maximum at 310–350 K (depending on the actual composition), which is a convenient temperature region for dielectric studies. Studies of the thermal behavior of this relaxor ferroelectric turned out, however, to be fairly complicated by the fact that the observed effects depend on the measurement time and thermal history of the sample under investigation and do not greatly exceed the attainable experimental accuracy. Nevertheless, some relations could be established.

We studied a $Sr_xBa_{1-x}Nb_2O_6$ (SBN) single crystal with $x = 0.61$ doped with La and Ce to concentrations of 0.44 and 0.023 at. %, respectively (the SBN single crystal was grown by L. Ivleva at GPI, RAS). The maximum in the quasi-static dielectric permittivity of this single crystal was reached at $T_m \approx 310$ K. The sample prepared for the heat capacity measurements was cut from a single crystal used earlier in comprehensive studies of the polarization relaxation in an external electric field [2]. The heat capacity was measured using modulation calorimetry. This method makes use of a variable heat flux Q, and the heat capacity is derived from the relation

$$C_p \sim \frac{Q_0}{\omega \Delta T_0}, \quad Q \sim \exp[i\omega t], \tag{1}$$

where ΔT_0 is the measured amplitude of temperature oscillations, Q_0 is the part of the heat flux that is absorbed, and ω is its modulation frequency. This frequency is necessarily chosen (from measurements of the $\Delta T_0(\omega)$ relation) such that $\Delta T_0 \sim 1/\omega$, thus ensuring that relation (1) holds. This means essentially that the temperature in the sample levels off in a time shorter than $1/\omega$ and that the heat is removed in a substantially longer time. The latter condition reduces the effect of the sample holder in the thermostat to a minimum (the condition of quasi-adiabaticity). The optimum modulation frequency $\omega/2\pi$ for the sample used in our studies, $2 \times 2 \times 0.2$ mm in size and about 5 mg in mass, was 1.7 Hz. The quantity Q_0 was not determined in our experiments; only the relative variation of the heat capacity was measured to within ≤0.1%. The measurements were performed in both the heating and cooling runs under stabilization of the average sample temperature. It is essential for what follows that the variation of the temperature in the thermostat and the establishment of the average sample temperature lasted for a time substantially shorter than the time taken for a single measurement.

Figure 1 displays the temperature dependence of the heat capacity of the SBN single crystal obtained within a broad temperature range in a cooling run. The deviation of the experimental points from the calculated phonon heat capacity (dashed line in Fig. 1) within an interval of ~100 K in the vicinity of T_m demonstrates the existence of an excess heat capacity. The inset to Fig. 1 shows, on a slightly modified scale, the results obtained in the heating–cooling–heating mode, which

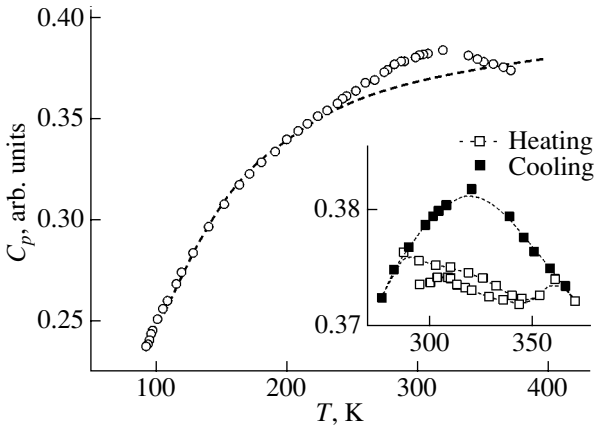

Fig. 1. Temperature dependence of the heat capacity of an SBN single crystal (dashed line is a fit with Eq. (4)). Inset shows the heat capacity obtained under thermal cycling.

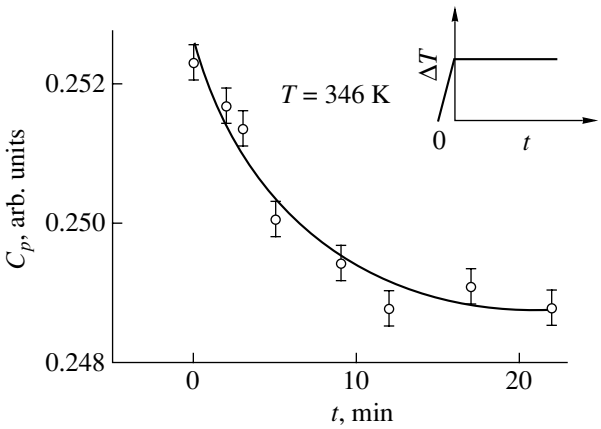

Fig. 2. Heat capacity relaxation of an SBN single crystal for $T > T_m$.

clearly reveal a temperature hysteresis. The maximum value of the excess heat capacity depends substantially on two parameters, the duration of a single measurement t_0 and the rate of sample temperature variation dT/dt. The experiment showed that the excess heat capacity is observed for $dT/dt \le 0.1$ K/min and $t_0 \ge 10$ min. It is in these conditions that the relation plotted in Fig. 1 was obtained. The excess heat capacity was found to be ~2%.

Relaxation of the heat capacity under thermal cycling of the sample was observed clearly only in the heating mode. Figure 2 shows the time variation of the heat capacity for $T > T_m$ following a single heating by ~3 K. The solid line in Fig. 2 plots an exponential $C_p(t) \sim \exp[-t/\tau]$ with $\tau \sim 10$ min. On longer time scales, a more complex prolonged relaxation and a nonexponential $C_p(t)$ behavior can be observed. However, this is not seen at the attainable accuracy of heat capacity measurements; likewise, a dependence of the heat capacity on time for $T < T_m$ is also not observed. As follows from general features in the behavior of nonergodic systems, the measurement results should depend on the time a sample is maintained at $T > T_m$ and $T < T_m$, i.e., on the ageing time; however, the times available in our experiments, as well as the measurement precision attained, do not warrant any conclusions of this type.

Remarkably, it is in the cooling mode that the SBN crystal reveals an excess heat capacity (or it is the largest in this case). This situation differs from the one observed in such fundamentally nonergodic systems as glasses; indeed, the anomaly in the heat capacity found under conventional glass formation follows a reverse hysteresis, because destruction of the glass state takes up a larger amount of heat. A similar pattern is observed to occur in spin glasses as well. At the same time, the dependence of the excess heat capacity on the rate of temperature variation measured in the SBN relaxor ferroelectric is in no way unique and, for instance, resembles that observed under structural vitrification of polymers [3]. Qualitatively, this becomes clear already from an analysis of the standard thermodynamics of a system consisting of two components, N_0 and N_1, which can transform into each other. For the SBN relaxor ferroelectric, these components may be ordered nanodomains and disordered microregions residing at quasi-equilibrium ($dN_0 = -dN_1 = dN$). Thus, if the enthalpy of the system is $H = H(T, p, N)$, then the heat capacity is given by

$$C_p = C_{p,N} + \left(\frac{\partial H}{\partial N}\right)_{T,p}\left(\frac{\partial N}{\partial T}\right), \qquad (2)$$

and the variation of configurational heat capacity, including the evolution of $N(t)$, is

$$\Delta C_p = \left(\frac{\partial H}{\partial N}\right)_{T,p}\left(\frac{dN}{dt}\right)\left(\frac{dT}{dt}\right)^{-1}. \qquad (3)$$

The quantity $\partial H/\partial N$ is an implicit function of time, and Eq. (3) actually describes the relaxation heat capacity. As is evident from Eqs. (2) and (3), if the rate of variation of nanodomain order dN/dt is much less than that of the temperature, then the configurational heat capacity is small and $C_p \approx C_{p,N}$. In the case where the temperature variation is slow enough, the quasi-static heat capacity is determined and the excess heat capacity can be analyzed quantitatively for any observation time longer than the characteristic relaxation times.

We determined the excess heat capacity as the difference between the measured heat capacity and the calculated phonon heat capacity, $\Delta C_p = C_p - C_p^0$. The phonon contribution to the total heat capacity was derived from the low-temperature experimental points and approximated by the sum of the Debye (D) and Einstein (E) functions

$$C_p^0 \sim [D(\Theta_D/T) + E(\Theta_E/T)], \qquad (4)$$

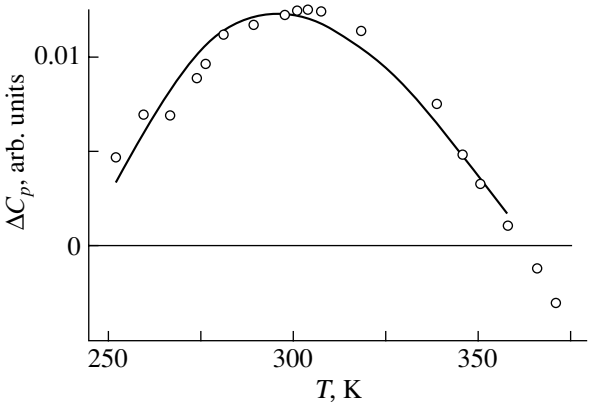

Fig. 3. Excess heat capacity of an SBN single crystal in the vicinity of T_m (solid line is a fit with Eq. (5)).

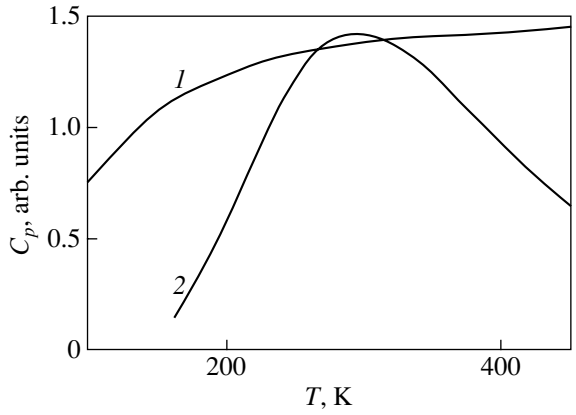

Fig. 4. Temperature dependences of (*1*) the phonon and (*2*) excess heat capacities calculated from Eqs. (4) and (5), respectively.

where Θ_D and Θ_E are the characteristic Debye and Einstein temperatures. For the Debye function, we used an expansion in powers of Θ_D/T. The dashed line in Fig. 1 is a least squares fit of Eq. (4). We readily see that, within a fairly broad temperature interval outside the T_m region, the model relation (4) adequately describes the experimental data. The values of the parameters Θ_D and Θ_E are ~310 and ~280 K, respectively. The deviations of the measured heat capacity from its calculated phonon part observed within a broad temperature region in the vicinity of T_m actually represent the excess heat capacity.

The pattern of the heat capacity anomaly $\Delta C_p(T)$ isolated in this way (Fig. 3) makes it possible to consider it as a manifestation of two-level states (the so-called Schottky anomaly). Two-level systems may in this case be both nanodomains separated by an energy barrier ΔE and certain atoms (groups of atoms) capable of occupying two structurally equivalent positions. Both versions are in line with the present-day concepts of the SBN relaxor ferroelectric [4]. Obviously enough, such two-level (or multilevel) systems allowing thermally activated transitions may account for the dielectric relaxation near T_m as well. In terms of the two-level model, the heat capacity anomaly can be written as (see, e.g., [5])

$$\Delta C_p \sim \left(\frac{\Delta E}{kT}\right)^2 \frac{\exp\left(\frac{\Delta E}{kT}\right)}{\left(1 + D\exp\left(\frac{\Delta E}{kT}\right)\right)^2}, \qquad (5)$$

where D is the ratio of the numbers of low-energy and high-energy states. Figure 3 presents a standard least squares fit of Eq. (5) to the heat capacity anomaly. The model parameters found in this manner are $D \approx 0.03$ and $\Delta E \approx 0.1$ eV. For $\ln(D^{-1}) \gg 1$, the temperature at which the excess heat capacity is maximal can be estimated as $T_m \sim \Delta E/\ln(D^{-1}) \approx 320$ K. While the experiment agrees fairly well with the calculated curve, this agreement, as well as the above numerical estimates, should be considered as having only a qualitative significance in view of the smallness of the experimentally determined quantity ΔC_p.

In view of the multilevel states characteristic of a relaxor ferroelectric, a more appropriate expression for the excess heat capacity should be

$$\Delta C_p \sim \int_0^{E_{\max}} n(E) f(E/kT) dE, \qquad (6)$$

where $n(E)$ is the distribution function of the relevant states (and, accordingly, of the relaxation times). A comparison of the experimental data with functional (6) would be, however, not only difficult to perform but also unreasonable, because the $n(E)$ function itself is implicitly dependent on time and the two-level states contributing to the heat capacity anomaly are only those for which the time of transition τ is shorter than the measurement time, $t_0 > \tau \sim \exp(\Delta E/kT)$. Thus, the use of Eq. (5) in this case is valid. The quantity ΔE found in this way is obviously the average height of the barrier separating these states. The barrier ΔE and, accordingly, the relaxation time depend on the volume of the ordered regions (similar to the situation in superparamagnets) and, thus, determine both the measurement duration and the temperature variation rate. The temperature hysteresis observed in the heat capacity measurements can originate from the asymmetry of a two-level system; namely, under cooling, the effective height of the barrier is lower for a transition from the high-energy to the low-energy state.

Note that the qualitative character of the comparison of the experimental data with Eq. (5) is also accounted for by the fact that in this region of fairly high temperatures the "two-level anomaly" in the heat capacity is masked by the large phonon contribution. This is evi-

dent from Fig. 4, which plots the temperature dependences of the heat capacity calculated for a broad range of temperatures using model relations (4) and (5) with the above parameters.

Thus, the character of the observed dependence of the excess heat capacity of the SBN relaxor ferroelectric on temperature and time convincingly demonstrates the absence of any thermodynamic phase transition near the temperature of the maximum in dielectric permittivity. The concept of a diffuse phase transition for the SBN relaxor ferroelectric is not thermodynamically valid either. The nanostructural nonuniformity of this compound contributes to the heat capacity only under certain thermal and temporal measurement conditions. This makes experimental observation of the corresponding heat capacity anomaly an artifact in a certain sense and may obviously impose a constraint on the application potential of barium–strontium niobate single crystals.

ACKNOWLEDGMENTS

This study was supported by the Russian Foundation for Basic Research, project no. 02-02-16823.

REFERENCES

1. E. D. Yakushkin, in *Abstracts of the 7th Symposium on Ferroelectricity (RCBJSF-7)* (St. Petersburg, 2002), p. 166.
2. V. V. Gladkiĭ, V. A. Kirikov, and T. R. Volk, Fiz. Tverd. Tela (St. Petersburg) **44** (2), 351 (2002) [Phys. Solid State **44**, 365 (2002)].
3. B. Wunderlich and H. Baur, *Heat Capacities of Linear High Polymers* (Springer, Berlin, 1970; Mir, Moscow, 1972), p. 147.
4. L. E. Cross, Ferroelectrics **76**, 241 (1987).
5. L. D. Landau and E. M. Lifshitz, *Course of Theoretical Physics*, Vol. 5: *Statistical Physics*, 3rd ed. (Nauka, Moscow, 1976; Pergamon, Oxford, 1980).

Translated by G. Skrebtsov

Physics of the Solid State, Vol. 46, No. 2, 2004, pp. 339–344. Translated from Fizika Tverdogo Tela, Vol. 46, No. 2, 2004, pp. 329–334.
Original Russian Text Copyright © 2004 by Shmyt'ko, Afonikova, Arnautova.

MAGNETISM AND FERROELECTRICITY

Anomalous States of the Structure of $[Rb_{0.7}(NH_4)_{0.3}]_2SO_4$ Crystals in the Temperature Range 4.2–300 K

I. M. Shmyt'ko, N. S. Afonikova, and E. A. Arnautova

Institute of Solid-State Physics, Russian Academy of Sciences, Chernogolovka, Moscow oblast, 142432 Russia
e-mail: shim@issp.ac.ru

Received May 19, 2003; in final form, July 16, 2003

Abstract—Crystals of $[Rb_{0.7}(NH_4)_{0.3}]_2SO_4$ solid solutions are studied using x-ray diffractometry in the temperature range 4.2–300 K. No anomalies are revealed in the temperature dependences of the lattice parameters and the volume of the host unit cell. A series of superstructure reflections observed along the basis axes corresponds to the guest lattice formed in the matrix of the host structure. From analyzing the axial ratio of these structures and their temperature dependences, it is concluded that the structure of the crystal has the form of an incommensurate composite. The guest structure of the composite at room temperature can be considered a set of chains that are not correlated along the **b** direction. In the plane perpendicular to the chain axes, these chains form a regular framework that is also incommensurate to the host lattice. © *2004 MAIK "Nauka/Interperiodica".*

1. INTRODUCTION

At present, the notion of aperiodic crystals has been widely used in the literature. Apart from quasicrystals and incommensurately modulated phases, this notion refers to crystalline composites or incommensurate intergrowth compounds. The first representative of this family of aperiodic crystals, namely, $Hg_{3-\delta}AsF_6$, was discovered in 1974 [1–3]. The structure of this compound consists of two nonequivalent (host and guest) substructures. The host substructure is composed of AsF_6 groups, which, in turn, form a basis tetragonal lattice with free channels along the **a** and **b** directions. These noncrossing channels contain chains of Hg atoms whose period does not coincide with the lattice spacing of the host structure (for the host structure, the lattice parameter $a = b = 7.54$ Å does not amount to three Hg–Hg distances, which are equal to 7.92 Å inside the chain). Therefore, the substructure consisting of Hg–Hg atoms (guest substructure) is incommensurate to the host substructure composed of AsF_6 groups.

More recently, many new composites were discovered and described (see, for example, review by van Smaalen [4]). There are three types of incommensurate composite structures. Composites of the first type have channels structures similar to the structure of the $Hg_{3-\delta}AsF_6$ compound. The second type can be described as structures with two sorts of columns that are packed parallel to each other and have different periodicities inside the columns. Structures of the third type belong to so-called layered compounds whose structure consists of alternating, chemically different, atomic layers. Composites of all the above types are composed of several chemical elements. It should be noted that elemental composites represented by high-pressure phases of Ba, Sr, Bi, and Rb [5–8] have also been discovered in the last few years.

The main feature of the incommensurate composites known prior to our investigations is that they are all incommensurate only along one crystallographic direction (or several symmetrically equivalent directions) specified by the direction of the channels, columns, or packing. In crystals of rubidium ammonium sulfate solid solutions of the general formula $[Rb_x(NH_4)_{1-x}]_2SO_4$ (x = 0.0, 0.1), we discovered a new fourth type of composite structure. The distinguishing characteristic of this type of composite structure is that the host and guest substructures are incommensurate along three independent directions [9, 10]. It was shown that crystals of pure ammonium sulfate undergo a sequence of thermally stimulated structural transformations from incommensurate structures into commensurate (along one of the crystallographic directions) composite structures. The last circumstance is of considerable importance, because it makes it possible to obtain the nonstructural characteristics necessary for elucidating the physical mechanism of formation of crystalline composite phases in these compounds. In particular, the stability of commensurate phases at low temperatures and their transformation into incommensurate phases with an increase in the temperature indicate that the composite structures are thermally activated. For pure ammonium sulfate, the characteristic energy of interaction between the host and guest substructures is approximately equal to 0.01 eV.

1063-7834/04/4602-0339$26.00 © 2004 MAIK "Nauka/Interperiodica"

Lattice parameters of $[Rb_{0.7}(NH_4)_{0.3}]_2SO_4$ crystals (space group *Pnma*) at 300 K

a, Å Δa	*b*, Å Δb	*c*, Å Δc	α, deg $\Delta\alpha$	β, deg $\Delta\beta$	γ, deg $\Delta\gamma$
7.8261	10.4517	5.9738	90.027	90.009	89.957
0.0013	0.0015	0.0004	0.008	0.009	0.012

It was also established that the axial ratios of coexisting substructures considerably change even in crystals with a rather low rubidium content of 10%. In this respect and taking into account that crystals with a rubidium content in the range $0 < x < 0.6$ undergo low-temperature ferroelectric phase transitions, it was of interest to investigate the real structure of crystals of the above family with the aim of analyzing the possibility of forming incommensurate composite phases in compounds whose properties do not exhibit temperature anomalies. The $[Rb_{0.7}(NH_4)_{0.3}]_2SO_4$ crystal was chosen as the object of our investigation.

2. SAMPLE PREPARATION AND EXPERIMENTAL TECHNIQUE

The quality of the studied samples was controlled using the traditional Laue and rolling-crystal methods. The determination of the space symmetry group and measurements of the unit cell parameters were performed on a Rigaku AFC6S diffractometer (MoK_α radiation) at room temperature. For x-ray diffraction analysis, samples were prepared in the form of balls ~0.25–0.35 mm in diameter. The angular distribution of substructure elements of the samples (ω scan mode) did not exceed 0.1°. The measured lattice parameters of $[Rb_{0.7}(NH_4)_{0.3}]_2SO_4$ crystals at room temperature are presented in the table.

The superstructure reflections were measured on a Siemens D500 x-ray diffractometer. The diffractometer was modified using special programs with the aim of recording one-dimensional and two-dimensional reciprocal lattice maps of the single-crystal sections. The samples were prepared in the form of parallelepipeds $2 \times 3 \times 3$ mm in size with faces parallel to the basal planes of the unit cell. This made it possible to perform measurements for different crystallographic sections with the same sample.

The low-temperature precision measurements of the unit cell parameters were carried out in the range 4.2–300 K with the use of a helium cryostat designed at the Institute of Solid-State Physics, Russian Academy of Sciences [11, 12].

3. RESULTS AND DISCUSSION

Figure 1 shows the characteristic one-dimensional sections of the reciprocal lattice of the $[Rb_{0.7}(NH_4)_{0.3}]_2SO_4$ crystal along the basis axes. It can be seen from this figure that, along all the basis axes, the main reflections are accompanied by satellite reflections. The positions of the main and satellite reflections correspond to the two coexisting substructures (host and guest, respectively). At room temperature, the lattice parameters of these substructures are as follows:

$$a_{host} = 7.826 \text{ Å}, \quad a_{guest} = 7.429 \text{ Å},$$
$$(a_{host}/a_{guest}) = 1.053;$$

$$b_{host} = 10.452 \text{ Å}, \quad b_{guest} = 10.711 \text{ Å},$$
$$(b_{host}/b_{guest}) = 0.976;$$

$$c_{host} = 5.974 \text{ Å}, \quad c_{guest} = 6.607 \text{ Å},$$
$$(c_{host}/c_{guest}) = 0.904.$$

It was revealed that, for the host substructure, the (100), (300), and (700) reflections have a finite intensity, even though these reflections are forbidden by the symmetry of space group *Pnma*. At the same time, the guest substructure is characterized only by the (300) reflection. The (500) reflection is absent for both the host and guest substructures. It is significant that the integrated intensity ratio $|(300)_{guest}/|(300)_{host}$ for the (300) forbidden reflection is considerably larger than the integrated intensity ratios $|(200)_{guest}/|(200)_{host}$ and $|(400)_{guest}/|(400)_{host}$ for the (200) and (400) allowed reflections. The above characteristics clearly demonstrate the differences in the atomic structure and symmetry of the coexisting (host and guest) substructures and justify the term "incommensurate intergrowth compounds," which is frequently used for this class of aperiodic crystals.

The temperature dependences of the lattice parameters and the unit cell volume of the host substructure are depicted in Fig. 2. It can be seen that structural anomalies are absent in the range 4.2–300 K. A substantial change in the thermal expansion coefficients in the range 4.2–50 K is not specific to crystals belonging to the ammonium sulfate family and merely corresponds to the freezing of anharmonic atomic vibrations at low temperatures, which is observed for all materials. A similar behavior of the structural parameters is also characteristic of the guest substructure. As an illustration, Fig. 3 shows the diffracted intensity distributions of the Bragg and satellite reflections at different temperatures. The constancy of the relative positions of these reflections with a variation in the temperature confirms the absence of structural anomalies in the guest substructure, on the one hand, and indicates that the studied composite is commensurate along the **a*** direction, on the other hand. From the relationship $Na_{host} = (N + m)a_{guest}$, we obtain $N = 75$, $m = 4$, and the distance $L_a = N \times a_{host} = 586.96$ Å at which the host and guest substructures most closely approach each other

along the **a** axis. For the **b** and **c** axes, we have $N = 161$, $m = 4$, and $L_b = 1724.53$ Å and $N = 66$, $m = 7$, and $L_c = 436.06$ Å, respectively.

In order to investigate the real structure of the composite phase in more detail, we measured two-dimensional reciprocal lattice maps in the vicinity of the characteristic points. Figure 4 shows the reciprocal lattice maps corresponding to the one-dimensional reciprocal lattice sections depicted in Figs. 1a and 1b. First and foremost, it is worth noting that, for the (050) reflection, there are two satellites in the form of rods perpendicular to the vector **b*** of the reciprocal lattice (Fig. 4b).[1] The coexistence of two satellites and one Bragg reflection suggests that the composite structure consists of one host substructure and two guest substructures, namely, the guest$_1$ and guest$_2$ substructures. The rodlike satellites in the reciprocal space correspond to the guest substructures in the real space. These substructures have the form of disordered periodic chains lying along the *b* direction with periods $b_{\text{guest1}} = 10.711$ Å and $b_{\text{guest2}} = 10.46$ Å. A similar chain structure of guest substructures was observed earlier in high-pressure phases of Ba, Bi, Sr, Rb, etc. [5–8]. The distinguishing feature of the $[Rb_{0.7}(NH_4)_{0.3}]_2SO_4$ crystal as compared to the aforementioned single-component, high-pressure, composite phases is that the two guest structures incommensurate to the host matrix coexist along one direction.

The behavior of the rodlike reflections with a variation in the temperature is illustrated in Fig. 4c, which shows the diffracted intensity distribution in the vicinity of the (050) point upon cooling of the sample to a temperature of 224 K. It can be seen from Fig. 4c that the intensity of the rodlike guest reflections decreases significantly, their width along the basis axis is small, and the intensity of the host reflection increases appreciably. It is characteristic that a decrease in the intensity of the guest$_1$ and guest$_2$ reflections is attended by a change in the their positions with respect to the position of the host reflection along the **b*** direction. This circumstance indicates that the composite is actually incommensurate along the **b*** direction. It is interesting to note that, owing to the low intensity, the satellite guest reflections are not observed at all in the one-dimensional diffraction patterns at 224 K (Fig. 5). A further decrease in the temperature leads to the complete disappearance of rodlike satellite reflections in the reciprocal lattice maps.

The subsequent heating to room temperature did not lead to the appearance of satellites (at least, during the recording of the diffraction patterns over a period of several hours). Moreover, even after heating above room temperature (to ~40°C), the crystal did not revert to the original state. The initial intensity distribution of rodlike guest reflections was recovered only in the course of subsequent long-term holding of the sample at room temperature (for one and a half days).

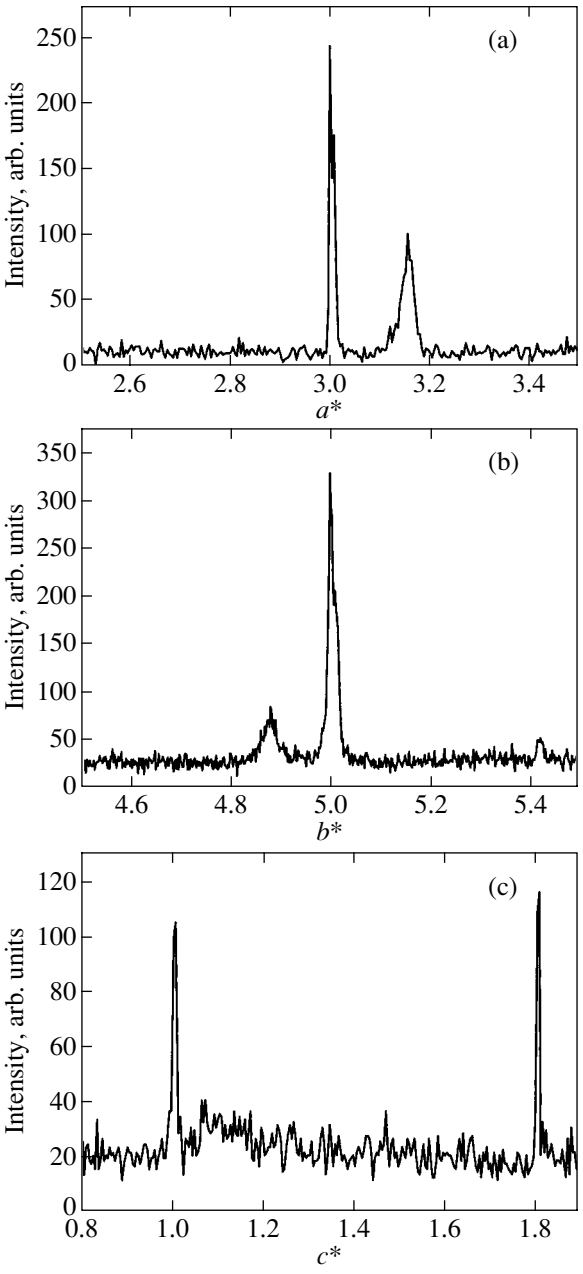

Fig. 1. Diffracted intensity distributions along the basis axes of the reciprocal lattice in the vicinity of the (a) (300), (b) (050), and (c) (002) points.

These observations clearly demonstrate that the formation of the composite phase proceeds through the thermally activated mechanism. At the first stage, the process involves the formation of periodic atomic chains. We assume that, with a further increase in the temperature, these chains are ordered to form a three-dimensional guest structure. This brings up a question

[1] The absence of the second satellite in the immediate vicinity of the (050) point in the one-dimensional section is explained by the fact that the intensity of this satellite is relatively low and its position almost coincides with the Bragg position along the direction of the reciprocal lattice vector at room temperature.

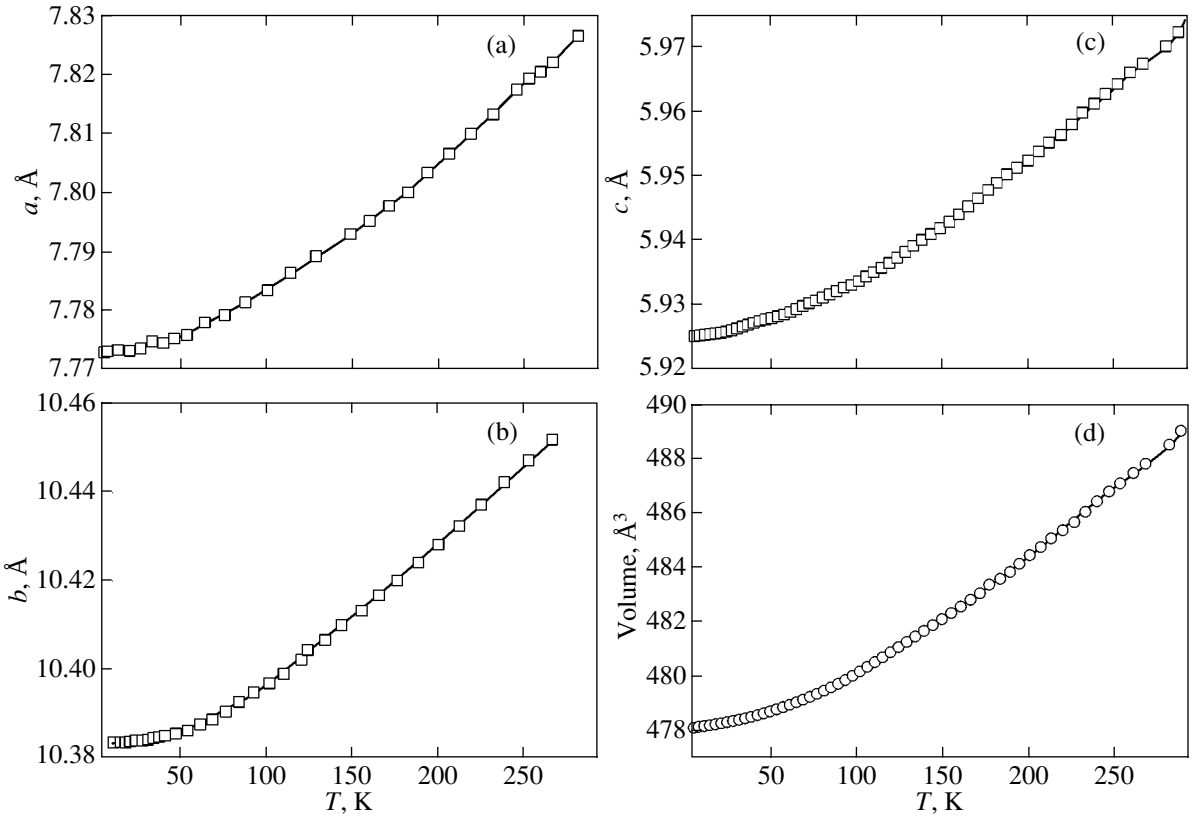

Fig. 2. Temperature dependences of the lattice parameters (a) *a*, (b) *b*, and (c) *c* and the temperature dependence of (d) the unit cell volume of the host structure.

as to the structural state of incommensurate composite phases at high temperatures, namely, whether these phases exist up to premelting temperatures or only in a limited (from above) temperature range. If the latter assumption holds true, the question arises as to the structural mechanism of high-temperature transition from the composite phase to the normal phase.[2]

It is also of interest to elucidate the mechanism of formation of initial atomic chains: whether statistically distributed point defects are originally formed in sites of future chains and, after reaching a sufficient concentration, make up these chains or an increase in the temperature brings about the immediate formation of chains. The results presented in this work provide answers to these questions. Indeed, a decrease in the temperature leads to a decrease in the intensity of rodlike satellites without changing their half-widths. In our opinion, this behavior corresponds to the mechanism of immediate formation of periodic chains from atoms (or atomic groups) rather than to the mechanism of ordering of point defects into chains. If the chains were to be formed through the ordering of point defects, we would initially observe smeared shifted diffuse reflections, which, with an increase in the temperature, would

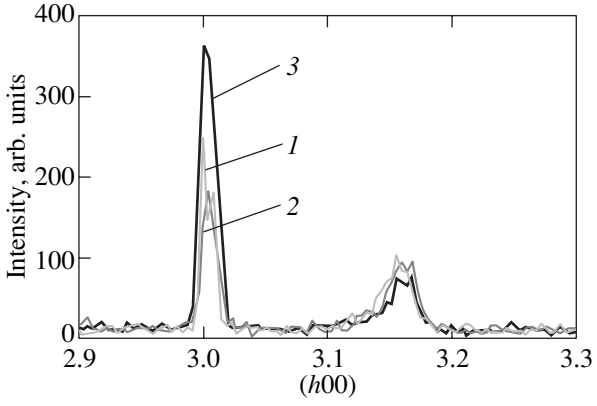

Fig. 3. Diffracted intensity distributions of the Bragg and satellite reflections in the vicinity of the (300) point at different temperatures *T* (K): (*1*) $T = T_{room}$, (*2*) 250, and (*3*) 118.

[2] Unfortunately, the technical capabilities of the cryostat were inadequate to provide an increase in the sample temperature above 50°C; hence, we failed to examine the dynamics of the composite structure at higher temperatures. In the immediate future, we intend to carry out these investigations with the use of a special medium-temperature chamber that makes it possible to perform x-ray diffraction experiments in the temperature range 300–700 K.

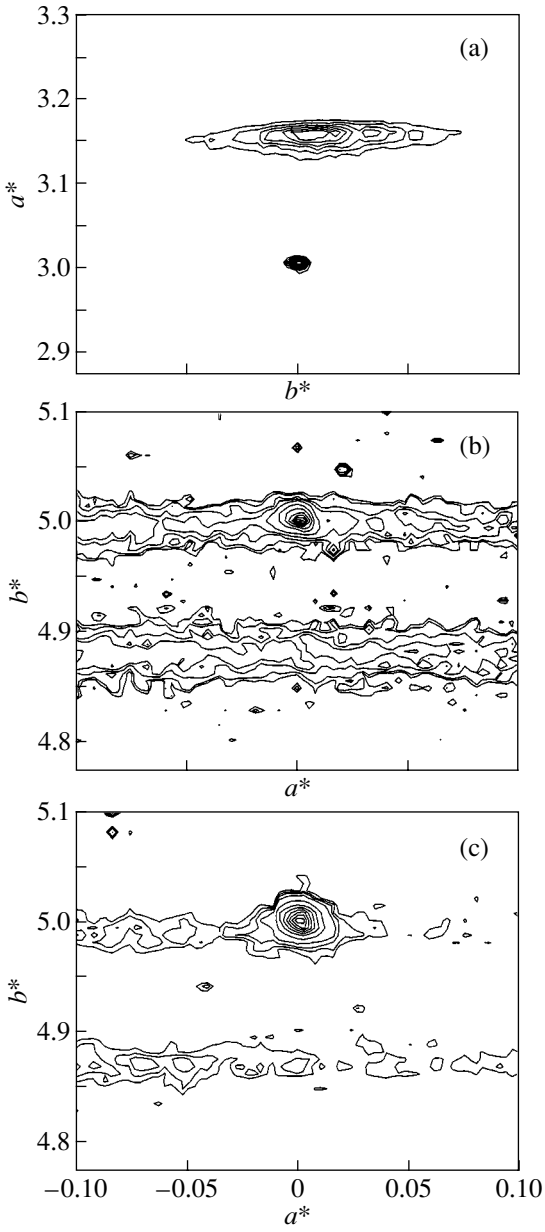

Fig. 4. Reciprocal lattice maps in the vicinity of the (a) (300) and (b, c) (050) points at temperatures of (a, b) 293 and (c) 224 K.

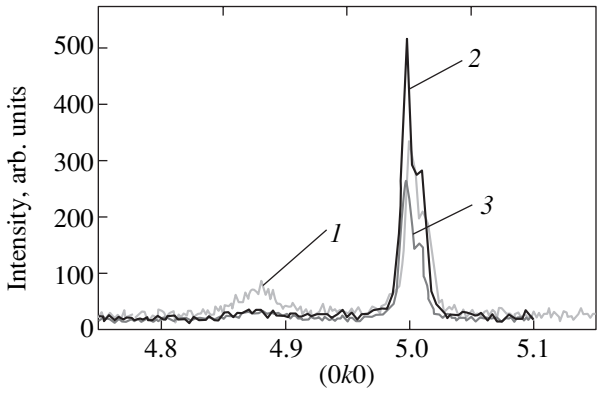

Fig. 5. Diffracted intensity distributions of the Bragg and satellite reflections in the vicinity of the (050) point upon cooling and heating: (*1*) at 293 K prior to cooling, (*2*) upon cooling to 224 K, and (*3*) upon heating to 317 K.

transform into rods due to narrowing along the reciprocal lattice vector and lengthening in the direction perpendicular to this vector.

For the purpose of establishing the structural mechanism of formation of incommensurate composite phases in crystals of the $[Rb_x(NH_4)_{1-x}]_2SO_4$ system, it is also important to answer the question as to why the guest reflections have such a very low intensity. For compositions with $x = 0.0$ and 0.1, the low intensity of these reflections could be explained by the low reflection power of (NH_4) groups. However, for the composition with $x = 0.7$, the reflection power of Rb substantially exceeds even the reflection power of SO_4 groups. Taking into account that the relative intensity of satellites with respect to the intensity of Bragg reflections even for pure ammonium sulfate [10] is considerably higher than that for the crystal with $x = 0.7$ (for example, $|(002)_{guest}/|(002)_{host} = 5.6 \times 10^{-2}$ for $(NH_4)_2SO_4$ and $=2.9 \times 10^{-5}$ for $[Rb_{0.7}(NH_4)_{0.3}]_2SO_4$), we can infer that the guest substructure is formed only by the remaining ammonium groups. This situation becomes possible when rubidium atoms are nonuniformly distributed over the positions of ammonium groups, which should lead to the precipitation of ammonium-enriched clusters followed by the formation of the composite structure. The validity of this model is confirmed by both the low intensity and large angular half-width of the guest reflections along the **a*** and **b*** directions (Figs. 3, 4a). The sizes of the reflecting regions of the guest composite phase along the basis axes can be estimated from the half-width of the θ–2θ diffraction curve under the assumption that the half-width is determined only by the small size of the scattering particles. According to these estimates, the sizes of the reflecting regions along the **a** and **b** axes are equal to 499.54 and 2310.40 Å, respectively.

It should be noted that the large half-width of the reflections along the direction perpendicular to the reciprocal lattice vector can be associated not only with the small sizes of scattering regions. We assume that the chain character of the guest substructure manifests itself not only along the **b** axis but also along the other basis axes. Consequently, partial ordering of chains along these axes should result in the contraction of the rodlike diffracted intensity distribution (which is characteristic of completely disordered chains) toward the center of the reciprocal lattice point. In turn, this should lead to the formation of normal reflections that are broadened in the direction perpendicular to the reciprocal lattice vector. Unfortunately, the structural data obtained are insufficient for making an unambiguous

choice of the model of the real structure of the observed composite states. In order to solve this problem, it is necessary to use direct methods of observing the atomic structure, in particular, high-resolution electron or atomic-force microscopy.

In our opinion, the coexistence of two guest substructures in the same host matrix is an anomalous phenomenon. However, this situation in principle can occur with ammonium sulfate and solid solutions based on ammonium sulfate with rubidium. In actual fact, according to the structural data, ammonium groups occupy two symmetrically inequivalent positions in the unit cell of ammonium sulfate [13, 14]. Making allowance for this fact and assuming that the guest lattice is formed only by ammonium groups, we can expect, in the general case, the formation of two symmetrically inequivalent guest substructures. As was shown earlier for the structure of the compound with $x = 0.1$, the NH_4II group, unlike the NH_4I group, is strongly localized and occupies a region with a relatively low background electron density in the unit cell.[3] We believe that this circumstance provides the ability of the NH_4II group to occupy different positions and, thus, leads to a substantial difference between the parameters of the $guest_2$ and host lattices. In turn, different arrangements of the NH_4I group are confined by a relatively high background electron density in the region where the group is located, which eventually leads to close parameters of the $guest_1$ and host lattices along the **b*** direction.

4. CONCLUSIONS

Thus, the results obtained in our investigation showed that the structure of the $[Rb_{0.7}(NH_4)_{0.3}]_2SO_4$ crystal, like the previously studied $[Rb_{0.1}(NH_4)_{0.9}]_2SO_4$ and $(NH_4)_2SO_4$ crystals, can be represented in the form of a three-dimensional incommensurate composite over a wide range of temperatures. The distinguishing feature of the composite structure of the $[Rb_{0.7}(NH_4)_{0.3}]_2SO_4$ crystal is that the two guest substructures with different lattice parameters along the **b*** direction coexist in the host structure. The assumption was made that both guest substructures are formed by ammonium groups located at symmetrically inequivalent positions in the unit cell. It was clearly demonstrated that the formation of composite structures is a thermally activated process. This process initially leads to the formation of randomly arranged periodic atomic chains, which, upon further heating, are hypothetically ordered into regular three-dimensional structures.

[3] The results of the structure solution and the electron density maps for the compound with $x = 0.1$ at 300 and 200 K will be published in a separate paper.

REFERENCES

1. I. D. Brown, B. D. Cutforth, C. G. Davies, *et al.*, Can. J. Chem. **52**, 791 (1974).
2. J. M. Hastings, J. P. Pouget, G. Shirane, *et al.*, Phys. Rev. Lett. **39** (23), 1484 (1977).
3. A. J. Schultz, J. M. Williams, N. D. Miro, *et al.*, Inorg. Chem. **17** (3), 646 (1978).
4. S. van Smaalen, Crystallogr. Rev. **4**, 79 (1995).
5. R. J. Nelmes, D. R. Allan, M. I. McMahon, and S. A. Belmonte, Phys. Rev. Lett. **83**, 4081 (1999).
6. M. I. McMahon, T. Bovornratanaraks, D. R. Allan, *et al.*, Phys. Rev. B **61** (5), 3135 (2000).
7. M. I. McMahon, O. Degtyareva, and R. J. Nelmes, Phys. Rev. Lett. **85** (23), 4896 (2000).
8. M. I. McMahon, S. Rekhi, and R. J. Nelmes, Phys. Rev. Lett. **87** (5), 055501-1 (2001).
9. I. M. Shmyt'ko, N. S. Afonnikova, and V. I. Torgashev, Fiz. Tverd. Tela (St. Petersburg) **44** (11), 2069 (2002) [Phys. Solid State **44**, 2165 (2002)].
10. I. M. Shmyt'ko, N. S. Afonnikova, and V. I. Torgashev, Fiz. Tverd. Tela (St. Petersburg) **44** (12), 2204 (2002) [Phys. Solid State **44**, 2309 (2002)].
11. L. S. Kruts, G. S. Med'ko, and I. M. Shmyt'ko, USSR Inventor's Certificate No. 993,220.
12. I. M. Shmyt'ko, N. Ya. Donchenko, S. S. Klimyuk, *et al.*, USSR Inventor's Certificate No. 1,148,452.
13. K. Hasebe and S. Tanisaki, J. Phys. Soc. Jpn. **42** (2), 568 (1977).
14. K. Hasebe, J. Phys. Soc. Jpn. **50** (4), 1266 (1981).

Translated by O. Borovik-Romanova

Physics of the Solid State, Vol. 46, No. 2, 2004, pp. 345–350. Translated from Fizika Tverdogo Tela, Vol. 46, No. 2, 2004, pp. 335–340.
Original Russian Text Copyright © 2004 by Domashevskaya, Terekhov, Kashkarov, Manukovskiĭ, Turishchev, Molodtsov, Vyalykh, Khokhlov, Mashin, Shengurov, Svetlov, Chalkov.

LOW-DIMENSIONAL SYSTEMS AND SURFACE PHYSICS

Synchrotron Investigations of the Specific Features in the Electron Energy Spectrum of Silicon Nanostructures

É. P. Domashevskaya*, V. A. Terekhov*, V. M. Kashkarov*, É. Yu. Manukovskiĭ*, S. Yu. Turishchev*, S. L. Molodtsov, D. V. Vyalykh***, A. F. Khokhlov****, A. I. Mashin****, V. G. Shengurov****, S. P. Svetlov****, and V. Yu. Chalkov******

** Voronezh State University, Universitetskaya pl. 1, Voronezh, 394693 Russia*

*** Institut für Oberflächen- und Mikrostrukturphysik, Technische Universität, Dresden, Germany*

**** Institut für Experimentalphysik, Freie Universität Berlin, Berlin, Germany*

***** Nizhni Novgorod State University, pr. Gagarina 23, Nizhni Novgorod, 603600 Russia*

e-mail: root@ftt.vsu.ru

Received February 11, 2003

Abstract—The Si $L_{2,3}$ x-ray absorption near-edge structure (XANES) spectra of porous silicon nanomaterials and nanostructures with epitaxial silicon layers doped by erbium or containing germanium quantum dots are measured using synchrotron radiation for the first time. A model of photoluminescence in porous silicon is proposed on the basis of the results obtained. According to this model, the photoluminescence is caused by interband transitions between the energy levels of the crystalline phase and oxide phases covering silicon nanocrystals. The stresses generated in surface silicon nanolayers by Ge quantum dots or clusters with incorporated Er atoms are responsible for the fine structure of the spectra in the energy range of the conduction band edge and can stimulate luminescence in these nanostructures. © *2004 MAIK "Nauka/Interperiodica".*

1. INTRODUCTION

In recent years, crystalline and amorphous materials containing nanoclusters have attracted the particular attention of researchers owing to their unique physical properties. These clusters are characterized by a quasiatomic energy structure of valence electron states, high adsorptive capacity, and reactivity. However, up to now, the main regularities of the evolution of the electronic spectra and physical properties upon changing over to nanoobjects have not been adequately investigated. The specific features of the interaction of nanoclusters with the material of the surrounding matrix used for passivating these clusters and stabilizing their properties are also not clearly understood.

The purpose of this work was to measure and investigate the spectra of the quantum yield of electrons near the $L_{2,3}$ absorption edge with the use of synchrotron radiation both in porous silicon materials with nanoclusters and in nanostructures containing layers with germanium quantum dots or doped with erbium.

As is known, the spectrum of the quantum yield of electrons corresponds to the spectrum of the x-ray absorption near-edge structure (XANES) [1] and reflects the distribution of the local partial density of states. In turn, the local partial density of states corresponds to unoccupied states in the conduction band to within the probability factor, which is equal to the square of the matrix element of the transition of an electron from the ground level to free states in the conduction band [2]:

$$\mu(E) \sim \nu^3 \Sigma_f |M_{fi}|^2 \delta(E_f - E_i - h\nu). \quad (1)$$

Here, $M_{fi} = \int \varphi_f^* H' \varphi_i dr$ is the matrix element of the probability of the transition of an electron from the core level with wave function φ_i and eigenvalue E_i to states in the conduction band with wave function φ_f, H' is the perturbation operator, and $h\nu$ is the energy of the absorbed synchrotron photon.

The measured XANES spectra were compared with the data obtained by ultrasoft x-ray emission spectroscopy (USXES). From analyzing the ultrasoft x-ray emission (USXE) spectra, it is possible to determine the local partial density of occupied states in the valence band of the material:

$$I(E) \sim \nu^3 \Sigma_j |M_{ij}|^2 \delta(E_i - E_j h\nu). \quad (2)$$

Here, $M_{ij} = \int \varphi_i^* H' \varphi_j dr$ is the matrix element of the probability of the transition of an electron from the valence band with wave function φ_j and eigenvalue E_j to a vacancy at the core level with wave function φ_i, H' is the perturbation operator, and $h\nu$ is the energy of the emitted photon.

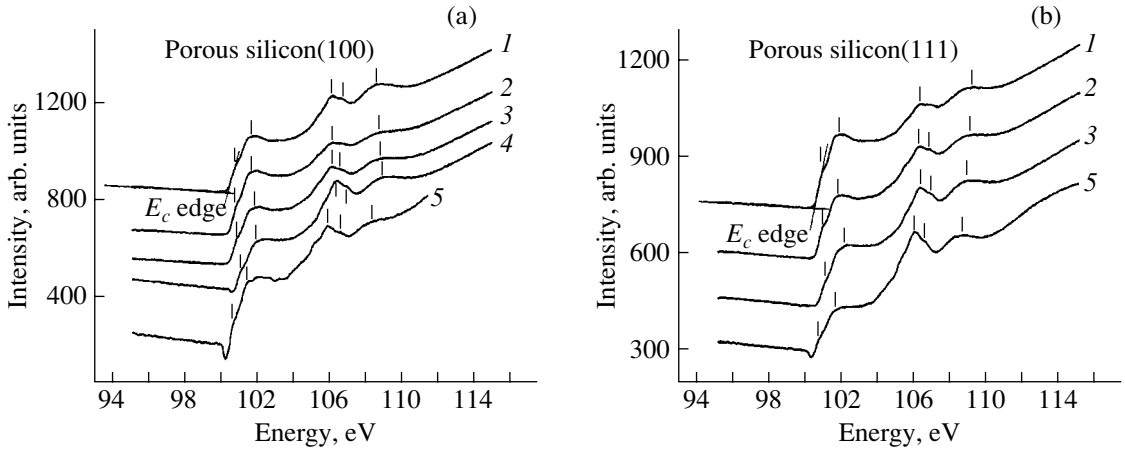

Fig. 1. Si $L_{2,3}$ XANES spectra of the samples of porous silicon on (a) *c*-Si(100) and (b) *c*-Si(111) substrates at different etching times (E_c is the energy at the conduction band bottom). Etching time, min: (*1*) 1, (*2*) 3, (*3*) 5, (*4*) 10, and (*5*) 10 (with subsequent additional etching in HCl).

Comparison of the XANES and USXE spectra on a unified energy scale with respect to the 2*p* core level for the $L_{2,3}$ spectra allows one to estimate the band gap from the partial densities of *s* and *d* states.

In this work, nanomaterials of two types were studied using synchrotron radiation. Samples of the first type consisted of porous silicon prepared by electrochemical etching of single-crystal silicon of two orientations, namely, (100) and (111). Samples of the second type were composed of nanostructures with epitaxial silicon layers doped with erbium or containing germanium quantum dots. These samples were also grown on Si(100) single-crystal substrates.

2. SAMPLE PREPARATION AND EXPERIMENTAL TECHNIQUE

The Si $L_{2,3}$ XANES spectra were measured on the Russian–German beamline at the BESSY II synchrotron. The x-ray optical design of the XANES measurements involved four mirrors with a golden coating and four gratings (600 grs/mm) covered with gold. The energy resolution was 0.03 eV. The thickness of the analyzed layer of the studied samples was limited by the depth of electron escape and did not exceed ~20 nm.

Porous silicon was prepared by standard electrochemical etching of Si(100) and Si(111) single-crystal wafers in an alcohol solution of hydrofluoric acid at different etching times. It is known that the etching time determines the thickness of the porous layer and the mean size of pores in the layer [3]. For example, the mean pore size in the studied samples at an etching time of 10 min and a current density of 15 mA/cm^2 was approximately equal to 2–3 nm. Moreover, upon subsequent treatment (additional etching) of porous silicon in hydrochloric acid, the properties of the material are stabilized and the intensity of photoluminescence in the visible spectral region (1.8–2.2 eV) increases significantly [4].

Silicon nanolayers doped with erbium were grown by sublimation molecular-beam epitaxy [5]. Erbium was evaporated from a clean metal holder by heating under vacuum at a residual pressure of ~2.6×10^{-6} Pa and a temperature of 450–500°C. The growth rate was equal to 0.5 μm/h.

Silicon nanolayers containing germanium quantum dots were grown using a similar technique in a GeH_4 atmosphere on a silicon buffer layer ~100 nm thick. Single-crystal Si(100) was used as a substrate for the nanostructures with Ge quantum dots and epitaxial layers doped with Er.

3. RESULTS AND DISCUSSION

3.1. Porous Silicon

The Si $L_{2,3}$ XANES spectra of porous silicon prepared on *c*-Si(111) and *c*-Si(100) single-crystal substrates are depicted in Fig. 1. For comparison, Fig. 2 shows the Si $L_{2,3}$ XANES spectrum of amorphous hydrogenated silicon *a*-Si:H, which was measured using synchrotron radiation, and also the Si $L_{2,3}$ absorption edges for different silicon oxides, namely, *c*-Si + SiO_2, quartz α-SiO_2, and thermal SiO_2 [6]. The energy positions of the specific features in the XANES spectra with respect to the Si $2p_{1/2,3/2}$ core level are given in Table 1.

The results obtained (Fig. 1, Table 1) demonstrate that the energy features observed in the XANES spectra of the samples of porous silicon prepared on the Si single crystals with (111) and (100) orientations are nearly identical. Comparison of these spectra with the spectra of reference compounds (Fig. 2) shows that surface layers of porous silicon contain three main phases: amorphous silicon, silicon oxide, and crystalline silicon [6].

However, additional etching of porous silicon in an HCl solution results in a substantial transformation of the XANES spectra (Fig. 1). The slope of the spectral curves becomes steeper, and the fine structure of the XANES spectra in the energy range corresponding to the oxide phase is more pronounced. These changes more clearly manifest themselves for the sample of porous silicon on the Si(100) substrate due to an increase in the relative intensity of the Si absorption edge. This is a manifestation of the different types of reactivity of the silicon atoms that occupy nonequivalent positions in the surface layer of porous silicon depending on the orientation of the crystalline substrate subjected to electrochemical etching [7].

In our earlier work [8], we proposed a technique for determining the phase composition of surface layers of porous silicon. This technique consists in decomposing the experimental USXE spectra into reference spectra and comparing the simulated and the experimental spectra. Figure 3 shows the experimental Si $L_{2,3}$ USXE spectra of the porous silicon samples (Fig. 3a) and the reference spectra (Fig. 3b). Table 2 presents the phase compositions determined according to the technique proposed in [8]. As reference spectra in the simulation, we used the Si $L_{2,3}$ USXE spectra of the following phases: crystalline silicon *c*-Si, amorphous hydrogenated silicon *a*-Si:H, slightly coordinated silicon *a*-Si(*lc*) (this phase with a coordination number of ~2.5–3 was observed in amorphous Si films in our previous work [9]), and two silicon oxides (suboxide $SiO_{1.3}$ and silicon dioxide SiO_2). Note that the above phases were chosen from the results of the computer simulation using the data obtained by other methods of studying porous silicon [8].

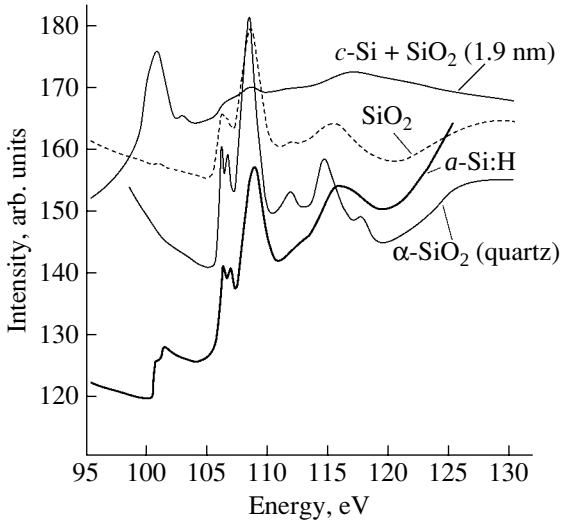

Fig. 2. Si $L_{2,3}$ absorption edges of *c*-Si + SiO_2, SiO_2, and α-SiO_2 (quartz) references samples [6] and the Si $L_{2,3}$ XANES spectrum of *a*-Si:H with inclusions of Si nanocrystals.

According to the USXES data, the porous layer contains the following phases: *a*-Si:H, SiO_2, *c*-Si, *a*-Si(*lc*), and $SiO_{1.3}$. Therefore, in addition to the *c*-Si, *a*-Si:H, and SiO_2 phases found by the XANES method, the USXES method revealed two additional phases,

Table 1. Energy positions of the main features in the XANES and USXE spectra of porous silicon on *c*-Si(100) and *c*-Si(111) substrates

Sample/substrate	Edge, eV		Energy positions of spectral features, eV		
	USXES, E_V	XANES, E_c			
1 min/(111)	99.2	100.3	101.7	106.2; 106.8	109
3 min/(111)	99.5	100.4	101.7	106.1; 106.7	108.9
5 min/(111)	–	100.4	102.0	106.2; 106.8	108.8
10 min, additional etching in HCl/(111)	99.9	100.3	101.8	105.8; 106.4	108.4
1 min/(100)	–	100.2	101.7	106.1; 106.5	108.9
3 min/(100)	–	100.3	101.9	106.2; 106.6	108.8
5 min/(100)	–	100.3	102.0	106.1; 106.7	108.7
10 min/(100)	–	100.5	102.3	106.3; 106.9	109.2
10 min, additional etching in HCl/(100)	–	100.1	102.0	105.8; 106.5	108.5
a-Si:H (Si nanocrystalline inclusions)	99.2	100.2	101.2	106.2; 106.7	108.6
SiO_2	98.5	105.3	–	106.2/106.6	108.7
α-SiO_2	98.5	105.4	–	106.1/106.4	108.2

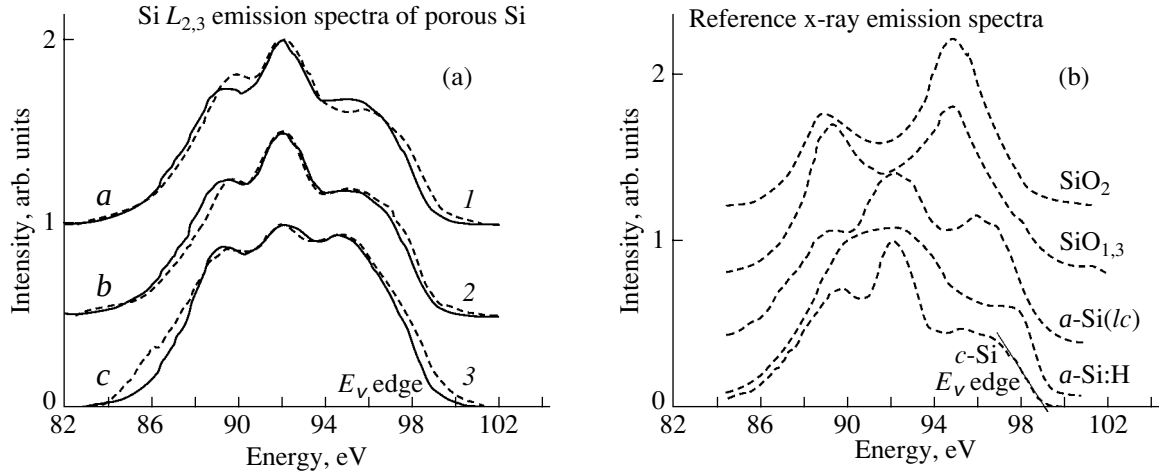

Fig. 3. (a) Si $L_{2,3}$ USXE spectra of the porous silicon samples prepared at etching times of (*1*) 1, (*2*) 2, and (*3*) 10 min. Dashed lines are the experimental spectra, and solid lines represent the simulated spectra. (b) Si $L_{2,3}$ USXE spectra of the reference samples used in the simulation.

namely, slightly coordinated silicon and $SiO_{1.3}$ suboxide.

Comparison of the XANES and USXE spectra shows that porous silicon is a multiphase system formed by silicon nanocrystalline clusters covered with amorphous and oxide phases. Laser excitation of the visible photoluminescence can result in a transfer of electrons from states in the vicinity of the valence band top (98.5 eV) of the oxide phases to states of the silicon conduction band (101–102 eV), which leads to the appearance of a broad luminescence band in the range 1.8–2.4 eV [10]. Analysis of the characteristic features in the XANES and USXE spectra of silicon and silicon oxides (Table 1) shows that there are energy levels for electron transitions between these phases that correspond to the visible photoluminescence of porous silicon.

3.2. Silicon-Based Nanostructures

The Si $L_{2,3}$ XANES spectra of multilayer nanostructures grown on *c*-Si(100) single-crystal substrates are depicted in Fig. 4. We examined multilayer nanostructures of two types under synchrotron radiation. Nanostructures of the first type involved structures with Er-doped epitaxial silicon layers grown by sublimation molecular-beam epitaxy [5]. Nanostructures of the second type consisted of layers with germanium quantum dots, which were grown by sublimation epitaxy in GeH_4. All the studied structures containing quantum dots were covered with a cladding silicon layer ~50 nm thick.

As follows from the results presented in Fig. 4 and Table 3, the spectra of all the nanostructures with layers containing germanium quantum dots and layers doped with erbium exhibit a specific fine structure in the energy range 101–104 eV. This fine structure near the $L_{2,3}$ absorption edge was observed for the first time. The transitions between the energy levels in the conduction band can contribute to the luminescence. Of particular interest is the fact that the spectra of the samples with quantum dots are very similar to the spectra of the nanostructures with erbium-doped layers. It should be remembered that the surfaces of nanostructures of both types are covered with a cladding epitaxial silicon layer ~50 nm thick, whereas the depth of the analyzed layer is approximately equal to 20 nm. This implies that the stresses generated at the boundaries of Ge quantum dots or nanoclusters containing Er extend over the whole cladding layer, provided it is sufficiently

Table 2. Phase composition of the samples of porous silicon on the *c*-Si(111) substrate

Time of etching of the *c*-Si substrate during the preparation of porous Si, min	Depth of USXES data collection, nm	Phase composition of porous silicon samples, %				
		c-Si	*a*-Si:H	*a*-Si(*lc*)	$SiO_{1,3}$	SiO_2
1	10	42.8	6.0	36.8	2.9	11.5
2	10	21.1	40.4	38.0	0.5	0.0
10	18	11.0	15.8	29.0	16.0	22.8

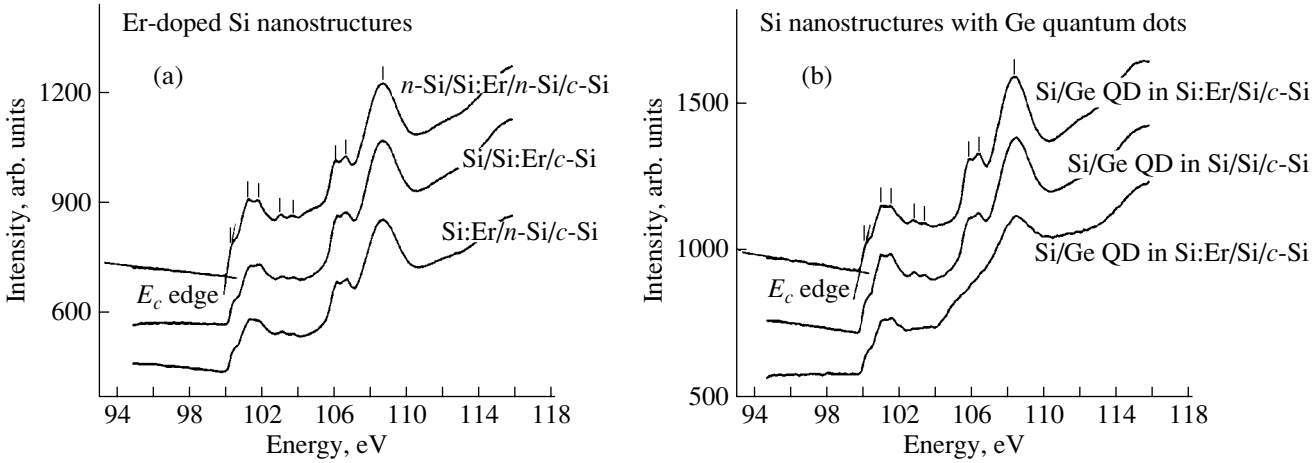

Fig. 4. (a) Si $L_{2,3}$ XANES spectra of nanostructures with epitaxial silicon layers doped with erbium and (b) Si $L_{2,3}$ XANES spectra of silicon nanostructures with Ge quantum dots.

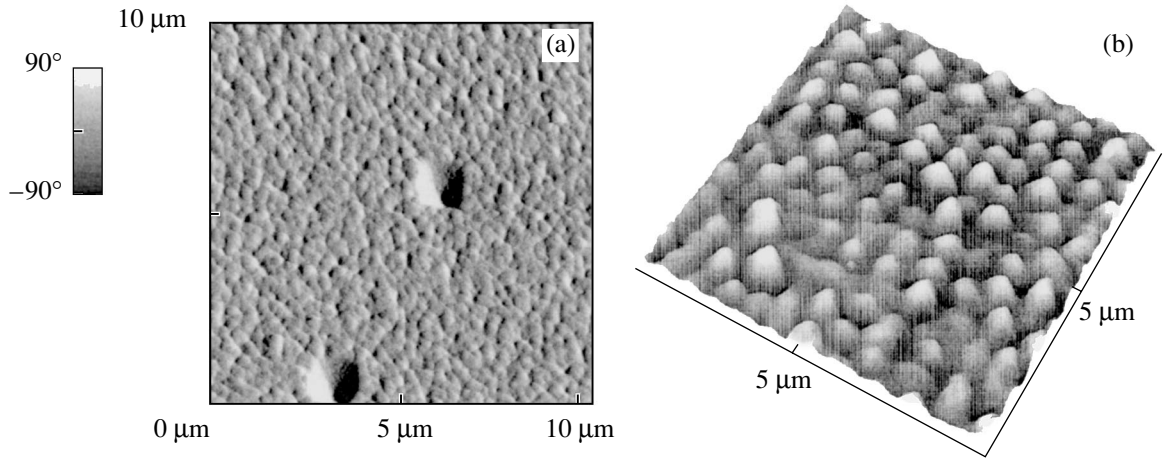

Fig. 5. Morphology of the surfaces of the nanostructures with (a) Er-doped silicon layers and (b) silicon layers with Ge quantum dots according to atomic-force microscopy.

thin (<50 nm). In the case when the multilayer nanostructure with Ge quantum dots is covered with a thicker Si layer (approximately 100 nm), the spectrum has a less pronounced fine structure (lower curve in Fig. 4b).

The morphology of the samples of the nanostructures with quantum dots and erbium-doped layers was examined by atomic-force microscopy (AFM). The AFM images of the surfaces of these nanostructures are given in Fig. 5.

Table 3. Energy positions of the main features in the XANES spectra of multilayer silicon nanostructures doped with Er and nanostructures with Ge quantum dots (QD)

Sample	XANES edge E_c, eV	Energy positions of XANES spectral features, eV			
n-Si/Si:Er/*n*-Si/*c*-Si	100.2	101.4; 101.9	103.0; 103.8	106.2; 106.7	108.8
Si/Si:Er/*c*-Si	100.2	101.4; 101.9	103.2; 103.8	106.3; 106.8	108.8
Si:Er/*n*-Si/*c*-Si	100.2	101.6	103.2; 103.8	106.2; 106.8	108.8
Si/Ge QD in Si:Er/Si/*c*-Si	100.1	101.3; 101.8	103; 103.7	106.2; 106.6	108.7
Si/Ge QD in Si/Si/*c*-Si	100.1	101.3; 101.8	103; 103.7	106.2; 106.7	108.8
Si/Ge QD in Si:Er/Si/*c*-Si	100.2	101.3; 101.9	–	–	108.8

It should also be noted that all the nanostructures are oxidized to some extent. This can be judged from the peaks in the XANES spectra in the energy range 106.2–108.8 eV, which are characteristic of silicon oxides (cf. Figs. 2, 3).

4. CONCLUSIONS

Thus, the main results obtained in this work can be summarized as follows.

The phase composition of surface layers and the energy spectrum of porous silicon were determined from the Si $L_{2,3}$ XANES and Si $L_{2,3}$ USXE spectra. It was found that porous silicon contains silicon nanocrystalline clusters covered with amorphous silicon and silicon oxides.

A model of photoluminescence in porous silicon was proposed. According to this model, the visible luminescence is caused by the electron transitions between the energy levels of the oxide and crystalline phases. The analysis of the XANES and USXE spectra of these phases demonstrated that there are energy levels for optical transitions in the range 1.8–2.4 eV, which corresponds to the photoluminescence in porous silicon.

The fine structure of the Si $L_{2,3}$ XANES spectra of silicon nanostructures containing layers with Ge quantum dots or Er-doped layers was revealed for the first time. The appearance of this structure in the energy range 102–103 eV ($E = E_c + 1$–2 eV) is associated with the stresses generated in silicon surface nanolayers by Ge quantum dots or clusters with incorporated Er atoms. The transitions between the energy levels in the conduction band can contribute to the photoluminescence in silicon nanostructures.

ACKNOWLEDGMENTS

We would like to thank the management of the Berlin Synchrotron Society for providing the opportunity to perform synchrotron radiation experiments on the Russian–German beamline at the BESSY II synchrotron.

REFERENCES

1. T. M. Zimkina and V. A. Fomichev, *Ultrasoft X-ray Spectroscopy* (Leningr. Gos. Univ., Leningrad, 1971).
2. A. S. Vinogradov, E. O. Filatova, and T. M. Zimkina, Pis'ma Zh. Tekh. Fiz. **15** (1), 84 (1989) [Sov. Tech. Phys. Lett. **15**, 35 (1989)].
3. R. V. Yung, S. Shin, and D. L. Kwong, J. Electrochem. Soc. **140** (10), 3046 (1993).
4. S. M. Prokes, W. E. Carlos, L. Seals, and J. L. Gole, Phys. Rev. B **62** (3), 1878 (2000).
5. P. S. Svetlov, V. Yu. Chalkov, and V. G. Shengurov, Prib. Tekh. Éksp., No. 4, 141 (2000).
6. E. O. Filatova, Doctoral Dissertation (St. Petersburg State Univ., 2000).
7. J. L. Gole, J. A. de Vincentis, L. Seals, *et al.*, Phys. Rev. B **61** (8), 5615 (2000).
8. V. M. Kashkarov, E. Yu. Manukovskii, A. V. Schukarev, *et al.*, J. Electron Spectrosc. Relat. Phenom. **114–116**, 895 (2001).
9. A. I. Mashin, A. F. Khokhlov, É. P. Domashevskaya, *et al.*, Fiz. Tekh. Poluprovodn. (St. Petersburg) **35** (8), 995 (2001) [Semiconductors **35**, 956 (2001)].
10. L. T. Canham, Appl. Phys. Lett. **57** (10), 1046 (1990).

Translated by O. Borovik-Romanova

Physics of the Solid State, Vol. 46, No. 2, 2004, pp. 351–356. Translated from Fizika Tverdogo Tela, Vol. 46, No. 2, 2004, pp. 341–346.
Original Russian Text Copyright © 2004 by Ganeev, Ryasnyansky, Stepanov, Usmanov.

LOW-DIMENSIONAL SYSTEMS AND SURFACE PHYSICS

Nonlinear Optical Response of Silver and Copper Nanoparticles in the Near-Ultraviolet Spectral Range

R. A. Ganeev[1], A. I. Ryasnyansky[2], A. L. Stepanov[3, 4], and T. Usmanov[1]

[1] *Akadempribor Research-and-Production Association, National Academy of Sciences of Uzbekistan, Tashkent, 700143 Uzbekistan*

[2] *Navoi State University, Samarkand, 703005 Uzbekistan*

[3] *Physical Institute of the Rhenish–Westphalian Technical University, Aachen, 52056 Germany*

[4] *Zavoiskiĭ Physicotechnical Institute, Kazan Scientific Center, Russian Academy of Sciences, Sibirskiĭ trakt 10/7, Kazan 29, 420029 Tatarstan, Russia*

Received May 16, 2003

Abstract—The nonlinear optical response of silver and copper nanoparticles synthesized by ion implantation in silica glasses is studied in the near-ultraviolet spectral range at a wavelength of 354.7 nm. The real and imaginary parts of the third-order nonlinear susceptibility $\chi^{(3)}$ of composite materials are measured. It is shown that the quantity $\mathrm{Im}\chi^{(3)}$ is due to saturated absorption, while $\mathrm{Re}\chi^{(3)}$ is due to the self-defocusing effect in composite materials. © *2004 MAIK "Nauka/Interperiodica".*

1. INTRODUCTION

Dielectric materials containing metal nanoparticles (NPs) are of interest because of their potential for application as a basis of optical switches with an ultrashort time response [1] and as optical limiters of laser radiation intensity [2, 3]. Moreover, such composite structures can exhibit nonlinear saturated absorption, which can be used for laser mode locking [4].

Most of the previous studies of the nonlinear-optical characteristics of NP metals in various dielectric matrices were carried out using lasers operating at wavelengths lying in the spectral range near the peak of the surface plasma resonance (SPR) of particles. For example, in a glass matrix, the SPR peaks of silver, copper, and gold NPs are at ~415, ~565, and ~525 nm, respectively [5–7]. The nonlinear response of metal NPs is most pronounced under conditions of resonant excitation of conduction electrons, i.e., at SPR frequencies. An example is the results published in [1], where silica glasses with silver NPs were studied to estimate their potential for application in optical switches. The third-order nonlinear susceptibility $\chi^{(3)}$ of these composite materials is high (1.5×10^{-7} esu) under irradiation with second-harmonic picosecond pulses (wavelength (λ = 400 nm) of a sapphire titanate laser.

It is of interest to determine nonlinear-optical characteristics of materials with metal NPs exposed to laser radiation in optical spectral ranges that have not been considered previously, in particular, in the near-ultraviolet spectral range. Up to now, there have also been few studies done on the nonlinear-optical properties of nonmetallic nanometer materials in the ultraviolet range. Nevertheless, it has been found that, e.g., in the case of silicon NPs irradiated with a Nd : YAG laser beam (τ = 8 ns) at a wavelength of 355 nm, the quantity $\chi^{(3)}$ is very large, 2.28×10^{-5} esu [8].

In this work, the nonlinear-optical properties of silver and copper NPs synthesized by ion implantation in silica glasses are studied in the near-ultraviolet region. Measurements were carried out using picosecond laser pulses at a wavelength of 354.7 nm and the *Z*-scanning technique.

2. EXPERIMENTAL

As a composite-material substrate, Suprasil silica glass (SG), characterized by a high optical transparency of ~90% in the spectral range 250–1100 nm, was used. Glass was shaped as plates 2×2 cm in size and 1 mm thick. Nanoparticles were synthesized through implantation of Ag^+ (with a dose of 4.0×10^{16} cm^{-2} and an energy of 60 keV) and Cu^+ ions (with a dose of 8.0×10^{16} cm^{-2} and an energy of 50 keV) at a beam current density of 10 μA/cm^2. The average size of synthesized metal NPs was estimated using x-ray reflectometry [6]. The optical transmittance of glasses doped by silver (SG : Ag) and copper ions (SG : Cu) was measured using a two-beam Perkin Elmer Lambda 19 spectrophotometer in the wavelength range 300–1100 nm.

The nucleation and growth of metal NPs in glass during implantation are initiated as the metal atomic concentration exceeds the solubility limit, which corresponds to an ion dose of $\sim 1 \times 10^{16}$ cm^{-2} at an energy of 50–60 keV [9, 10]. The formation of metal NPs in the samples under study was detected using x-ray measurements, which made it possible, in particular, to estimate the average size of copper particles as 3.5–4.5 nm [11]. The samples implanted by silver ions were character-

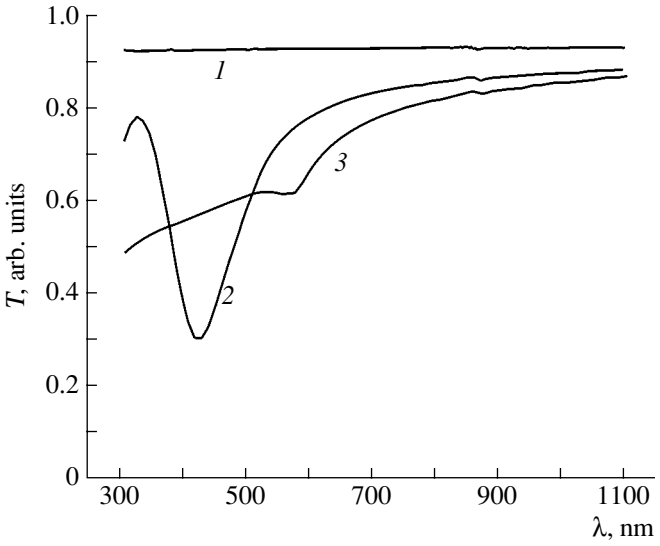

Fig. 1. Optical transmission spectra of (*1*) SG, (*2*) SG : Ag, and (*3*) SG : Cu samples.

ized by a wider spread in NP sizes, from 2 to 18 nm, which was confirmed by electron-microscopy studies [10]. For the selected implantation energies, metal NPs were formed in glasses at a depth less than 60 nm [9, 12]. The thickness L corresponding to this depth was then used to measure and quantitatively estimate the linear absorption coefficient α_0 of SG, SG : Ag, and SG : Cu samples at the operating wavelength.

The formation of metal NPs is also characterized by selective absorption bands arising in the optical transmission spectra of implanted glasses in the visible region (in the ranges 400–450 and 550–600 nm), (Fig. 1). These bands are caused by SPR absorption in silver and copper particles, respectively [13]. Under various conditions, implantation of accelerated ions into silica glasses causes radiation defects, which can stimulate reversible and irreversible changes in the material structure [10]. Various types of structural changes were detected, such as the formation of extended and point defects, local crystallization and amorphization, the formation of a new phase from atoms composing the glass structure or from implanted ions, etc. The formation of metal particles in a glass increases its volume and causes internal stresses in the implanted layer. Radiation defects increase the glass absorption at the edge of fundamental absorption in the near-ultraviolet region (the short-wavelength spectral region in Fig. 1).

To determine the nonlinear-optical characteristics of the samples, we used a Z-scanning system with the confining diaphragm described in detail in [14]. The diaphragm radius was 1.5 mm, which corresponded to a transmittance of ~20%. The experiments were carried out using the third harmonic of the Nd : YAG laser with the following parameters: a pulse duration of 55 ps, a pulse energy of 0.1 mJ, and wavelength $\lambda = 354.7$ nm. The focal spot size in the waist region was 42 μm. To prevent the influence of the thermal effects produced by many pulses on the measured optical characteristics, their repetition frequency did not exceed 2 Hz. The laser beam intensity I_0 used for measurements was varied within the range 10^9–5×10^9 W cm^{-2}, since the optical breakdown intensity for glasses doped with both ion types was ~10^{10} W cm^{-2}. Each point in the experimental dependences shown in this paper was obtained by averaging over 20 laser pulses.

3. EXPERIMENTAL RESULTS AND DISCUSSION

In actual practice, a conventional Z-scanning technique with a confining diaphragm [15, 16] is used to determine the nonlinear refractive index n_2 entering the expression for the total refractive index $n = n_0 + n_2|E|^2$ (where n_0 is the linear refractive index and E is the amplitude of the electromagnetic field strength of the laser beam). This approach also allows one to determine the sign of n_2 of a material. In particular, if n_2 becomes negative, the following feature is observed in the normalized transmittance $T(z)$ variation during scanning over the sample focal plane along the Z axis: when the sample is far from the lens focus, the laser beam intensity is relatively small and only linear optical processes manifest themselves. In this case, $T(z)$ is close to unity. As a sample approaches the lens focus, the intensity of the focused laser beam and, hence, the influence of the negative coefficient n_2 increase and the total refractive index n of the nonlinear medium decreases. The medium acts as a scattering matrix, which causes convergence of the passing laser beam at the varying diaphragm, thus increasing the measured transmittance. The transmittance peak is achieved at a certain sample position z_0 not coinciding with the lens focus. As the sample further approaches the focus and the laser beam intensity increases, self-defocusing begins to cause beam divergence and, hence, decreases $T(z)$. As the sample reaches the lens focus, $T(z)$ again becomes equal to unity. The sample motion along the Z axis beyond the focus causes a reverse process due to the n_2 variation, i.e., an increase in n followed by its decrease. Thus, the $T(z)$ dependence corresponding to a negative n_2 is similar to a sinusoidal curve, which first rises, then descends after reaching a certain maximum, then reaches a minimum, and returns to the initial level. This optical nonlinearity corresponds to self-defocusing of the laser beam. In a structurally homogeneous sample in the absence of nonlinear absorption, the $T(z)$ dependence for the sample positions in front of and behind the focus is centrosymmetric with respect to the position at the focus. The laser beam self-focusing that occurs at positive values of n_2 is characterized by similar, but reversed $T(z)$ variations; i.e., the minimum in the curve precedes the maximum.

As practice shows, the *Z*-scanning technique can be efficiently applied to determine n_2 only using a confining diaphragm passing through 1–5% of light [16]. Such a small size of the confining diaphragm requires that the sample under study be sufficiently transparent. Previously, we efficiently employed such small diaphragms to study nonlinear processes in the near-IR region in glasses with metal NPs [17, 18]. However, in the near-ultraviolet region, composite materials feature a low transmittance due to strong absorption at the edge of fundamental absorption of metal silver and the glass matrix (Fig. 1). Therefore, a confining diaphragm with a high transmittance (20%) was used in these experiments. A specific feature of measurements with such diaphragms is that the $T(z)$ dependence to be determined can be affected not only by nonlinear refraction of a sample but also by its nonlinear absorption, if the latter is inherent to the sample material [19]. In this case, because of the influence of both nonlinear processes, the experimental $T(z)$ curve becomes asymmetric with respect to the lens focus.

Above all, we note that no nonlinear refraction and absorption were observed at the selected laser wavelength in an undoped silica glass. Figure 2 shows the $T(z)$ curve measured using the *Z*-scanning scheme with a confining diaphragm for an SG : Ag sample. We can see that the gradual increase in $T(z)$ followed by an abrupt decrease as the sample position varies is indicative of a contribution from the negative n_2 and, therefore, of the laser beam self-defocusing. The noticeable asymmetry in the $T(z)$ dependence with respect to the lens focus, which manifests itself in the amplitude at the transmittance maximum being larger than the amplitude at the minimum, as well as in the $T(z)$ maximum shifting to the region in front of the lens focus, is a manifestation of nonlinear saturated absorption in the sample under study [16]. If the amplitude were to be larger at the transmittance minimum in the $T(z)$ curve than at the maximum, it could be concluded that there exists nonlinear-induced absorption, such as two-photon or reverse saturated absorption. However, as follows from the dependence shown in Fig. 2, these types of nonlinear absorption can be excluded from consideration. We note that the nonlinear (saturated or induced) absorption has no effect on the n_2 sign and, hence, on the self-action processes (self-focusing or self-defocusing).

In general, if various nonlinear processes occur in a sample under study, then, in the case of an axially symmetric laser beam, the $T(z)$ dependence measured using the *Z*-scanning scheme with a confining diaphragm can be written as [20]

$$T(z) = 1 + T_{\Delta\Phi}(z) + T_{\Delta\Psi}(z), \quad (1)$$

where $T_{\Delta\Phi}(z)$ and $T_{\Delta\Psi}(z)$are the contributions from nonlinear refraction and nonlinear absorption, respectively.

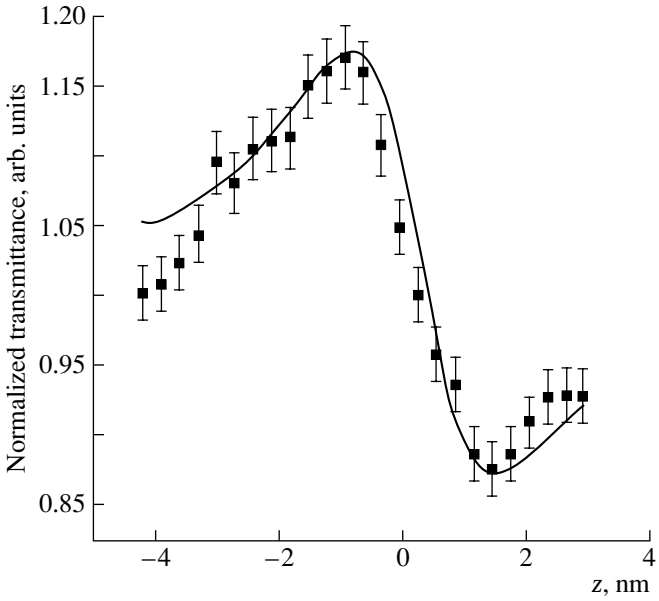

Fig. 2. Dependence of the normalized transmittance on the sample position measured for SG : Ag using the *Z*-scanning technique with a confining diaphragm (solid curve represents a calculation).

This dependence can be written as [20]

$$T(z) = 1 - \frac{4x}{(x^2+9)(x^2+1)}\Delta\Phi_0 - \frac{2(x^2+3)}{(x^2+9)(x^2+1)}\Delta\Psi_0, \quad (2)$$

where $x = z/z_0$, $z_0 = kw_0^2/2$ is the beam diffraction length, w_0 is the beam radius at the focus at the level of $1/e^2$ of the intensity distribution (which is 42 μm in this study), and $k = 2\pi/\lambda$ is the wave vector; $\Delta\Phi_0 = k\gamma I_0 L_{\text{eff}}$ and $\Delta\Psi_0 = \beta I_0 L_{\text{eff}}/2$ are parameters defining the phase shift of an electromagnetic wave near the focus due to nonlinear refraction and nonlinear absorption, respectively (γ is the nonlinear refractive index measured in SI units). In practice [16], the transition to the esu system is given by n_2 [esu] = $\frac{cn_0}{40\pi}\gamma$ [m^2 W^{-1}] (here, the speed of light c is measured in m s^{-1}). The quantity β is the nonlinear absorption coefficient and I_0 is the minimum intensity of the laser beam at the focus at which it was possible to detect the manifestation of optical nonlinearities in samples with NPs in this experiment. The parameter $L_{\text{eff}} = [1 - \exp(-\alpha_0 L)]/\alpha_0$ is the effective thickness of a glass sample containing implanted NPs, whose actual thickness is $L = 60$ nm, and α_0 is the linear absorption coefficient. The values of I_0 and α_0 for the samples under study are listed in the table. From these values it follows that nonlinearities in SG : Ag occur at a lower beam intensity than in the case of SG : Cu.

Nonlinear-optical parameters of SG : Ag and SG : Cu samples at a wavelength of 354.7 nm

Sample	a_0, 10^4 cm^{-1}	I_0, 10^9 W cm^{-2}	n_2, 10^{-7} esu	β, 10^{-6} cm W^{-1}	Re $\chi^{(3)}$, 10^{-8} esu	Im $\chi^{(3)}$, 10^{-9} esu	$\lvert\chi^{(3)}\rvert$, 10^{-8} esu
SG : Ag	8.8	1.25	–2.7	–14.25	–6.025	–6.14	6.056
SG : Cu	10.7	4.1	–0.6	–6.67	–1.34	–2.87	1.36

It can be shown that $\Delta\Psi_0 = \rho\Delta\Phi_0$, where $\rho = \beta/2k\gamma$ [20]. In this case, Eq. (2) reduces to

$$T(z) = 1 + \frac{2(-\rho x^2 - 2x - 2\rho)}{(x^2+9)(x^2+1)}\Delta\Phi. \qquad (3)$$

In this study, the $T(z)$ dependence was simulated using Eq. (3). The best fit of the calculated curve to the experimental data was attained at $\rho = -0.07$ and $\Delta\Phi_0 = -0.75$ (solid line in Fig. 2). With these values of ρ and $\Delta\Phi_0$, using the relation between $\Delta\Psi_0$, ρ, and $\Delta\Phi_0$, we get $n_2 = -2.7 \times 10^{-7}$ esu and $\beta = -14.25 \times 10^{-6}$ cm W^{-1} for SG : Ag.

In general, if nonlinear refraction and nonlinear absorption occur simultaneously in a material, the Kerr susceptibility is a complex quantity, $\chi^{(3)} = \mathrm{Re}\chi^{(3)} + i\mathrm{Im}\chi^{(3)}$. The real and imaginary parts of $\chi^{(3)}$ are related to n_2 [21] and to β [22], respectively; namely, $\mathrm{Re}\chi^{(3)} = n_0 n_2/3\pi$ and $\mathrm{Im}\chi^{(3)} = n_0\varepsilon_0 c^2\beta/\omega$, where ω is the laser radiation frequency and ε_0 is the permittivity. Knowing n_2 and β, the values of $\mathrm{Re}\chi^{(3)}$ and $\mathrm{Im}\chi^{(3)}$ can be found to be -6.025×10^{-8} and -6.14×10^{-9} esu, respectively. In this case, the magnitude $|\chi^{(3)}| = [(\mathrm{Re}\chi^{(3)})^2 + (\mathrm{Im}\chi^{(3)})^2]^{1/2}$ is 6.056×10^{-8} esu. From the values obtained it follows that the major contribution to $|\chi^{(3)}|$ is made by $\mathrm{Re}\chi^{(3)}$.

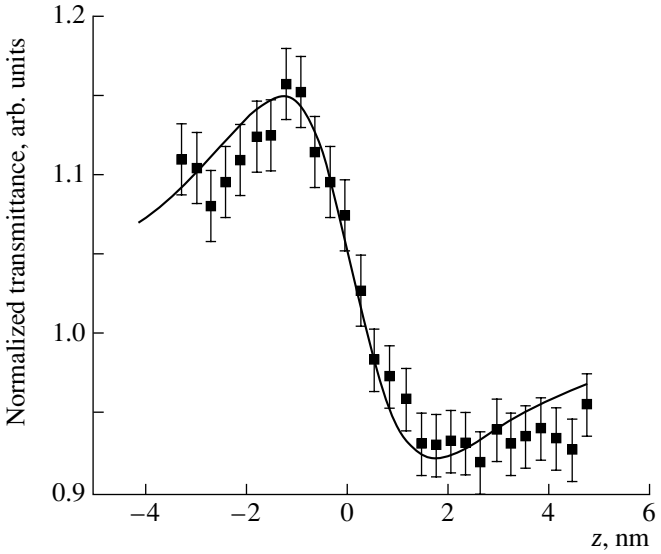

Fig. 3. Same as in Fig. 2, but for SG : Cu.

The experimental $T(z)$ dependence for an SG : Cu sample is shown in Fig. 3. We can see that the curve and the nonlinearity n_2 sign are similar to those for the SG : Ag sample. However, there is also a difference; indeed, the difference between the amplitudes at the points of the maximum and minimum of $T(z)$ is smaller in the former case, which allows one to assume that the contribution from nonlinear saturated absorption in SG : Cu is smaller than in SG : Ag. Applying a similar approach to simulating the $T(z)$ dependence (solid line in Fig. 3), we obtained $\rho = -0.15$ and $\Delta\Phi_0 = -0.548$, which made it possible to determine $n_2 = -0.6 \times 10^{-7}$ esu and $\beta = -6.67 \times 10^{-6}$ cm W^{-1}, as well as $\mathrm{Re}\chi^{(3)} = -1.34 \times 10^{-8}$ esu and $\mathrm{Im}\chi^{(3)} = -2.87 \times 10^{-9}$ esu. The magnitude $|\chi^{(3)}|$ for SG : Cu is found to be 1.36×10^{-8} esu. For convenient comparison, all the nonlinear-optical parameters are listed in the table.

As in the previous study of the nonlinear-optical properties of similar glasses with metal NPs in the IR region [17], we analyze the experimental data assuming the composite material to be an effective homogeneous medium. This approach is valid due to the small NP sizes in comparison with the radiation wavelength. An effective homogeneous condensed medium in which resonant transitions occur can be described using the conventional two-level energy diagram [21] and the corresponding equation for n_2:

$$n_2(\omega_i) = -2\pi N\frac{|\mu_{i0}|^4}{n_0\hbar(\omega_{i0}-\omega_p)^3}, \qquad (4)$$

where ω_p is the SPR frequency of metal NPs, ω_{i0} is the laser radiation frequency, the subscript i indicates one- or two-photon process in a material, and N is the concentration of active nonlinear-excitation centers, which are considered dipoles to a first approximation and can be associated with NPs in a sample in the case under study; μ_{i0} is the dipole moment of the transition at frequencies ω_{i0}.

As can be seen from Eq. (4), the n_2 sign is independent of N and μ_{i0} and is defined only by the sign of detuning from resonance, $\Delta = \omega_{i0} - \omega_p$. Since $\mathrm{Re}\chi^{(3)}$ is linearly proportional to n_2 [21], the sign of the nonlinearity of a composite medium can be determined from the relation

$$\mathrm{Re}\,\chi^{(3)} \propto -(\omega_{i0} - \omega_p). \qquad (5)$$

Let us consider this relation for the laser radiation frequency $\omega_{10} \sim 28193$ cm^{-1} (354.6 nm) used in this study and for the SPR frequencies in SG : Ag and SG : Cu samples. In the case of copper NPs, the SPR peak occurs at $\omega_p = 17699.1$ cm^{-1} (565 nm). Therefore, for the frequency ω_{10}, the detuning Δ is positive and $\mathrm{Re}\chi^{(3)}$ is negative. The same is true for SG : Ag, whose SPR peak is at $\omega_p = 24096.4$ cm^{-1} (415 nm). Positive values of Δ correspond to laser beam self-defocusing, which is observed in the experiment with SG : Cu and SG : Ag samples.

The laser beam pulses used in this work were rather short ($\tau = 55$ ps). Nevertheless, let us consider the possible influence of the thermal effect on the nonlinear refraction processes, since the samples under study are characterized by high linear absorption in the near-ultraviolet region. To this end, we estimate the change in the refractive index of glass caused by its heating, e.g., through heat transfer from metal NPs heated by laser radiation or through direct absorption of light by the matrix.

The change in the refractive index due to the contribution from nonlinearity in a local region of the isotropic dielectric (glass) in the case of the thermal effect of laser radiation can be written as [23]

$$\Delta n_{\mathrm{therm}}(r, z, t) = (\delta\sigma)^{-1}(dn/dT)\Delta E(r, z, t), \quad (6)$$

where δ and σ are the specific heat and the silica glass density, equal to 0.703 J g^{-1} K^{-1} and 2.203 g cm^{-3}, respectively. The quantity $dN/dT = 11.9 \times 10^{-6}$ K^{-1} is the thermal-optical coefficient of glass and $\Delta E(r, z, t)$ is the laser radiation energy per unit volume of the material absorbed over time t.

To calculate the value of $\Delta E(r, z, t)$ corresponding to an individual laser pulse of duration 55 ps, we consider the case of a sample positioned near the lens focus. The values of the absorbed radiation energy E in SG : Cu and SG : Ag were determined to be 7.63×10^{-6} and 2.78×10^{-6} J, respectively. For a 60-nm-thick nonlinear layer and a beam radius of 42 μm at the focus, the volume under study is 3.32×10^{-10} cm^3. Therefore, the values of $\Delta E(r, z, t)$ for SG : Cu and SG : Ag are 2.3×10^4 and 8.61×10^3 J cm^{-3}, respectively. With these numerical estimates, the values of $\Delta n_{\mathrm{therm}}$ are found to be 0.176 in SG : Cu and 6.61×10^{-2} in SG : Ag.

On the other hand, using the obtained values of the phase shifts $\Delta\Phi_0$ due to nonlinear refraction and taking into account the relation $\Delta\Phi_0 = k\Delta n_{\mathrm{exp}} L_{\mathrm{eff}}$ [16] between this parameter and Δn, we determined the values Δn_{exp} corresponding to our experiment to be –0.516 and –0.7 for SG : Cu and SG : Ag, respectively. It is evident that these values appreciably exceed (in magnitude) the values of $\Delta n_{\mathrm{therm}}$ calculated from the thermal effect and differ from them in sign. Hence, the contribution from $\Delta n_{\mathrm{therm}}$ can be neglected and the Kerr nonlinearities are dominant in the samples studied under the conditions of our nonlinear-optical experiment.

Let us determine the pulse durations at which the quantity $\Delta n_{\mathrm{therm}}$ due to the thermal effect will become comparable to Δn_{exp} due to the Kerr effect. The values of Δn_{exp} exceed $\Delta n_{\mathrm{therm}}$ in magnitude by a factor of 3 and 10 for SG : Cu and SG : Ag, respectively. We note that the thermal effect and the Kerr effect are determined by the energy and power density of radiation, respectively [24]. If we increase the beam pulse duration by a factor of 3 and 10 for SG : Cu and SG : Ag samples, respectively, and simultaneously increase the radiation energy by the same factors, then the power density (and the change in n due to the Kerr effect) will remain unchanged but the value of $\Delta n_{\mathrm{therm}}$ will increase n by a factor of 3 and 10, respectively. In this case, the values of Δn_{exp} for both effects in question will become equal. Therefore, for the samples under study, the thermal nonlinearities at a wavelength of 354.7 nm will become significant at a pulse duration τ longer than 165 and 550 ps for SG : Cu and SG : Ag, respectively.

4. CONCLUSIONS

Thus, we have studied the nonlinear-optical characteristics at a wavelength of 354.7 nm of silica glasses containing silver and copper NPs synthesized by ion implantation. The real and imaginary parts of the third-order nonlinear susceptibility $\chi^{(3)}$ of the composite materials were measured. It was shown that $\mathrm{Im}\chi^{(3)}$ is due to saturated absorption in metal NPs, whereas $\mathrm{Re}\chi^{(3)}$ is due to the self-defocusing effect in the composite materials. The influence of the thermal effect on nonlinear refraction of the glass matrix was analyzed numerically. It was shown that glass heating is insignificant in comparison with the optical nonlinearities caused by metal NPs at the wavelength and pulse duration of laser radiation used in the experiment.

ACKNOWLEDGMENTS

This study was supported by the Russian Foundation for Basic Research (project no. 00-15-96615), Uzbek Scientific and Technical Center (grant no. Uzb-29), Science and Technology Center of Uzbekistan (grant no. 2.1.22), and the Alexander von Humboldt Foundation.

REFERENCES

1. H. Inouye, K. Tanaka, I. Tanahashi, *et al.*, Jpn. J. Appl. Phys. **39**, 5132 (2000).
2. Y.-P. Sun, J. E. Riggs, H. W. Rollins, and R. Guduru, J. Phys. Chem. B **103**, 77 (1999).
3. J. Staromlynska, T. J. McKay, and P. Wilson, J. Appl. Phys. **88**, 1726 (2000).
4. K. Wundke, S. Potting, and J. Auxier, Appl. Phys. Lett. **76**, 10 (2000).

5. J. Olivares, J. Requejo-Isidro, R. Del Coso, *et al.*, J. Appl. Phys. **90**, 1064 (2001).
6. F. Hache, D. Ricard, C. Flytzanis, and U. Kreibig, J. Appl. Phys. **47**, 354 (1988).
7. K. Ushida, S. Kaneko, S. Omi, *et al.*, J. Opt. Soc. Am. B **11**, 1236 (1994).
8. S. Vijayalakshmi, M. A. George, and H. Grebel, Appl. Phys. Lett. **70**, 708 (1997).
9. A. L. Stepanov and D. E. Hole, Recent Res. Devel. Appl. Phys. **5**, 1 (2002).
10. P. D. Townsend, P. J. Chandler, and L. Zhang, *Optical Effects of Ion Implantation* (Cambridge Univ. Press, Cambridge, 1994), p. 157.
11. A. Nadon and D. Thaiaudiere, J. Appl. Crystallogr. **30**, 822 (1997).
12. A. L. Stepanov, V. A. Zhikharev, and I. B. Khaĭbullin, Fiz. Tverd. Tela (St. Petersburg) **43**, 733 (2001) [Phys. Solid State **43**, 766 (2001)].
13. U. Kreibig and M. Vollmer, *Optical Properties of Metal Clusters* (Springer, Berlin, 1995), p. 533.
14. R. A. Ganeev, A. I. Ryasnyansky, S. R. Kamalov, *et al.*, J. Phys. D: Appl. Phys. **34**, 1602 (2001).
15. M. Sheik-Bahae, A. A. Said, and E. W. Van Stryland, Opt. Lett. **14**, 955 (1989).
16. M. Sheik-Bahae, A. A. Said, T. Wei, *et al.*, IEEE J. Quantum Electron. **26**, 760 (1990).
17. R. A. Ganeev, A. I. Ryasnyansky, A. L. Stepanov, *et al.*, Opt. Spektrosk. (2003) (in press).
18. R. A. Ganeev, A. I. Ryasnyansky, A. L. Stepanov, and T. Usmanov, Fiz. Tverd. Tela (St. Petersburg) **45** (7), 1292 (2003) [Phys. Solid State **45**, 1355 (2003)].
19. M. Kyong and M. Lee, Bull. Korean Chem. Soc. **21**, 26 (2000).
20. M. Yin, H. P. Li, S. H. Tang, and W. Ji, Appl. Phys. B **70**, 587 (2000).
21. J. F. Reintjes, *Nonlinear Optical Parametrical Processes in Liquids and Gases* (Academic, Orlando, 1984; Mir, Moscow, 1987).
22. R. Rangel-Rojo, T. Kosa, E. Hajto, *et al.*, Opt. Commun. **109**, 143 (1994).
23. G. A. Swartzlander, B. L. Justus, A. L. Huston, *et al.*, Int. J. Nonlinear Opt. Phys. **2**, 577 (1993).
24. C. S. Mehendale, S. R. Mishra, K. S. Bindra, *et al.*, Opt. Commun. **133**, 273 (1997).

Translated by A. Kazantsev

Physics of the Solid State, Vol. 46, No. 2, 2004, pp. 357–363. Translated from Fizika Tverdogo Tela, Vol. 46, No. 2, 2004, pp. 347–352.
Original Russian Text Copyright © 2004 by Parfen'eva, Smirnov, Misiorek, Mucha, Jezowski, Prokof'ev, Assmus.

LOW-DIMENSIONAL SYSTEMS AND SURFACE PHYSICS

Spinon Thermal Conductivity of –(CuO_2)– Spin Chains in $LiCuVO_4$

L. S. Parfen'eva*, I. A. Smirnov*, H. Misiorek, J. Mucha**, A. Jezowski**, A. V. Prokof'ev***, and W. Assmus*****

** Ioffe Physicotechnical Institute, Russian Academy of Sciences, Politekhnicheskaya ul. 26, St. Petersburg, 194021 Russia*
e-mail: igor.smirnov@pop.ioffe.rssi.ru
*** Institute of Low-Temperature and Structural Research, Polish Academy of Sciences, Wroclaw, 50-950 Poland*
**** Institute of Physics, Goethe University, Frankfurt am Main, 60054 Germany*
Received June 16, 2003

Abstract—The thermal conductivity κ_{tot}^{b} of the quasi-one-dimensional ($S = 1/2$) Heisenberg antiferromagnet $LiCuVO_4$ with uniform (–CuO_6–) spin chains aligned parallel to the *b* axis in a crystal with an orthorhombically distorted inverse spinel structure is measured in the temperature range 10–300 K. The spinon component κ_m^{chain} of the thermal conductivity is separated out. © *2004 MAIK "Nauka/Interperiodica".*

1. INTRODUCTION

Since 2000, thermal conductivity of low-dimensional magnetic materials and, especially, one-dimensional spin systems, such as one-dimensional ($S = 1/2$) Heisenberg antiferromagnets, have attracted the particular attention of experimenters and theorists at leading laboratories in Switzerland, Germany, the United States, France, Japan, and Russia [1–9]. This interest stems from the fact that elementary excitations in these objects are provided by quantum solitons (rather than by magnons) with spin $S = 1/2$, which are referred to as spinons [4–10].

Heat transfer by spinons and their contribution to the thermal conductivity κ_m have been observed in one-dimensional materials with spin ladders (κ_m^{ladd}, $(Sr,Ca,La)_{14}Cu_{24}O_{41}$ systems) [1, 2, 5–7] and spin chains (κ_m^{chain}, Sr_2CuO_3 and $SrCuO_2$) [3, 4].

This effect most clearly manifests itself in materials with spin ladders when the heat flux in crystals is directed along the ladders. With an increase in the temperature above $T > 50$ K, the thermal conductivity drastically increases and, in the range 100–150 K, exhibits a second maximum whose intensity is considerably higher than the intensity of the low-temperature phonon maximum which is typical of crystalline solids.

The above materials have orthorhombic symmetry. The spin chains and spin ladders in these compounds are formed by Cu^{2+} and O^{2-} ions (–Cu–O–Cu– bonds) and are characterized by the constants of exchange coupling between the nearest neighbor ions Cu^{2+} in chains (J^{chain}) and ladders (J_{leg}^{ladd} for the coupling along ladders and J_{rung}^{ladd} for the rung coupling).

In the Sr_2CuO_3 compound, uniform chains with $J^{chain} \sim 2150$–3000 K consist of square CuO_4 units, which are shared by vertices and lie along the *b* axis [11–14].

The structure of chains in the $SrCuO_2$ compound is similar to that in the Sr_2CuO_3 compound. Although the chains in $SrCuO_2$ are shared in pairs on common sides of squares, the magnetic coupling between spins of adjacent chains is small in magnitude. The chains are aligned parallel to the *c* axis, and, as in the case of Sr_2CuO_3, the exchange coupling constant J^{chain} is approximately equal to 2150–3000 K [11–14].

Compounds in the $(Sr,Ca,La)_{14}Cu_{24}O_{41}$ system have more complex structures. Specifically, the Cu_2O_3 two-leg spin ladders with $J_{leg}^{ladd} \sim 1500$ K and $J_{rung}^{ladd} \sim 835$ K [15] and the dimerized CuO_2 chains with J_1^{chain} (intradimer) ~ 116–130 K and J_2^{chain} (interdimer) ~ 9–13 K [15–17][1] coexist in the crystal and are arranged along the *c* axis. This makes the interpretation of experimental data on the thermal conductivity more difficult. However, Sologubenko *et al.* [2] and Kudo *et al.* [7] asserted that, for compounds in the $(Sr,Ca,La)_{14}Cu_{24}O_{41}$ system, the thermal conductivity obeys the inequality $\kappa_m^{ladd} \gg \kappa_m^{chain}$. This inference was drawn from an analysis of the available experimental data for the

[1] In [15–17], these data were obtained for the $Sr_{14}Cu_{24}O_{41}$ compound.

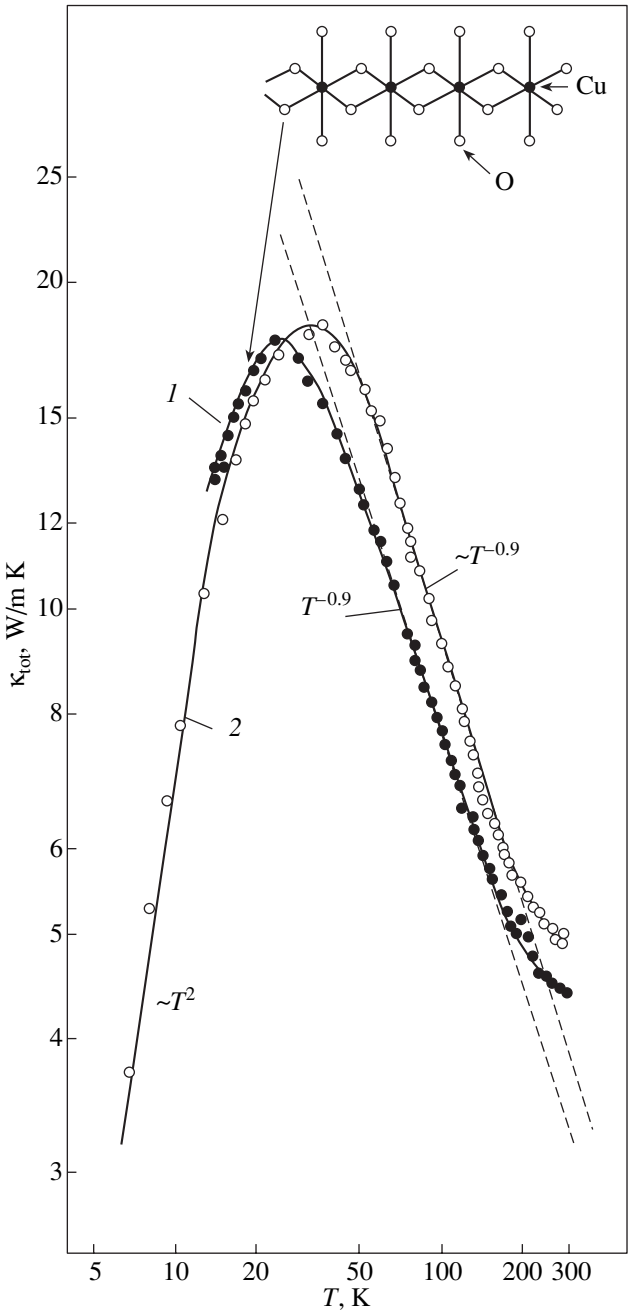

Fig. 1. Temperature dependences of the thermal conductivities (*1*) $\kappa_{tot}^{b}(T)$ and (*2*) $\kappa_{tot}^{a}(T)$ [21] for the $LiCuVO_4$ single crystal. The inset shows the structure of a copper spin chain in the $LiCuVO_4$ crystal.

$Sr_{14}Cu_{24}O_{41}$ compound in the $(Sr,Ca,La)_{14}Cu_{24}O_{41}$ system on the basis of the following facts.

(1) For the $Sr_{14}Cu_{24}O_{41}$ compound, the magnetic coupling in spin chains is considerably weaker than that in spin ladders ($J^{ladd} \gg J^{chain}$) [15–17].

(2) According to the neutron scattering data [17], the magnetic excitation spectra of CuO_2 chains are characterized by a very weak dispersion of the branches along the *c* axis. Therefore, the thermal conductivity κ_m^{chain} of spin chains should be small in magnitude.

However, to the best of our knowledge, no direct measurements that could provide reliable information on the thermal conductivity κ_m^{chain} for compounds with small values of exchange coupling constants J^{chain} were performed.

The aim of the present work was to measure the thermal conductivity κ_m^{chain} of a quasi-one-dimensional compound that belongs to one-dimensional ($S = 1/2$) Heisenberg antiferromagnets and has spin chains with exchange coupling constants J^{chain} close to the values of J^{chain} for spin chains in the $Sr_{14}Cu_{24}O_{41}$ compound.

It was also of interest to measure the thermal conductivity κ_m^{chain} of a compound of another class of materials and to compare the results of measurements with the data obtained earlier for $(Sr,Ca,La)_{14}Cu_{24}O_{41}$, Sr_2CuO_3, and $SrCuO_2$ compounds. This was another purpose of our work.

For these purposes, we chose the $LiCuVO_4$ compound. As will be shown below, this compound completely satisfies the aforementioned requirements. The $LiCuVO_4$ compound crystallizes in an orthorhombically distorted inverse spinel structure in which the nonmagnetic V^{5+} ions occupy tetrahedral holes and nonmagnetic Li^+ and magnetic Cu^{2+} ($S = 1/2$) ions are located in octahedral holes of the anionic sublattice in an ordered manner [18, 19]. The CuO_6 octahedra form magnetic chains (see inset in Fig. 1), and the LiO_6 octahedra make up nonmagnetic chains. These magnetic and nonmagnetic chains in the $LiCuVO_4$ structure are aligned parallel to the *b* and *a* axes, respectively.

In the $LiCuVO_4$ structure, the exchange coupling inside the spin chains is characterized by $J^{chain} \sim 22$ K [20], whereas the constant of exchange coupling between the Cu^{2+} ions located in adjacent chains is $J^{interchain} \sim 1$ K [20].

The basic properties of $LiCuVO_4$ (the crystal structure; magnetic susceptibility; specific heat; EPR, NMR, optical IR spectra) have been investigated in sufficient detail.[2] The thermal conductivity κ_{tot}^{a} has been measured only in the case when the heat flux is directed along the nonmagnetic LiO_6 chains (the *a* axis) [21].

[2] References to the works dealing with these properties are given in [21].

2. SAMPLE PREPARATION AND EXPERIMENTAL TECHNIQUE

For measurements of the thermal conductivity, $LiCuVO_4$ single crystals were grown by slow cooling of an $LiCuVO_4$ solution in an $LiVO_3$ melt from 650 to 580°C. The growth technique was described in detail in [22]. In the terminology used in [21], these single crystals belong to the "high-temperature" crystals (unlike the "low-temperature" $LiCuVO_4$ crystals grown in the course of slow cooling of an $LiCuVO_4$ solution in a 53 wt % $LiVO_3$–47 wt % LiCl melt from 580 to 520°C).

According to the chemical analysis, the high- and low-temperature single crystals have the statistically averaged compositions $Li_{0.92}Cu_{1.03}VO_{4-x}$ and $Li_{0.97}Cu_{1.00}VO_{4-x}$, respectively. As was noted in [21], attempts to prepare compounds of stoichiometric composition $LiCuVO_4$ either in the form of single crystals or in the form of powders have failed.

In this work, the thermal conductivity was measured with a high-temperature single crystal $3.5 \times 2 \times 0.6$ mm in size. The heat flux was directed parallel to the long side of the sample, which corresponded to the *b* axis.

The thermal conductivity κ_{tot}^{b} was measured in the temperature range 10–300 K on a setup similar to that used in [23].

3. RESULTS AND DISCUSSION

The experimental data on the total thermal conductivity $\kappa_{tot}^{b}(T)$ of the $LiCuVO_4$ single crystal are presented in Fig. 1. For comparison (and also for the subsequent analysis of the experimental results), Fig. 1 shows the dependence $\kappa_{tot}^{a}(T)$ (taken from our previous work [21]) for the $LiCuVO_4$ single crystal grown using the low-temperature technique.

The thermal conductivity $\kappa_{tot}^{b}(T)$ (like the thermal conductivity $\kappa_{tot}^{a}(T)$ [21]) does not involve the electronic component κ_e. Actually, the electrical conductivities measured in the $LiCuVO_4$ single crystal along the *a* and *b* axes are approximately equal to 10^{-5}–10^{-7} Ω^{-1} cm^{-1}; in this case, the value of κ_e appears to be negligible.

It can be seen from Fig. 1 that the thermal conductivities $\kappa_{tot}^{b}(T)$ and $\kappa_{tot}^{a}(T)$ only slightly increase at $T >$ 150–200 K. According to [21], this increase is associated with the superionic state of the $LiCuVO_4$ crystal and will not concern us in the present work.

As was shown in [21], the thermal conductivity κ_{tot}^{a} of the $LiCuVO_4$ crystal in the range 5–200 K satisfies the equality $\kappa_{tot}^{a} = \kappa_{ph}^{a}$ (where κ_{ph}^{a} is the thermal conductivity of the crystal lattice).

It can be assumed that, unlike the thermal conductivity $\kappa_{tot}^{a}(T)$, the thermal conductivity $\kappa_{tot}^{b}(T)$ in the temperature range 10–150 K should satisfy the relationship

$$\kappa_{tot}^{b}(T) = \kappa_{ph}^{b}(T) + \kappa_{m}^{chain}(T). \quad (1)$$

However, the curve $\kappa_{tot}^{b}(T)$ depicted in Fig. 1 gives no indication of both the contribution from the spinon component $\kappa_{m}^{chain}(T)$ to the total thermal conductivity

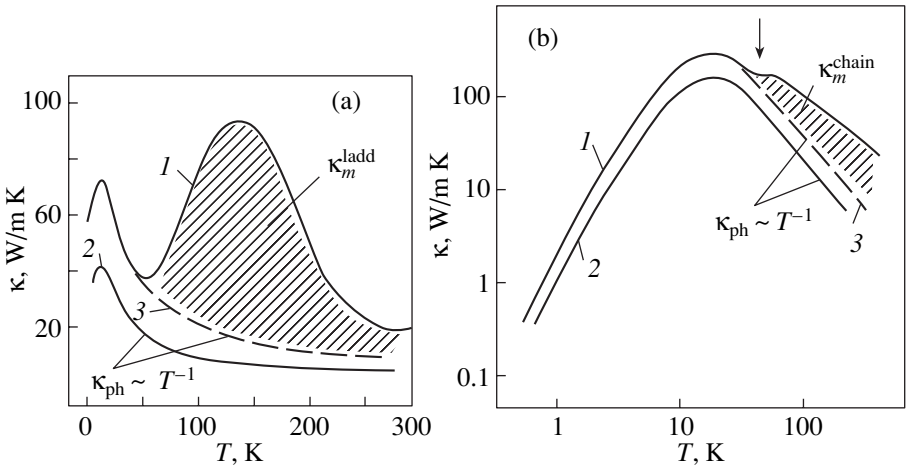

Fig. 2. Schematic diagram illustrating the separation of the thermal conductivity components (a) κ_{m}^{ladd} and (b) κ_{m}^{chain} from (*1*) the experimental thermal conductivity κ_{tot} [1, 2, 5, 6], (*2*) the thermal conductivity measured along the crystallographic directions in which spin ladders and spin chains are absent, and (*3*) the thermal conductivity extrapolated according to the relationship $\kappa_{ph} \sim T^{-1}$.

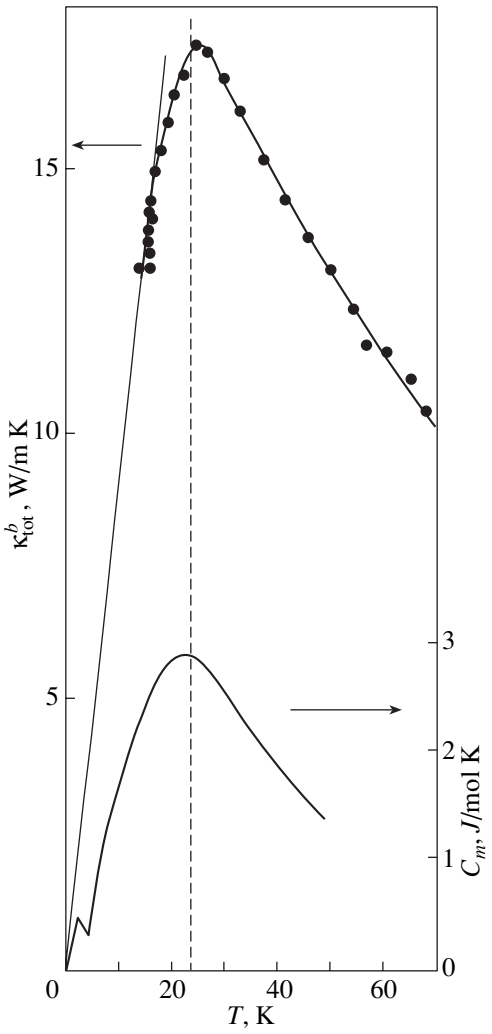

Fig. 3. Temperature dependences of the thermal conductivity κ^b_{tot} and the magnetic specific heat [24] of the $LiCuVO_4$ compound.

$\kappa^b_{tot}(T)$ and the temperature range corresponding to this contribution. This problem did not arise when the contributions of the components $\kappa^{ladd}_m(T)$ and $\kappa^{chain}_m(T)$ were separated from the total thermal conductivity $\kappa_{tot}(T)$ measured along the spin ladders [1, 2, 5, 6] and spin chains [3, 4] in the $(Sr,Ca,La)_{14}Cu_{24}O_{41}$ system and Sr_2CuO_3 and $SrCuO_2$ compounds. For these materials, the reference data were obtained by measuring the thermal conductivity along the crystallographic directions in which spin ladders and spin chains were absent. In these directions, the thermal conductivity of the crystal lattice varied as the reciprocal of the temperature ($\kappa_{ph} \sim T^{-1}$), which is consistent with the theoretical dependence of the phonon component of the thermal conductivity at $T \geq \Theta/3$ (where Θ is the Debye temperature).

For compounds with spin ladders, the contribution of the component $\kappa^{ladd}_m(T)$ could be determined as the difference between the total thermal conductivity κ_{tot}, which corresponds to the second maximum, and the values of $\kappa_{ph}(T)$, which were extrapolated according to the relationship $\kappa_{ph} \sim T^{-1}$ from the temperature boundary of the first maximum toward the high-temperature range (see the scheme shown in Fig. 2a).

The dependences of the thermal conductivity $\kappa_{tot}(T)$ of the compounds with spin chains did not exhibit second maxima but involved a characteristic shoulder (marked by an arrow in Fig. 2b). In this case, too, the contribution of the component $\kappa^{chain}_m(T)$ was determined as the difference between the total thermal conductivity $\kappa_{tot}(T)$ and the values of $\kappa_{ph}(T)$, which were extrapolated using the relationship $\kappa_{ph} \sim T^{-1}$ from the initial point of the shoulder toward the high-temperature range (Fig. 2b). Nothing of the kind is observed in our experimental curves $\kappa^b_{tot}(T)$ for the $LiCuVO_4$ crystal (Fig. 1, curve *1*).

It was assumed that, since the exchange coupling constant J^{chain} for the $LiCuVO_4$ crystal is small, the contribution of the component $\kappa^{chain}_m(T)$ to the total thermal conductivity $\kappa^b_{tot}(T)$ can be observed at lower temperatures as compared to those for the Sr_2CuO_3 and $SrCuO_2$ compounds, for which J^{chain} lies in the range 2150–3000 K and the dependences $\kappa^{chain}_m(T)$ exhibit maxima at 80 and 50 K, respectively [3, 4]. If this assumption is valid, the maximum in the dependence $\kappa^{chain}_m(T)$ for the $LiCuVO_4$ crystal can be located in the vicinity of the maximum corresponding to the phonon thermal conductivity.

In order to verify this assumption, we compared the temperature dependence of the thermal conductivity $\kappa^b_{tot}(T)$ with the temperature dependence of the magnetic component of the specific heat $C_m(T)$ for the $LiCuVO_4$ compound [24] (Fig. 3).

For systems with spin ladders and spin chains, the temperatures of the maxima in the dependences $\kappa^{ladd}_m(T)$ and $\kappa^{chain}_m(T)$ approximately coincide with those in the dependences $C_m(T)$.

According to Yamaguchi *et al.* [24], the dependence $C_m(T)$ of $LiCuVO_4$ exhibits a maximum at ~30 K (Fig. 3). Therefore, taking into account the aforesaid, the maximum of the curve $\kappa^{chain}_m(T)$ for this compound should be observed near the same temperature.

This confirms our assumption but appreciably complicates the separation of the component $\kappa^{chain}_m(T)$ from

the experimental dependence $\kappa^b_{tot}(T)$, because the curve $\kappa^b_{tot}(T)$ has a maximum at a temperature of ~30 K (Fig. 3). Recall that, in this temperature range, the experimental thermal conductivity can be substantially affected not only by the components κ^{chain}_m and κ_{ph} but also by impurities and defects [25], which leads to additional error in the determination of the contribution from the component $\kappa^{chain}_m(T)$.

Let us now attempt to estimate (even if approximately) the thermal conductivity $\kappa^{chain}(T)$ for the $LiCuVO_4$ crystal.

As was noted above, the contribution from the component $\kappa^{chain}_m(T)$ to the thermal conductivity of the $LiCuVO_4$ crystal cannot be separated by the standard technique used earlier for the $(Sr,Ca,La)_{14}Cu_{24}O_{41}$ system and Sr_2CuO_3 and $SrCuO_2$ compounds.

We applied another approach to the separation of the contribution from the component $\kappa^{chain}_m(T)$. This approach is based on the specific features in the behavior of the temperature dependence of the anisotropy coefficient $\beta = \kappa^b_{ph}(T)/\kappa^a_{ph}(T)$.

Sologubenko *et al.* [4] revealed that the temperature dependences of the anisotropy coefficient β for systems with spin ladders $[(Sr,Ca,La)_{14}Cu_{24}O_{41}]$ and compounds with spin chains (Sr_2CuO_3, $SrCuO_2$) exhibit unusual behavior. The anisotropy coefficient β weakly depends on the temperature (or remains constant) in the temperature range in which the contribution from κ^{chain}_m (or κ^{ladd}_m) to the measured thermal conductivity is absent (or small) and increases (or even passes through a maximum) when the contribution from this additional components of the thermal conductivity becomes significant (Fig. 4).[3] The same inference follows from a comparison of the dependences $\beta(T)$ [4] and $\kappa^{ladd}_m(T)$ [5] for the $Sr_{14}Cu_{24}O_{41}$ compound (see inset in Fig. 4).

Figure 5a depicts the temperature dependence of the anisotropy coefficient $\beta = \kappa^b_{tot}/\kappa^a_{tot}$, which was determined from the data presented in Fig. 1 for the $LiCuVO_4$ crystal. For comparison, Fig. 5b shows the dependence $\beta(T)$ for the $Sr_{14}Cu_{24}O_{41}$ compound [4].

The high-temperature maximum in the dependence $\beta(T)$ for $Sr_{14}Cu_{24}O_{41}$ is associated with the contribution from the component $\kappa^{ladd}_m(T)$ to the measured thermal conductivity. By analogy with the $Sr_{14}Cu_{24}O_{41}$ compound, we can assume that the maximum in the dependence $\beta(T)$ for the $LiCuVO_4$ crystal is due to the contribution from the component $\kappa^{chain}_m(T)$ to the total thermal conductivity $\kappa^b_{tot}(T)$.

In the range 50–150 K, the anisotropy coefficient $\beta(T)$ for the $LiCuVO_4$ crystal only weakly depends on the temperature (Fig. 5a). In our previous work [21], we showed that, in the temperature range 5–150 K, the thermal conductivity κ^a_{tot} obeys the equality $\kappa^a_{tot} = \kappa^a_{ph}$ (Fig. 1). Probably, the thermal conductivity κ^b_{tot} in the range 50–150 K satisfies the same condition; i.e., $\kappa^b_{tot} = \kappa^b_{ph}$. This assumption is confirmed by the fact that, in

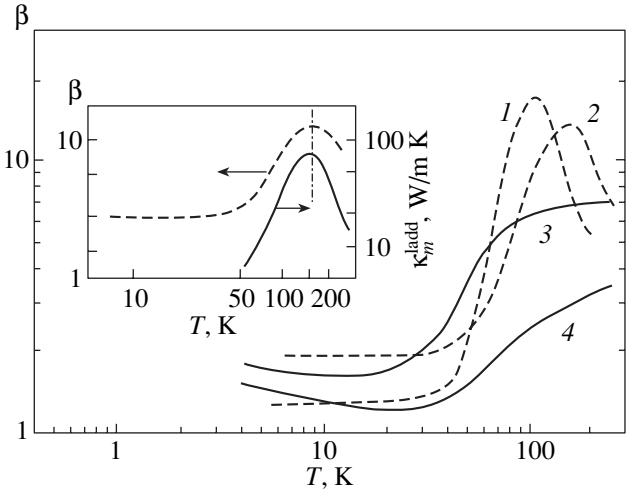

Fig. 4. Temperature dependences of the anisotropy coefficient β for (*1*) $Sr_{12}Ca_2Cu_{24}O_{41}$, (*2*) $Sr_{14}Cu_{24}O_{41}$, (*3*) $SrCuO_2$, and (*4*) Sr_2CuO_3 [4]. For explanation of the anisotropy coefficient β, see the text (Footnote 3). The inset shows the temperature dependences of the anisotropy coefficient β [4] and the thermal conductivity κ^{ladd}_m [5] for the $Sr_{14}Cu_{24}O_{41}$ compound.

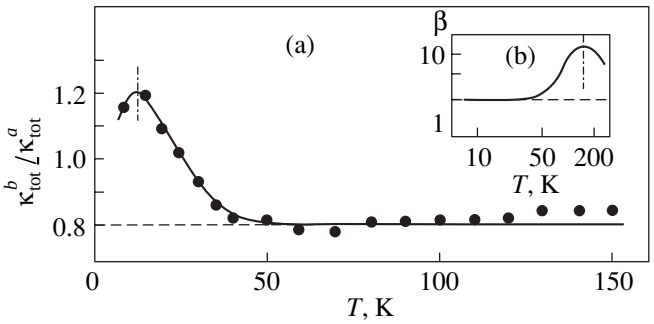

Fig. 5. Temperature dependences of the anisotropy coefficient β for (a) $LiCuVO_4$ (our data) and (b) $Sr_{14}Cu_{24}O_{41}$ [4].

[3] In the system $(Sr,Ca,La)_{14}Cu_{24}O_{41}$ ($\beta = \kappa^c/\kappa^a$), spin ladders are arranged along the *c* axis. In the compounds $SrCuO_2$ ($\beta = \kappa^c/\kappa^a$) and Sr_2CuO_3 ($\beta = \kappa^b/\kappa^c$), spin chains are aligned along the *c* and *b* axes, respectively.

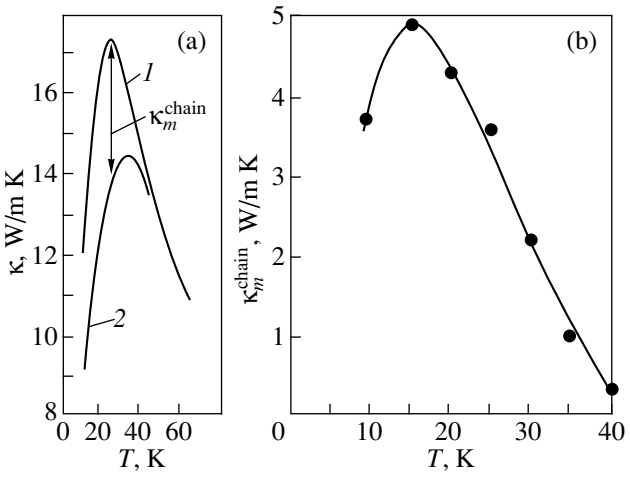

Fig. 6. Temperature dependences of the thermal conductivities (a) (*1*) κ_{tot}^{b}, (*2*) κ_{ph}^{b}, and (b) κ_m^{chain} for the $LiCuVO_4$ compound.

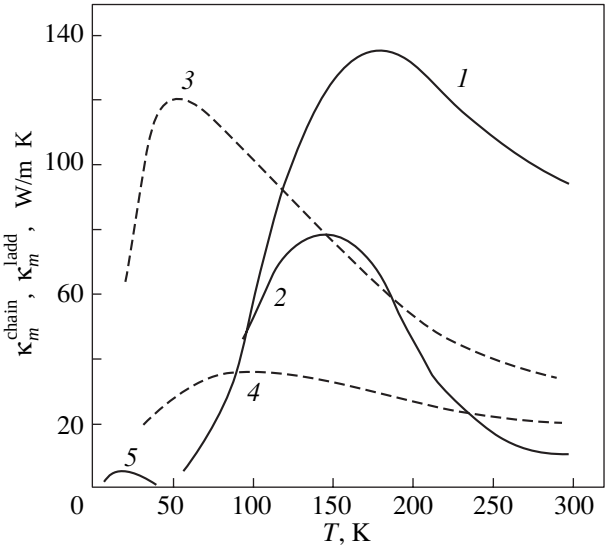

Fig. 7. Temperature dependences of the thermal conductivities κ_m^{ladd} and κ_m^{chain} for (*1*) $Ca_9La_5Cu_{24}O_{41}$ [5] and (*2*) $Sr_{14}Cu_{24}O_{41}$ [5] compounds with spin ladders and (*3*) $SrCuO_2$ [3, 4], (*4*) Sr_2CuO_3 [3, 4], and (*5*) $LiCuVO_4$ compounds with spin chains.

the temperature range under consideration, the dependences $\kappa_{tot}^{a}(T)$ and $\kappa_{tot}^{b}(T) \sim T^{-0.9}$ exhibit identical behavior (Fig. 1). These dependences are similar to the theoretical dependence $\kappa_{ph} \sim T^{-1}$ at $T \geq \Theta/3$ for ideal defect-free crystals. Since the experimental thermal conductivities of both samples vary as $\sim T^{-0.9}$ rather than as T^{-1}, the samples contain small amounts of defects. Although defects in each sample can be different in nature, they equally affect the thermal conductivities $\kappa_{ph}^{b}(T)$ and $\kappa_{ph}^{a}(T)$. Therefore, the equality $\beta(T) = \kappa_{ph}^{b}(T)/\kappa_{ph}^{a}(T)$ for the $LiCuVO_4$ compound can be considered to be satisfied in the temperature range 50–150 K.

Let us now consider the low-temperature range 10–50 K (Fig. 5a). In this range, we have $\beta(T) = \kappa_{tot}^{b}(T)/\kappa_{ph}^{a}(T) = \kappa_{ph}^{b}(T) + \kappa_m^{chain}(T)/\kappa_{ph}^{a}(T)$. Under the assumption that $\beta(T) = \text{const} \sim 0.8$ over the entire range 10–150 K, the values of κ_{ph}^{b} in the range 10–150 K can be estimated from the relationship $\kappa_{ph}^{b}(T) = 0.8\kappa_{ph}^{a}$. The results of these calculations are presented in Fig. 6a (curve *2*). Then, the thermal conductivity $\kappa_m^{chain}(T)$ for the $LiCuVO_4$ crystal can be determined from the relationship $\kappa_m^{chain}(T) = \kappa_{tot}^{b}(T) - \kappa_{ph}^{b}(T)$ (Fig. 6b).

However, it should be noted once again that the procedure of separating the component $\kappa_m^{chain}(T)$ from the total thermal conductivity $\kappa_{tot}^{b}(T)$ for the $LiCuVO_4$ compound is rather approximate because of the large number of assumptions and simplifications.

Figure 7 illustrates the main results obtained in our work. In this figure, the calculated dependence $\kappa_m^{chain}(T)$ for the $LiCuVO_4$ crystal is compared with the data available in the literature on the dependences $\kappa_m^{ladd}(T)$ for the $Ca_9La_5Cu_{24}O_{41}$ and $Sr_{14}Cu_{24}O_{41}$ compounds [5] and the dependences $\kappa_m^{chain}(T)$ for the $SrCuO_2$ and Sr_2CuO_3 compounds [4].

It can be seen from Fig. 7 that, in materials with large values of exchange coupling constants J^{ladd} and J^{chain} for spin ladders and spin chains (1500 and 2150–3000 K, respectively [11–15]), the components κ_m^{ladd} and κ_m^{chain} make a significant contribution to the thermal conductivity when the heat flux in crystals is directed along the ladders and chains. The contribution from the component κ_m^{chain} to the measured thermal conductivity is considerably less for materials with small values of J^{chain} ($J^{chain} \sim 22$ K for spin chains in $LiCuVO_4$ [20]).

ACKNOWLEDGMENTS

This work was performed in the framework of bilateral agreements between the Russian Academy of Sciences, the Polish Academy of Sciences, and Deutsche Forschungsgemeinschaft and was supported by the Russian Foundation for Basic Research (project no. 02-02-17657).

REFERENCES

1. A. V. Sologubenko, K. Gianno, H. R. Ott, *et al.*, Physica B (Amsterdam) **284–288**, 1595 (2000).
2. A. V. Sologubenko, K. Gianno, H. R. Ott, *et al.*, Phys. Rev. Lett. **84** (12), 2714 (2000).
3. A. V. Sologubenko, E. Felder, K. Gianno, *et al.*, Phys. Rev. B **62** (10), R6108 (2000).
4. A. V. Sologubenko, K. Gianno, H. R. Ott, *et al.*, Phys. Rev. B **64**, 054412 (2001).
5. C. Hess, C. Baumann, U. Ammerahl, *et al.*, Phys. Rev. B **64**, 184305 (2001).
6. C. Hess, U. Ammerahl, C. Baumann, *et al.*, Physica B (Amsterdam) **312–313**, 612 (2002).
7. K. Kudo, S. Ishikawa, T. Noji, *et al.*, J. Phys. Soc. Jpn. **70** (2), 437 (2001).
8. J. V. Alvarez and G. Gros, cond-mat/0201300 (2002).
9. F. Heidrich-Meisner, A. Honecker, D. C. Cabra, and W. Brenig, cond-mat/0208282 (2002).
10. L. D. Faddeev and L. A. Takhtajan, Phys. Lett. A **85**, 375 (1981).
11. T. Ami, M. K. Crawford, R. L. Harlow, *et al.*, Phys. Rev. B **51**, 5994 (1995).
12. H. Suzuura, H. Yasuhara, A. Furusaki, *et al.*, Phys. Rev. Lett. **76**, 2579 (1996).
13. N. Motoyama, H. Eisaki, and S. Uchida, Phys. Rev. Lett. **76**, 3212 (1996).
14. D. C. Johnston, Acta Phys. Pol. A **91**, 181 (1997).
15. R. S. Eccleston, M. Uehara, J. Akimitsu, *et al.*, Phys. Rev. Lett. **81**, 1702 (1998).
16. L. P. Regnault, J. P. Boucher, H. Moudden, *et al.*, Phys. Rev. B **59** (2), 1055 (1999).
17. M. Matsuda, T. Yosihava, K. Kokurai, and G. Shirane, Phys. Rev. B **59** (2), 1060 (1999).
18. M. A. Lafontaine, M. Lablanc, and G. Ferey, Acta Crystallogr. C **45**, 1205 (1989).
19. M. O. Keeffe and S. Andersson, Acta Crystallogr. A **33**, 914 (1977).
20. A. N. Vasil'ev, L. A. Ponomarenko, H. Manaka, *et al.*, Phys. Rev. B **64**, 024419 (2001).
21. L. S. Parfen'eva, A. I. Shelykh, I. A. Smirnov, *et al.*, Fiz. Tverd. Tela (St. Petersburg) **45** (11), 1991 (2003) [Phys. Solid State **45**, 2093 (2003)].
22. A. V. Prokofiev, D. Wichert, and W. Assmus, J. Cryst. Growth **220**, 345 (2000).
23. A. Jezowski, J. Mucha, and G. Pompe, J. Phys. D: Appl. Phys. **7**, 1247 (1974).
24. M. Yamaguchi, T. Furuta, and M. Ishikawa, J. Phys. Soc. Jpn. **65** (9), 2998 (1996).
25. V. S. Oskotskiĭ and I. A. Smirnov, *Defects in Crystals and Thermal Conductivity* (Nauka, Leningrad, 1972).

Translated by O. Borovik-Romanova

Physics of the Solid State, Vol. 46, No. 2, 2004, pp. 364–370. Translated from Fizika Tverdogo Tela, Vol. 46, No. 2, 2004, pp. 353–359.
Original Russian Text Copyright © 2004 by Kyutt, Shcheglov, Davydov, Usikov.

LOW-DIMENSIONAL SYSTEMS AND SURFACE PHYSICS

Deformation of AlGaN/GaN Superlattice Layers According to X-ray Diffraction Data

R. N. Kyutt, M. P. Shcheglov, V. Yu. Davydov, and A. S. Usikov

Ioffe Physicotechnical Institute, Russian Academy of Sciences, Politekhnicheskaya ul. 26, St. Petersburg, 194021 Russia

Received June 23, 2003

Abstract—Three-crystal x-ray diffractometry is used for structural studies of nitride AlGaN/GaN superlattices (SLs) grown by metal-organic chemical vapor deposition on sapphire with GaN and AlGaN buffer layers with widely varied SL period (from 50 to 3500 Å), Al content in $Al_xGa_{1-x}N$ layers ($0.1 \le x \le 0.5$), and buffer layer composition. Satellite peaks characteristic of SLs are well pronounced up to the third order in θ–2θ scans of symmetric Bragg reflections and θ scans of the symmetric Laue geometry. The corresponding curves are well modeled by kinematic formulas. The average SL parameters, as well as the thickness, composition, and strain of individual layers, are determined using a combination of symmetric Bragg and Laue reflections. It is shown that all the samples under study are partially relaxed structures in which the elastic stresses between the entire SL and the buffer layer, as well as between individual layers, are relaxed. The AlGaN layers are stretched and the GaN layers are compressed. The GaN layer compression is larger in magnitude than the AlGaN layer tension because of thermoelastic stresses. © *2004 MAIK "Nauka/Interperiodica".*

1. INTRODUCTION

Gallium and aluminum nitrides, as well as solid solutions made on their basis, are promising materials for optoelectronic devices operating in the blue and violet spectral regions. The AlGaN solid solution attracts close attention due to its application not only in laser structures (as cladding layers) but also in field-effect transistors operating under high voltage and at high temperatures. Due to the large piezoelectric coefficient and stresses arising between GaN and AlGaN layers in AlGaN/GaN heterostructures, strong electric fields can be induced, which promote the formation of a two-dimensional electron gas of high concentration at interfaces between the layers.

Beginning with the paper by Nakamura *et al.* [1], AlN/GaN and AlGaN/GaN superlattices became a widely used object in optical and electrical studies [2–5]. The physical properties of these structures heavily depend on SL layer stresses and defects generated during their relaxation. For this reason, studies of the strain state of SL layers, their relaxation, and defect generation are of great significance.

X-ray diffractometry (XRD) is the best instrument for determining the SL structure parameters. This method is also applied to study nitride structures [6–17]. In most of these works, attention was focused on the determination of the limits of coherent growth for AlGaN/GaN SLs with various Al concentrations, periods, and total thicknesses [6, 7, 10–12]. Hence, the XRD analysis was restricted to only the determination of the layer composition and the degree of total relaxation of an SL with respect to the buffer. The elastic stress relaxation and its mechanism in AlGaN/GaN SLs were considered in most detail in [13], where they were studied using optical microscopy, XRD, and photoluminescence spectroscopy. In [15], it was shown that the growth of an AlGaN/AlN SL as a buffer allows a significant decrease in the density of growth dislocations. In [16], the defect structure of the AlGaN/GaN system on the GaN buffer was studied and its influence on the transport properties was shown.

This paper is devoted to performing detailed XRD studies of AlGaN/GaN SLs in wide ranges of layer thicknesses, Al concentrations, and buffer layer compositions. Since both single GaN epitaxial layers and multilayer systems made on their basis are significantly imperfect structures with a high defect density [17–19], special emphasis was placed on the determination of the SL parameters using combinations of XRD reflections.

2. DIFFRACTION FROM SUPERLATTICES AND DETERMINATION OF THE STRUCTURAL PARAMETERS

The diffraction curves from SLs contain periodically arranged satellite peaks caused by periodic variation of the strain $\varepsilon(z)$ and the scattering power (structure factor) $F(z)$ over the SL depth. The relative intensity of satellites depends on the distribution of these parameters over one period. For symmetric reflections, the strain $\varepsilon(z)$ is expressed in terms of the variation in the interplanar distance $d(z)$ for a measured reflection (for asymmetric reflections, $\varepsilon(z)$ also depends on the mutual rotations of the reflecting planes arising in coherently joined or not completely relaxed SL layers). In most cases, epitaxial SLs can be represented as consisting of

two alternating layers of different composition separated by a sharp interface; therefore, the distributions of d and F over a period are characterized by the two interplanar distances d_1 and d_2, structure factors F_1 and F_2, and thicknesses t_1 and t_2 of these layers. For layers of ternary solid solutions, the structure factors are immediately defined by their composition x_1 and x_2; the interplanar distance depends not only on the composition but also on the strain state of these layers, which can in turn be described by the relaxation parameters. Thus, there are six independent structural parameters (x_1, x_2, t_1, t_2, and two relaxation parameters). These parameters define the diffraction pattern and can be obtained from a diffraction analysis. In the case of the GaN/$Al_xGa_{1-x}N$ system, where one layer is a pure substance and the other is a solid solution, the number of independent parameters decreases to five.

In wurtzite-structure films growing along the hexagonal ⟨0001⟩ axis, the lattice parameters a and c define the interplanar distances in the interface plane and along the normal to it, respectively. Let a_i and c_i be the actual (measured) lattice parameters of the ith layer in the system and let a_i^b and c_i^b be the corresponding lattice parameters of the layer of the given composition in the stress-free state, respectively, where the subscript $i = 0$, 1, and 2 indicates the buffer layer and the first and second SL sublayers, respectively. The elastic strain of SL layers is given by

$$\varepsilon_i = \frac{a_i - a_i^b}{a_i^b}, \quad (1)$$

and the actual lattice parameter is $c_i = c_i^b(1 - p\varepsilon_i)$, where $p = 2c_{13}/c_{33}$ is the Poisson ratio. The elastic stress relaxation in SLs can be characterized by the change $\Delta a_i = a_i - a_{i-1}$ in the lattice parameter a at the interface or by the relative relaxation

$$r_i = \frac{a_i - a_{i-1}}{a_i^b - a_{i-1}} = \frac{\Delta a_i}{a_i^b - a_{i-1}}, \quad (2)$$

where Δa_1 and r_1 correspond to relaxation at the lower interface (between the buffer layer and the first SL layer) and Δa_2 and r_2 characterize relaxation at the interfaces between individual layers (Fig. 1). For the unrelaxed coherent structure, we have $\Delta a_1 = \Delta a_2 = 0$. If the individual SL layers remain coherent and the SL relaxes as a unit with respect to the buffer, we have $\Delta a_2 = 0$ and Δa_1 can be negative or positive depending on the buffer layer composition. In the general case of a relaxed incoherent SL, both changes in the lattice parameter are nonzero and the magnitude of Δa_2 should be the same at all SL interfaces for the structure to be periodic.

The diffraction curve of a symmetric Bragg reflection allows direct determination of the period T (from the distance $\delta\theta$ between the satellites) and the average lattice parameter $\langle c \rangle$ [from the angular position of the central peak (zero satellite)] in the 2θ angle scale. An analysis of the formulas of the kinematic scattering theory for a two-layer SL with sharp interfaces [20] shows that the ratio I_n/I_0 of the intensities of the nth-order satellite and the zero satellite is given by a simple analytical expression and depends on three quantities, namely, the ratio of the thicknesses of the two layers t_2/t_1, the ratio of their structure factors F_2/F_1, and a strain parameter; for a symmetric Bragg reflection, this parameter can be written as

$$B = \frac{2\pi\sin(\theta)}{\lambda}\Delta\varepsilon_\perp\frac{t_1 t_2}{t_1 + t_2}. \quad (3)$$

Taking into account relaxation between layers, the difference $\Delta\varepsilon_\perp$ of the strains of the two SL layers is given by

$$\Delta\varepsilon_\perp = \frac{c_{AlN} - c_{GaN}}{c_{GaN}}x + p\frac{a_{AlN} - a_{GaN}}{a_{GaN}}x - p\frac{\Delta a_2}{a_{GaN}}, \quad (4)$$

where c_{GaN}, a_{GaN}, and c_{AlN}, a_{AlN} are the tabulated lattice parameters of GaN and AlN, respectively, and the Poisson ratio $p = 2c_{13}/c_{33}$ is taken to be identical for the GaN and AlGaN layers. All other conditions being equal, the larger B, the higher the intensities of side satellites with respect to the zero satellite. At $B > 1.5$, the zero satellite can become weaker than the other peaks and the problem of its identification arises. These three parameters (B, t_2/t_1, F_2/F_1) can be calculated from the relative intensity of satellites if their number in the experimental curve is larger than three.

Notwithstanding the fact that all five independent SL parameters can be determined in this way by analyzing a single curve for a symmetric Bragg reflection, the accuracy of their determination is not very high, especially at low Al concentrations in the solid solution layer. Therefore, as an additional parameter, we used

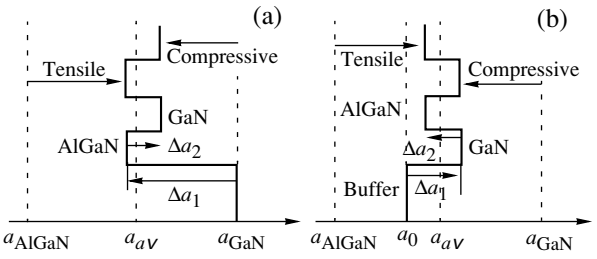

Fig. 1. Schematic diagram of variations in the parameter a over the depth of a relaxed incoherent AlGaN/GaN superlattice grown on (a) a GaN and (b) an AlGaN buffer layer. In the latter case, the Al content in the buffer layer is higher than the average Al content for the superlattice. Dashed lines are the lattice parameters of GaN and AlGaN in the stress-free state, as well as the parameter a averaged over the SL. Δa_1 and Δa_2 are the changes in the lattice parameter at the interfaces between the buffer and SL and between the SL layers, respectively.

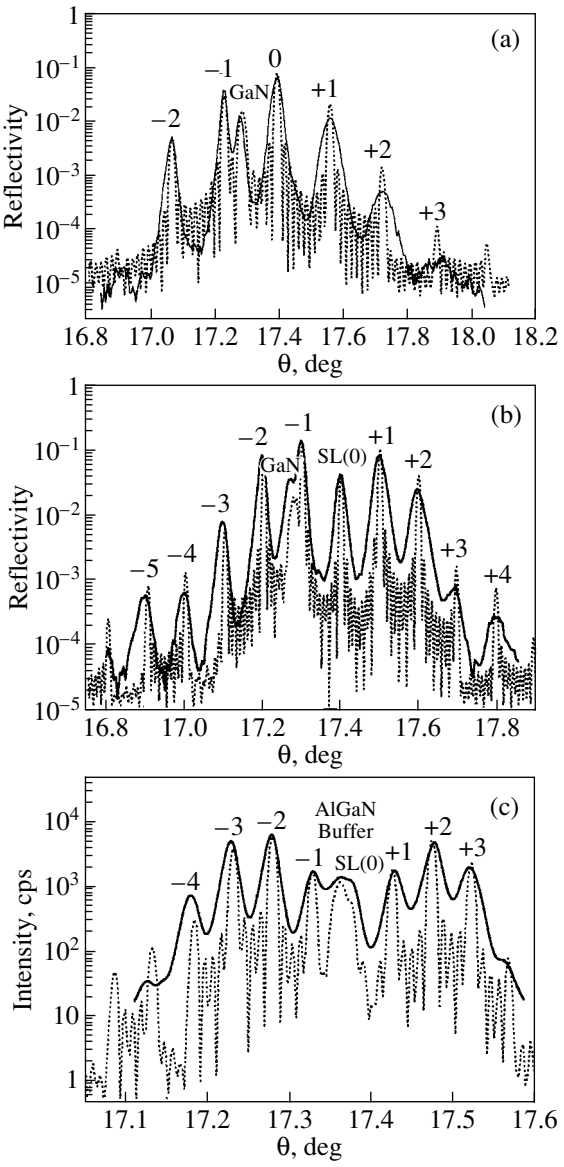

Fig. 2. Three-crystal diffraction curves of θ–2θ scanning of the symmetric (0002) Bragg reflection for samples with various SL periods. The solid curve represents the experimental data, and the dashed curve is calculated for the SL with the parameters listed in Tables 2 and 3. The period T is (a) 281, (b) 470, and (c) 950 Å.

the 2θ-angle position of the central peak in the curve of a symmetric Laue reflection from the SL. This parameter allows direct calculation of the average lattice parameter a of the SL:

$$\langle a \rangle = (a_1 t_1 + a_2 t_2)/T. \quad (5)$$

Given B, t_2/t_1, $\langle c \rangle$, and $\langle a \rangle$, we determined the actual lattice parameters c and a of both SL layers and then the Al content in the AlGaN layer and the relaxation parameters Δa_1 and Δa_2. The analytical approach described above contains a number of approximations (the absence of a transition layer between GaN and AlGaN layers and constancy of the structure factors over the angular interval under study). For this reason, the obtained parameters were used as initial parameters when calculating the diffraction curves and their values were then refined by comparing the calculated and experimental curves. In this study, the reflection curves were calculated within the kinematic approximation [20]; the calculation procedure is described in [21].

The calculated reflection curves characterize a perfect superlattice without structural defects. In the case of defect structures, such as the system under study, the satellite peaks are broadened due to defects. However, practice has shown that all the SL satellites are distorted identically (if only the influence of defects is considered rather than distortions of the SL periodicity). This allows comparison of the calculated (for perfect SLs) and experimental reflection curves in terms of the relative height of satellites or their integral intensity.

When determining the SL characteristics, the following parameters were used: a = 3.189 and 3.113 Å, c = 5.1851 and 4.9816 Å, and p = 0.53 and 0.49 for GaN and AlN, respectively [22, 23].

3. EXPERIMENTAL

AlGaN/GaN superlattices were grown by metal-organic chemical vapor deposition (MOCVD) on (0001) sapphire substrates with a buffer layer approximately 1 μm thick. Three series of samples were studied. In two series, SLs consisted of layers of the same thickness, with an Al content of ~26 at. % in one of the two layers; the period varied from 5 to 320 nm. In one of these series, layers were grown on a GaN buffer, and in the other, on an AlGaN buffer. The SLs in the third series had the same period (~10 nm), but the Al content was varied from 10 to 50 at. %. The total SL thickness was the same in all series (~3 μm).

X-ray diffraction measurements were carried out using a three-crystal diffractometer with CuK_α radiation. The θ and θ–2θ diffraction curves were measured in two diffraction geometries, namely, for the symmetric Bragg (0002) reflection and symmetric Laue (1010) reflection. The θ–2θ curves were measured using the absolute scale of scattering angles 2θ. For a number of samples, the total intensity distribution around the reciprocal-lattice site was measured. The monochromator and analyzer reflections were selected so as to attain the highest intensity and the lowest dispersion of the resulting signal, depending on the reflection from the sample.

4. RESULTS AND DISCUSSION

The two-crystal integral curves of symmetric Bragg reflections do not reveal any fine structure and exhibit a common broadened peak from the entire buffer–SL layer. However, the fine structure is well pronounced in the three-crystal θ–2θ scans (Fig. 2). Depending on the

SL parameters, the curves contain satellites up to the fifth order, which is an indication of good periodicity of the grown structures. Apart from the SL peaks, reflection from the buffer layer can also be detected in most of the curves. For some samples (with SL periods of 20–80 Å), satellites are also detected in the symmetric Laue geometry (in the θ scans), although their intensity is much lower than that of the central peak of the SL reflection. An example of such a scan is shown in Fig. 3a.

Such a difference in the number of satellites observed in the diffraction curves is explained by the specific dislocation structure of GaN films. It consists mostly of straight screw and edge dislocations perpendicular to the interface. Due to dislocations, the intensity distribution around the reciprocal-lattice sites is extended in the direction parallel to the surface [24, 25]. The reflection broadening along the normal to the surface is much narrower. Since the additional reflection centers (satellites) are also distributed along the normal (the direction of periodic variation in the composition of the crystalline layer), they can be detected in the curves representing a cross section of reciprocal lattice sites in this direction, i.e., for θ–2θ scans in the symmetric Bragg geometry and in the θ curves in the symmetric Laue case.

Figure 2 shows that the (0002)-reflection curves notably change shape as the SL period T increases at fixed x. The intensity of the central peak decreases, while the intensities of the side satellites increase. At longer periods ($T > 1600$ Å), the curve splits into two sets of oscillations localized near reflection centers of the two (GaN and AlGaN) layers. This transformation is caused by the strain parameter B increasing with the SL period. As for the angular position of the central peak, it is almost the same for SLs with periods of 50–400 Å.

For SLs with identical technological parameters but grown on different buffer layers (GaN or AlGaN), the diffraction curves differ both in position and in satellite intensity only slightly. In the case of symmetric Laue diffraction, the angular position of the SL central peak, determined by the analyzer angle in the 2θ-scanning mode, also varies only slightly with the period and is independent of the buffer layer composition (Fig. 3b).

As the Al content in SL layers increases, the satellite positions shift toward smaller angles, the relative intensity of the zero satellite decreases, and that of the side satellites increases. The change in the satellite intensity is caused by the increase in the strain difference Δε of the two layers and, hence, in the parameter B.

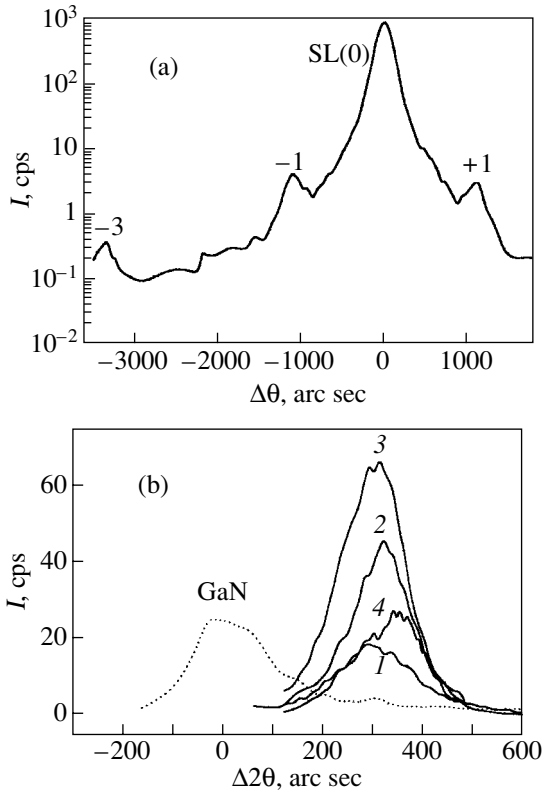

Fig. 3. Diffraction curves for symmetric (1010) Laue reflection. (a) The three-crystal curve of θ scanning for sample 1044 (the SL period 570 Å) and (b) the SL central peaks (solid lines) in the curves of 2θ scanning for samples (*1*) 1059, (*2*) 1044, (*3*) 927, and (*4*) 870 and for the GaN buffer layer (dashed line).

The parameters determined immediately from the diffraction curves (SL period, average lattice parameters $\langle a \rangle$, $\langle c \rangle$) are listed in Table 1. The degree of relaxation of the entire SL can be determined from the ratio $\langle c \rangle / \langle a \rangle$. Figure 4 shows these values as a function of the SL period (for samples of series 1, 2) and of the average Al content in SLs (for samples of series 3). The experimental points in Fig. 4 lie far from the lines characterizing pseudomorphic strained structures and are slightly higher than the curves calculated for total relaxation, which suggests that all the SLs are in a com-

Table 1. Average parameters of superlattices determined from x-ray diffraction curves

Buffer layer	GaN				AlGaN						
Sample	1055	1054	1051	1044	1072	1059	927	870	1070	1074	1075
Period, Å	53.5	129	281	470	92	238	570	950	119	142	142
$\langle c \rangle$, Å	5.1543	5.1523	5.1526	5.1543	5.1492	5.1543	5.1621	5.1598	5.1703	5.1340	5.1224
$\langle a \rangle$, Å	3.1759	3.1761	3.1766	3.1748	3.1721	3.1755	3.1757	3.1752	3.1812	3.1664	3.1620

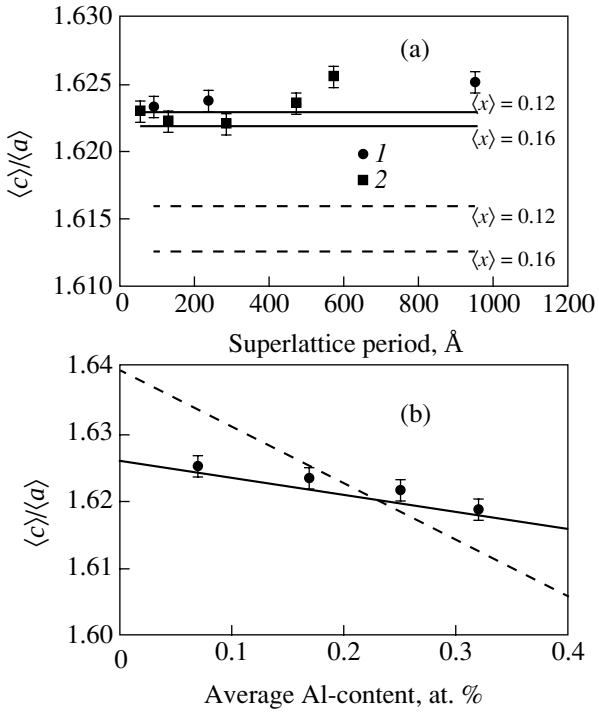

Fig. 4. Ratio of the experimental average parameters $\langle c\rangle$ and $\langle a\rangle$ of the AlGaN/GaN superlattice as a function (a) of the SL period at a fixed average composition and (b) of the average SL composition at a fixed SL period for samples grown on (*1*) GaN and (*2*) AlGaN buffer layers. The solid and dashed lines in panel (a) are calculations for a completely relaxed SL and for the unrelaxed state with respect to the GaN buffer layer, respectively. The dashed line in panel (b) is calculated for the unrelaxed state with respect to the AlGaN buffer layer with composition $x_0 = 0.22$.

pressed state. Therefore, the SLs under study are relaxation structures and the compression is caused by strains resulting from the difference in the thermal expansion coefficients α of the sapphire substrate ($\alpha = 7.2 \times 10^{-6}$ K^{-1}) and the GaN and AlGaN layers ($\alpha_{GaN} = 5.6 \times 10^{-6}$ K^{-1}, $\alpha_{AlN} = 4.2 \times 10^{-6}$ K^{-1}). We can see from Fig. 4a that the points corresponding to the SLs grown on a GaN buffer lie, in general, lower than the values of $\langle c\rangle/\langle a\rangle$ for the structures with an AlGaN buffer layer. This result can be due to the fact that, apart from the contribution from thermoelastic strains, there are residual strains resulting from incomplete relaxation of the mismatch stresses between the buffer layer and the entire SL at the relaxation temperature. The residual strains are tensile in the former case and compressive in the latter (if the Al content in the buffer layer is higher than that in the SL on average). Figure 4a shows a certain increase in the ratio $\langle c\rangle/\langle a\rangle$ with the SL period. As the Al content increases, the ratio $\langle c\rangle/\langle a\rangle$ decreases in full agreement with the dependence calculated for relaxed SLs (Fig. 4b).

The parameters of individual SL layers were determined analytically using the technique described above and were refined by comparing the experimental and calculated reflection curves (see Table 2 for the first two series and Table 3 for the third series). The curves calculated using these parameters are shown in Fig. 2 (dashed line). The relative satellite intensities calculated using the kinematic theory for the perfect superlattice fit the experimental curves well, notwithstanding the fact that the total SL thickness exceeds the extinction length.

The determined values of the period and thickness of sublayers, as well as the AlGaN layer composition, significantly differ from the preset growth parameters. In most cases, the SL period exceeds the expected one by ~20%. The anticipated equality of the AlGaN and GaN layer thicknesses also does not take place (the solid-solution layer is thicker than the GaN layer in most of the structures). The Al content in the barrier layer is not equal to the preset value $x = 0.26$ and varies from sample to sample in the first two series. We note that this complicates analysis of the strains in the SLs under study, since this does not allow the use of technological parameters and requires determination of all these values from diffraction measurements.

We can see from Tables 2 and 3 that the GaN and solid-solution layers are in the compression ($\varepsilon_{GaN} < 0$) and tension $\varepsilon_{AlGaN} > 0$) states, respectively. This takes place for all the structures under study irrespective of the buffer layer composition (except for the sample with the lowest Al content). The data from Table 2 show that the strain varies from sample to sample, although there is no dependence on the SL period. The GaN layer compression is, on average, identical in the structures

Table 2. Layer parameters of AlGaN/GaN superlattices with various periods (see Table 1), determined from x-ray diffraction curves

Sample	1055	1054	1051	1044	1059	927	870
t_{AlGaN}/t_{GaN}	1.25	1.05	1.15	1.05	1	1.1	1.1
x	0.286	0.31	0.30	0.31	0.30	0.25	0.25
ε_{GaN}, 10^{-3}	–2.4	–4.0	–2.6	–4.4	–3.1	–3.6	–3.3
ε_{AlGaN}, 10^{-3}	1.3	3.5	2.2	2.9	2.3	1.4	1.1
Δa_1, Å	–0.018	–0.012	–0.016	–0.014	0.008	0.001	0.003
Δa_2, Å	0.010	0	0.008	0	–0.007	–0.003	–0.006

grown on GaN and AlGaN buffer layers; however, in the latter case, the solid-solution layers are subject to weaker tensile strains. In the series of structures characterized by approximately identical periods but different Al contents, the strains in both SL sublayers increase (in magnitude) with the Al content.

The compressive strains in the GaN layers are larger in magnitude than the tensile strains in the AlGaN layers. This difference is mainly caused by thermoelastic strains. They can be calculated assuming that relaxation occurs at the growth temperature or can be estimated empirically from the angular position of the reflection peak of the GaN buffer layer in the symmetric Laue geometry (Fig. 3a). The thermoelastic contribution $\delta\varepsilon_T$ to the strains is calculated to be -2.8×10^{-3} in the former case and -1.2×10^{-3} in the latter. The former value seems to be too large in magnitude, since its subtraction from the values of ε listed in Tables 2 and 3 suggests that the SLs as a whole are in the tension state at the growth temperature. This can be so in the case of growth on a relaxed GaN buffer layer but cannot be explained for the structures growing on a solid-solution buffer with an Al content higher than that in the SL on average. The empirical value of $\delta\varepsilon_T$ is closer to reality. However, it can be used if the following two conditions are satisfied. First, the difference in the thermoelastic strains of GaN and AlGaN layers should not be very appreciable and, second, all relaxation processes that occur in the buffer layer on sapphire and in SL layers grown on buffer layers of various composition should take place at the same temperature lower than the growth temperature.

If we subtract the thermoelastic contribution, then the values of ε_{GaN} and ε_{AlGaN} become close in magnitude, which is an indication that (as mentioned above) relaxation close to 100% takes place at the lower interface in all SLs under study, i.e., that the stresses between the entire SL and the buffer layer are relieved. This is not unexpected if we take into account that the total SL thickness is ~3 μm and that the relative mismatch between the SL as a whole and the GaN buffer layer is ~0.32% or higher (reasoning from the average SL composition $\langle x \rangle = 0.15$); as a result, the arising stresses are a priori stronger than the critical values. The last conclusion is also valid for growth on a solid-solution buffer layer if the Al content in the buffer layer differs substantially from its average value for the SL. Using the data from Tables 2 and 3, we calculated the strains averaged over the SL period at the relaxation temperature. The calculated values show the existence of residual tensile strains $\langle\varepsilon\rangle \approx (0.6–1.2) \times 10^{-3}$ in the samples grown on a GaN buffer layer and almost total (within the determination error) stress relief in the structures grown on an AlGaN buffer layer (except for sample 1070, which has the lowest Al content).

However, the data obtained show that stresses are relieved not only at the lower interface between the SL and the buffer layer but also at the interfaces between individual SL layers. This is indicated by the nonzero values of the parameter Δa_2 which vary from sample to sample, exhibiting no dependence on the SL period or Al content. Almost total stress relaxation between layers takes place in the sample with the lowest Al content. A large degree of relaxation (~0.5) is also observed in the SL with the shortest period. In most of the structures, the relative relaxation degree r_2 is 0.1–0.3; the layers of SLs 1044 and 1054 are coherent ($\Delta a_2 = 0$). Such a spread can be explained by the fact that relaxation between layers depends on the defect structure of the buffer layers and films. This structure depends, to a significant extent, on the growth conditions of the sample.

Table 3. Layer parameters of AlGaN/GaN superlattices with various Al contents in the $Al_xGa_{1-x}N$ solid solution layer

Sample	1070	1072	1074	1075
t_{AlGaN}/t_{GaN}	1.1	1.2	1.3	1.3
x	0.15	0.31	0.44	0.54
ε_{GaN}, 10^{-3}	−0.3	−4.6	−5.5	−6.8
ε_{AlGaN}, 10^{-3}	−0.8	1.6	2.1	3.4
Δa_1, Å	0.013	0.004	0.0012	−0.004
Δa_2, Å	−0.013	−0.004	−0.009	−0.009

Several ways of providing stress relief in the AlGaN/GaN structures can be conceived. If relaxation involves dislocations, then the stresses between individual layers can be relieved in part by the bending of growth dislocations of mixed type with the formation of horizontal fragments at the interfaces between layers during growth (this mechanism was considered in [26]). As for the stresses between the entire SL and the buffer layer, they can relax via the formation of a dislocation network or of growth dislocations with large horizontal projections when the critical SL thickness is reached. In [13], another mechanism of stress relaxation in AlGaN/GaN SLs is suggested, according to which SL layers first grow coherently with respect to each other and to the buffer layer. On reaching the critical thickness, the stresses produced by the GaN buffer layer are relieved through the formation of cracks, which thread the entire structure and are sources of dislocation generation at the interfaces between individual layers. However, such a process can take place only in SLs subjected to moderate tensile stresses with respect to the buffer layer, i.e., grown either on a GaN buffer layer or on a solid-solution buffer with an Al content lower than its average for the SL (samples 1074 and 1075 in the case under consideration). Unfortunately, the x-ray diffraction data are insufficient for making a conclusion concerning a concrete relaxation mechanism.

5. CONCLUSIONS

X-ray diffractometry has been applied to study AlGaN/GaN superlattices grown on sapphire with GaN or AlGaN buffer layers in a wide range of the SL periods and Al contents. On the basis of an analysis and simulation of diffraction curves for a symmetric Bragg reflection and using the data on the symmetric Laue reflection, we determined the average lattice parameters, as well as the composition, thickness, and strains for individual SL layers. The following conclusions can be drawn.

(1) Both SL sublayers are in the strain state; more specifically, the GaN layers suffer compressive strain with respect to their free state, while the AlGaN layers are subject to tensile strain.

(2) In the SLs under study, almost complete relaxation takes place at the lower interface between the entire SL and the buffer layer; the stresses between individual layers are relieved in part.

(3) The GaN layer compression is larger (in magnitude) than the AlGaN layer tension; therefore, the structures as a whole are in the compression state, which is caused by the contribution from thermoelastic stresses.

ACKNOWLEDGMENTS

This study was supported by the Russian Foundation for Basic Research (project nos. 03-02-16164, 03-02-17562) and the Ministry of Education of the Russian Federation (project no. E02-3.4-182).

REFERENCES

1. S. Nakamura, M. Senoh, S. Nagahama, *et al.*, Appl. Phys. Lett. **72**, 211 (1998).
2. O. Ambacher, J. Smart, J. R. Shealy, *et al.*, J. Appl. Phys. **85**, 3222 (1999).
3. V. Yu. Davydov, A. A. Klochikhin, I. E. Kozin, *et al.*, Phys. Status Solidi A **188**, 863 (2001).
4. P. Kozodoy, M. Hansen, S. P. DenBaars, and M. K. Mishra, Appl. Phys. Lett. **74**, 3681 (1999).
5. S. Tripathy, S. J. Chua, P. Chen, and Z. L. Miao, J. Appl. Phys. **92**, 3503 (2002).
6. D. Korakakis, K. F. Ludwig, and T. D. Moustakas, Appl. Phys. Lett. **72**, 1004 (1998).
7. R. Langer, J. Simon, O. Konovalov, *et al.*, MRS Internet J. Nitride Semicond. Res. **3**, 46 (1998).
8. Cho Yong-Hoon, F. Feller, R. J. Hauenstein, *et al.*, J. Appl. Phys. **85**, 3006 (1999).
9. A. Saxler, P. Debray, R. Perrin, *et al.*, J. Appl. Phys. **87**, 369 (2000).
10. J. Bai, T. Wang, and S. Sakai, J. Appl. Phys. **90**, 1740 (2001).
11. S. Yamaguchi, M. Kosaki, Y. Watanabe, *et al.*, Appl. Phys. Lett. **79**, 3062 (2001).
12. A. Dadgar, J. Christen, T. Riemann, *et al.*, Appl. Phys. Lett. **78**, 2211 (2001).
13. S. Einfeldt, H. Heinke, V. Kirchner, and D. Hommel, J. Appl. Phys. **89**, 2160 (2001).
14. M. A. Tagliente, L. De Caro, L. Tapfer, *et al.*, J. Appl. Phys. **92**, 70 (2002).
15. H.-M. Wang, J.-P. Zhang, C.-Q. Chen, *et al.*, Appl. Phys. Lett. **81**, 604 (2002).
16. Z. Zhong, O. Ambacher, A. Link, *et al.*, Appl. Phys. Lett. **80**, 3521 (2002).
17. B. Heying, X. H. Wu, S. Keller, *et al.*, Appl. Phys. Lett. **68**, 643 (1996).
18. T. Metzger, R. Hopler, E. Born, *et al.*, Philos. Mag. A **77**, 1013 (1998).
19. R. Kyutt, V. Ratnikov, G. Mosina, and M. Scheglov, Fiz. Tverd. Tela (St. Petersburg) **41**, 30 (1999) [Phys. Solid State **41**, 25 (1999)].
20. V. S. Speriosu and T. Vreeland, J. Appl. Phys. **56**, 1591 (1984).
21. R. N. Kyutt, A. A. Toropov, T. V. Shubina, *et al.*, Appl. Surf. Sci. **166**, 341 (2000).
22. H. Angeger, D. Brunner, F. Freudenberg, *et al.*, Appl. Phys. Lett. **71**, 1504 (1997).
23. D. Polan, M. Grimsditch, and I. Grzegory, J. Appl. Phys. **79**, 3343 (1996).
24. V. Ratnikov, R. Kyutt, T. Shubina, *et al.*, J. Appl. Phys. **88**, 6252 (2000).
25. V. V. Ratnikov, R. N. Kyutt, T. V. Shubina, *et al.*, J. Phys. D: Appl. Phys. **34**, A30 (2001).
26. C. G. Jiao and D. Cherns, Inst. Phys. Conf. Ser. **169**, 327 (2001).

Translated by A. Kazantsev

Physics of the Solid State, Vol. 46, No. 2, 2004, pp. 371–377. Translated from Fizika Tverdogo Tela, Vol. 46, No. 2, 2004, pp. 360–366.
Original Russian Text Copyright © 2004 by Gall', Rut'kov, Tontegode.

LOW-DIMENSIONAL SYSTEMS AND SURFACE PHYSICS

Interaction of Silver Atoms with Iridium and with a Two-Dimensional Graphite Film on Iridium: Adsorption, Desorption, and Dissolution

N. R. Gall', E. V. Rut'kov, and A. Ya. Tontegode

Ioffe Physicotechnical Institute, Russian Academy of Sciences, Politekhnicheskaya ul. 26, St. Petersburg, 194021 Russia

e-mail: gall@ms.ioffe.rssi.ru

Received June 11, 2003

Abstract—The initial stages in the interaction of silver with the (111)Ir surface and with a two-dimensional graphite film (2D GF) on (111)Ir were studied by high-resolution electron Auger spectroscopy in ultrahigh vacuum. The growth mechanisms of silver films and the desorption fluxes of Ag atoms were determined, and their desorption energies estimated. It was found that the Ag desorption fluxes from a 2D GF on Ir and from a thick silver film on the pure metal are similar and considerably (an order of magnitude) smaller than the sublimation fluxes from bulk silver at the same temperatures. The activation energy for desorption from a submonolayer film varies from 3.2 eV for coverage $\theta = 1$ to 3.7 eV at $\theta \sim 0$. It was shown that silver atoms do not penetrate into the substrate bulk throughout the temperature range covered (300–1800 K). *© 2004 MAIK "Nauka/Interperiodica".*

1. INTRODUCTION

Even though the adsorption of silver on metals has been the subject of more than one investigation [1–3], this issue has not lost its importance because of the large number of discrepancies in the quoted figures. Moreover, there are still no data on the adsorption of silver atoms on the iridium surface, although platinum-group metals, such as Pt and Ru, have been studied in considerable detail. There is practically no information on silver adsorption on film systems [4], although such data are certainly of scientific interest and have application potential; indeed, carbon films are present on metal surfaces in many technological processes [5]. Furthermore, the presence of atoms of a third species on the metal surface could be employed for purposes of calibration in studies of adsorption.

Of particular interest in this respect is the adsorption of silver on top of two-dimensional graphite films (2D GFs) on metals. As shown by us earlier, silver is the only element studied thus far (Cs, K, Ba, Na, Pt, Si, C, Ir, Mo, etc.) that does not intercalate spontaneously under a 2D GF, i.e., does not penetrate into the space between the 2D GF and the metal surface [6].

There is practically no reliable information on the desorption of silver, particularly in film systems. As far as we know, no studies have attempted to separate the two possible mechanisms (desorption into vacuum and dissolution in the volume of the substrate) through which Ag atoms can escape from a surface [7]. It therefore became evident that studying the desorption of Ag atoms both from a pure-iridium surface and from iridium coated by a graphite monolayer would be of interest for establishing the physical mechanism of this phenomenon.

2. EXPERIMENTAL TECHNIQUES

The experiments were carried out in a high-resolution, ultrahigh-vacuum Auger spectrometer ($\Delta E/E < 0.1\%$) using a prism analyzer described in detail in [8]. We could measure Auger spectra of a high-temperature adsorbate directly within the range 300–2000 K. The substrate used was a predominantly (111)-oriented ribbon of textured polycrystalline Ir measuring $1 \times 40 \times 0.02$ mm heated directly by passing an electric current through it. The substrate was cleaned by annealing it successively in an oxygen ambient ($p_{O_2} = 10^{-6}$ Torr) at $T = 1500$ K and in ultrahigh vacuum at $T = 2000$ K for many hours. The temperature was measured with a micropyrometer or (in the region not accessible pyrometrically) by linearly extrapolating the dependence of the ribbon temperature on the heater current. The error in measuring the temperature was $\Delta T \sim 20$ K.

Silver was deposited uniformly onto the whole operating surface of the ribbon using a special extended source. After the proper ageing procedure, the deposited layers produced silver Auger peaks only.

The Auger peaks used in quantitative estimates were as follows: for Ag, the second peak of the doublet at $E = 356$ eV (peak-to-peak); for Ir, the triplet with the energies $E = 154$, 162, and 171 eV (from the top of the $E = 154$ eV peak to the bottom of the peak at $E = 171$ eV);

1063-7834/04/4602-0371$26.00 © 2004 MAIK "Nauka/Interperiodica"

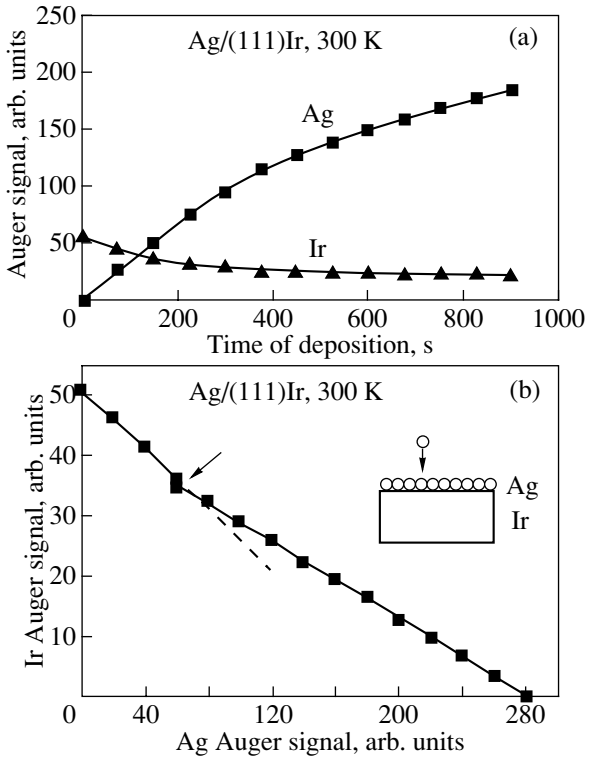

Fig. 1. Deposition of Ag atoms on (111)Ir in a constant flux at 300 K. (a) Variation of Auger signals of silver and iridium and (b) the Auger signal of iridium plotted vs. that of silver; the arrow indicates the point at which a monolayer film forms. Inset shows a scheme of the processes.

and for C, the peak at $E = 272$ eV (from the bottom of the peak to the background level).

3. PREPARATION AND CHARACTERIZATION OF TWO-DIMENSIONAL GRAPHITE FILMS ON (111)Ir

A 2D GF was prepared on the iridium surface by the technique described in [4]; namely, carbon was deposited on the iridium surface either in a flux of C atoms from a special source [9] or through the adsorption of benzene molecules on a metal surface heated to ~1700 K. The benzene molecules impinging on the metal surface at $T = 1600$–1800 K break up, with the hydrogen desorbing and the carbon remaining in the adlayer. Rather than dissolving in the bulk of iridium, C atoms form two-dimensional graphite islands, which merge to produce a continuous graphite film of exactly monolayer thickness on the surface. The latter method of preparing 2D GFs was found to be preferable, because in this case the film becomes two-dimensional automatically; indeed, C_6H_6 molecules are neither adsorbed nor break up on the passive graphite layer, thus terminating the influx of carbon into the adlayer. On completion of the carbon deposition, the benzene vapors are pumped out and all subsequent measurements are performed in ultrahigh vacuum.

As shown by us earlier [4, 5], the physicochemical properties of 2D GFs are practically independent of the substrate, the choice of iridium being motivated only by the convenience of operating with it. A 2D GF on iridium remains stable under any variation of the temperature for $T < 1900$ K, which makes such a film an appropriate subject for the investigation of adsorption–desorption processes. Atoms intercalating under a film do not noticeably affect either its structure or its physicochemical properties; their action reduces to pushing the graphite layer away from the metal surface, just as graphite layers are pushed apart in bulk intercalated compounds.

4. ADSORPTION OF SILVER ATOMS

Figure 1a shows the variation of silver and iridium Auger signals under deposition of Ag atoms on (111)Ir in a constant flux at $T = 300$ K. We readily see that by a time of 600–700 s the iridium Auger signal decreases by a factor ~2.5 compared to its initial magnitude, after which further deposition of silver brings about nothing more than slight variations in this signal. At the same time, the silver Auger signal continues to grow with each new deposited amount, but significantly slower than in the initial stages of the process.

This somewhat unusual behavior of the Auger signals suggests a possible islandlike film growth on the metal surface [10]. To clarify this point, the silver flux was increased by about eight times. The results obtained are presented in Fig. 1b in the form $I_{Ir} = f(I_{Ag})$, which is convenient for analyzing the growth mechanisms of adsorbed films [11]. The graph is seen to have a break, with the slope of the initial part being larger than that of the final part. This behavior suggests the following mechanism of film growth. In the initial stage, all adsorbing atoms build up in the first layer on the surface of the substrate; this stage should be identified with the straight line to the left of the arrow in Fig. 1b and with the fast initial growth of the silver Auger signal paralleled by a noticeable weakening of the substrate Auger signal in Fig. 1a. After the adsorption layer has reached a certain critical concentration (a monolayer, indicated by an arrow in Fig. 1b), three-dimensional islands of the adsorbate start to nucleate and grow on top of it; then the islands merge and produce a thick film through the Stranski–Krastanow mechanism [11]. The growth of island films under adsorption of silver on platinum at room temperature was also reported in [2].

Let us turn now to the adsorption of silver on a 2D GF-coated (111)Ir at 300 K. The variation in the Auger signals measured under deposition of Ag atoms is displayed in Fig. 2a. After about 1000 s of adsorption, the substrate Auger signal is seen to diminish by a factor 1.6 and to vary only weakly thereafter. While the silver

Auger signal also varies weakly, it continues to grow slowly under deposition. Therefore, islands are likely to grow in this case as well.

As with pure iridium, in order to measure the Auger signal of a thick film of silver, its flux was increased by 6–8 times. The results are depicted in Fig. 2b. All the experimental points are seen to fit with sufficient accuracy one straight line without breaks, which, in accordance with the classification proposed in [10, 11], corresponds to the Folmer–Weber mechanism, more specifically, to the growth of three-dimensional islands directly on the substrate (in our case, on the 2D GF surface) without preliminary formation of a monolayer film. The growth of three-dimensional silver islands on the graphite surface [(0001)HOPG face] was also observed using STM in [12].

It would be of interest to know the concentration of silver atoms in a monolayer on (111)Ir. Unfortunately, we did not have an absolutely calibrated flux of atomic silver at our disposal and did not have the possibility of preparing a reliably characterized surface coating containing silver with a known surface concentration. Therefore, as a means of calibration, we calculated the coefficients of elemental sensitivity (ESCs) for silver [13, 14] using our experimental data. The use of the ESCs tabulated, for instance, in [14] would be wrong, because the transmission function of our prism analyzer [15] differs from that of the cylindrical mirror-type analyzer employed in [14].

Table 1 presents experimental data on the Auger signal intensities for the clean metal surface and for thick and monolayer films of graphite and silver on iridium obtained at the same sensitivity. The ESCs were calculated using the following relations (these relations are derived under the assumption of the layer from which the Auger electrons escape being uniform and are valid for both a bulk crystal and a film system, provided the film thickness exceeds the mean free path of the corresponding Auger electrons):

$$I_A = K_A n_A \lambda_A T_0, \quad (1)$$

where A indicates the substance (iridium, silver, or carbon), n_A is its atomic concentration, λ_A is the mean free path for the Auger electrons of the given substance,

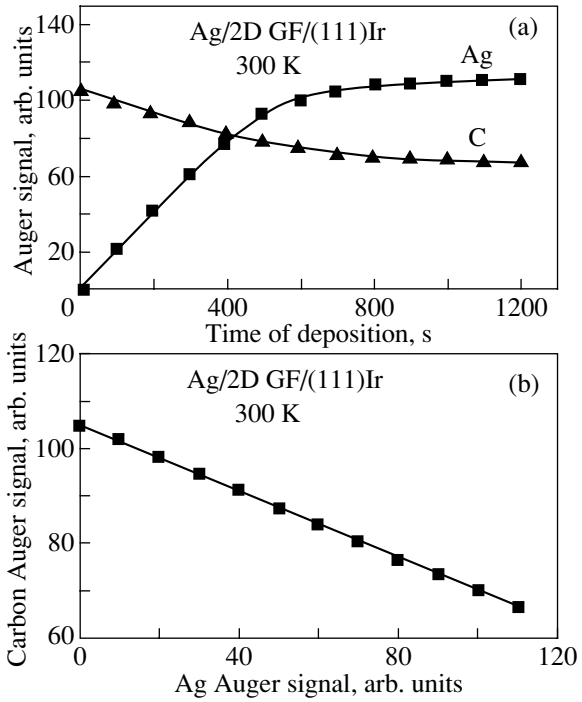

Fig. 2. Deposition of Ag atoms on top of 2D GF on (111)Ir in a constant flux at 300 K. (a) Variation of Auger signals of silver and carbon and (b) dependence of the carbon Auger signal on the silver Auger signal.

T_0 is the instrumental function, and K_A is the corresponding ESC. Equation (1) does not contain the usual fast-electron backscattering coefficients, because all the materials studied are deposited on the same substrate, Ir (a crystal can be considered as a film lying on top of a substrate of the same composition), and the film thicknesses are small compared to the escape depths of fast electrons (~200–300 Å); therefore, this coefficient is the same in all three cases.

The results of a self-consistent calculation are presented in the last column of Table 1. They differ slightly from the ones reported in [14], apparently because of the prism energy analyzer having a higher transmission at low energies than that of the cylindrical mirror arrangement.

Table 1. Elemental sensitivity coefficients of Ag, Ir, and C and data needed for their calculation

Film system	I_{Ir}	I_C	I_{Ag}	λ_A, Å	n, 10^{22} cm^{-3}	K_A
Clean Ir	51			6	7.1	1
Multilayer graphite film on Ir		260		8	13	1.8 ± 0.5
Multilayer silver film on (111)Ir			390	8	5.8	5.4 ± 1
2D GF/(111)Ir		97				
Ag(1 ML)/(111)Ir			80 ± 10			

Note: I_{Ir}, I_C, and I_{Ag} are the Auger signal intensities of clean iridium, of a thick graphite film on iridium, and of a thick silver film on iridium, respectively; λ_A is the mean free path of the corresponding Auger electrons [14]; n is the atomic concentration of the corresponding material; and K_A is the ESC in relative units.

Table 2. Silver concentrations in a "monolayer" on various substrates and on the (111) face of single-crystal silver

System	N^{ML}, 10^{15} cm^{-2}	Method of determination	References
Ag/(111)Ir	1.3 ± 1.3	AES	This work
Ag/(111)Pt	1.5	AES, TDS	[2]
Ag/(111)Ru	1.45	AES, LEED	[3]
(111)Ag	1.39	*X*-ray diffraction	[7]

Note: AES stands for Auger electron spectroscopy, TDS for thermal desorption spectroscopy, and LEED for low-energy electron diffraction.

The atomic concentration of silver in a "monolayer" was calculated from the following relation, which is valid for both a silver monolayer and a 2D GF on (111)Ir:

$$I_A^{ML} = K_A N_A T_0, \quad (2)$$

where I_A^{ML} is the Auger signal intensity from the corresponding monolayer film and N_A is the surface concentration of adsorbate atoms in it. Knowing the ESCs, the Auger signal intensities (Table 1), and the surface concentration of carbon in the 2D GF on (111)Ir, we determined the Ag concentration in a silver monolayer. The results of the calculation are listed in Table 2, which compares them with the silver concentrations (available in the literature) in monolayer coatings on other platinum-group metals.

The results obtained by us for silver on the surface of iridium are seen to agree well with the literature data for silver adsorption on other platinum-group metals. The (111) iridium face used is smooth and closely packed, and it is very unlikely that it can pattern the structure of the adsorbate layer noticeably. In our case, the "compressed silver layer" discussed in [3], i.e., the layer containing more atoms than are present in the close-packed (111) face of single-crystal silver, was not observed, but one cannot rule out its existence, because the surface concentration corresponding to it lies within the experimental error with which the Ag concentration on (111)Ir was determined.

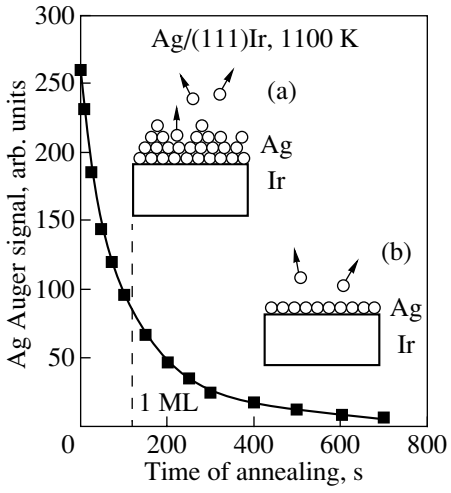

Fig. 3. Variation of the silver Auger signal under isothermal annealing of an Ag film deposited on top of (111)Ir at 300 K. Annealing temperature is 1100 K and Ag film thickness is ~(5–6) × 10^{15} cm^{-2}. Dashed line corresponds to one silver monolayer. Insets show schemes of the process of desorption from (a) a multilayer and (b) a monolayer film.

5. SILVER DESORPTION

Desorption of silver from the iridium surface has a clearly pronounced threshold character; indeed, it is not seen for $T < 1000$ K, whereas at $T = 1300$ K all of the silver escapes from the surface in a time shorter than 5 s. Figure 3 presents the variation in the silver Auger signal measured under isothermal annealing of an Ag film ~5–6 monolayers thick [N_{Ag} = (5–6) × 10^{15} cm^{-2}] at 1100 K. We readily see that, in a time of ~700 s, the silver Auger signal decreases by more than two orders of magnitude to become washed out by noise, which indicates that the surface is now completely clean of adsorbed silver. At the same time, the iridium Auger signal recovers its initial amplitude.

The dashed line in Fig. 3 specifies the level of the surface concentration of a silver monolayer. The rate with which Ag atoms leave the surface is seen to decrease substantially as one goes from a thick adsorbate film to a monolayer. Indeed, about four to five monolayers left the surface during the first 120 s, whereas the remaining layer desorbs in ~600 s. Let us consider these two stages separately.

We assume that, in the case of a submonolayer film, the adlayer is uniform and desorption in these conditions is a first-order process. We can then write

$$\nu_{des} = N_{Ag} C \exp[-E_{des}/kT], \quad (3)$$

where N_{Ag} is the surface concentration of silver, C is a frequency factor, and E_{des} is the activation energy for desorption. Both E_{des} and C can be dependent on the silver concentration in the adlayer. The desorption flux density and the desorption activation energy for N_{Ag} = (5–6) × 10^{15} cm^{-2} calculated under the assumption that $C = 10^{13}$ s^{-1} [7] are given in Table 3. According to literature data (mass-spectrometric measurements reported in [1–3]), silver desorbs from metal surfaces practically only in the form of single atoms; it is most likely that in our case desorption also occurs through this mechanism.

The data in Fig. 3 are not sufficient for estimating the desorption energy at low coverages with a reasonable accuracy. To do this, a special experiment was performed: silver was deposited on the (111)Ir surface in an amount N_{Ag} = (5–6) × 10^{13} cm^{-2} (i.e., about

Table 3. Data on silver desorption from the iridium surface at 1100 K

Adlayer	Silver desorption flux, $cm^{-2}\ s^{-1}$	Desorption activation energy, eV	References
Thick Ag film on (111)Ir	4.2×10^{13}		This work
Ag monolayer on (111)Ir	1.2×10^{13}	3.3	"
0.5 Ag monolayer on (111)Ir;	4.1×10^{12}	3.4	"
0.1 Ag monolayer on (111)Ir	1.2×10^{13}*	3.7	"
Thick Ag film on top of 2D GF on (111)Ir	4×10^{13}		"
Bulk silver	8.5×10^{14}	2.7**	[16]
	$\sim 10^{16}$		[17]

* At 1250 K.

** Sublimation energy.

1/20 monolayer) and desorbed at $T = 1250$ K. The values of the binding energy calculated under the same conditions are listed in Table 3.

Let us turn back to the initial part of the plot in Fig. 3. During the first 120 s, about 5×10^{15} Ag atoms/cm^2 desorb from the surface. Thus, the average desorption flux was $\nu_{des} = 5 \times 10^{15}/120 = 4.2 \times 10^{13}\ cm^{-2}\ s^{-1}$. In this case, Eq. (3), relating the flux of desorption to its energy and entropy parameters (E_{des}, C, respectively), cannot be applied because desorption definitely takes place from a nonuniform adlayer.

We see that the silver desorption flux changes very little as one goes from a multi- to monolayer film; indeed, the change lies within the measurement error. The variation in desorption energy within a monolayer is more substantial; as one switches from one monolayer to $N_{Ag} \sim 0$, E_{des} increases by 0.4 eV, apparently as a result of the decreasing role played by the lateral interactions in the adsorption layer.

Figure 4 shows the results obtained for annealing a silver film deposited on top of a 2D GF on (111)Ir. The silver concentration in the film was approximately $(4–6) \times 10^{15}\ cm^{-2}$. As shown earlier, the film grows, most likely, in the form of three-dimensional islands, which makes measurement of its thickness in monolayers meaningless.

As is evident from the graph in Fig. 4, the surface becomes completely cleaned of silver in a time shorter than 100 s. The average desorption flux was found to be $\nu_{des} = (4–6) \times 10^{15}/80 = 4 \times 10^{13}\ cm^{-2}\ s^{-1}$, which coincides, with good accuracy, with the desorption flux calculated above for a thick silver film on (111)Ir.

Let us compare this value of the flux with data on the sublimation of silver. The data quoted in the literature refer, as a rule, to the equilibrium vapor pressure of an element, which can then be used to derive the flux of interest to us here from the Herz–Knudsen equation

$$\nu_{des} = p/(2\pi mkT)^{1/2}, \qquad (4)$$

where p is the saturated vapor pressure, m is the mass of the particle (atom or molecule), T is the temperature, and k is the Boltzmann constant [10]. Table 3 presents the data on the desorption flux of silver from a surface under equilibrium conditions calculated from Eq. (4) using data on the equilibrium silver vapor pressure collected in [16]. Because the saturated vapor above a silver surface has a complex composition and consists primarily of Ag atoms and Ag_2 and Ag_3 molecules in an approximate ratio of 1 : 3 : 2 (this ratio depends on the temperature and varies slightly according to various authors [16, 18]), we took the weighted average for the particle mass, as recommended in [18]. The discrepancies with the data reported in [17] are even larger, nearly two orders of magnitude (see Table 3).

Note that the desorption flux calculated in this way far exceeds the values obtained in our experiments. This might mean that thin silver films adsorbed even on

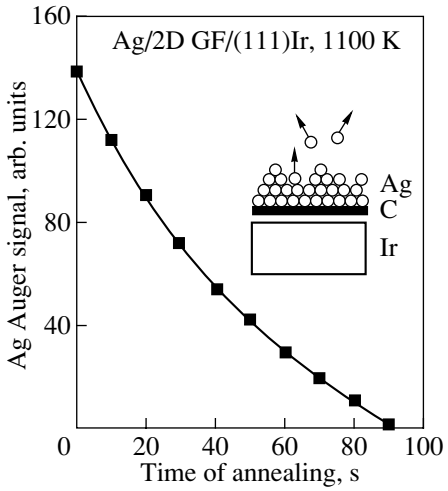

Fig. 4. Variation of the silver Auger signal under isothermal annealing of an Ag film deposited on top of a 2D GF on (111)Ir at 300 K. Annealing temperature is 1100 K and Ag film thickness is $(4–5) \times 10^{15}\ cm^{-2}$. Inset shows a scheme of the process.

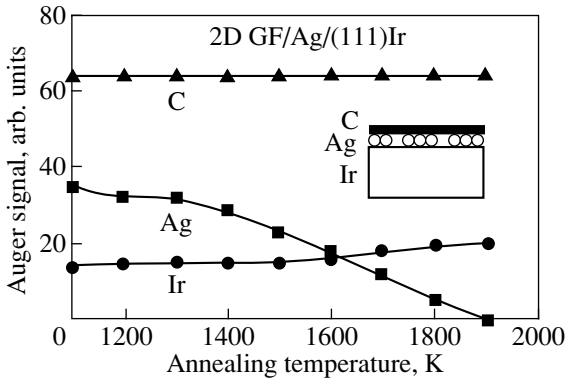

Fig. 5. Variation of the Auger signals of carbon, iridium, and silver under stepped annealing (in steps of 100 K) of an Ag film intercalated under a 2D GF on (111)Ir at 1100 K. Holding time at each point 20 s. Inset shows a scheme of the film system obtained by intercalation of silver under a 2D GF on (111)Ir at $T = 1100$ K.

a passive substrate, such as graphite, differ in their desorption properties from bulk samples, a point that should be taken into account when using the constants listed in handbooks to calculate the characteristics of film systems. These differences are probably due to the microrelief of the surface from which the silver evaporates (drops, atomic steps).

6. DISSOLUTION OF SILVER

Let us consider now the physical nature of the process by which silver escapes from the surface. In Section 5, we assumed thermal desorption to be the only channel by which Ag atoms leave the iridium surface. Generally speaking, the adsorbate can escape from the surface in three ways: through desorption, dissolution in the substrate material, and migration over the substrate surface (for instance, to the sample holders). This relates naturally only to well-cleaned samples and ultrahigh-vacuum conditions, where one may disregard chemical reactions with both residual-gas molecules and the impurity atoms segregating from the substrate bulk. As for the migration, the shape of the sample employed (a long narrow ribbon fixed at the ends only) and the uniform deposition of silver over the whole ribbon surface make this channel inefficient; by contrast, the part played by dissolution needs to be discussed.

The curves displayed in Figs. 3 and 4 are practically independent of the sample prehistory, more specifically, of the regime of sample cleaning employed, preliminary Ag deposition, etc. Therefore, it is unlikely that dissolution of the adsorbate is significant, because otherwise the kinetics would be extremely sensitive to preliminary saturation of the surface layer by the adsorbate [19].

The fact that here we have desorption rather than dissolution is proved unambiguously by our experiments dealing with silver intercalation under a 2D GF on iridium. Unlike many atomic species studied by us, silver atoms do not penetrate spontaneously under a graphite monolayer on a metal. Nevertheless, we found the conditions favoring realization of this process; indeed, it turned out that Ag atoms can penetrate under a 2D GF if silver is deposited on a graphite film intercalated preliminarily with Cs to saturation, i.e., on a film that contains both intercalated (under the film) and adsorbed (on top of the film) Cs atoms in about equal concentration, $N_{Cs} = (3–4) \times 10^{14}$ cm^{-2} [6]. Subsequent annealing at 1100 K removes all the cesium from the system, with silver substituting for it under the 2D GF. In this case, the carbon Auger signal completely recovers its initial amplitude. This implies that there are no adsorbates on top of the graphite film at $T > 1100$ K [6].

The results of the annealing of this film system are plotted in Fig. 5. The carbon Auger signal is seen to remain strictly constant up to 1900 K, which means there are no adsorbates on the graphite. The silver Auger signal decreases gradually with increasing temperature while remaining observable up to 1800 K, where the lifetime of the Ag adatom on an open iridium surface should be less than 10^{-5} s. In the course of the annealing, the Auger signal of iridium grows slowly, apparently because of the screening by silver atoms becoming weaker.

Thus, silver present as an intercalant remains in direct adsorption contact with the metal surface up to temperatures exceeding the temperature of its thermal desorption by 500–700 K. The intercalated silver adds up to less than one monolayer, and it stays on the iridium surface up to very high temperatures, 1800–1900 K. The gradual decrease in the silver surface concentration, proportional to the Auger signal at submonolayer adsorbate concentrations, may be due to both partial penetration of Ag atoms through the graphite coating or partial dissolution in the bulk of the substrate. This sets a lower bound on the activation energy for this process, $E_{sol} > 5$ eV, and allows us to conclude that all the silver Auger signal variations seen in Figs. 3 and 4 are indeed due to desorption.

7. DISCUSSION OF THE RESULTS

While both silver and iridium crystallize in an fcc lattice, the volume per atom in the silver crystal is ~21% larger than that in iridium [20]. This means that the incorporation of a silver atom into the iridium lattice should give rise to two energetically unfavorable processes, namely, substantial local Ir lattice strains and contraction of the valence electronic shells of the Ag atoms. It is possibly this excess of the atomic volume of silver over that of iridium that makes the penetration of Ag atoms into the iridium crystal difficult. Thermal desorption turns out to be preferable under these conditions, and it accounts for the escape of silver from the surface at substantially lower temperatures than required for the dissolution to begin. One could

also conceive of thermodynamic reasons for the absence of dissolution; indeed, it is known that a spontaneous onset of a process is possible only if it entails a decrease in the corresponding thermodynamic potential (in the Gibbs energy in our case). While the entropy part of the Gibbs energy always decreases when atoms are mixed, the increase in the energy part may outweigh the former for the above reasons, in which case there will be no dissolution even at equilibrium. Indeed, it is known that silver dissolves very poorly in iridium with a solubility limit of less than 1% [21], which likewise attests to the validity of the above considerations.

Interestingly, adsorbed silver differs strongly in behavior from, for instance, aluminum atoms, which, while being practically of the same size, dissolve readily in refractory metals and form stable surface compounds on their surface [22–24]. In particular, on iridium, aluminum forms surface aluminide Ir_5Al with a concentration $N_{Al} \sim 3.5 \times 10^{14}$ cm^{-2}, with all Al atoms in excess of the surface aluminide dissolving in the bulk of the metal. Al adatoms escape from the iridium surface at T = 1500–1600 K, apparently through thermal desorption [23]. As for silver, it does not dissolve in the bulk and does not form fixed surface compounds. The nature of these differences still remains unclear.

8. CONCLUSIONS

We have studied in considerable detail the initial stages in the interaction of silver with the (111)Ir surface and with two-dimensional graphite films on iridium over a broad temperature range (300–1800 K). Adsorption was shown to have an island pattern at room temperature, the growth of islands on a clean metal surface being preceded by the formation of a monolayer film. Under isothermal conditions, the desorbing flux varies weakly in going from an island to a monolayer film and was found to be substantially smaller than the equilibrium silver sublimation flux at the same temperatures. It was shown that silver does not penetrate into the bulk of the substrate up to at least 1800 K. The adsorption properties of silver were established to differ substantially from those of Al (which has practically the same atomic size) in that, unlike aluminum, silver does not dissolve in the bulk of the substrate and does not form surface compounds.

ACKNOWLEDGMENTS

This study was supported by the state program of the Russian Federation "Physics of Solid State Nanostructures," project no. 8G158.

REFERENCES

1. P. W. Davies, M. A. Quinlan, and G. A. Somorjai, Surf. Sci. **121**, 290 (1982).
2. J. Kovaczkievich, Surf. Sci. **183**, 251 (1987).
3. C. Park, Surf. Sci. **203**, 395 (1988).
4. N. R. Gall, E. V. Rut'kov, and A. Ya. Tontegode, Int. J. Mod. Phys. B **11** (16), 1865 (1997).
5. A. Ya. Tontegode and E. V. Rut'kov, Usp. Fiz. Nauk **163** (11), 57 (1993) [Phys. Usp. **36**, 1053 (1993)].
6. N. R. Gall', E. V. Rut'kov, and A. Ya. Tontegode, Pis'ma Zh. Éksp. Teor. Fiz. **75**, 28 (2002) [JETP Lett. **75**, 26 (2002)].
7. M. W. Roberts and C. S. McKee, *Chemistry of the Metal–Gas Interface* (Clarendon, Oxford, 1978; Mir, Moscow, 1981), pp. 33–58.
8. N. R. Gall, S. N. Mikhailov, E. V. Rut'kov, and A. Ya. Tontegode, Surf. Sci. **191**, 185 (1987).
9. N. R. Gall, E. V. Rut'kov, A. Ya. Tontegode, *et al.*, Chem. Vap. Deposition **5** (4), 1 (1997).
10. J. F. Biberian and G. A. Samorjai, Appl. Surf. Sci. **2**, 352 (1979).
11. C. Argile and G. E. Rhead, Surf. Sci. Rep. **10** (6/7), 277 (1989).
12. A. Jablonsky, S. Eper, and K. Wandelt, in *Proceedings of 3rd International Conference on Solid Films and Surfaces, Sydney, Australia* (1984), p. 98.
13. A. Ioshi and P. W. Palmberg, in *Methods of Surface Analysis*, Ed. by A. W. Czanderna (Elsevier, New York, 1975; Mir, Moscow, 1979).
14. L. E. Davis, N. C. MacDonald, P. W. Palmberg, G. E. Riach, and R. E. Weber, *Handbook of Auger Electron Spectroscopy* (Physical Electronics Industries, Eden Prairie, 1976).
15. Yu. A. Nevinnyĭ, N. A. Kholin, and E. M. Yakushev, *Theory and Calculation of Electrostatic Prismatic Spectrometer* (Akad. Nauk SSSR, Leningrad, 1988).
16. *Properties of Elements: A Handbook*, Ed. by M. E. Drits (Metallurgiya, Moscow, 1985), pp. 71–79.
17. V. F. Kovalenko, *Thermophysical Processes and Vacuum Tubes* (Sovetskoe Radio, Moscow, 1975), p. 197.
18. N. A. Nesmeyanov, *Vapor Pressure of Chemical Elements* (Akad. Nauk SSSR, Moscow, 1961; Elsevier, New York, 1963).
19. N. R. Gall, E. V. Rut'kov, A. Ya. Tontegode, and M. M. Usufov, Phys. Low-Dimens. Semicond. Struct., No. 4/5, 75 (1996).
20. C. Kittel, *Introduction to Solid State Physics*, 5th ed. (Wiley, New York, 1976; Nauka, Moscow, 1978).
21. E. M. Savitskiĭ, V. P. Polyakova, N. B. Gorina, and N. R. Roshan, *Materials Science of Platinum-Group Metals* (Metallurgiya, Moscow, 1975), pp. 221–223.
22. N. R. Gall', E. V. Rut'kov, and A. Ya. Tontegode, Fiz. Tverd. Tela (St. Petersburg) **44** (7), 1179 (2002) [Phys. Solid State **44**, 1394 (2002)].
23. M. Parschan and K. Cristmann, Surf. Sci. **347**, 63 (1996).
24. N. R. Gall', E. V. Rut'kov, and A. Ya. Tontegode, Fiz. Tekh. Poluprovodn. (St. Petersburg) **36** (3), 295 (2002) [Semiconductors **36**, 276 (2002)].

Translated by G. Skrebtsov

Physics of the Solid State, Vol. 46, No. 2, 2004, pp. 378–382. Translated from Fizika Tverdogo Tela, Vol. 46, No. 2, 2004, pp. 367–371.
Original Russian Text Copyright © 2004 by Suzdal'tsev, Yafarov.

LOW-DIMENSIONAL SYSTEMS AND SURFACE PHYSICS

Microtopography and Field Emission Properties of Carbon Films Grown in a Microwave Gas Discharge Plasma

S. Yu. Suzdal'tsev and R. K. Yafarov

Institute of Radio Engineering and Electronics, Russian Academy of Sciences, Saratov, 410009 Russia

e-mail: pirpc@renet.ru

Received February 20, 2003; in final form, May 12, 2003

Abstract—Graphite-like carbon films are grown in an ethanol vapor plasma in a microwave gas discharge. The electrical parameters controlling the microtopography and electronic properties of carbon films are determined. It is shown that electron bombardment affects the fine structure of graphite-like nanocrystallites and their emissive power with characteristics close to those of carbon nanotubes. The emission properties of layered graphite-like films can be improved by metal (cadmium) impurity doping. For nanocrystalline graphite-like films, emission currents with a density of 0.3 A/cm^2 are induced at an electric field strength of less than 7 V/μm in the gap.
© 2004 MAIK "Nauka/Interperiodica".

1. INTRODUCTION

The preparation of nanocrystalline carbon film materials with different structures for use as field emission cathodes in flat displays and devices for vacuum microwave microelectronics is an important problem in solid-state electronics [1]. Carbon cathodes hold considerable promise owing to their stability to bombardment with residual gas ions (which occurs in devices operating under technical vacuum and high voltage) and the possibility of reducing the work function for structural modifications that are characteristic of both valence electrons of carbon atoms with a diamond-type hybridization of bonds and open carbon nanotubes with a graphite structure [2, 3]. Gulyaev *et al.* [4, 5] were the first to succeed in producing an efficient electron emission in nanotubular "tubelene" structures.[1] Since these structures were reported at the Conference on Vacuum Microelectronics in Paris in 1994, many research laboratories in the world have performed extensive investigations in this direction.

The purpose of this work was to determine the conditions for growing and modifying carbon layers in order to prepare graphite-like nanocrystalline and microcrystalline film materials with desired field emission properties.

2. EXPERIMENTAL TECHNIQUE AND RESULTS

Carbon films were deposited on glass substrates in an ethanol vapor plasma in a microwave gas discharge with electron cyclotron resonance. The experimental setup was described earlier in [6]. The thickness of the deposited films was determined using laser ellipsometry and interference microscopy. The microtopography of the film surface was thoroughly examined with a scanning atomic-force microscope (AFM). The film structure was investigated on a DRON-3.0 x-ray powder diffractometer. The field emission current was measured under high vacuum (10^{-5} Pa) with the use of a diode structure, which made it possible to change the electrode spacing with an accuracy of 1 μm. The diameter of the operating surface of an anode fabricated from an MPG-6 carbon material was equal to 3 mm.

The carbon films were deposited in the plasma at an ethanol vapor pressure of 0.05 Pa and different accelerating voltages at the substrate holder. The temperature of the substrate holder was 350°C. The microwave power of the plasma source was 250 W. The thickness of the deposited films varied from 0.25 to 0.30 μm. According to the x-ray diffraction analysis, the films predominantly contained a finely crystalline graphite phase (interplanar spacing d = 3.36 Å [7]).

Figure 1 depicts typical dependences of the emission current density on the electric field strength in a diode structure based on graphite-like carbon films grown at different accelerating potentials. The distance between the sample and the anode was equal to 120 μm. The lowest emission threshold was observed for carbon films grown at an accelerating potential of +300 V at the substrate holder.

The curves shown in Fig. 1 were used to calculate the amplification factor K of the electric field in the microdiode. This factor is equal to the ratio of the electric field strength E_1 at a single protrusion in the microdiode gap to the electric field strength E in the same gap, which is determined by the cathode–anode potential difference and the interelectrode spacing without regard for the film roughness in the gap:

[1] Tubelenes are fullerene species having the shape of a tube (rather than a sphere) that is a few nanometers across and capped with fullerenes at the ends.

$K = E_1/E$. In order to calculate the amplification factor of the electric field, the dependences shown in Fig. 1 were represented in the form of an analytical relationship between the emission current density j and the electric field strength E in the microdiode gap [8], that is,

$$j = AE^2 e^{B/E},$$

where A and B are coefficients.

From the same dependences plotted in the Fowler–Nordheim coordinates

$$\log\left(\frac{j}{E^2}\right) = f\left(\frac{1}{E}\right),$$

we determined the slopes of the experimental curves. These slopes and the amplification factors K are related by the expression

$$K = \frac{B\log e}{\tan\alpha}.$$

Figure 2 shows the amplification factor of the electric field in the diode structure, the measured surface electrical resistance, and the mean height of microprotrusions on the surface of the carbon films as a function of the accelerating potential in the course of the film synthesis. The mean height of microprotrusions for three different regions of the film surface was determined with the data processing program package (for the atomic-force microscope). The typical AFM images of the surfaces of the carbon films grown at different accelerating potentials are given in Fig. 3. As can be seen from Figs. 1 and 2, the more positive the accelerating potential at the substrate holder and the higher the surface electrical resistance of the grown films, the lower the threshold values of the electric field strengths corresponding to an efficient field emission from graphite-like films and the larger the amplification factors of the electric field at the tips of the emitting structures. Note that the dependence of the size of the microcrystallites on the carbon film surface on the potential at the substrate holder is nearly symmetric with respect to zero potential.

For the purpose of elucidating how the surface modification affects the emission properties of the carbon films, the films were subjected to treatment with argon ions and metal impurity doping. In experiments on metal (cadmium) impurity doping, the carbon film on a glass substrate was mounted in a grounded substrate holder positioned perpendicularly to a plasma stream in a vacuum plasma setup. The sputtered metal platelike target was located at a distance of 1.5–2.0 cm and an angle of 120° to the substrate holder. Cadmium was deposited in a microwave gas discharge plasma in an argon atmosphere at a pressure of 0.05 Pa and an accelerating potential of 80–90 V. The thickness of the deposited cadmium layer was equal to 10 nm. After the cadmium deposition, the sample was heated to 180–200°C for 2 h in the same setup at a residual pressure of

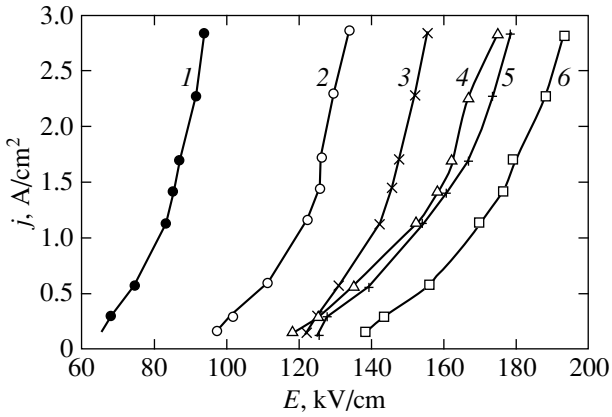

Fig. 1. Typical dependences of the emission current density j on the electric field strength E in a diode structure based on graphite-like carbon films grown at accelerating potentials U = (*1*) +300, (*2*) +200, (*3*) +100, (*4*) –100, (*5*) –300, and (*6*) –200 V. The diode gap is 120 μm.

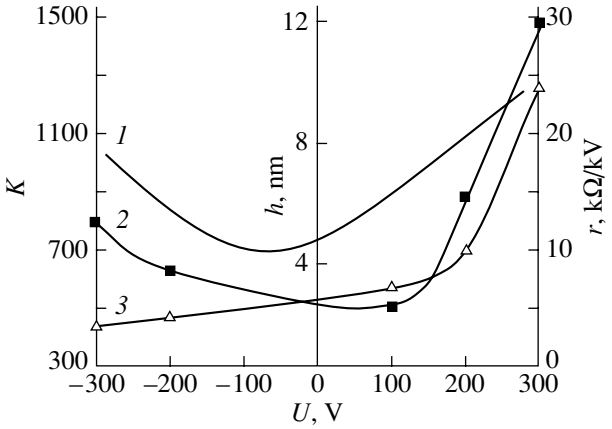

Fig. 2. Dependences of (*1*) the mean height h of microprotrusions on the surface, (*2*) the amplification factor K of the electric field in the microdiode with a gap of 120 μm, and (*3*) the surface electrical resistance r of the carbon films on the accelerating potential U at the substrate holder in the course of film synthesis.

1 Pa in the vacuum chamber in order to provide diffusion of the cadmium into the carbon film. Thereafter, the film was exposed to an argon plasma beam with the aim of removing the remaining cadmium from the surface. Cadmium was removed at an accelerating potential of 150 V at the substrate holder for a time equal to the time of deposition of a cadmium layer.

The influence of the dopant on the electronic properties of the surface was analyzed using three groups of samples, namely, carbon films doped with cadmium according to the above procedure (Fig. 4a), carbon films treated in the argon plasma without doping (Fig. 4b), and the initial carbon films (Fig. 3b). The graphite-like films grown at an accelerating potential of

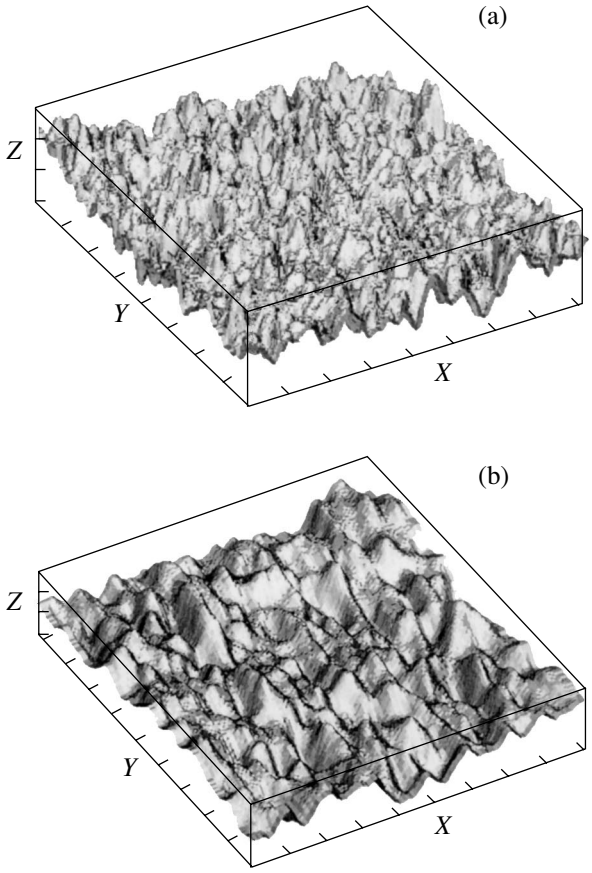

Fig. 3. Typical AFM images of the surfaces of the carbon films grown at accelerating potentials of (a) +300 and (b) –300 V. The scale divisions along the *X*, *Y*, and *Z* axes are equal to 1 μm, 1 μm, and 10 nm, respectively.

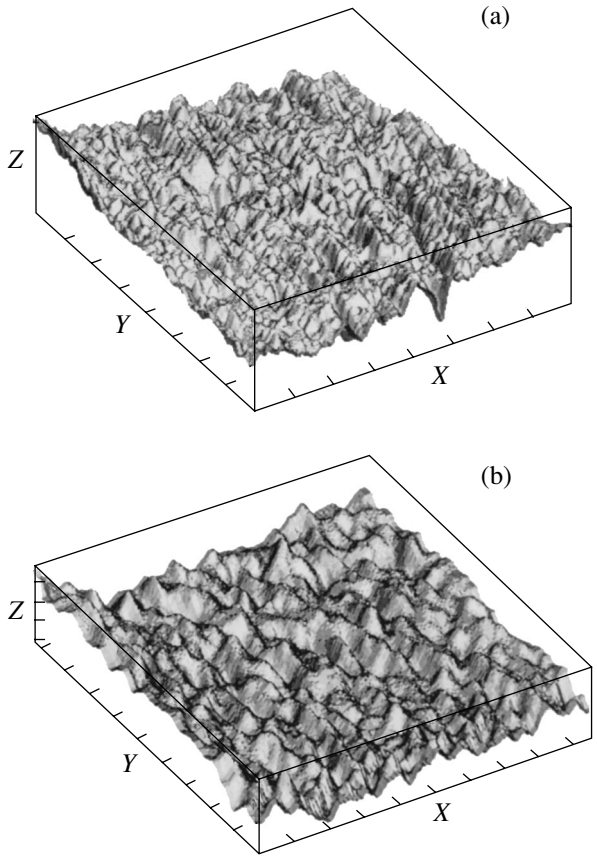

Fig. 4. AFM images of the surfaces of the carbon films (a) doped with cadmium and (b) treated in a low-energy argon plasma without doping. The scale divisions along the *X*, *Y*, and *Z* axes are equal to 1 μm, 1 μm, and 10 nm, respectively.

–300 V at the substrate holder served as the initial films. It can be seen from Fig. 1 that the initial films possess the minimum surface electrical resistance but the lowest emissive power as compared to those of the films grown under other conditions.

Figure 5 shows typical experimental dependences of the field emission current on the electric field strength in the microdiode with a gap of 120 μm for three groups of samples. As can be seen, the emissive power of the films substantially increases upon doping with cadmium and decreases after treatment in the low-energy argon plasma.

The effect of cadmium doping and treatment of undoped carbon films in the low-energy argon plasma on the amplification factor of the electric field in the microdiode gap is illustrated in Fig. 6. The amplification factors for all groups of carbon films were calculated under the assumption that the work functions of the films were identical and equal to the work function of graphite. It can be seen that the field amplification coefficient for all microdiode gaps depends on the procedure of modifying the sample surface.

3. DISCUSSION

The experimental results demonstrate that intensive electron bombardment during the growth of graphite-like carbon films is of crucial importance in decreasing the threshold field strength of the field emission from these films. An increase in the field emission efficiency is accompanied by an increase both in the amplification factor of the electric field at the tips of the emitting structures and in the surface electrical resistance of the films. These quantities are characterized by asymmetric dependences on the accelerating potential at the substrate holder (Fig. 2). Actually, depending on the sign of the potential at the substrate holder, the field amplification factor changes almost twofold, namely, from 800 at a potential of –300 V to 1500 at a potential of +300 V. On the other hand, the dependence of the microcrystallite size on the potential at the substrate holder is nearly symmetric with respect to zero potential. Consequently, the geometric (size) factor of the electric field amplification at the emitter tips cannot be responsible for the asymmetric dependence of the field emission properties of carbon nanocrystallites on the potential at the substrate holder during their synthesis. Therefore, these

findings indicate that, although the geometric parameters of the microcrystallites grown under different conditions are identical, they can have different structures.

The emission current density and the strength of the macroscopic field of the efficient field emission from nanocrystalline carbon films grown in the course of intensive electron bombardment (Fig. 1) are close to those of carbon nanotube films [9]. This can be explained by the fact that the microstructure of the prepared films involves nanocrystallites consisting of several tens of ordered atomic microsheets of graphite-like carbon whose electronic structure is similar to the electronic structure of carbon atoms at the ends of open nanotubes. These nanotubes are composed of the same atomic sheets rolled up into tubes and are predominantly orientated perpendicularly to the substrate plane. The spatial orientation of the nanocrystallites is confirmed by the fact that the amplification factor of the electric field at the tips and the emissive power correlate with the surface electrical resistance of the graphite-like carbon films prepared under intensive electron bombardment of the growth surface (Fig. 2).

Earlier [10], we showed that the deposition rate of carbon films and their roughness in the course of high-vacuum microwave plasma deposition are governed, to a large extent, by the energy and type of charged particles bombarding the films during the growth. Low negative potentials at the substrate holder (from 0 to –200 V, Fig. 2) provide nearly ideal conditions for growth of graphite films through the layered mechanism. This is associated with the absence of supersaturation of atomic carbon in the gaseous phase and the high surface mobility of carbon atoms due to a change in the potential relief of the surface under low-energy ion bombardment. Moreover, this is supported by the fact that the graphite-like films which were grown at negative potentials at the substrate holder and possessed a higher electrical conductivity but a low emissive power also had a better metallic luster typical of single-crystal graphite.

For positive potentials of higher than +100 V at the substrate holder, the bombardment of the surface with electrons and negative ions leads to an increase in the electron current passing through the substrate and, hence, to an increase in the sticking coefficient of carbon atoms; as a result, the nucleation is enhanced and the growth of the graphite-like film becomes more chaotic. This manifests itself in an increase in the number and size of particular nanocrystallites that are misoriented with respect to the direction of the layered growth and most likely represent a set of nanosheets made up of carbon atoms forming a hexagonal lattice. Since the electrical properties of graphite are anisotropic, this growth is attended by an increase in the surface electrical resistance of the film and the emissive power perpendicular to the film surface. According to our experimental data, the emissive power of the carbon films becomes close to that of carbon nanotube films.

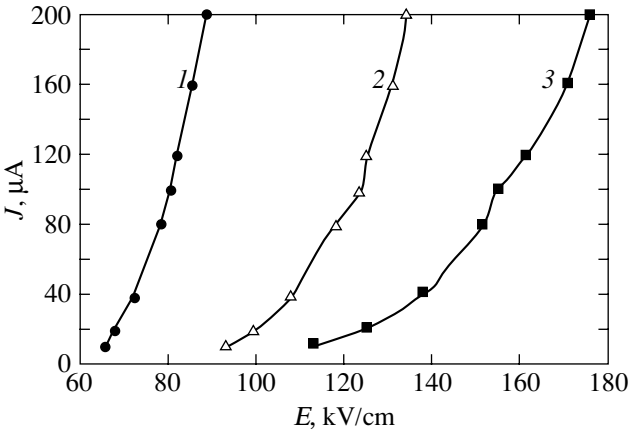

Fig. 5. Dependences of the field emission current J on the electric field strength E in the microdiode with a gap of 120 μm for (*1*) the cadmium-doped carbon film, (*2*) the initial carbon film, and (*3*) the carbon film treated in an argon plasma.

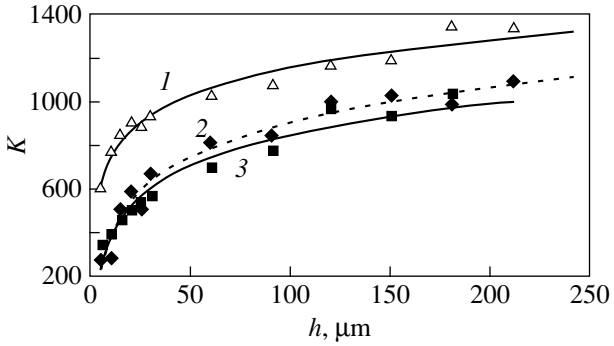

Fig. 6. Effect of cadmium doping and treatment of carbon films in an argon plasma on the amplification factor of the electric field in the microdiode gap: (*1*) the cadmium-doped carbon film, (*2*) the initial carbon film, and (*3*) the carbon film treated in an argon plasma.

For sufficiently high negative accelerating potentials (higher than –200 V), the increase in the roughness of the graphite-like carbon films is caused by their etching with hydrogen ions and hydrogen atoms that come from the ethanol vapor plasma and penetrate into the surface layers. The etching (erosion) processes are initiated in regions initially involving growth surface defects [11], such as atomic vacancies or growth steps. In the regions where one or several carbon bonds are dangling, hydrogen more readily enters into the chemical reaction and forms a volatile hydrocarbon compound. This is accompanied by the removal of carbon atoms from the upper layer and, as a consequence, the formation of the roughness. The carbon atoms located along the roughness boundary become potential centers of electron emission. Note that this mechanism of for-

mation of the roughness in the carbon film does not affect the electrical conductivity anisotropy. Therefore, in the case when the negative potentials at the substrate holder are relatively high during the growth of the graphite-like film in the microwave gas discharge plasma, an increase in the emission power correlates only with the roughness as a constant or decreasing longitudinal electrical resistance of the film (Fig. 2). The electronic surface properties of these films are more uniform; specifically, the field amplification factors and the field emission thresholds of the films grown under the above conditions are less than those of the films synthesized at positive potentials at the substrate holder.

As follows from the experimental data, the surface modification upon exposure to argon ions either does not change or even decreases the field amplification factor. At the same time, the doping with cadmium results in a substantial increase in the field amplification factor. This fact indicates that the work function of the carbon films doped with cadmium decreases, because the surface roughnesses and the related geometric factors of electric field amplification for all three groups of samples remain virtually unchanged after doping and treatment of the films in the low-energy argon plasma. This was confirmed by examining the surfaces of the carbon films with the use of a scanning atomic-force microscope.

The comparative analysis of the current–voltage characteristics in the Fowler–Nordheim coordinates [8] demonstrated that the work function decreases by approximately 20% for the carbon films doped with cadmium and increases by approximately 2% for the films treated in the low-energy argon plasma as compared to the work function of the initial carbon films.

Thus, apart from the topographic amplification of the electric field on the surface of the nanocrystalline carbon film, the decrease in the work function is associated with the nature of surface roughness, the structure of carbon emission centers (which depend on the deposition conditions in the microwave gas discharge plasma), and the electrical properties of the nanostructured material, such as the electrical conductivity (in the direction of emission current) increasing the efficiency of electron transfer to emission centers inside the solid.

REFERENCES

1. A. F. Bobkov, E. V. Davydov, S. V. Zaĭtsev, *et al.*, Zh. Tekh. Fiz. **71** (6), 95 (2001) [Tech. Phys. **46**, 736 (2001)].
2. A. N. Obraztsov, I. Yu. Pavlovskiĭ, and A. P. Volkov, Zh. Tekh. Fiz. **71** (11), 89 (2001) [Tech. Phys. **46**, 1437 (2001)].
3. M. Dieter Gruen, in *Proceedings of the International Topical Meeting on Field Electron Emission from Carbon Materials (ITM-FEECM 2001)* (Moscow, 2001), p. 14.
4. Yu. V. Gulyaev, L. A. Chernozatonskii, Z. Ya. Kosakovskaya, *et al.*, in *Proceedings of the 7th International Vacuum Microelectronics Conference (IVMC'94)* (Grenoble, 1994); Vide Couches Minces, Suppl. **271**, 322 (1994).
5. L. A. Chernozatonskii, Z. Ya. Kosakovskaya, Yu. V. Gulyaev, *et al.*, J. Vac. Sci. Technol. B **14** (3), 2080 (1996).
6. N. N. Bylinkina, S. P. Mushtakova, V. A. Oleĭnik, *et al.*, Pis'ma Zh. Tekh. Fiz. **22** (6), 43 (1996) [Tech. Phys. Lett. **22**, 245 (1996)].
7. A. Ubbelohde and F. Lewis, *Graphite and Its Crystal Compounds* (Clarendon Press, Oxford, 1960; Mir, Moscow, 1965).
8. M. I. Elinson and G. F. Vasil'ev, in *Nonincandesced Cathodes*, Ed. by M. I. Elinson (Nauka, Moscow, 1974), p. 278.
9. L. A. Chernozatonskii, K. R. Izrael'yants, E. F. Kukovitsky, and A. L. Musatov, in *Proceedings of the 4th IEEE International Vacuum Electron Source Conference (IVESC 2002)* (Saratov, 2002), p. 116.
10. S. Yu. Suzdal'tsev and R. K. Yafarov, Pis'ma Zh. Tekh. Fiz. **27** (15), 77 (2001) [Tech. Phys. Lett. **27**, 656 (2001)].
11. Z. Waqar, E. A. Denisov, T. N. Kompaniets, *et al.*, Zh. Tekh. Fiz. **71** (6), 133 (2001) [Tech. Phys. **46**, 773 (2001)].

Translated by O. Borovik-Romanova

Physics of the Solid State, Vol. 46, No. 2, 2004, pp. 383–391. Translated from Fizika Tverdogo Tela, Vol. 46, No. 2, 2004, pp. 372–379.
Original Russian Text Copyright © 2004 by Savin, Savina.

FULLERENES AND ATOMIC CLUSTERS

Nonlinear Dynamics of Carbon Molecular Lattices: Soliton Plane Waves in Graphite Layers and Supersonic Acoustic Solitons in Nanotubes

A. V. Savin* and O. I. Savina**

** Semenov Institute of Chemical Physics, Russian Academy of Sciences, ul. Kosygina 4, Moscow, 117977 Russia*
e-mail: asavin@center.chph.ras.ru
*** Russian State University for Trade and Economy, Moscow, 125817 Russia*
Received March 25, 2003; in final form, June 2, 2003

Abstract—The dynamics of solitary plane waves in graphite layers and supersonic acoustic solitons in an ideal single-layer carbon nanotube are numerically studied. It is shown that stable solitary waves exist only in flat graphite layers. In nanotubes, only soliton-like excitations can exist and their supersonic motion is always accompanied by phonon emission. The lifetime of such excitations depends on their energy and on the nanotube radius. © *2004 MAIK "Nauka/Interperiodica".*

1. INTRODUCTION

Carbon nanotubes are cylindrical macromolecules with a diameter exceeding half a nanometer and a length of up to several microns. Similar structures were obtained more than 50 years ago through thermal decomposition of carbon oxide at an iron contact [1]. However, nanotubes themselves were obtained only ten years ago as by-products of the synthesis of fullerene C_{60} [2]. Carbon nanotubes now attract attention due to their unique properties [3]. A nanotube is a quasi-1D molecular structure with pronounced nonlinear properties. It was shown in [4] that in the continuum approximation the nonlinear dynamics of such structures can be described by the Korteweg–de Vries equation, i.e., that supersonic longitudinal compression solitons can exist in nanotubes.

The aim of this paper is to study numerically the motion of supersonic acoustic solitons in single-wall carbon nanotubes. If the nanotube radius is infinitely increased, the nanotube assumes the form of a flat graphite layer and acoustic waves in it become plane waves in the layer. It is shown that stable solitary waves (solitons) exist only in flat layers. Supersonic motion of such excitations in carbon nanotubes is always accompanied by continuous phonon emission; this emission is due to the variation in the nanotube diameter in the region of localization of the excitation, and its intensity decreases with increasing nanotube radius. Phonon emission results in the decay of supersonic solitons; therefore, they have a finite lifetime.

2. STRUCTURE OF GRAPHITE LAYERS

A graphite layer is a plane covered by regular hexagons with carbon atoms at their vertices (Fig. 1a). In this two-dimensional lattice, each carbon atom is bonded to the three neighboring atoms by valence bonds, which form regular hexagons. It is convenient to denote lattice sites by the two indices i and j. Let $x_{i,j}$, $y_{i,j}$, $z_{i,j}$ be the coordinates of the lattice site with the corresponding indices. In equilibrium, we have

$$x^0_{i,j} = ia_x, \quad y^0_{i,j} = (-1)^{i+j}\rho_0/4 + ja_y, \quad z^0_{i,j} = 0, \quad (1)$$

where $a_x = \rho_0\sqrt{3}/2$, $a_y = 3\rho_0/2$, and ρ_0 is the equilibrium valence bond length.

Here and in what follows, we take into account only the interaction between the nearest neighbor carbon atoms connected by valence bonds and we describe the interaction itself by the many-particle Brenner potential [5]. To specify the electrostatic interaction energy between two carbon atoms with two-dimensional indices **i** and **j**, we must also know the positions of other carbon atoms bonded to these two atoms. Let $r_{\mathbf{ij}}$ be the bond length and let $\theta_{\mathbf{i},1}$, $\theta_{\mathbf{i},2}$, $\theta_{\mathbf{j},1}$, and $\theta_{\mathbf{j},2}$ be the angles formed by the valence bonds (Fig. 2).

Then, the interaction energy is

$$U_{\mathbf{ij}} = V_R(r_{\mathbf{ij}}) - \frac{1}{2}(B_{\mathbf{ij}} + B_{\mathbf{ji}})V_A(r_{\mathbf{ij}}), \quad (2)$$

where the repulsive part of the potential is

$$V_R(r) = \frac{D}{S-1}\exp[-\sqrt{2S}\beta(r-r_0)],$$

the attractive part is

$$V_A(r) = \frac{DS}{S-1}\exp[-\sqrt{2/S}\beta(r-r_0)],$$

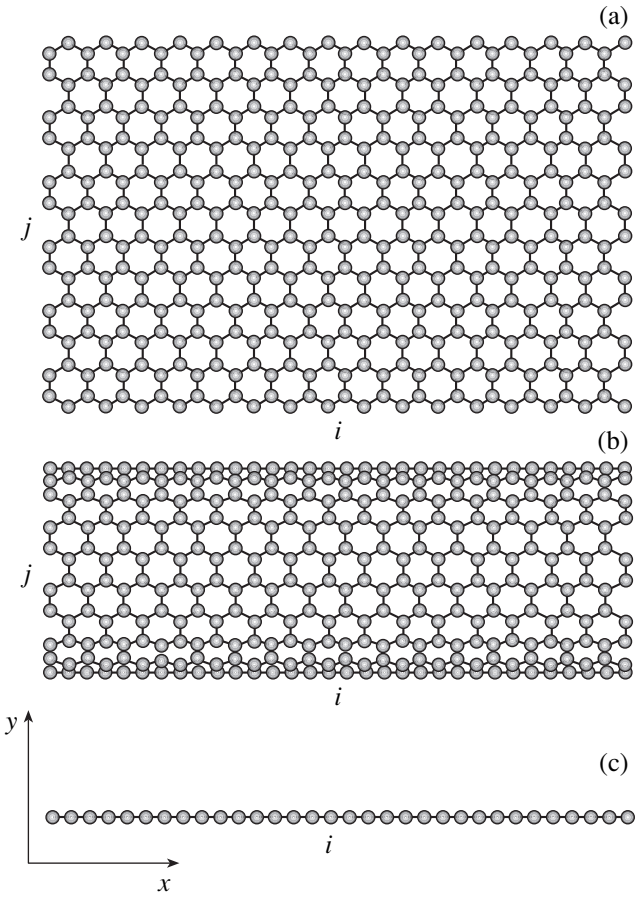

Fig. 1. Structure of (a) a flat graphite layer, (b) carbon nanotube with chirality (10, 10), and (c) reduced one-dimensional chain used to describe the propagation of symmetric plane waves.

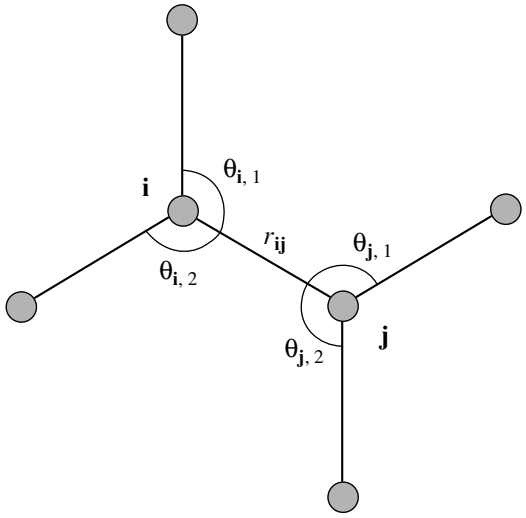

Fig. 2. Carbon structure in the vicinity of the valence bond between carbon atoms **i** and **j** (schematic).

and the parameters are $r_0 = 1.315$ Å, $D = 6.325$ eV, $\beta = 1.5$ Å^{-1}, and $S = 1.29$. We also have

$$B_{\mathbf{ij}} = [1 + G(\theta_{\mathbf{i},1}) + G(\theta_{\mathbf{i},2})]^{-\delta},$$

$$B_{\mathbf{ji}} = [1 + G(\theta_{\mathbf{j},1}) + G(\theta_{\mathbf{j},2})]^{-\delta},$$

where

$$G(\theta) = a_0\left[1 + \frac{c_0^2}{d_0^2} - \frac{c_0^2}{d_0^2 + (1 + \cos\theta)^2}\right],$$

and the parameters are $a_0 = 0.011304$, $c_0 = 19$, $d_0 = 2.5$, and $\delta = 0.80469$.

To find the equilibrium valence bond length in the graphite lattice described by Eq. (1), it is necessary to solve the minimum problem

$$U_{\mathbf{ij}} \longrightarrow \min_{r_{\mathbf{ij}}} \tag{3}$$

with the constraints $\theta_{\mathbf{i},1} = \theta_{\mathbf{i},2} = \theta_{\mathbf{j},1} = \theta_{\mathbf{j},2} = 2\pi/3$. The numerical solution of problem (3) yields $R_0 = 1.419$ Å, which is in good agreement with the experimental valence bond length |CC| = 1.42 Å. The valence bond energy is $E_0 = -U_{\mathbf{ij}}(R_0) = 4.92$ eV.

3. DISPERSION EQUATION FOR PLANE WAVES IN A GRAPHITE LAYER

Let us consider a symmetric plane wave propagating along the x axis in a graphite layer. For such motion, all sites with the same value of index i always have equal displacements, $x_{i,j} \equiv x_i$, $y_{i,j} \equiv y_i$, $z_{i,j} \equiv z_i$. Therefore, instead of the dynamics of a two-dimensional lattice (Fig. 1a), it suffices to consider the dynamics of a reduced one-dimensional chain (Fig. 1c) described by the Hamiltonian

$$H = \sum_i \left\{\frac{1}{2}M(\dot{\mathbf{r}}_i, \dot{\mathbf{r}}_i) + V(\mathbf{r}_{i-1}, \mathbf{r}_i, \mathbf{r}_{i+1}, \mathbf{r}_{i+2})\right\}, \tag{4}$$

where $M = 12m_p$ is the mass at a site of the reduced chain (double the carbon atomic mass) and $m_p = 1.67261 \times 10^{-27}$ kg is the proton mass. The position vector $\mathbf{r}_i = (x_i, y_i, z_i)$ specifies site i, and the intersite interaction potential is

$$V(\mathbf{r}_{i-1}, \mathbf{r}_i, \mathbf{r}_{i+1}, \mathbf{r}_{i+2}) = U_{i,1} + U_{i,2} + U_{i,3}. \tag{5}$$

Here, the potential $U_{i,1}$ is given by Eq. (2) and describes the valence bond between the sites $(i-1, j)$ and (i, j) of the layer j, the potential $U_{i,2}$ describes the bond between the sites (i, j) and $(i, j+1)$, and the potential $U_{i,3}$ describes the bond between the sites (i, j) and $(i+1, j)$.

Using Hamiltonian (4), we obtain the following system of equations of motion:

$$-M\ddot{\mathbf{r}}_i = F_1(\mathbf{r}_i, \mathbf{r}_{i+1}, \mathbf{r}_{i+2}, \mathbf{r}_{i+3}) + F_2(\mathbf{r}_{i-1}, \mathbf{r}_i, \mathbf{r}_{i+1}, \mathbf{r}_{i+2}) + F_3(\mathbf{r}_{i-2}, \mathbf{r}_{i-1}, \mathbf{r}_i, \mathbf{r}_{i+1}) + F_4(\mathbf{r}_{i-3}, \mathbf{r}_{i-2}, \mathbf{r}_{i-1}, \mathbf{r}_i), \quad (6)$$

where

$$F_k = \frac{\partial}{\partial \mathbf{r}_k} U(\mathbf{r}_i, \mathbf{r}_2, \mathbf{r}_3, \mathbf{r}_4), \quad k = 1, 2, 3, 4.$$

For convenience, we pass from the absolute coordinates $\mathbf{r}_i(t)$ to the relative displacements $\mathbf{u}_i(t) = \mathbf{r}_i(t) - \mathbf{r}_i^0$, where $\mathbf{r}_i^0$ is the equilibrium position of site i. We use a linear approximation in analyzing low-amplitude vibrations. Therefore, for small displacements $|\mathbf{u}_i| \ll \rho_0$, we go from the nonlinear system of equations of motion (6) to the linear system

$$-M\ddot{\mathbf{u}}_i = B_1\mathbf{u}_i + B_2(\mathbf{u}_{i-1} + \mathbf{u}_{i+1}) + B_3(\mathbf{u}_{i-2} + \mathbf{u}_{i+2}) + B_4(\mathbf{u}_{i-3} + \mathbf{u}_{i+3}), \quad (7)$$

where $B_1 = F_{11} + F_{22} + F_{33} + F_{44}$, $B_2 = F_{12} + F_{23} + F_{34}$, $B_3 = F_{13} + F_{24}$, and $B_4 = F_{14}$ are matrices, with

$$F_{kl} = \frac{\partial^2 V}{\partial \mathbf{u}_k \partial \mathbf{u}_l}(\mathbf{0}, \mathbf{0}, \mathbf{0}, \mathbf{0}), \quad k, l = 1, 2, 3, 4.$$

We seek the solution of system (7) in the form of a wave,

$$\mathbf{u}_i(t) = \mathbf{A}\exp[i(qi - \omega t)], \quad (8)$$

where ω is the wave frequency, $\mathbf{A}$ is the amplitude vector, and $q \in [0, \pi]$ is the dimensionless wave number. After substituting Eq. (8) into the linear system (7), we obtain the dispersion equation

$$\left|B_1 + 2\cos(q)B_2 + 2\cos(2q)B_3 + 2\cos 3qB_4 - \omega^2 E\right| = 0, \quad (9)$$

where E is the unit matrix.

The dispersion equation (9) is a third-order polynomial with respect to ω^2. The corresponding algebraic curve has three branches: $0 \le \omega_z(q) \le \omega_y(q) \le \omega_x(q)$ (Fig. 3a). The first branch $\omega = \omega_z(q)$ describes the dispersion of transverse plane waves in the graphite layer, with the lattice sites being displaced from the layer plane along the z axis. The second branch $\omega = \omega_y(q)$ corresponds to dispersion of transverse plane waves with the lattice sites remaining in the plane of the two-dimensional lattice and moving along the y axis. The third branch $\omega = \omega_x(q)$ corresponds to dispersion of plane longitudinal waves with the lattice sites remaining in the plane of the two-dimensional lattice and moving along the x axis.

The dispersion curves are shown in Fig. 3a. All three frequencies vanish for the wave number $q = 0$ and increase monotonically with q. Their maximal values are reached at $q = \pi$ and are equal to $\omega_x(\pi) = 121$ cm^{-1}, $\omega_y(\pi) = 97$ cm^{-1}, and $\omega_z(\pi) = 54$ cm^{-1}. The velocities of the corresponding long-wavelength phonons are found to be

$$v_x = a_x \lim_{q \to 0} \omega_x(q)/q = 15\,878.5 \text{ m/s}$$

for plane longitudinal phonons and

$$v_y = a_x \lim_{q \to 0} \omega_y(q)/q = 10\,670.7 \text{ m/s},$$

for plane transverse phonons, and the ratio of the velocities is $v_y/v_x = 0.672$. Nonplanar phonons have a zero velocity,

$$v_z = a_x \lim_{q \to 0} \omega_x(q)/q = 0.$$

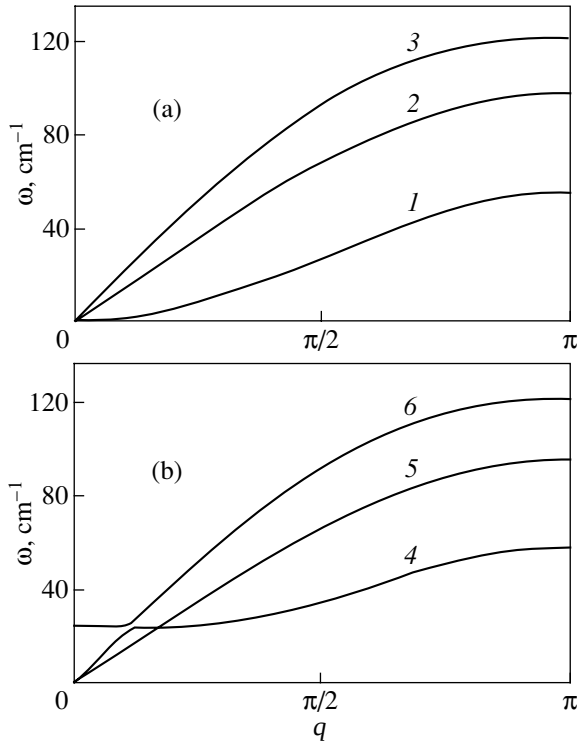

Fig. 3. Dispersion curves for (a) a flat graphite layer and (b) a carbon nanotube with chirality (5, 5): (*1*) $\omega = \omega_z(q)$, (*2*) $\omega = \omega_y(q)$, (*3*) $\omega = \omega_x(q)$, (*4*) $\omega = \omega_o(q)$, (*5*) $\omega = \omega_t(q)$, and (*6*) $\omega = \omega_l(q)$.

4. SOLITARY PLANE WAVES IN A GRAPHITE LAYER

To find a solitary plane wave (soliton), we use the pseudospectral method [6, 7]. A detailed description of the application of this method can be found in [8, 9], where the dynamics of solitary plane waves was numerically modeled for the two-dimensional hexagonal lattice [8] and for the I_h ice crystal [9]. In virtually the same way, this method can be applied for studying sol-

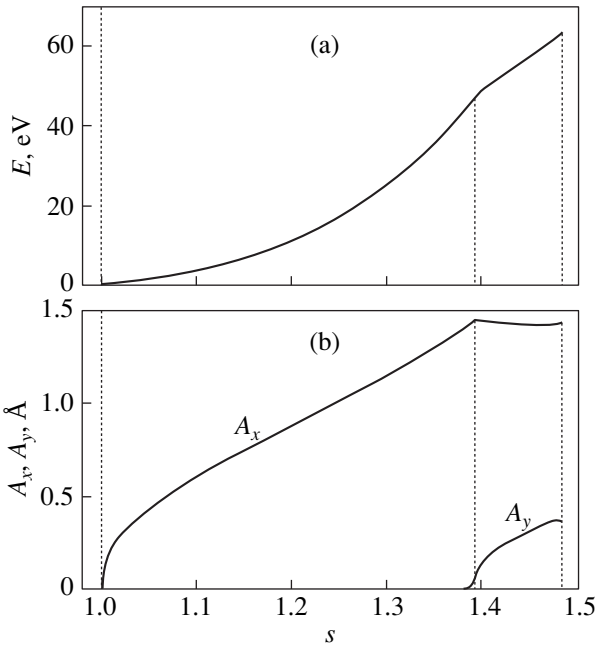

Fig. 4. (a) Energy E and (b) amplitudes A_x and A_y for a plane soliton wave in a graphite layer as functions of dimensionless velocity $s = v/v_x$.

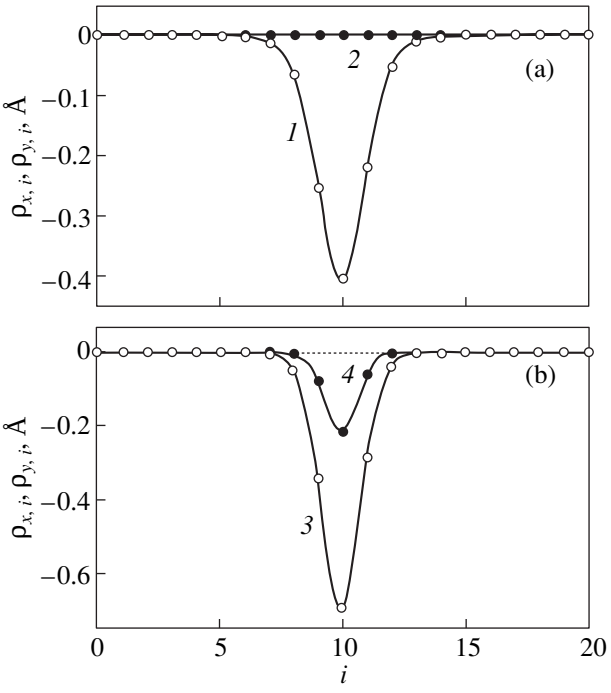

Fig. 5. Profile of a soliton wave in a graphite layer for dimensionless velocity (a) $s = 1.25$ and (b) 1.47. The relative displacements (*1*, *3*) along the x axis $\rho_{x,i} = u_{x,i+1} - u_{x,i}$ and (*2*, *4*) along the y axis $\rho_{y,i} = u_{y,i+1} - u_{y,i}$ are shown.

itary plane waves in graphite layers. Therefore, we omit the description of the method and directly state the results.

The pseudospectral method can give an unambiguous answer to the problem of existence of wide solitons, as well as of narrow solitons, whose width is comparable to the chain period. For relative displacements $\mathbf{u}_i(t)$, the system of equations of motion (6) takes the form

$$\begin{aligned} -M\ddot{\mathbf{u}}_i &= F_1(\mathbf{u}_i, \mathbf{u}_{i+1}, \mathbf{u}_{i+2}, \mathbf{u}_{i+3}) + F_2(\mathbf{u}_{i-1}, \mathbf{u}_i, \mathbf{u}_{i+1}, \mathbf{u}_{i+2}) \\ &+ F_3(\mathbf{u}_{i-2}, \mathbf{u}_{i-1}, \mathbf{u}_i, \mathbf{u}_{i+1}) + F_4(\mathbf{u}_{i-3}, \mathbf{u}_{i-2}, \mathbf{u}_{i-1}, \mathbf{u}_i), \\ i &= 0, \pm 1, \pm 2, \ldots. \end{aligned} \quad (10)$$

We seek the solution of the system of nonlinear equations (10) in the form of a solitary wave of stationary profile $\mathbf{u}_i(t) = \mathbf{u}(\xi) = (u_x(\xi), u_y(\xi), u_z(\xi))$, where the wave variable is $\xi = a_x t - vt$. The vector function $\mathbf{u}(\xi)$ determines the shape of the wave propagating along the x axis with constant velocity v; as $\xi \longrightarrow \pm\infty$, the derivatives of all three components of this function must tend to zero, $\mathbf{u}' \longrightarrow 0$ (solitariness condition).

Numerical analysis of the system of nonlinear equations (10) showed that only solitary waves of longitudinal compression can exist in a flat graphite layer and that their supersonic dimensionless velocities lie in the finite interval $1 < s = v/v_x < s_2 = 1.48$.

The soliton wave $\mathbf{u}$ is characterized by the energy

$$E = \sum_i \left\{ \frac{1}{2} M v^2 (\mathbf{u}'(ia_x), \mathbf{u}'(ia_x)) + V[\mathbf{u}((i-1)a_x), \mathbf{u}(ia_x), \mathbf{u}((i+1)a_x), \mathbf{u}((i+2)a_x)] \right\}$$

and by the vector amplitude $\mathbf{A} = (A_x, A_y, A_z)$, where

$$\begin{aligned} A_x &= \max_\xi [u_x(\xi + 1) - u_x(\xi)], \\ A_y &= \max_\xi [u_y(\xi + 1) - u_y(\xi)], \\ A_z &= \max_\xi [u_z(\xi + 1) - u_z(\xi)]. \end{aligned}$$

For all allowed values of the solitary-wave velocity, the site displacements occur in the lattice plane, i.e., $A_z = 0$. The wave energy E increases monotonically with propagation velocity (Fig. 4a). The amplitude A_x of lattice compression along the x axis also grows monotonically for $1 < s < s_1 = 1.39$ (Fig. 4b). Moreover, the displacement amplitude $A_y = 0$; i.e., the lattice sites are only displaced along the x axis. This component of the displacement has the form of a soliton wave (Fig. 5a). For velocities in the interval $s_1 < s < s_2$, the second component of the site displacement is also nonzero. Moreover, only the amplitude A_y increases monotonically with

velocity and now the displacements look like a solitary wave in two components, x and y (Fig. 5b).

Numerical integration of the system of equations (10) showed that plane soliton waves are stable for all values of the dimensionless velocity in the range $1 < s < s_2$. They propagate along the chain with constant velocity and completely conserve their initial shape. It was shown in [8] that the plane soliton wave in a two-dimensional hexagonal lattice can propagate in any direction (only the maximum velocity depends on the direction of propagation).

5. STRUCTURE OF CARBON NANOTUBES

An ideal single-wall carbon nanotube (Fig. 1b) is a cylindrically convoluted flat graphite layer ribbon. The direction of the convolution determines the chirality of a carbon nanotube, denoted by the set of symbols (m, n). For convenience of calculation, we consider carbon nanotubes with equal chirality symbols (m, m). Note that all results obtained are also valid for any carbon nanotube, regardless of the symbols (m, n).

Carbon nanotubes with chirality (10, 10) are most stable. Such a nanotube is shown in Fig. 1b. The equilibrium positions of carbon atoms in the infinite (m, m) nanotube are

$$x^0_{i,j} = i\Delta_x, \quad y^0_{i,j} = R\cos\varphi_{i,j}, \quad z^0_{i,j} = R\sin\varphi_{i,j}, \quad (11)$$

where the subscripts i ($i = 0, \pm1, \pm2, \ldots$) and j ($j = 1, 2, \ldots, m + m$) define the positions of the sites in the nanotube along the longitudinal and transverse directions, respectively; Δx is the longitudinal step; and R is the nanotube radius. The angles are

$$\varphi_{i,j} = (j-1)\frac{\pi}{m} - \frac{1}{2}[1-(-1)^{i+j}]\Delta\varphi,$$

where $\Delta\varphi$ is the angle of transverse displacement. Stationary values of the parameters Δx_0, R_0, and $\Delta\varphi_0$ correspond to minima of the function

$$E(\Delta x, R, \Delta\varphi) = \frac{1}{3}(E_1 + E_2 + E_3),$$

where E_1 is the energy of the valence bond between sites (1, 1) and (1, 2) given by Eq. (2), E_2 is the bonding energy between sites (1, 1) and (2, 1), and E_3 is the bonding energy between sites (1, 1) and (0, 1). The values of Δx_0, R_0, and $\Delta\varphi_0$ and the energy of the valence bond E_0 are given in Table 1. As $m \longrightarrow \infty$, the radius of the nanotube tends to infinity and the nanotube becomes a two-dimensional lattice (graphite layer).

6. DISPERSION EQUATION FOR LONGITUDINAL WAVES IN A NANOTUBE

Let $x_{i,j}$, $y_{i,j}$, and $z_{i,j}$ be the coordinates of site (i, j) in the nanotube. We pass from Cartesian coordinates to cylindrical coordinates $h_{i,j}$, $r_{i,j}$, and $\phi_{i,j}$:

Table 1. Dependence of the longitudinal step Δx_0, radius R_0, angle of transverse displacement $\Delta\varphi_0$, and energy of one valence bond E_0 on chirality symbols (m, m) of the nanotube

m	Δx_0, Å	R_0, Å	$\Delta\varphi_0$, deg	E_0, eV
5	1.23387	3.42	11.89	4.8655
7	1.23153	4.76	8.53	4.8912
10	1.23036	6.79	5.99	4.9048
15	1.22975	10.18	4.00	4.9120
20	1.22954	13.56	3.00	4.9146
30	1.22939	20.34	2.00	4.9164
50	1.22932	33.89	1.20	4.9173
100	1.22929	67.77	0.60	4.9177
∞	1.22928	∞	0	4.9178

$$\begin{aligned} x_{i,j} &= i\Delta_x + h_{i,j}, \\ y_{i,j} &= (R + r_{i,j})\cos(\varphi_{i,j} + \phi_{i,j}), \\ z_{i,j} &= (R + r_{i,j})\sin(\varphi_{i,j} + \phi_{i,j}) \end{aligned} \quad (12)$$

(in equilibrium, we have $h_{i,j} = 0$, $\phi_{i,j} = 0$, $r_{i,j} = 0$). Next, we assume that the displacements of atoms with the same second indices j are equal, i.e., that

$$h_{i,j} \equiv h_i, \quad r_{i,j} \equiv r_i, \quad \phi_{i,j} \equiv \phi_i.$$

Then, the Hamiltonian assumes the form

$$H = \sum_i \left\{ \frac{1}{2}M[\dot r_i^2 + (R + r_i)^2\dot\phi_i^2 + \dot h_i^2] + V_i \right\}, \quad (13)$$

where

$$\begin{aligned} V_i = V(&r_{i-1}, \phi_{i-1}, h_{i-1}; r_i, \phi_i, h_i; r_{i+1}, \phi_{i+1}, h_{i+1}; \\ &r_{i+2}, \phi_{i+2}, h_{i+2}) = U_{i,1} + U_{i,2} + U_{i,3}. \end{aligned}$$

Here, the potential $U_{i,1}$ is given by Eq. (2) and describes the valence bond between the sites ($i - 1$, j) and (i, j) of the nanotube, the potential $U_{i,2}$ describes the bond between the sites (i, j) and (i, $j + 1$), and the potential $U_{i,3}$ describes the bond between the sites (i, j) and ($i + 1$, j).

It is convenient to analyze low-amplitude vibrations by introducing orthogonal local coordinates:

$$\begin{aligned} u_{i,1} &= (R + r_i)\cos\phi_i - R, \\ u_{i,2} &= (R + r_i)\cos\phi_i, \\ u_{i,3} &= h_i. \end{aligned}$$

In these coordinates, the Hamiltonian of the system has the form

$$H = \sum_i \left\{ \frac{1}{2}M(\dot{\mathbf{u}}_i, \dot{\mathbf{u}}_i) + V(\mathbf{u}_{i-1}, \mathbf{u}_i, \mathbf{u}_{i+1}, \mathbf{u}_{i+2}) \right\}, \quad (14)$$

Table 2. Dependence of the limiting values of the frequencies $\omega_l(0)$, $\omega_0(\pi)$, $\omega_t(0)$, and $\omega_l(\pi)$ (cm^{-1}) and velocities of long-wavelength phonons v_t and v_l (m/s) on chirality symbols (m, m) of the nanotube

m	$\omega_l(0)$	$\omega_0(\pi)$	$\omega_t(\pi)$	$\omega_l(\pi)$	v_t	v_l
5	24.5	56.7	94.7	120.6	10442.3	15766.1
7	17.6	55.5	95.6	120.8	10551.5	15782.8
10	12.4	54.9	96.1	120.9	10611.4	15792.9
15	8.3	54.5	96.4	120.9	10644.2	15798.5
20	6.2	54.3	96.5	121.0	10655.7	15808.2
30	4.1	54.2	96.6	121.0	10664.0	15820.7
50	2.5	54.2	96.6	121.0	10668.3	15848.5
100	1.2	54.2	96.6	121.0	10670.1	15877.1
∞	0	54.2	96.6	121.0	10670.7	15878.5

where $\mathbf{u}_i = (u_{i,1}, u_{i,2}, u_{i,3})$. In the linear approximation, the system of equations (7) corresponds to Hamiltonian (14).

We again search for a solution of the linear system in the form of a linear wave (8). Then, the dispersion equation with respect to the frequency squared ω^2 is a cubic equation. The corresponding algebraic curve has three branches, $0 \le \omega_o(q) \le \omega_t(q) \le \omega_l(q)$ (Fig. 3b). The first branch $\omega = \omega_o(q)$ describes optical (transverse) nanotube vibrations, for which the strains are mostly due to variations in the local radius r_i. The second branch $\omega = \omega_t(q)$ describes torsional nanotube vibrations, for which the strains are due to variations in the local angles ϕ_i and the third branch $\omega = \omega_l(q)$ corresponds to longitudinal vibrations, for which the strains are due to variations in the local longitudinal displacements h_i. Note that, for small values of the dimensionless wave number q, the frequencies $\omega_o(q)$ and $\omega_l(q)$ correspond to longitudinal and transverse vibrations of the nanotube, respectively.

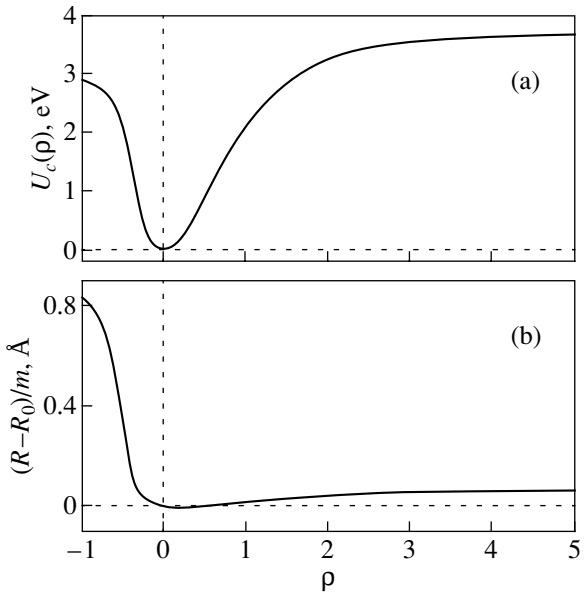

Fig. 6. Variations in (a) the strain energy U_c and (b) radius $R(m, m)$ of the nanotube (m = 5, 10, 20) as a function of the compression ρ of the nanotube step.

The dispersion curves are shown in Fig. 3b. For q = 0, the frequencies $\omega_o(q)$ and $\omega_t(q)$ vanish and $\omega_l(q) > 0$. The frequency $\omega_l(q) \longrightarrow 0$ as the nanotube radius increases. The frequencies increase monotonically with q and reach their maximum values for $q = \pi$. We define the velocity of long-wavelength torsional phonons as

$$v_t = \Delta x \lim_{q \to 0} \omega_t(q)/q$$

and the velocity of longitudinal phonons as

$$v_l = \Delta x \lim_{q \to 0} \omega_o(q)/q.$$

The dependences of the limiting values of frequencies and velocities of long-wavelength phonons v_t and v_l on chirality symbols (m, m) for carbon nanotubes are given in Table 2.

With increasing index m (i.e., with increasing radius R), a carbon nanotube becomes a flat layer and the dispersion curves $\omega_o(q)$, $\omega_t(q)$, and $\omega_l(q)$ approach the corresponding curves $\omega_z(q)$, $\omega_y(q)$, and $\omega_x(q)$ for a flat layer. To put it differently, we have $\omega_o(q) \longrightarrow \omega_z(q)$, $\omega_t(q) \longrightarrow \omega_y(q)$, $\omega_l(q) \longrightarrow \omega_x(q)$, $v_t \longrightarrow v_y$, and $v_l \longrightarrow v_x$ as $m \longrightarrow \infty$.

7. SOLITON-LIKE NANOTUBE EXCITATIONS

To analyze the nonlinear nanotube dynamics, it is useful to consider its effective potential of longitudinal compression,

$$U_c(\rho) = \min_{R, \Delta\varphi}[E(\Delta x_0 + \rho, R, \Delta\varphi) - E(\Delta x_0, R_0, \Delta\varphi_0)],$$

which describes the variation of the valence bond energy of the nanotube when each longitudinal bond is stretched by ρ. When the nanotube is stretched, both its energy and its radius are changed. The effective poten-

tial $U_c(\rho)$ and the nanotube radius R are shown in Fig. 6 as functions of longitudinal compression ρ. It is seen in Fig. 6 that in the ground state we have $\rho = 0$, the radius of the spiral is $R = R_0$, and the strain energy is $U_c(0) = 0$. Both compression and stretching of the nanotube increase its radius. The shape of the $U_c(\rho)$ curve indicates that the nanotube has a pronounced negative anharmonicity; namely, the strain energy increases much faster for compression of the nanotube than for stretching.

The negative anharmonicity indicates that supersonic solitons of longitudinal compression can exist in the nanotube. This was noted for the first time in [4], where it was shown that, in the continuum approximation (without taking into account variations in the nanotube radius), the nanotube nonlinear dynamics can be described by a Korteweg–de Vries equation having soliton solutions.

Let us also consider the one-dimensional effective torsional potential of the nanotube,

$$U_t(\phi) = \min_{\Delta x, R}[E(\Delta x, R, \Delta\varphi_0 + \varphi) - E(\Delta x_0, R_0, \Delta\varphi_0)],$$

which describes the nanotube energy variation when each link of the nanotube is twisted by angle ϕ. The torsional potential is shown in Fig. 7, from which we can see that the nanotube has negative anharmonicity of the fourth order with respect to the angular variable. This anharmonicity does not ensure the existence of acoustic solitons (soliton solutions can only exist for systems with positive quartic anharmonicity). Therefore, one should not expect the existence of torsional solitary waves in nanotubes.

Using Hamiltonian (13), we obtain the following equations of motion:

$$\begin{aligned} M\ddot{r}_i - M(R + r_i)\dot{\phi}_i^2 + \frac{\partial}{\partial r_i}P &= 0, \\ M(R + r_i)^2\ddot{\phi}_i + 2M(R + r_i)\dot{\phi}_i\dot{r}_i + \frac{\partial}{\partial \phi_i}P &= 0, \\ M\ddot{h}_i + \frac{\partial}{\partial h_i}P &= 0, \\ i &= 0, \pm1, \pm2, \ldots, \end{aligned} \tag{15}$$

where the potential energy is

$$P = \sum_i V(r_{i-1}, \phi_{i-1}, h_{i-1}; r_i, \phi_i, h_i; r_{1+1}, \phi_{i+1}, h_{i+1}; r_{i+2}, \phi_{i+2}, h_{i+2}).$$

Numerical analysis of the discrete system (15) showed that, in contrast to the case of a graphite layer, the equations of motion for a nanotube have no exact solutions describing the propagation of solitary waves (solitons) of longitudinal compression along the chain.

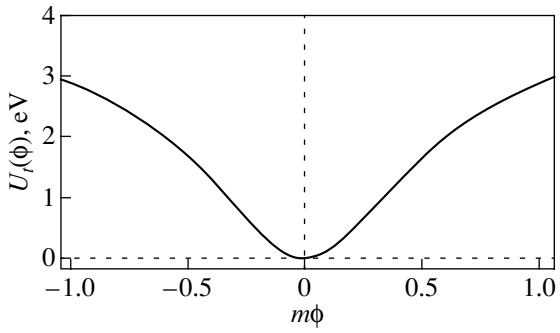

Fig. 7. Variation in the strain energy $U_t(m, m)$ of the nanotube (m = 5, 10, 20) as a function of torsion angle ϕ.

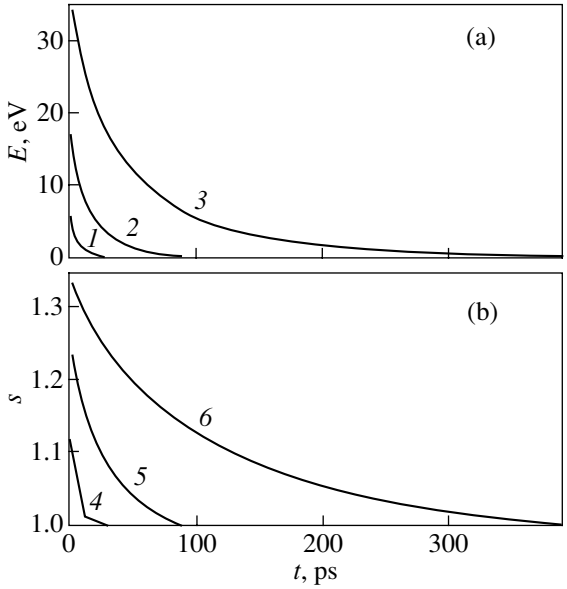

Fig. 8. Variations in (a) the energy E and (b) the dimensionless velocity $s = v/v_l$ of a soliton-like excitation propagating along the (m, m) nanotube for m = (*1*, *4*) 10, (*2*, *5*) 20, and (*3*, *6*) 40.

The fundamental difference between a flat layer and a nanotube is that compression of a nanotube modifies the surface curvature, whereas a graphite layer always remains flat. If we forbid transverse displacements in the equations of motion (15) for a nanotube, i.e., if we set all $r_i \equiv 0$, then exact soliton solutions appear and describe longitudinal compression solitons in a finite supersonic velocity range, just as for a graphite layer. However, if the possibility of transverse displacement of the sites appears, then these solutions are no longer exact. Therefore, one can only consider soliton-like excitations. They move with supersonic velocities $v > v_l$, but while moving they always emit longitudinal acoustic phonons. The emission intensity depends on the nanotube radius; namely, the smaller the radius, the greater the emission rate. Accordingly, the energy and velocity of a moving excitation decrease in time

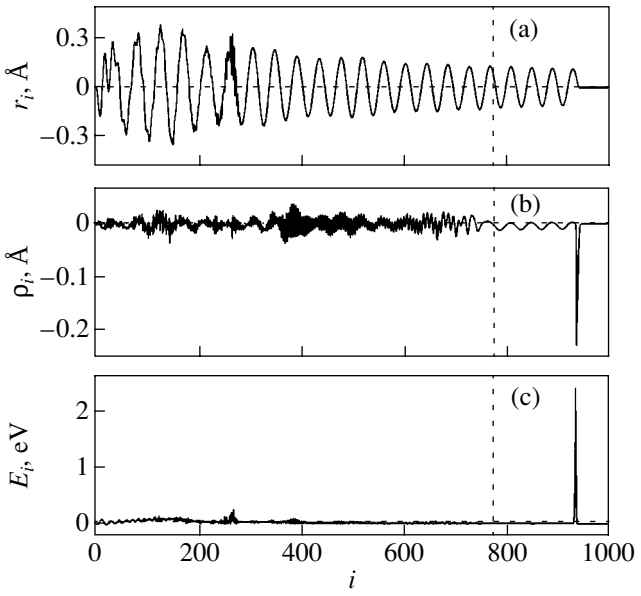

Fig. 9. Distribution of (a) transverse displacements r_i, (b) longitudinal compression $\rho_i = h_{i+1} - h_i$, and (c) energy E_i for the (10, 10) nanotube at time t = 6 ps. The initial strains are $A_r = 0$, $A_h = 1$ Å, and $A_\phi = 0$. Vertical dotted lines are the boundaries of the region in which long-wavelength longitudinal phonons propagate during the numerical integration.

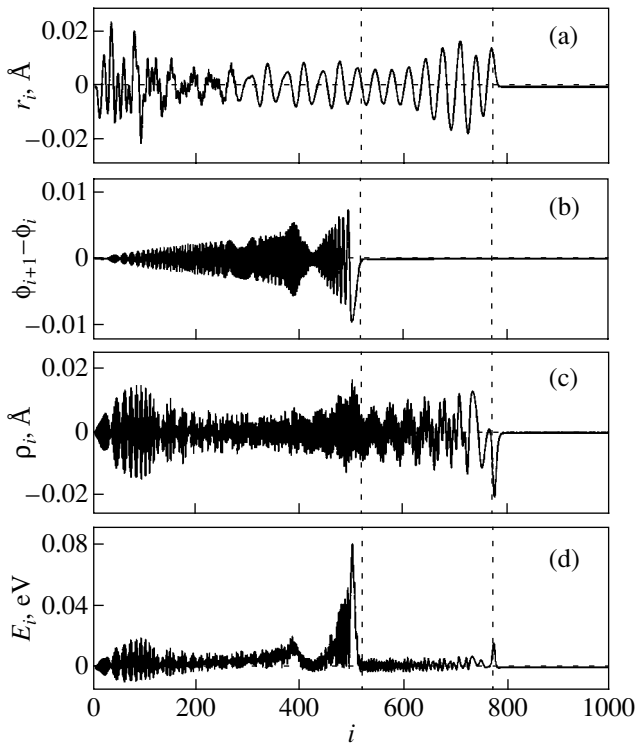

Fig. 10. Formation of two oscillating wave packets caused by initial torsion of a finite fragment of the (10, 10) nanotube (the amplitudes are $A_r = 0$, $A_h = 0$, $A_\phi = \Delta\varphi/3$). The distributions of (a) transverse displacements r_i, (b) relative rotations $\phi_{i+1} - \phi_i$, (c) longitudinal compression $\rho_i = h_{i+1} - h_i$, and (d) energy E_i along the chain at time t = 6 ps are shown. Vertical dotted lines are the boundaries of the region in which long-wavelength torsional phonons and longitudinal strain phonons propagate during the numerical integration.

(Fig. 8). Therefore, soliton excitations in carbon nanotubes have a finite lifetime, which monotonically increases with the nanotube radius. The equations of motion (15) have no solutions describing the propagation of solitary longitudinal torsional waves along the nanotube.

Thus, for carbon nanotubes there can be only soliton-like solutions describing the propagation of localized regions of longitudinal compression, which is always accompanied by phonon emission. To verify this assumption, we numerically modeled the excitation dynamics in a finite fragment of a nanotube with fixed ends.

We considered the equations of motion (15) with i = 1, 2, …, 1000 and used the condition of fixed ends by setting $\dot{r}_i$, $\dot{h}_i$, and $\dot{\phi}_i$ equal to zero for i = 1 and 1000. Then, we integrated the system of equations with the initial conditions corresponding to the ground state ($r_i = 0$, $\dot{r}_i = 0$, $h_i = 0$, $\dot{h}_i = 0$, $\phi_i = 0$, $\dot{\phi}_i = 0$ for i = 2, 3, …, 1000) with the first link displaced, namely, with $r_1(0) = A_r$, $h_1(0) = A_x$, and $\phi_1(0) = A_\phi$. The results of the numerical integration are shown in Figs. 9 and 10.

The system of equations (15) was numerically integrated using the standard fourth-order Runge–Kutta method with a constant integration step. The integration precision was estimated using the conservation of the total-energy integral (13). For the integration step $\Delta t = 0.5 \times 10^{-15}$ s, the energy of the system was conserved to within six significant digits for the entire time of numerical integration.

To be specific, let us consider a carbon nanotube with symbols (10, 10). For longitudinal compression of the first link by 1 Å ($A_r = 0$, $A_x = 1$ Å, $A_\phi = 0$), a localized region of longitudinal compression appears in the chain and propagates with a supersonic velocity $v > v_l$ (Fig. 9). The propagation of this soliton-like excitation is accompanied by the emission of longitudinal phonons. In addition, an oscillating wave packet is formed that propagates with a subsonic velocity $v < v_l$. The main part of the initial strain energy is concentrated in the soliton-like excitation, but then it is completely spent for phonon emission in further motion.

In the initially twisted nanotube ($A_r = 0$, $A_x = 0$, $A_\phi = \Delta\varphi/3$), only two oscillating wave packets appear (Fig. 10). The first one is formed by torsional phonons and moves with velocity $v = v_t$; the second one is formed by longitudinal phonons and moves with a higher velocity, $v = v_l$.

Thus, the numerical modeling of the dynamics of carbon molecular lattices has confirmed the conclusion that acoustic solitons do not exist in carbon nanotubes. There are only soliton-like excitations, whose propagation is always accompanied by the emission of longitudinal phonons. The emission intensity decreases with increasing carbon nanotube radius but is never equal to zero.

ACKNOWLEDGMENTS

The study was supported by the Russian Foundation for Basic Research, project no. 98-03-333-66a.

REFERENCES

1. L. V. Radushkevich and V. M. Luk'yanovich, Zh. Fiz. Khim. **26** (1), 88 (1952).
2. S. Iijima, Nature **354**, 56 (1991).
3. A. V. Eletskiĭ, Usp. Fiz. Nauk **172** (4), 401 (2002) [Phys. Usp. **45**, 369 (2002)].
4. T. Yu. Astakhova, O. D. Gurin, M. Menon, and G. A. Vinogradov, Phys. Rev. B **64** (4), 035418 (2001).
5. D. W. Brenner, Phys. Rev. B **42** (15), 9458 (1990).
6. J. C. Eilbeck and R. Flesch, Phys. Lett. A **149**, 200 (1990).
7. D. K. Campbell, M. Peyrard, and P. Sodano, Physica D (Amsterdam) **19**, 165 (1986).
8. Y. Zolotaryuk, A. V. Savin, and P. L. Christiansen, Phys. Rev. B **57** (22), 14213 (1998).
9. O. I. Savina, Mat. Model. **11** (12), 67 (1999).

Translated by I. Zvyagin

Physics of the Solid State, Vol. 46, No. 2, 2004, pp. 392–394. Translated from Fizika Tverdogo Tela, Vol. 46, No. 2, 2004, pp. 380–382.
Original Russian Text Copyright © 2004 by V. Pokropivny, A Pokropivny.

FULLERENES AND ATOMIC CLUSTERS

Structure of "Cubic Graphite": Simple Cubic Fullerite C_{24}

V. V. Pokropivny and A. V. Pokropivny

Institute for Problems of Materials Science, National Academy of Sciences of Ukraine, Kiev, 03142 Ukraine

e-mail: pokr@ipms.kiev.ua

Received February 11, 2003; in final form, July 8, 2003

Abstract—The structure of an intermediate carbon phase, the so-called "cubic graphite," is determined. Close agreement between the calculated and experimental lattice constants (A = 0.5545 nm), densities (ρ = 2.80 g/cm^3), and all lines of the Debye powder pattern indicates that cubic graphite has a simple cubic lattice formed by C_{24} fullerene molecules copolymerized by the square faces. © *2004 MAIK "Nauka/Interperiodica".*

Intermediate carbon phases and, in particular, the so-called "cubic graphite" have been revealed experimentally by many researchers [1–5]. However, the structures of these phases have not been determined yet. The possible existence of a C_{24} molecule and other three-dimensional carbon networks (in essence, fullerenes) was predicted by Balaban *et al.* [6]. In their comprehensive review of the prefullerene era, Stankevich *et al.* [7] stated that, apart from diamond and graphite, whose structures are well understood, there exist carbon modifications (up to eight carbine forms, metallic carbon, carbon C_8 (and C_{24}), etc.) that are described in the literature, but their structures remain to be elucidated [7]. Similar phases, which are intermediate in density between diamond-like sphalerite and graphite-like BN, are also observed in boron nitride [8–10], and their structure is a subject of considerable discussion [2–4, 11].

Cubic graphite was first synthesized by Aust and Drickamer [1] from natural graphite at temperatures T = 77 and 296 K and pressures P > 150 kbar; this could be judged from a sharp increase in the electrical conductivity. It was established that cubic graphite belongs to the cubic system with lattice constant A = 0.5545 nm, density ρ = 2.80 g/cm^3, and number of atoms per unit cell Z = 24. Fedoseev *et al.* [3] synthesized cubic graphite during the preparation of ultrafine diamond powders from methane and other hydrocarbons. Graphite polycrystals of octahedral and cubic form have been revealed in the Earth's crust [4] and meteorites.

Smolyar *et al.* [5] synthesized a carbon phase on a specially designed high-pressure apparatus at temperatures T > 1000°C and pressures P < 1 GPa. This phase crystallizes in the cubic system with mean parameters A = 0.56 nm and ρ = 2.78 g/cm^3. The crystals are opaque and have an octahedral or cubic form. The intermediate hardness is equal to 1–5 GPa. The table presents the interplanar distances, and Fig. 1 shows the x-ray diffraction pattern of sample **2** [5]. For comparison, we also presented available experimental data [12] and the angles of reflection for the x-ray diffraction pattern. The angles of reflection were calculated according to the Wulf–Bragg formula $n\lambda = 2d_{hkl}\sin\theta$, where n = 1; λ = 0.15405 nm (Cu$K_{\alpha 1}$ radiation); $d_{hkl} = A/(h^2 + k^2 + l^2)^{1/2}$; and h, k, and l are the Miller indices. The results of the comparison can be summarized as follows: (i) the data obtained by Aust and Drickamer [1] and Smolyar *et al.* [5] are in good agreement and correspond to the cubic graphite phase and (ii) the x-ray diffraction patterns of the studied samples are characterized by theo-

Interplanar distances d_{hkl} (nm) in the structure of cubic graphite and the calculated $2\theta_{hkl}$ angles in the x-ray diffraction pattern of the simple cubic fullerite C_{24}

hkl	d_{hkl} [1, 10]	d_{hkl} [3]	d_{hkl} [5], sample **1**	d_{hkl} [5], sample **2**	d_{hkl} [5], sample **3**	d_{hkl}, calculation	$2\theta_{hkl}$, calculation
111	0.3208	0.3192	0.322	0.318	0.316	0.32014	27.84
200	0.2770	0.2730	0.282	0.277	0.287	0.27725	32.26
210	0.2467		0.233	0.252	0.249	0.24798	36.19
220	0.1961	0.1985		0.209	0.1965	0.19605	46.27
221; 300	0.1844	0.1834	0.181		0.182	0.18483	49.26
222	0.1600		0.1653	0.1607	0.1655	0.16007	57.73
321	0.1485	0.1450		0.1451		0.14820	62.63

1063-7834/04/4602-0392$26.00 © 2004 MAIK "Nauka/Interperiodica"

retical angles of reflection of cubic graphite and, moreover, exhibit lines of different intensities due to other intermediate carbon phases.

Since the determination of the structure of cubic graphite involves considerable experimental difficulties that have not yet been surmounted, we consider the theory and its implications. It should be noted that it is hopeless to construct stable molecular crystals from covalently bonded icosahedral fullerenes, for example, C_{20} or C_{60}, except quasicrystals of fullerenes.

All possible cubic unit cells containing 24 carbon atoms can be constructed in the following manner: (1) the diamond lattice from eight C_3 clusters, (2) the lonsdaleite lattice from four C_6 clusters, (3) the face-centered cubic lattice from four C_6 clusters, (4) the body-centered cubic lattice from two C_{12} clusters, and (5) the simple cubic lattice from a single C_{24} molecule. The quantum-chemical calculations carried out in this work and by other authors [13–15] demonstrate that configurations of C_3 and C_6 clusters in the form of either linear chains or rings are energetically favorable and stable. These configurations can only be used to construct either molecular crystals bound through weak van der Waals forces or polymers. Since their density is lower than the density of graphite, lattices (1)–(3) should be rejected as candidates for the structure of cubic graphite. The other C_N clusters, beginning from a C_8 prismane (a polyhedron with eight vertices [14]), can form bulk cages, but they become stable only beginning from a dodecahedron with $N = 20$ [15]. Therefore, C_{12} clusters, in particular, icosahedra, should also be rejected because these clusters are metastable and, moreover, have none of the faces necessary for constructing a lattice.

Thus, the C_{24} fullerene molecule is a unique candidate for the unit cell of cubic graphite (Fig. 2). The inclusion of the relaxation, for example, in the MNDO calculations performed in our previous work [16] or in the MINDO calculations carried out by Stankevich *et al.* [17], leads to a slight distortion of the molecular configuration due to the equilibration of the bonds, but the molecules remain stable. Moreover, C_{24} is the smallest sized molecule satisfying the law of isolated squares, which, by analogy with the law of isolated pentagons for the C_{60} buckminsterfullerene, serves as a criterion of stability due to the conservation of valence 4 for all atoms of the molecule. The molecule has T_h symmetry and is characterized by the following parameters: the atomization energy per atomic pair E_a = 11.875 kcal/mol; the lengths of the bonds shared by two hexagons and a hexagon–square $a_{6,6}$ = 0.138 nm and $a_{6,4}$ = 0.1503 nm, respectively [17]; the mean radius $R = (5/2)^{1/2}a_{C-C}$ (where a_{C-C} is the length of the C–C bond); and the radii from the center of the molecule to the centers of the square face and the hexagonal face $R_4 = (2)^{1/2}a_{C-C}$ and $R_6 = (3/2)^{1/2}a_{C-C}$, respectively.

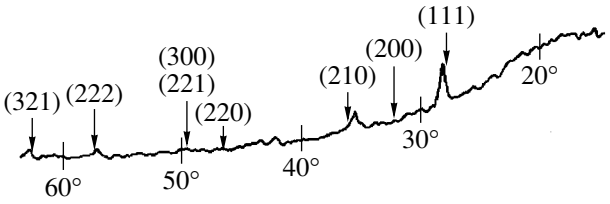

Fig. 1. X-ray diffraction pattern of the cubic graphite sample (Carbex Ltd., Kiev) obtained by the gas method at $T <$ 1000°C and $P < 1$ GPa [5].

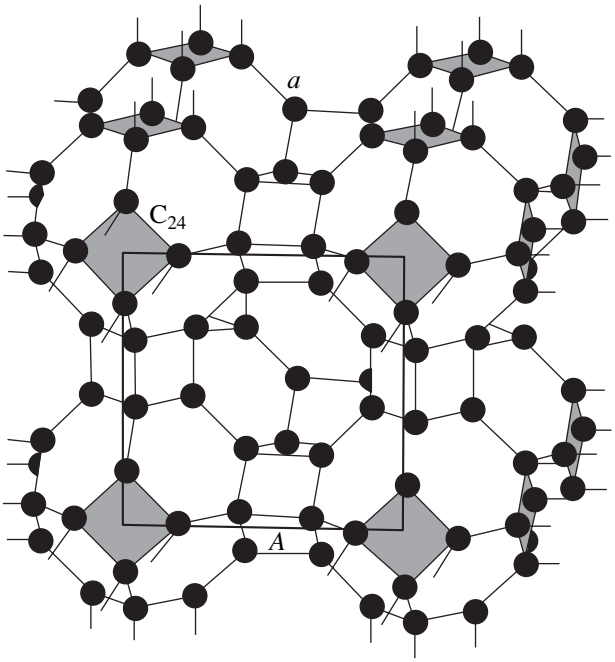

Fig. 2. Unit cell of the simple cubic lattice formed by a C_{24} fullerene molecule [18, 19]. Designations: *A* is the lattice constant, and *a* is the bond length in the molecule.

The possibility of forming cubic lattices (including a simple cubic lattice) from $B_{12}N_{12}$ and C_{24} molecules was first predicted in our recent works [18, 19]. The C_{24} fullerene is the smallest sized polyhedron that has a sufficient number of faces (six squares and eight hexagons) to provide the formation of cubic lattices, including a simple cubic lattice in which C_{24} molecules are bound by the covalent bonds arising between adjacent square faces upon copolymerization (Fig. 2). It is reasonable to refer to this lattice as a simple cubic fullerite C_{24}. In the case when the adjacent hexagons are brought closer together under pressure, double sp^2 bonds break to form four sp^3 hybridized bonds between adjacent molecules. Consequently, all carbon atoms in the simple cubic fullerite C_{24} are linked by sp^3 hybridized bonds, as is the case with diamond.

Let us calculate the parameters of the simple cubic fullerite C_{24}. Under the assumption that the intermediate bond length for the intermediate phase is the mean of the bond lengths $a_{6,6}$ and $a_{6,4}$ in the C_{24} molecule ($a_{C–C}$ = 0.14484 nm), we obtain the unit cell parameter of the simple cubic lattice $A = 2R_4 + a_{C–C}$ = 0.5545 nm and the density $\rho = Zm_C/A^3$ = 2.808 g/cm^3, where m_C = 19.94522×10^{-24} g is the mass of the carbon atom. The calculated and experimental values of A and ρ are in almost complete agreement. This cannot be an accidental coincidence. On the contrary, the coincidence of the lattice constants, the densities, and the lines of the x-ray diffraction pattern is convincing proof that the structure of cubic graphite is the simple cubic fullerite C_{24}. The spatial angles between the bonds (~90° and ~120°) differ from the equilibrium value (109.47°). This raises a problem regarding stability. According to preliminary first principles calculations, performed by the full-potential linearized augmented-plane-wave (FLAPW) method without optimization of the structure, the simple cubic fullerite C_{24} is a stable carbon phase, because the dependence of the total energy on the bond length $a_{C–C}$ is similar to that of diamond and has a minimum. The discrepancy between the theoretical and experimental bond lengths is insignificant and is associated with errors.

Earlier [18, 19], we also predicted the possible formation of "hyperdiamond" with a diamond- or lonsdaleite-type lattice, whose sites are occupied by C_{24} molecules, and body-centered cubic fullerites (bccf), for example, bccf–Me_2–$B_{12}N_{12}$ and bccf–Me_2–C_{24} (doped by a light donor Me = Li, Be, etc.), with a density (ρ = 4.11–5.28 g/cm^3) higher than that of diamond. Moreover, we predicted the possible formation of other cubic forms of boron nitride and carbon from $B_{24}N_{24}$ and C_{48} fullerene molecules capable of forming simple cubic, body-centered cubic, and face-centered cubic lattices, which have not yet been discovered.

Piskoti *et al.* [20] synthesized hexagonal close-packed crystals composed of C_{36} molecules with an intermolecular distance of 0.668 nm. However, they did not determine the structure of the crystals synthesized, because, in the authors' opinion [20], the thin platelike samples had a large form factor.

Undoubtedly, the results obtained in the present work can give a clue to the definite proof of the structure of cubic graphite and to the identification of other phases of carbon and boron nitride.

Similar to zeolites, the structure of the simple cubic fullerite C_{24} involves a two-dimensional lattice of cylindrical nanopores with diameter D = 0.41 nm, which can be used as molecular sieves. As in the case of mesoporous silicon, the size effect observed at a wavelength $\lambda \sim R$ can give rise to unusual optical properties, but in the x-ray range. Probably, the manifestation of this masking quantum effect makes the determination of the structure of fullerene-like crystals difficult. Without doubt, the aforementioned fullerene-like phases of carbon and boron nitride will exhibit new interesting properties and find various applications.

REFERENCES

1. R. B. Aust and H. C. Drickamer, Science **140**, 817 (1963).
2. F. P. Bundy and J. S. Kasper, J. Chem. Phys. **46**, 3437 (1967).
3. D. V. Fedoseev, V. V. Deryagin, V. P. Varnin, *et al.*, Dokl. Akad. Nauk SSSR **228**, 371 (1976).
4. V. V. Slodkevich, Dokl. Akad. Nauk SSSR **253**, 697 (1980).
5. A. S. Smolyar, I. Yu. Sozin, V. A. Barkholenko, *et al.*, Sverkhtverd. Mater., No. 2, 79 (2002).
6. A. T. Balaban, C. C. Rentia, and E. Ciupitu, Rev. Roum. Chim. **13** (2), 231 (1968).
7. I. V. Stankevich, M. V. Nikerov, and D. A. Bochvar, Usp. Khim. **53**, 1101 (1984).
8. A. V. Kurdyumov and A. N. Pilyankevich, in *Boron: Production, Structure, and Properties* (Nauka, Moscow, 1984), p. 181.
9. T. Akashi, H. R. Pack, and A. B. Sawaoka, J. Mater. Sci. **21**, 4060 (1986).
10. S. S. Batsanov, L. J. Kopaneva, and E. V. Lazareva, Propellants, Explos., Pyrotech. **18**, 352 (1993).
11. A. S. Smolyar, Sverkhtverd. Mater., No. 5, 13 (1996).
12. *Diamond: A Handbook*, Ed. by N. V. Novikov (Naukova Dumka, Kiev, 1981).
13. K. Raghavachari and J. S. Binkley, J. Chem. Phys. **87**, 2191 (1987).
14. L. A. Openov and V. E. Elesin, Pis'ma Zh. Éksp. Teor. Fiz. **68**, 695 (1998) [JETP Lett. **68**, 726 (1998)].
15. R. O. Jones and G. Seifert, Phys. Rev. Lett. **79**, 443 (1997).
16. D. M. Sheichenko, A. V. Pokropivny, and V. V. Pokropivny, Semicond. Phys. Quantum Electron. Optoelectron. **3** (4), 545 (2000).
17. I. V. Stankevich, A. L. Chistyakov, E. G. Gal'pern, and N. P. Gambaryan, Zh. Strukt. Khim. **36**, 976 (1995).
18. V. V. Pokropivny, A. V. Pokropivny, V. V. Skorokhod, and A. V. Kurdyumov, Dopov. Nats. Akad. Nauk Ukr. **4**, 112 (1999).
19. V. V. Pokropivny, V. V. Skorokhod, G. S. Oleinik, *et al.*, J. Solid State Chem. **154**, 214 (2000).
20. C. Piskoti, J. Yargert, and A. Zettl, Nature **393**, 773 (1998).

Translated by O. Moskalev